Production of High-Mass Pairs of Direct Photons and Neutral Mesons in a Tevatron Fixed-Target Experiment

by

Michael Begel

Submitted in Partial Fulfillment

of the

Requirements for the Degree

Doctor of Philosophy

Supervised by

Professor Paul Slattery

Department of Physics and Astronomy
The College
Arts and Science

University of Rochester
Rochester, New York

1999

Curriculum Vitae

Michael Begel was born in New York City in 1969. He spent his undergraduate years at Reed College in Portland, Oregon where he received a Bachelor of Arts degree. During that time he earned a Senior Reactor Operator's License for the college's research reactor and wrote a thesis on single photon interference. He entered the graduate program in physics at the University of Rochester in 1991; earning a Master of Arts degree in 1993. During this time he was awarded a Department of Education Fellowship. He began his association with the E706 collaboration at FNAL as a summer student during the 1991 Fixed Target run and never left.

Acknowledgments

E706 is an experiment with a long and illustrious history. It took many people to design, build, and operate the spectrometer, to write the code, and to analyze the data and I wish to thank everyone who contributed to this experiment. E706 was first proposed while I was in sixth grade and started taking beam while I was still in high school, but since joining in 1991, I've had the opportunity to take part in, and contribute to, this extraordinary experiment. There have been order 40 theses based on the Meson West Spectrometer, both from E706 and from our colleagues on E672. This represents one of the last theses that will be written on our data and is the culmination of many years of hard work.

I must first thank my professors at the University of Rochester: my advisor, Paul Slattery, for his invaluable support and guidance over these many years, Tom Ferbel for being a proper nudnik, and the late Fred Lobkowicz, who taught me to appreciate many of the subtleties inherent in the electromagnetic calorimeter. I would also like to thank Michigan State University professors Carl Bromberg, for forcing me to repeatedly reexamine and strengthen my conclusions in the face of his vigorous arguments, and Joey Huston, for his work in the QCD trenches.

I would especially like to thank our senior researchers, Marek Zieliński, without whom this thesis analysis could not have been finished, and George Ginther, without whom most of the E706 thesis analyses couldn't have been finished.

There are too many people who have impacted my life here to mention in the brief space allotted (this thesis is long enough!). Still, I've had the pleasure of working with some very talented individuals. David Striley, who could type faster (and harder) than almost anyone I've ever met and with whom I worked, for many a long night, getting the Čerenkov detector operational (we never achieved a $\bar{p}$

tag, but there are some rather nice π^+ tagged data in Chapters 8 and 12). Lee Sorrell, our trigger guru and resident Klingon, who kept trying to show me his martial arts moves. And, of course, Lenny Apanasevich, who has the dubious honor of having the other last E706 thesis, and who has had to put up with a lot while I finished this document.

I would also like to thank all the theorists I've interacted with over the years, particularly Jeff Owens and Csaba Balázs, for their many helpful discussions and for providing their QCD calculations.

I would also like to thank my physics professors at Reed College: David Griffiths, Mary James, Johnny Powell, Bob Reynolds, and Nick Wheeler. My senior thesis was on single photons [1] so, of course, my Ph.D. thesis is on double photons.

I need to thank the late Betty Cook, Barbara Warren, Connie Jones, and Judy Mack at the University of Rochester, who've taken care of all the pesky details while I'm here at Fermilab.

I would particularly like to thank my parents, who've always encouraged me, even when they didn't understand what I was doing, and my Uncle Shep, who always made sure to feed me steak vegetables whenever I needed them. I would also like to thank my friends, Paul Bloom and Tamara Neuberger, for occasionally forcing me to stop working and spend time away from lab.

I thank the U.S. Department of Energy, the National Science Foundation including its Office of International Programs, and the Universities Grants Commission of India, for their support of this research.

Finally, I would like to thank Gen. Thompson Mead for all of his sage advice.

Preface

The Creation of Elohim

In the Beginning

(Genesis 1:1)

When the King conceived ordaining
He engraved engravings in the luster on high.
A blinding spark flashed
within the Concealed of the Concealed
from the mystery of the Infinite,
a cluster of vapor in formlessness,
set in a ring,
not white, not black, not red, not green,
no color at all.
When a band spanned, it yielded radiant colors.
Deep within the spark gushed a flow
imbuing the colors below,
concealed within the concealed of the mystery of the Infinite.
The flow broke through and did not break through its aura.
It was not known at all
until, under the impact of breaking through,
one high and hidden point shone.
Beyond that point, nothing is known.
So it is called Beginning,
the first command of all.

From the Zohar as translated by Daniel Matt.

Abstract

The production of high-mass pairs of direct photons, π^0's, and η's has been measured by Fermilab experiment E706. The experimental apparatus included a large, finely segmented lead–liquid argon electromagnetic calorimeter and a charged particle spectrometer consisting of silicon microstrip detectors in the target region and multiwire proportional chambers and straw tube drift chambers downstream of an analysis magnet. The experiment triggered on localized high-p_T depositions in the electromagnetic calorimeter; the high-mass pair data required two depositions on opposite sides of the calorimeter. Correlations between high-p_T particles are used to extract information about the transverse momentum of partons (k_T). Comparisons are made between the diphoton data and the results of next-to-leading order perturbative Quantum Chromodynamic (NLO pQCD) calculations. The shapes of the NLO pQCD results are inconsistent with the data distributions. A resummed NLO pQCD calculation, which incorporates the effects of multiple soft-gluon emission, provides reasonable matches to the shapes of the data distributions. Similar distributions of $\pi^0\pi^0$ and $\gamma\pi^0$ pairs are compared with leading order pQCD calculations which approximates initial-state k_T effects by a Gaussian smearing technique. These calculations, using $\langle k_T \rangle$ values consistent with the diphoton data, successfully reproduce the shapes of the data distributions. The theory can provide a good representation of k_T-insensitive distributions, such as the mass of the pair and particle p_T. Results from the high-mass pair data are used as input to a phenomenological k_T-smearing model which provides a consistent description of the observed deviations of NLO pQCD calculations from the inclusive direct-photon and π^0 data.

Table of Contents

Curriculum Vitae — **iii**

Acknowledgments — **v**

Preface — **vii**

Abstract — **ix**

List of Tables — **xvii**

List of Figures — **xxvii**

Chapter 1 Introduction — **1**

1.1 Standard Model 1

1.2 Hard Scatters 5

1.2.1 Factorization 6

1.2.2 Direct Photons 10

1.2.3 Kinematics 14

1.2.4 Parton Transverse Momentum 17

1.3 Experimental Methods 22

1.4 Summary 25

Chapter 2 The Meson West Spectrometer — **29**

2.1 Introduction 29

2.1.1 Coordinate System 29

2.2 Beamline and Target 30

2.2.1 Accelerator 30

2.2.2 Meson West Beamline 30

2.2.3 Beamline Čerenkov Detector 34

2.2.4 Hadron Shield and Veto Walls 34

2.2.5 Beam and Interaction Counters 34
2.2.6 Target 37
2.3 Charged Particle Spectrometer 40
2.3.1 Silicon Strip Detectors 40
2.3.2 Magnet 40
2.3.3 Proportional Wire Chambers 42
2.3.4 Straw Drift Tubes 42
2.4 Calorimetry 47
2.4.1 Liquid Argon Calorimeter Cryostat and Gantry 47
2.4.2 Electromagnetic Calorimeter 49
2.4.3 Hadronic Calorimeter 51
2.4.4 Forward Calorimeter 54
2.5 Muon Spectrometer 55
Chapter 3 Trigger and Data Acquisition 57
3.1 Trigger 57
3.1.1 Beam and Interaction 57
3.1.2 Pretrigger 59
3.1.3 Local Triggers 63
3.1.4 Global Triggers 63
3.1.5 Double-Octant Trigger 64
3.2 Data Acquisition 66
Chapter 4 Event Reconstruction 71
4.1 Overview 71
4.2 Tracking Reconstruction 72
4.2.1 Downstream Tracking 73
4.2.2 Upstream Tracking and Linking 75

4.2.3 Vertex Finding 75
4.2.4 Relinking 76
4.3 Electromagnetic Reconstruction 76
4.3.1 Unpacker, Pedestals, and Gains 76
4.3.2 Group Finding 77
4.3.3 Active Pedestal Subtraction 78
4.3.4 Peak Finding 78
4.3.5 Gamma Reconstruction 81
4.3.6 Gamma Correlation and Photon Reconstruction 83
4.3.7 Photon Timing 83
4.4 Event Database 91
4.5 Particle Zoo 91
Chapter 5 Detector Simulation 101
5.1 Full Monte Carlo 101
5.1.1 Event Generator 101
5.1.2 Event Selection 104
5.1.3 Detector Simulation 105
5.1.4 Reconstruction Efficiencies 114
5.2 Parameterized Monte Carlo 114
5.2.1 Generator 114
5.2.2 Detector Simulation 120
5.2.3 Direct Photon Background Calculation 125
5.2.4 Spectral Unsmearing 129
Chapter 6 Energy Scale Calibration 135
6.1 Introduction 135

6.2 Samples 138
6.2.1 Data 138
6.2.2 Full Monte Carlo 140
6.2.3 Parameterized Monte Carlo 141
6.2.4 Mass Reference 142
6.2.5 Momentum Scale 142
6.3 EMLAC Alignment 144
6.4 Energy Scale Methodology 145
6.4.1 Photons and Electrons 147
6.4.2 Full Monte Carlo 150
6.5 Data Energy Corrections 150
6.5.1 Initial Scale and Time Dependence 150
6.5.2 Octant-to-Octant 152
6.5.3 Inner/Outer ϕ Boundary 152
6.5.4 Correction for Material Energy Loss 155
6.5.5 Dependence of the Energy Scale on Radial Position 155
6.5.6 Results and Linearity 160
6.6 Electron Cross Checks 167
6.6.1 Search for Residual Corrections Using the γe^+e^- Sample 167
6.6.2 Another Look at Electrons 169
6.7 Full Monte Carlo Energy Scale 176
6.7.1 Initial Scale 176
6.7.2 Radial Dependence and Absolute Scale 176
6.7.3 Results 179
6.8 Systematic Uncertainty 183
6.8.1 Energy Scale Calibration 183

6.8.2 Mesons versus Photons 191
6.8.3 P_T Scale 192
6.8.4 Cross-Section Uncertainties 194

Chapter 7 Event Selection and Analysis 201

7.1 Cross Section Definition 201
7.2 Normalization 201
7.2.1 Beam 201
7.2.2 Target 202
7.2.3 Integrated Luminosity 207
7.3 Trigger 209
7.4 Photon Definition 212
7.5 EMLAC Geometrical Acceptance 215
7.6 Signal Definitions 218
7.6.1 Meson–Meson Background Subtraction 221
7.6.2 Direct Photon–Meson Background Subtraction 221
7.6.3 Double Direct Photon Background Subtraction 224
7.7 Systematic Uncertainties 226

Chapter 8 Production of High-Mass Pion Pairs 229

8.1 Cross Section Measurements 229
8.1.1 Mass Distributions 229
8.1.2 Pion Transverse Momentum 240
8.1.3 Angular Distributions 240
8.2 Kinematic Correlations 247

Chapter 9 Production of High-Mass Eta and Pion Pairs 259

9.1 Eta–Pion Production 259
9.2 Eta–Eta Production 264

Chapter 10 Production of Photon—Pion Pairs **265**

10.1 Cross Section Measurements 265

10.1.1 Mass Distributions 265

10.1.2 Transverse Momentum and the Fragmentation Function 268

10.1.3 Angular Distributions 270

10.2 Kinematic Correlations 270

Chapter 11 Production of High-Mass Direct Photon Pairs **279**

Chapter 12 Conclusions **289**

References **307**

Appendix A Tabulated Cross Sections: $\pi^0\pi^0$ **321**

Appendix B Tabulated Cross Sections: $\eta\pi^0$ **369**

Appendix C Tabulated Cross Sections: $\gamma\pi^0$ **375**

List of Tables

1.1 Fundamental forces in the Standard Model and their mediating bosons. .. 3

1.2 Properties of mediating bosons in the Standard Model [10]. 3

1.3 Leptons in the Standard Model with their masses and charges [10]. Neutrinos are regarded as massless in Standard Model calculations. The ν_τ has not yet been experimentally detected. 4

1.4 Quarks in the Standard Model, with their masses and charges [10]. 4

1.5 The order in α_{s} and α_{em} of the various subprocesses contributing to the production of single and double direct photons in hadron–hadron collisions [21]. 11

1.6 Methodology and choice of calorimeter technology for some experiments that have published results on direct-photon production. 23

1.7 Fixed target experiments that have published direct-photon results. 26

1.8 Hadron collider experiments that have published direct-photon results. .. 26

1.9 Statistical significance of published double direct-photon results. 27

2.1 Primary beam intensity at the production target required to generate $\approx 2 \times 10^8$ particles on the experimental target [73]. 32

2.2 Target materials, positions, and dimensions in the 1990 and 1991 configurations. The fiducial length of the hydrogen target is defined by a cut that excludes regions compromised by the proximity of the container material. 39

2.3 Elements of the charged particle spectrometer upstream of the analysis magnet. This table describes the 1990 configuration. During the 1991 fixed target run, beam SSDs 2 and 3 were moved farther upstream to make room for an expanded target. 44

2.4 Elements of the charged particle spectrometer downstream of the analysis magnet. This table describes the 1990 configuration. 45

3.1 Trigger characteristics during the 1990 fixed target run. Many events satisfied more than one trigger. Some prescale factors changed during the run. 59

4.1 Distance and χ^2/DOF requirements for tracks in various detector systems. This information is for the first iteration only. Subsequent iterations had somewhat different requirements. See [84] for more details. 73

5.1 Monte Carlo filters with their particle requirements. Also listed are the particle p_T requirements with respect to p_T^{MIN}. 104

5.2 Full Monte Carlo statistics (in thousands of events). This Monte Carlo was intended to generate π^0 and η events using the `HERWIG` event generator. No direct-photon events are included in these samples. Numbers in parenthesis represent full Monte Carlo events generated with the 1990 beam and target configuration that were processed by the appropriate 1991 preprocessor. 106

5.3 Full Monte Carlo statistics (in thousands of events). This Monte Carlo was intended to generate direct-photon events using the `HERWIG` event generator. All events were produced with filters 2 or $2'$. Numbers in parenthesis represent full Monte Carlo events generated with the 1990 beam and target configuration that were processed by the appropriate 1991 preprocessor. 107

5.4 Full Monte Carlo statistics (in thousands of events). This Monte Carlo was intended to generate either π^0 and η events using reconstructed data events as an input to the full Monte Carlo. Only events from the 1990 run were utilized for this purpose. 107

5.5 Particle decays and associated branching ratios [10] simulated in the parameterized Monte Carlo. 125

5.6 Target configuration in the parameterized Monte Carlo. The vertex was generated at (0,0) cm in the X-Y plane. The front face of the EMLAC was at (0,0,900) cm. 125

6.1 Summary table listing the data sections used in the energy scale analysis. 138

6.2 The masses of particles used in the energy scale calibrations. 142

6.3 Reconstructed masses of the neutral mesons in the data. All of the standard cuts are applied. All mesons have $p_T > 5$ GeV/c. The π^0 is measured on the outside of the detector (R > 50 cm) only. The 1990 data sample includes both the early and late samples. 167

6.4 The systematics associated with the energy scale calibration of the EMLAC for the data composed with the Monte Carlo and their respective uncertainties. 190

7.1 Average weight for beam absorption and photon conversion for the various materials in the 1990 and 1991 target configurations. 204

7.2 Luminosity as a function of beam and target for data samples used in this analysis. 207

7.3 Candidate and sideband ranges for π^0's and η's reconstructed from two-photon combinations. 218

11.1 Effective $\langle k_T \rangle$ values from several diphoton distributions. 287

A.1 Differential cross section per nucleon, $d\sigma/dM$, for several minimum $p_T^{\pi^0}$ requirements for $\pi^0\pi^0$ events produced in π^-Be interactions at 515 GeV/c. Additional requirements on the combinations contributing to this distribution are summarized at the beginning of Appendix A. .. 322

A.2 Differential cross section per nucleon, $d\sigma/dM$, for various targets for $\pi^0\pi^0$ from the 515 GeV/c π^- sample. Additional requirements on the combinations contributing to this distribution are summarized at the beginning of Appendix A. 323

A.3 Differential cross section per nucleon, $d\sigma/dM$, for various targets for $\pi^0\pi^0$ from the 515 GeV/c π^+ sample. Additional requirements on the combinations contributing to this distribution are summarized at the beginning of Appendix A. 323

A.4 Differential cross section per nucleon, $d\sigma/dM$, for several minimum $p_T^{\pi^0}$ requirements for $\pi^0\pi^0$ events produced in pBe interactions at 530 GeV/c. Additional requirements on the combinations contributing to this distribution are summarized at the beginning of Appendix A. .. 324

A.5 Differential cross section per nucleon, $d\sigma/dM$, for various targets for $\pi^0\pi^0$ events from the 530 GeV/c proton sample. Additional requirements on the combinations contributing to this distribution are summarized at the beginning of Appendix A. 325

A.6 Differential cross section per nucleon, $d\sigma/dM$, for several minimum $p_T^{\pi^0}$ requirements for $\pi^0\pi^0$ events produced in pBe interactions at 800 GeV/c. Additional requirements on the combinations contributing to this distribution are summarized at the beginning of Appendix A. .. 326

A.7 Differential cross section per nucleon, $d\sigma/dM$, for various targets for $\pi^0\pi^0$ from the 800 GeV/c proton sample. Additional requirements on the combinations contributing to this distribution are summarized at the beginning of Appendix A. 327

A.8 Differential cross section per nucleon, $d\sigma/dp_T$, for several targets for $\pi^0\pi^0$ from the 515 GeV/c π^- sample. There are two entries per pair. Additional requirements on the combinations contributing to this distribution are summarized at the beginning of Appendix A. 328

A.9 Differential cross section per nucleon, $d\sigma/dp_T$, for several targets for $\pi^0\pi^0$ from the 515 GeV/c π^+ sample. There are two entries per pair. Additional requirements on the combinations contributing to this distribution are summarized at the beginning of Appendix A. 328

A.10 Differential cross section per nucleon, $d\sigma/dp_T$, for several targets for $\pi^0\pi^0$ from the 530 GeV/c proton sample. There are two entries per pair. Additional requirements on the combinations contributing to this distribution are summarized at the beginning of Appendix A. 329

A.11 Differential cross section per nucleon, $d\sigma/dp_T$, for several targets for $\pi^0\pi^0$ from the 800 GeV/c proton sample. There are two entries per pair. Additional requirements on the combinations contributing to this distribution are summarized at the beginning of Appendix A. 330

A.12 Differential cross section per nucleon, $d\sigma/dYdM$, for several targets for $\pi^-N \longrightarrow \pi^0\pi^0$ at 515 GeV/c. Additional requirements on the combinations contributing to this distribution are summarized at the beginning of Appendix A. 331

A.13 Differential cross section per nucleon, $d\sigma/dY$, for $\pi^+Be \longrightarrow \pi^0\pi^0$ at 515 GeV/c. Additional requirements on the combinations contributing to this distribution are summarized at the beginning of Appendix A. .. 332

A.14 Differential cross section per nucleon, $d\sigma/dYdM$, for various targets for $pN \longrightarrow \pi^0\pi^0$ at 530 GeV/c. Additional requirements on the combinations contributing to this distribution are summarized at the beginning of Appendix A. 333

A.15 Differential cross section per nucleon, $d\sigma/dYdM$, for various targets for $pN \longrightarrow \pi^0\pi^0$ at 800 GeV/c. Additional requirements on the combinations contributing to this distribution are summarized at the beginning of Appendix A. 334

A.16 Differential cross section per nucleon, $d\sigma/d|\cos\theta^\star|$. To avoid rapidity biases, we require $|\eta_{\rm boost}| < 0.25$. To avoid biases due to the p_T requirements, there is a minimum mass requirement of 7.5 GeV/c for the π^- beam and 7.0 GeV/c for the proton beam. Additional requirements on the combinations contributing to this distribution are summarized at the beginning of Appendix A. 335

A.17 Differential cross section per nucleon, $d\sigma/d\Delta\phi$, for various targets for $\pi^0\pi^0$ from the 515 GeV/c π^- sample. Additional requirements on the combinations contributing to this distribution are summarized at the beginning of Appendix A. 336

A.18 Differential cross section per nucleon, $d\sigma/d\Delta\phi$, for $\pi^+\mathrm{Be} \longrightarrow \pi^0\pi^0$ at 515 GeV/c. Additional requirements on the combinations contributing to this distribution are summarized at the beginning of Appendix A. 336

A.19 Differential cross section per nucleon, $d\sigma/d\Delta\phi$, for various targets for $\pi^0\pi^0$ from the 530 GeV/c proton sample. Additional requirements on the combinations contributing to this distribution are summarized at the beginning of Appendix A. 337

A.20 Differential cross section per nucleon, $d\sigma/d\Delta\phi$, for various targets for $\pi^0\pi^0$ from the 800 GeV/c proton sample. Additional requirements on the combinations contributing to this distribution are summarized at the beginning of Appendix A. 337

A.21 Differential cross section per nucleon, $d\sigma/dQ_T$, for various targets for $\pi^0\pi^0$ from the 515 GeV/c π^- sample. Additional requirements on the combinations contributing to this distribution are summarized at the beginning of Appendix A. 338

A.22 Differential cross section per nucleon, $d\sigma/dQ_T$, for $\pi^0\pi^0$ from the 515 GeV/c π^+Be sample. Additional requirements on the combinations contributing to this distribution are summarized at the beginning of Appendix A. 338

A.23 Differential cross section per nucleon, $d\sigma/dQ_T$, for various targets for $\pi^0\pi^0$ from the 530 GeV/c proton sample. Additional requirements on the combinations contributing to this distribution are summarized at the beginning of Appendix A. 339

A.24 Differential cross section per nucleon, $d\sigma/dQ_T$, for various targets for $\pi^0\pi^0$ from the 800 GeV/c proton sample. Additional requirements on the combinations contributing to this distribution are summarized at the beginning of Appendix A. 339

A.25 Differential cross sections per nucleon $d\sigma/dp_{OUT}$ and $d\sigma/dp_{OUT}dM$ for $\pi^-\mathrm{Be} \longrightarrow \pi^0\pi^0$ at 515 GeV/c. There are two entries per pair. Additional requirements on the combinations contributing to this distribution are summarized at the beginning of Appendix A. 340

A.26 Differential cross section per nucleon, $d\sigma/dp_{OUT}$, for various targets for $\pi^0\pi^0$ from the 515 GeV/c π^- sample. There are two entries per pair. Additional requirements on the combinations contributing to this distribution are summarized at the beginning of Appendix A. 341

A.27 Differential cross section per nucleon, $d\sigma/dp_{OUT}$, for various targets for $\pi^0\pi^0$ from the 515 GeV/c π^+ sample. There are two entries per pair. Additional requirements on the combinations contributing to this distribution are summarized at the beginning of Appendix A. 341

A.28 Differential cross sections per nucleon $d\sigma/dp_{OUT}$ and $d\sigma/dp_{OUT}dM$ for pBe $\longrightarrow \pi^0\pi^0$ at 530 GeV/c. There are two entries per pair. Additional requirements on the combinations contributing to this distribution are summarized at the beginning of Appendix A. 342

A.29 Differential cross section per nucleon, $d\sigma/dp_{OUT}$, for various targets for $\pi^0\pi^0$ from the 530 GeV/c proton sample. There are two entries per pair. Additional requirements on the combinations contributing to this distribution are summarized at the beginning of Appendix A. 343

A.30 Differential cross sections per nucleon $d\sigma/dp_{OUT}$ and $d\sigma/dp_{OUT}dM$ for pBe $\longrightarrow \pi^0\pi^0$ at 800 GeV/c. There are two entries per pair. Additional requirements on the combinations contributing to this distribution are summarized at the beginning of Appendix A. 344

A.31 Differential cross section per nucleon, $d\sigma/dp_{OUT}$, for various targets for $\pi^0\pi^0$ from the 800 GeV/c proton sample. There are two entries per pair. Additional requirements on the combinations contributing to this distribution are summarized at the beginning of Appendix A. 345

A.32 Differential cross section per nucleon $d\sigma/dp_{IN}dM$ for π^-Be $\longrightarrow \pi^0\pi^0$ at 515 GeV/c. There are two entries per pair. Additional requirements on the combinations contributing to this distribution are summarized at the beginning of Appendix A. 346

A.33 Differential cross section per nucleon, $d\sigma/dp_{IN}$, for various targets for $\pi^0\pi^0$ from the 515 GeV/c π^- sample. There are two entries per pair. Additional requirements on the combinations contributing to this distribution are summarized at the beginning of Appendix A. 347

A.34 Differential cross section per nucleon, $d\sigma/dp_{IN}$, as a for various targets for $\pi^0\pi^0$ from the 515 GeV/c π^+ sample. There are two entries per pair. Additional requirements on the combinations contributing to this distribution are summarized at the beginning of Appendix A. 347

A.35 Differential cross section per nucleon $d\sigma/dp_{IN}dM$ for pBe $\longrightarrow \pi^0\pi^0$ at 530 GeV/c. There are two entries per pair. Additional requirements on the combinations contributing to this distribution are summarized at the beginning of Appendix A. 348

A.36 Differential cross section per nucleon, $d\sigma/dp_{IN}$, for various targets $\pi^0\pi^0$ from the 530 GeV/c proton sample. There are two entries per pair. Additional requirements on the combinations contributing to this distribution are summarized at the beginning of Appendix A. 349

A.37 Differential cross sections per nucleon $d\sigma/dp_{IN}dM$ for pBe $\longrightarrow \pi^0\pi^0$ at 800 GeV/c. There are two entries per pair. Additional requirements on the combinations contributing to this distribution are summarized at the beginning of Appendix A. 350

A.38 Differential cross section per nucleon, $d\sigma/dp_{IN}$, for various targets for $\pi^0\pi^0$ from the 800 GeV/c proton sample. There are two entries per pair. Additional requirements on the combinations contributing to this distribution are summarized at the beginning of Appendix A. 351

A.39 Differential cross section per nucleon $d\sigma/dzdM$ for π^-Be $\longrightarrow \pi^0\pi^0$ at 515 GeV/c. There are two entries per pair. Additional requirements on the combinations contributing to this distribution are summarized at the beginning of Appendix A. 352

A.40 Differential cross section per nucleon, $d\sigma/dz$, for various targets for $\pi^0\pi^0$ from the 515 GeV/c π^- sample. There are two entries per pair. Additional requirements on the combinations contributing to this distribution are summarized at the beginning of Appendix A. 353

A.41 Differential cross section per nucleon, $d\sigma/dz$, for various targets for $\pi^0\pi^0$ from the 515 GeV/c π^+ sample. There are two entries per pair. Additional requirements on the combinations contributing to this distribution are summarized at the beginning of Appendix A. 354

A.42 Differential cross section per nucleon $d\sigma/dzdM$ for pBe $\longrightarrow \pi^0\pi^0$ at 530 GeV/c. There are two entries per pair. Additional requirements on the combinations contributing to this distribution are summarized at the beginning of Appendix A. 355

A.43 Differential cross section per nucleon, $d\sigma/dz$, for various targets for $\pi^0\pi^0$ from the 530 GeV/c proton sample. There are two entries per pair. Additional requirements on the combinations contributing to this distribution are summarized at the beginning of Appendix A. 356

A.44 Differential cross section per nucleon $d\sigma/dzdM$ for pBe $\longrightarrow$ $\pi^0\pi^0$ at 800 GeV/c. There are two entries per pair. Additional requirements on the combinations contributing to this distribution are summarized at the beginning of Appendix A. 357

A.45 Differential cross section per nucleon, $d\sigma/dz$, for various targets for $\pi^0\pi^0$ from the 800 GeV/c proton sample. There are two entries per pair. Additional requirements on the combinations contributing to this distribution are summarized at the beginning of Appendix A. 358

A.46 Averages of several kinematic quantities as functions of mass for π^-Be $\longrightarrow$ $\pi^0\pi^0$ at 515 GeV/c. Additional requirements on the combinations contributing to this distribution are summarized at the beginning of Appendix A. 359

A.47 Averages of several kinematic quantities as functions of mass for π^-Cu $\longrightarrow$ $\pi^0\pi^0$ at 515 GeV/c. Additional requirements on the combinations contributing to this distribution are summarized at the beginning of Appendix A. 360

A.48 Averages of several kinematic quantities as functions of mass for π^-p $\longrightarrow$ $\pi^0\pi^0$ at 515 GeV/c. Additional requirements on the combinations contributing to this distribution are summarized at the beginning of Appendix A. 361

A.49 Averages of several kinematic quantities as functions of mass and target for $\pi^0\pi^0$ events from the 515 GeV/c π^+ sample. Additional requirements on the combinations contributing to this distribution are summarized at the beginning of Appendix A. 362

A.50 Averages of several kinematic quantities as functions of mass for pBe $\longrightarrow$ $\pi^0\pi^0$ at 530 GeV/c. Additional requirements on the combinations contributing to this distribution are summarized at the beginning of Appendix A. 363

A.51 Averages of several kinematic quantities as functions of mass for pCu $\longrightarrow$ $\pi^0\pi^0$ at 530 GeV/c. Additional requirements on the combinations contributing to this distribution are summarized at the beginning of Appendix A. 364

A.52 Averages of several kinematic quantities as functions of mass for pp $\longrightarrow$ $\pi^0\pi^0$ at 530 GeV/c. Additional requirements on the combinations contributing to this distribution are summarized at the beginning of Appendix A. 365

A.53 Averages of several kinematic quantities as functions of mass for pBe $\longrightarrow$ $\pi^0\pi^0$ at 800 GeV/c. Additional requirements on the combinations contributing to this distribution are summarized at the beginning of Appendix A. 366

A.54 Averages of several kinematic quantities as functions of mass for pCu $\longrightarrow$ $\pi^0\pi^0$ at 800 GeV/c. Additional requirements on the combinations contributing to this distribution are summarized at the beginning of Appendix A. 367

A.55 Averages of several kinematic quantities as functions of mass for pp $\longrightarrow$ $\pi^0\pi^0$ at 800 GeV/c. Additional requirements on the combinations contributing to this distribution are summarized at the beginning of Appendix A. 368

B.1 Differential cross section per nucleon, $d\sigma/dM$, for $\pi^0\pi^0$ and $\eta\pi^0$ events. Additional requirements on the combinations contributing to this distribution are summarized at the beginning of Appendix B. 370

B.2 Differential cross section per nucleon, $d\sigma/dY$, for $\eta\pi^0$ events. Additional requirements on the combinations contributing to this distribution are summarized at the beginning of Appendix B. 371

B.3 Differential cross section per nucleon, $d\sigma/dQ_T$, for $\eta\pi^0$ events. Additional requirements on the combinations contributing to this distribution are summarized at the beginning of Appendix B. 372

B.4 Differential cross section per nucleon, $d\sigma/d\Delta\phi$, for $\eta\pi^0$ events. Additional requirements on the combinations contributing to this distribution are summarized at the beginning of Appendix B. 372

B.5 Differential cross section per nucleon, $d\sigma/dp_{OUT}$, for $\eta\pi^0$ events. There are two entries per pair. Additional requirements on the combinations contributing to this distribution are summarized at the beginning of Appendix B. 373

C.1 Differential cross section per nucleon, $d\sigma/dM$, for several minimum $p_T{}^\gamma$ requirements for $\gamma\pi^0$ events produced in π^-Be interactions at 515 GeV/c. Additional requirements on the combinations contributing to this distribution are summarized at the beginning of Appendix C. .. 376

C.2 Differential cross section per nucleon, $d\sigma/dM$, for several targets for $\gamma\pi^0$ from the 515 GeV/c π^- sample. Additional requirements on the combinations contributing to this distribution are summarized at the beginning of Appendix C. 376

C.3 Differential cross section per nucleon, $d\sigma/dp_T{}^{\gamma}$, for π^-Be $\longrightarrow$ $\gamma\pi^0$ at 515 GeV/c. These direct photons are opposite π^0's with $p_T{}^{\pi^0} >$ 2.5 GeV/c. Additional requirements on the combinations contributing to this distribution are summarized at the beginning of Appendix C. .. 377

C.4 Differential cross section per nucleon, $d\sigma/dp_T{}^{\pi^0}$, for π^-Be $\longrightarrow$ $\gamma\pi^0$ at 515 GeV/c. These π^0's are opposite direct photons with $p_T{}^{\gamma} > 4.0$ GeV/c and $p_T{}^{\gamma} > 4.5$ GeV/c. Additional requirements on the combinations contributing to this distribution are summarized at the beginning of Appendix C. 377

C.5 Differential cross section per nucleon, $d\sigma/dYdM$, for π^-Be $\longrightarrow$ $\gamma\pi^0$ at 515 GeV/c. Additional requirements on the combinations contributing to this distribution are summarized at the beginning of Appendix C. 378

C.6 Differential cross section per nucleon, $d\sigma/d|\cos\theta^{\star}|$ for π^-Be $\longrightarrow$ $\gamma\pi^0$ at 515 GeV/c. To avoid rapidity biases, we require $|\eta_{\rm boost}| < 0.25$. To avoid biases due to the p_T requirements, there is a minimum mass requirement of 7.5 GeV/c. Additional requirements on the combinations contributing to this distribution are summarized at the beginning of Appendix C. .. 378

C.7 Differential cross section per nucleon, $d\sigma/d\Delta\phi$, for π^-Be $\longrightarrow$ $\gamma\pi^0$ at 515 GeV/c. Additional requirements on the combinations contributing to this distribution are summarized at the beginning of Appendix C. .. 379

C.8 Differential cross section per nucleon, $d\sigma/dp_{\rm OUT}$, for π^-Be $\longrightarrow$ $\gamma\pi^0$ at 515 GeV/c. There are two entries per pair. Additional requirements on the combinations contributing to this distribution are summarized at the beginning of Appendix C. 379

C.9 Differential cross section per nucleon, $d\sigma/dQ_T$, for π^-Be $\longrightarrow$ $\gamma\pi^0$ at 515 GeV/c. Additional requirements on the combinations contributing to this distribution are summarized at the beginning of Appendix C. .. 380

List of Figures

1.1 Schematic diagram of a two-body reaction, $A + B \longrightarrow C + D$, which has been factorized according to the prescriptions of pQCD. Here a is a parton from hadron A with distribution $G_{a/A}(x_a, Q^2)$. Similarly for parton b. Partons a and b interact to form partons c and d via the hard-scattering process $d\hat{\sigma}/dt(a + b \longrightarrow c + d)$. Parton c fragments into particle C with probability $D_{C/c}(z_c, Q^2)$. Similarly for parton d. 6

1.2 Two parton distribution functions used in this analysis, CTEQ4L [17] and GRV92LO [18]. They were calculated using `PDFLIB` [19] at $Q^2 = 10$ GeV^2. 8

1.3 Probability that a given parton will fragment into a π^0 as a function of the momentum fraction, z, of the π^0. These leading-order fragmentation functions [20] were evaluated at $Q^2 = 10$ GeV^2. 9

1.4 The lowest order diagrams for direct-photon production. 10

1.5 The fractional contribution of the leading-order diagrams for the inclusive production of direct photons calculated using LO pQCD [11]. 13

1.6 Two important diagrams for the production of two direct photons. 14

1.7 Cartoon illustrating the impact of multiple soft-gluon emission in the hard scatter of two partons. Partons a and b (from hadrons A and B respectively), emit soft-gluons prior to the hard scatter which produces particles c and d. This gives rise to a p_T imbalance between the outgoing particles. 17

1.8 Mean transverse momentum, $\langle Q_T \rangle$, of pairs of muons, photons, and jets produced in hadronic collisions versus $\sqrt{s}$. 19

1.9 An illustration of a two arm configuration in the p_T plane (beam is oriented along the Z-axis). The lengths of the vectors represent their p_T. The angle between the two vectors is $\Delta\phi$. The projection of a p_T-vector onto the plane formed by the other vector and the beam axis yields p_{OUT}. 21

1.10 The observed single γ to π^0 ratio for signal+background (•) and background (curve) from the π^-Be data at 515 GeV/c. 24

2.1 A schematic drawing of the Fermilab accelerator complex during the 1991 fixed target run. 31

2.2 A schematic drawing of the Meson West beamline showing the most important elements. 33

2.3 A schematic drawing of the beamline Čerenkov counter (top) and its phototube placement (bottom). Each ring of photomultiplier tubes is labeled according to the particle it was designed to tag. 35

2.4 A schematic drawing of the Meson West Spectrometer in the 1991 configuration. 36

2.5 Configuration of the target region during the 1990 run. 38

2.6 Configuration of the target region during the 1991 run. 38

2.7 The silicon strip detectors in their 1990 configuration. The instrumented regions of each plane are marked by the shaded areas. 41

2.8 Arrangement of the sense wires in each proportional wire chamber module. 43

2.9 Cut view of a straw drift tube bundle. 46

2.10 A cut-away view of the liquid argon calorimeter and gantry. Both the electromagnetic and hadronic calorimeters are visible within the cryostat. 48

2.11 An exploded view of the electromagnetic calorimeter. 50

2.12 A cell from the hadronic calorimeter. 52

2.13 The pad structure used in the hadronic calorimeter. A typical hadronic shower is shown in the inset. 53

2.14 Diagram of the forward calorimeter. 54

3.1 The π^0 number distribution prior to trigger corrections. Where two triggers overlap, the trigger corrections allow for the use of the higher-threshold trigger, along with its higher statistics. 60

3.2 A block diagram of the EMLAC based trigger system. 61

3.3 Selected inner (left) and outer (right) PRETRIGGER HIGH turn-ons for few (solid) and many (dashed) groups from the 1991 data. The error bars above the turn-on region are intended to provide an estimate of the statistical uncertainty of the measurement, and should not be taken to imply that the efficiency could exceed 100%. 62

3.4 The p_T summing for the local triggers. 64

3.5 LOCAL LOW (top) and LOCAL HIGH (bottom) turn-ons for selected inner and outer locals as a function of trigger-p_T from the 1991 data. The error bars above the turn-on region are intended to provide an estimate of the statistical uncertainty of the measurement, and should not be taken to imply that the efficiency could exceed 100%. 65

3.6 A block diagram of the data acquisition system. 67

3.7 A block diagram of the LAC amplifiers. 68

4.1 An event from one EMLAC quadrant before the active pedestal subtraction has been applied. Note the ramp in Left R and the level difference between the left and right sides of Outer ϕ. 79

4.2 An event from one EMLAC quadrant (the same event as in Figure 4.1) following the application of the active pedestal subtraction. 80

4.3 Photon shower shape function for the summed section. 82

4.4 An event from one EMLAC quadrant showing how the gammas are correlated together. Dashed lines mark the locations of the boundaries in the other view. Showers tagged with the same number were correlated together. 84

4.5 Pedestal corrected TVC distribution in ADC counts for groups of four LAC strips. There is a minimum requirement of 4 GeV on the total energy of the four strips. The peaks at low ADC counts represent electronic jitter due to the BEFORE gate. 86

4.6 Raw TVC efficiency for groups of four LAC strips. Both master and slave values were used in these plots and the noise due to the BEFORE gate has been excluded. 87

4.7 The time of π^0's having $p_T > 3$ GeV/c when there were two latched interactions—one in-time, and one approximately 38 ns later. Insets show the $\gamma\gamma$ mass distributions for combinations restricted to the indicated time intervals. 89

4.8 The time of π^0's having $p_T > 3$ GeV/c for specific configurations of beam–target interactions. Each configuration requires an interaction in-time (beam bucket 8) and one and only one interaction in buckets 5 through 13. Each overlay is peak normalized in the in-time bucket. The peak representing the case when there was only one recorded interaction (the in-time bucket) has been hatched for reference. 90

4.9 Mesons that decay into photons. Signals are reconstructed with combinations of converted (ZMP) and non-converted photons. 92

4.10 Reconstructed mesons that decay into pions. 94

4.11 The invariant mass of all matched ZMPs in the combined data sample. The mass is determined from tracking information only. 96

4.12 ΔS_Y distributions for the 1991 π^- sample. The effect for the various cuts on the ΔS_Y distribution: a) all oppositely charged tracks; b) $188 <$ ZXI < 208 cm; c) at least one ZMP track matched with a shower having $E_{FRONT}/E_{TOTAL} > 0.5$; d) both ZMP tracks matched with showers. Each plot contains the requirements of the previous one. 98

4.13 Z–X intersection distributions for the 1991 π^- sample. The effect for the various cuts on the ZXI distributions: a) all oppositely charged tracks; b) $|\Delta S_Y| < 3$ mrad; c) at least one ZMP track matched with a shower having $E_{FRONT}/E_{TOTAL} > 0.5$; d) both ZMP tracks matched with showers. Each plot contains the requirements of the previous one. 99

5.1 Comparison between the number of reconstructed photons in the triggering octant (top) and the total number of reconstructed tracks (bottom) in PYTHIA, HERWIG, and the data for events containing π^0's with p_T > 3.5 GeV/c. 102

5.2 A comparison of the shapes of data (•) and the HERWIG (histogram) photon multiplicity distributions binned in rapidity for two choices of p_T. This is from the 800 GeV/c proton beam sample. 103

5.3 A shape comparison of photon $E_R - E_\phi$ distributions in eight photon energy bins between the data (•) and the full Monte Carlo (histogram). This is from the 800 GeV/c proton beam sample for events containing π^0's with $p_T > 3.5$ GeV/c. 109

5.4 A shape comparison of the photon E_{FRONT}/E_{TOTAL} distributions in nine photon energy bins between the data (•) and the full Monte Carlo (histogram). This is from the 530 GeV/c proton beam sample for events containing π^0's with $p_T > 3.5$ GeV/c. 110

5.5 A shape comparison of the photon radial view shower energy χ^2 distributions in six photon energy bins between the data (•) and the full Monte Carlo (histogram). This is from the 515 GeV/c π^- beam sample for events containing π^0's with $p_T > 3.5$ GeV/c. 111

5.6 Comparison between data (•) and the full Monte Carlo (histogram) from the 530 GeV/c proton beam sample for $\gamma\gamma$ combinations in the π^0 and η mass regions. 112

5.7 Comparison of the π^0 energy asymmetry distribution in data (•) and the full Monte Carlo (histogram) for the 800 GeV/c proton beam sample. Shown are the comparisons for two p_T intervals, $4.0 < p_T < 5.5$ GeV/c and $5.5 < p_T < 7.0$ GeV/c. 113

5.8 Probability for reconstructing direct photons with the TWO GAMMA trigger as a function of the photon's p_T and rapidity. This was taken from the 515 GeV/c π^- full Monte Carlo (1991 configuration). 115

5.9 Probability for reconstructing π^0's with the TWO GAMMA trigger as a function of the π^0's p_T and rapidity. The rise at low-p_T (backwards rapidity) is due to the trigger turn-on, the dip at high p_T (forwards rapidity) is due to the coalescence of the two decay photons. This was taken from the 515 GeV/c π^- full Monte Carlo (1991 configuration). 116

5.10 Probability for reconstructing η's with the TWO GAMMA trigger as a function of the η's p_T and rapidity. The rise at low-p_T is due to the trigger turn-on. This was taken from the 515 GeV/c π^- full Monte Carlo (1991 configuration). 117

5.11 The π^0 cross section versus p_T and rapidity from the 530 GeV/c proton beam sample. The parameterization is overlayed on the data. 118

5.12 Measured ratio for the production of η's with respect to π^0's as a function of p_T for the three major samples considered in this analysis. The line represents a simple flat line fit to the data. 119

5.13 Comparison between data (•) and the parameterized Monte Carlo (curve) for distributions in mass, $\Delta\phi$, p_{OUT}, and Q_T for π^0 pairs from the 515 GeV/c π^- beam sample. 121

5.14 Fractional widths of the $E_R - E_\phi$ distributions plotted as functions of the total energy of the shower, for showers in the outer and inner regions of the detector. The data are isolated single photons from the 515 GeV/c π^- beam sample. The curves represent fits to the data. 122

5.15 Comparison between data (•) and the parameterized Monte Carlo (curve) from the 530 GeV/c proton beam sample. Top) $\gamma\gamma$ combinations in the π^0 and η mass regions; bottom) π^0 energy asymmetry. The combinatorial background in the data has been removed through a simple subtraction for this comparison. 123

5.16 Mass plots from the parameterized Monte Carlo for the π^0, η, ω, and converted η with smeared $p_T > 3.5$ GeV/c. This is from the 515 GeV/c π^- beam sample. 124

5.17 Probability for an electron to be reconstructed in the EMLAC as a function of the electron's reconstructed momentum. This function was extracted from a sample of e^+e^- pairs in the 515 GeV/c π^- data. 126

5.18 Probability that the two photons from a π^0 decay are reconstructed as a single photon. This function was extracted from the full Monte Carlo for the 515 GeV/c π^- beam sample. 127

5.19 The fraction of direct-photon background arising from various sources in $\pi^0 \longrightarrow \gamma\gamma$ events as a function of photon p_T. This was extracted from the parameterized Monte Carlo for the 515 GeV/c π^- beam sample. 128

5.20 The fraction of the direct-photon background arising from π^0's, η's, ω's, and all other sources as a function of photon p_T. This was extracted from the parameterized Monte Carlo for the 515 GeV/c π^- beam sample. .. 130

5.21 The photon definition efficiency for (•) direct photons, and (○) background photons in the full Monte Carlo. This was extracted from the 530 GeV/c proton beam sample. 131

5.22 A comparison of the direct-photon background as a function of p_T between the parameterized Monte Carlo (line) and the full Monte Carlo (•). The background (b_γ) was normalized to the π^0 cross section (s_{π^0}). 132

5.23 Illustration showing the effect of energy resolution on a steeply falling p_T spectrum. For any given reconstructed p_T bin, there are more contributions from bins with lower generated p_T than from bins with higher generated p_T, leading to a net shift in the p_T spectrum. 133

5.24 Impact of the EMLAC energy resolution on the mean π^0 $E_{smeared}/E_{generated}$ as functions of generated p_T (solid) and smeared p_T (dashed) both prior to (top) and after (bottom) the energy calibration. Following the energy calibration procedure (which used smeared quantities), the average smeared energy is smaller than the average generated energy when binned in generated p_T. 134

6.1 Inclusive differential cross sections as a function of p_T for the production of photons and mesons in π^-Be interactions at 515 GeV/c. 136

6.2 The systematic uncertainty in a π^0 cross section as a function of p_T due to the uncertainty in the energy scale. Three different values are displayed. This is for the production of π^0's in π^-Be interactions at 515 GeV/c. . 137

6.3 Two photon invariant mass spectrum with $p_T > 3$ GeV/c from the 1991 data sample. The lower, dashed, curve represents $\gamma\gamma$ pairs with energy asymmetry less than 0.5. The peaks are due to reconstructed π^0 and η mesons. 140

6.4 a) $\pi^+\pi^-$ invariant mass in the K^0_S mass region for secondary vertices upstream of the analysis magnet; b) $\mu^+\mu^-$ invariant mass in the J/ψ mass region. 143

6.5 The position resolution for the EMLAC as a function of energy. The contribution to this resolution from the tracking system has been subtracted out in quadrature. 146

6.6 The top plot shows a comparison of reconstructed π^0 mass as a function of the separation between the two photons from the π^0 decay in the data (•) and the full Monte Carlo (∘) for the 1990 π^- sample with $p_T > 3.5$ GeV/c. The bottom plot shows the comparison of the mean reconstructed to generated π^0 energy in the full Monte Carlo versus the separation in the EMLAC between the photons from the π^0 decay. 148

6.7 Uncalibrated relative values for the reconstructed masses of the π^0 and η signals as a function of beam days during the 1990 and 1991 runs. The triangles represent the EMLAC response to 50 GeV/c incident electron beams. Both the π^0 and η signals were reconstructed with $p_T > 5$ GeV/c and $R > 50$ cm. 151

6.8 The ratio of the reconstructed π^0 mass to its nominal value as a function of octant number in the 1991 data sample. 153

6.9 Radial dependence of the reconstructed π^0 mass from the 1991 data relative to its accepted value using as photon energy top) twice the R gamma energy or bottom) twice the ϕ gamma energy. The dashed lines represent ± 5 cm around the inner/outer ϕ boundary. 154

6.10 The accumulated number of radiation lengths passed through by a photon originating in the target and pointing towards the center of an EMLAC quadrant. The cryostat accounts for most of the material upstream of the EMLAC as measured in radiation lengths. This is taken from the GEANT Monte Carlo. 156

6.11 The functions used to correct for the energy loss in the material in front of the EMLAC. 157

6.12 Radial dependence of the reconstructed π^0 and η masses from the 1991 data sample. Also shown is the radial dependence of the E/P ratio for ZMP electrons with P $\approx$ 20 GeV/c adjusted for Section 6.6.2. 158

6.13 Radial dependence of the reconstructed π^0 mass shown for various values of the BEFORE/AFTER gate time. 159

6.14 Radial dependence of the reconstructed π^0 mass with $p_T > 3.0$ GeV/c relative to its accepted value by octant from 1991. 161

6.15 The calibrated two-photon mass distribution in the π^0 mass region for $\gamma\gamma$ pairs with $p_T > 3$ GeV/c and R > 50 cm from the 1991 data sample. .. 162

6.16 The calibrated two-photon mass distribution in the π^0 mass region for $\gamma\gamma$ pairs with $p_T > 5$ GeV/c and R > 50 cm from the 1991 data sample. The peak at low mass is due to muon bremsstrahlung. See Section 7.3 for more details. 163

6.17 The calibrated two-photon mass distribution in the η mass region for $\gamma\gamma$ pairs with $p_T > 5$ GeV/c from the 1991 data sample. 164

6.18 The calibrated $\gamma\pi^0$ mass distribution in the ω mass region for $\gamma\pi^0$ $p_T >$ 5 GeV/c from the 1991 data sample. 165

6.19 The mean η mass as a function of the η's energy (top) and p_T (bottom) from the 1991 data sample. 166

6.20 The γe^+e^- mass distribution from the combined 1990 and 1991 data samples. 168

6.21 Ratio of the η mass to its nominal value when one of its photons converted into an e^+e^- pair versus the energy of the other photon. To fill in the low energy region, the same ratio is shown for the away-side π^0 mass. 170

6.22 Ratio of the π^0 mass to its nominal value versus the number of radiation lengths of target material traversed by the photons. The closed circles (•) represent the π^0 mass ratio when one of the photons converted to an e^+e^- pair with the three particle γe^+e^- system $p_T > 0.8$ GeV/c. The open circles (○) represent π^0's with $p_T > 3.0$ GeV/c reconstructed from non-converted photons. The lines are fits to the data. 170

6.23 The J/ψ mass in its e^+e^- and $\mu^+\mu^-$ decay modes. These data are from the 1990 sample. 171

6.24 The $e^+e^-e^+e^-$ invariant mass distribution from the 1990 π^- sample with $p_T > 0.5$ GeV/c. The π^0 peak is clearly visible. Only information from the tracking system was used in this mass calculation. The electrons were not required to match with showers in the calorimeter. 172

6.25 The dependence of ZMP electron's reconstructed energy to its measured momentum as a function of its energy. The line at 1.0 is intended to guide the eye. These data are from the 1991 sample. 174

6.26 The ratio of a ZMP electron's reconstructed energy to its measured momentum for $E > 40$ GeV. Here the π^0 p_T cut has been raised to 3 GeV/c. The mean E/P is 1.000 ± 0.003 (Gaussian fit). These data are from the 1991 sample. 175

6.27 The relative change in the energy scale as a function of radius due to the energy resolution of the EMLAC (Figure 5.14). This was determined using the parameterized Monte Carlo (Section 5.2). The dashed line at 1.0 is intended to guide the eye. 177

6.28 The π^0 (top) and η (bottom) masses versus p_T^{MIN} from the 1990 515 GeV/c π^- full Monte Carlo. This data is untriggered and is a composite of all the available filters. The π^0 mass is from the outside of the detector ($R > 50$ cm). 178

6.29 The π^0 (top) and η (bottom) masses versus p_T^{MIN} from the 1990 515 GeV/c π^- full Monte Carlo for different filter types. This data is untriggered. The π^0 mass is from the outside of the detector ($R > 50$ cm). 180

6.30 The π^0 (top) and η (bottom) masses versus p_T^{MIN} from the 1990 515 GeV/c π^- full Monte Carlo for the local triggers. This data is a composite of the available filters. The π^0 mass is from the outside of the detector ($R > 50$ cm). 181

6.31 E_{REC}/E_{GEN} from the 1990 515 GeV/c π^- full Monte Carlo sample for π^0's and η's as functions of their reconstructed p_T values. Overlayed on each are the results from the parameterized Monte Carlo (Section 5.2). 182

6.32 The relative change between Monte Carlo and data in the mean π^0 mass when the "high-mass bump" has been removed from consideration. ... 184

6.33 Residual systematic uncertainty in the radial correction for the 1991 data sample. 186

6.34 Residual systematic uncertainty in the absolute energy scale from the 1991 data sample. 189

6.35 E_{REC}/E_{GEN} from the 1991 800 GeV/c proton full Monte Carlo sample for π^0's and direct photons as functions of their generated p_T values. The top plot is for the standard energy scale sample, the bottom plot has additional requirements assuring that all photons were reconstructed in the same manner by `EMREC`. 193

6.36 The systematic uncertainty in the π^0 cross section as functions of the π^0 p_T (top) and rapidity (bottom) for the data displayed in Figure 6.1. The energy scale systematic uncertainty was taken to be 0.5%. 195

6.37 The systematic uncertainty in the direct-photon cross section as functions of p_T (top) and rapidity (bottom) for the data displayed in Figure 6.1. The energy scale systematic uncertainty was taken to be 0.6%. 196

6.38 The systematic uncertainty in the $\pi^0\pi^0$ cross section as functions of mass (top), Q_T (bottom-right), and p_{OUT} (bottom-left) for the 515 GeV π^- data. 197

6.39 The systematic uncertainty in the direct photon–π^0 cross section as functions of mass (top), Q_T (bottom-right), and p_{OUT} (bottom-left) for the 515 GeV π^- data. 198

6.40 The systematic uncertainty in the double direct-photon cross section as functions of mass (top), Q_T (bottom-right), and p_{OUT} (bottom-left) for the 515 GeV π^- data. 199

7.1 Pressure curves for the pion, kaon, and proton tags with incident +530 GeV/c beam. Each curve is labeled by tag logic. Peaks/plateaus are labeled by the associated particle type. The solid vertical line represents a typical Čerenkov operating pressure. The line clearly passes through the desired peaks for tagging each particle type with the appropriate coincidence logic [76]. 203

7.2 The longitudinal distribution of reconstructed vertices for 1990 (top) and 1991 (bottom) target configurations. The events contributing to these plots were selected by requiring a π^0 with $p_T > 4.0$ GeV/c. 205

7.3 X–Y distribution of vertices in the copper and beryllium targets for the 1990 515 GeV/c π^- data and the 1991 530 GeV/c proton data. Each event required a π^0 with $p_T > 3.5$ GeV/c. The solid lines mark the edges of the target; the dashed lines represent the instrumented region of the beam SSDs; the dotted circle is the beam hole counter. Vertices outside the Cu and Be target area in the 1990 data are primarily due to interactions in the Rohacell target stand [119]. 206

7.4 The ratio of inclusive differential π^0 cross sections as a function of p_T from the 515 GeV/c π^-Be data for the 1990 and 1991 fixed target runs. The luminosities (and most of the corrections) were calculated independently for these two samples. The line is a fit; the ratio is 0.998 ± 0.007. 208

7.5 The ratio of $\pi^0\pi^0$ cross sections as a function of mass from the 515 GeV/c π^-Be data for the 1990 and 1991 fixed target runs. The luminosities (and most of the corrections) were calculated independently for these two samples. The line is a fit; the ratio is 0.96 ± 0.06. 208

7.6 Comparison of $\pi^0\pi^0$ events for the TWO GAMMA trigger and for the SINGLE LOCAL HIGH trigger from the 800 GeV/c pBe data sample. These data are from independent run ranges. The π^0 was required to have ${p_T}^{\pi^0} > 4$ GeV/c to conform with the SINGLE LOCAL HIGH turn-on. 210

7.7 The π^0 mass plot with $p_T > 7.0$ GeV/c and R > 50 cm for top) the SINGLE LOCAL HIGH trigger and bottom) the TWO GAMMA trigger. The rise at low mass (M < 0.1 GeV/c^2) is due to muon bremsstrahlung. The *all muon cuts* includes all requirements listed in [79]. 211

7.8 The distance to the nearest track for direct-photon candidates having $p_T > 4$ GeV/c. The dashed line is a representation of the cut value. Entries to the left of the line are primarily electrons. 213

7.9 E_{FRONT}/E_{TOTAL} distribution for (•) electromagnetic showers (ZMP electrons) and (∘) hadronic showers ($\pi^\pm$ from K^0_S decays). 214

7.10 The positions of photons reconstructed in the EMLAC from the 1990 data. Each photon is required to fall within the EMLAC's fiducial volume. The octant structure is clearly visible. 216

7.11 Geometrical acceptance for $\gamma\gamma$, $\gamma\pi^0$, $\pi^0\pi^0$, and $\eta\pi^0$ pairs as a function of $\Delta\phi$. The maxima and minima reflect the octant boundaries and the Δoctant cut. The line is a parameterization of the $\gamma\gamma$ geometrical acceptance. 217

7.12 The π^0 and η masses showing the candidate and sideband regions used in this analysis. 219

7.13 The energy asymmetry distribution for π^0 mesons ($4.0 < p_T < 5.5$ GeV) in the top) candidate region; middle) sideband region; bottom) sideband subtracted (signal region). 220

7.14 Candidate and side-band distributions for $\pi^0\pi^0$ events as a function of mass from the 530 GeV/c pBe sample. 222

7.15 Comparison of signal and background for $\gamma\pi^0$ data from the 515 GeV/c π^-Be sample. The ratios c_γ/s_{π^0} and b_γ/s_{π^0} are plotted for the case when a π^0 with ${p_T}^{\pi^0} > 2.5$ GeV/c is reconstructed on the other side of the calorimeter. 223

7.16 Comparison of signal and background for $\gamma\gamma$ data from the 515 GeV/c π^-Be sample. The ratios c_γ/s_{π^0} and b_γ/s_{π^0} are shown for the case when a photon (c_γ) with $p_T{}^\gamma > 4.0$ GeV/c is reconstructed on the other side of the calorimeter. 225

7.17 Difference in the time between left) two π^0's with $p_T{}^{\pi^0} > 2.5$ GeV/c from the 530 GeV/c proton sample and right) two direct-photon candidates with $p_T{}^\gamma > 4$ GeV/c from the 515 GeV/c π^- sample. A fit to shape of the $\pi^0\pi^0$ distribution has been overlayed on the diphoton data. 227

8.1 The dipion mass distribution produced by 515 GeV/c π^- incident on beryllium. The results of corresponding LO theory calculations [11] for several choices of scale are also shown. 230

8.2 The dipion mass distribution for several different minimum $p_T{}^{\pi^0}$ requirements. Systematic uncertainties have only been displayed for the $p_T{}^{\pi^0} >$ 1.5 GeV/c points. The results of corresponding LO theory calculations [11] are also shown. 232

8.3 The dipion mass distribution produced by interactions of various beams on beryllium. The results of corresponding LO theory calculations [11] are also shown. 233

8.4 The dipion mass distribution produced by interactions of various beams on hydrogen. The results of corresponding LO theory calculations [11] are also shown. 234

8.5 Data to theory comparison for $\pi^0\pi^0$ data produced in pp interactions from NA24, E706, and CCOR. Each sample has the same kinematic requirements. The LO theory [11] is described in the text; the theory in the top plot has $\langle k_T \rangle = 0$ GeV/c, the theory in the bottom plot has $\langle k_T \rangle$ as described in the text. 236

8.6 Data to theory comparison for $\pi^0\pi^0$ data produced in pp interactions from NA24, E706, and CCOR. The NA24 and CCOR data are the same as in Figure 8.5; the E706 data has the kinematic requirements used in Figure 8.4. The LO theory is described in the text; the theory in the top plot has $\langle k_T \rangle = 0$ GeV/c, the theory in the bottom plot has $\langle k_T \rangle$ as described in the text. 237

8.7 Comparison between the $\pi^0\pi^0$ cross section measured by E706 and the $\pi^+\pi^-$ cross section measured by E711 in pBe interactions at 800 GeV/c. For this comparison, the E711 kinematic requirements were placed on the E706 data. The E711 charged dipion cross section was reduced by a factor of two to account for the difference in the final states. 239

8.8 The dipion $p_T{}^{\pi^0}$ distribution produced by 800 GeV/c protons incident on beryllium. There are two entries per pair. The results of corresponding LO theory calculations [11] for several choices of scale are also shown. . 241

8.9 The dipion $p_T^{\pi^0}$ distribution produced by interactions of various beams on beryllium. There are two entries per pair. The results of corresponding LO theory calculations [11] are also shown. 242

8.10 The dipion $p_T^{\pi^0}$ distribution produced by interactions of various beams on hydrogen. There are two entries per pair. The results of corresponding LO theory calculations [11] are also shown. 243

8.11 Dipion distributions in $\cos\theta^\star$ for the 515 GeV/c π^-Be data (M > 7.5 GeV/c) and the 530 GeV/c pBe data (M > 7.0 GeV/c). The parameterization refers to Equation 1.9 (dashed curve); the data was normalized at $\cos\theta^\star = 0$ using this function. Also overlayed are the results from the LO theory calculation [11] (solid curve). 245

8.12 The dipion rapidity distribution in several mass bins produced by 530 GeV/c protons incident on beryllium. Additional requirements on the combinations contributing to this distribution are summarized at the beginning of Chapter 8. The results of corresponding LO theory calculations [11] are also shown. 246

8.13 Average values of $\Delta\phi$ as a function of mass for $\pi^0\pi^0$ pairs. Curves from the LO theory [11] are overlayed on the data. 248

8.14 The dipion $\Delta\phi$ distribution produced by interactions of various beams on beryllium. The results of corresponding LO theory calculations [11] are also shown. 249

8.15 The dipion $\Delta\phi$ distribution produced by interactions of various beams on hydrogen. The results of corresponding LO theory calculations [11] are also shown. 251

8.16 Average values of selected kinematic quantities as functions of mass for $\pi^0\pi^0$ pairs produced by pBe interactions at 800 GeV/c. Curves from the LO theory [11] are overlayed on the data. 252

8.17 The dipion p_{OUT} distribution produced by interactions of various beams on beryllium. There are two entries per pair. The results of corresponding LO theory calculations [11] are also shown. 253

8.18 The dipion p_{IN} distribution produced by interactions of various beams on beryllium. There are two entries per pair. The results of corresponding LO theory calculations [11] are also shown. 254

8.19 The dipion Q_T distribution produced by interactions of various beams on beryllium. The results of corresponding LO theory calculations [11] are also shown. 255

8.20 The dipion z distribution produced by interactions of various beams on beryllium. There are two entries per pair. The results of corresponding LO theory calculations [11] are also shown. 256

8.21 The dipion p_{OUT} distribution produced by interactions of various beams on hydrogen. There are two entries per pair. The results of corresponding LO theory calculations [11] are also shown. 257

8.22 The dipion p_{IN} distribution produced by interactions of various beams on hydrogen. There are two entries per pair. The results of corresponding LO theory calculations [11] are also shown. 258

9.1 Ratio of $\sigma(\eta\pi^0)$ to $\sigma(\pi^0\pi^0)$ as a function of mass. Additional requirements on the combinations contributing to this distribution are summarized at the beginning of Chapter 9. Twice the measured inclusive ratio $\sigma(\eta)/\sigma(\pi^0)$ (Figure 5.12) is presented as an overlay. 260

9.2 Shape comparison in $\Delta\phi$ between $\eta\pi^0$ (points) and $\pi^0\pi^0$ events (histogram). Additional requirements on the combinations contributing to this distribution are summarized at the beginning of Chapter 9. 261

9.3 Shape comparison in p_{OUT} between $\eta\pi^0$ (points) and $\pi^0\pi^0$ events (histogram). There are two entries per pair. Additional requirements on the combinations contributing to this distribution are summarized at the beginning of Chapter 9. 262

9.4 Shape comparison in Q_T between $\eta\pi^0$ (points) and $\pi^0\pi^0$ events (histogram). Additional requirements on the combinations contributing to this distribution are summarized at the beginning of Chapter 9. 263

10.1 The $\gamma\pi^0$ mass distribution produced by 515 GeV/c π^- incident on beryllium. The results of corresponding LO theory calculations [11] for two choices of scale are also shown. 266

10.2 The $\gamma\pi^0$ mass distribution for several different minimum ${p_T}^\gamma$ requirements. The results of corresponding LO theory calculations [11] are also shown. 267

10.3 Pseudo-fragmentation function, $(1/\sigma_\gamma)d\sigma/dz$, where pseudo-z = ${p_T}^{\pi^0}/{p_T}^\gamma$. On the left is a comparison between the data and the results of the LO theory calculation. On the right is a comparison between the same data and the results from a study of charged hadrons in a jet opposite an isolated direct photon from the pBe at 800 GeV/c sample [146]. 269

10.4 Distributions in $\cos\theta^\star$ for the 515 GeV/c π^-Be $\longrightarrow \gamma\pi^0$ data with M > 7.5 GeV/c. Additional requirements on the combinations contributing to this distribution are summarized at the beginning of Chapter 10. The parameterization refers to Equation 1.9 (dashed curve); the data was normalized at $\cos\theta^\star = 0$ using this function. The dipion result from Figure 8.11 is shown as the dotted curve. Also overlayed are the results from the LO theory calculation [11] (solid curve). 271

10.5 The $\gamma\pi^0$ rapidity distribution in three mass bins produced by 515 GeV/c π^- incident on beryllium. Additional requirements on the combinations contributing to this distribution are summarized at the beginning of Chapter 10. The results of corresponding LO theory calculations [11] are also shown. 272

10.6 Average values of selected kinematic quantities as functions of mass for $\gamma\pi^0$ events. Additional requirements on the combinations contributing to this distribution are summarized at the beginning of Chapter 10. Curves from the LO theory are overlayed on the data. 275

10.7 The $\gamma\pi^0$ $\Delta\phi$ distribution produced by 515 GeV/c π^- incident on beryllium. The results of corresponding LO theory calculations [11] are also shown. 276

10.8 The $\gamma\pi^0$ p_{OUT} distribution produced by 515 GeV/c π^- incident on beryllium. There are two entries per pair. The results of corresponding LO theory calculations [11] are also shown. 277

10.9 The $\gamma\pi^0$ Q_T distribution produced by 515 GeV/c π^- incident on beryllium. The results of corresponding LO theory calculations [11] are also shown. 278

11.1 The diphoton mass distribution produced by 515 GeV/c π^- incident on beryllium. Overlayed on the data are the results from NLO [149] (dashed) and resummed [150] (solid) calculations. 280

11.2 The diphoton p_T^γ distribution produced by 515 GeV/c π^- incident on beryllium. There are two entries per pair. Overlayed on the data are the results from NLO [149] (dashed) and resummed [150] (solid) calculations. 281

11.3 The diphoton $\Delta\phi$ distribution produced by 515 GeV/c π^- incident on beryllium. Overlayed on the data are the results from NLO [149] (dashed) and resummed [150] (solid) calculations. `PYTHIA` [121] results (dotted) with $\langle k_T \rangle = 1.1$ GeV/c are also shown. 283

11.4 The diphoton p_{OUT} distribution produced by 515 GeV/c π^- incident on beryllium. There are two entries per pair. Overlayed on the data are the results from NLO [149] (dashed) and resummed [150] (solid) calculations. `PYTHIA` [121] results (dotted) with $\langle k_T \rangle = 1.1$ GeV/c are also shown. (The dip at $p_{OUT} = 0$ GeV/c is an artifact of `RESBOS` and is not intentional.) 284

11.5 The diphoton Q_T distribution produced by 515 GeV/c π^- incident on beryllium. Overlayed on the data are the results from NLO [149] (dashed) and resummed [150] (solid) calculations. `PYTHIA` [121] results (dotted) with $\langle k_T \rangle = 1.1$ GeV/c are also shown. 285

11.6 The diphoton z distribution produced by 515 GeV/c π^- incident on beryllium. There are two entries per pair. Overlayed on the data are the results from NLO [149] (dashed) and resummed [150] (solid) calculations. `PYTHIA` [121] results (dotted) with $\langle k_T \rangle = 1.1$ GeV/c are also shown. .. 286

11.7 Distributions in $\cos\theta^\star$ for the 515 GeV/c π^-Be $\longrightarrow \gamma\gamma$ data with M > 9.5 GeV/c. Additional requirements on the combinations contributing to this distribution are summarized at the beginning of Chapter 11. The parameterization refers to Equation 1.9 (dashed curve); the data was normalized at $\cos\theta^\star = 0$ using this function. The parameterization of the dipion result from Figure 8.11 is shown as the dotted curve. Also overlayed are the results from the resummed theory calculation [150] (solid curve). 288

12.1 Comparison between proton-induced direct-photon data and NLO pQCD calculations for several experiments as a function of photon x_T. 290

12.2 Comparison between π^- induced direct-photon data and NLO pQCD calculations for several experiments as a function of photon x_T. 291

12.3 $\langle Q_T \rangle$ of pairs of muons, photons, and jets produced in hadronic collisions versus $\sqrt{s}$. The data point from Chapter 11 has been included on this plot. 292

12.4 Diphoton $\Delta\phi$, p_{OUT}, Q_T, and z distributions produced by 515 GeV/c π^- incident on beryllium. The p_{OUT} and z distributions have two entries per pair. Overlayed on the data are the results from NLO [149] (dashed) and resummed [150] (solid) calculations. PYTHIA [121] results (dotted) with $\langle k_T \rangle = 1.1$ GeV/c are also shown. 294

12.5 p_{OUT} distributions for $\gamma\gamma$, $\pi^0\pi^0$, $\gamma\pi^0$, and $\eta\pi^0$ produced by 515 GeV/c π^- incident on beryllium. There are two entries per pair. Overlayed on the diphoton data are the results from NLO [149] and resummed [150] pQCD calculations. PYTHIA [121] results with $\langle k_T \rangle = 1.1$ GeV/c are also shown. Overlayed on the $\pi^0\pi^0$ and $\gamma\pi^0$ are the results from LO pQCD calculations [11] for various values of $\langle k_T \rangle$ and fixed $\langle q_T \rangle = 0.6$ GeV/c. The $\pi^0\pi^0$ data has been overlayed on the $\eta\pi^0$ data for comparison. ... 295

12.6 Charged D meson production for 515 GeV/c π^-N interactions as a function of the p_T of the charged D. Overlayed are the results of NLO calculations with and without k_T [158]. 297

12.7 Top: The photon and π^0 cross sections at $\sqrt{s} = 31.1$ GeV compared to the k_T-enhanced NLO calculations. Bottom: The quantity (Data - Theory)/Theory for direct-photon production. 298

12.8 Comparison between a threshold resummed and a NLO theory calculation for direct-photon production for two scale choices: $p_T/2$ and $2p_T$ [164]. The threshold resummed theory exhibits a smaller dependence on scale than the NLO calculation and corresponds to the NLO theory with $\mu = p_T/2$. 299

12.9 The variation of k_T enhancements, $K(p_T)$, for the 530 GeV/c pBe data. 300

12.10 Invariant differential cross sections per nucleon for direct-photon and π^0 production in π^-Be and π^+Be interactions at 515 GeV/c and pBe interactions at 530 GeV/c and 800 GeV/c. Cross sections are shown as a function of p_T averaged over the full rapidity range. Overlayed on the data are the results of the NLO calculation with k_T enhancements for several values of $\langle k_T \rangle$. 301

12.11 Isolated direct-photon cross sections from CDF and DØ at $\sqrt{s} = 1.8$ TeV. Overlayed on the data are the results of the NLO calculations with (solid) and without (dashed) k_T enhancements for $\langle k_T \rangle = 3.5$ GeV/c. 303

12.12 Preliminary, isolated direct-photon cross section for CDF at $\sqrt{s} = 630$ GeV [168]. Overlayed on the data are the results of the NLO calculations with (solid) and without (dashed) k_T enhancements for $\langle k_T \rangle = 2.5$ GeV/c. 304

12.13 Invariant cross sections for direct-photon and π^0 production from WA70 (top) and UA6 (bottom). Overlayed on the data are the results of the NLO calculation with k_T enhancements for several values of $\langle k_T \rangle$. 305

Chapter 1 Introduction

1.1 Standard Model

> *In any subject which has principles, causes, and elements, scientific knowledge and understanding stems from a grasp of these, for we think we know a thing only when we have grasped its first causes and principles and have traced it back to its elements.*
>
> *Aristotle*
> Physics

For more than two millenia two conflicting models were used to explain most phenomena. One was an atomic theory where fundamental particles interacted in reaction to specific forces [3]. The other consisted of four general constituents that reacted according to certain fundamental laws of nature [4]. In the first theory, the universe consisted of tiny, indestructible, indivisible, pieces of matter that interacted in a fathomless void. The second theory, which arose separately in Greece, India, and China, considered everything in the universe to be created from, and resolved into, four elements: Earth, Water, Air, and Fire. Both theories were sufficient to describe, in rational terms, all observed phenomena.

Over the course of the past few centuries [5], particularly during the last three decades [6], a different model of nature has arisen. The Standard Model is a blend of experimental observations supported by a theoretical framework that describes the universe in terms of four fundamental forces and numerous fundamental particles. Many excellent reviews of the Standard Model exist [7, 8, 9]; a brief synopsis follows.

The four forces are Gravity, Strong, Weak, and Electromagnetic (Table 1.1). Gravity[1] binds together gross matter in the universe; it is very weak and has

[1] Gravity is not typically considered in Standard Model calculations.

a negligible effect on nuclear and sub-nuclear particles. The strong force acts at very short distances; it binds quarks together to make nucleons and binds nucleons together to make nuclei. The weak force is responsible for nuclear decays; it plays a critical role in the generation of energy in the sun and in the synthesis of heavy elements. The electromagnetic force provides the attraction between electrons and nuclei that build atoms and molecules. These forces are mediated by the exchange of particles called gauge bosons (Table 1.2).

There are two other classes of particles, both fermions, in the Standard Model: leptons (Table 1.3), and quarks (Table 1.4). For each lepton and quark there is a corresponding anti-lepton and anti-quark with opposite quantum numbers (electrical charge of -1 goes to $+1$, red color goes to anti-red, etc). There are six leptons, organized into three generations. Each generation consists of a massive charged particle and a nearly massless neutrino. Similarly, there are six flavors of quarks that are also organized into three generations. Bound states of quarks are called hadrons. There are two types of hadrons: mesons, which contain a quark–anti-quark combination, and baryons, which contain three quarks. For example, a π^+ meson is $u\bar{d}$, a proton is uud, and a neutron is udd, where u and d are the two first generation quarks.

The theory that describes the interaction of quarks and gluons (collectively called partons) is Quantum Chromodynamics (QCD), which takes its name from the color charge associated with the strong force. Since both quarks and gluons have color, strong interactions are qualitatively different in character than electromagnetic interactions. Gluons can couple to gluons while photons cannot couple to photons. The strength of the strong coupling constant, α_s, depends on the distance between the interacting particles. The potential energy required to separate two quarks increases with the distance between them until there is

Interaction	Mediating Bosons	Source	Impacts
Gravitational	gravitons	Mass/Energy	everything
Strong	gluons	Color	quarks, gluons
Weak	W^+, W^-, Z	Flavor	quarks, leptons
Electromagnetic	photons	Electric charge	electrically charged

Table 1.1 Fundamental forces in the Standard Model and their mediating bosons.

Mediating Boson	Mass (GeV/c^2)	Electric Charge	Color
graviton	0	0	no
gluon	0	0	yes
W^-	80.4	-1	no
W^+	80.4	$+1$	no
Z	91.1	0	no
γ	0	0	no

Table 1.2 Properties of mediating bosons in the Standard Model [10].

Lepton	Symbol	Mass (GeV/c^2)	Electric Charge
electron	e	0.000511	-1
electron neutrino	ν_e	$< 1 \times 10^{-8}$	0
muon	μ	0.106	-1
muon neutrino	ν_μ	< 0.0002	0
tau	τ	1.78	-1
tau neutrino	ν_τ	< 0.02	0

Table 1.3 Leptons in the Standard Model with their masses and charges [10]. Neutrinos are regarded as massless in Standard Model calculations. The ν_τ has not yet been experimentally detected.

Quark	Symbol	Mass (GeV/c^2)	Electric Charge
down	d	0.003	$-1/3$
up	u	0.003	$+2/3$
strange	s	0.1	$-1/3$
charm	c	1.3	$+2/3$
bottom	b	4.3	$-1/3$
top	t	175	$+2/3$

Table 1.4 Quarks in the Standard Model, with their masses and charges [10].

sufficient energy to produce a quark–anti-quark pair. So, the effect of injecting energy into a hadron is not simply to separate the quarks, but to create new hadrons. The "harder" the probe used to study the hadron, the more influence gluons and virtual quark–anti-quark pairs have on the measurement. The bound state quarks ($q\bar{q}$ and qqq) are referred to as *valence* quarks, while the others are referred to as *sea* quarks. Hadrons are observed to be colorless; this is referred to as color confinement in QCD [7].

Exact QCD calculations that describe experimentally measurable quantities have not yet been achieved. Instead, approximate calculations are performed using perturbation theory (pQCD) with expansions in the strong coupling constant, α_s. In terms of the momentum transferred between two partons (Q^2), α_s can be defined as

$$\alpha_s(Q^2) = \frac{12\pi}{(33 - 2n_f)\ln(Q^2/\Lambda)}, \tag{1.1}$$

where n_f is the number of flavors. The characteristic scale, Λ, is on the order of several hundred MeV. This expression is presented in the leading log approximation where the expansion has been summed to all orders, retaining only terms containing the leading-order logarithm [11]. Equation 1.1 illustrates another concept associated with QCD, asymptotic freedom. As $Q^2 \to \infty$ (distance$\to 0$), $\alpha_s \to 0$. Asymptotic freedom justifies the use of perturbative calculations in the high-Q^2 regime.

1.2 Hard Scatters

One method for investigating certain fundamental aspects of nature is to collide particles together and observe what comes out. By carefully studying the kinematic distributions of the outgoing objects, we can draw conclusions about

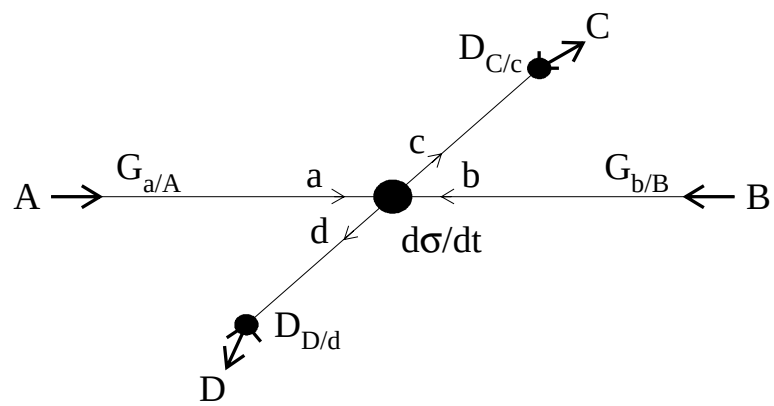

Figure 1.1 Schematic diagram of a two-body reaction, $A + B \longrightarrow C + D$, which has been factorized according to the prescriptions of pQCD. Here a is a parton from hadron A with distribution $G_{a/A}(x_a, Q^2)$. Similarly for parton b. Partons a and b interact to form partons c and d via the hard-scattering process $d\hat{\sigma}/dt(a + b \longrightarrow c + d)$. Parton c fragments into particle C with probability $D_{C/c}(z_c, Q^2)$. Similarly for parton d.

the internal dynamics that produced them. Such an approach led to the discovery that the atom has a small nucleus [12] and to the discovery that the proton was composed of partons [13, 14].

1.2.1 Factorization

A schematic diagram for a large transverse momentum reaction in the parton model, $A+B \longrightarrow C+D$, is presented in Figure 1.1 [15]. In this $2 \rightarrow 2$ hard scatter, parton a from hadron A interacts with parton b from hadron B to form partons c and d. The interaction has been *factorized*, that is, the long distance aspects have been separated from the short distance aspects [16]. The long distance aspects are considered independent of the underlying hard-scattering process, described by $d\hat{\sigma}/dt$, and are assumed to be universal properties of the hadrons. The long

distance aspects of the collision are described by the parton distribution function (PDF) and the fragmentation function.

The PDF, designated by $G_{a/A}(x_a, Q^2)$ (Figure 1.2), is the probability of finding parton a in hadron A with a fraction x_a of the hadron's momentum. The PDFs within pQCD represent the non-perturbative pieces of the cross section (small Q^2). The scale distinguishing between the perturbative and non-perturbative pieces is μ; physics with scales $\ll 1/\mu$ are not included in the perturbative calculation. The physical cross section cannot depend upon the choice of scale so a pQCD calculation is considered stable if its results are stable for large changes in μ. Typically, μ is related to an experimental observable such as the transverse momentum of an outgoing particle, the mass of the pair of outgoing particles, or the total center-of-mass energy available in the reaction. PDFs are different for each type of parton and for each type of hadron (Figure 1.2). They are extracted via global analyses of many different experimental observations [16].

Outgoing partons undergo the process of *hadronization* in which gluons and quark–anti-quark pairs are pulled out of the vacuum and combined to form colorless outgoing particles. The probability of finding a given hadron C with a fraction z_c of the original parton's longitudinal momentum is given by $D_{C/c}(z_c, Q^2)$ (Figure 1.3). This fragmentation function also has a scale associated with it, μ_F, which typically is related to the transverse momentum of hadron C.

The short-distance aspect of the hard-scattering process is represented by the perturbative cross section, $d\hat{\sigma}/dt$. It is calculated within pQCD up to some order in α_s. Leading order (LO) and next-to-leading order (NLO) pQCD calculations are available for most processes. Higher order pQCD calculations are rare.

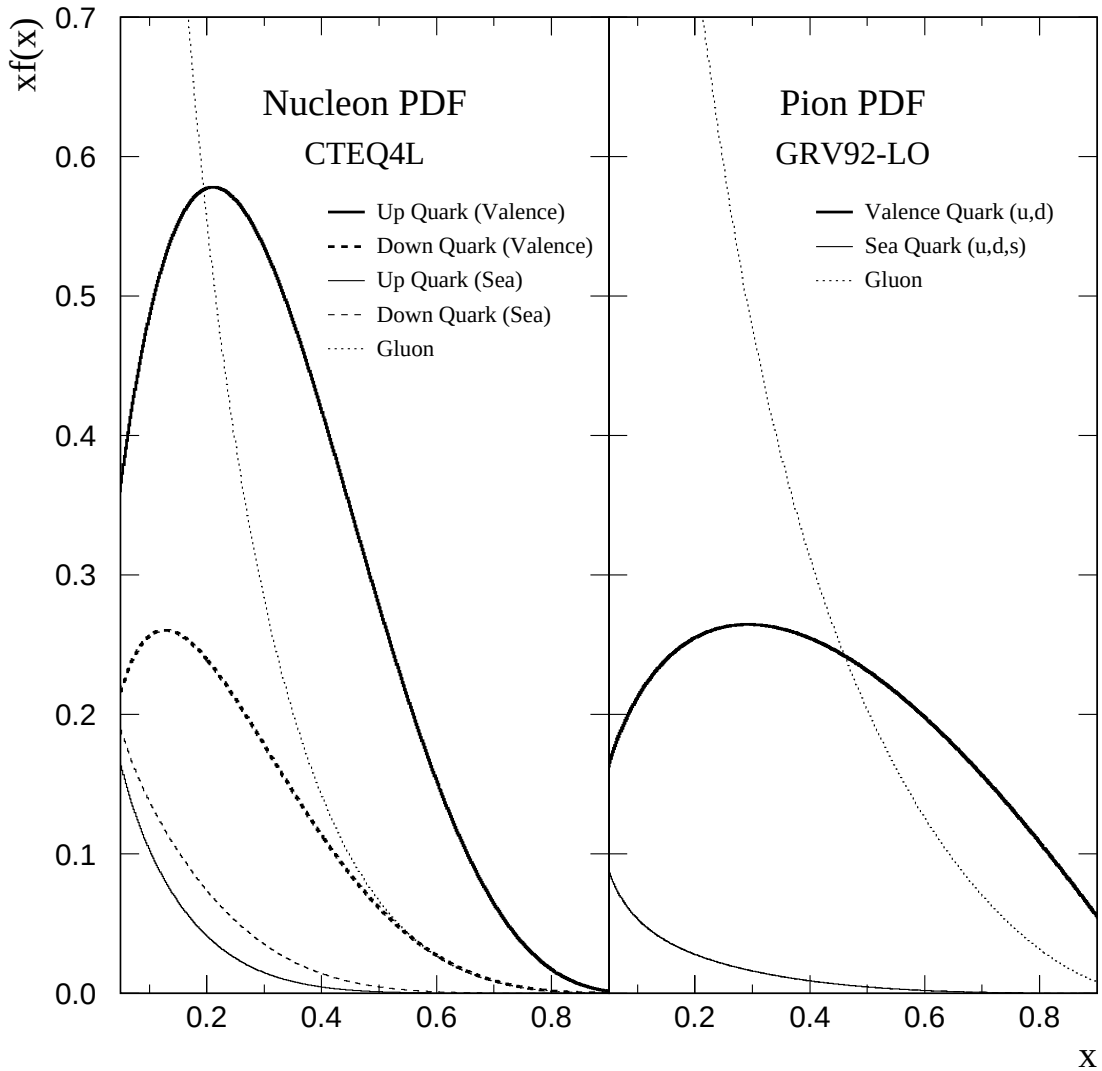

Figure 1.2 Two parton distribution functions used in this analysis, CTEQ4L [17] and GRV92LO [18]. They were calculated using `PDFLIB` [19] at $Q^2 = 10$ GeV^2.

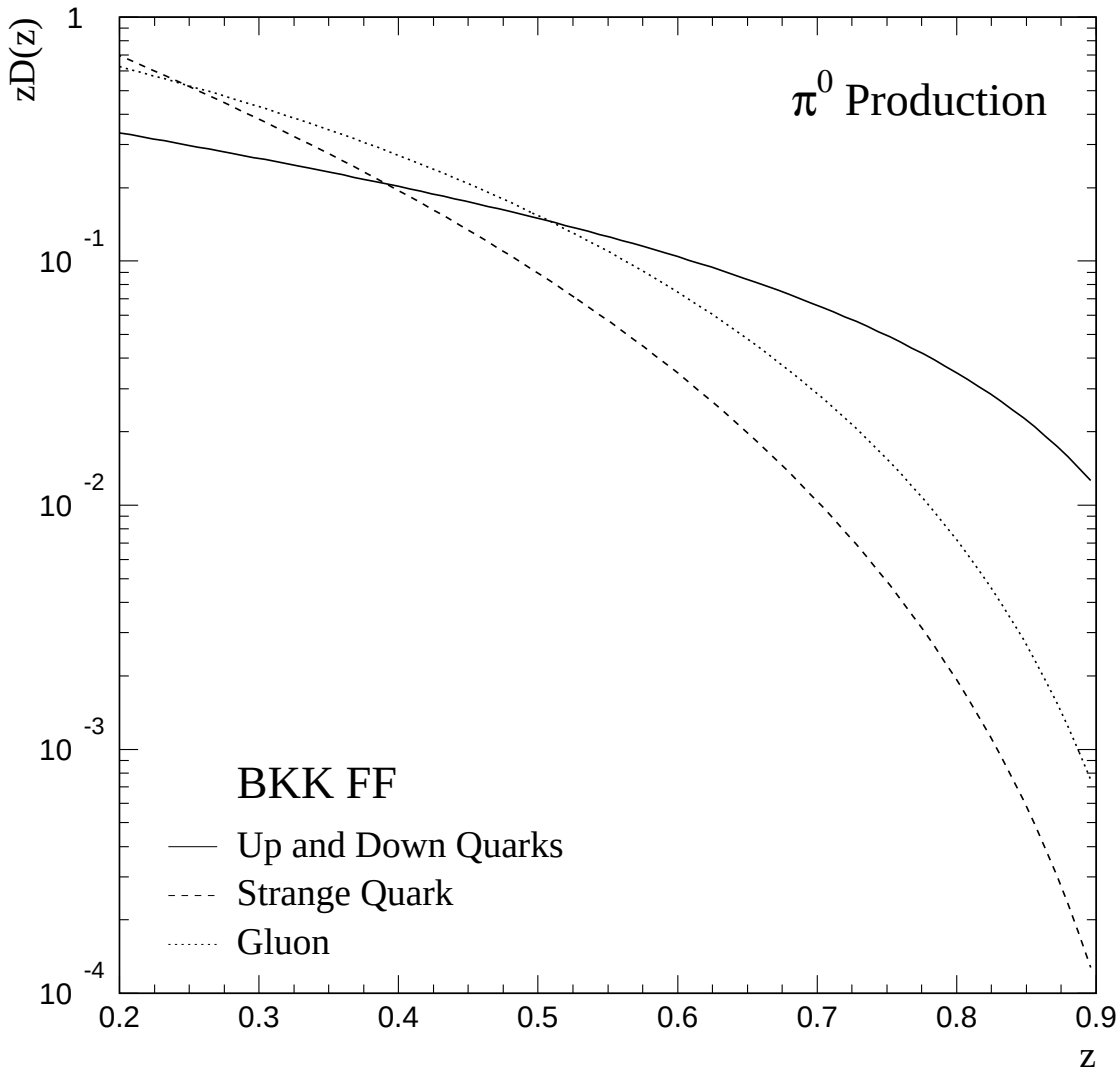

Figure 1.3 Probability that a given parton will fragment into a π^0 as a function of the momentum fraction, z, of the π^0. These leading-order fragmentation functions [20] were evaluated at $Q^2 = 10$ GeV^2.

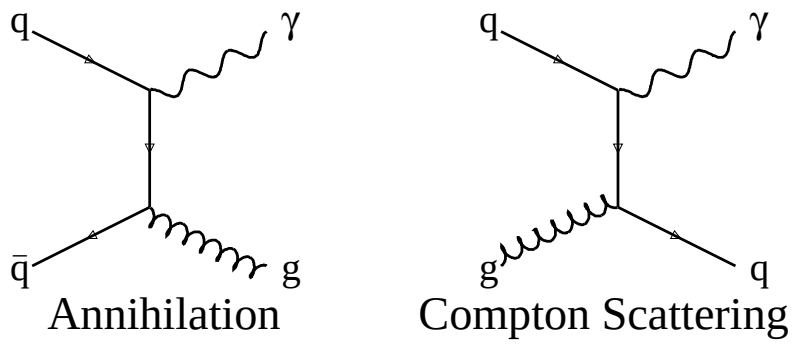

Figure 1.4 The lowest order diagrams for direct-photon production.

1.2.2 Direct Photons

Direct photons are photons produced in the hard scatter that are not the decay products of other particles. Processes that give rise to direct photons are summarized in Table 1.5 [21]. At leading order in α_s, direct photons are produced through quark–anti-quark annihilation and quark–gluon Compton scattering (Figure 1.4). Unlike colored objects such as quarks and gluons, these photons emerge unaltered from the hard scatter, and therefore provide valuable information about the hard scatter. This is not the case for *jets*, collimated collections of particles arising from the fragmentation of quarks and gluons, since is it generally not possible to precisely and unambiguously define all the remnants of a single quark or gluon.

Since, at leading order, direct-photon production via Compton scattering has a gluon in the initial-state, direct photons can be used to measure the gluon distribution function of hadrons [16]. Direct photons can also be produced with

Description	Order	Subprocess
annihilation	$\alpha_{\mathrm{em}}\alpha_{\mathrm{s}}$	$\mathrm{q\bar{q}} \to \gamma\mathrm{g}$
Compton	$\alpha_{\mathrm{em}}\alpha_{\mathrm{s}}$	$\mathrm{qg} \to \gamma\mathrm{q}$
single bremsstrahlung	$\alpha_{\mathrm{em}}\alpha_{\mathrm{s}}^2$	$\mathrm{qq} \to \mathrm{q}(\mathrm{q} \to \gamma)$
		$\mathrm{gq} \to \mathrm{g}(\mathrm{q} \to \gamma)$
		$\mathrm{qg} \to \mathrm{q}(\mathrm{g} \to \gamma)$
		$\mathrm{gg} \to \mathrm{g}(\mathrm{g} \to \gamma)$
QCD-induced $\mathrm{g}\gamma$ coupling	$\alpha_{\mathrm{em}}\alpha_{\mathrm{s}}^3$	$\mathrm{gg} \to \gamma\mathrm{g}$
QED annihilation	α_{em}^2	$\mathrm{q\bar{q}} \to \gamma\gamma$
single bremsstrahlung	$\alpha_{\mathrm{em}}^2\alpha_{\mathrm{s}}$	$\mathrm{qg} \to \gamma(\mathrm{q} \to \gamma)$
double bremsstrahlung	$\alpha_{\mathrm{em}}^2\alpha_{\mathrm{s}}^2$	$\mathrm{qq} \to (\mathrm{q} \to \gamma)(\mathrm{q} \to \gamma)$
		$\mathrm{gq} \to (\mathrm{g} \to \gamma)(\mathrm{q} \to \gamma)$
		$\mathrm{gg} \to (\mathrm{g} \to \gamma)(\mathrm{g} \to \gamma)$
Quark Box	$\alpha_{\mathrm{em}}^2\alpha_{\mathrm{s}}^2$	$\mathrm{gg} \to \gamma\gamma$

Table 1.5 The order in α_{s} and α_{em} of the various subprocesses contributing to the production of single and double direct photons in hadron–hadron collisions [21].

a gluon in the final state via the annihilation process. Consequently, direct photons can be used to examine differences between gluon and quark jets [11]. By comparing production rates from different incident hadrons, specific information about the hard scatter can be extracted. For example, most direct photons measured in pN interactions are produced (at leading order) via the Compton scattering diagram (Figure 1.5), so this data is particularly useful for extracting information about the gluon distribution. High transverse momentum direct photons produced in π^-N interactions are better suited to measuring the gluon fragmentation function since they typically are produced by the annihilation diagram. Differences in production rates between π^-N and π^+N, and between pp and p$\bar{\text{p}}$ can be used to study individual subprocesses [22].

Occasionally two direct photons can be produced in the hard scatter (Table 1.5). At lowest order these photons are produced in quark–anti-quark annihilation (Figure 1.6) with a production rate $\approx 1\%$ of that for single direct photons. One higher order diagram that can contribute a significant portion of the cross section [21] is the quark box diagram shown in Figure 1.6. Double direct-photon production is an inherently "cleaner" process than single direct-photon production since there are no outgoing jets produced in the $2 \rightarrow 2$ hard scatter. A measurement of the 4-vectors for each of the two photons fixes the kinematics of the hard scatter and provides a superior probe into the underlying physics of the interaction. As there are no factors of α_{s} in the lowest order diphoton subprocess, a comparison of double direct-photon production to single direct-photon production (Equation 1.2) can be used to study α_{s} and extract information about the charges of the quarks [22].

$$\frac{\text{E}d^3\sigma/dp^3(\pi^- \longrightarrow \gamma\gamma + \text{X})}{\text{E}d^3\sigma/dp^3(\pi^- \longrightarrow \gamma + \text{X})} = \frac{3}{4}\,\frac{\alpha_{\text{em}}}{\alpha_{\text{s}}}\,\text{e}_{\text{u}}^2 = \frac{1}{3}\,\frac{\alpha_{\text{em}}}{\alpha_{\text{s}}} \tag{1.2}$$

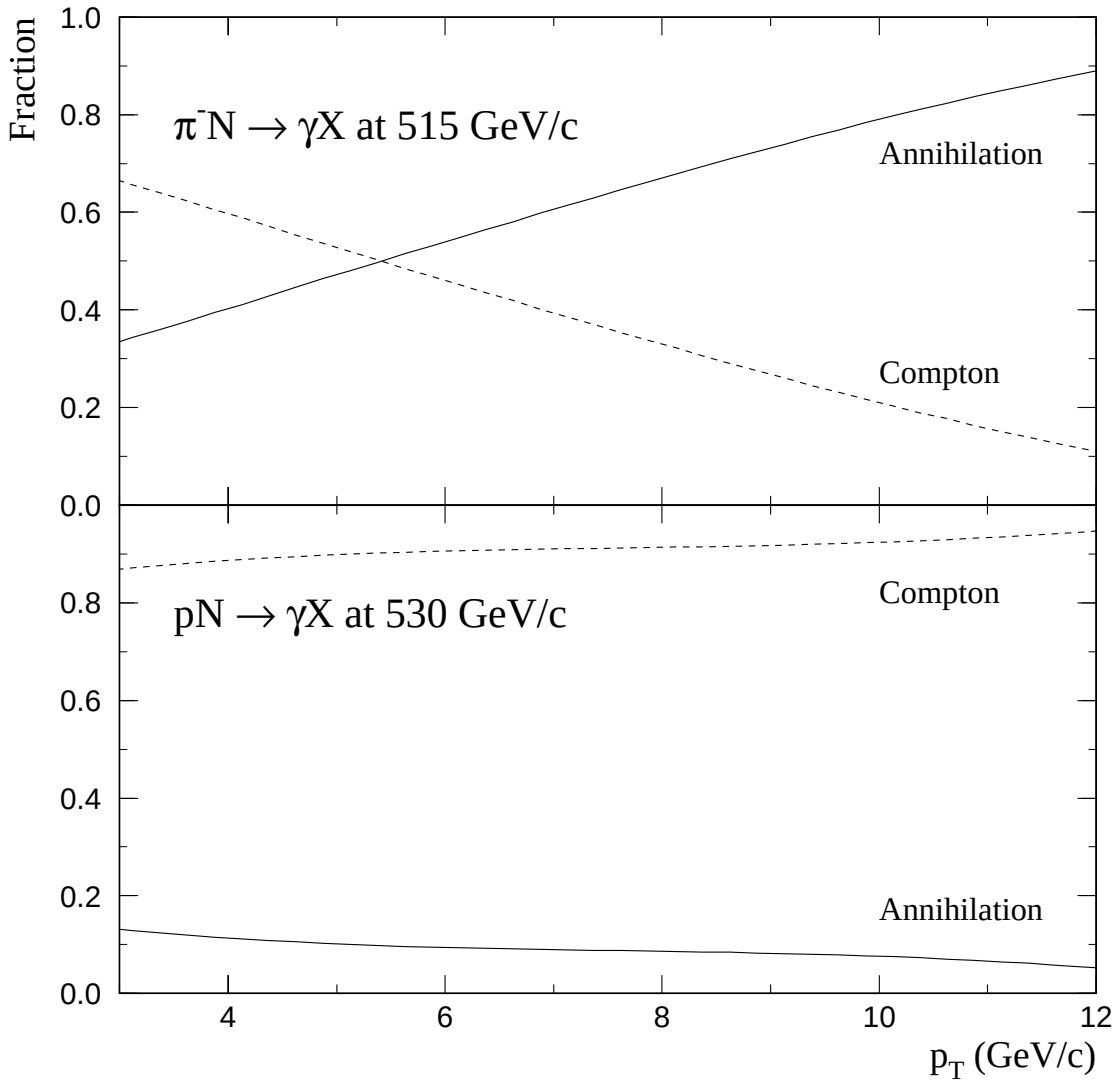

Figure 1.5 The fractional contribution of the leading-order diagrams for the inclusive production of direct photons calculated using LO pQCD [11].

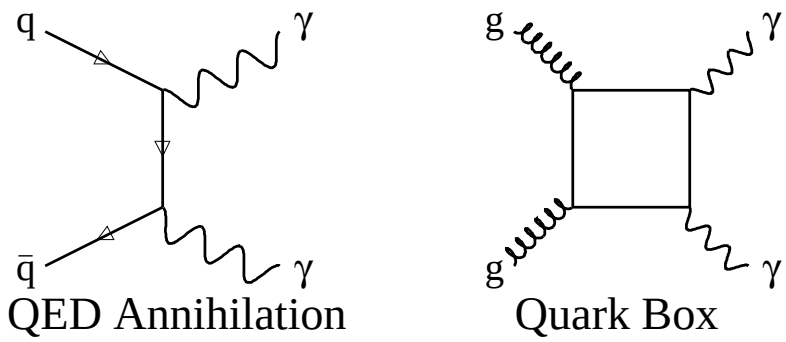

Figure 1.6 Two important diagrams for the production of two direct photons.

1.2.3 Kinematics

At the parton level, the collision in Figure 1.1 is a simple $2 \rightarrow 2$ process with well-defined initial and final states. A complete kinematical description is provided by the Mandelstam invariants s, t, and u [7]. The Mandelstam variables corresponding to the interacting partons are denoted by $\hat{s}$, $\hat{t}$, and $\hat{u}$, while those corresponding to the hadrons are denoted by s, t, and u. These variables are defined in terms of the incoming and outgoing parton 4-vectors as follows:

$$\hat{s} = (p_a + p_b)^2 \qquad \hat{t} = (p_a - p_c)^2 \qquad \hat{u} = (p_a - p_d)^2 \tag{1.3}$$

For the hadron states, the Mandelstam variables are defined as:

$$s = (p_A + p_B)^2 \qquad t = (p_A - p_C)^2 \qquad u = (p_A - p_D)^2 \tag{1.4}$$

The variable s is simply the square of the center-of-mass energy, while t and u are the squares of the 4-momentum transfers from partons a and b to c and d,

respectively. The Mandelstam variables obey the sum rule

$$\hat{s} + \hat{t} + \hat{u} = \sum_i m_i^2, \tag{1.5}$$

where m_i is the mass of the ith particle entering or exiting the interaction. For massless quarks and gluons the sum rule becomes $\hat{s} + \hat{t} + \hat{u} = 0$.

The kinematics of the underlying partonic hard scatter can be related to experimental quantities. In the initial state, parton a carries fraction x_a of hadron A's momentum, and parton b has a momentum fraction x_b. The mass of the outgoing system (M), x_a, x_b, s, and $\hat{s}$ are related by

$$\hat{s} = x_a x_b s = M^2 = (p_c + p_d)^2 . \tag{1.6}$$

Instead of $\hat{s}$ or M, the dimensionless variable τ is generally used in the analysis of Drell-Yan pairs[2] where $\tau = \hat{s}/s = x_a x_b = M^2/s$.

The transverse and longitudinal momentum components of a particle with respect to the interaction axis are denoted by p_T and p_z, respectively. Occasionally, these variables are expressed as dimensionless variables x_T and x_F with $x_T = 2p_T/\sqrt{s}$ and $x_F = 2p_z/\sqrt{s}$. Another important variable is rapidity, y, defined as

$$y = \frac{1}{2} \ln \frac{E + p_z}{E - p_z}. \tag{1.7}$$

The shape of the rapidity spectrum is invariant under Lorentz boosts in the z-direction. The rapidity of a pair of particles is denoted by Y. When evaluated for a massless particle, y reduces to $\ln \cot \theta/2$, where θ is the center-of-mass scattering angle. For a massive particle, the quantity $\ln \cot \theta/2$ is called the pseudorapidity and is denoted by η. In the parton–parton center of momentum frame, where

[2] Drell-Yan production refers to the direct production of lepton pairs in hadronic collisions.

the outgoing particles are produced back-to-back, the production angle in the parton–parton rest frame ($\theta^\star$) and in the incident particle frame (θ) are equal. For the case where c and d are both photons, the cross section in Figure 1.1 can be expressed as [11]

$$\frac{d\sigma}{dx_a dx_b d\cos\theta^\star} = \frac{x_a x_b s}{2} \sum_{ab} G_{a/A} G_{b/B} \frac{d\sigma}{d\hat{t}} (ab \to \gamma\gamma) . \tag{1.8}$$

The angular distribution can be parameterized as [11]

$$\frac{d\sigma}{d\cos\theta^\star} \Big/ \frac{d\sigma}{d\cos\theta^\star}\Big|_{\cos\theta^\star=0} = \frac{1}{2}\left[\frac{1}{(1+\cos\theta^\star)^\alpha} + \frac{1}{(1-\cos\theta^\star)^\alpha}\right] . \tag{1.9}$$

Since the $\cos\theta^\star$ distribution is a weighted average of all available subprocesses, the parameter α depends on the parton distribution functions that contribute to the reaction, and to the strong coupling constant. For example, $\alpha = 2.02$ for $gg \to gg$, 2.15 for $gq \to gq$, 2.6 for $qq \to qq$, and 0.9 for $gq \to \gamma q$ in a LO pQCD theory calculation [11].

Assuming the incident system has no net p_T, then the 4-vectors for partons a and b can be expressed as

$$p_a = \frac{x_a\sqrt{s}}{2}(1,0,0,1) \qquad p_b = \frac{x_b\sqrt{s}}{2}(1,0,0,1) \tag{1.10}$$

where the positive z axis is taken to be along the direction of the incident hadron A. If the scattered parton c has transverse momentum p_T and rapidity y_c, then its 4-vector is just $p_c = p_T(\cosh y_c, 1, 0, \sinh y_c)$. The Mandelstam variables $\hat{t}$ and $\hat{u}$ can be expressed as $\hat{t} = -x_a p_T\sqrt{s}\, e^{-y_c}$ and $\hat{u} = -x_b p_T\sqrt{s}\, e^{y_c}$. In terms of the rapidity and p_T of the outgoing partons, x_a and x_b can be expressed as

$$x_a = \frac{p_T}{\sqrt{s}}\left(e^{y_c} + e^{y_d}\right) , \tag{1.11}$$

and,

$$x_b = \frac{p_T}{\sqrt{s}}\left(e^{-y_c} + e^{-y_d}\right) . \tag{1.12}$$

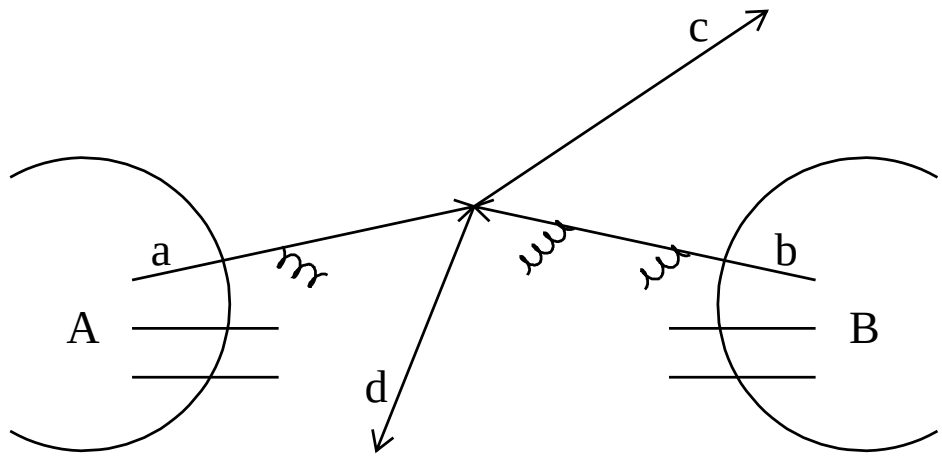

Figure 1.7 Cartoon illustrating the impact of multiple soft-gluon emission in the hard scatter of two partons. Partons a and b (from hadrons A and B respectively), emit soft-gluons prior to the hard scatter which produces particles c and d. This gives rise to a p_T imbalance between the outgoing particles.

1.2.4 Parton Transverse Momentum

Correlations between high-p_T particles probe aspects of the hard scatter not easily accessible via studies of single inclusive particle production. In particular, studies of high-mass pairs of particles such as direct photons and π^0's can be used to extract information about the transverse momentum of the partons prior to the hard scatter.

In a two-body hard scatter, parton a from hadron A interacts with parton b from hadron B giving rise to particles c and d (Figure 1.1). In the parton–parton center-of-momentum frame, partons a and b are collinear and particles c and d are produced back-to-back with equal p_T. However, in the hadron–hadron center-of-momentum frame the two partons may no longer be collinear; that is, they can

have some transverse momentum, k_T, with respect to each other. As illustrated in Figure 1.7, k_T gives a boost in the direction of one of the outgoing particles.

Such k_T can arise from several sources. For example, there is a primordial k_T due to confinement of the partons of order the hadron size, approximately 300 MeV. The majority of such transverse momentum can, however, be attributed to the emission of multiple soft-gluons by the partons prior to the hard scatter. Whatever the source, any transverse momentum between the partons will appear as a net p_T imbalance among the outgoing particles. To examine this effect, one can look at the total p_T (vector sum) of the outgoing particles, Q_T. If the outgoing particles are photons or leptons, then this variable should provide a good measure of k_T with $\langle k_T \rangle$/parton $\approx \langle Q_T \rangle/\sqrt{2}$. Evidence of significant k_T has long been observed in the production of Drell-Yan and diphoton pairs. A collection of measurements of $\langle Q_T \rangle$ is presented in Figure 1.8 for a wide range of center-of-mass energies ($\sqrt{s}$) [23—29]. When the outgoing particles are partons, they will hadronize and the reconstructed jets should yield a measure of k_T. These dijet k_T measurements (Figure 1.8) agree qualitatively with the dimuon and diphoton results, though they have somewhat higher mean values. This shift is expected since there is also potential for final-state soft-gluon emission in dijet events.

It is often simpler to measure individual parton fragments, in particular, high-p_T hadrons, than to reconstruct entire jets. Nevertheless, studies of dihadron pairs should also provide reasonable measures of k_T. The difficulty with such measurements is that the fragments carry only a fraction, z, of the total p_T of the outgoing partons. Assuming that partons fragment independently, there will always be some $Q_T = |z_C - z_D| p_T$ describing the difference in transverse momentum between any two outgoing particles, even in the absence of k_T. However, since fragmentation functions have been measured in the relatively clean environment

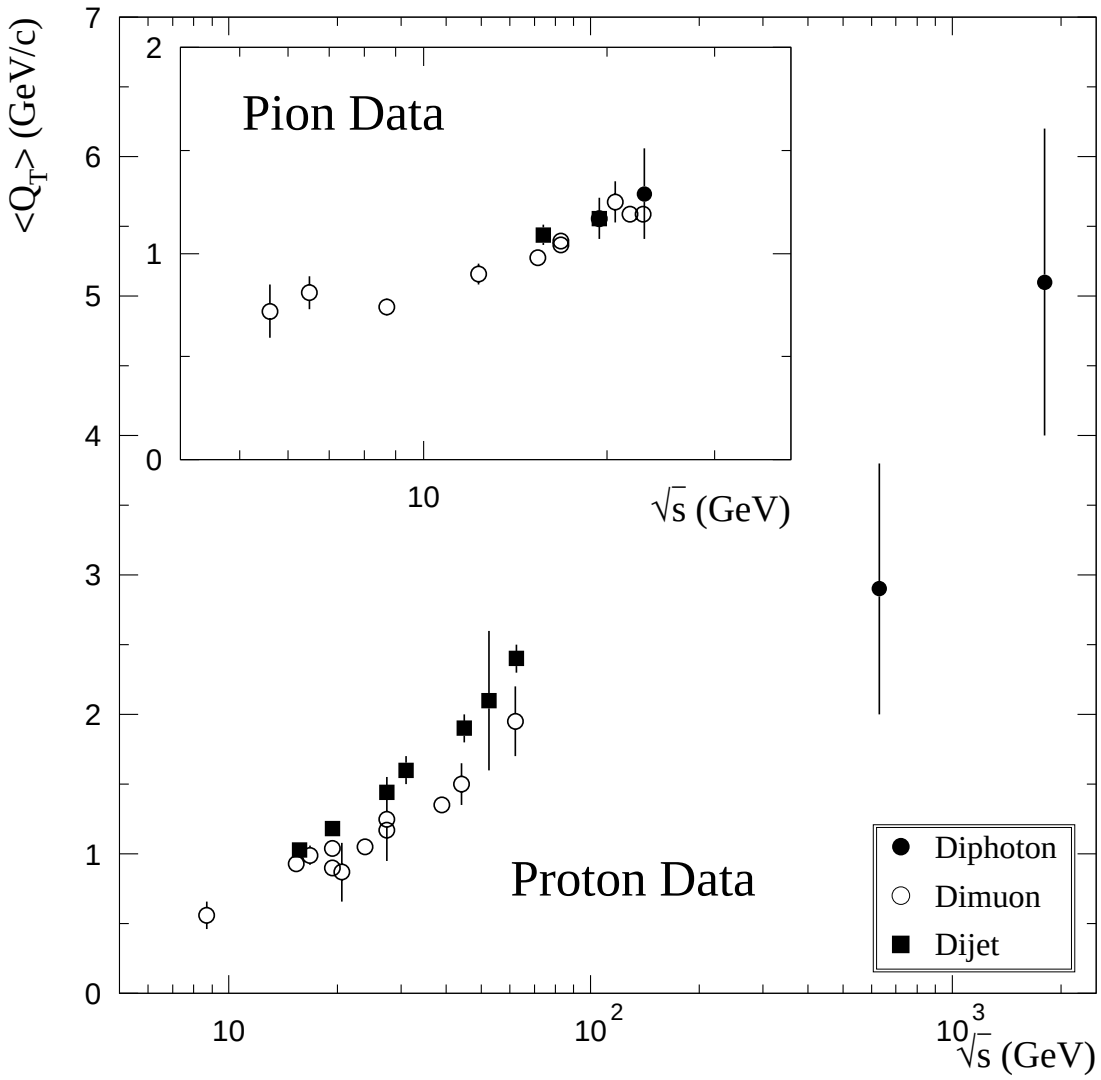

Figure 1.8 Mean transverse momentum, $\langle Q_T \rangle$, of pairs of muons, photons, and jets produced in hadronic collisions versus $\sqrt{s}$.

of e^+e^- colliders [20], this "z–smearing" can be accommodated in the examination of k_T. Another difficulty with individual hadrons is that jet fragments have a small transverse momentum, q_T, with respect to the jet. This issue has been studied by several groups [28, 29]. They have found that, on average, leading particles (high z) have $\langle q_T \rangle \approx 600$ MeV/c with respect to the jet axis. This is in contrast to soft particles (low z) in the jet, which have $\langle q_T \rangle \approx 350$ MeV/c.

The p_T imbalance between the outgoing particles can be examined using kinematic variables other than Q_T. Given a non-zero k_T, the outgoing particles no longer emerge back-to-back; the azimuthal angle between the particles, $\Delta\phi$, will differ from π. This distribution is relatively unbiased with respect to longitudinal fragmentation effects (z–smearing) although it is still sensitive to q_T. Another variable insensitive to z–smearing is the out-of-plane momentum, p_{OUT}. This is the projection of one p_T-vector onto the relative plane formed by the other p_T-vector and the beam axis. There are two such values for any pair of hadrons. These variables are illustrated in Figure 1.9. Additional variables sensitive to z–smearing include the in-plane momentum, p_{IN}, and the p_T-balance between the particles, denoted[3] by z.

$$z = -\frac{\vec{p}_{T1} \bullet \vec{p}_{T2}}{p_{T2}^2} = \frac{p_{T2}}{p_{T1}} \cos \Delta\phi \tag{1.13}$$

Each of these variables has two possible values per pair.

There are also several variables that are insensitive to k_T effects and can therefore be used to study the underlying physics of the hard scatter. Two such variables are the invariant mass of the pair (M), and the particle p_T (one entry per particle) [30]. The angular variables, rapidity and $\cos\theta^\star$, are also sensitive to the production dynamics.

[3] It is unfortunate that the p_T-balance variable and the longitudinal momentum fraction of a hadron in a jet are both denoted by the same variable, z. However, the correct interpretation should be clear from the context.

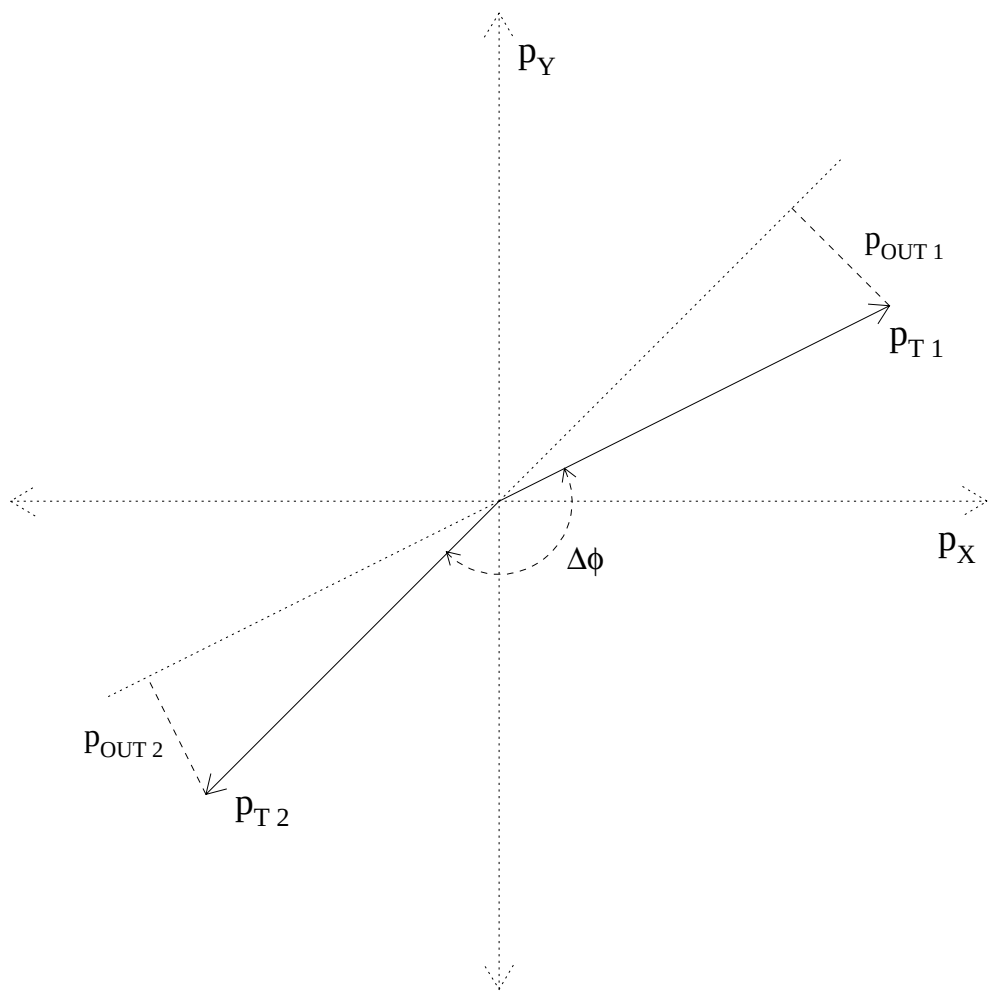

Figure 1.9 An illustration of a two arm configuration in the p_T plane (beam is oriented along the Z-axis). The lengths of the vectors represent their p_T. The angle between the two vectors is $\Delta\phi$. The projection of a p_T-vector onto the plane formed by the other vector and the beam axis yields p_{OUT}.

1.3 Experimental Methods

There are several challenges associated with the measurement of direct-photon production. Due to the difference in the relative strengths of the electromagnetic and strong coupling constants, the cross section for direct-photon production is three orders of magnitude smaller than the cross section for jet production. Consequently, jet constituents that decay electromagnetically can produce significant backgrounds in the direct-photon sample. The decay of π^0 mesons into two photons forms the largest background contribution since π^0's are copiously produced (about one out of three particles in a jet).

There are several general experimental methods employed to measure direct-photon production (Table 1.6). In the direct approach, a calorimeter with good resolution and fine segmentation is used to identify individual photons from a π^0 or η decay. These photons are excluded from the direct-photon sample. This method is used by E706 and several other fixed target experiments. Since not all background photons can be individually identified, a Monte Carlo simulation is used to evaluate the remaining background contributions, which are subtracted statistically from the measured direct-photon signal. The level of this background is traditionally illustrated by a comparison of the single photon yield to the measured π^0 cross section (Figure 1.10).

There are other techniques for separating the direct-photon signal from the background. The first of these is the conversion method. Photons that pass through material can convert into e^+e^- pairs. A π^0 usually decays into two photons, so the conversion probability for the π^0 decay products is greater than for a single photon. The measured conversion fraction in the candidate sample can be used to statistically extract the yield of direct photons. Already existing material

Experiment	Method	Calorimeter
CDF [31]	Shower prof./Conv. + isol.	Pb/Steel–Scintillator
DØ [32]	Conversion +isol.	U–Liquid Argon
E629 [33]	Direct	Pb–Liquid Argon
E704 [34]	Direct + isol.	Pb–Glass
E706 [35]	Direct	Pb–Liquid Argon
NA3 [36, 37]	Direct/Conv.	Pb–Scintillator
NA24 [38, 39]	Direct	Pb–Scintillator
R108 [40]	Conversion	Pb–Glass
R110 [41]	Conv. + Shower prof.	Pb–Glass/Scintillator + MWPC
R806 [42]	Direct	Pb–Liquid Argon
R807/8 [43, 44]	Direct	NaI + U/Cu Scintillator
UA1 [45]	Shower profile + isolation	Pb–Scintillator
UA2 [46]	Conv. + isolation	Pb–Scintillator
UA6 [47]	Direct	Pb–Proportional tubes
WA70 [48]	Direct	Pb–Liquid Scintillator

Table 1.6 Methodology and choice of calorimeter technology for some experiments that have published results on direct-photon production.

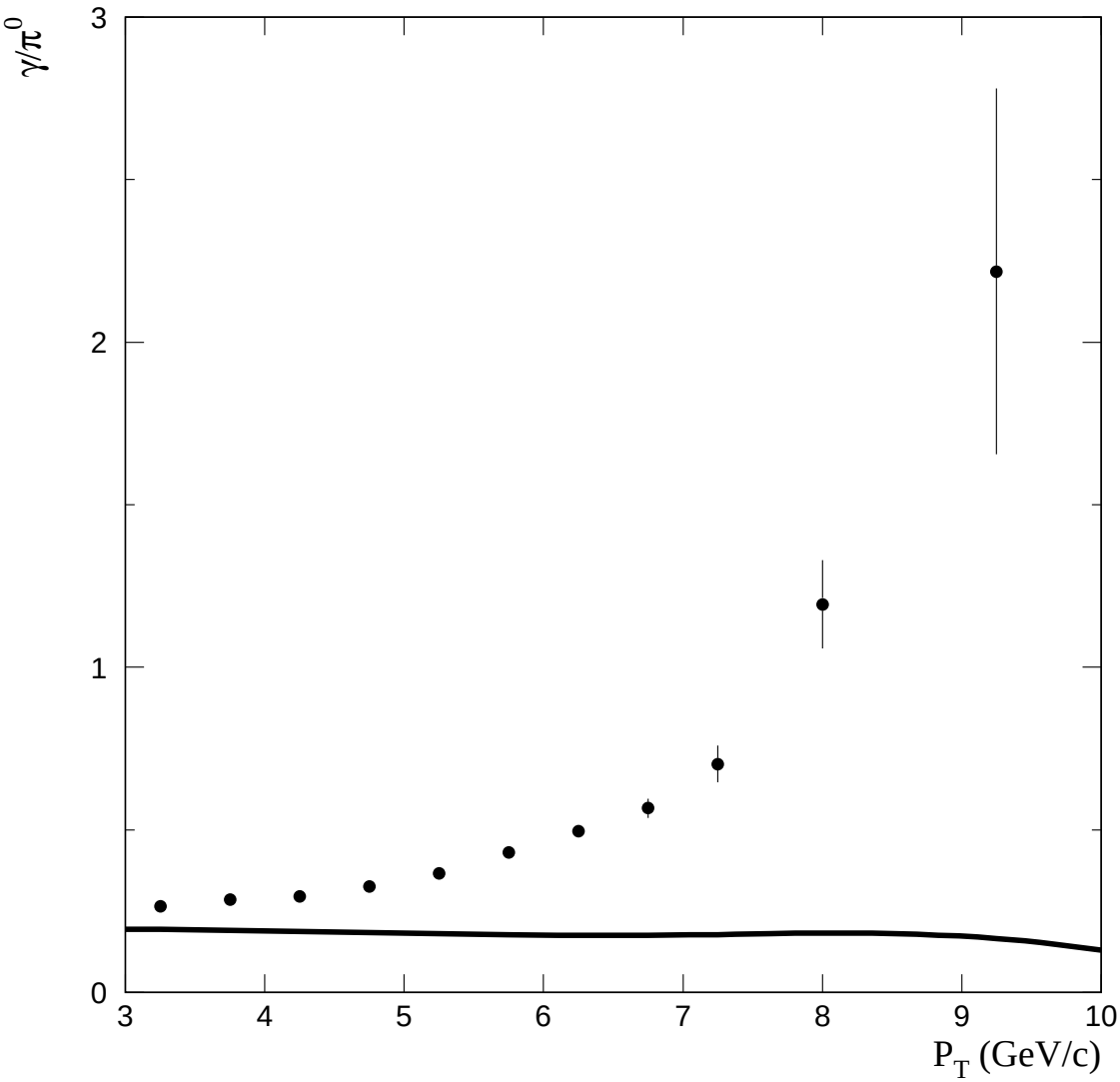

Figure 1.10 The observed single γ to π^0 ratio for signal+background (•) and background (curve) from the π^-Be data at 515 GeV/c.

is typically used as the converter (e.g., magnet coils, support structures). Another, similar, technique uses the difference in the profile of the showers deposited in the electromagnetic calorimeter. The two photons from π^0 decay result in a broader and shallower reconstructed shower than that from a single photon of the same energy. The shower profiles of photon candidates can be used to statistically extract the direct-photon cross section. These methods are typically employed in large-$\sqrt{s}$ environments (Table 1.6), where it is difficult to resolve the individual photons from π^0 decays.

The amount of energy surrounding photon candidates can also be used to discriminate between signal and background. True direct photons should be relatively isolated (ignoring production through quark bremsstrahlung) compared to π^0's that are part of a jet. Isolation criteria can also be applied, and are used routinely in the collider environment (Table 1.6).

Only a few experiments have measured the hadronic production of direct photons. Most of these are listed in Tables 1.7 and 1.8. Even fewer experiments have managed to extract a double direct-photon signal. These are listed in Table 1.9, along with the statistical significance of their result. General reviews of direct-photon measurements can be found in [49, 50, 11].

1.4 Summary

Fermilab experiment E706 was a fixed-target experiment specifically designed to measure the production of direct photons and their associated particles. The experiment featured a large, finely segmented, lead and liquid argon electromagnetic calorimeter and a high resolution charged particle spectrometer. In addition to measurements of single direct-photon production, the original proposal for experiment E706 [51] also contained provision for the measurement

Experiment	Beam Energy (GeV)	$\sqrt{s}$ (GeV)	Target	Sensitivity (pb^{-1})			
				π^-	$\bar{p}$	π^+	p
E629 [52]	200	19.4	C	—	—	-?-	-?-
NA3 [53]	200	19.4	C	-?-	—	-?-	-?-
E704 [34]	200	19.4	H_2	—	—	—	-?-
WA70 [54, 55]	280	23.0	H_2	3.5	—	1.3	5.2
NA24 [56]	300	23.8	H_2	1.3	—	0.2	0.5
UA6 [57, 58]	315	24.3	H_2	—	3.5	—	6.1
E706 [59]	500	30.6	Be, Cu	0.5	—	—	0.8
E706	515	31.1	H_2, Be, Cu	11.6	—	0.3	—
E706	530	31.6	H_2, Be, Cu	—	—	—	8.4
E706	800	38.8	H_2, Be, Cu	—	—	—	10.6

Table 1.7 Fixed target experiments that have published direct-photon results.

Experiment	$\sqrt{s}$ (GeV)	Interaction	Sensitivity (pb^{-1})
R806 [60]	31,45,53,63	pp	50
R807/8 [61]	53	pp, $p\bar{p}$	16
R108 [40]	62.4	pp	76
R110 [41]	63	pp	85
UA1 [45]	546	$p\bar{p}$	0.1
UA1 [45]	630	$p\bar{p}$	0.6
UA2 [62]	630	$p\bar{p}$	13.2
CDF [63]	630, 1800	$p\bar{p}$	35
DØ [64]	1800	$p\bar{p}$	12.9

Table 1.8 Hadron collider experiments that have published direct-photon results.

Experiment	$\sqrt{s}$ (GeV)	Interaction	Statistical Significance (Standard Deviations)
NA3 [65]	19.4	π^-C,pC	3
WA70 [66, 23]	23	π^-p	6
NA24 [67]	23.7	π^-p	2.9
R806 [68]	63	pp	2
R807/8 [69]	63	pp	2
UA1 [45]	630	p$\bar{\text{p}}$	2
UA2 [70]	630	p$\bar{\text{p}}$	4.3
CDF [24]	1800	p$\bar{\text{p}}$	3.2
DØ [71]	1800	p$\bar{\text{p}}$	5.8

Table 1.9 Statistical significance of published double direct-photon results.

of pairs of direct photons. The study of double direct-photon production is the principal subject of this thesis. Correlations between direct photons will be used to extract information about the transverse momentum of partons. In addition, results will be presented on the production of pairs of neutral mesons ($\pi^0\pi^0$, $\eta\pi^0$) and on the production of π^0's in association with direct photons ($\gamma\pi^0$). Studies of these systems will be used to improve our understanding of k_T effects in the production of single photons and π^0's.

The rest of this thesis is organized as follows: Chapters 2, 3, and 4 briefly describe the spectrometer, its trigger and readout, and the methods used to reconstruct photons and charged particles. Chapter 5 describes the detector

simulation. Chapter 6 contains a detailed description of the calibration of the energy response of the electromagnetic calorimeter (the analysis of the energy scale was among the author's primary responsibilities). The basic analysis techniques for studying high-mass $\pi^0\pi^0$, $\eta\pi^0$, $\gamma\pi^0$, and $\gamma\gamma$ events are presented in Chapter 7, followed in the ensuing chapters and appendices by discussions of their production cross sections.

Chapter 2 The Meson West Spectrometer

2.1 Introduction

The Meson West spectrometer was a large acceptance, multi-purpose spectrometer designed to measure direct-photon and dimuon production. The spectrometer had three major sub-systems. The first was a spectrometer used to measure the trajectories of charged particles emerging from beam–target interactions. The second sub-system consisted of a series of calorimeters to identify particle energies and positions. Finally, there was a muon spectrometer. All three sections of the Meson West spectrometer are discussed in more detail below.

The Meson West spectrometer was commissioned during the 1987–8 fixed target run and was used during the 1990 and 1991 fixed target runs. The spectrometer underwent several important upgrades between the 1987–8 and the 1990 runs [72]; the discussion below is limited to the Meson West spectrometer in its 1990 and 1991 configurations.

2.1.1 Coordinate System

A right handed coordinate system with the Z-axis oriented along the nominal beam direction was adopted. The X-axis was in the horizontal direction and the Y-axis was in the vertical direction (positive pointed up). Coordinates were signed according to the beam direction, downstream being more positive in Z and upstream more negative. The origin of the coordinate system was defined by a surveyor's plug located near the target box.

2.2 Beamline and Target

2.2.1 Accelerator

The Fermilab accelerator complex consisted of five particle accelerators (Figure 2.1). Negative hydrogen ions were accelerated by a Cockcroft–Walton to 750 keV. They were then accelerated in a linear accelerator to 400 MeV, stripped of their electrons, and injected into a 500 foot diameter, rapid cycling synchrotron (Booster) and accelerated to 8 GeV. The beam was extracted into a 4 mile circumference proton synchrotron (Main Ring) which accelerated the protons to 150 GeV. Some of these protons were directed into a target. Anti-protons produced in the resulting collision were stored in the Accumulator Ring for subsequent injection into the Main Ring.

The Tevatron is a 4 mile circumference, superconducting, proton synchrotron capable of simultaneously accelerating protons and anti-protons up to 0.9 TeV. The Tevatron can be operated in two modes: collider and fixed target. In collider mode, the proton and anti-proton beams can be forced to cross at up to four locations, including B0/CDF and D0/DØ. In fixed target mode, protons were accelerated by the Tevatron to 0.8 TeV and delivered to various experiments through a switch-yard complex. There were three principal experimental areas served by the switch-yard: Proton, Neutrino, and Meson. Each area had several beamlines that served the various fixed target experiments.

2.2.2 Meson West Beamline

E706 was located at the end of the Meson West beamline [73], which was capable of transporting either 0.8 TeV protons from the Tevatron or secondary beams of either polarity. Primary protons were delivered during a 23 second

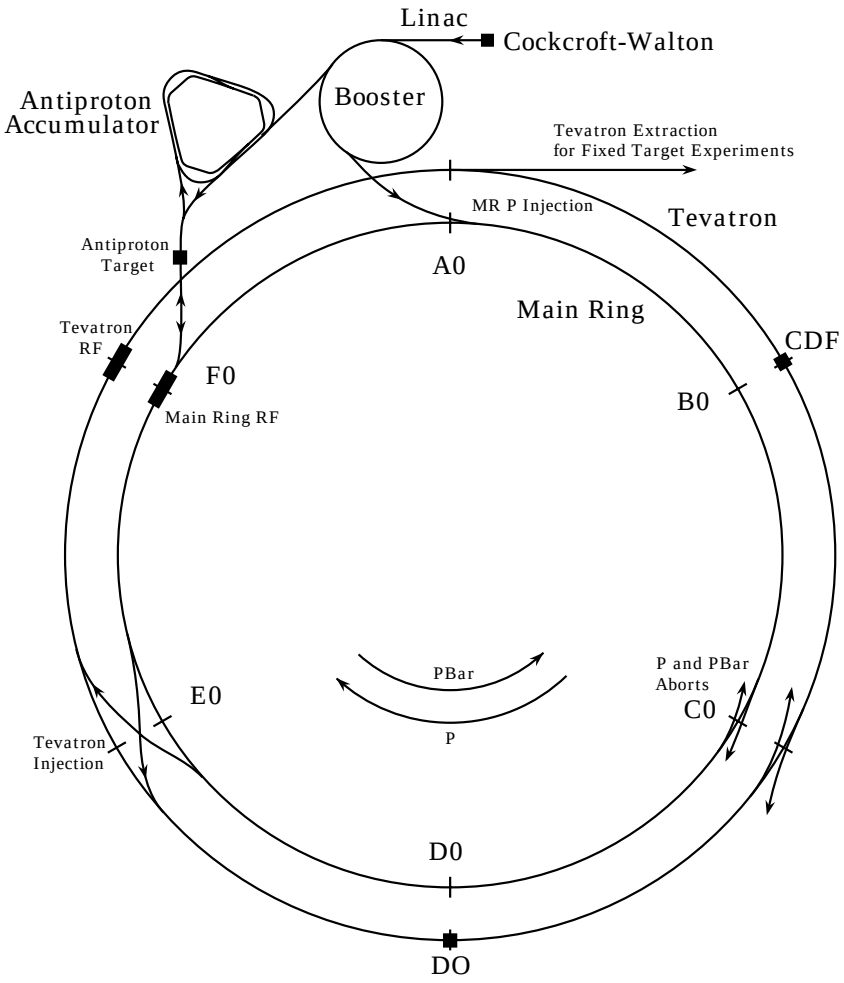

Figure 2.1 A schematic drawing of the Fermilab accelerator complex during the 1991 fixed target run.

Primary Beam Flux (protons/spill)	Mean Beam Momentum (GeV/c)	Majority Beam Particle
2×10^{11}	800	p
2×10^{12}	530	p
5×10^{12}	515	π^-

Table 2.1 Primary beam intensity at the production target required to generate $\approx 2 \times 10^8$ particles on the experimental target [73].

spill; spills were separated by 34 seconds. The beam was time localized into *buckets* $\approx$ 1 ns wide and $\approx$ 19 ns apart. This 19 ns (53 MHz) RF structure was an important timing reference. During normal operations, the Tevatron beam intensity was $\approx 10^{13}$ protons/spill.

To generate 0.5 TeV/c secondary beams of pions, kaons, and protons, the primary proton beam was directed into a $\approx$ 1 interaction length beryllium target[1] [74] (Table 2.1). For calibration purposes, we also transported 25–100 GeV/c mixed electron (40%) and hadron (60%) beams and 200–400 GeV/c hadron beams [75].

The polarity of the secondary beam was chosen by a series of magnets; the most important elements of the beamline optics are shown in Figure 2.2. The pinhole collimators controlled primary beam intensity. The Segmented Wire Ion Chambers (SWICs) and the Secondary Emission Monitors (SEMs) were used to measure beam position and intensity, respectively. Spoiler magnets swept away muons and hadrons that otherwise traveled parallel to the beamline.

[1] The primary target was 1.14 interaction lengths during the 1990 run. In 1991, the production target was reduced to 0.75 interaction lengths.

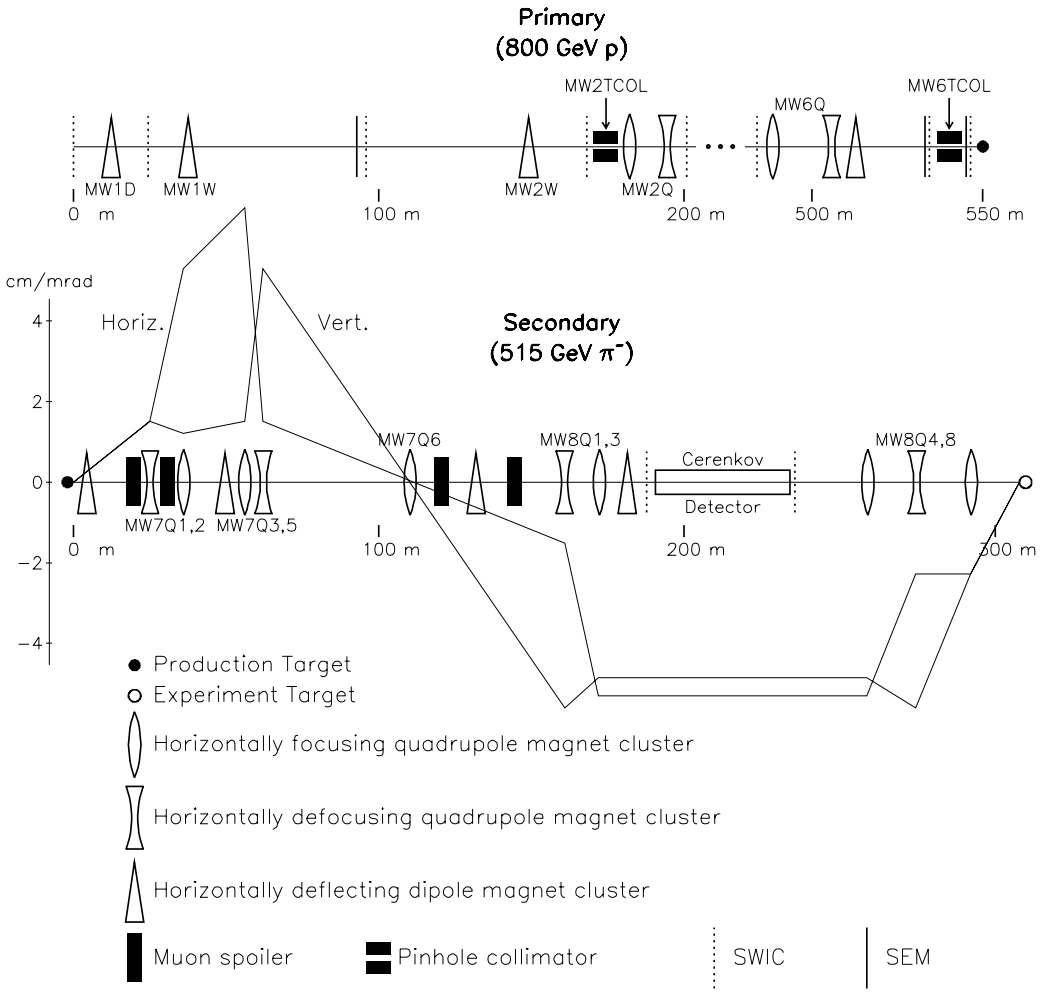

Figure 2.2 A schematic drawing of the Meson West beamline showing the most important elements.

2.2.3 Beamline Čerenkov Detector

A differential Čerenkov counter [76, 77] was installed in the beamline to identify (*tag*) incident pions, kaons, and protons in the secondary beams. This helium filled counter was 43.4 m long and was located $\approx$ 100 m upstream of the experimental target (Figure 2.2). Three concentric rings of photomultiplier tubes detected photons in order to simultaneously identify the secondary beam particles (Figure 2.3). A precision gas system controlled the helium pressure so that the Čerenkov light could be scanned across the photomultiplier tubes for calibration purposes. The typical operating pressure was between 6.0 and 6.5 psia.

2.2.4 Hadron Shield and Veto Walls

A 4.7 m long stack of battleship steel was placed between the last beamline magnet and the target box (Figure 2.4) to absorb hadrons and identify muons not swept away by the spoiler magnets. A water tank was placed on the downstream end of the steel to absorb neutrons. Scintillator walls were placed upstream and downstream of the steel to identify penetrating muons. These *veto walls* were used in both the online trigger definition [78] and in the offline analysis [79] to discriminate against beam halo muons. Two scintillator walls were located downstream of the hadron shield and two upstream.[2]

2.2.5 Beam and Interaction Counters

Trigger information was provided by scintillators in the target region [80]. Position and timing information for incident beam particles was provided by a hodoscope [81] located between the hadron shield and the target region (Figure 2.4). The hodoscope had three layers forming X, Y, and U views. Each

[2] Only one upstream wall was in place during the 1990 run.

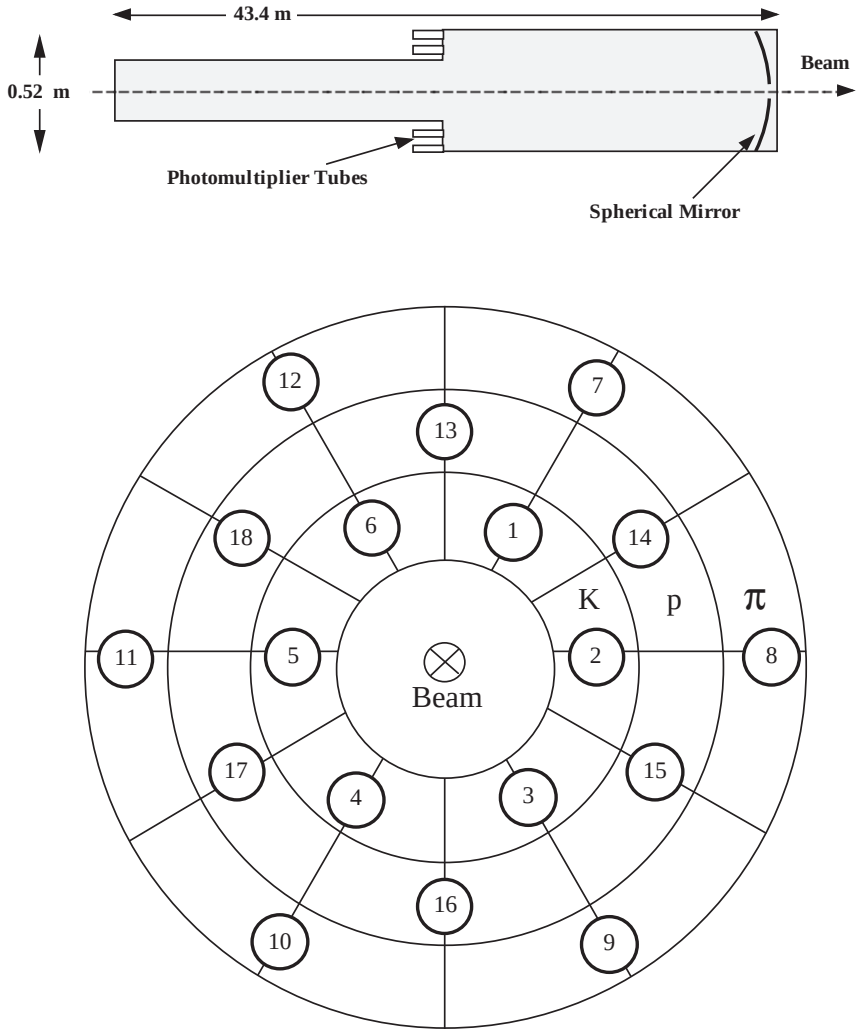

Figure 2.3 A schematic drawing of the beamline Čerenkov counter (top) and its phototube placement (bottom). Each ring of photomultiplier tubes is labeled according to the particle it was designed to tag.

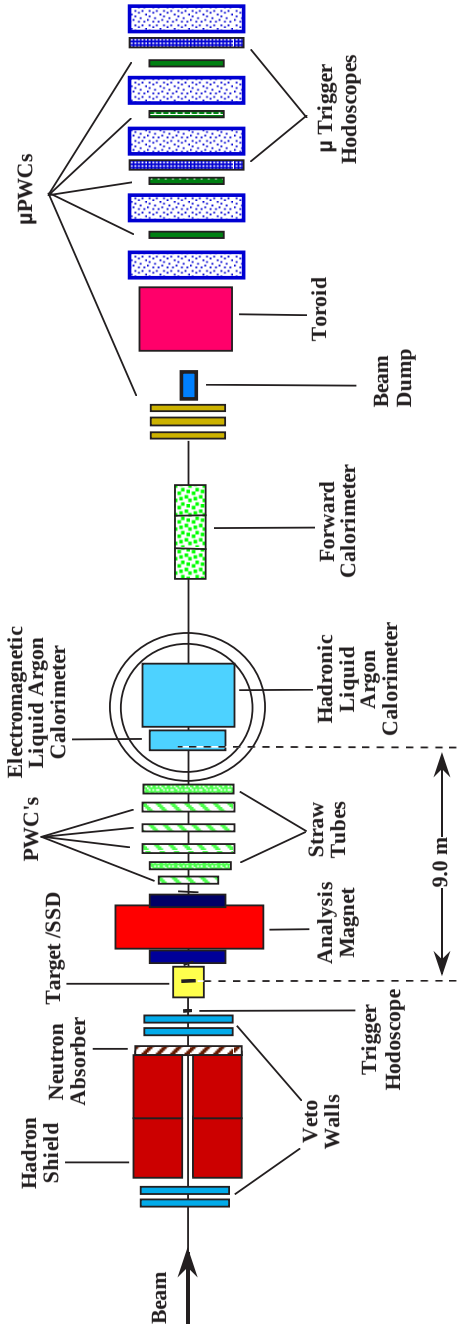

Figure 2.4 A schematic drawing of the Meson West Spectrometer in the 1991 configuration.

view consisted of twelve 3.5 cm long scintillator strips. The strip widths varied with the thinnest strips (1 mm) located in the beam region.

A scintillator counter with a 0.375 inch diameter hole was placed in the target region to define the transverse beam size. This counter was used as a beam veto in the trigger logic. A single piece of scintillator was used during the 1990 run; this was replaced with four pieces, covering approximately the same area, for the 1991 run.

E706 used thin targets corresponding to between 10% and 15% of an interaction length. To identify buckets in which an interaction occurred, four planes of scintillator were placed downstream of the target. Two were located upstream of the analysis magnet (Section 2.3.2) and two downstream. Holes were cut out of the center of the planes, 0.75 inches diameter in the case of the upstream pair and 1.5 inches diameter for the downstream pair, to eliminate non-interacting beam particles.

2.2.6 Target

Targets (Table 2.2) were located between the hodoscope and the interaction counters. Arrayed around the targets were silicon strip detectors used to reconstruct the beam particles and the interaction vertex. The targets were hydrogen [82], beryllium, and copper arranged as in Figures 2.5 and 2.6.

The experimental target during the 1990 fixed target run (Figure 2.5) consisted of two pieces of copper and two pieces of beryllium. The copper targets were 0.08 cm thick and had a circular shape (2.54 cm diameter) with the sides cut off; this resulted in a cross-sectional shape that was circular on top and bottom and rectangular in the middle. The beryllium targets were 2 cm diameter cylinders. The upstream piece was 3.7 cm long, while the downstream piece was 1.1 cm long.

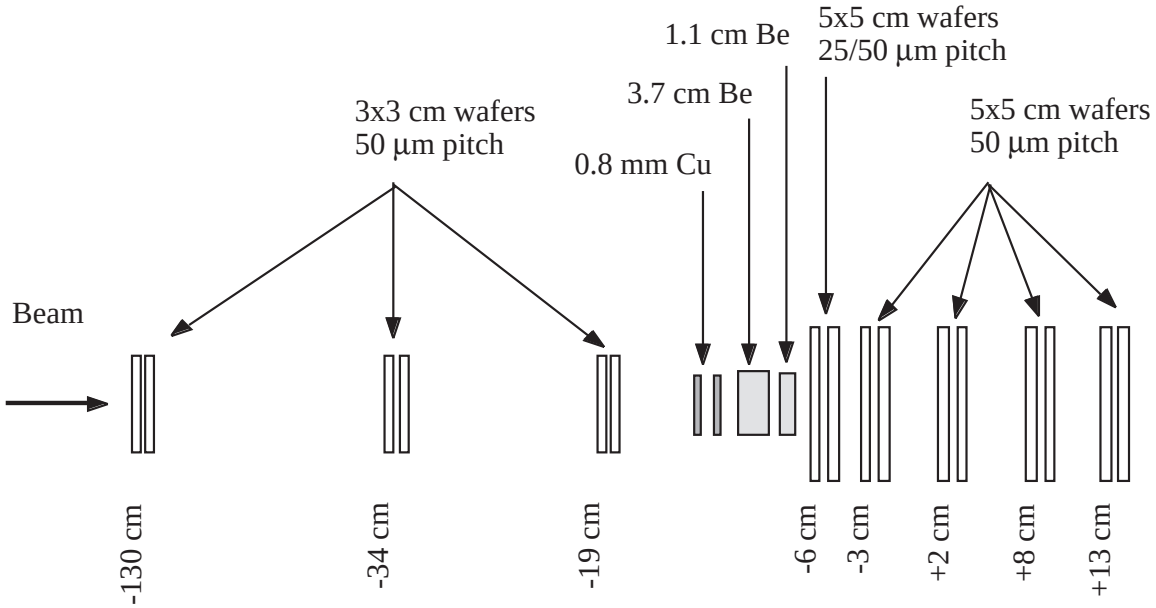

Figure 2.5 Configuration of the target region during the 1990 run.

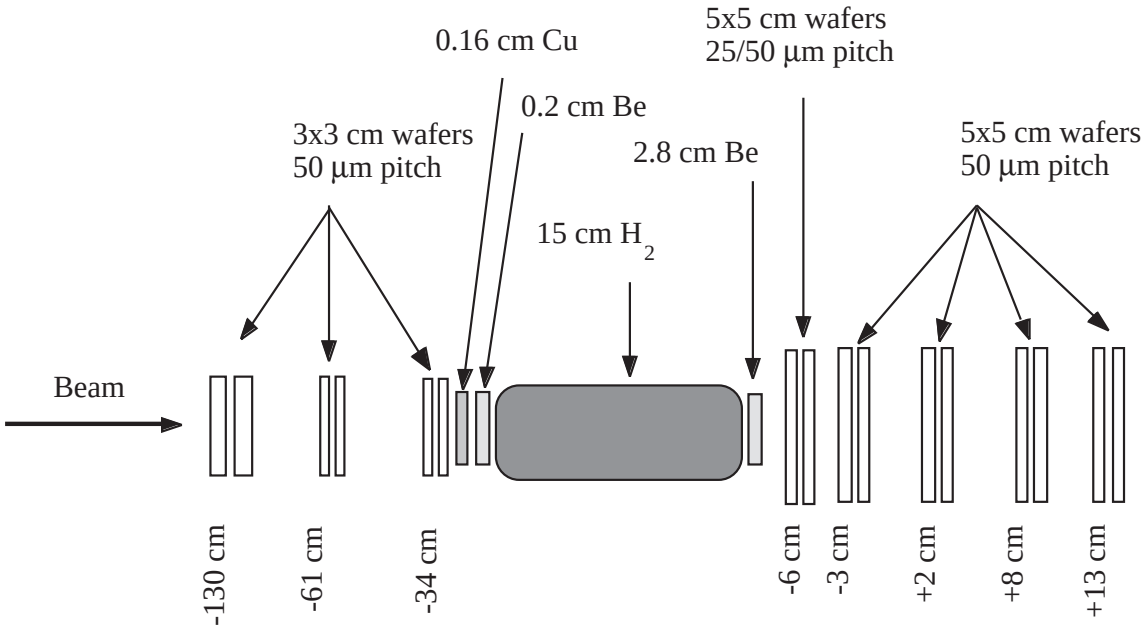

Figure 2.6 Configuration of the target region during the 1991 run.

Run	Material	$Z_{upstream}$ (cm)	Diameter (cm)	Length (cm)
1990	Cu	−15.54	2.54	0.0780
	Cu	−15.22	2.54	0.0781
	Be	−14.65	2.08	3.7092
	Be	−9.92	2.06	1.1201
1991	Cu	−30.44	2.54	0.0780
	Cu	−29.95	2.54	0.0781
	Be	−28.36	8.1	0.249
	H	−26.9	6.35	15.3
	Be	−10.52	9.9	0.282
	Be	−10.8	2.54	2.5397

Table 2.2 Target materials, positions, and dimensions in the 1990 and 1991 configurations. The fiducial length of the hydrogen target is defined by a cut that excludes regions compromised by the proximity of the container material.

A hydrogen target was added for the 1991 fixed target run (Figure 2.6). The liquid hydrogen was contained in a 15 cm long mylar flask. The flask was a 6 cm diameter cylinder (oriented along the Z-axis) housed within a stainless steel vacuum jacket equipped with beryllium windows at both ends. The 1991 target configuration also included two 0.08 cm thick copper targets upstream of the hydrogen target; the copper pieces were circular with a diameter of 2.5 cm. Downstream of the hydrogen target (adjacent to the downstream beryllium window) was a 2.54 cm long beryllium cylinder with a diameter of 2.54 cm.

2.3 Charged Particle Spectrometer

The tracking system was designed to measure the location of the beam–target interaction, the location of heavy particles decays, and the momenta of charged particles. For these purposes silicon strip detectors (SSDs) were placed in the target region, and proportional wire chambers (PWCs) and straw drift tubes (SDTs) were placed downstream of a dipole magnet.

2.3.1 Silicon Strip Detectors

The SSD system [83, 84] consisted of 16 silicon microstrip detectors [85, 86] arranged into 8 modules. In each module, the upstream plane was oriented vertically and the downstream plane was oriented horizontally; planes were supported by a 1/4 inch thick aluminum frame. The planes were ≈ 300 μm thick with a 50 μm strip pitch[3]. Three modules were placed upstream of the target and five downstream. The angular resolution of the SSD system was ≈ 0.06 mrad. Figure 2.7 is a diagram of the SSD system showing the instrumented regions. The entire system can be seen in Figures 2.5 and 2.6. The characteristics of the SSD planes can be found in Table 2.3.

2.3.2 Magnet

An analysis magnet [87] was located between the SSDs and the PWCs (Figure 2.4). It produced a dipole magnetic field of 6.2 kG to provide a 0.44 GeV/c transverse momentum impulse in the horizontal plane. Mirror plates were installed at both ends of the magnet aperture (at Z $\approx$ 53 cm and Z $\approx$ 360 cm) to minimize fringe field effects. A helium bag filled the magnet aperture to reduce multiple scattering.

[3] The first plane downstream of the target was a hybrid plane having a central region of 25 μm pitch and an outer region with 50 μm pitch.

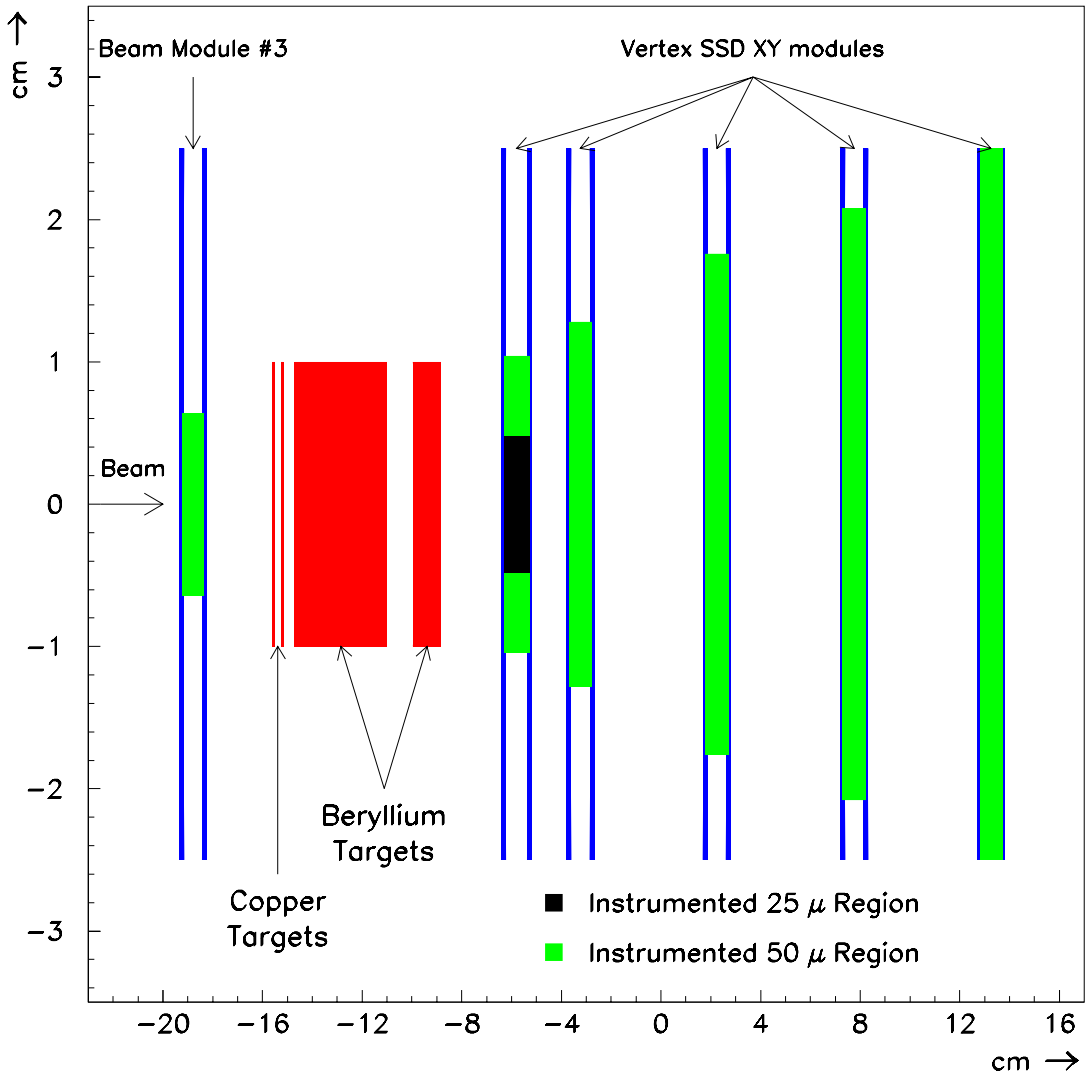

Figure 2.7 The silicon strip detectors in their 1990 configuration. The instrumented regions of each plane are marked by the shaded areas.

2.3.3 Proportional Wire Chambers

The PWC system [88] consisted of four modules of four anode planes each. The planes were oriented horizontally, vertically, and in two stereo views, U ($+37°$) and V ($-53°$). Each anode plane was surrounded by two cathode planes as illustrated in Figure 2.8. The cathode planes were capable of supporting independent high voltages in three regions: *beam*, *diffractive*, and *main*. Although the four modules were nearly identical in design, the active areas increased with increasing Z to provide nearly constant acceptance for charged particles bent by the magnet (Table 2.4). The angular resolution of the PWC system was ≈ 0.30 mrad.

The anodes were 0.8 mil gold plated tungsten wire while the cathodes were graphite coated 1.0 mil thick mylar sheets glued to a supporting G-10 frame. Anode wires were placed 0.1 inches apart and there was 0.226 inches between the cathode planes and the anodes. The cathode planes were operated at -3 kV while the anodes were grounded. The ionizing medium was a mixture of 80.4% argon, 18% isobutane, 0.1% freon, and 1.5% isopropyl alcohol.

2.3.4 Straw Drift Tubes

The SDT system [89, 90] consisted of two modules of eight planes each. The first four planes of each module were oriented vertically and the second four planes were oriented horizontally. SDTs were interspersed with the PWC system (Figure 2.4) to increase the resolution of the tracking system downstream of the analysis magnet.

The straws were made from two spiral wrapped layers of 150 μm mylar with a layer of 8 μm aluminum coated on the inner surface of the inner layer. The tube diameter was 1.04 cm in the first straw chamber and 1.63 cm in the second

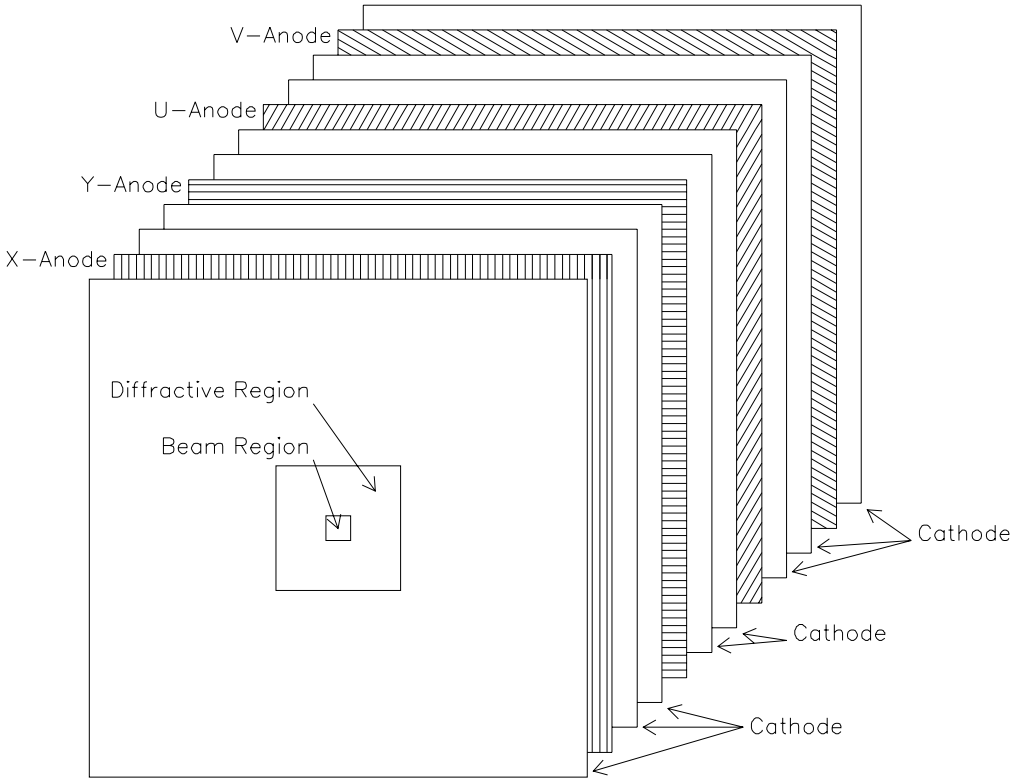

Figure 2.8 Arrangement of the sense wires in each proportional wire chamber module.

Module	Orientation	Elements	Pitch (μm)	Active Region (cm)	Z Position (cm)
Beam SSD 1	X	256	50	1.28	-130.2
	Y	256	50	1.28	-129.3
Beam SSD 2	X	256	50	1.28	-34.2
	Y	256	50	1.28	-33.3
Beam SSD 3	X	256	50	1.28	-19.2
	Y	256	50	1.28	-18.3
Vertex SSD 1	X	384	25	0.96	-6.3
		256	50	1.28	
	Y	384	25	0.96	-5.3
		256	50	1.28	
Vertex SSD 2	X	512	50	2.56	-3.7
	Y	512	50	2.56	-2.8
Vertex SSD 3	X	704	50	3.52	1.8
	Y	704	50	3.52	2.7
Vertex SSD 4	X	832	50	4.16	7.3
	Y	832	50	4.16	8.2
Vertex SSD 5	X	1000	50	5.00	12.8
	Y	1000	50	5.00	13.7

Table 2.3 Elements of the charged particle spectrometer upstream of the analysis magnet. This table describes the 1990 configuration. During the 1991 fixed target run, beam SSDs 2 and 3 were moved farther upstream to make room for an expanded target.

Module	Orientation	Elements	Spacing (mm)	Active Region (cm)	Z Position (cm)
PWC 1	X	640	2.54	122	379.0
	Y	480	2.54	122	380.8
	U	704	2.54	122	382.5
	V	672	2.54	122	384.2
SDT 1	X	160	10.4	167	426.2
	X	160	10.4	167	427.1
	X	160	10.4	167	428.1
	X	160	10.4	167	429.0
	Y	128	10.4	126	434.0
	Y	128	10.4	126	434.9
	Y	128	10.4	126	435.9
	Y	128	10.4	126	436.8
PWC 2	X	800	2.54	203	472.3
	Y	800	2.54	203	474.0
	U	896	2.54	203	475.8
	V	896	2.54	203	477.5
PWC 3	X	800	2.54	203	567.4
	Y	800	2.54	203	569.1
	U	896	2.54	203	570.9
	V	896	2.54	203	572.6
PWC 4	X	960	2.54	244	660.1
	Y	960	2.54	244	661.9
	U	1120	2.54	244	663.7
	V	1120	2.54	244	665.4
SDT 2	X	160	16.3	280	743.9
	X	160	16.3	280	745.3
	X	160	16.3	280	747.0
	X	160	16.3	280	748.4
	Y	160	16.3	280	750.3
	Y	160	16.3	280	751.8
	Y	160	16.3	280	753.4
	Y	160	16.3	280	754.8

Table 2.4 Elements of the charged particle spectrometer downstream of the analysis magnet. This table describes the 1990 configuration.

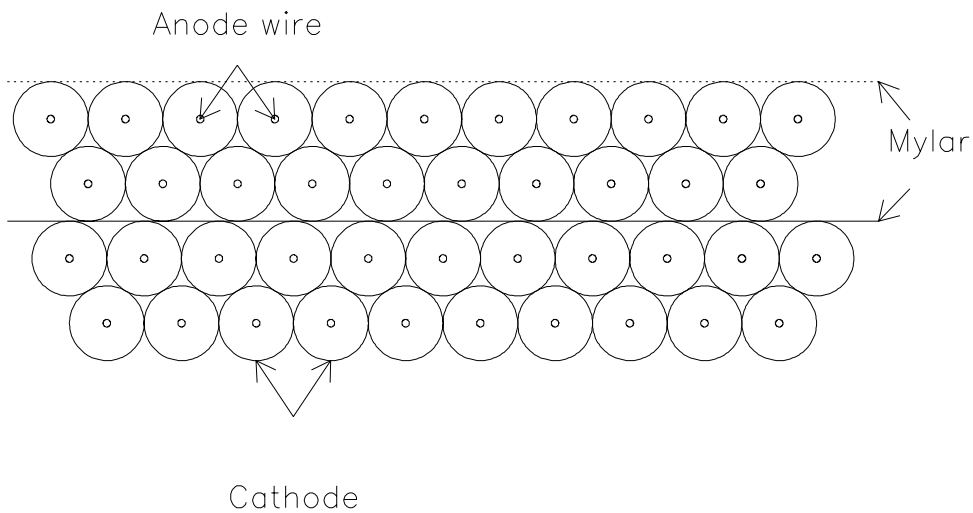

Figure 2.9 Cut view of a straw drift tube bundle.

(Table 2.4). The cathode was grounded. The anode, running down the center of each straw, was a 20 μm gold-plated tungsten wire held at ≈ 1.8 kV. The ionizing medium in the straws was a mixture of 50% argon and 50% ethane bubbled through ethyl alcohol at 0°C.

Straws were glued together to form bundles arranged in a staggered fashion for better coverage (Figure 2.9). Information about hit straws as well as timing information from the charge collection was recorded; this improved the downstream tracking resolution to ≈ 0.06 mrad, comparable to the SSD system.

2.4 Calorimetry

Three sampling calorimeters were located downstream of the SDTs to measure the energies of photons, electrons, and hadrons (Figure 2.4). Two calorimeters used liquid argon as the active medium (LAC). The electromagnetic calorimeter (EMLAC) was very finely segmented to accurately measure the energies and positions of photons. A hadronic calorimeter (HALAC) was located downstream within the same cryostat. A scintillator calorimeter (FCAL) was placed further downstream to increase coverage in the forward (positive rapidity) region.

2.4.1 Liquid Argon Calorimeter Cryostat and Gantry

The EMLAC and HALAC were located within a cryostat [91] suspended from a gantry (Figure 2.10). The cryostat was filled with $\approx$ 17000 liters of liquid argon; the argon was checked for purity prior to use [35]. Argon pressure was controlled by liquid nitrogen cooling coils. The vessel consisted of two pieces connected by a bolted flange with a very large O-ring; the flange was at room temperature. Electrical feedthroughs were installed at the top of the cryostat for the signal and high voltage lines. These were "warm" feedthroughs; while the detectors were submerged in liquid argon, the top of the cryostat was filled with gaseous argon. A steel-jacketed vessel filled with Rohacell was used to exclude argon from the front of the EMLAC; this filler vessel significantly reduced the energy lost in material upstream of the detector (Section 6.5.4). Another steel-jacketed vessel filled with gaseous helium spanned the entire length of the cryostat; it filled the hollow centers of both calorimeters to minimize further interactions with the beam.

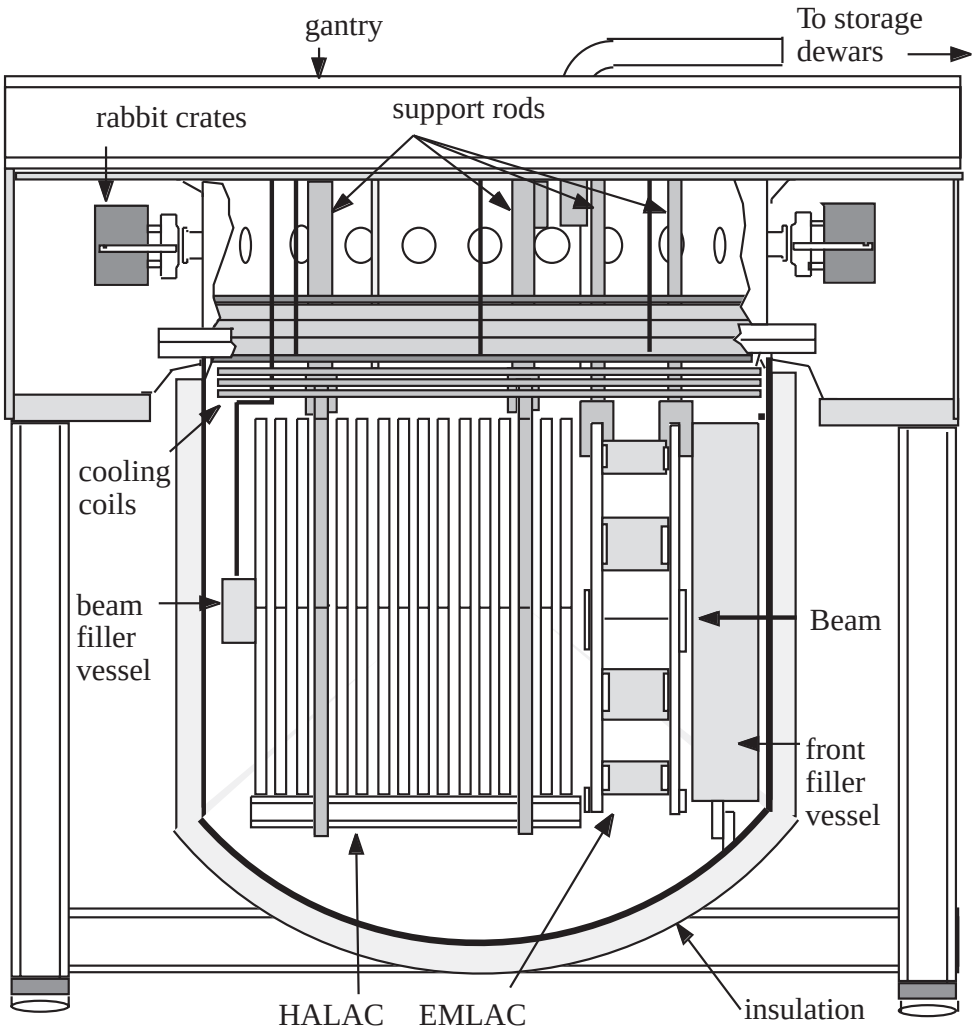

Figure 2.10 A cut-away view of the liquid argon calorimeter and gantry. Both the electromagnetic and hadronic calorimeters are visible within the cryostat.

The gantry consisted of a steel I-beam frame capable of supporting the cryostat, 105 tons of liquid argon, and 225 tons of detectors. It was capable of very fine motion transverse to the beam for detector calibration (Section 6.3). The gantry also supported the *Faraday Room*, a shielded and electrically isolated room containing the feedthroughs and detector electronics.

2.4.2 Electromagnetic Calorimeter

The EMLAC [92, 75] had a cylindrical geometry with an inner radius of 20 cm and an outer radius of 165 cm. It was divided into four mechanically independent quadrants that were further subdivided to create octants. The calorimeter had 33 longitudinal cells read out in two sections: an 11 layer front (about 8.5 radiation lengths) and a 22 layer back (about 18 radiation lengths). This front/back split was used for shower matching in photon reconstruction (Section 4.3.6), for measuring the direction of incidence of the showering particle [35], and for discriminating between electromagnetic and hadronic showers (Section 7.4). The longitudinal layers consisted of a 2 mm thick lead sheet (cathode)[4], a double-sided copper–clad G-10 anode board (radial), another 2 mm thick lead sheet (cathode), and another double-sided copper–clad G-10 anode board (azimuthal). Between each of these components was a 2.5 mm argon gap. The physical layout is illustrated in Figure 2.11. The cathodes were operated at -2.5 kV; the anodes were grounded through the amplifiers.

The radial coordinate readout consisted of 254 concentric strips in each octant; the strips were focussed[5] in a tower–like fashion towards the target 9 m upstream of the detector. The azimuthal coordinate readout was subdivided at 40 cm (radius)

[4] The first layer has an aluminum cathode rather than a lead cathode.
[5] These strips are 5.45 mm wide on the first radial board.

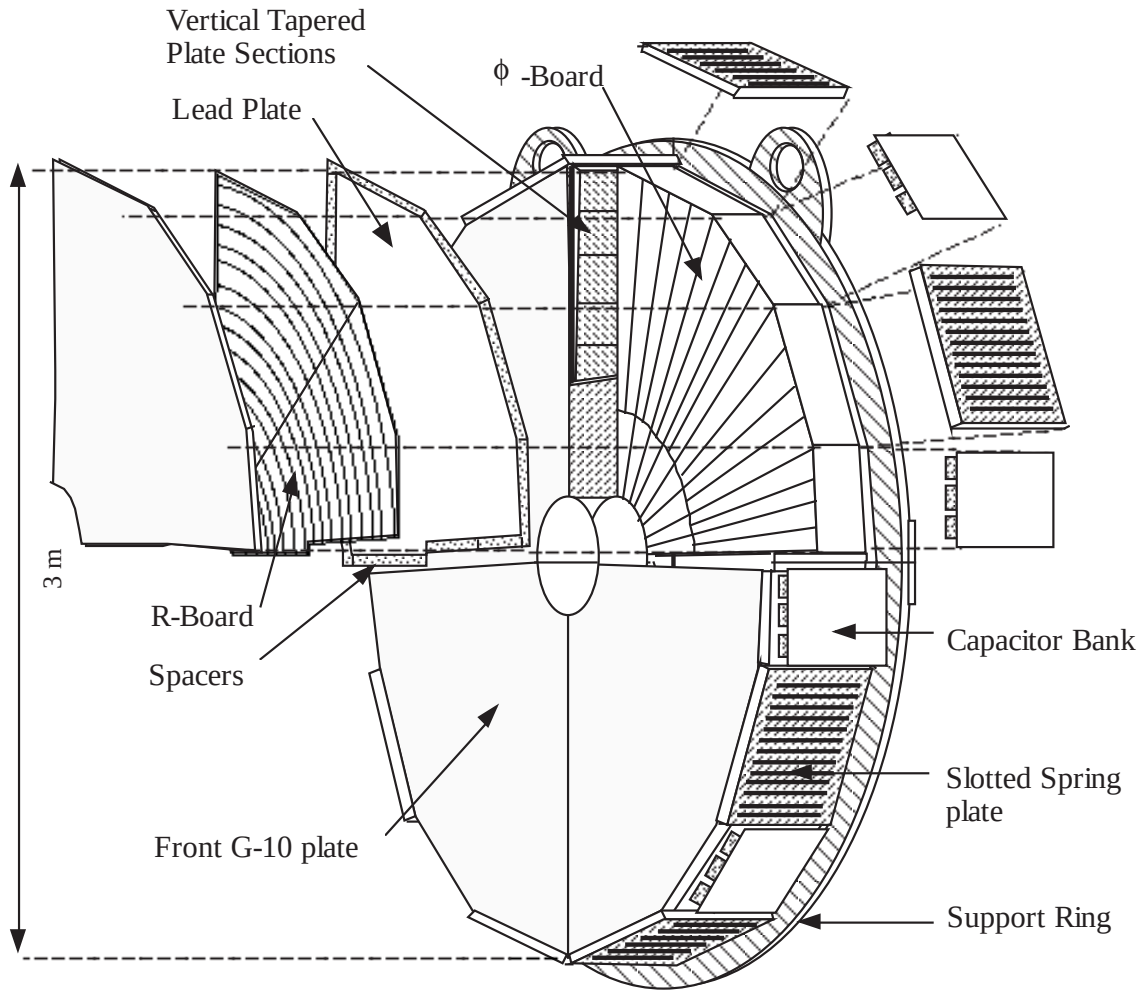

Figure 2.11 An exploded view of the electromagnetic calorimeter.

into inner and outer segments; each inner strip subtended an azimuthal angle of $\pi/192$ radians, while each outer strip covered $\pi/384$ radians. This subdivision of the azimuthal strips on the outer portion of the detector was used to improve both position and energy resolution of reconstructed photons. It also reduced R–ϕ correlation ambiguities in the reconstruction caused by multiple showers in the same octant of the calorimeter (Section 4.3.6).

2.4.3 Hadronic Calorimeter

The HALAC [75, 87] had 53 longitudinal cells read out in 2 sections: a 14 layer front (about 2 interaction lengths), and a 39 layer back (about 6 interaction lengths). Each cell consisted of a detector plane (*cookie*) with a 0.125 inch effective argon gap and a 1 inch thick steel plate (Figure 2.12). Cookies had two anode planes formed from single-sided copper-clad G-10 boards glued together back-to-back and separated by vertical G-10 strips for mechanical support. The anode planes were bracketed by two double-sided copper-clad G-10 boards. The side facing the anode board was held at -2.5 kV, the other side was grounded. The anode boards were grounded through their amplifiers. The high voltage boards were separated from the anodes by 3 mm thick horizontal strips of G-10. The area covered by the G-10 strips was not instrumented for readout; to avoid gaps in the acceptance, these non-instrumented regions were staggered vertically within the cookie.

Anodes were cut into pads in a triangular pattern (Figure 2.13), which was focussed in a tower-like fashion on the target. Pads ranged in height from 10.9 cm in the front to 13.3 cm in the back. The typical hadronic shower was contained within a six-pad area.

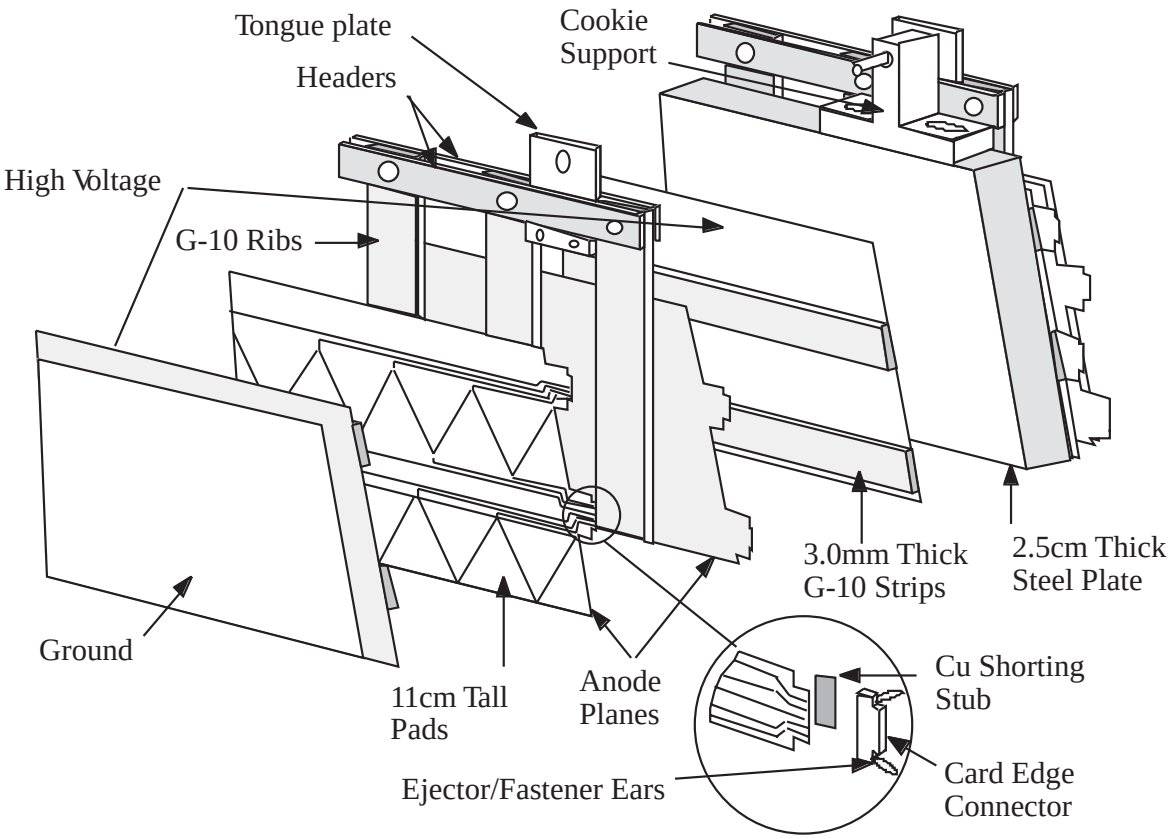

Figure 2.12 A cell from the hadronic calorimeter.

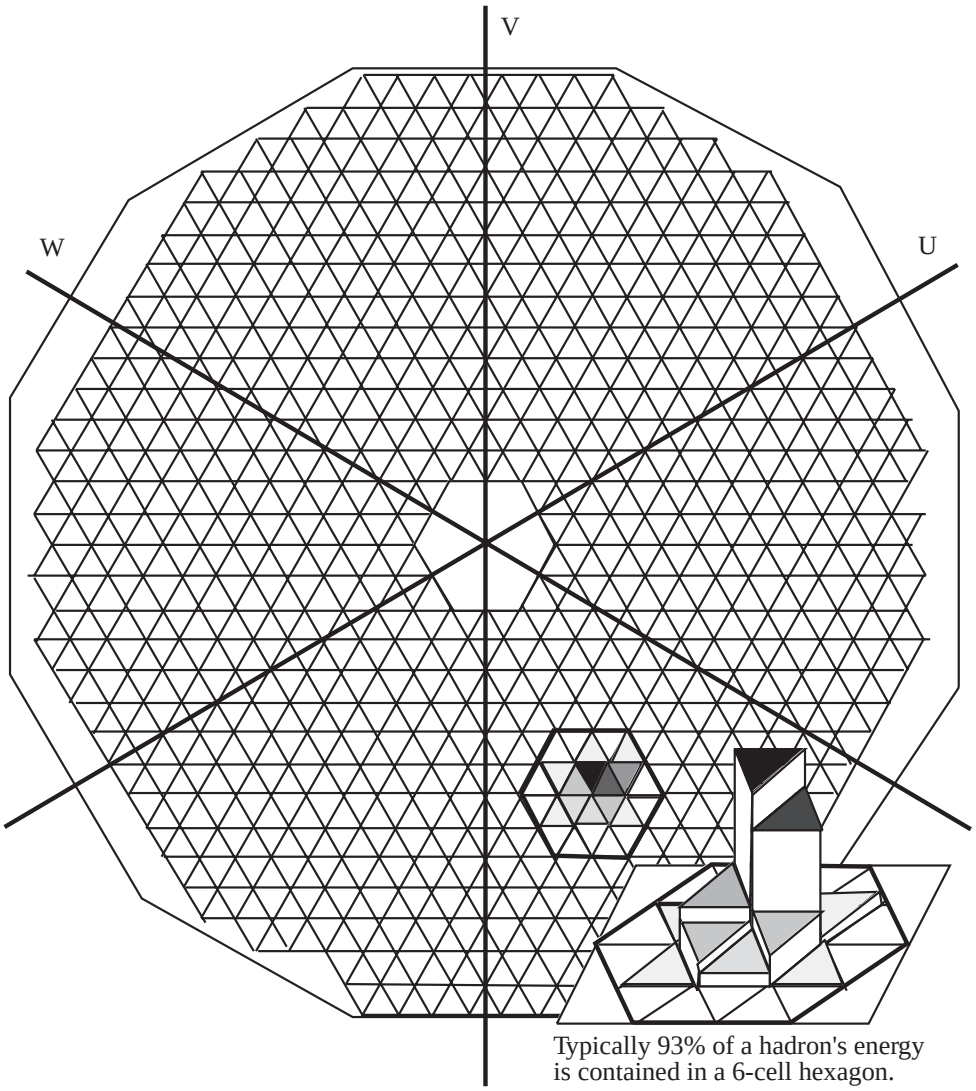

Figure 2.13 The pad structure used in the hadronic calorimeter. A typical hadronic shower is shown in the inset.

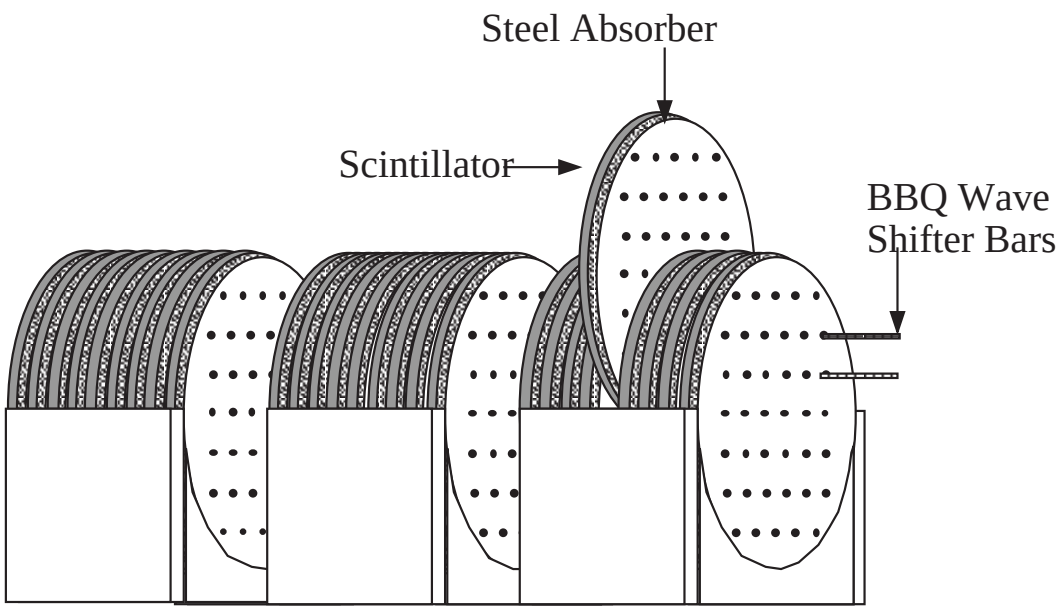

Figure 2.14 Diagram of the forward calorimeter.

2.4.4 Forward Calorimeter

A steel and scintillator calorimeter (Figure 2.14) was located downstream of the LAC (Figure 2.4) to measure energy in the forward direction [93, 94]. The FCAL acceptance covered the LAC beam hole. It was split into three similar sections, each composed of alternating layers of 1.9 cm steel absorber plates and 4.8 mm acrylic scintillator sheets. The downstream module had 32 layers of steel absorber plates and 33 layers of scintillator sheets, the other two modules had 28 layers of steel absorber plates and 29 layers of scintillator sheets. The steel plates were 114 cm in diameter and were separated by 6.9 mm. The three modules constituted ≈ 10.5 interaction lengths. Holes were drilled through the steel and scintillator with 1.27 cm and 1.12 cm diameters respectively. Wavelength shifter rods were inserted through these holes and were used to guide the collected light to

photomultiplier tubes. The photomultiplier tubes were located at the downstream end of the downstream module and at both ends of the other two modules.

2.5 Muon Spectrometer

In addition to its use in E706, the Meson West spectrometer was simultaneously used by another experiment, E672. E672 was a high-mass dimuon experiment investigating the hadroproduction of J/ψ [95, 96], ψ' [95], χ_c [97], and B [98] mesons. The E672 collaboration was principally responsible for the spectrometer elements downstream of the forward calorimeter as shown in Figure 2.4. These elements consisted of a toroidal magnet, hodoscopes, and proportional wire chambers. E706 and E672 shared trigger logic, data acquisition, and event reconstruction programs. Information from many aspects of the spectrometer contributed to their analyses and data from their triggers were used for several of our studies and calibrations [for example, the J/$\psi \longrightarrow \mu^+\mu^-$, as identified by the E672 trigger, was used in our tracking momentum scale calibration (Section 6.2.5)]. We also jointly published results obtained using the dimuon trigger [95—98].

Chapter 3 Trigger and Data Acquisition

This chapter describes the experimental method that selected the data and the system that read out the spectrometer.

3.1 Trigger

The trigger system [78, 80, 94] selected a sample of rare, high-p_T events ($\approx$ 1 in every 10^5 beam-target interactions). There were four classes of triggers implemented for the Meson West spectrometer: scintillator triggers, single-octant EMLAC based triggers, double-octant EMLAC based triggers, and a dimuon trigger. The scintillator triggers relied on signals from the beam hodoscope and interaction counters. The single-octant triggers required localized deposits of transverse momentum in the EMLAC. The double-octant triggers required two localized deposits of transverse momentum in the EMLAC azimuthally separated by at least 90°; they were intended to mimic a two-arm spectrometer arrangement. The dimuon trigger required downstream muon hodoscope information; it was the principle trigger of E672[1].

3.1.1 Beam and Interaction

The initial stage of the trigger used timing information from the hodoscope and interaction counters (Section 2.2.5). Trigger signals were issued depending upon specific coincidences of the hodoscope and interaction counter information. One coincidence was BEAM. A BEAM signal occurred when two or more planes of the hodoscope fired during the same RF bucket. This signal had no discrimination between one and more than one beam particles in the RF bucket making it difficult

[1] There was also an online processor that performed a quick track reconstruction to pick out high-mass dimuon events.

to normalize. BEAM1 was defined to provide this discrimination; it had the same requirements as BEAM plus additional restrictions on the pattern of lit fingers in the hodoscope planes.

The interaction signal, INT, required at least two interaction counters fired in the same RF bucket. An INT1 signal was issued when the INT signal was in coincidence with BEAM1. The downstream trigger electronics (Faraday room) were unable to handle interactions that were too close together in time. For this reason, at least three non-interacting RF buckets (CLEAN) were required on either side of the INT[2]. Since the tracking system's gate was ≈ 100 ns, the CLEAN filter also had the advantage of minimizing overlapping events detected in the tracking system electronics.

Once a trigger was issued, the computer issued a busy signal that was maintained until all the event information was read out. Upon completion of this process, a computer ready signal (CMPRDY) was issued and the system was ready for the next event. The final live interaction definition was

$$\text{LIVE INT1} = \text{INT1} \otimes \text{CLEAN} \otimes \text{CMPRDY} \otimes \overline{\text{BH}}, \tag{3.1}$$

where $\overline{\text{BH}}$ indicated that no signal was observed in the beam hole counter. These signals were taken in coincidence with two signals provided by the accelerator, BEAM GATE, which indicated that a spill was in progress, and RF CLOCK. Signals were stored for 15 RF buckets by the Minnesota latches [93]. This information (centered in-time on BEAM) was read out by the data acquisition system.

A small fraction of BEAM and INT signals were used to trigger the experiment (Table 3.1). These scintillator triggers were primarily used for studies requiring

[2] The late CLEAN requirement was removed for runs > 14606 to gauge the impact of ringing in the interaction counters [80].

Trigger	Prescale Factor	Fraction of Events (%)
BEAM	15^6	2
INTERACTION	15^5	3
PRETRIGGER	2925	7
SINGLE LOCAL LOW	40	18
SINGLE LOCAL HIGH	1	40
LOCAL GLOBAL LOW	40	20
LOCAL 1/2 GLOBAL HIGH	1	35
LOCAL GLOBAL HIGH	1	35
TWO GAMMA	1	20
DIMUON	1	20

Table 3.1 Trigger characteristics during the 1990 fixed target run. Many events satisfied more than one trigger. Some prescale factors changed during the run.

a low-bias sample. The π^0 number distribution measured with INT1 is shown in Figure 3.1; this data merges smoothly into the single-octant EMLAC triggers.

3.1.2 Pretrigger

It was important to make trigger decisions quickly to reduce dead-time. Because of the EMLAC rise time ($\approx$ 350 ns), a *fast-output* was implemented ($\approx$ 180 ns) for the trigger. The fast-out energy estimates were less accurate than the values obtained from the longer integration time ($\approx$ 800 ns for the actual energy measurement), but they were sufficient for rejecting low-p_T events. Fast-out energies from pairs of neighboring radial strips were added together and output to attenuator cards that weighted the energy by $\sin\theta$ to form *trigger*-p_T. Every four pairs of strips were added together to form a *sum-of-eight*; there were 32 sums-

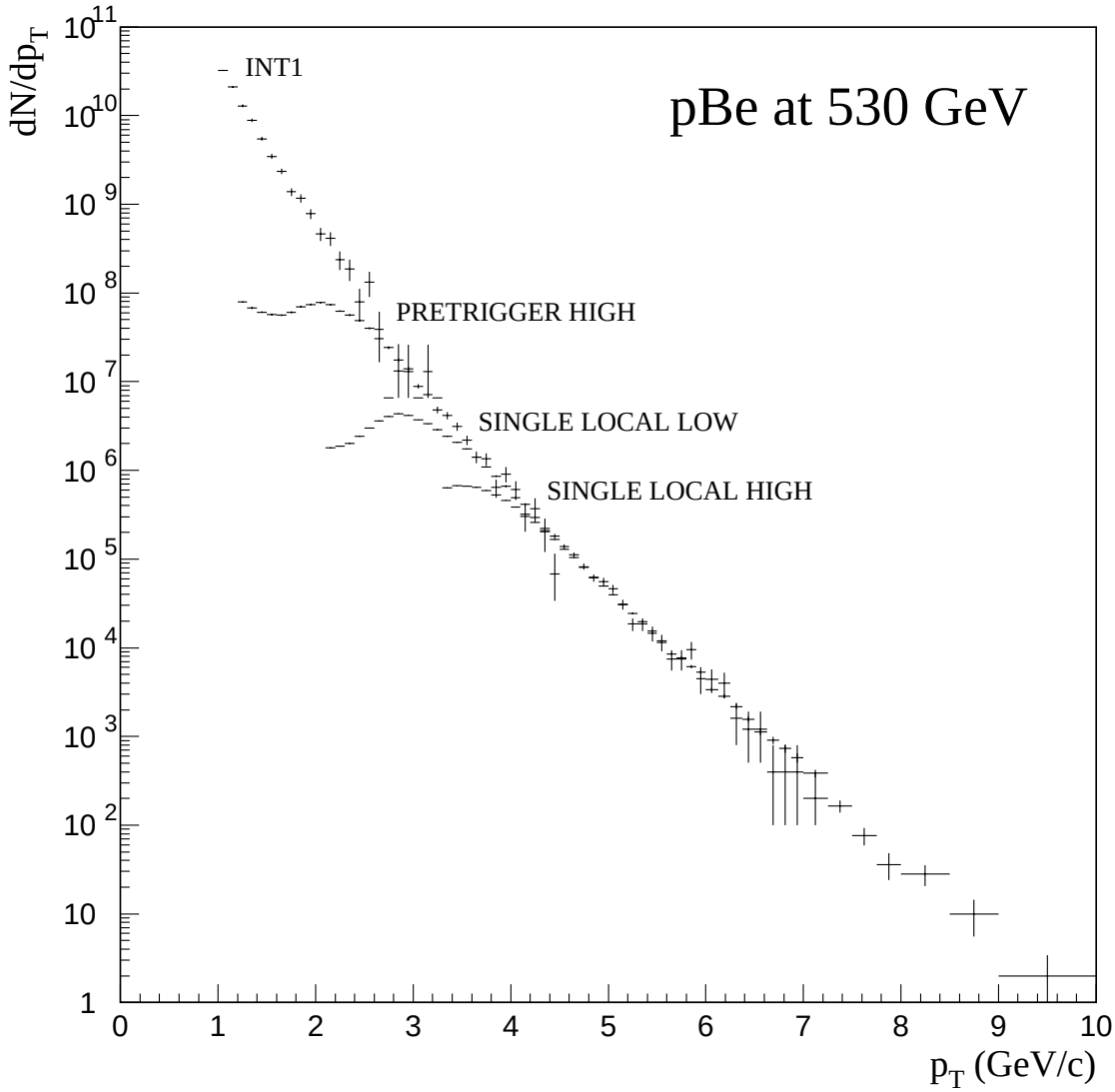

Figure 3.1 The π^0 number distribution prior to trigger corrections. Where two triggers overlap, the trigger corrections allow for the use of the higher-threshold trigger, along with its higher statistics.

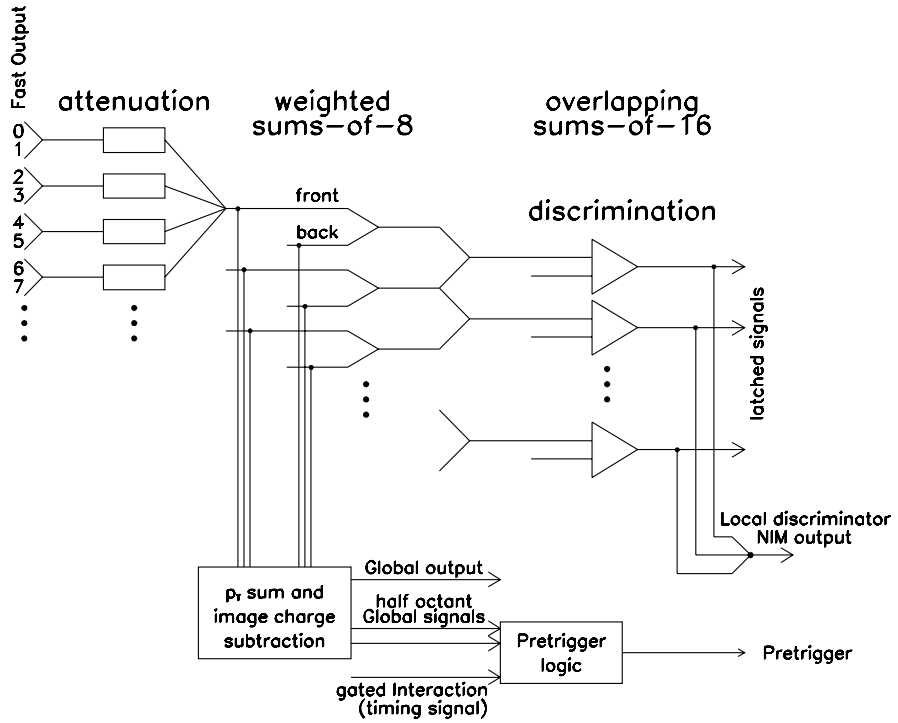

Figure 3.2 A block diagram of the EMLAC based trigger system.

of-eight in each octant. These sums-of-eight were sent to the biased p_T adder cards [80] and the local discrimination cards (Figure 3.2).

The PRETRIGGER was based on this fast trigger-p_T estimate. It rejected a large fraction of very low-p_T events quickly; in addition, it provided EMLAC timing information. The biased p_T adder cards summed the total trigger-p_T in a half octant[3]. The half octant trigger-p_T was sensitive to noise and image-charge effects [80]; to minimize these effects a small threshold requirement was placed on each sum-of-eight. The adder cards output was then sent to a zero-crossing

[3] This is half the radial view, i.e. 128 strips, not the inner/outer ϕ boundary used elsewhere in this document.

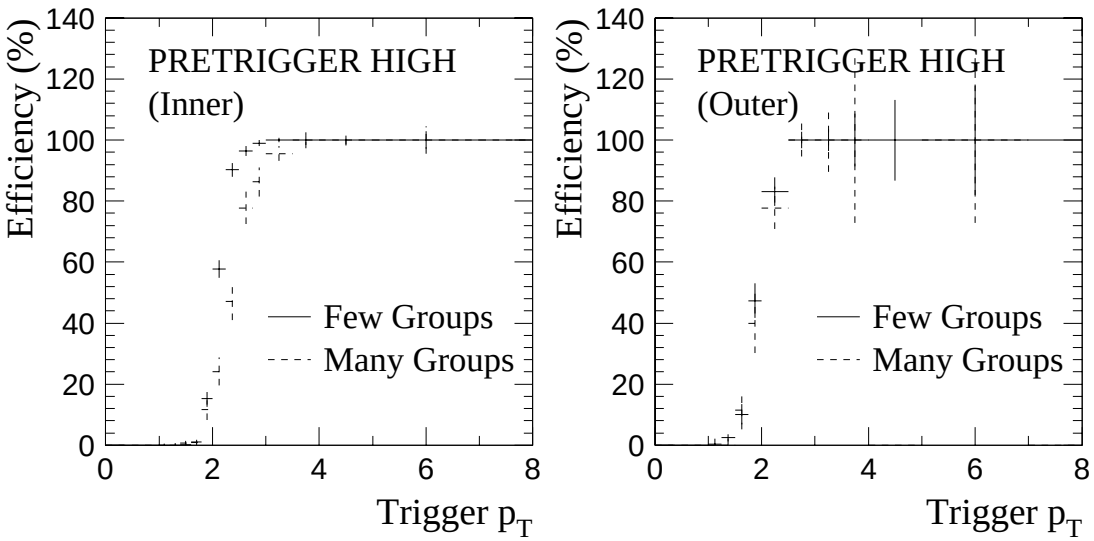

Figure 3.3 Selected inner (left) and outer (right) PRETRIGGER HIGH turn-ons for few (solid) and many (dashed) groups from the 1991 data. The error bars above the turn-on region are intended to provide an estimate of the statistical uncertainty of the measurement, and should not be taken to imply that the efficiency could exceed 100%.

discriminator that provided a timing reference for the EMLAC signals. This zero-crossing time was then compared to INT1 to form the PRETRIGGER.

Several vetoes were applied to the PRETRIGGER signal. PRETRIGGERS were vetoed when they came in coincidence with Faraday room power supply noise spikes (400 Hz). Pileup and image-charge effects were reduced by requiring there be no significant trigger-p_T in the half octant in the 350 ns prior to the PRETRIGGER signal. Spurious triggers due to muon bremsstrahlung were avoided by using the veto walls (Section 2.2.4). Coincidences between signals in the upstream and downstream sets of veto walls with the PRETRIGGER signal was cause to veto the event.

Surviving PRETRIGGER signals were then compared against a pair of level discriminators. The higher threshold discriminator (PRETRIGGER HIGH) was used to create the single-octant trigger (Figure 3.3). The lower threshold discriminator (PRETRIGGER LOW) was used for the double-octant trigger (TWO GAMMA PRETRIGGER); it also required a valid PRETRIGGER LOW signal in another octant (one of the opposite three octants for a total of 12 possible trigger combinations).

3.1.3 Local Triggers

A trigger sensitive to single photons, π^0's, and η's was implemented using the local structure of the sums-of-eight. Pairs of sums-of-eight were combined to form overlapping *sums-of-sixteen*; there were 31 overlapping sums-of-sixteen in each octant (Figure 3.4). Each overlapping sum-of-sixteen was compared to a pair of level discriminators (Figure 3.5). Both thresholds were utilized for the single-octant triggers (LOCAL LOW and LOCAL HIGH) (Figure 3.1); the lower threshold was also used for the double-octant trigger (TWO GAMMA).

3.1.4 Global Triggers

A set of jet triggers were also implemented where the trigger-p_T was summed over the half or full octant (Figure 3.4). These signals, which also had to satisfy the local requirements, were compared against a pair of discriminators to provide low and high triggers. These triggers were not used in this analysis. More details can be found elsewhere [80].

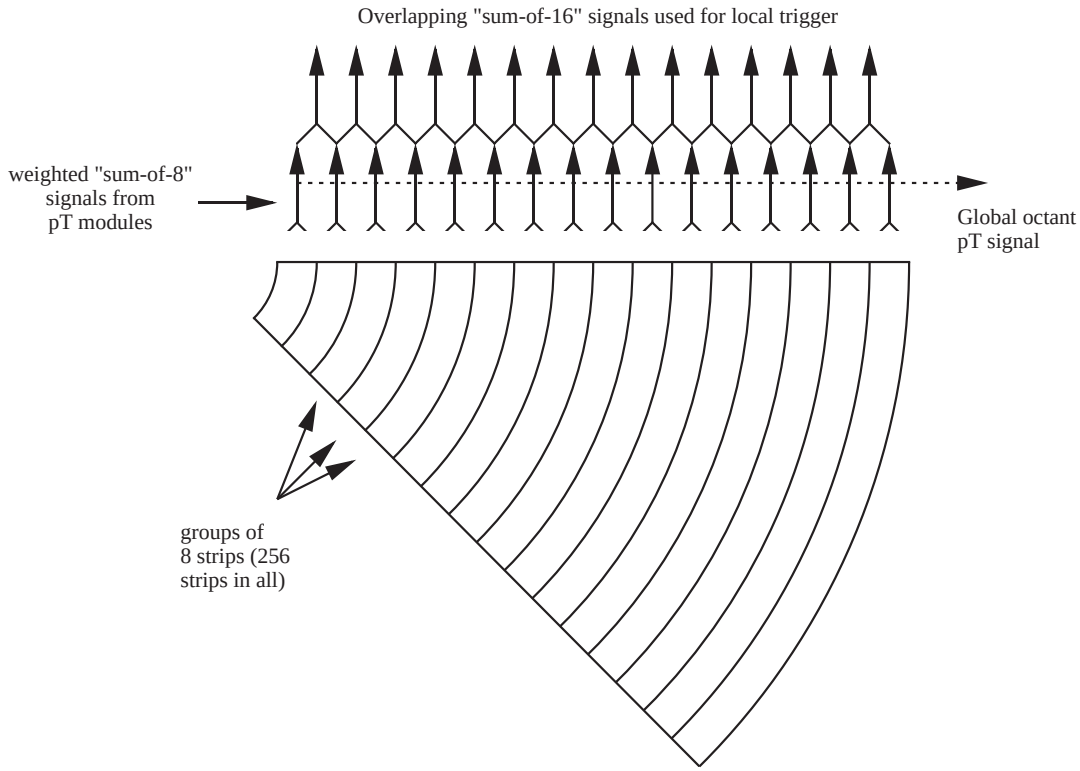

Figure 3.4 The p_T summing for the local triggers.

3.1.5 Double-Octant Trigger

The double-octant trigger, TWO GAMMA, was intended for the investigation of double direct-photon production (hence the name). It was also used to measure two-arm event structure where there were high-p_T neutral particles on opposite sides of the detector. Low-p_T thresholds were used for this trigger as this class of events is very rare. The trigger required the TWO GAMMA PRETRIGGER in coincidence with a LOCAL LOW in two octants. There were 12 allowed octant configurations: the four opposite octant combinations (1+5, 2+6, 3+7, and 4+8), and the eight adjacent-opposite octant combinations (1+4, 1+6, 2+5, 2+7, 3+6, 3+8, 4+7, and 5+8).

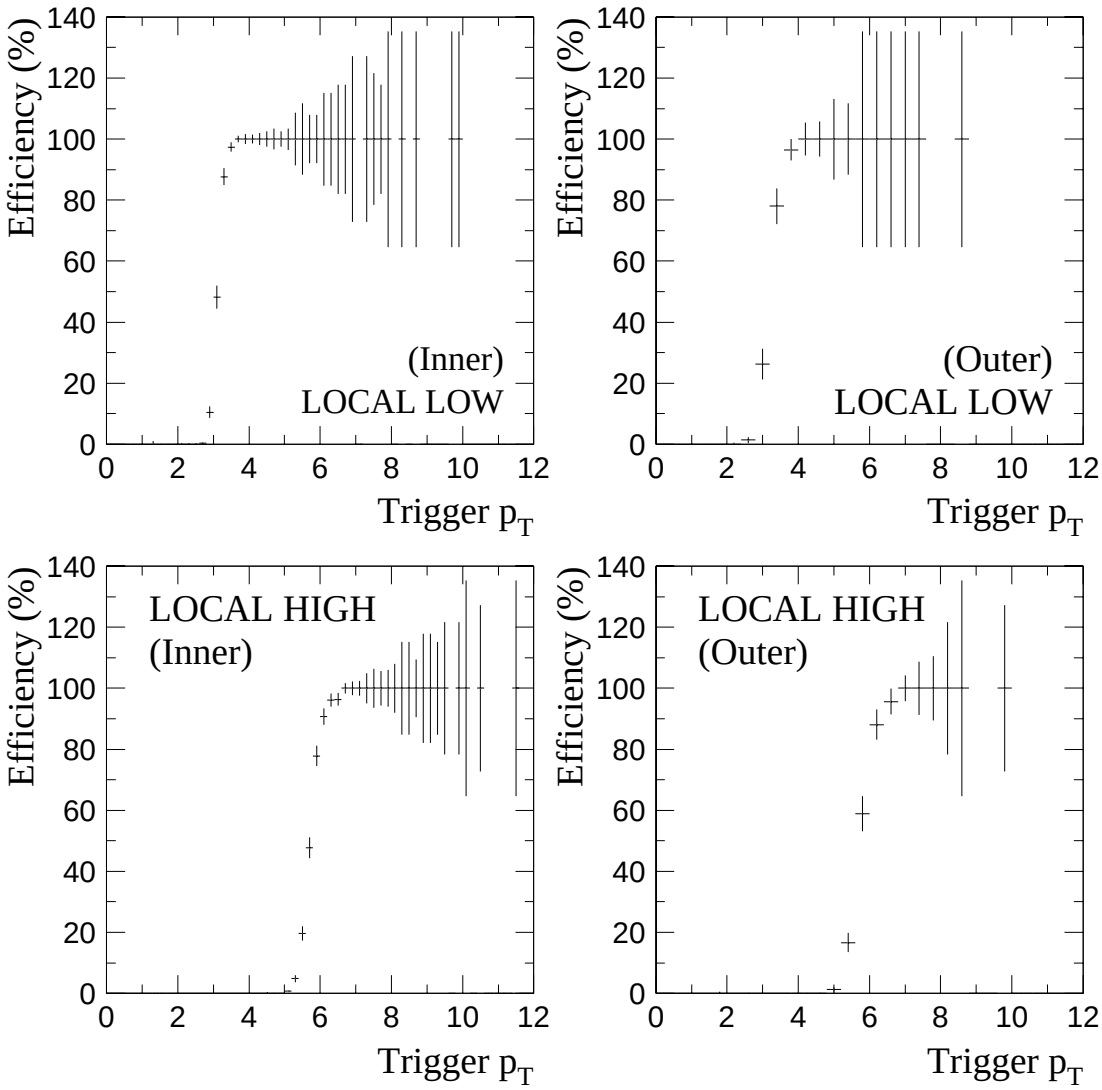

Figure 3.5 LOCAL LOW (top) and LOCAL HIGH (bottom) turn-ons for selected inner and outer locals as a function of trigger-p_T from the 1991 data. The error bars above the turn-on region are intended to provide an estimate of the statistical uncertainty of the measurement, and should not be taken to imply that the efficiency could exceed 100%.

> [The 1991 fixed-target] run had occasional episodes of intensity-dependent instability in the spill...The extent of the problem for experimenters ranged from negligible to bothersome...Finally, near the end of the run, the problem was isolated in the RF system...
>
> Craig Moore [99]

The accelerator experienced significant beam related instabilities during the first portion of the 1991 fixed target run. Symptoms related to these instabilities were RF buckets with large numbers of particles and long strings of RF buckets each having a particle. The beam related instabilities caused the TWO GAMMA trigger to operate erratically; the trigger had to be removed for part of the run. The beam problems were mostly cleared up by run 13599 (when the trigger was reinstalled). This was early enough in the fixed target run that all of the 0.5 TeV/c running could be salvaged. However, the majority of the 0.8 TeV/c proton running could not; only the final portion of the run was usable (Tables 6.1 and 7.2).

3.2 Data Acquisition

The data acquisition system (DAQ) collected the raw electronic signals from the Meson West spectrometer [100, 73]. In particular, information collected by the DAQ from the electromagnetic calorimeter was used to form the trigger (Section 3.1.2). Once the trigger was satisfied, the DAQ concatenated the information from the various subsystems (Figure 3.6) and wrote the event to tape.

Low impedance cables carried the charge collected on the EMLAC anode boards through the LAC feedthroughs at the top of the gantry to the RABBIT crates [101] located in the Faraday room. The signals were then amplified, integrated, and digitized by specially designed amplifier cards [102]. Each card had 16 channels, one per detector strip (Figure 3.7). There were three outputs:

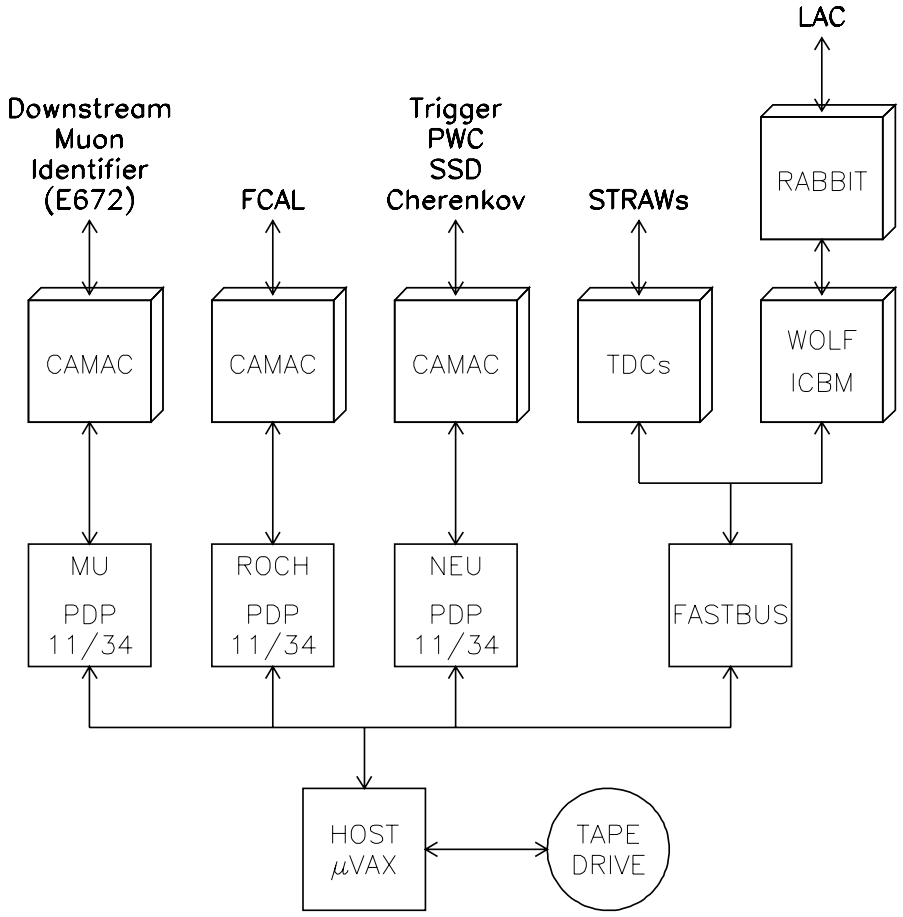

Figure 3.6 A block diagram of the data acquisition system.

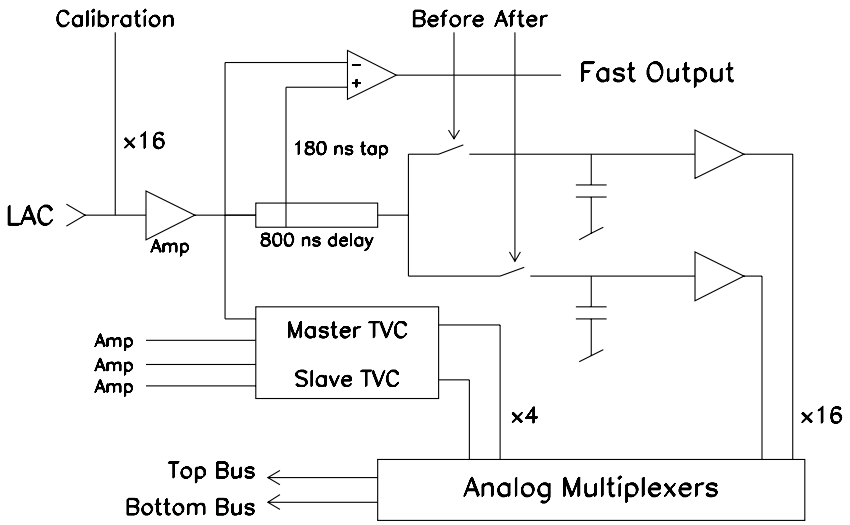

Figure 3.7 A block diagram of the LAC amplifiers.

fast-out, sample-and-hold, and the time-to-voltage converter (TVC). The fast-output was the difference between the amplified EMLAC signal and its 180 ns delayed copy; this signal was sent to the trigger electronics (Section 3.1.2). If the event was accepted by the trigger, then a BEFORE signal was issued. This signal was followed after a specified time by an AFTER signal (Table 6.1). Upon receipt of the BEFORE, the voltage level of the amplifier prior to the event was sampled (the amplifier signal was delayed by 800 ns for this purpose). The AFTER caused the integrated amplifier signal to be sampled. The difference between these two voltages was digitized and represented the amplified strip energy.

The TVC was intended to make a trigger-independent measurement of the photon's time [103]. Every four adjacent LAC channels were added together. The output of these amplifiers was differentiated and compared to a crate–wide threshold. If the signal was above threshold then the timing circuit was engaged.

The circuit had a common stop—the timing ended upon receipt of the BEFORE gate. Once the circuit was triggered, a second circuit could be enabled in case of another energy deposition above threshold in the same LAC channels. That circuit was also stopped by the same BEFORE signal. The first circuit was referred to as the master; the second, the slave. The timing circuits reset if there was no trigger signal within $\approx 1.5\mu$s.

The EMLAC was monitored, calibrated, and read-out by the FASTBUS system [104] through the RABBIT crates [105, 101]. The FASTBUS system also read out the HALAC and the STDs. The other detector subsystems were read out by three PDP-11 minicomputers through parallel and serial CAMAC units [106]. A DEC μVAX then concatenated information from the subsystems and wrote out the event to a pair of 8 mm magnetic tape drives. The μVAX was also responsible for run control through `VAXONLINE` [107]. Events were grouped into runs; each run containing a maximum of 65535 events. Under normal running conditions, a new run was started every two hours. The DAQ was reinitialized periodically (every eight hours) at which point calibration data (pedestals, etc) were recorded for the spectrometer. Calibration data was also recorded between accelerator spills.

Chapter 4 Event Reconstruction

4.1 Overview

More than 70 million events were accumulated during the 1990 and 1991 fixed target runs. These data were processed by a large FORTRAN software package which interpreted the recorded electronic signals as photons and charged particles. Event reconstruction was controlled by a single steering routine, `MAGIC` [108], which performed data unpacking and called other routines to independently reconstruct data from specific spectrometer elements. Data were organized by the `ZEBRA` [109] dynamic memory system (banks). `ZEBRA` was also used to write events in a machine architecture independent format.

The reconstruction code was developed on VAX computers[1] with some work performed on Silicon Graphics (SGI) machines. Extreme care was taken to ensure the output was architecture and operating system independent. Selected events were reconstructed on SGIs during data taking to monitor data quality. Full reconstruction took place on parallel processing computer clusters run by the Fermilab Computing Division. These *farms* consisted of a single I/O node and many worker nodes. Each worker node processed, in full, a single event. Reconstructed events were concatenated together and written to tape. Three different architectures were employed by this experiment for event reconstruction: SGI, Sun, and IBM.

[1] The VAXes ran the VMS operating system. All other computers used for event reconstruction ran variants of the UNIX operating system.

`MAGIC` is a flexible framework that calls reconstructor programs according to a user-controlled scheme. There were six independent reconstruction packages:

- `DLREC`: Trigger and Čerenkov logic [110];
- `PLREC`: Charged particles and associated vertices in the charged particle spectrometer [84, 87, 90];
- `EMREC`: Positions and energies of photons and electrons in the EMLAC [73];
- `HCREC`: Positions and energies of hadrons in the HALAC [87];
- `FCREC`: Forward energy in the FCAL [93, 94];
- `MUREC`: Muons in the downstream muon spectrometer [95].

Summaries of two reconstructors important to the analyses described in this document, `PLREC` and `EMREC`, are presented below.

4.2 Tracking Reconstruction

The reconstructor for the charged particle spectrometer, `PLREC` (PLanes REConstructor), was responsible for converting hits detected by the tracking chamber electronics (SSDs, PWCs, and SDTs) into tracks representing the trajectories of charged particles through the spectrometer. The momentum of each charged particle was measured using this information combined with the action of the dipole magnet (Section 2.3.2). `PLREC` was also responsible for reconstructing the location of the beam–target interaction (*primary vertex*) as well as vertices due to heavy particle decays or secondary interactions.

The general methodology for charged particle reconstruction was to identify tracks using combinations of pairs of hits on so-called seed-planes with hits on all other planes. Every view (X, Y, etc) of each detector (beam SSDs, vertex SSDs, PWCs, and SDTs[2]) was examined independently. Hits were identified with

[2] Straw tracks used PWC tracks as seeds.

Detector	Track hits	Distance (wire spacing)	χ^2/DOF
beam SSDs	3	1.5	3.0
	2	1.5	1.0
PWCs - view	4	1.0	3.0
	3	1.0	2.0
PWCs - space	> 13	1.5	3.0
	13	1.5	2.0
vertex SSDs	5	1.5	5.0
	4	1.5	4.0

Table 4.1 Distance and χ^2/DOF requirements for tracks in various detector systems. This information is for the first iteration only. Subsequent iterations had somewhat different requirements. See [84] for more details.

particular tracks according to their distance from the track and the associated χ^2 per degree of freedom (Table 4.1). The maximum number of hits per track per view per detector was a 3-hit beam SSD track, a 5-hit vertex SSD track, a 4-hit PWC track, and a 16-hit SDT (straw) track. Once all such tracks for a particular view were found, hits associated with these tracks were removed from consideration and the remaining hits were used to progressively find the remaining tracks (down to 2-hit tracks in most cases). These view tracks were then combined to find their three dimensional analogues, *space tracks*. Finally, space tracks from the different detectors were *linked* together to yield tracks representing charged particle trajectories through the spectrometer.

4.2.1 Downstream Tracking

`PLREC` used the PWCs and SDTs to reconstruct space tracks downstream of the analysis magnet. These tracks were used to measure charged particle momenta

and to identify electron-initiated showers in the EMLAC. Track reconstruction began with the PWC data; seed-planes were defined as the outermost pair of PWC planes in each view. Once view tracks were identified, candidate space tracks were formed from pairs of tracks in the X and Y views. These candidate space tracks were then projected onto the U and V views. Candidates were accepted if there were a sufficient number of hits in the U and V views corresponding to the space track. The procedure was repeated, starting with the U and V views and projecting onto the X and Y views, picking up any missed tracks.

PWC space tracks were then used as seeds for the SDT tracks. Space tracks were projected onto the SDTs and hits were assigned to the track if the track–hit distance[3] was less than 3.5 mm. Following this procedure, each space track was refit using only SDT hits. The error associated with each hit was primarily a function of its TDC time [90]. The mean SDT hit resolution was approximately 250 μm. The search window was decreased with each iteration, from 3.5 mm to 1.3 mm to 0.8 mm. SDT tracks also had chamber-hit configuration requirements. During the first iteration, straw track candidates were required to be at least 8-hit space tracks with 4-hit tracks in each view having at least two hits in each of the two SDT modules. These requirements were relaxed in later iterations.

Finally, each downstream track was refit using both the PWC and the SDT information. Since SDT hits provided better resolution, the results of the fit were dominated by the SDTs.

[3] This search window accounted for the uncertainty in the projection of the PWC tracks onto the SDTs.

4.2.2 Upstream Tracking and Linking

Tracks reconstructed in the vertex SSDs were used to locate the beam–target interaction point and to identify vertices attributed to secondary interactions and heavy particle decays. View tracks upstream of the analysis magnet were matched (*linked*) with tracks downstream of the magnet [87]. This provided an additional constraint which improved the resolution of the upstream tracks [84].

The three pairs of SSDs upstream of the target were used to track incident beam particles. The measured beam track was used to improve the resolution of the primary vertex and was used as a reference for the p_T measurement of particles emerging from the beam–target interaction.

4.2.3 Vertex Finding

Precision measurements of the beam–target interaction location were essential for the physics goals of E706. Upstream tracks with the best links to downstream tracks were used to ensure good quality vertices. At least three upstream tracks were required for a vertex to be reconstructed in a view.

The vertex position was determined by a χ^2 minimization of the impact parameter [111, 84]. If a relevant beam track was found, it was included in the vertex location fit. The Z position of the vertex was determined by a weighted average of the positions calculated in the X and Y views. If more than one vertex was identified by this procedure, then the most upstream vertex was assumed to represent the location of the beam–target interaction. The closest beam track to the primary vertex with an impact parameter less than 100 μm was designated as the interacting beam particle that produced the event.

4.2.4 Relinking

Once the primary vertex was located, it was used as an additional constraint on the tracks upstream of the analysis magnet. These tracks were then relinked to the tracks downstream of the magnet to improve the resolution of the entire system. Using a full Monte Carlo simulation of the spectrometer (Section 6.2.2), the fractional momentum resolution of the tracking system was determined to be [84]

$$\sigma(\mathrm{p})/\mathrm{p} = 0.0076 + 0.00026\mathrm{p}, \tag{4.1}$$

where p is the charged particle's momentum in GeV/c.

4.3 Electromagnetic Reconstruction

The reconstructor for the electromagnetic calorimeter, `EMREC` (ElectroMagnetic REConstructor), reconstructed showers from the EMLAC amplifier signals. First, raw amplifier signals were converted into an energy equivalent. Then the reconstructor searched for patterns in the data: *groups* of channels with energies above threshold, and *peaks* within the groups. An energy independent shower shape was used to fit the peaks to evaluate their energies and positions. These *gammas* were then matched by shape and location to form photons. The showers in each detector quadrant were independently reconstructed.

4.3.1 Unpacker, Pedestals, and Gains

ONE RING TO BIND THEM AND IN THE DARKNESS RULE THEM.

— *Comment card for* `UNPCAL`

The unpacker for the electromagnetic calorimeter organized raw data into `ZEBRA` banks and converted raw amplifier counts into energy. Strip energies were

adjusted for amplifier pedestals [105, 79] and relative gains [112]. Pedestals and gains information for the LAC amplifier cards were collected by the FASTBUS system each time the DAQ was reinitialized (about once per eight hours). Online pedestals were measured for each LAC channel by averaging the results of at least 128 consecutive readouts in the absence of incident beam. The pedestals were refined by analyzing non-interacting BEAM triggered events [105]. This offline analysis typically shifted the pedestal value a few counts compared to the online constants. Gains were measured by injecting charge into the amplifiers; this charge was collected and read out through the data pathways. These gains were stable over time to the $\pm 0.2\%$ level [35, 112].

The adjusted ADC counts were converted into energy using a factor determined from initial detector studies with incident electron beams [75]. The conversion factor was 3.1 MeV/count [102]. A correction was made for the time-dependent EMLAC energy response (Section 6.5.1). Finally, the few dead channels in the EMLAC ($< 0.3\%$ of the total) were assigned energies based on the contents of neighboring strips.

A *summed* section was formed by adding corresponding strips from the front and back. The summed section was used for group and peak finding and to correlate gammas.

4.3.2 Group Finding

A *group* was defined as a series of adjacent strips each of whose energies exceeded 80 MeV (95 MeV in outer ϕ). At least one strip was required to have an energy greater than 300 MeV (350 MeV in outer ϕ) and the total energy of the group had to exceed 600 MeV. Finally, the group had to contain at least 3 strips above threshold. This last requirement was reduced to 2 strips for outer ϕ where

the strips are relatively wide and was reduced to a single strip for groups adjacent to the flash[4] in the R views (but only if there was significant energy deposited in the flash).

4.3.3 Active Pedestal Subtraction

Some events contained obvious residual pedestals. These features were attributed to a variety of sources including image-charge effects and overlapping events. An example of this type of event is shown in Figure 4.1. These features were corrected event-by-event by fitting the regions between groups (the event background) in the R views. The resulting function was subtracted (in all channels) from the R view and was used to determine the ϕ view correction. This procedure was performed iteratively by varying the group thresholds [94]. The impact of the active pedestal subtraction upon the event shown in Figure 4.1 is illustrated in Figure 4.2.

4.3.4 Peak Finding

Groups were scanned to find the local maxima and minima (with special care taken near group boundaries). A *peak* was defined as a significant maxima surrounded by minima. Significant, in this case, meant the height of the peak above the surrounding valleys (the minima) was at least 2.5 standard deviations above that expected from energy fluctuations in the strips (Equation 4.3).

Following completion of the summed section peak finding, a second search was implemented in the front section to determine whether the peaks resulted from multiple showers. If additional peaks were found in the front section, valleys for

[4] The flash was an irregularly shaped strip on the innermost and outermost edges of the radial and azimuthal views.

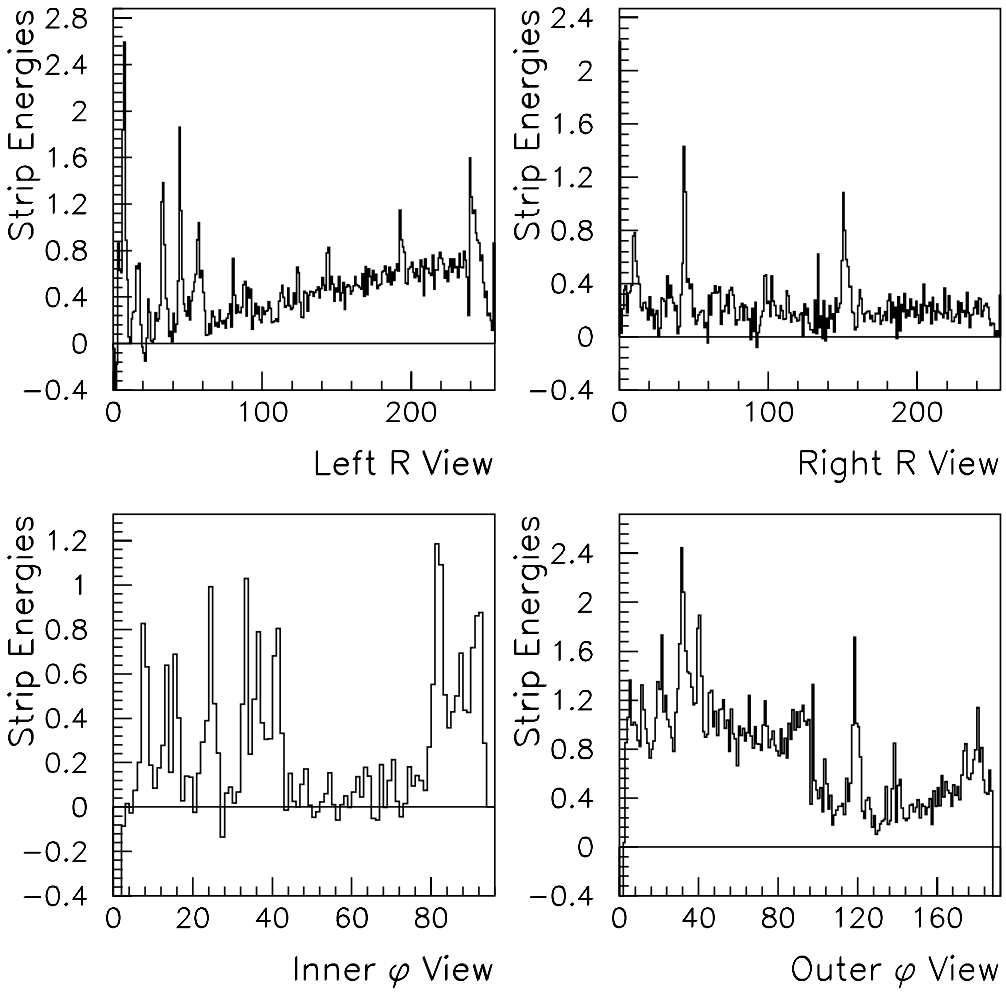

Figure 4.1 An event from one EMLAC quadrant before the active pedestal subtraction has been applied. Note the ramp in Left R and the level difference between the left and right sides of Outer ϕ.

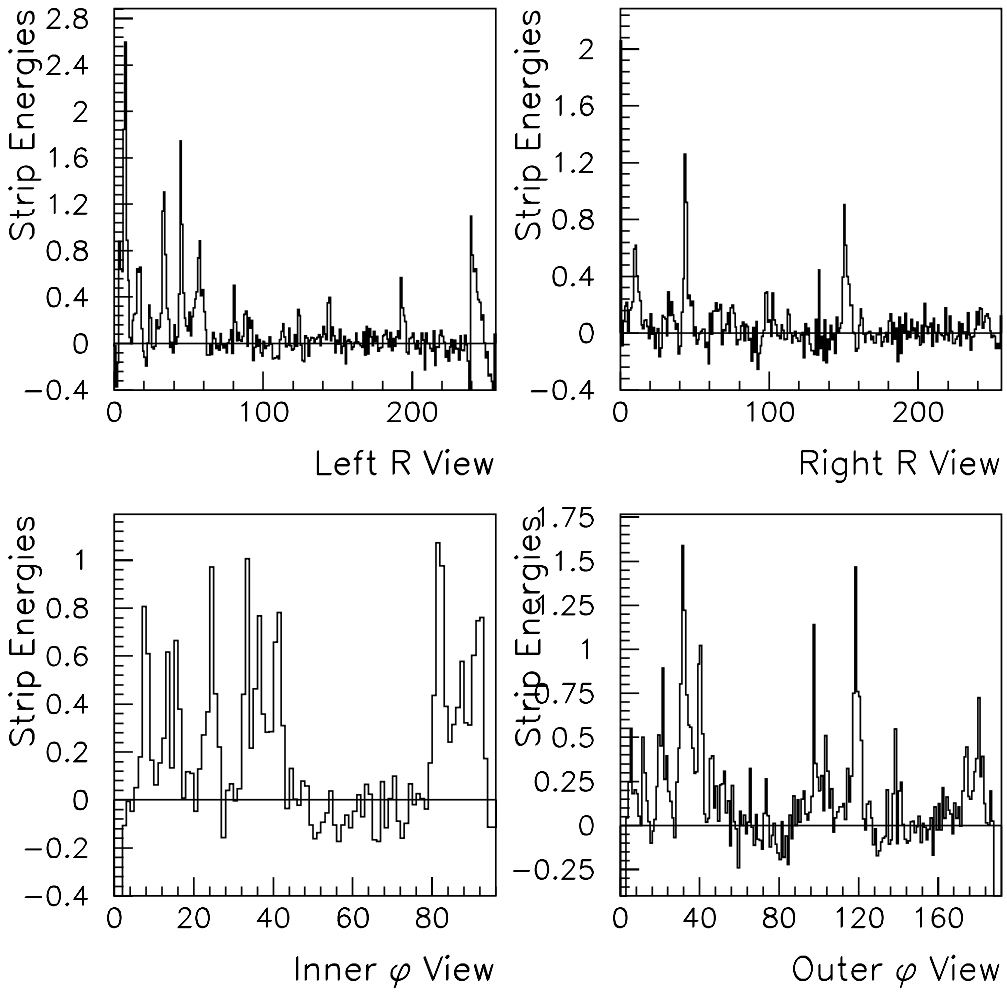

Figure 4.2 An event from one EMLAC quadrant (the same event as in Figure 4.1) following the application of the active pedestal subtraction.

each of them were re-evaluated and the peak significance checked. If a peak was found in the front section, then the corresponding peak was searched for in the back section as well.

It is possible two showers, such as those from the decay of a high-p_T π^0, overlap to such an extent that there is no significant valley between the peaks. In this case, one of the photons can show up as a shoulder on one side of the peak. A search for shoulders was initiated whenever a single peak was found in both the front and summed sections with an integrated energy (between the valleys) of at least 35 GeV. An ideal shower has an approximately exponential shape (Figure 4.3), so a peak in the logarithmic derivative of the strip energy with respect to the distance from the peak position would indicate the presence of a shoulder. Once a shoulder was found, its significance was checked.

Peak positions and energies were estimated to help perform shower shape fits.

4.3.5 Gamma Reconstruction

The energies and positions of peaks were identified precisely using a shower shape fit (Figure 4.3). The shower shape was parameterized independently in the front and back. The summed section shower shape was determined by adding together those for the front (70%) and the back (30%). The shower shape fit was performed by minimizing the χ^2,

$$\chi^2 = \sum_i \frac{(E_i - z_i E)^2}{\sigma_i^2}, \tag{4.2}$$

where the E_i are the strip energies in GeV, the z_i are the fraction of shower energy deposited in the strip, and σ_i was the nominal resolution [73] of the EMLAC given by

$$\sigma_i^2(E) = (0.22)^2 + (0.16)^2 E_i + (0.01)^2 E_i^2. \tag{4.3}$$

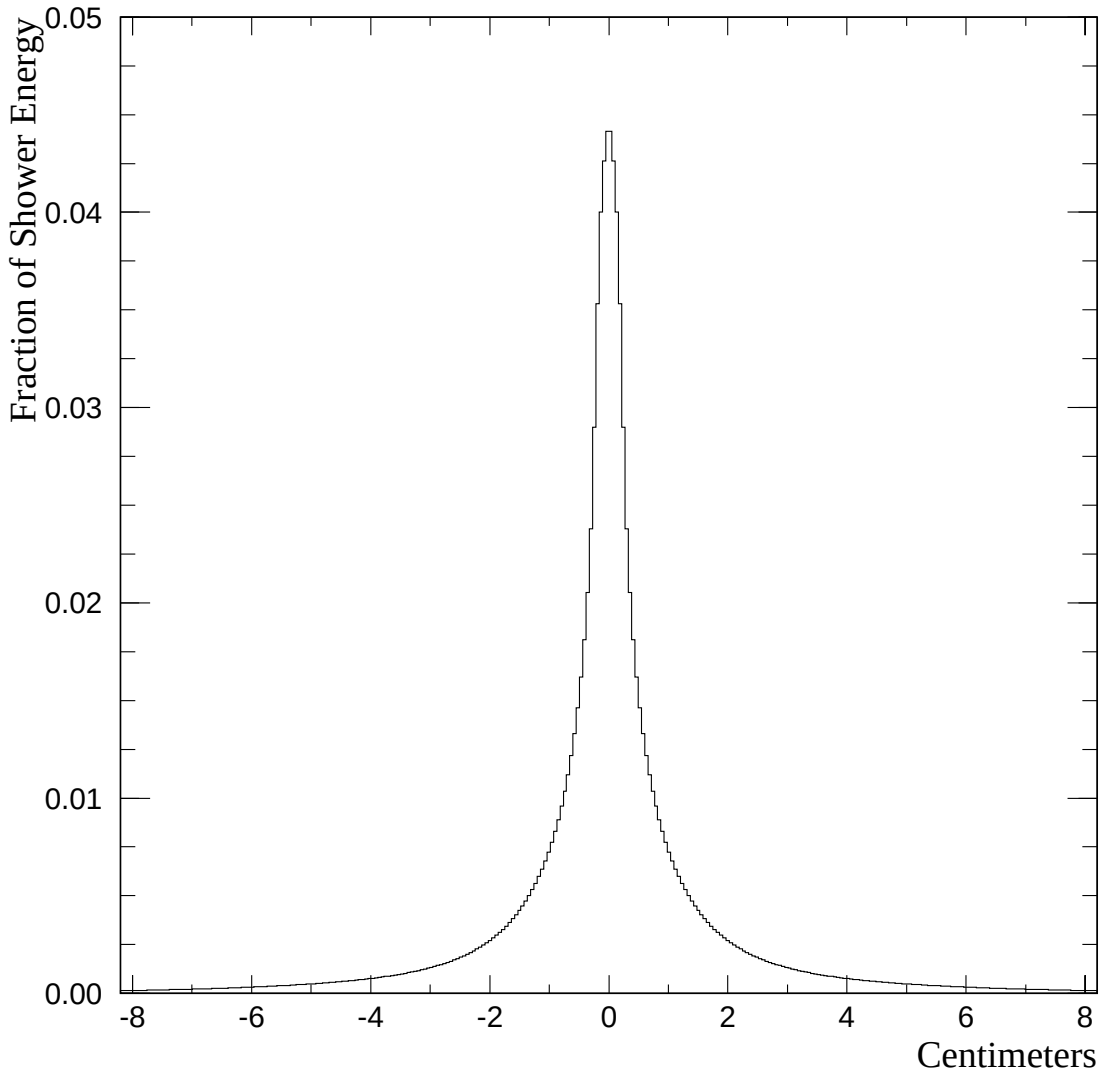

Figure 4.3 Photon shower shape function for the summed section.

The shower shape was parameterized in terms of distance from shower center; it fit unambiguously in the radial views. In the azimuthal views, estimates of the radial position were made first; these were based on shower width measurements. The ϕ energies were refit at a later stage in the reconstruction process (Section 4.3.6).

Once the gammas were identified, their shower energies were corrected for losses at the quadrant and view boundaries and for the fraction of shower energy deposited in strips lying outside the valleys (tails).

4.3.6 Gamma Correlation and Photon Reconstruction

Gammas from the radial and azimuthal views were correlated together to measure the positions of the reconstructed showers and improve the energy measurement. The correlation procedure relied on the segmentation of the detector into left/right and inner/outer regions. For example, radial gammas with R $<$ 40 cm were only correlated with inner ϕ gammas (Figure 4.4). There were also special configurations relating gammas near the view boundaries and overlapping gammas (shoulders) [73]. Since photons deposited roughly the same energy in the radial and azimuthal views, the correlation was performed based on the gamma energy. Two gammas were considered the radial and azimuthal projections of the same shower if their summed, as well as front and back, energies were similar. The correlation procedure was performed twice to improve measurement of the ϕ energies.

4.3.7 Photon Timing

The TVCs (Section 3.2) were used to determine photon arrival times with respect to the trigger. TVC pedestals were calculated somewhat differently than those for the LAC amplifiers (Section 4.3.1). While there was an online calibration

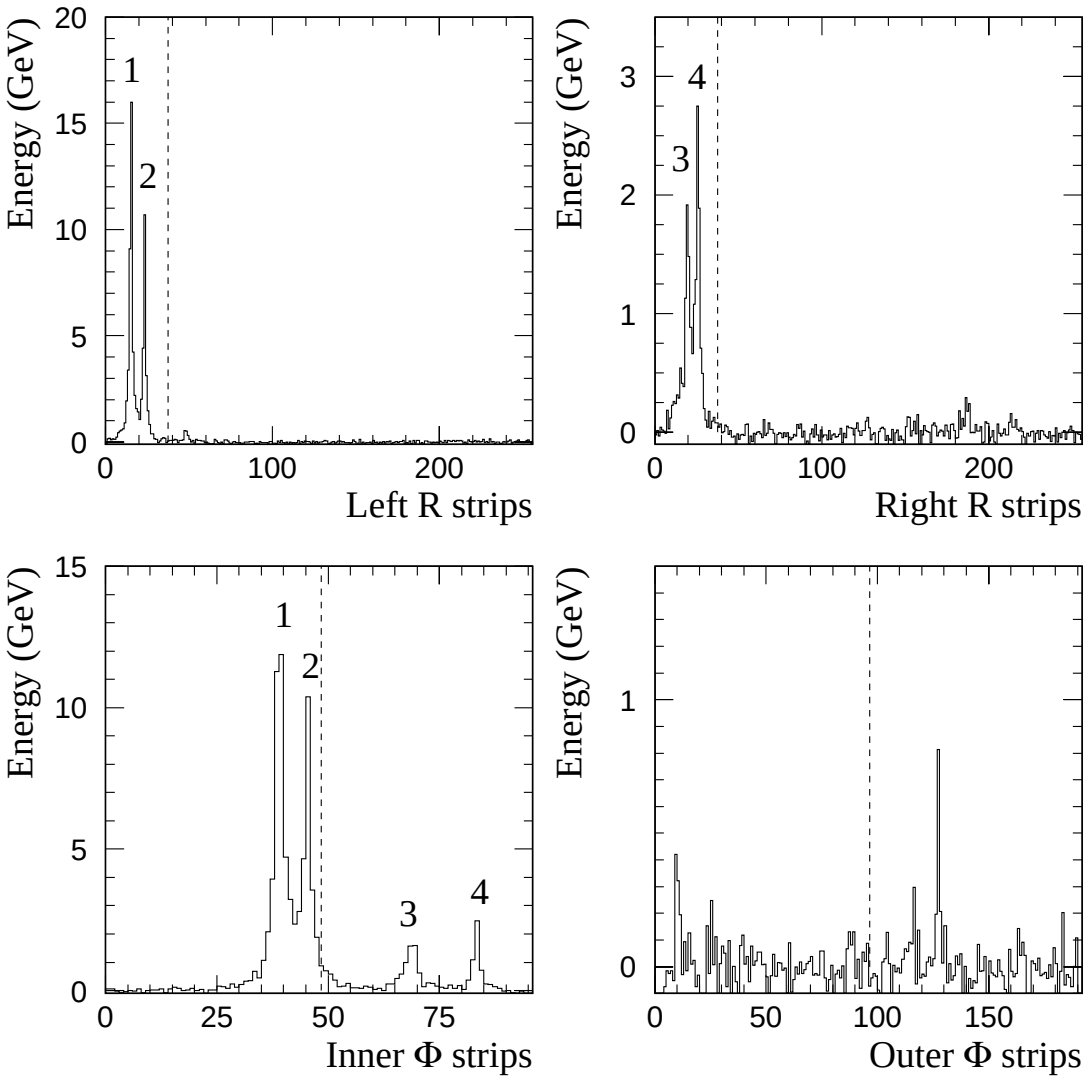

Figure 4.4 An event from one EMLAC quadrant showing how the gammas are correlated together. Dashed lines mark the locations of the boundaries in the other view. Showers tagged with the same number were correlated together.

system [113, 114], pedestals for the 1991 data set were calculated offline. TVC pedestals were based on energy deposited in the EMLAC. The ADC counts within a timing window were collected and the peak of the resulting distribution was used to represent the time of the trigger. The pedestal value was the difference from 34000 ADC counts, the nominal time of the trigger.

The sampling window was established by examining the distribution of TVCs for the EMLAC in ADC counts. A sample of this spectrum from an 800 GeV run is shown in Figure 4.5. The smaller the number of ADC counts, the later the photon arrived with respect to the trigger[5]. Two distinct features appear in the time spectrum. The large peak centered on 34000 ADC counts represents those photons which arrived in time with the trigger. The smaller peaks near 6000 ADC counts are noise that occurs when the TVC circuit is triggered by the action of the BEFORE gate. The window for pedestals determination was 24000 to 44000 ADC counts.

TVCs were adjusted during unpacking for pedestals, gains, and energy slewing. The TVCs are efficient in all views. A set of efficiency plots for R and ϕ views are shown in Figure 4.6. In both views the turn-on occurs at ≈ 4 GeV with a full efficiency of $\approx 95\%$ by 8 GeV. A minimum requirement of 4 GeV was enforced within the unpacker for each group of four LAC strips to ensure TVCs fired by low energy noise were excluded from consideration in the determination of the photon's time.

Photon times were based on the TVC value that occurred most often. In case of a tie, the time of the TVC group with the highest energy was chosen.

[5] The TVCs began accumulating voltage when the energy in the strips went above threshold. The voltage level was sampled once the BEFORE was issued. This signal was delayed by ≈ 800 ns from the trigger.

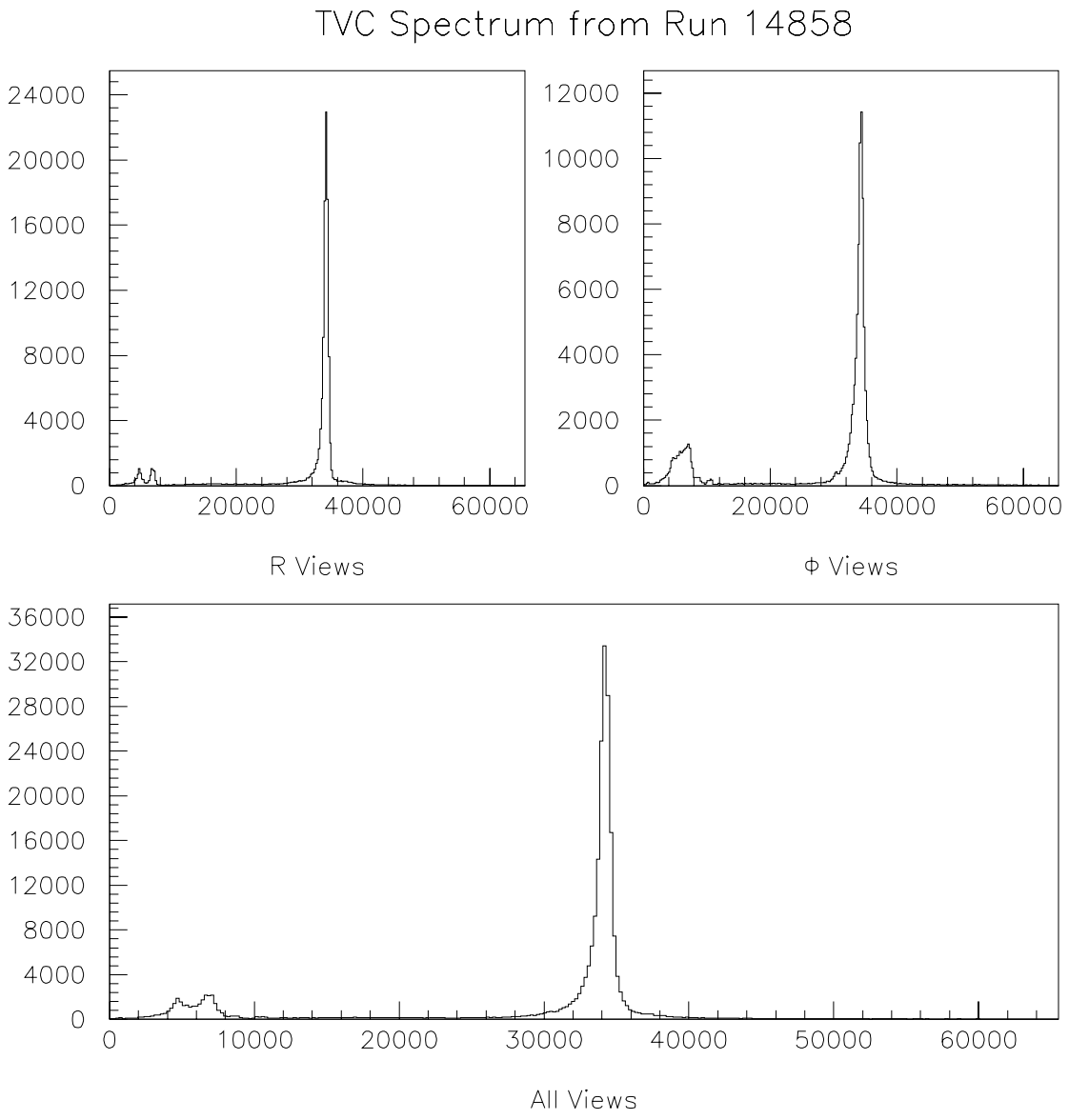

Figure 4.5 Pedestal corrected TVC distribution in ADC counts for groups of four LAC strips. There is a minimum requirement of 4 GeV on the total energy of the four strips. The peaks at low ADC counts represent electronic jitter due to the BEFORE gate.

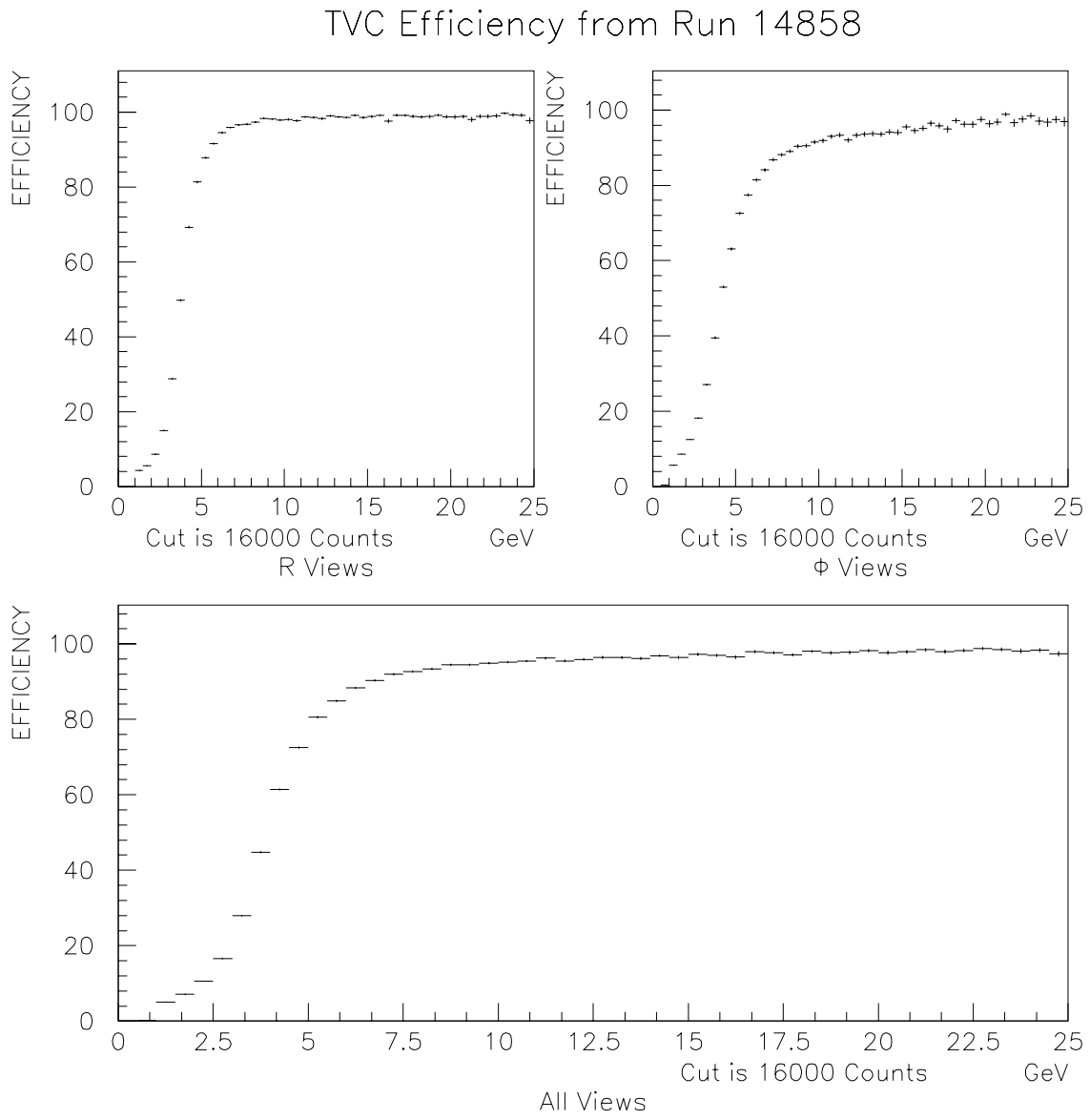

Figure 4.6 Raw TVC efficiency for groups of four LAC strips. Both master and slave values were used in these plots and the noise due to the BEFORE gate has been excluded.

Masters and slaves carried equal weight for the purpose of finding a time. Times were calculated in nanoseconds with an in-time value of zero ns. The time axis was reversed so that positive times were late (following the trigger) and negative times early (prior to the trigger). The conversion from counts to nanoseconds was 0.0229 ns/count.

The trigger system stored timing information about beam–target interactions. This data was used to examine the ability of the TVCs to distinguish between photons coming from different interactions in a single event record. The reconstructed times for π^0's with $p_T > 3$ GeV/c is shown in Figure 4.7 for a rare but illustrative configuration ($< 2\%$ of all events) of beam–target interactions. Here the interaction that triggered the DAQ is followed by another one approximately 38 ns later. The times associated with reconstructed π^0's for these events clearly show the different interactions.

The general ability of the TVCs to distinguish between different buckets can be better examined by overlaying π^0 times from events with similar configurations. Each event in Figure 4.8 was required to have an in-time interaction (bucket 8) and one interaction in another bucket (5–13 only). Each of the overlays has been peak normalized to the in-time signal to see the resolution smearing of the TVCs away from in-time. The peak representing the case when there was only one interaction (the in-time bucket) has been hatched for reference. This peak shape is present in each of the displayed configurations as each event requires (by definition) an interaction in the in-time bucket. While it is clear the TVCs can distinguish between buckets, their resolution is not fine enough to be able to easily discriminate between interactions at the single bucket level in the general analysis. TVC resolution is sufficient to distinguish between interactions at the two bucket level and was therefore used extensively in studies of the trigger system.

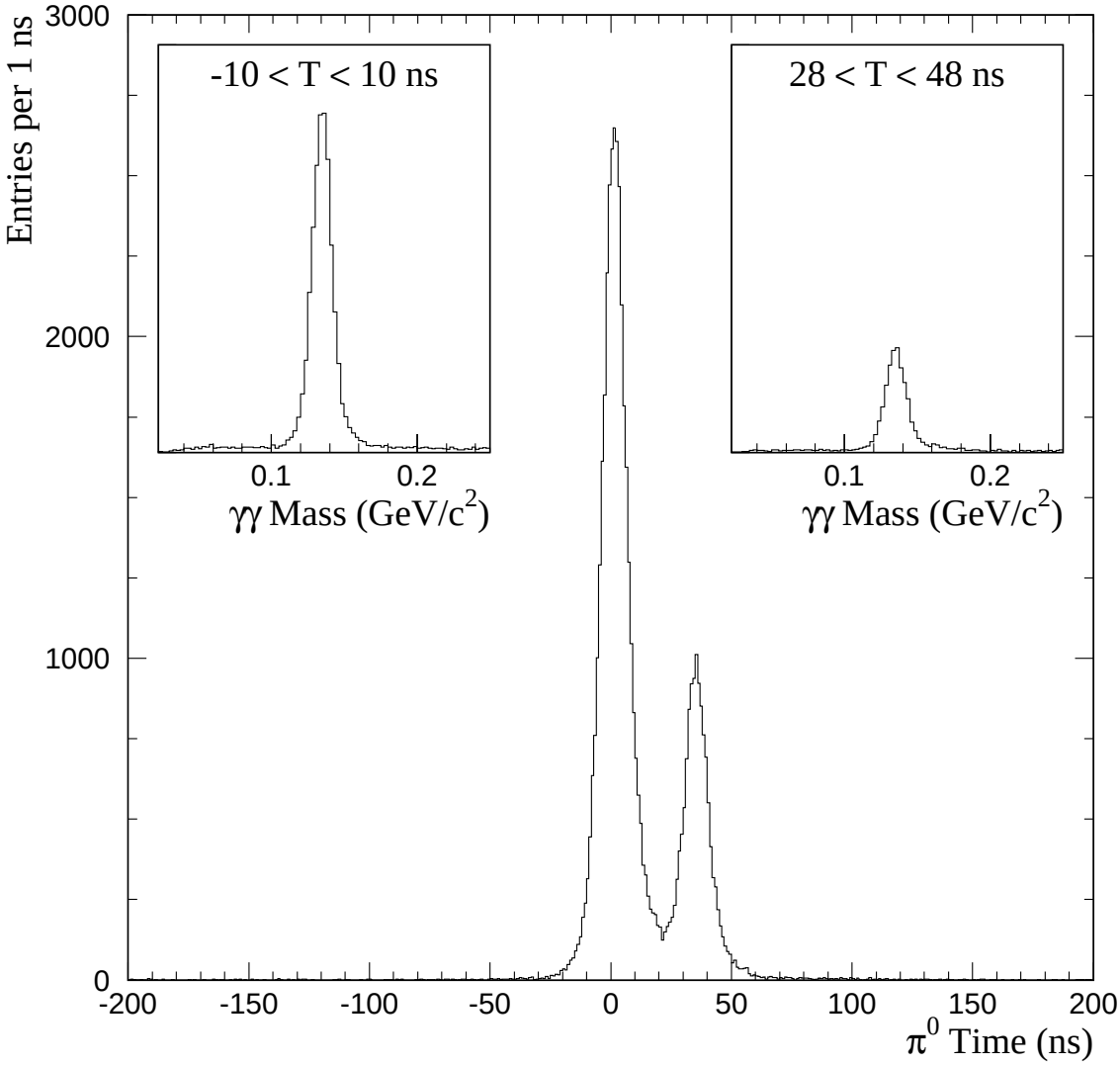

Figure 4.7 The time of π^0's having $p_T > 3$ GeV/c when there were two latched interactions—one in-time, and one approximately 38 ns later. Insets show the $\gamma\gamma$ mass distributions for combinations restricted to the indicated time intervals.

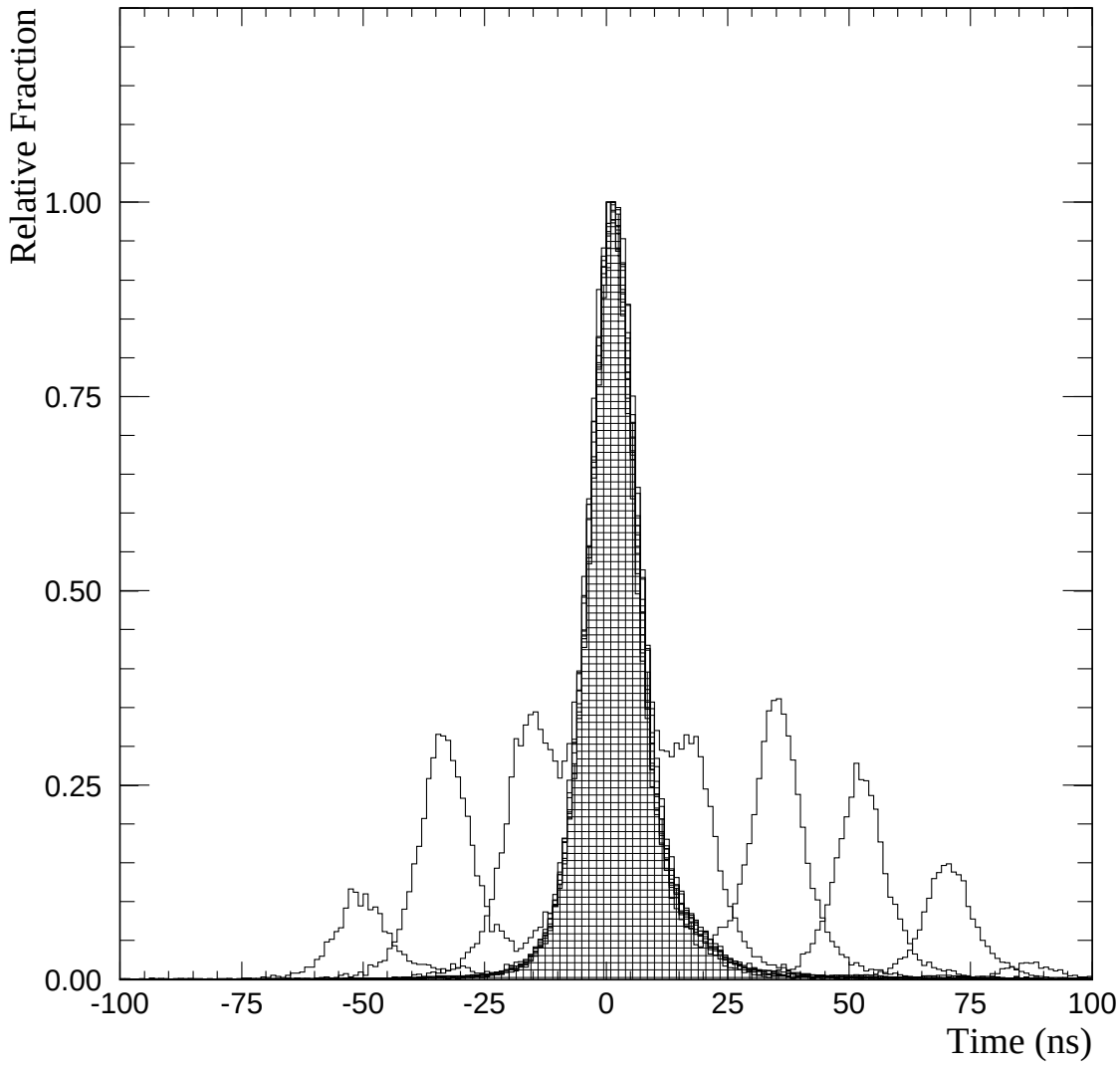

Figure 4.8 The time of π^0's having $p_T > 3$ GeV/c for specific configurations of beam–target interactions. Each configuration requires an interaction in-time (beam bucket 8) and one and only one interaction in buckets 5 through 13. Each overlay is peak normalized in the in-time bucket. The peak representing the case when there was only one recorded interaction (the in-time bucket) has been hatched for reference.

4.4 Event Database

Reconstructed tracks, showers, etc., were written in `ZEBRA` format to *Data Summary Tapes* (DSTs). These were event based files, organized by run number, which allowed for higher level analysis by comparing reconstructed information from different spectrometer elements. More precise detector calibrations were determined and applied to the data at this level. Also, the DSTs allowed for better particle identification; for example, electrons could be identified by correlating charged tracks with EMLAC showers.

Events were organized into object-based databases (NTUPLEs) using `HBOOK` [115]. The `NTUPLE` code was capable of creating NTUPLEs for the following event classes: one-photon (direct photon), two-photon (π^0, η), three-photon (ω), two-photon plus one-charged-track ($\rho^\pm$), two-photon plus two-charged-track (η, ω), two-arm ($\pi^0\pi^0$, $\pi^0\eta$, $\eta\eta$, $\gamma\pi^0$, $\gamma\eta$, $\gamma\gamma$, $\pi^0\pi^\pm$, $\gamma\pi^\pm$), two-electron (J/ψ, Drell Yan), one-electron (converted photons), one-photon plus two-electrons (π^0, η), four-electron (π^0), strange (K^0_S, $\Lambda^\pm$), and jet (π^0j, γj). These NTUPLEs were the principle structures used for the calibration and cross-section analyses.

4.5 Particle Zoo

The invariant mass distribution of photon pairs reconstructed in the Meson West spectrometer is displayed in Figure 4.9 (top). Peaks in this distribution represent the decays of π^0 and η mesons. Several criteria were used to select these photon pairs:

- Each photon was reconstructed within the fiducial volume of the detector (Section 7.5);
- Each photon deposited at least 20% of its energy within the front section of the calorimeter;

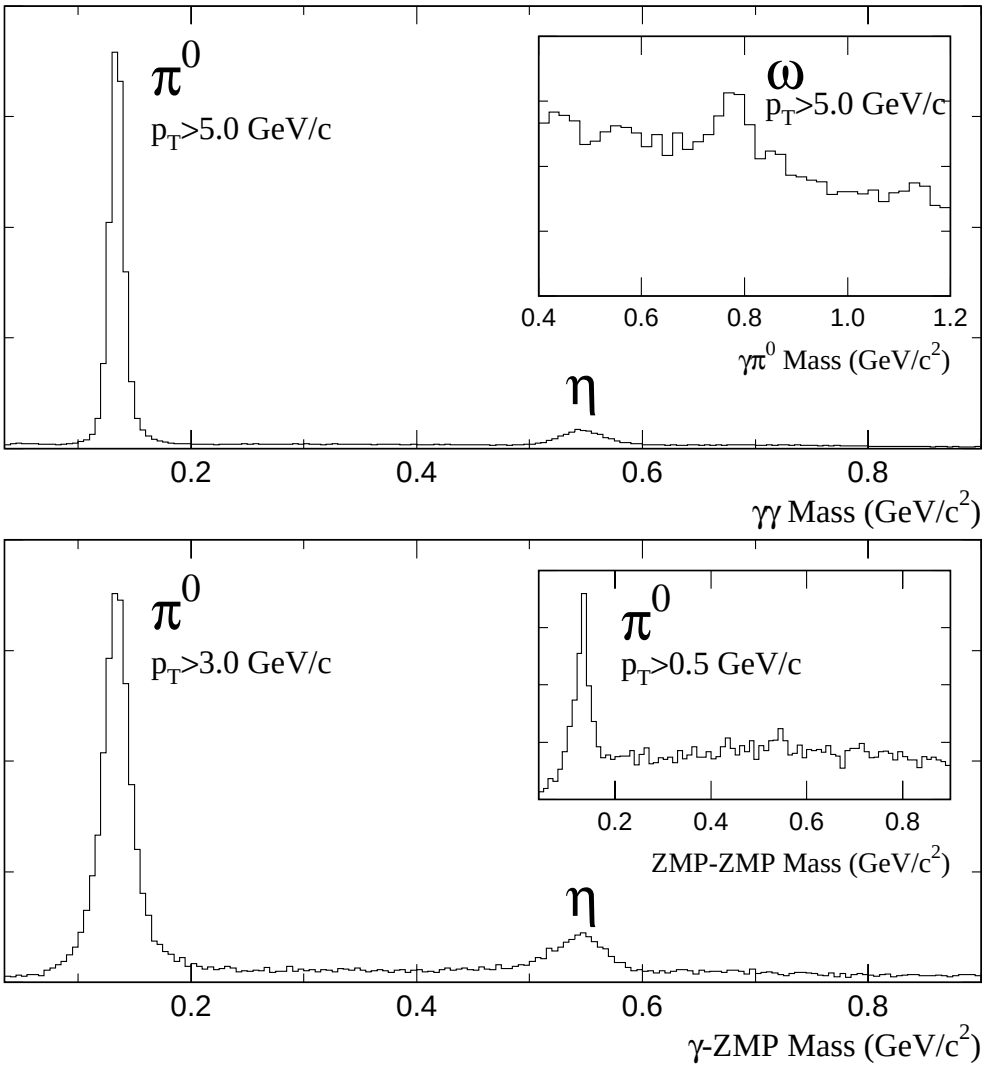

Figure 4.9 Mesons that decay into photons. Signals are reconstructed with combinations of converted (ZMP) and non-converted photons.

- Each photon in the pair was reconstructed in the same octant;
- Each pair was associated with a valid trigger;
- A minimum p_T was required for the pair;
- An energy asymmetry cut was applied to the pair.

The fiducial volume requirement ensures the photons are reconstructed a sufficient distance from the EMLAC boundaries to avoid anomalous energy losses. The E_{FRONT}/E_{TOTAL} requirement biases against hadronic showers. Requiring the two photons be reconstructed within the same triggered octant reduces trigger and reconstruction biases. The combinatorial background is reduced by the minimum p_T requirement and by the cut on energy asymmetry. The asymmetry is defined as

$$A = \frac{|E_1 - E_2|}{E_1 + E_2}, \tag{4.4}$$

where E_1 and E_2 represent the photon energies. Requiring a maximum energy asymmetry reduces the combinatorial background due to several low energy photons paired with a single high energy photon.

The invariant mass distribution for combinations of three photons is displayed in the inset of Figure 4.9 (top). All three photons were reconstructed in the same octant; two of the photons were consistent with a π^0 decay. The above criteria were required to be satisfied with an additional requirement that the $\pi^0\gamma$ asymmetry be less than 0.6. The peak in this spectrum is due to the decay of the ω meson.

The invariant mass distribution for combinations of photon pairs (consistent with π^0 decays) and single charged tracks (assumed to be charged pions) is shown in the top of Figure 4.10. These peaks are due to charged ρ decays. The lower left plot in the figure contains the invariant mass distribution for two oppositely

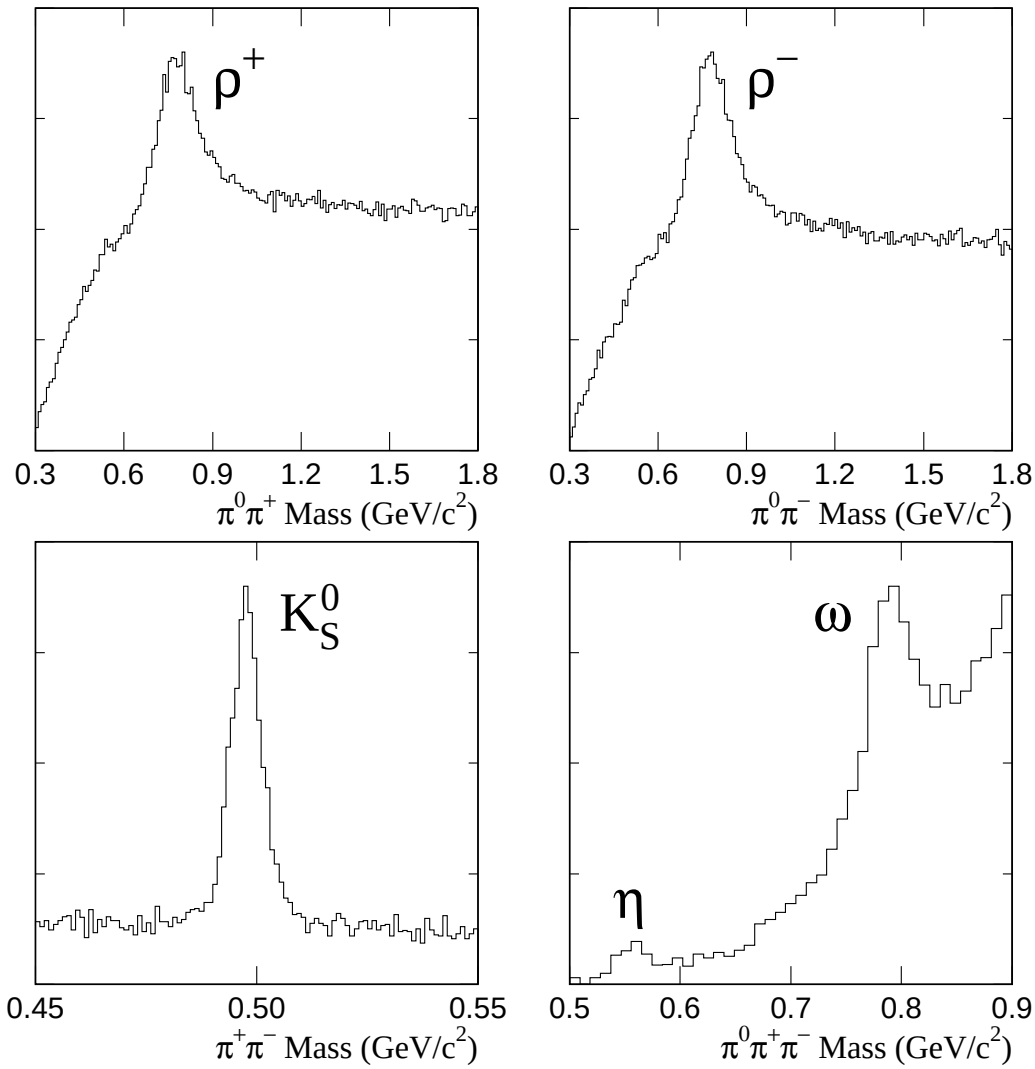

Figure 4.10 Reconstructed mesons that decay into pions.

charged tracks (assuming both to be pions) in the K^0_S mass region. Finally, the invariant mass distribution for $\pi^0\pi^+\pi^-$ combinations is shown in the lower right of Figure 4.10. The peaks represent the decays of the η and ω mesons.

A photon passing through material can convert into an electron–positron pair if its energy is greater than the two–electron mass threshold. For photons with energies greater than 1 GeV, the probability, P, for pair creation is approximately constant with energy and is given by [116, 117]

$$P = 1 - e^{-7x/9}, \tag{4.5}$$

where x is the thickness of the material in radiation lengths. The primary source of photons in our data are the electromagnetic decays of π^0 and η mesons, and these photons are the principle source of electron-positron pairs. Most of these conversions take place within the target material upstream of the magnet. The electron–positron pair has an invariant mass of $\approx 2m_e$ (Figure 4.11); converted photons are referred to as *Zero Mass Pairs* (ZMPs).

The ZMP opening angle is approximately $2m_e/E_\gamma$ which, for a 10 GeV photon, is approximately 0.1 mrad. This is comparable to the angular resolution of the SSDs (Section 2.3.1) and so many ZMPs are reconstructed as a single track upstream of the magnet. When the electron–positron pair passes through the magnet the particles diverge as the magnetic field bends them in the X direction. The ZMP is therefore frequently reconstructed downstream of the magnet as two separate tracks in the X, U, and V views, and as one track in the Y view. This provides the basis for a geometrical definition of the ZMP.

ZMP selection was based upon the following geometrical characteristics:

- Oppositely charged tracks;

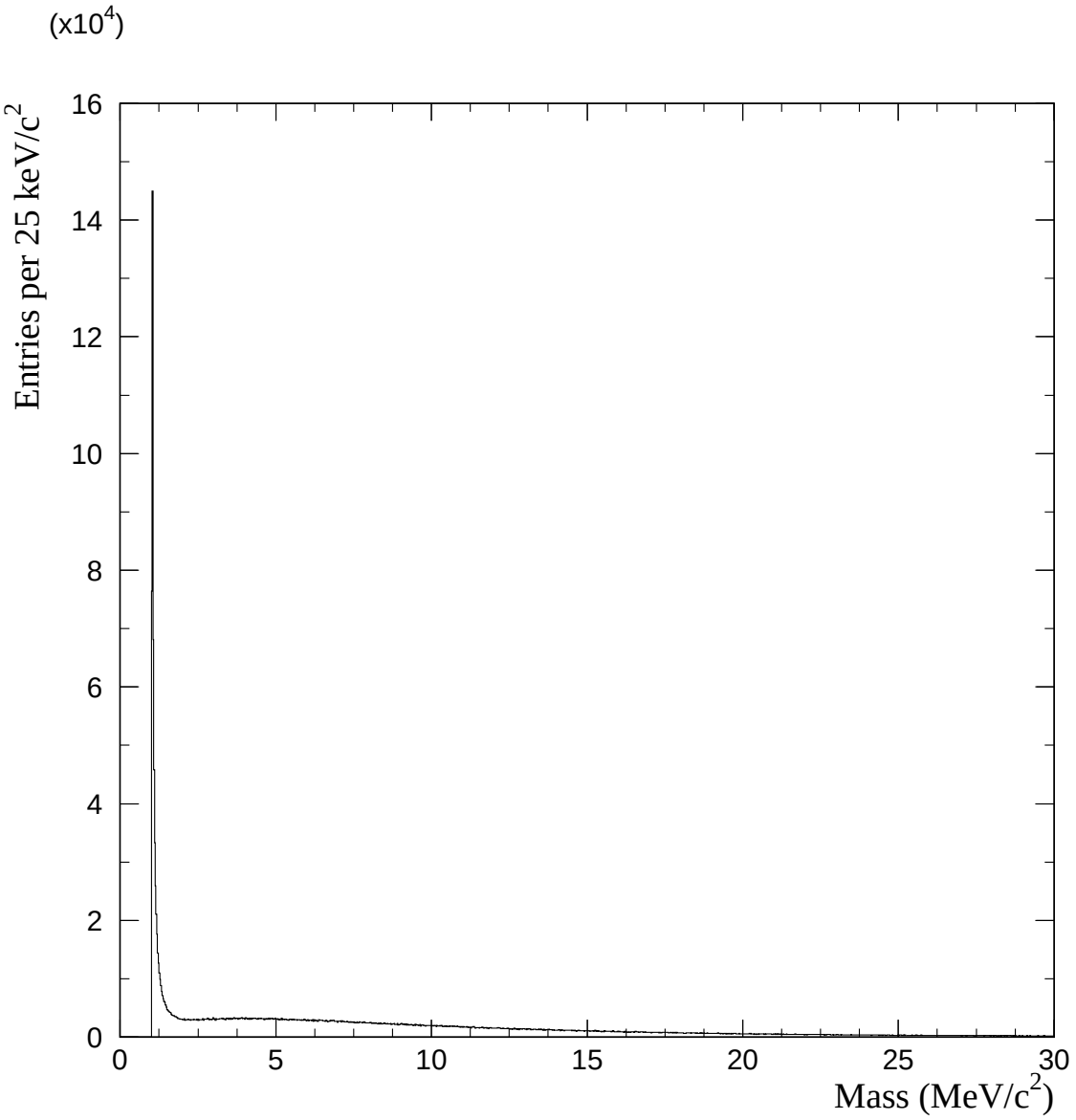

Figure 4.11 The invariant mass of all matched ZMPs in the combined data sample. The mass is determined from tracking information only.

- Both tracks had similar slopes in the Z–Y projection plane;
- Both tracks intersected near the center of the magnet in the Z–X projection plane.

During reconstruction, the candidate ZMP electron tracks were flagged in order to readily identify these events during the data analysis. After the selection of a pair of oppositely charged tracks, the following requirements were used to identify ZMPs in the data:

ΔS_Y: Difference between the Z–Y slopes of the two tracks less than 3 mrad (Figure 4.12);

ZXI: Z–X intersection point between 188 and 208 cm (Figure 4.13);[6]

ΔR: Distance between the projected track position at the front face of the EMLAC and the closest shower position less than 2 cm, specifically $\Delta R = \sqrt{(X_{track} - X_{shower})^2 + (Y_{track} - Y_{shower})^2} < 2$ cm.

The ΔS_Y distribution for all oppositely charged tracks is shown in Figure 4.12a. The ZMP signal becomes even more pronounced with the additional imposition of the ZXI cut (Figure 4.12b). If we also require at least one ZMP track to match with an EMLAC shower having $E_{FRONT}/E_{TOTAL} > 0.5$ (Figure 7.9), then the signal becomes even cleaner as seen in Figure 4.12c. Requiring both ZMP tracks match provides the cleanest signal (Figure 4.12d). Similarly, the effects of these cuts on the ZXI distribution are shown in Figure 4.13. The cleanest signal is when we apply the ΔS_Y cut to the doubly matched oppositely charged tracks as shown in Figure 4.13d.

[6] The center of the magnet was at Z=197.3 (197.7) cm in 1990 (1991).

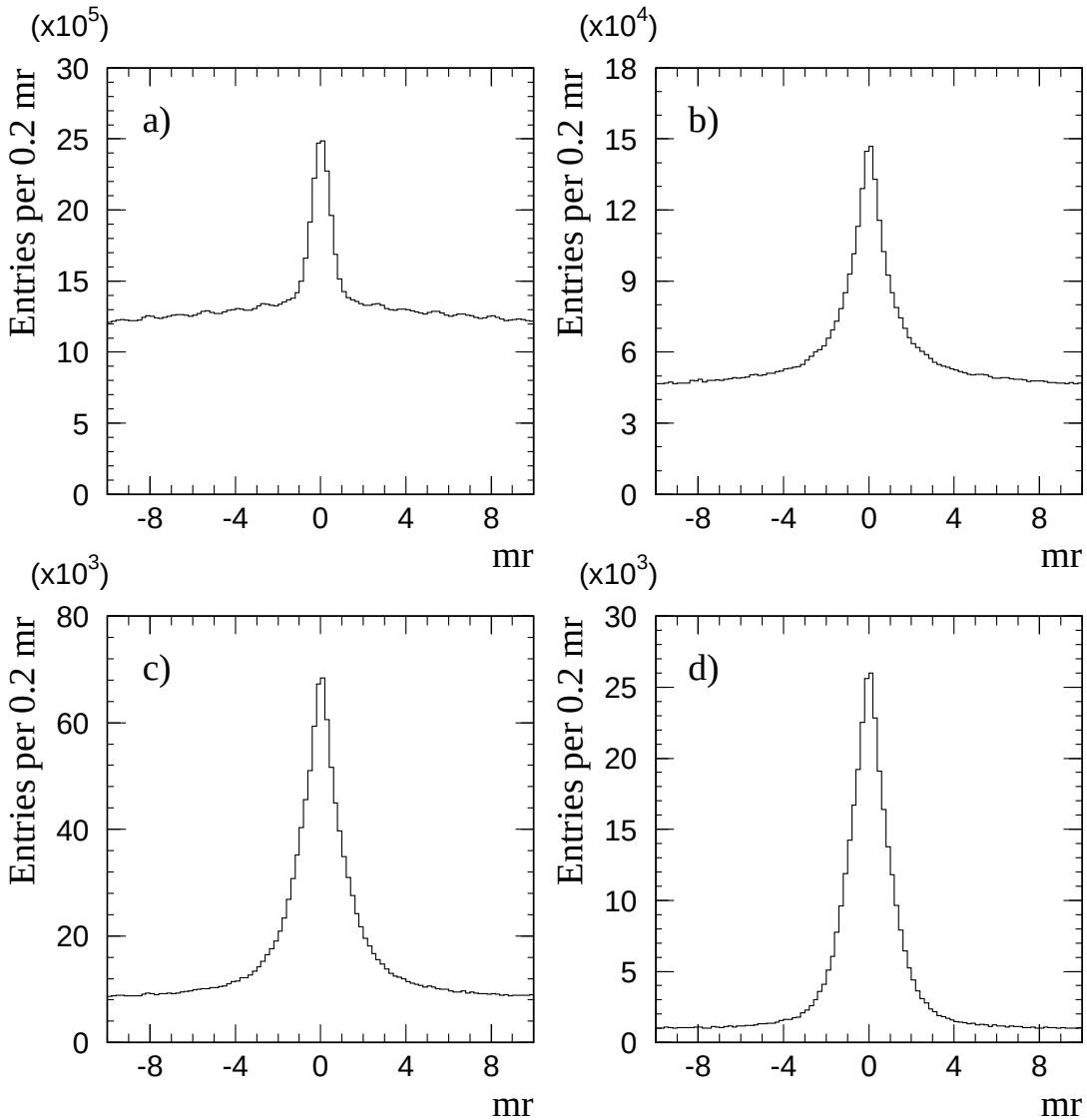

Figure 4.12 ΔS_Y distributions for the 1991 π^- sample. The effect for the various cuts on the ΔS_Y distribution: a) all oppositely charged tracks; b) $188 < ZXI < 208$ cm; c) at least one ZMP track matched with a shower having $E_{FRONT}/E_{TOTAL} > 0.5$; d) both ZMP tracks matched with showers. Each plot contains the requirements of the previous one.

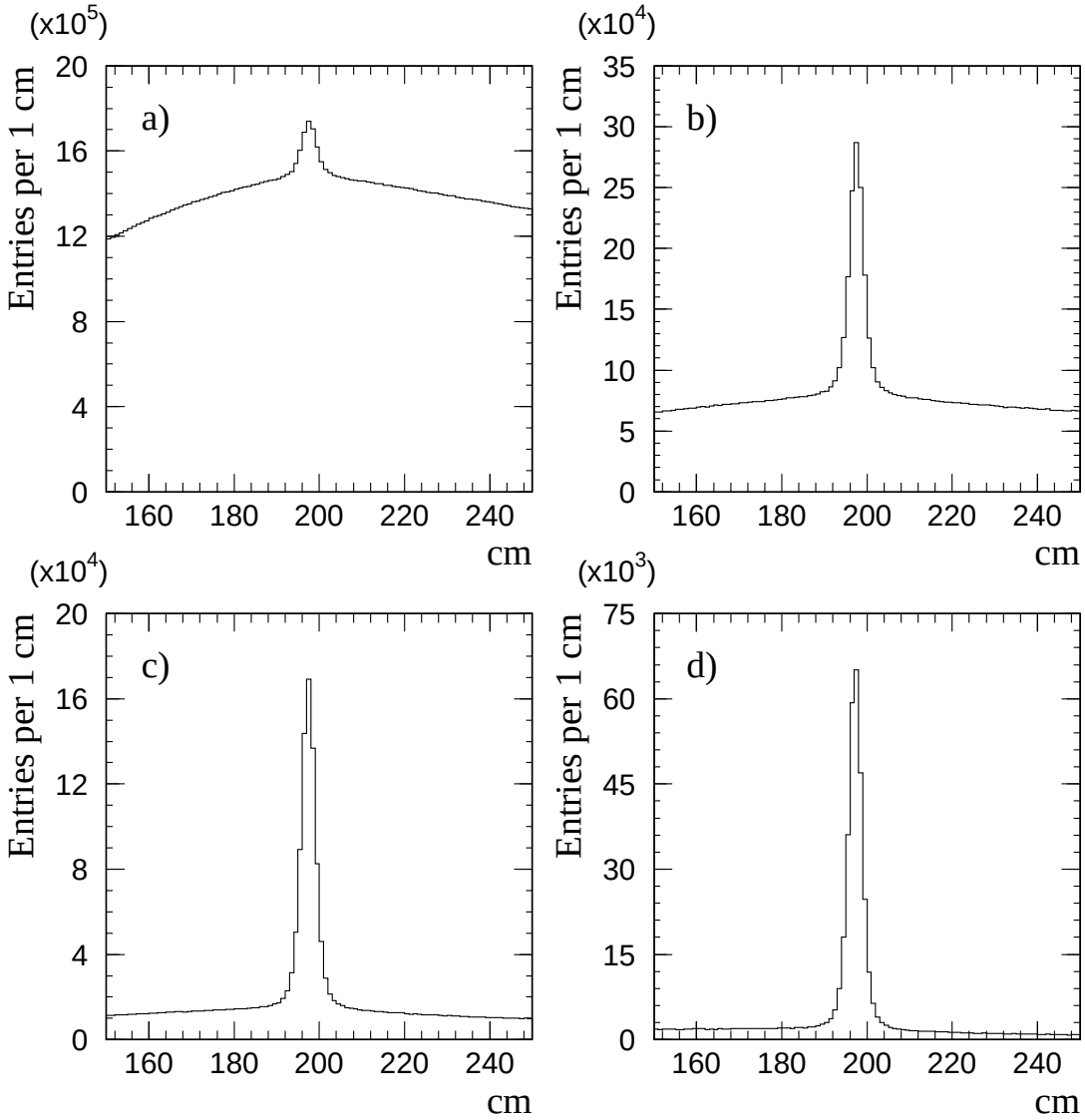

Figure 4.13 Z–X intersection distributions for the 1991 π^- sample. The effect for the various cuts on the ZXI distributions: a) all oppositely charged tracks; b) $|\Delta S_Y| < 3$ mrad; c) at least one ZMP track matched with a shower having $E_{FRONT}/E_{TOTAL} > 0.5$; d) both ZMP tracks matched with showers. Each plot contains the requirements of the previous one.

We can reconstruct π^0 and η signals (Figure 4.9) by combining ZMPs and photons. Here, the four-vectors for the ZMP are obtained from the tracking system while calorimeter information is used for the photon. For this signal, there is no trigger requirement in the photon's octant, and the minimum p_T is taken as low as 0.8 GeV/c. We can also reconstruct π^0 signals by combining ZMP pairs (Figure 4.9).

Chapter 5 Detector Simulation

The Meson West spectrometer was simulated to study its response in a controlled environment [118, 119]. Simulations were used for numerous purposes including studying geometrical acceptance (Section 7.5), reconstructor biases and efficiencies (Section 5.1.4), and calculating background contributions to direct-photon production (Section 5.2.3).

Three Monte Carlo implementations were used to simulate the response of the spectrometer. The first employed a standard physics event generator and a detailed spectrometer model (Section 5.1). This Monte Carlo simulation was used for detailed studies. The second employed parameterizations of physics cross sections and detector responses (Section 5.2). It was used for studies that required large statistics. The third was a simple ray trace used to determine the fiducial acceptance of the EMLAC (Section 7.5).

5.1 Full Monte Carlo

5.1.1 Event Generator

The full Monte Carlo used two standard physics generators: `HERWIG` [120] and `PYTHIA` [121]. Photon and track multiplicities for the two generators are compared to the data in Figures 5.1 and 5.2. Based on these comparisons, `HERWIG` was chosen as the principal event generator. Potential biases in the physics generator were studied using reconstructed data events as an input to the detector simulation [119].

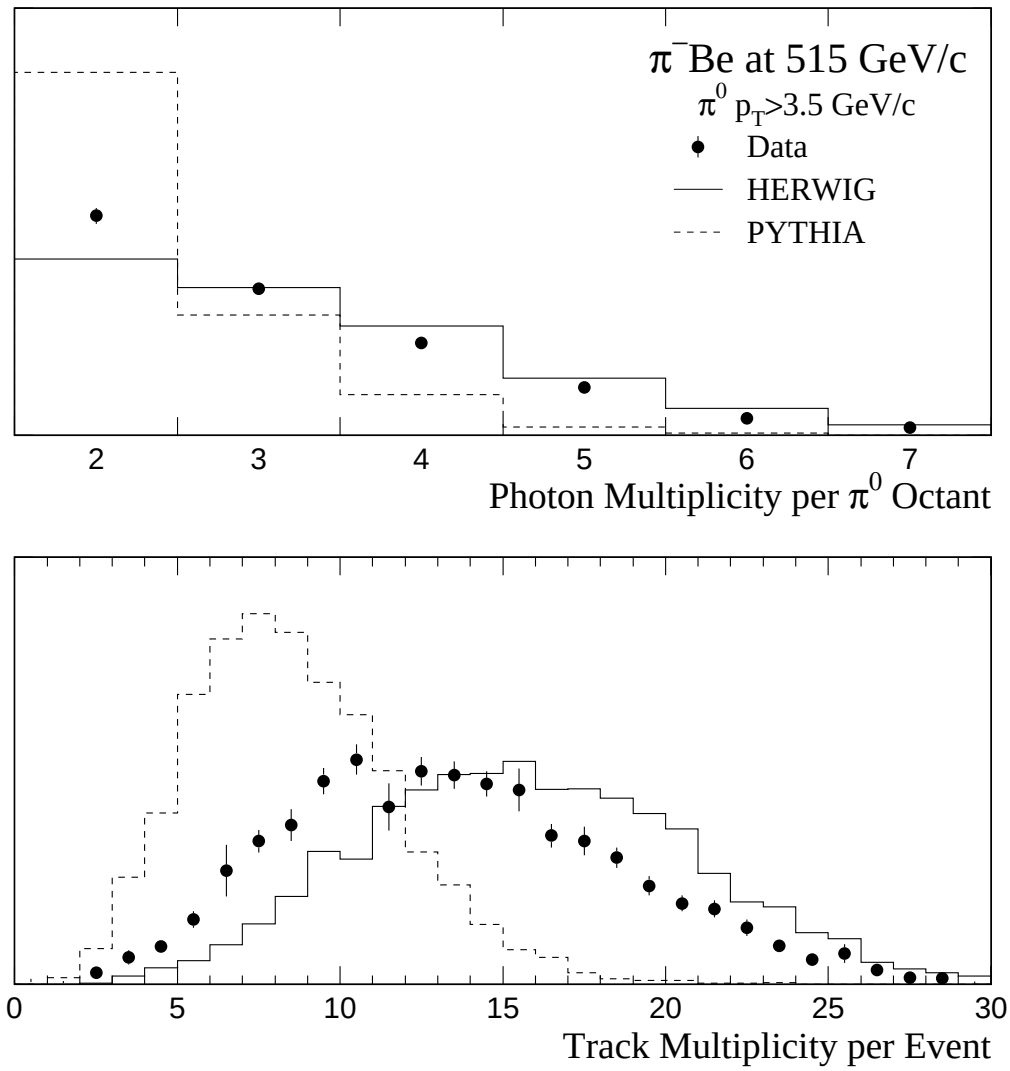

Figure 5.1 Comparison between the number of reconstructed photons in the triggering octant (top) and the total number of reconstructed tracks (bottom) in `PYTHIA`, `HERWIG`, and the data for events containing π^0's with $p_T > 3.5$ GeV/c.

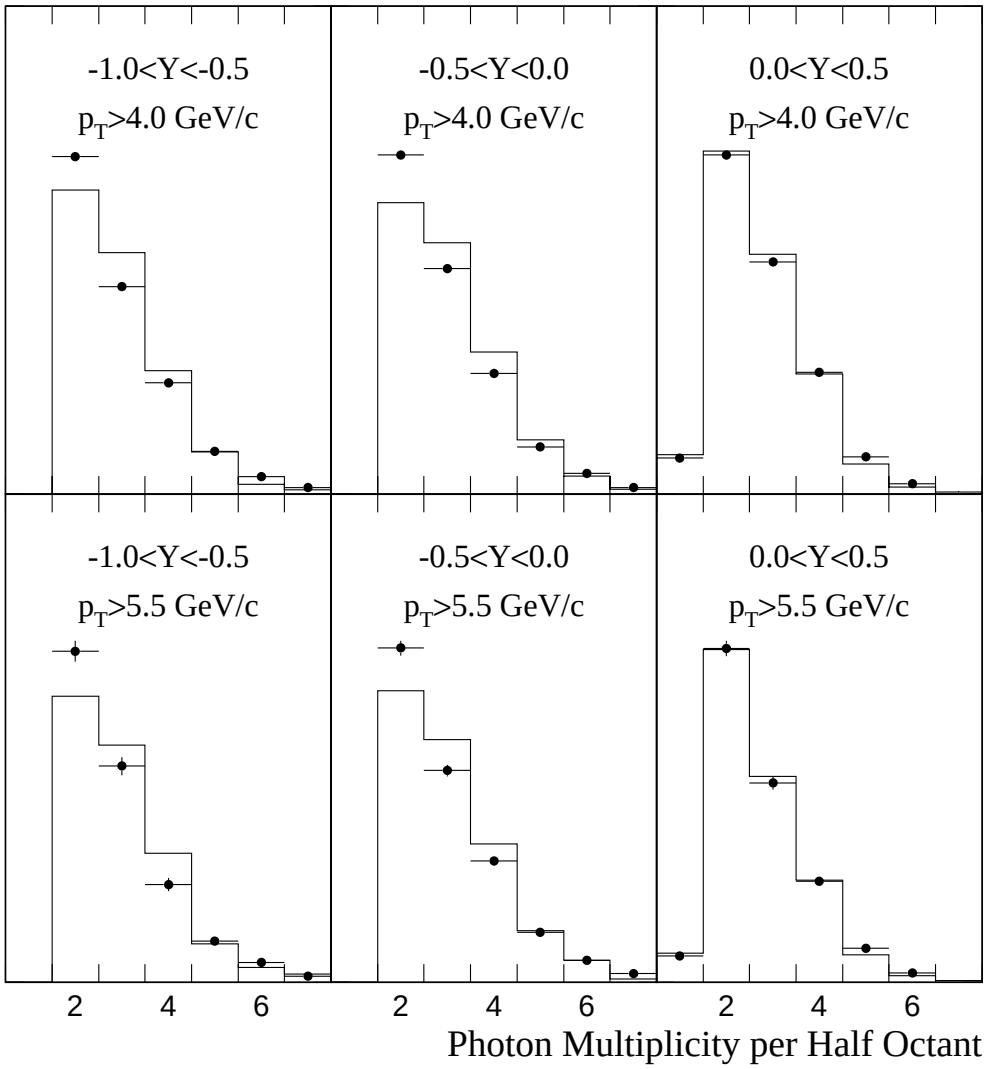

Figure 5.2 A comparison of the shapes of data (•) and the HERWIG (histogram) photon multiplicity distributions binned in rapidity for two choices of p_T. This is from the 800 GeV/c proton beam sample.

Filter	Specified Particles	p_T Requirement (GeV/c)
1	π^0	p_T^{MIN}
2	γ, $e^{\pm}$, π^0, K_S^0, K_L^0, η, ω, η', n	$p_T^{MIN} - 0.5$
2′		$p_T^{MIN} - 1.0^{\dagger}$
3	γ, $e^{\pm}$, π^0, K_S^0	p_T^{MIN}
4	η	p_T^{MIN}
4′		$p_T^{MIN\dagger}$
5	ω	p_T^{MIN}
6	$\pi^{\pm}$	p_T^{MIN}

† These filters have a `HERWIG` hard-scatter p_T requirement of $p_T^{MIN} - 0.5$ [119].

Table 5.1 Monte Carlo filters with their particle requirements. Also listed are the particle p_T requirements with respect to p_T^{MIN}.

5.1.2 Event Selection

Substantial computational resources are required to generate high statistics samples of the rare useful events. Consequently, special routines, called *filters*, were implemented to reject uninteresting events at an early stage in the processing [119]. Filters required specific particles with p_T above a specified threshold, p_T^{MIN}. There were six filters used in this analysis (Table 5.1). Filters 1, 4, 5, and 6 were simplistic; they required a high-p_T particle in the event. Filter 3 was more complicated; multiple particles could potentially deposit energy in the EMLAC. Filter 2 was the most complex; it operated in two stages. The first stage was similar to Filter 3; it required specific particles with $p_T > p_T^{MIN} - 0.5$. The second stage projected all generated photons and electrons to the EMLAC and calculated nominal sums-of-eight (Section 3.1.2). The filter was satisfied if any overlapping sum-of-sixteen was greater than p_T^{MIN}, or if any triggering particle satisfied $p_T > p_T^{MIN}$, or if the total p_T from photons and electrons in the

triggering quadrant was greater than p_T^{MIN}. Monte Carlo statistics by filter type are presented in Tables 5.2, 5.3, and 5.4.

5.1.3 Detector Simulation

`GEANT` [122] is a software package that simulates the passage of elementary particles through matter. The simulation includes all essential physics processes involved in electromagnetic shower development. `GEANT` provides a data base of standard geometrical shapes and materials used to model a wide variety of detectors. The Meson West spectrometer was extensively modeled [118, 119, 79] using this package.

Our understanding of direct-photon backgrounds depends critically upon the proper simulation of electromagnetic shower development. Typically, showers are developed (via bremsstrahlung and pair production processes) until the resulting particles reach the energy at which dissipative processes (e.g. ionization and excitation) become dominant. Once this cut-off energy is reached, `GEANT` stops tracking the particle and deposits the particle's energy. Comparisons between the Monte Carlo and the data for a sample of high quality single electrons gave adequate agreement for an energy cut-off of 1 MeV [118].

Every particle is tracked independently in `GEANT`, so this can be a very slow process. The Monte Carlo simulation was sped up (by a factor of 5) by increasing the energy cutoff to 10 MeV. This change resulted in a 50% loss in the deposited energy. The loss was accounted for using a special parameterization of the shower development [118] applied during the digitization process [119]. This shower parameterization was specifically designed to properly reproduce both the longitudinal and transverse shower shapes.

p_T^{MIN} (GeV/c)	1990 515 GeV π^-				1991 515 GeV π^-				1991 530 GeV p				1991 800 GeV p			
	F1	F2	F3	F4	F1	F2	F3	F4	F1	F2	F3	F4	F1	F2	F3	F4
0.50	208	-	-	-	(213)	-	-	-	(206)	-	-	-	-	97	-	-
1.50	-	221	-	-	-	(230)	-	-	-	(224)	-	-	-	331	-	-
2.00	-	-	-	184	-	-	-	(178)	-	-	-	(178)	-	-	-	-
2.25	-	303	-	-	-	(313)	-	-	-	(306)	-	-	-	-	-	198
2.50	-	-	-	-	-	-	-	-	-	-	-	-	-	197	-	-
3.00	-	344	151	186	-	(371)	(138)	(161)	-	(368)	(136)	(211)	-	184	-	-
3.50	-	-	-	-	-	-	-	-	-	-	-	-	-	851	-	236
4.00	-	233	-	-	-	(218)	-	-	-	(243)	-	-	-	-	-	-
5.00	-	77	124	38	-	96 (81)	(136)	(40)	-	109 (81)	(122)	142 (40)	-	266	-	93
6.50	-	42	120	20	-	-	(44)	(20)	-	-	(44)	(20)	-	151	-	-
7.00	-	-	-	-	-	-	-	-	-	99	-	-	-	-	-	44
7.50	-	-	-	12	-	-	-	(12)	-	-	-	(12)	-	-	-	-
8.00	-	-	66	-	-	-	(35)	-	-	50	(35)	-	-	115	-	-
9.00	-	30	10	-	-	(30)	-	-	-	24 (30)	-	-	-	35	-	40

Table 5.2 Full Monte Carlo statistics (in thousands of events). This Monte Carlo was intended to generate π^0 and η events using the `HERWIG` event generator. No direct-photon events are included in these samples. Numbers in parenthesis represent full Monte Carlo events generated with the 1990 beam and target configuration that were processed by the appropriate 1991 preprocessor.

p_T^{MIN}	1990 515 GeV π^-	1991 515 GeV π^-	1991 530 GeV p	1991 800 GeV p
3.00	440	(439)	(453)	347
3.50	-	-	-	437
5.00	203	(206)	(203)	210
7.00	91	(78)	(90)	83
8.50	10	(10)	(10)	48

Table 5.3 Full Monte Carlo statistics (in thousands of events). This Monte Carlo was intended to generate direct-photon events using the `HERWIG` event generator. All events were produced with filters 2 or 2′. Numbers in parenthesis represent full Monte Carlo events generated with the 1990 beam and target configuration that were processed by the appropriate 1991 preprocessor.

p_T^{MIN}	Trigger Class	π^0	η	two arm
2.50	TWO GAMMA	-	-	44
3.00	LOCAL LOW	301	84	-
3.50	LOCAL HIGH	723	171	-

Table 5.4 Full Monte Carlo statistics (in thousands of events). This Monte Carlo was intended to generate either π^0 and η events using reconstructed data events as an input to the full Monte Carlo. Only events from the 1990 run were utilized for this purpose.

Shape comparisons between the Monte Carlo simulation and the data for $E_R - E_\phi$ and the fraction of energy deposited in the front section of the EMLAC, E_{FRONT}/E_{TOTAL}, are presented in Figures 5.3 and 5.4. The Monte Carlo simulation agrees well with the data for these distributions indicating the simulation properly treats shower development in the EMLAC. There is good agreement in the results of the shower shape fit (Section 4.3.5) to both Monte Carlo and data photons (Figure 5.5) further indicating photons are reasonably simulated in the EMLAC. A comparison between the data and the full Monte Carlo for the reconstructed mass of photon pairs in the π^0 and η mass regions is shown in Figure 5.6. The full Monte Carlo reproduces both the signal widths and the combinatorial background level.

It was important to ensure the Monte Carlo faithfully reproduced real detector effects. A *preprocessor* was used to convert `GEANT` information into the hits and strip energies measured by various detectors. The preprocessor also applied hardware effects, such as channel noise and gains, to the generated events. Monte Carlo events were written to tape, processed through the same reconstruction software used in the data analysis, formed into DSTs, and processed into NTUPLEs. This allowed us to account for inefficiencies and biases in the reconstruction algorithms (Section 5.1.4). That the Monte Carlo simulation accurately describes the losses of very low-energy photons can be seen in Figure 5.7 which shows a comparison between the Monte Carlo and the data for the π^0 energy asymmetry.

Rather than employ the Monte Carlo "predictions" of p_T and rapidity spectra for our studies, the π^0, η, and direct-photon spectra were weighted to the data results in an iterative fashion so that final corrections were based on the data distributions rather than on the choice of a physics generator [119].

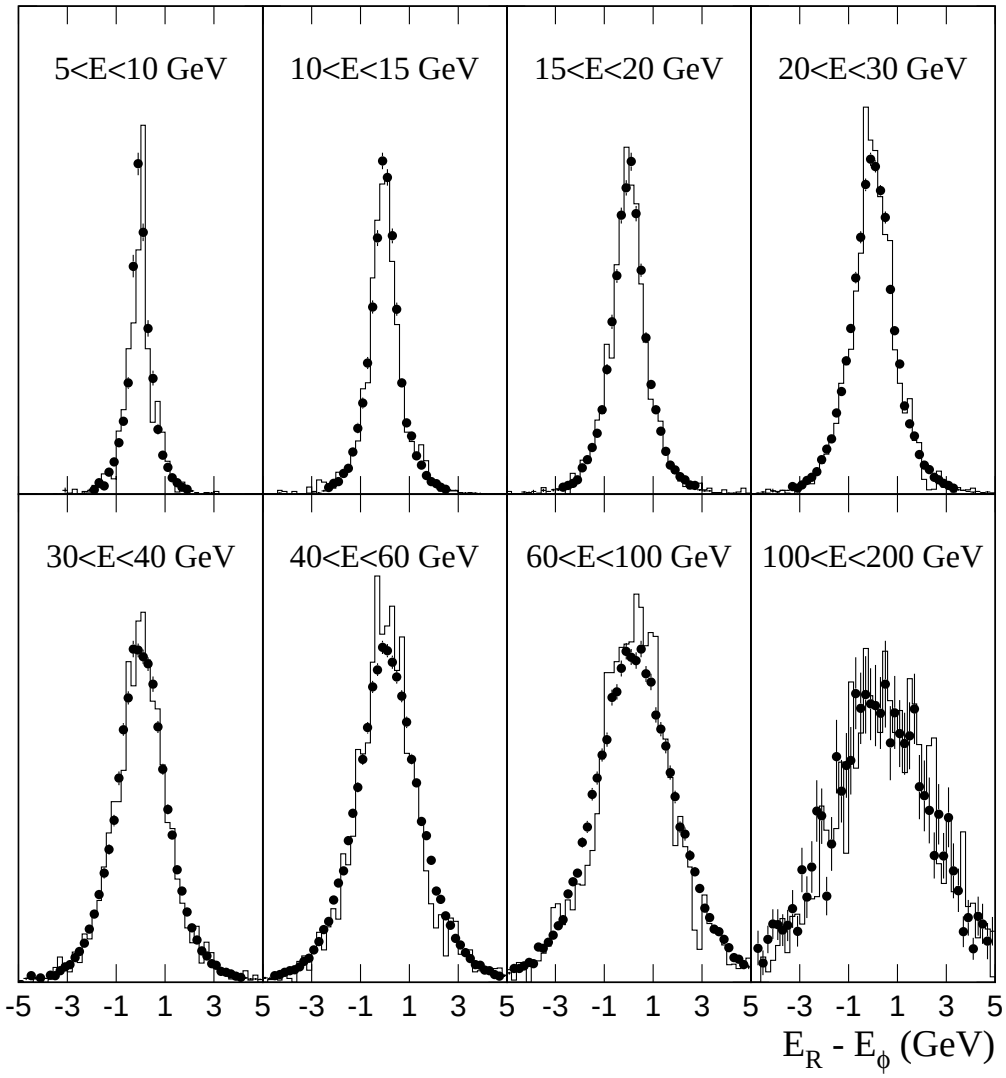

Figure 5.3 A shape comparison of photon $E_R - E_\phi$ distributions in eight photon energy bins between the data (•) and the full Monte Carlo (histogram). This is from the 800 GeV/c proton beam sample for events containing π^0's with $p_T > 3.5$ GeV/c.

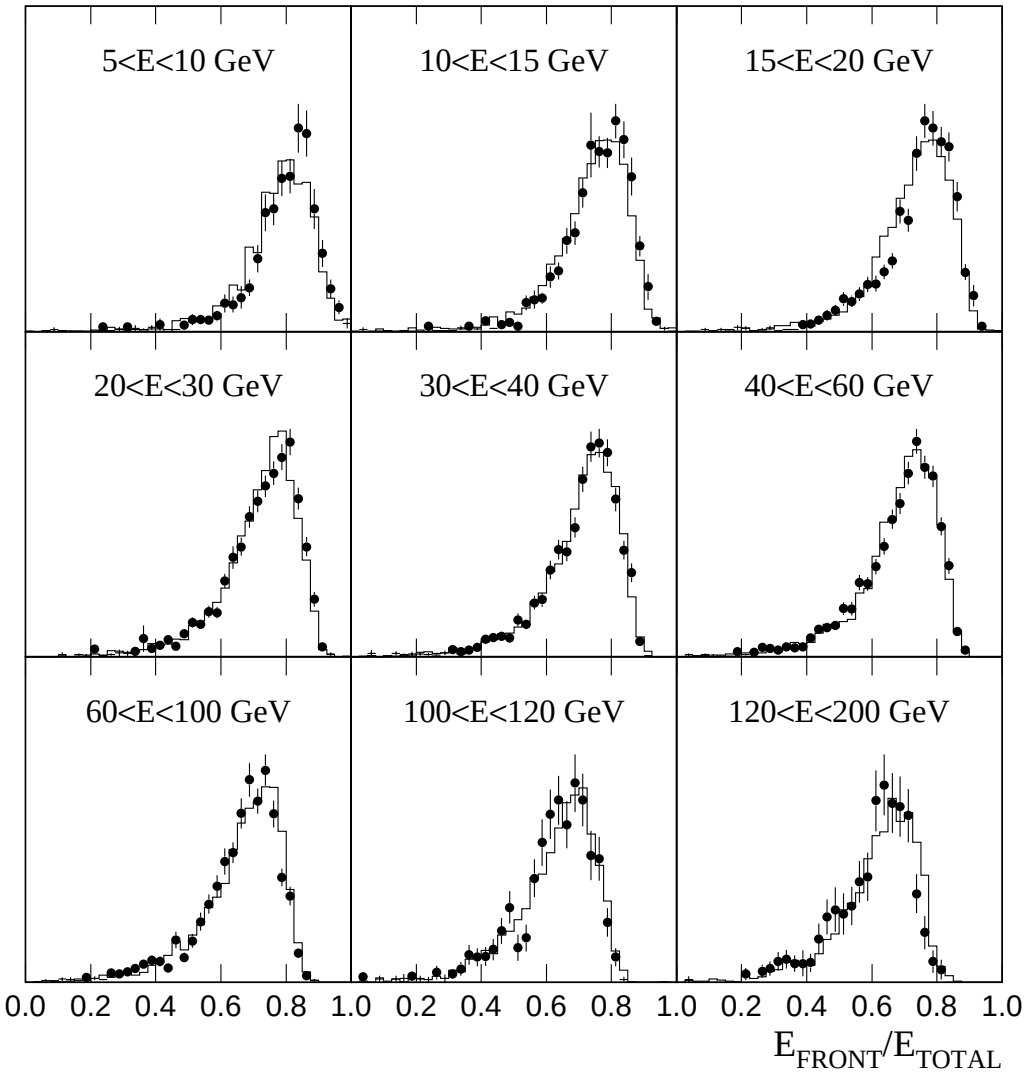

Figure 5.4 A shape comparison of the photon E_{FRONT}/E_{TOTAL} distributions in nine photon energy bins between the data (•) and the full Monte Carlo (histogram). This is from the 530 GeV/c proton beam sample for events containing π^0's with $p_T > 3.5$ GeV/c.

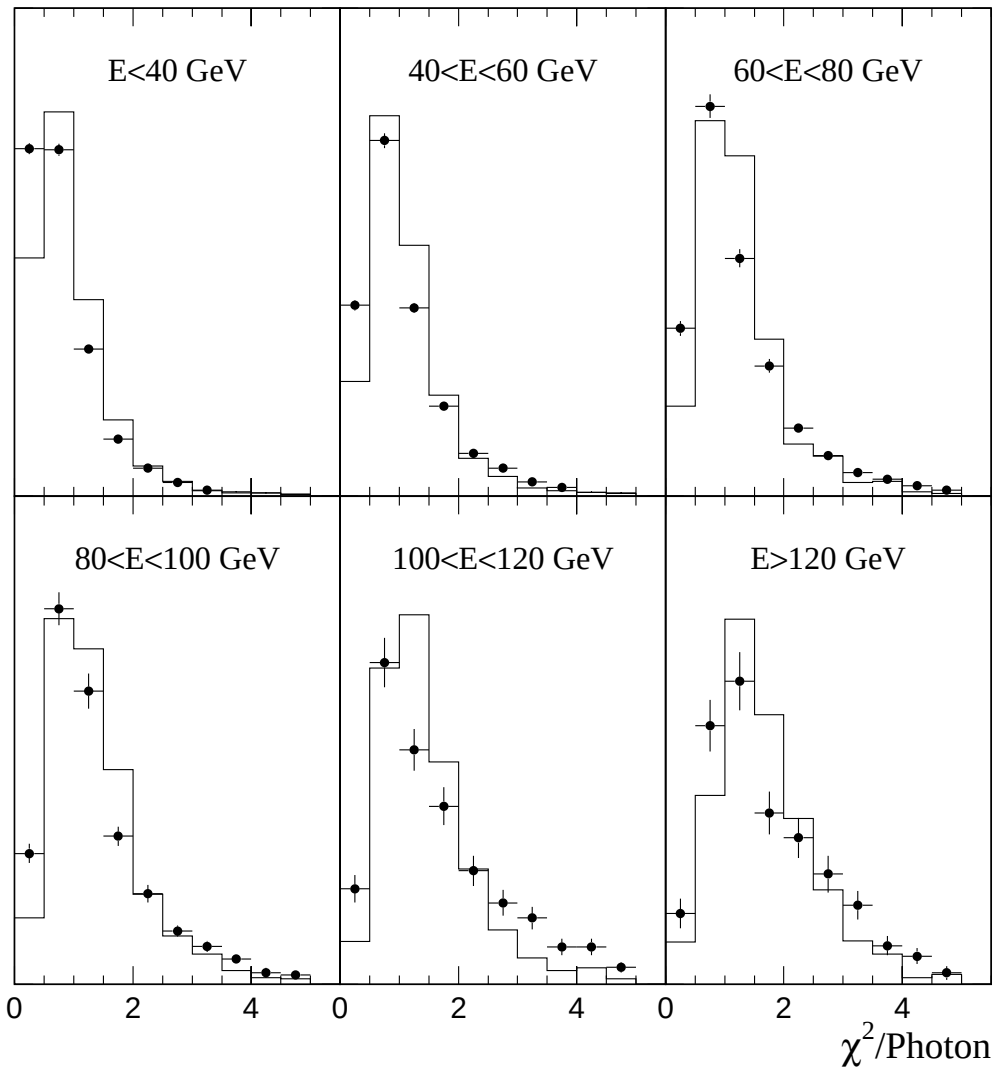

Figure 5.5 A shape comparison of the photon radial view shower energy χ^2 distributions in six photon energy bins between the data (•) and the full Monte Carlo (histogram). This is from the 515 GeV/c π^- beam sample for events containing π^0's with $p_T > 3.5$ GeV/c.

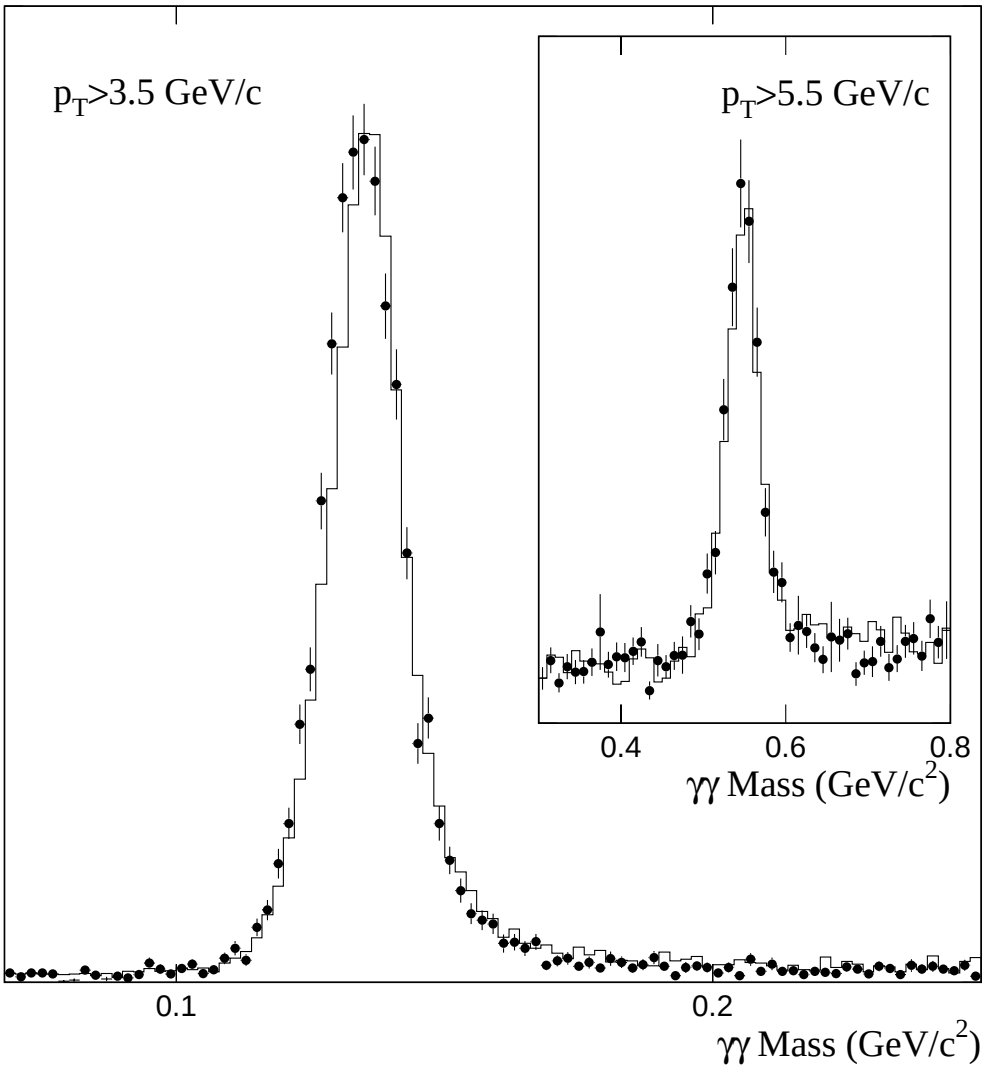

Figure 5.6 Comparison between data (•) and the full Monte Carlo (histogram) from the 530 GeV/c proton beam sample for $\gamma\gamma$ combinations in the π^0 and η mass regions.

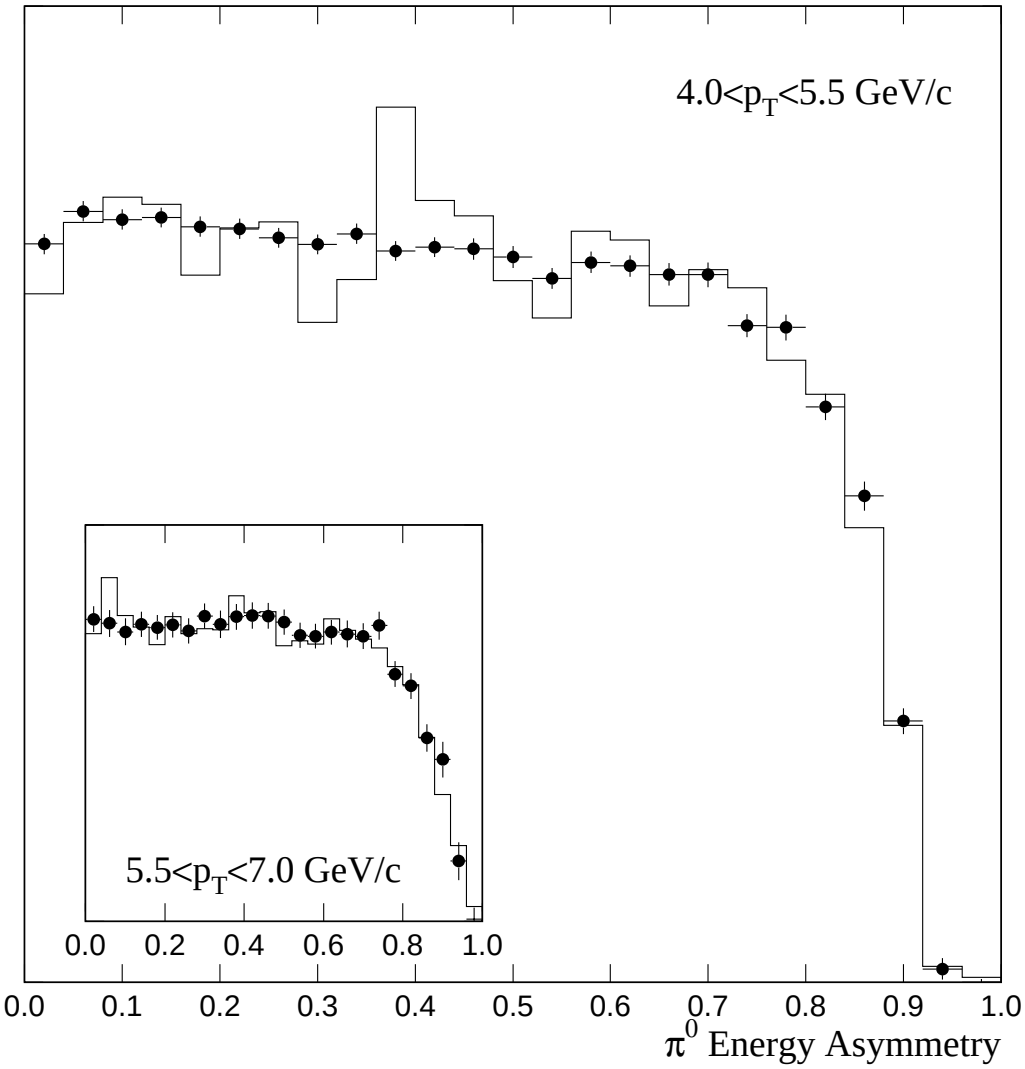

Figure 5.7 Comparison of the π^0 energy asymmetry distribution in data (•) and the full Monte Carlo (histogram) for the 800 GeV/c proton beam sample. Shown are the comparisons for two p_T intervals, $4.0 < p_T < 5.5$ GeV/c and $5.5 < p_T < 7.0$ GeV/c.

5.1.4 Reconstruction Efficiencies

The full Monte Carlo was used to evaluate the probability for reconstructing π^0's, η's, and direct photons. The reconstruction efficiency [119, 79] was determined using the the `HERWIG` event generator and `GEANT` Monte Carlo simulation of the detector. The efficiency was defined as the number of objects reconstructed (photons, π^0's, or η's) per number generated. Functions were produced as surfaces in p_T and rapidity (Figures 5.8, 5.9, and 5.10).

The efficiency also included corrections for the trigger probability cut (Section 7.3) and the E_{FRONT}/E_{TOTAL} cut (Section 7.4).

5.2 Parameterized Monte Carlo

The full Monte Carlo simulation of the Meson West spectrometer was very complex and produced events relatively slowly. A simpler, faster, Monte Carlo simulation was implemented to gain additional insights into the energy response of the EMLAC, the backgrounds to direct-photon production, and the structure of two armed events. This Monte Carlo simulation employed parameterizations of the production cross sections, spectrometer acceptance, and detector resolutions and efficiencies.

5.2.1 Generator

Parameterizations of the measured cross sections were used as an input to the Monte Carlo. The inclusive π^0 and direct-photon cross sections were parameterized as two dimensional surfaces in p_T and rapidity (Figure 5.11) [119]. The η, ω, and η' cross sections were parameterized using the η/π^0 [119, 72], ω/π^0 [112, 123], and η'/η [124, 125] ratios. The fraction η/π^0 is presented in Figure 5.12. The fraction ω/π^0 was assumed to be 1.0 for all samples; η'/η was assumed to be 1.7.

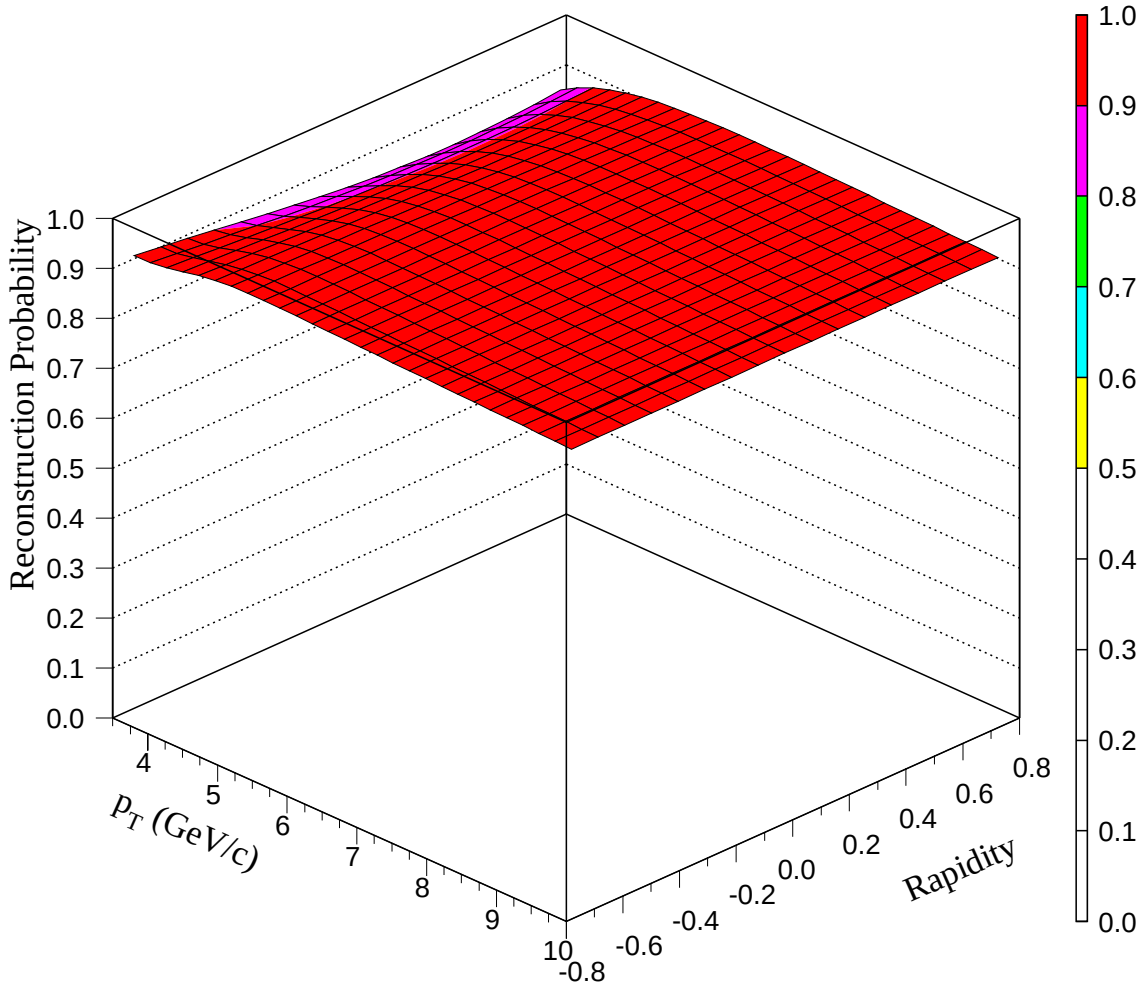

Figure 5.8 Probability for reconstructing direct photons with the TWO GAMMA trigger as a function of the photon's p_T and rapidity. This was taken from the 515 GeV/c π^- full Monte Carlo (1991 configuration).

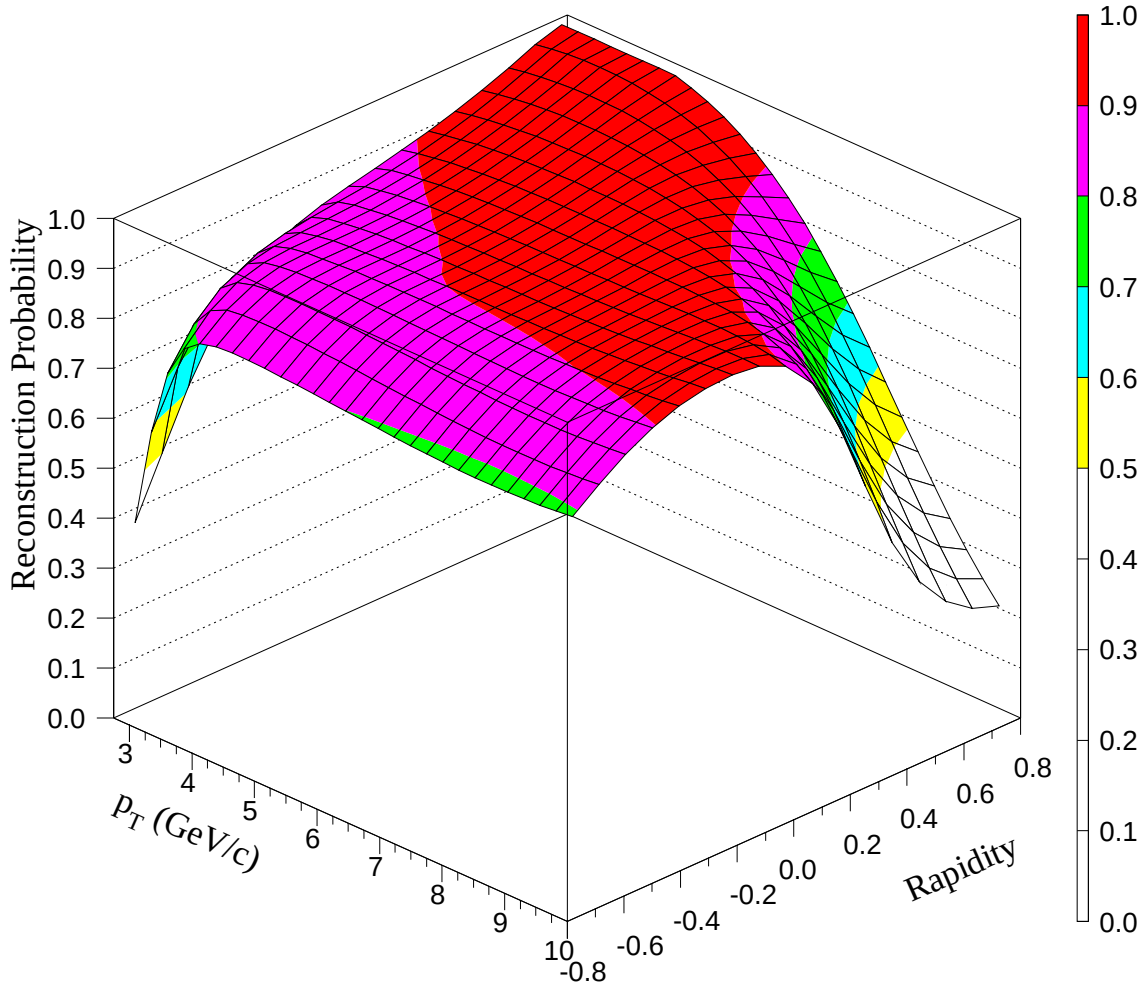

Figure 5.9 Probability for reconstructing π^0's with the TWO GAMMA trigger as a function of the π^0's p_T and rapidity. The rise at low-p_T (backwards rapidity) is due to the trigger turn-on, the dip at high p_T (forwards rapidity) is due to the coalescence of the two decay photons. This was taken from the 515 GeV/c π^- full Monte Carlo (1991 configuration).

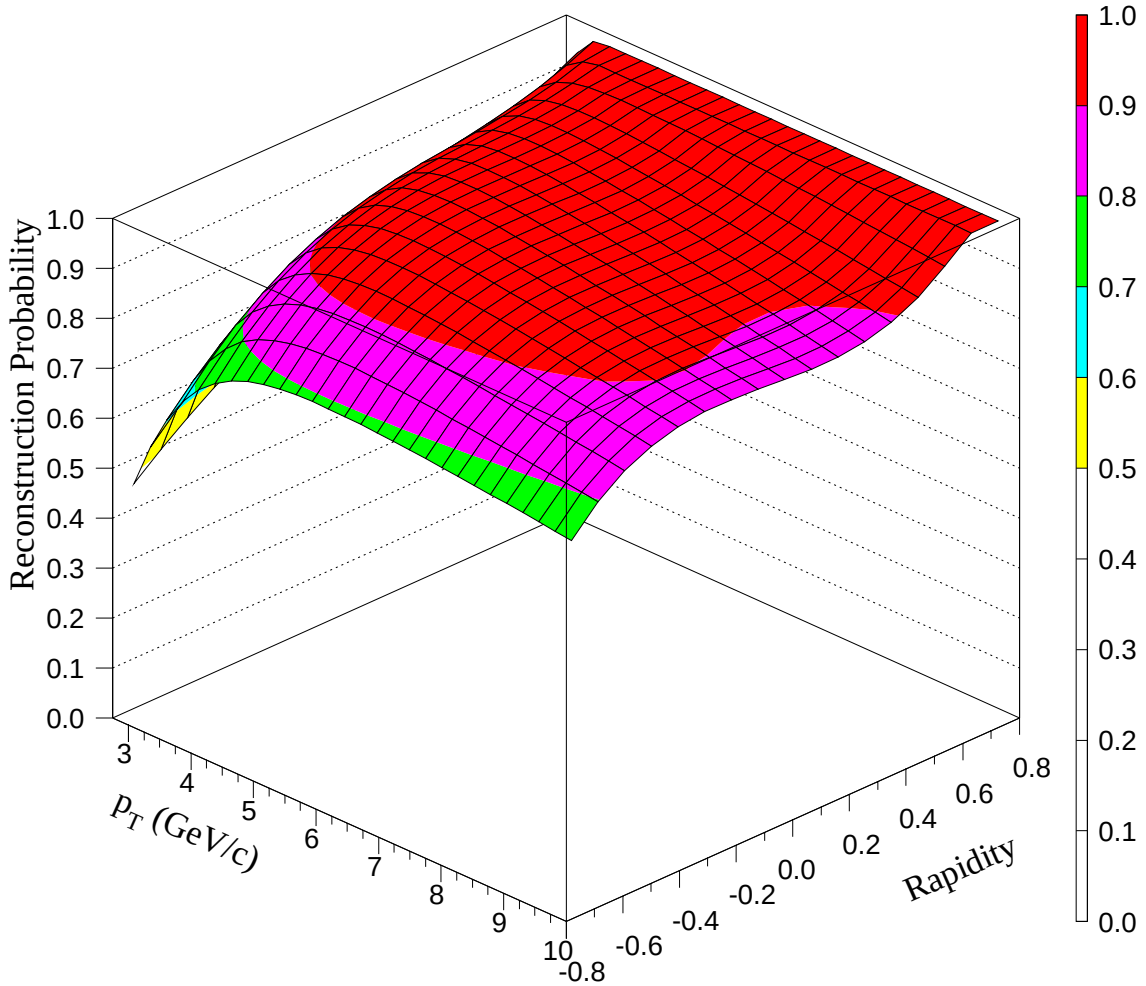

Figure 5.10 Probability for reconstructing η's with the TWO GAMMA trigger as a function of the η's p_T and rapidity. The rise at low-p_T is due to the trigger turn-on. This was taken from the 515 GeV/c π^- full Monte Carlo (1991 configuration).

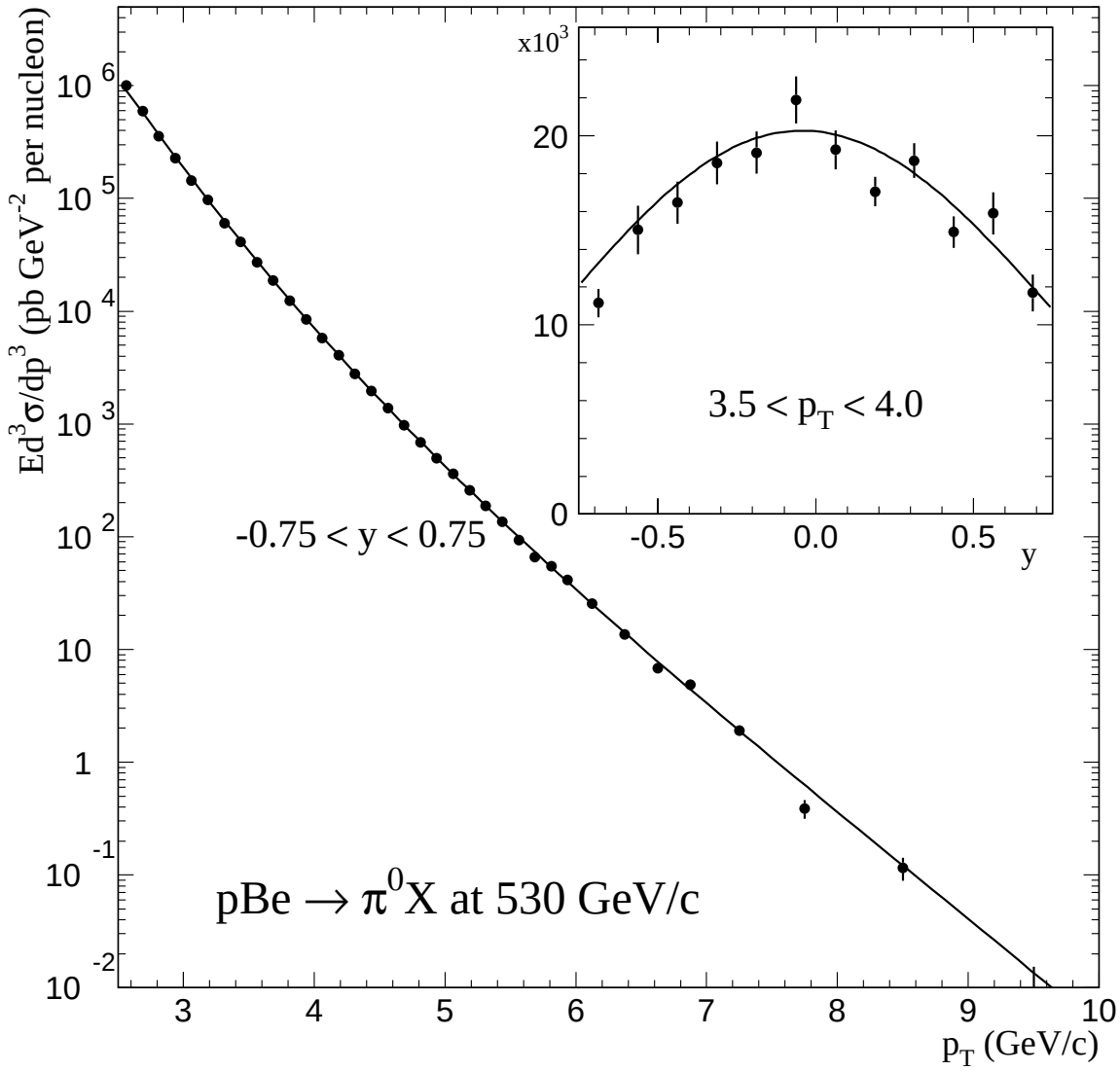

Figure 5.11 The π^0 cross section versus p_T and rapidity from the 530 GeV/c proton beam sample. The parameterization is overlayed on the data.

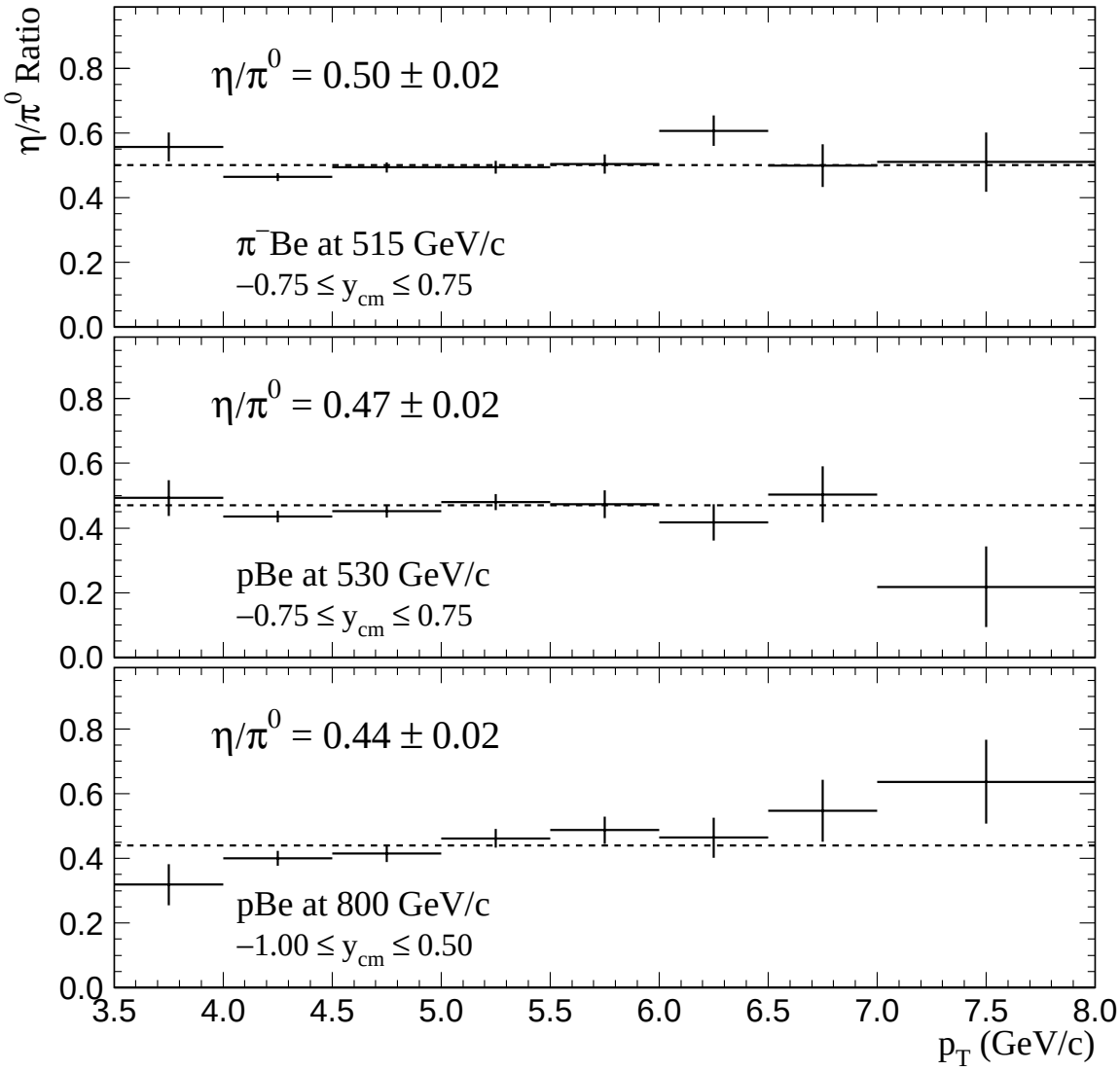

Figure 5.12 Measured ratio for the production of η's with respect to π^0's as a function of p_T for the three major samples considered in this analysis. The line represents a simple flat line fit to the data.

The cross sections for $\pi^0\pi^0$, $\gamma\pi^0$, and $\gamma\gamma$ production were parameterized as functions of the mass of the pair. A Gaussian k_T was applied in order to achieve proper agreement with Q_T, $\Delta\phi$, and p_{OUT} distributions. An additional Gaussian accounted for smearing due to the fragmentation process. Pairs containing η, ω, and η' mesons were produced using the values described above. Figure 5.13 displays the comparison between data and the parameterized Monte Carlo for $\pi^0\pi^0$ production as a function of several interesting variables.

5.2.2 Detector Simulation

Generated mesons were decayed into final state particles[1] (Table 5.5); photons were smeared for energy (Figure 5.14 and Section 6.5.4) and position (Section 6.3) resolution. A vertex was generated in the simulated target for every event (Table 5.6). Photons were allowed to convert into e^+e^- pairs; the energy of the resulting electrons was reduced using the `GEANT` function for bremsstrahlung radiation. Electron four-vectors were smeared for multiple scattering in the target and the resolution of the tracking system (Equation 4.1) [126, 84] and adjusted for the action of the magnet [87]. Figure 5.15 displays a comparison between the parameterized Monte Carlo and the data in the π^0 and η mass regions and for the π^0 energy asymmetry. The parameterized Monte Carlo provides a reasonable characterization of the data. This Monte Carlo reproduced the widths of the π^0 and η reconstructed as both $\gamma\gamma$ and as γe^+e^- (Figure 5.16). The ω width was also reproduced in its $\pi^0\gamma$ decay mode. Additionally, the observed shift in the mean mass of the γe^+e^- system (Section 6.6.1) was reproduced.

[1] Particles were produced according to inclusive spectra. Therefore, for example, π^0's from ω decays (Table 5.5) are already included in the generated π^0 sample. These particles (e.g., π^0's from η or ω decays) were treated as "ghosts" to avoid double counting.

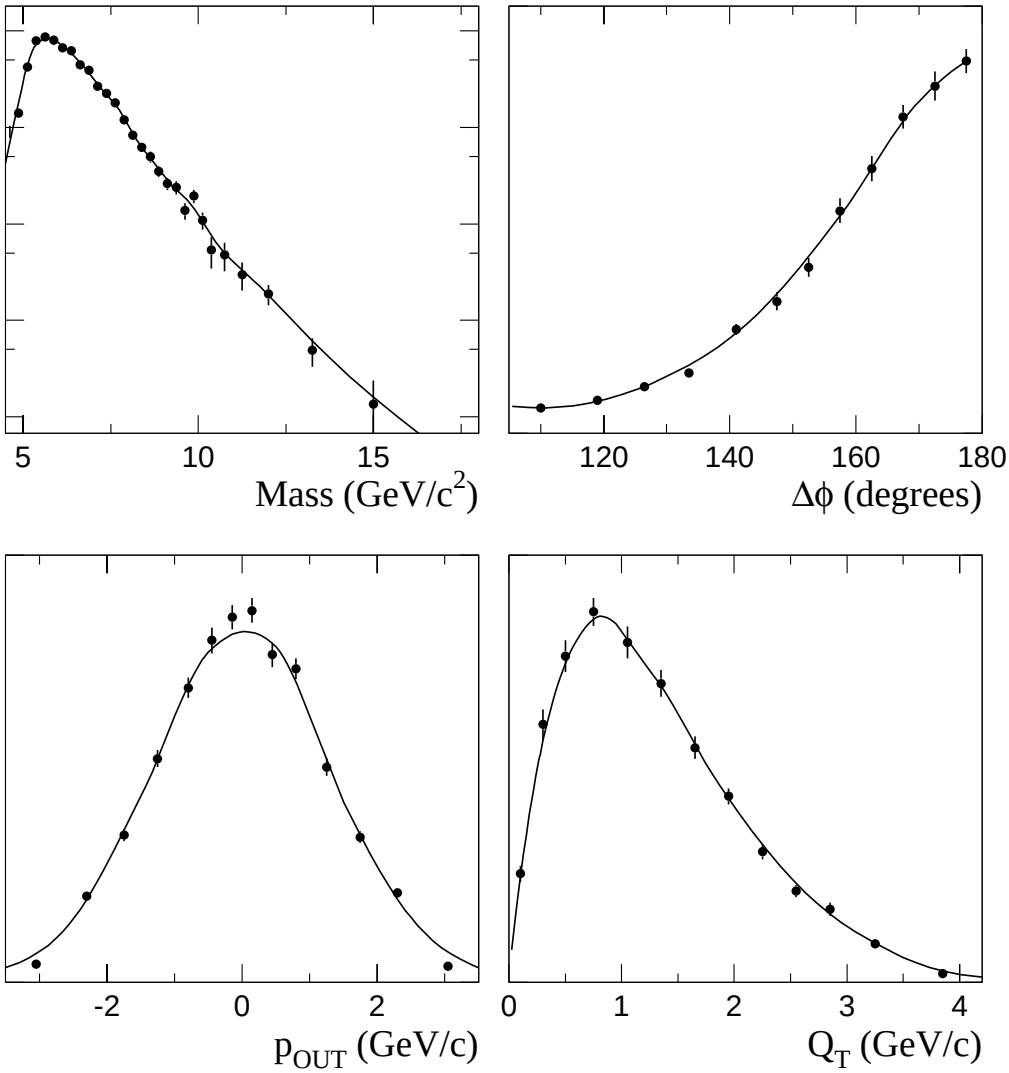

Figure 5.13 Comparison between data (•) and the parameterized Monte Carlo (curve) for distributions in mass, $\Delta\phi$, p_{OUT}, and Q_T for π^0 pairs from the 515 GeV/c π^- beam sample.

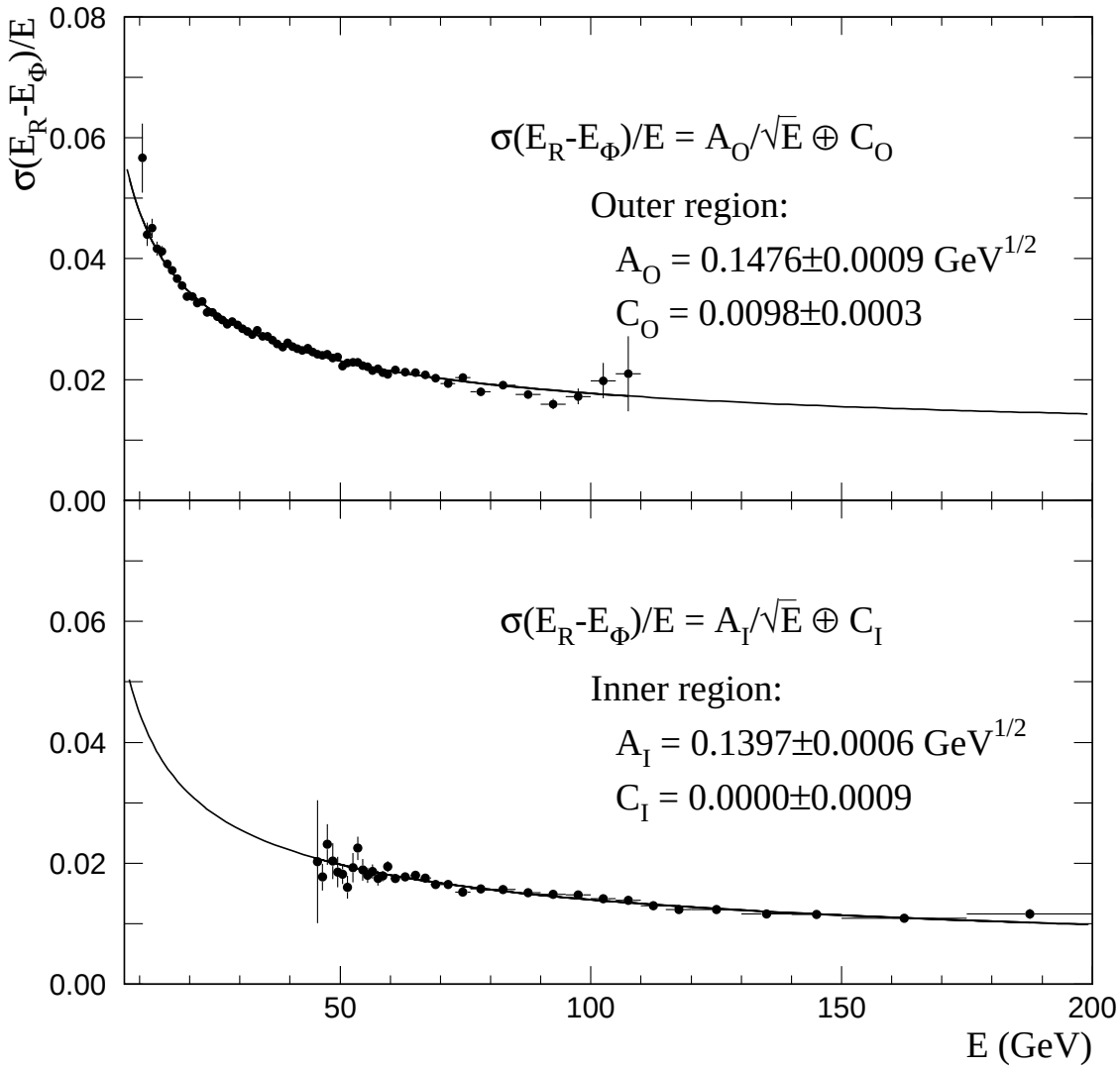

Figure 5.14 Fractional widths of the $E_R - E_\phi$ distributions plotted as functions of the total energy of the shower, for showers in the outer and inner regions of the detector. The data are isolated single photons from the 515 GeV/c π^- beam sample. The curves represent fits to the data.

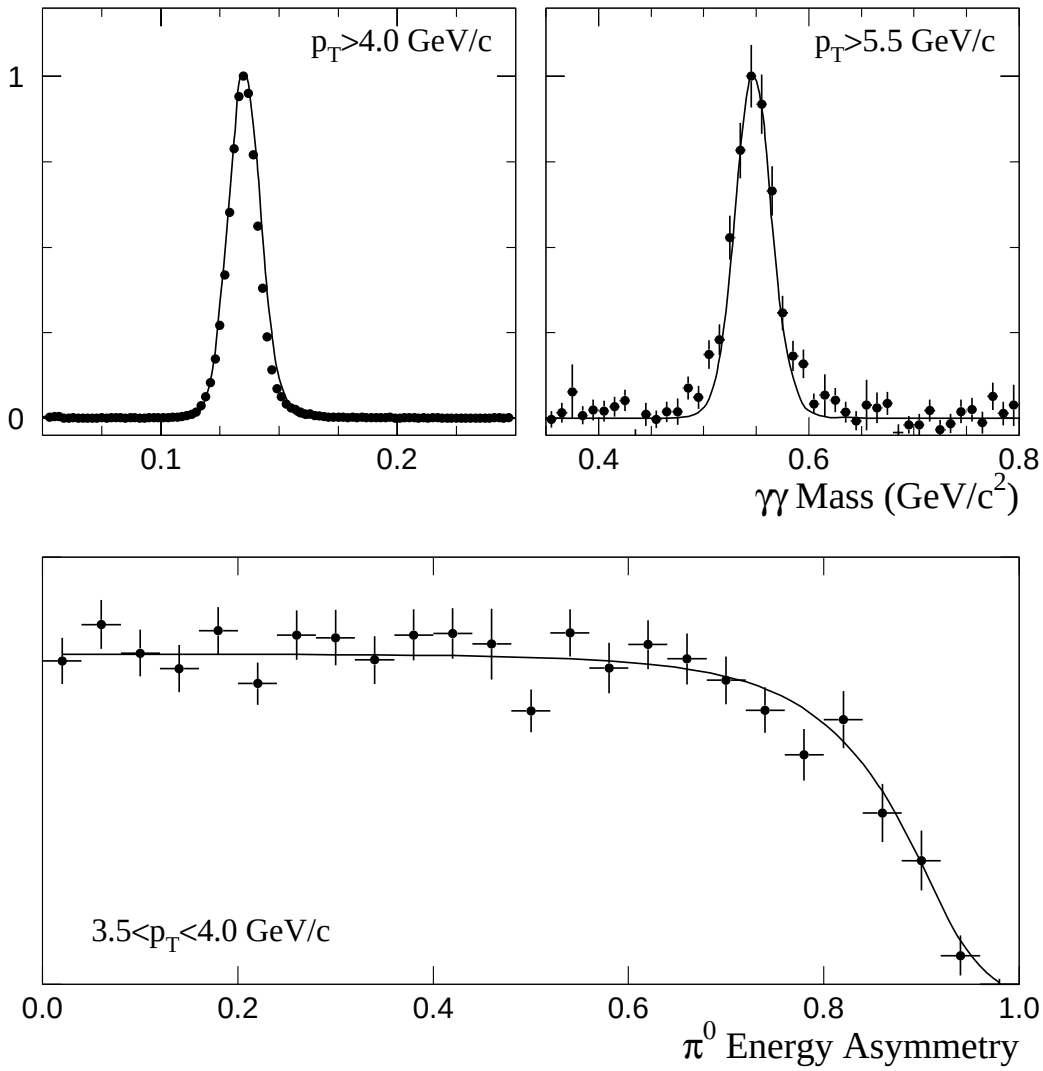

Figure 5.15 Comparison between data (•) and the parameterized Monte Carlo (curve) from the 530 GeV/c proton beam sample. Top) $\gamma\gamma$ combinations in the π^0 and η mass regions; bottom) π^0 energy asymmetry. The combinatorial background in the data has been removed through a simple subtraction for this comparison.

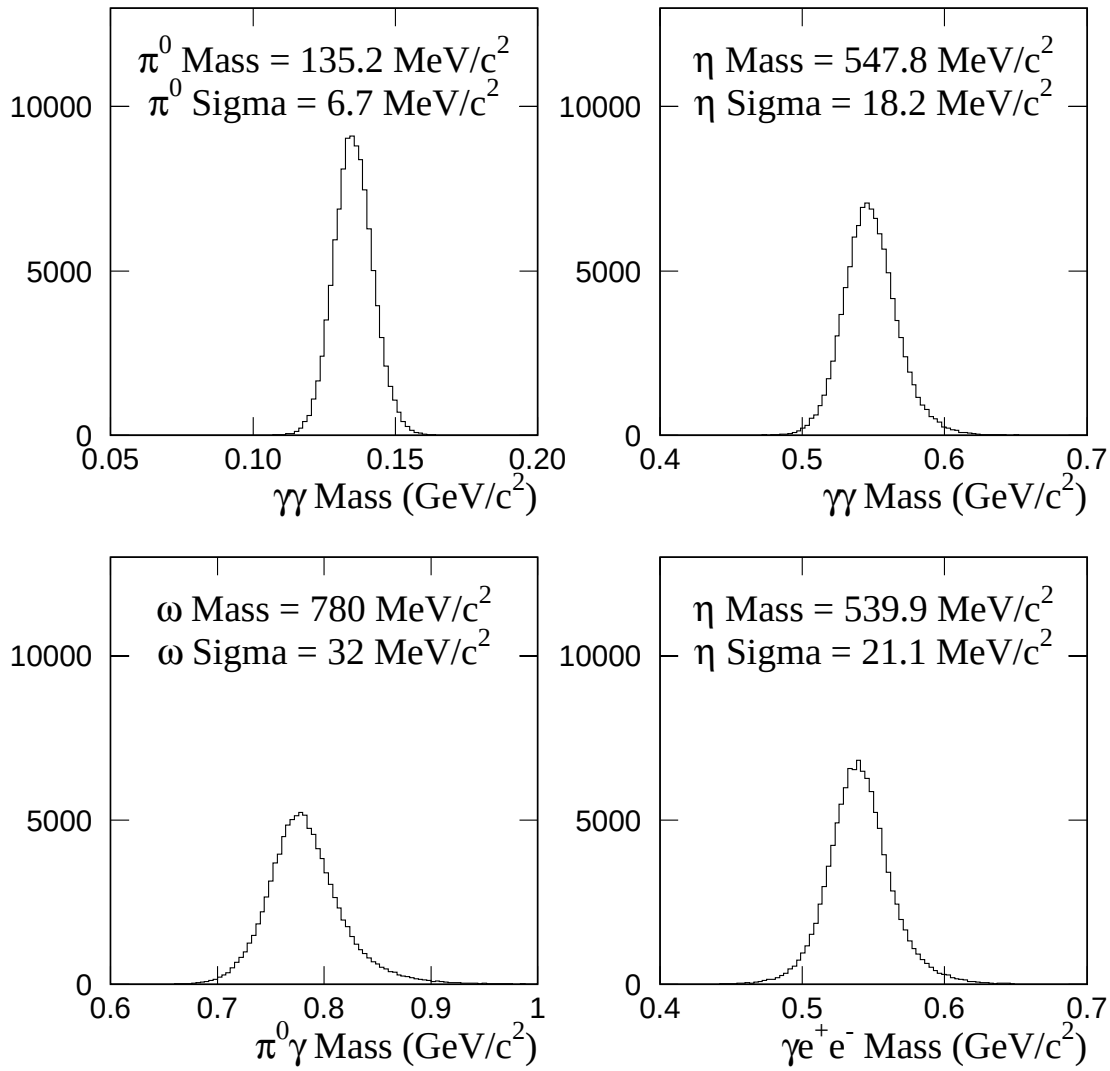

Figure 5.16 Mass plots from the parameterized Monte Carlo for the π^0, η, ω, and converted η with smeared $p_T > 3.5$ GeV/c. This is from the 515 GeV/c π^- beam sample.

Decay	Branching Ratio
$\pi^0 \longrightarrow \gamma\gamma$	0.98798
$\pi^0 \longrightarrow \gamma e^+e^-$	0.01198
$\eta \longrightarrow \gamma\gamma$	0.3921
$\omega \longrightarrow \pi^0\gamma$	0.085
$\eta' \longrightarrow \gamma\gamma$	0.0211
$\eta' \longrightarrow \rho\gamma$	0.302
$\eta' \longrightarrow \omega\gamma$	0.0301

Table 5.5 Particle decays and associated branching ratios [10] simulated in the parameterized Monte Carlo.

Beam	Target Material	Target Fraction	Z_{VERTEX} (cm)	Photon Conversion Probability
π^-	H	0.03	-20.0	0.11
	Be	0.82	-12.0	0.09
	Cu	0.15	-16.0	0.18
p	H	0.13	-20.0	0.11
	Be	0.69	-9.5	0.08
	Cu	0.18	-30.5	0.16

Table 5.6 Target configuration in the parameterized Monte Carlo. The vertex was generated at (0,0) cm in the X-Y plane. The front face of the EMLAC was at (0,0,900) cm.

5.2.3 Direct Photon Background Calculation

The full Monte Carlo was used to estimate background contributions to single inclusive direct-photon production. Since there were insufficient statistics to use these Monte Carlo samples for $\gamma\pi^0$ and $\gamma\gamma$ backgrounds, the parameterized Monte Carlo was used instead. This Monte Carlo estimated background contributions to direct-photon production due to mesons which decayed into photons (Table 5.5).

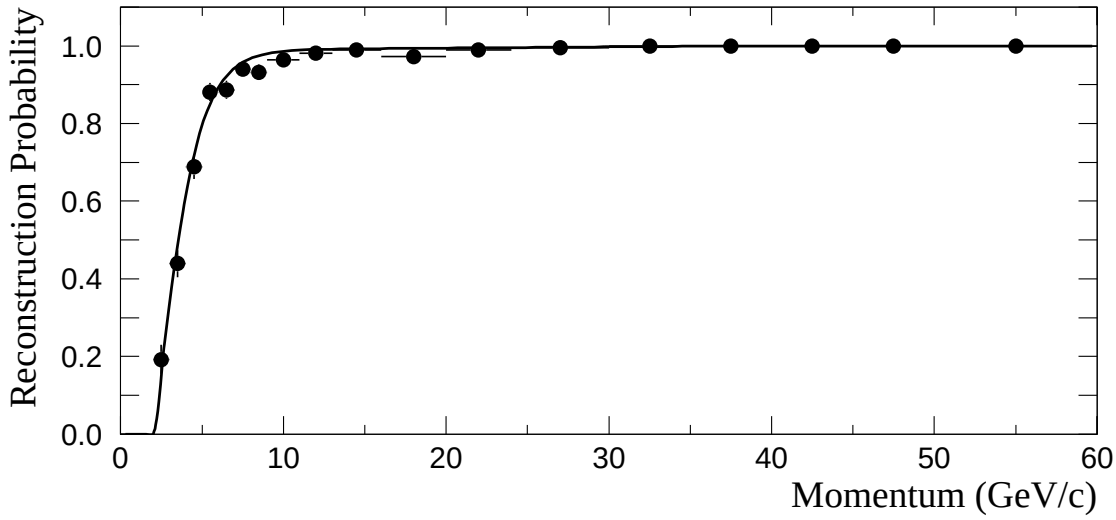

Figure 5.17 Probability for an electron to be reconstructed in the EMLAC as a function of the electron's reconstructed momentum. This function was extracted from a sample of e^+e^- pairs in the 515 GeV/c π^- data.

Photons were compared against a list of criteria developed from a detailed understanding of the analysis and studies of the full Monte Carlo [119].

For example, consider a π^0 that decays into two photons. If one photon converts into an e^+e^- pair in the material upstream of the EMLAC (Table 5.6), or doesn't shower within the fiducial volume of the EMLAC (Section 7.5), or isn't reconstructed (Figure 5.17), then the remaining photon contributes to the direct-photon background. Also, some fraction of the time, for high-p_T, forward rapidity π^0's, the two photons will be indistinguishable from a single photon (Figure 5.18). Additionally, photons showering in different octants both contribute to the background (Section 4.5). Finally, if the π^0 decays with $A > 0.75$ (Section 7.6) then both photons contribute to the background (Figure 5.19).

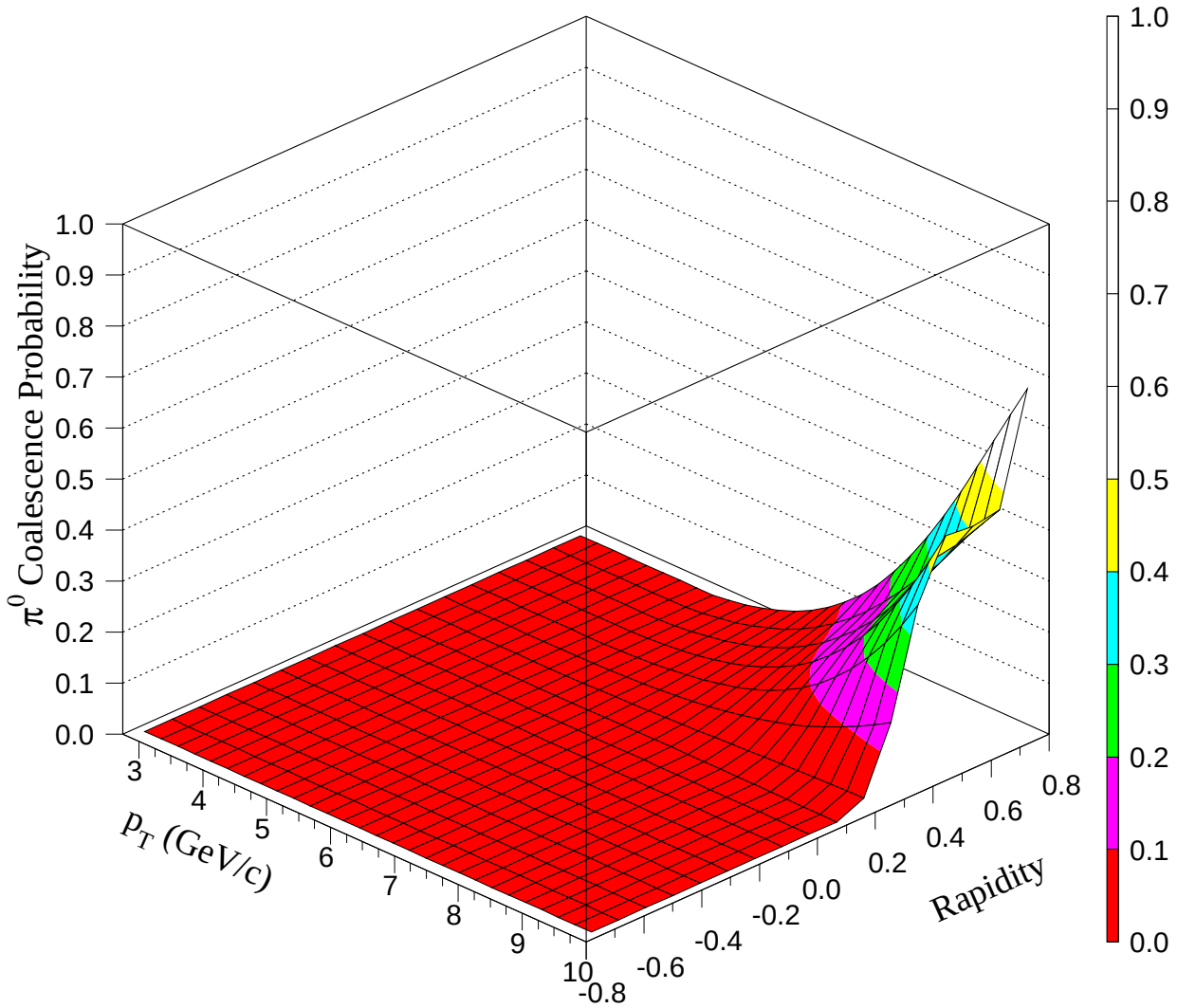

Figure 5.18 Probability that the two photons from a π^0 decay are reconstructed as a single photon. This function was extracted from the full Monte Carlo for the 515 GeV/c π^- beam sample.

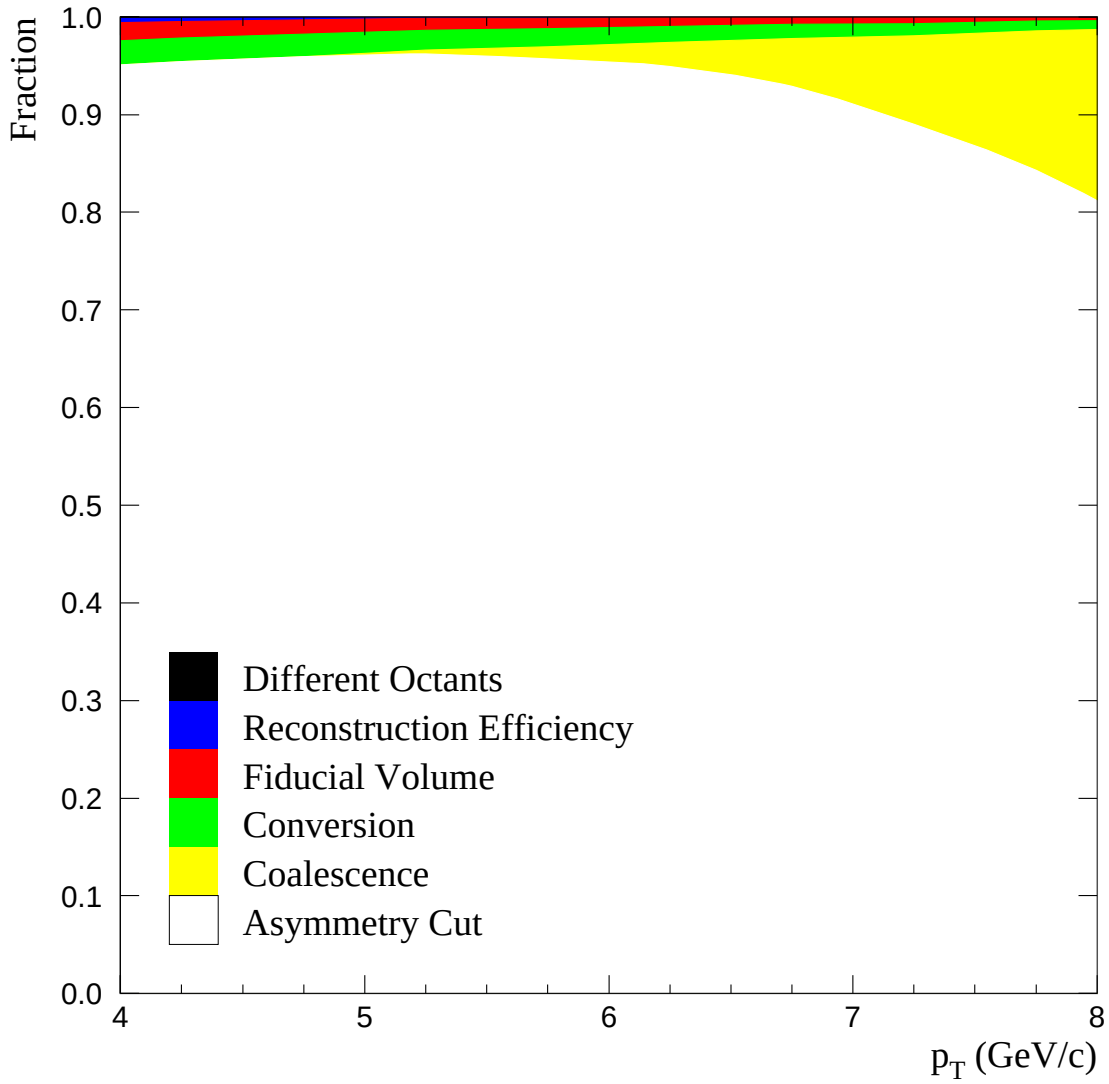

Figure 5.19 The fraction of direct-photon background arising from various sources in $\pi^0 \longrightarrow \gamma\gamma$ events as a function of photon p_T. This was extracted from the parameterized Monte Carlo for the 515 GeV/c π^- beam sample.

Similar considerations apply for background contributions from other mesons (Figure 5.20).

Additionally, the impact of $K_L^0 \longrightarrow \pi^0\pi^0$ (which has a displaced vertex) and contributions from $\pi^\pm$ were added to the overall background via simple weighting functions.

Background photons have a different event structure than direct photons; the response of the EMLAC to the two classes of photons also differs. For example, the energy response (Section 6.8.2) and the probability a photon passes the required cuts (Section 7.6 and Figure 5.21) are affected. Figure 5.22 shows a comparison between the fraction of background photons determined by the parameterized Monte Carlo for a single inclusive direct-photon sample, and the background fraction extracted from the full Monte Carlo. The good agreement indicates the parameterized Monte Carlo is successfully reproducing the background.

5.2.4 Spectral Unsmearing

The EMLAC resolution (Figure 5.14) smears the reconstructed photon energies relative to their actual (generated) values. The resolution function is approximately symmetric so that an approximately equal number of photons are smeared to lower and higher energy when binned as a function of reconstructed energy. However, since the cross sections are steeply falling functions of p_T, the lower energy photons (which have a higher cross section) which are reconstructed with higher energy due to smearing are a more significant factor in the higher energy bins (where the cross section is lower) while higher energy photons which have a smaller reconstructed energy due to smearing tend to have a negligible effect upon lower energy bins. This leads to a net shift in the p_T spectrum (Figure 5.23) when binned in reconstructed p_T bins. Similarly, the mean measured meson masses

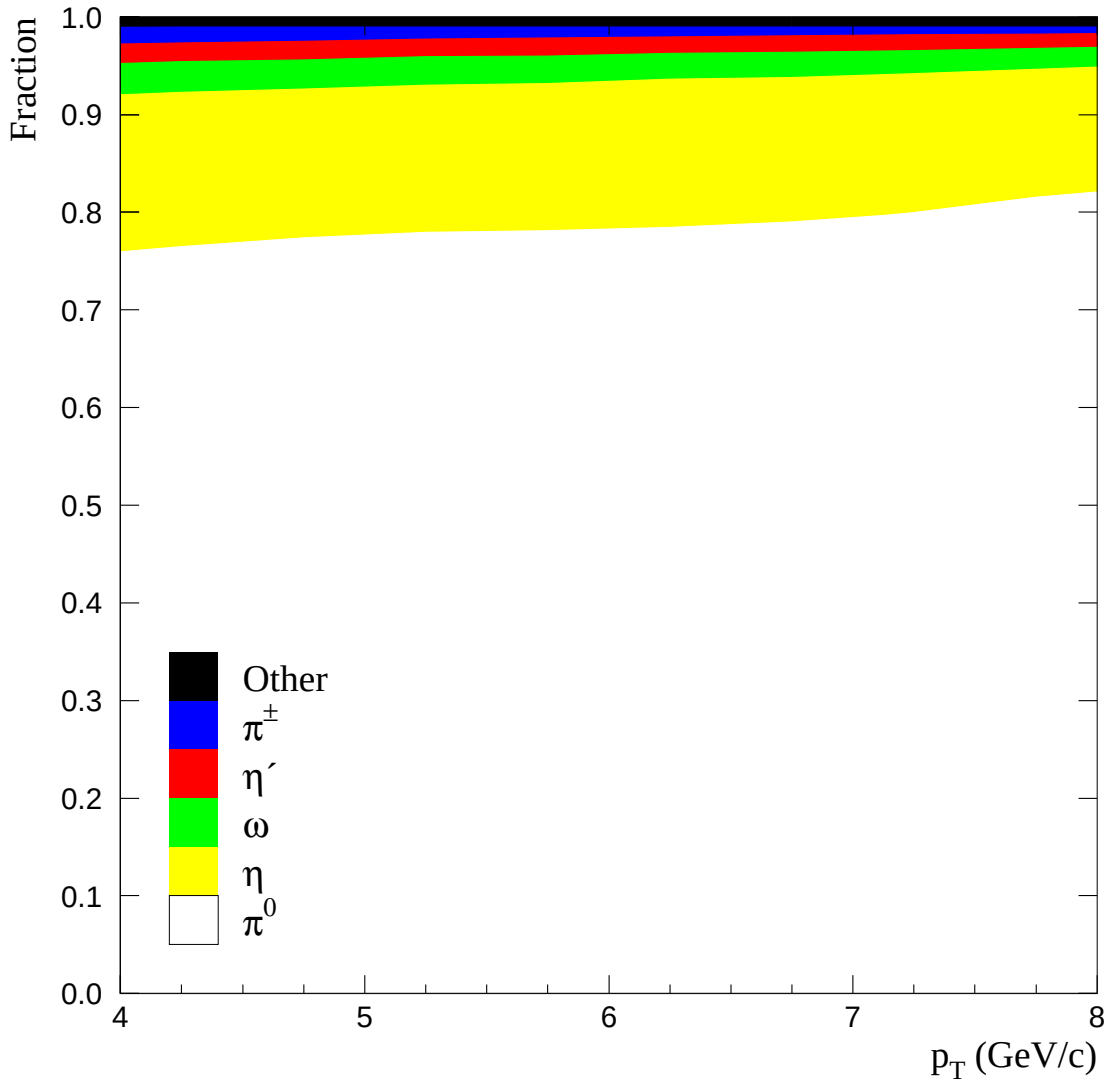

Figure 5.20 The fraction of the direct-photon background arising from π^0's, η's, ω's, and all other sources as a function of photon p_T. This was extracted from the parameterized Monte Carlo for the 515 GeV/c π^- beam sample.

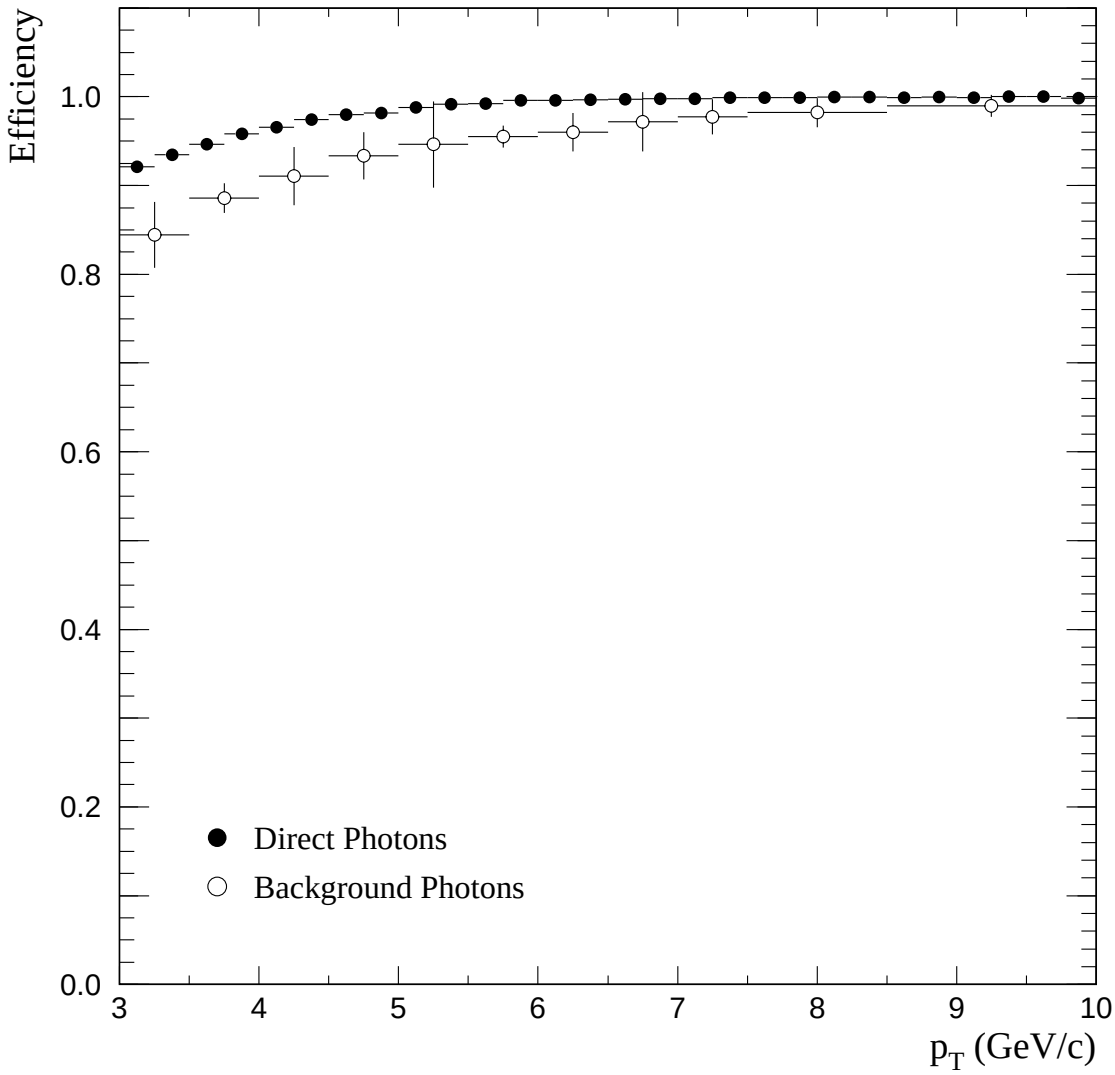

Figure 5.21 The photon definition efficiency for (•) direct photons, and (○) background photons in the full Monte Carlo. This was extracted from the 530 GeV/c proton beam sample.

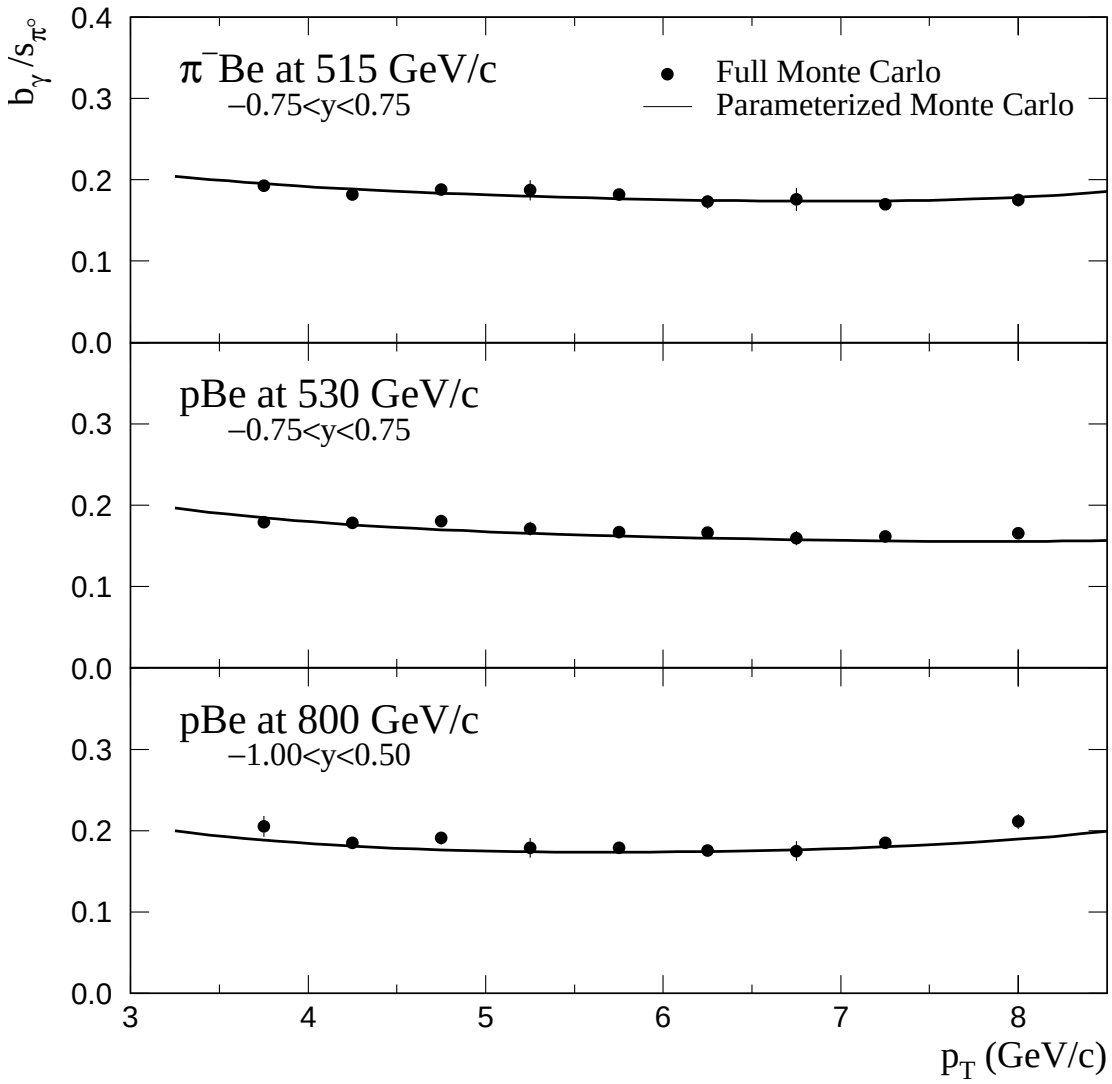

Figure 5.22 A comparison of the direct-photon background as a function of p_T between the parameterized Monte Carlo (line) and the full Monte Carlo (•). The background (b_γ) was normalized to the π^0 cross section (s_{π^0}).

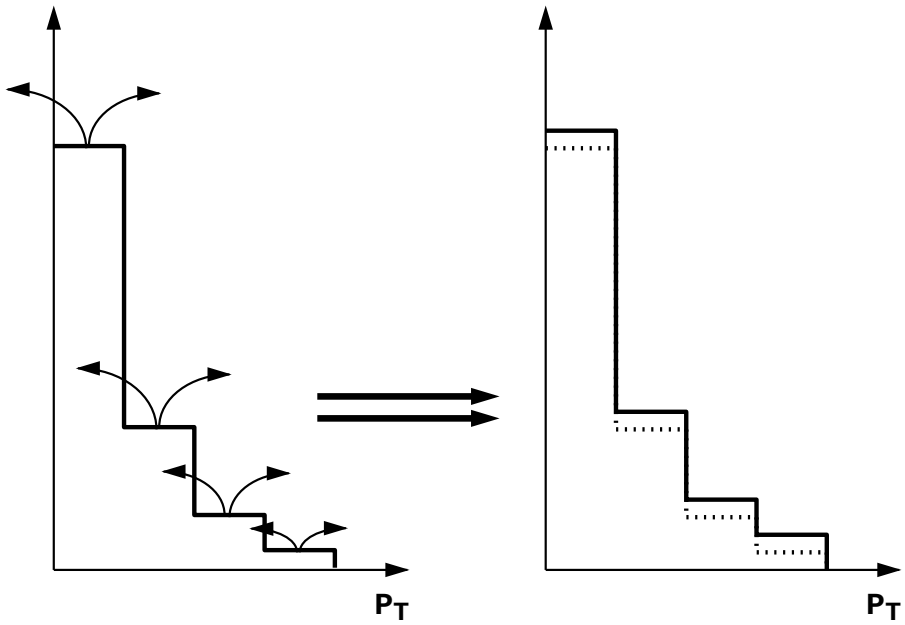

Figure 5.23 Illustration showing the effect of energy resolution on a steeply falling p_T spectrum. For any given reconstructed p_T bin, there are more contributions from bins with lower generated p_T than from bins with higher generated p_T, leading to a net shift in the p_T spectrum.

will be slightly higher than the generated values. Since these masses are used to calibrate the energy response of the calorimeter (Section 6.4.2), the net effect will be to reduce the reconstructed photon energies below the generated values (Figure 5.24).

The Monte Carlo simulations were used to correct for these smearing effects. For the single arm inclusive measurements, the reconstruction efficiencies (Section 5.1.4) were binned in reconstructed p_T and rapidity so that the data was unsmeared bin-by-bin. The parameterized Monte Carlo was used to evaluate unsmearing functions for the two armed measurements. These cross sections were unsmeared as functions of the mass of the pair.

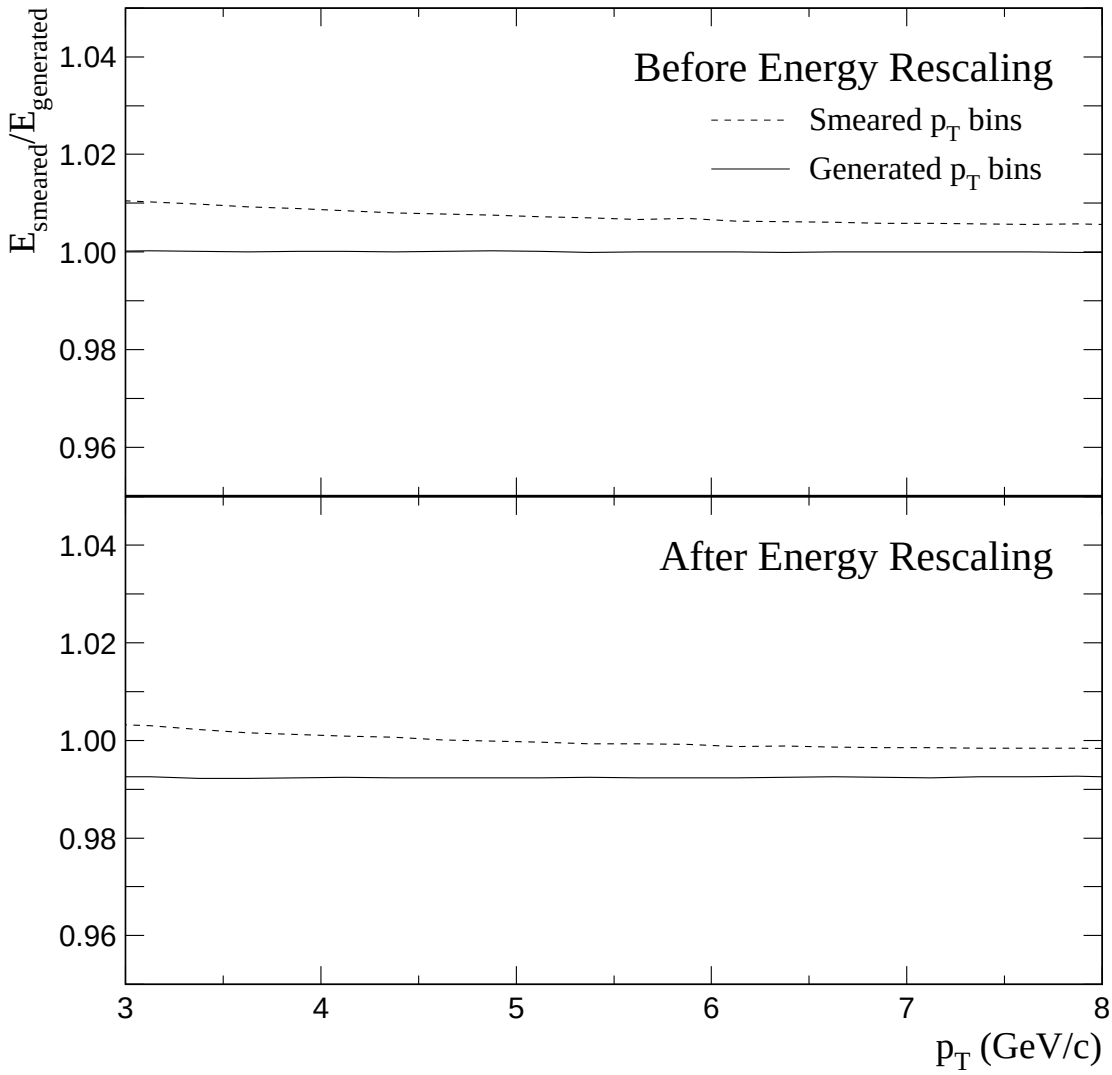

Figure 5.24 Impact of the EMLAC energy resolution on the mean π^0 $E_{smeared}/E_{generated}$ as functions of generated p_T (solid) and smeared p_T (dashed) both prior to (top) and after (bottom) the energy calibration. Following the energy calibration procedure (which used smeared quantities), the average smeared energy is smaller than the average generated energy when binned in generated p_T.

Chapter 6 Energy Scale Calibration

6.1 Introduction

The measurement of the energy response of the electromagnetic calorimeter was an important part of the E706 physics analysis. The *energy scale* calibration was intended to deal with systematic effects due to four potential sources: the physical detector, the data acquisition system, the simulated detector, and the reconstruction package. This calibration was difficult to accomplish as it was sensitive to almost every aspect of the experiment. Because of this complexity, most of the energy scale calibration was performed following full event reconstruction. Systematic effects were then identified and eliminated as necessary.

The cross sections measured by this experiment are sensitive to the calibration of the EMLAC energy response. An incorrect energy scale affects both the normalization and the shape of these cross sections. The energy scale is particularly important in the determination of the inclusive differential cross sections since these cross sections are rapidly falling functions of p_T (Figure 6.1). For example, a relative uncertainty of 1% in the energy scale results in a systematic error of 9% at $p_T = 4$ GeV/c in the measurement of the π^0 differential cross section (Figure 6.2). It is therefore critically important to obtain a self consistent energy scale. For this purpose, we examine electrons from converted photons and J/ψ decays, and photons from π^0, η, and ω decays.

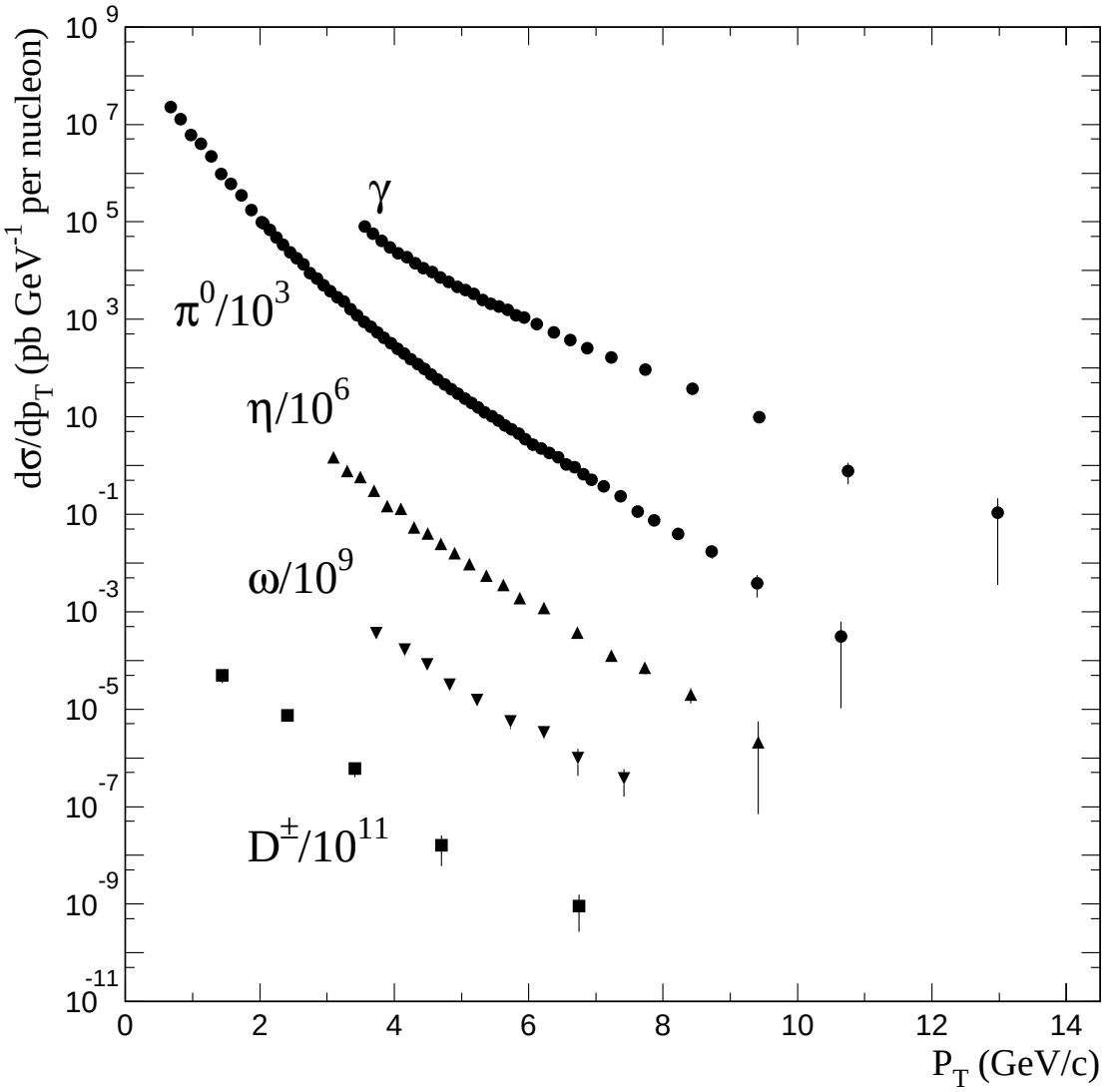

Figure 6.1 Inclusive differential cross sections as a function of p_T for the production of photons and mesons in π^-Be interactions at 515 GeV/c.

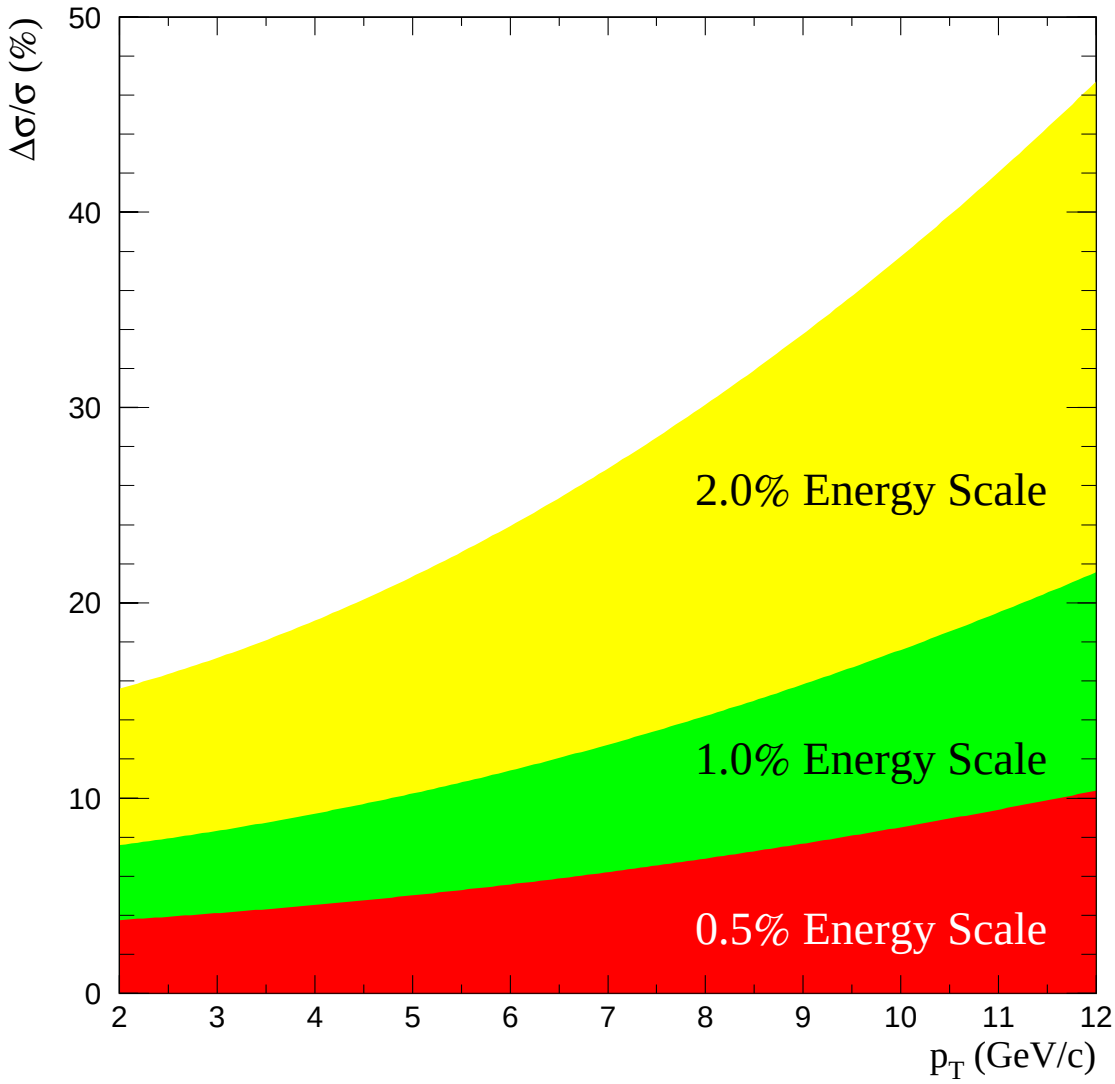

Figure 6.2 The systematic uncertainty in a π^0 cross section as a function of p_T due to the uncertainty in the energy scale. Three different values are displayed. This is for the production of π^0's in π^-Be interactions at 515 GeV/c.

Run	Majority Beam Particle	Beam Momentum (GeV/c)	BEFORE/AFTER (ns)	Run Number Range
1988	p/π^-	500	640	1672—3036
1990	π^-	515	400	7523—7907
			790	7908—9434
1991	p	800	840	12163—13648†
	p	530		13717—14302
	π^-	515		14303—14451
	p	530		14452—14701
	p	800		14702—14901

† The TWO GAMMA trigger was available for runs > 13599 (Section 3.1.5).

Table 6.1 Summary table listing the data sections used in the energy scale analysis.

6.2 Samples

6.2.1 Data

The data analyzed in this chapter (Table 6.1) were recorded during the 1990 and 1991 fixed target runs. Aside from small improvements, the spectrometer did not change between these two data runs. These data were analyzed separately. The data energy scale analysis presented below is primarily concerned with the 1991 data sample. A presentation of the energy scale devoted to the 1990 data sample can be found in [105, 127]. A combined summary of the calibration of the 1990 and 1991 data samples can be found in [35]. The energy scale for the 1988 data has been discussed extensively elsewhere [59, 88].

Every data event considered for the energy scale analysis was required to have a reconstructed vertex in the target region. Events were rejected if the veto-walls signaled possible muon contamination [79]. Photons were required to be

reconstructed in octants which fired one of the triggers. Most of this analysis was concerned with data from only two of these triggers, the TWO GAMMA (Section 3.1.5) and the SINGLE LOCAL HIGH (Section 3.1.3). The p_T cuts[1] were, respectively, $p_T > 3$ GeV/c and $p_T > 5$ GeV/c. These cuts were determined by taking into account the effects of the trigger on the energy scale distributions. In each case, the p_T requirement was chosen to minimize any trigger effects. For the ω (Figure 6.18), a SINGLE LOCAL HIGH trigger and $p_T > 5$ GeV/c were required.

A cut on the energy asymmetry, $A < 0.5$ (Equation 4.4), was used to minimize the sensitivity of the reconstructed mass to possible uncertainties in the energy scale as a result of two photons with large energy difference being close together (Figure 6.3). This requirement was placed on both data and Monte Carlo events.

For purposes of the energy scale calibration, ZMP cuts (Section 4.5) were tightened where necessary to provide the cleanest signal (with reasonable statistics) possible. Electron tracks were required to be linked, straw-X tracks that matched within 1.5 cm with an EMLAC shower having $E_{FRONT}/E_{TOTAL} > 0.4$. The ZMP mass was also required to be less than 5 MeV/c^2 (Figure 4.11).

ZMP electrons can be combined with photons to reconstruct π^0 and η signals (Figure 4.9). Here, the ZMP four-vectors are obtained from the tracking system. This is used to probe the single photon energy scale in the calorimeter and is used for an additional linearity cross check. No trigger requirement was placed on the photon's octant for this signal, and the minimum p_T is taken as low as 0.8 GeV/c.

[1] These are for the 1991 data analysis. Lower p_T cuts were used for the 1990 data analysis: 2.0 and 3.5 GeV/c respectively.

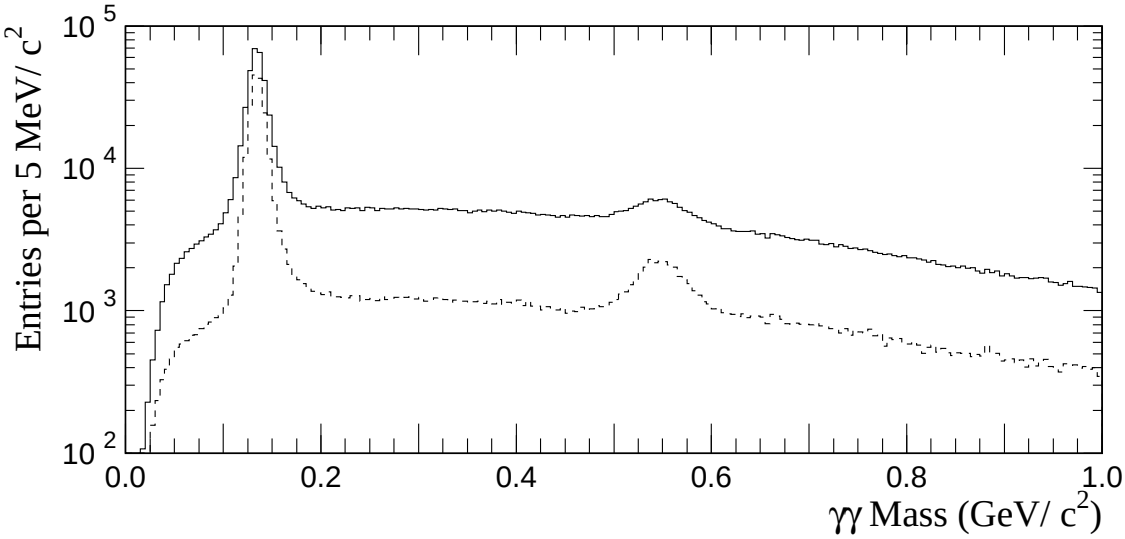

Figure 6.3 Two photon invariant mass spectrum with $p_T > 3$ GeV/c from the 1991 data sample. The lower, dashed, curve represents $\gamma\gamma$ pairs with energy asymmetry less than 0.5. The peaks are due to reconstructed π^0 and η mesons.

6.2.2 Full Monte Carlo

The energy response of the simulated EMLAC was studied in the same manner as the energy response of the real detector. Three Monte Carlo samples were considered in this analysis. The first consisted of QCD $2 \rightarrow 2$ hard-scatter events produced by the `HERWIG` event generator (Section 5.1.2). This was the principle sample used in the Monte Carlo energy scale calibration. The second sample consisted of `HERWIG` generated direct-photon events. The third sample consisted of reconstructed data events processed through the `GEANT` spectrometer simulation [119]. These latter two samples were only used for cross checks.

The cross sections for the production of photons and mesons are rapidly falling functions of p_T (Figure 6.1), so, a variety of p_T thresholds [119] were used in

the Monte Carlo event generation to populate the high-p_T regions. While these thresholds made it simpler to generate the statistics to perform other analyses (e.g. reconstruction efficiencies, direct-photon background subtractions), it made it very difficult to measure the energy response of the simulated EMLAC. Each threshold had very limited statistics (Tables 5.2, 5.3, and 5.4) making it difficult to accurately measure distributions such as the π^0 mass versus EMLAC radius. Additionally, the samples were cut 0.5 GeV/c above p_T^{MIN} to avoid threshold effects. This reduced statistics even further.

Monte Carlo spectra were weighted to the data results in an iterative fashion so that final corrections were based on the data distributions rather than on the choice of a physics generator [119]. The energy scale was dependent upon these spectra[2] and so it was important to apply the appropriate weighting functions (`HERWIG`-to-Data surfaces) when calibrating the simulated calorimeter.

6.2.3 Parameterized Monte Carlo

A simple Monte Carlo was implemented to better study the effects of various sources on the energy response of the detector (Section 5.2). Due to smearing effects (Section 5.2.4), an energy scale was implemented for this Monte Carlo equivalent to the data energy scale. This implementation was used to estimate the impact on the cross sections of systematic uncertainties associated with the calibration of the EMLAC energy response.

[2] A simple rule of thumb is that the energy scale changes by 0.5% for every factor of two change in slope versus p_T.

Particle	World Average Mass (MeV/c^2)	Full Monte Carlo Mass (MeV/c^2)
π^0	134.9764 ± 0.0006	134.973
η	547.45 ± 0.19	547.3
ω	781.94 ± 0.12	782.0
K^0_S	497.672 ± 0.031	497.67
J/ψ	3096.88 ± 0.04	3096.93

Table 6.2 The masses of particles used in the energy scale calibrations.

6.2.4 Mass Reference

Masses were set/compared to their world averages [10] as listed in Table 6.2. The masses for the particles used in the full Monte Carlo simulation were generated with an older set of world averages [128]. The energy scale in the full Monte Carlo was determined using these values rather than those used for the data. The parameterized Monte Carlo used the world averages. Throughout most of this document, the π^0 and η masses are presented relative to their nominal values. Thus a mass ratio of 1.0 indicates the mean meson mass was measured (using a Gaussian fit with linear background) to be at its nominal value (according to Table 6.2).

6.2.5 Momentum Scale

The momentum scale of the tracking system was calibrated using the decays $K^0_S \longrightarrow \pi^+\pi^-$ and $J/\psi \longrightarrow \mu^+\mu^-$. The K^0_S sample was reconstructed from pairs of oppositely charged tracks originating in secondary vertices. Events containing J/ψ's were selected by the E672 dimuon trigger [95], but the reconstructed parameters of the tracks were evaluated using only information from the SSDs, PWCs, and SDTs. Figures 6.4a and 6.4b show the K^0_S and J/ψ mass peaks

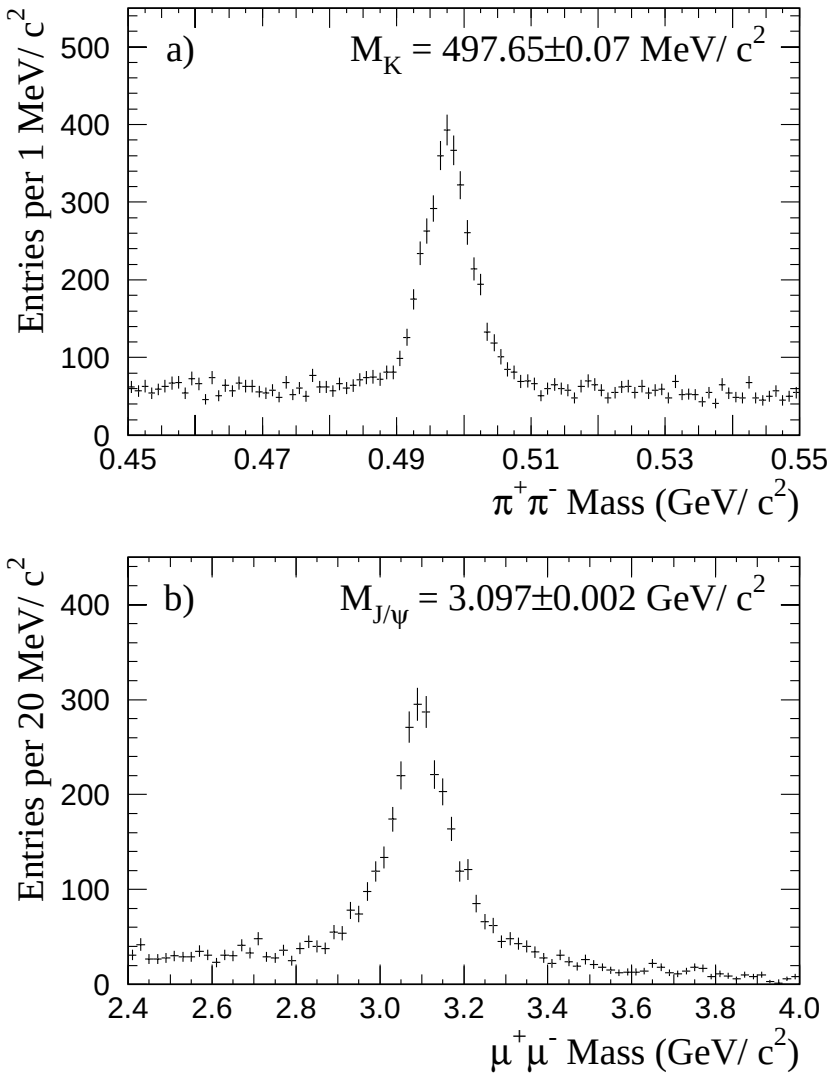

Figure 6.4 a) $\pi^+\pi^-$ invariant mass in the K^0_S mass region for secondary vertices upstream of the analysis magnet; b) $\mu^+\mu^-$ invariant mass in the J/ψ mass region.

respectively [129]. The reconstructed masses are within 0.1% of their accepted values.

6.3 EMLAC Alignment

The EMLAC was aligned to the tracking system using the ZMP sample. The EMLAC was independently aligned for the 1990 and 1991 data samples since the EMLAC was moved between runs for calibration purposes. Certain ZMP criteria were tightened as follows:

- $|\Delta S_Y| < 2.5$ mrad;
- Z–X intersection point within 10 cm of the center of the magnet;
- $P > 20$ GeV/c;
- $0.6 < E/P < 1.4$;
- Track–shower distance less than 1 cm;
- $E_{FRONT}/E_{TOTAL} > 0.5$;
- Electron shower was reconstructed within the EMLAC fiducial volume but not within 2.5 cm of the inner/outer ϕ boundary.

The same method was used to align the EMLAC to the tracking system as was used for the 1988 data [130]. This involved a χ^2 minimization (using `MINUIT` [131]) of the reconstructed shower positions of the ZMP electrons to their position determined by projecting the tracks onto the EMLAC. The minimization was performed in two steps; first the azimuthal rotation and Z-position of each of the four quadrants was determined. These were fixed (with a single overall Z-position for the EMLAC), and then the X and Y offsets were determined for each octant. Finally, each octant's alignment was cross checked to ensure there were no physical overlaps. Additionally, the alignment was checked independently for different run regions. These cross checks gave consistent results.

The position resolution for the EMLAC (Figure 6.5), using the ZMP electron data, is

$$\sigma_{\Delta \mathrm{R}}(\mathrm{E}) = \frac{1.65}{\mathrm{E}} + 0.045 \text{ cm}, \tag{6.1}$$

where E is measured in GeV. Here the contribution to the resolution from the tracking system has been removed in quadrature [129].

6.4 Energy Scale Methodology

A systematic study of the π^0 and η masses in their $\gamma\gamma$ decay mode can be used to set the energy scale since both particles are produced in large numbers and are well distributed throughout the EMLAC. Once the scale is set, the high quality electron sample is used to look for residual energy corrections. As a final cross check, the ω meson, in the $\pi^0\gamma$ decay mode, is examined. The agreement of its mass with the world average provides an independent measure of the internal consistency between the $\gamma\gamma$ and single photon energy scale.

The photon energies are corrected so that the $\gamma\gamma$ masses come to their nominal values. The mass is given by

$$\mathrm{M}^2 = 2\mathrm{E}_1\mathrm{E}_2(1 - \cos\theta), \tag{6.2}$$

where E_1 and E_2 are the energies of the photons reconstructed in the EMLAC and θ is the angle between them in the lab system. If two photons, such as those from a high–p_T π^0, are close together, then the tails of their showers overlap, and it is possible they will be reconstructed with compromised energies and positions. Studies have shown that the sum energy of the two photons does not change [132], but the mass calculated using the individual photon energies and positions is modified (Figure 6.6). This sensitivity could cause the two photon mass to exhibit

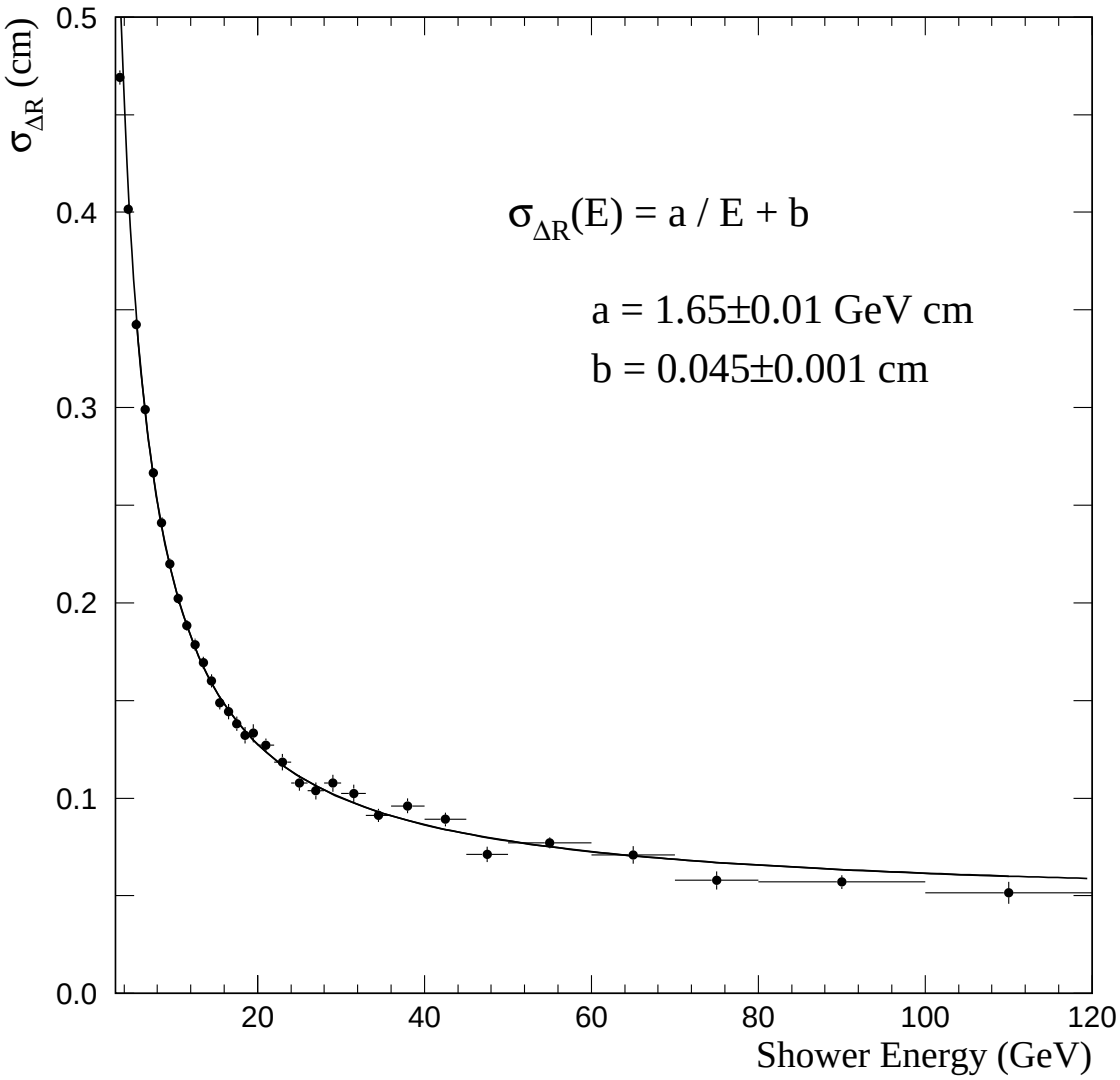

Figure 6.5 The position resolution for the EMLAC as a function of energy. The contribution to this resolution from the tracking system has been subtracted out in quadrature.

different characteristics (when measured as a function of p_T or EMLAC radius, for example) than corresponding measurements of a single photon's energy. For this reason, one must take care that the corrections evaluated using the meson masses do not compromise the energy measurement; thus, well-separated showers are required during evaluation of the energy scale corrections. The average separation of photons from π^0 decays decreases as the π^0 p_T increases; therefore samples containing low-p_T π^0's are used to measure most of the corrections.

6.4.1 Photons and Electrons

Since E706 has an excellent tracking system, it should be possible to calibrate the response of the electromagnetic calorimeter using electrons. In this case we would adjust the reconstructed energy of showers in the calorimeter to match the momenta measured in the tracking system. This method was used for the analysis of the 1988 data and an uncertainty of 0.9% in the energy scale was inferred [59, 88]. Unfortunately, this method also has its shortcomings. To begin with, the shower shapes for electrons and photons are different (electron initiated showers being broader than corresponding photon initiated showers). The electromagnetic reconstruction was specifically tuned to measure the energy of photon induced showers. The reconstructed energies of electron induced showers are not as well determined and are systematically low for the lower energy electrons where the tracking system momentum measurements dominate (Figure 6.25). This difference between electron and photon induced showers is exacerbated by the energy lost in the materials upstream of the active layers of the electromagnetic calorimeter (Section 6.5.4). A differential between electrons and the photons in terms of the effects of the energy loss correction on the reconstructed radial dependence of the detector (Section 6.5.5) can lead to relatively large changes in the inclusive cross sections measured as functions of rapidity.

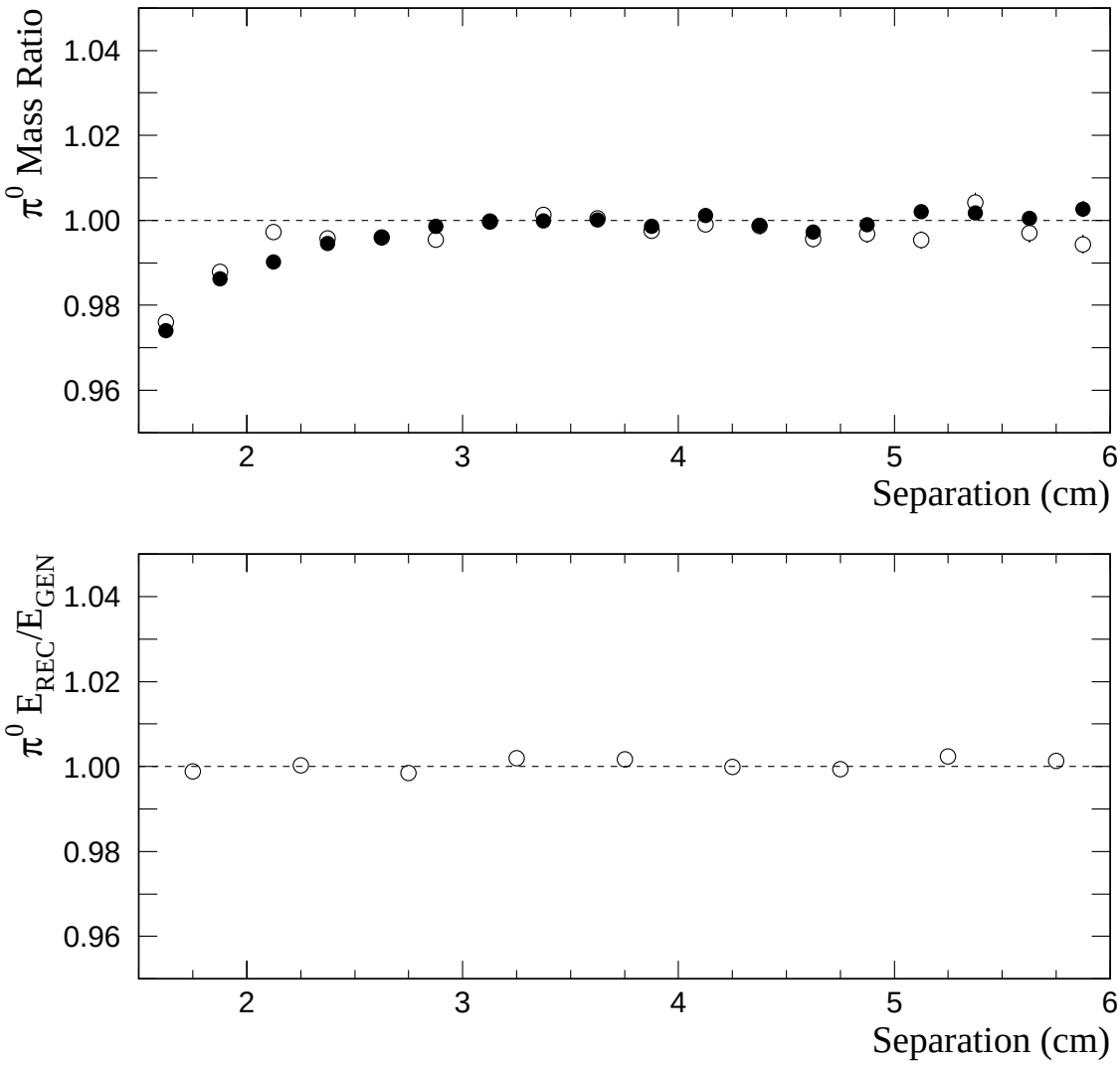

Figure 6.6 The top plot shows a comparison of reconstructed π^0 mass as a function of the separation between the two photons from the π^0 decay in the data (•) and the full Monte Carlo (∘) for the 1990 π^- sample with $p_T > 3.5$ GeV/c. The bottom plot shows the comparison of the mean reconstructed to generated π^0 energy in the full Monte Carlo versus the separation in the EMLAC between the photons from the π^0 decay.

Electrons are deflected in the X direction by the dipole magnet. This means they do not have the same spectrum as photons; additionally, the spectrum is different in X than it is in Y (the natural EMLAC variables being R and ϕ). This means the average distribution of showers in the detector as a function of energy is different for photons than for electrons and it differs from octant-to-octant. Any position dependent corrections will be somewhat biased when calculated using electrons and applied to photons. The effects of this spectral difference can be removed by unfolding the electron distribution, though this was not done for the 1988 data.

One of the major cross checks on the energy scale, when determined using electrons as it was for the 1988 data sample, is that the reconstructed π^0 mass is measured to be at its nominal value when one of the photons of that π^0 converted in the target materials into an e^+e^- pair. This cross check probes the applicability of the energy scale to the photon when it was determined using the electrons. As described below (Section 6.6.1), electrons lose energy in the target due to bremsstrahlung radiation (Figure 6.22). This energy is lost prior to the momentum measurement, and so the electron's energy and momentum still correspond to each other. However, the average γe^+e^- mass will be lower than its nominal value (Figure 6.20). The photon energy is still a decent probe for checking the relative energy scale, but the γe^+e^- is not adequate to check the absolute scale.

None of these effects are large, so electrons provide a valuable cross check for the energy scale calibration. However, the goal for the 1990 and 1991 data samples is to achieve an order 0.5% energy scale uncertainty. Given the size of these biases, we chose to use the π^0 and η in their $\gamma\gamma$ decay mode to measure the energy response of the electromagnetic calorimeter for the 1990 and 1991 data samples rather than using ZMP electrons as was done for the 1988 data sample.

6.4.2 Full Monte Carlo

There is, of course, more information about the photons available from `GEANT` than from the raw data. In particular, the actual energy of the generated photon is accessible. This gives the Monte Carlo a unique leverage with respect to measuring the calorimeter's energy response. Here, however, another difficulty comes to fore. As the interesting cross sections are steeply falling functions of p_T, small uncertainties in the energy determination can have large effects on the measured results. One such uncertainty comes from the intrinsic energy resolution of the EMLAC (Figure 5.14). This means the smeared energies, will not, bin by bin, agree with the generated energies (Section 5.2.4). One might imagine the energy scale prescription in this case would involve setting the smeared energies equivalent to the generated values. This is inappropriate since the data energy scale must be calibrated with the smeared energies[3]. Instead, to achieve parity, the Monte Carlo energy scale is measured in exactly the same way as the data—using the reconstructed masses of the π^0 and η mesons and ignoring the generated information.

6.5 Data Energy Corrections

6.5.1 Initial Scale and Time Dependence

The factor for converting amplifier voltage (ADC counts) to energy was measured using electron beams incident upon the EMLAC [75]. This factor was applied during the initial unpacking prior to the reconstruction phase (Section 4.3.1).

[3] The unsmearing calculation is included either in the reconstruction efficiencies (Section 5.1.4) or as a separate correction (Section 5.2.4) rather than in the energy scale.

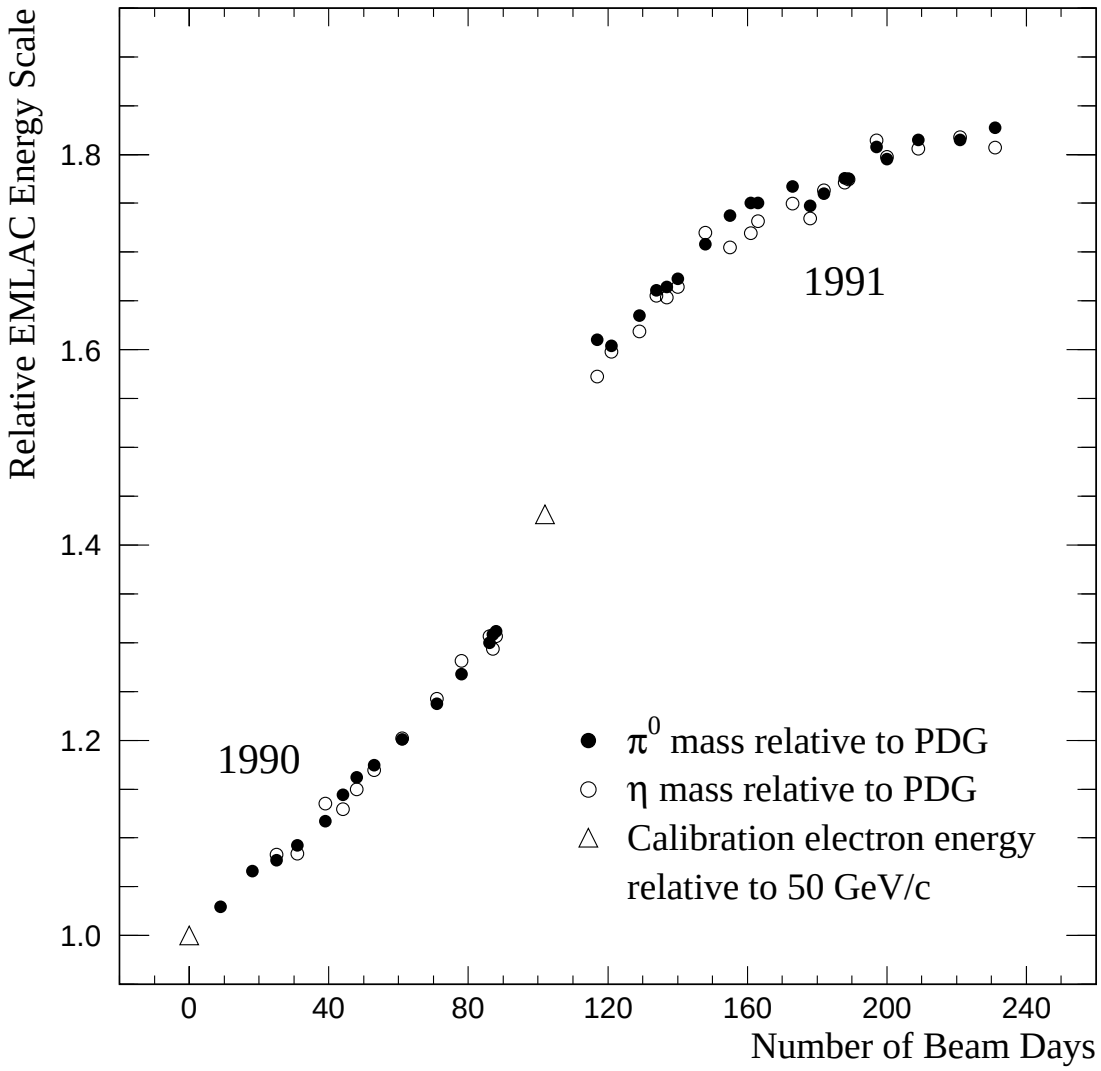

Figure 6.7 Uncalibrated relative values for the reconstructed masses of the π^0 and η signals as a function of beam days during the 1990 and 1991 runs. The triangles represent the EMLAC response to 50 GeV/c incident electron beams. Both the π^0 and η signals were reconstructed with $p_T > 5$ GeV/c and R > 50 cm.

A distinct dependence of the EMLAC energy response on time was observed. Figure 6.7 is plotted as a function of beam days, where a beam day signifies a day upon which beam was delivered to the experiment. The long shutdown between the 1990 and 1991 fixed target runs and the shorter shutdowns representing accelerator down-times do not appear in the plot. This dependence is discussed in more detail elsewhere [105, 35]. The time dependence was corrected prior to the reconstruction to allow consistent thresholds throughout the reconstruction (Section 4.3). Residuals to the smooth function used in the correction were removed as the first stage in the energy scale calibration.

6.5.2 Octant-to-Octant

A correction was implemented to account for the observed octant dependence of the mean calorimeter response (Figure 6.8). These variations in the energy scale are attributed to differences in the construction and operation of each octant (such as different lead thicknesses, readout electronics, high voltage variations, etc) and reconstruction biases (the left/right ordering, etc). The correction was determined using the low-p_T π^0 sample. To avoid any radial effects (Section 6.5.5), the π^0's were taken from the outside of the detector.

6.5.3 Inner/Outer ϕ Boundary

The reconstructor forms gammas independently in R and ϕ and correlates them together by shape and energy to form photons (Section 4.3.5). Since the energies of the ϕ gammas are over-corrected relative to the R gammas near the inner/outer ϕ boundary (as can be seen in Figure 6.9), in this region the photon energy is taken to be twice the R gamma energy rather than the sum of R and ϕ gamma energies.

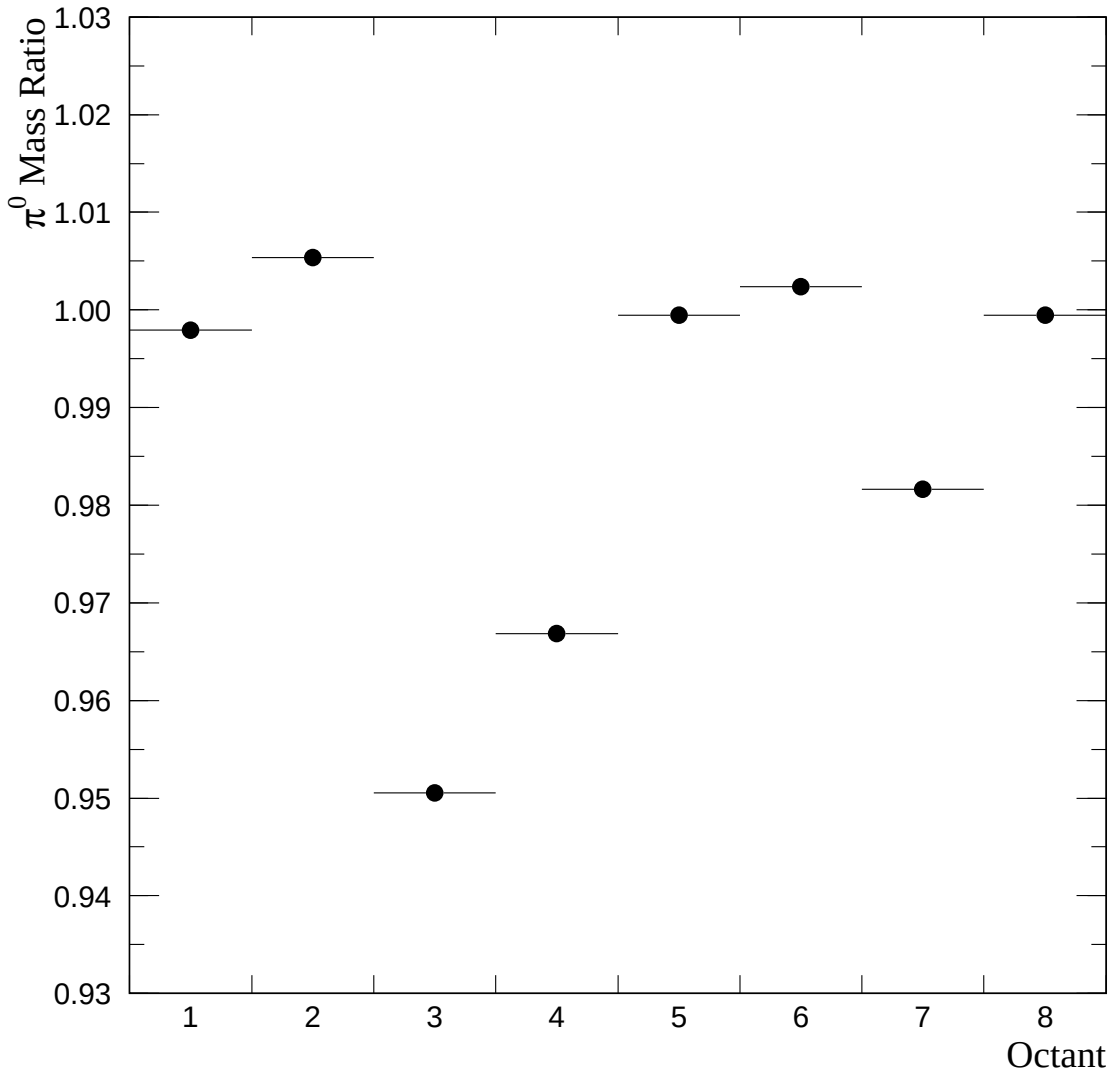

Figure 6.8 The ratio of the reconstructed π^0 mass to its nominal value as a function of octant number in the 1991 data sample.

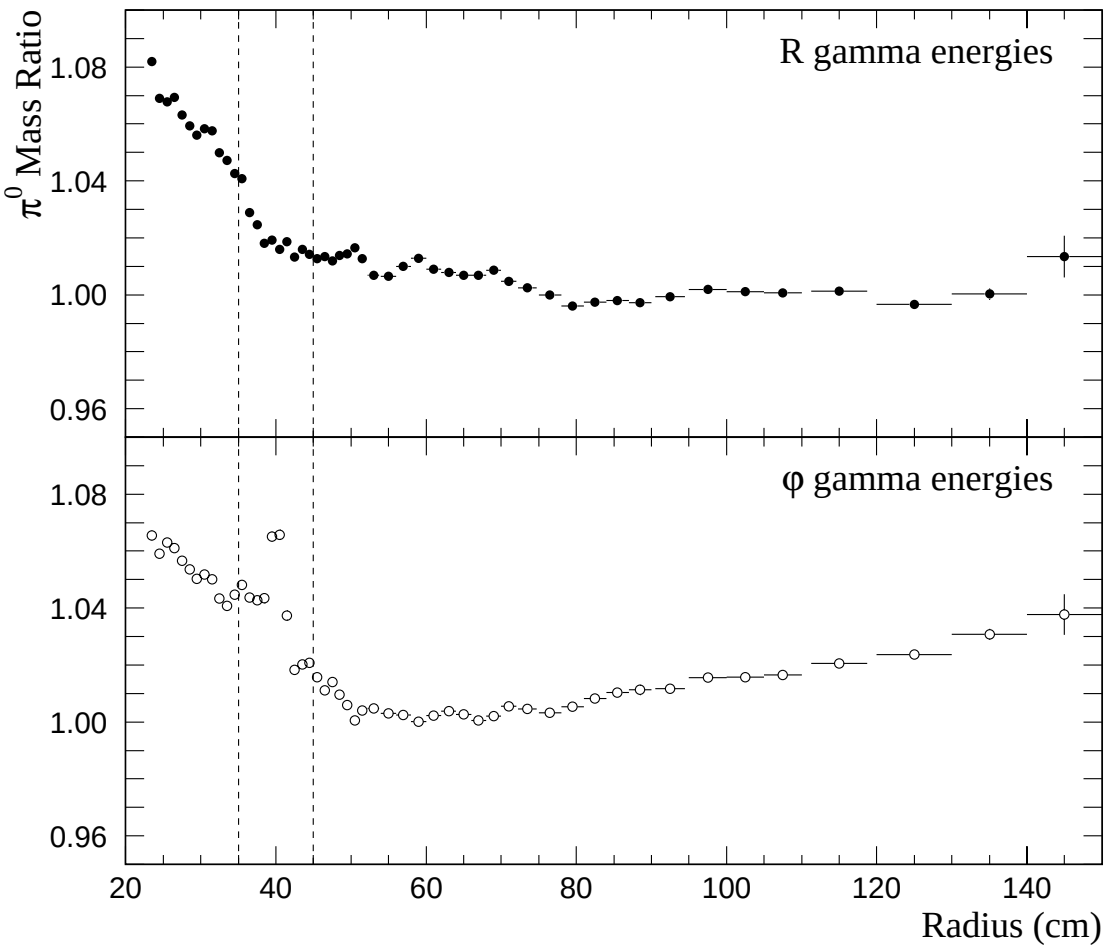

Figure 6.9 Radial dependence of the reconstructed π^0 mass from the 1991 data relative to its accepted value using as photon energy top) twice the R gamma energy or bottom) twice the ϕ gamma energy. The dashed lines represent ± 5 cm around the inner/outer ϕ boundary.

6.5.4 Correction for Material Energy Loss

A correction was made to account for the energy lost due to showering in the 2.8 radiation lengths of material upstream of the first active layer of the EMLAC (Figure 6.10). The `GEANT` Monte Carlo simulation of the spectrometer was used to determine this correction independently for photons and electrons. Figure 6.11 shows the average energy lost for photon and electron initiated showers as a function of their reconstructed energy. The amount of energy lost for photons was about 40% less than the energy lost for electrons.

The correction was parameterized as a function of energy, averaging over position dependent quantities such as the curvature of the cryostat. This is accounted for, on average, by applying the same corrections to the reconstructed energies in the Monte Carlo (thus affecting the reconstruction efficiencies as in Section 5.1.4). In addition to this, small differences in the material between the Monte Carlo simulation and the actual detector are accounted for, on an average basis, by the octant dependent radial dependence correction (Section 6.5.5). This solution comes at the cost of a using a gain-type correction to account for a pedestal-type effect; this leads to a small increase in the overall energy scale systematic uncertainty (Section 6.8.1).

6.5.5 Dependence of the Energy Scale on Radial Position

The radial dependence of the reconstructed π^0 and η masses, following the octant and material loss corrections, is shown in Figure 6.12. This dependence can also be seen in the adjusted ratio of the ZMPs energy (calorimeter) and momentum (tracking system). Since the radial dependence appears in both the $\gamma\gamma$ sample and the electron sample, it is attributed to a residual radial dependence of the EMLAC energy response. There are many effects which influence the radial

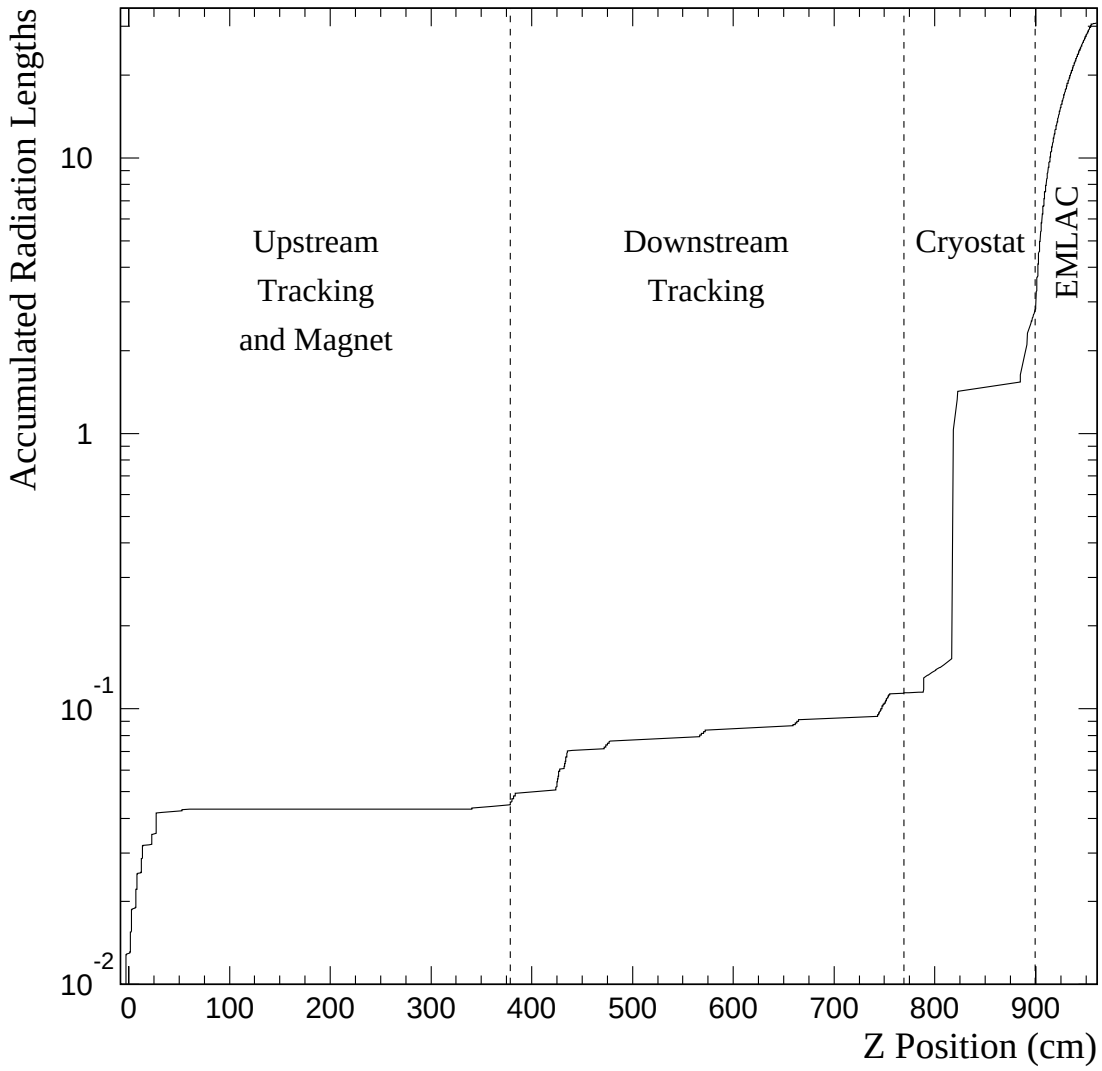

Figure 6.10 The accumulated number of radiation lengths passed through by a photon originating in the target and pointing towards the center of an EMLAC quadrant. The cryostat accounts for most of the material upstream of the EMLAC as measured in radiation lengths. This is taken from the `GEANT` Monte Carlo.

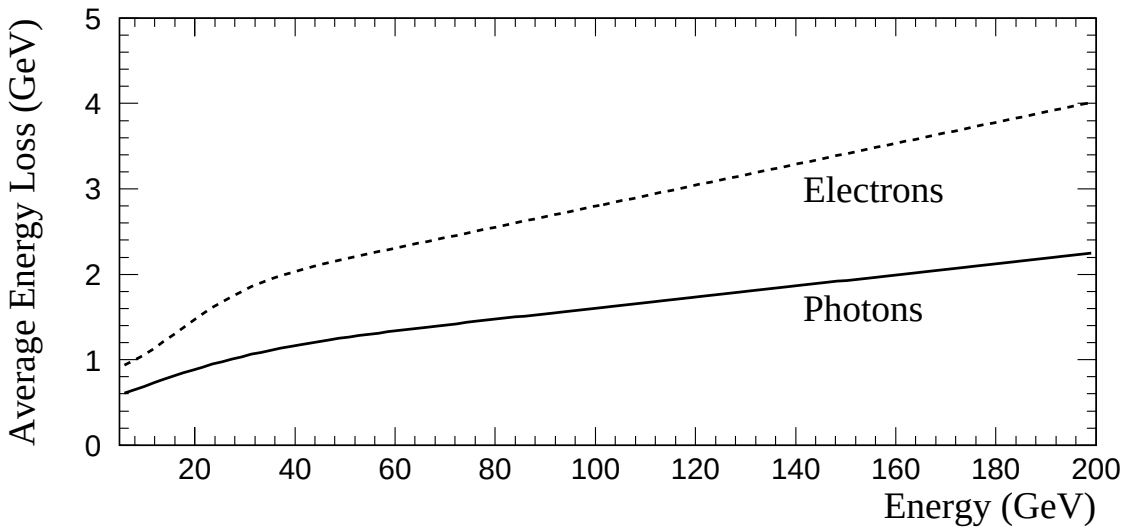

Figure 6.11 The functions used to correct for the energy loss in the material in front of the EMLAC.

dependence, such as reconstructor biases and event structure, but the dominant effect is due to the choice of the amplifier integration time. This can be seen in Figure 6.13 which displays the radial dependence of the reconstructed π^0 mass for four different values of the BEFORE/AFTER time. The BEFORE and AFTER were global calorimeter timing signals (Section 3.2). Upon receipt of the BEFORE, the voltage level of the amplifier prior to the event was sampled. The AFTER caused the integrated amplifier signal to be sampled. The difference between these two voltages was digitized and represented the "energy" seen by the amplifier. This time difference was chosen in order to minimize certain noise effects (such as cross talk between amplifiers) during the data taking [102]. However, the different amplifier integration times caused different signal regions to be sampled. These differences were not accounted for by the online amplifier gain measurements, and so the subsequent radial dependence needed to be removed offline.

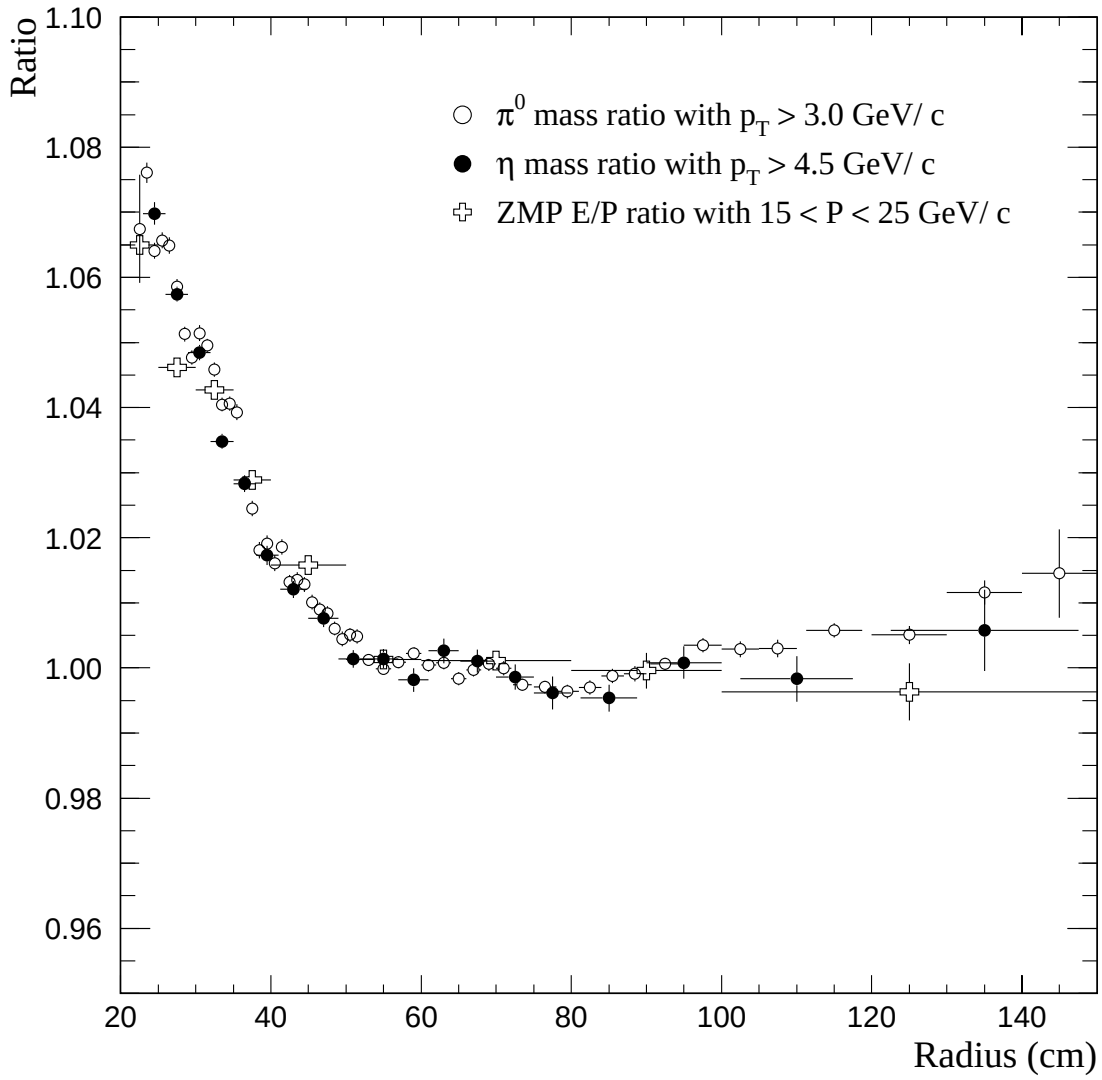

Figure 6.12 Radial dependence of the reconstructed π^0 and η masses from the 1991 data sample. Also shown is the radial dependence of the E/P ratio for ZMP electrons with P $\approx$ 20 GeV/c adjusted for Section 6.6.2.

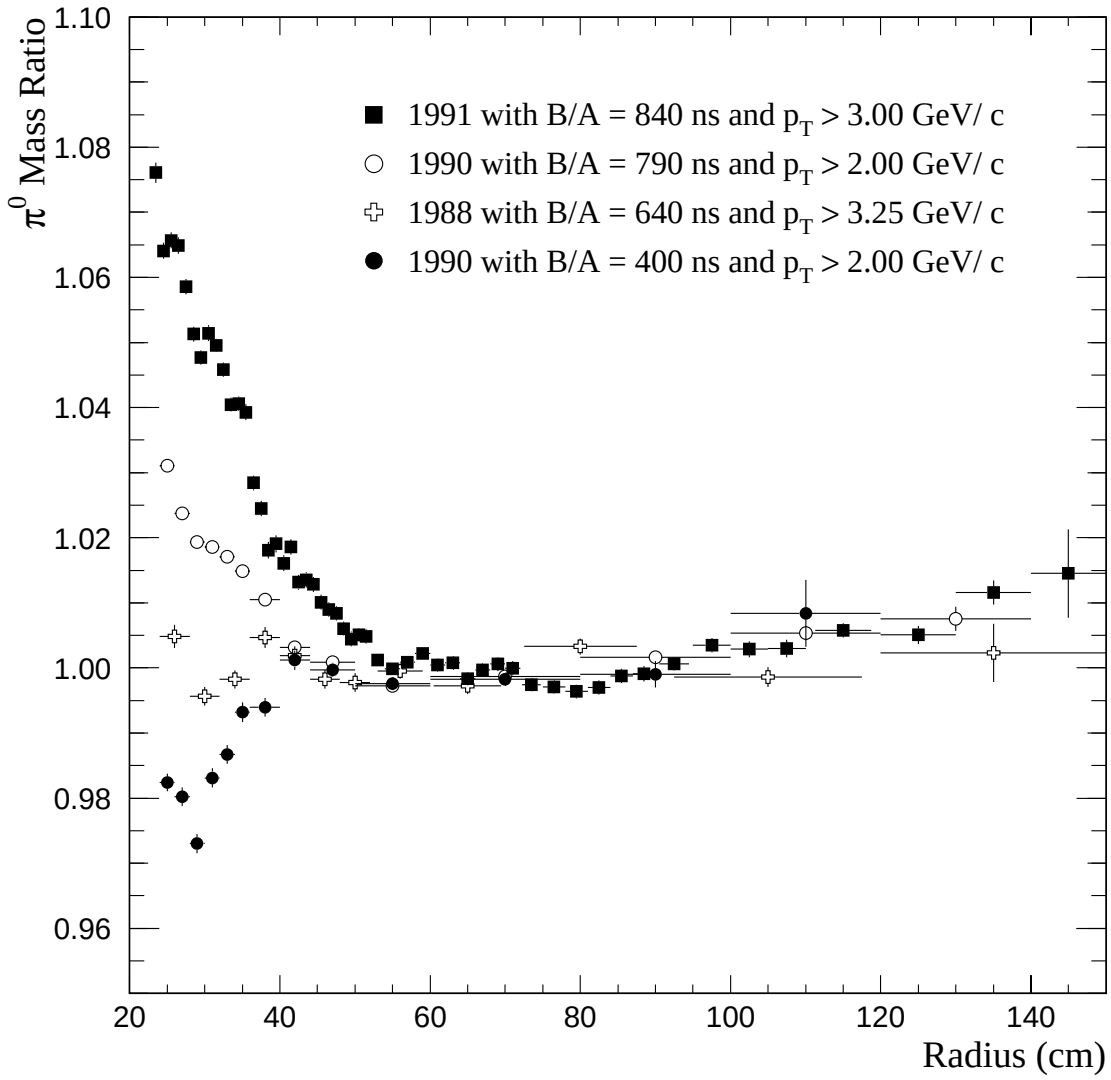

Figure 6.13 Radial dependence of the reconstructed π^0 mass shown for various values of the BEFORE/AFTER gate time.

For the 1991 data sample, the reconstructed π^0 and η masses start out high in the inner-R region and decrease with increasing radius. A correction was determined independently for each octant using the low-p_T π^0 sample since this sample had enough statistics to scan the EMLAC in small radial bins. In order to minimize the sensitivity of the reconstructed mass to any residual effects (such as reconstruction efficiency), the photons were required to have energies greater than 10 GeV. The data shown in Figure 6.14 were parameterized using an iterative procedure. The π^0 p_T used for this correction was unfortunately high enough that this correction was affected by separation effects. The higher-p_T η sample, averaged over all octants, was used to account for the residual dependence of the radial correction on separation, but was not used to alter the absolute energy scale.

6.5.6 Results and Linearity

Figures 6.15, 6.16, and 6.17 are the π^0 and η mass plots following completion of data energy scale corrections. The mean masses and widths of the signals are summarized in Table 6.3. The reconstructed ω mass (Figure 6.18) was approximately 0.5% lower than its nominal value (Tables 6.3 and 6.2). It should be noted, however, that the ω has a different slope in p_T than the π^0 or η (Figure 6.1) and so should be affected differently by the EMLAC resolution smearing. The results from the parameterized Monte Carlo (Section 5.2) indicate the ω mass should have been reconstructed approximately 0.25% lower than its nominal mass. The reconstructed ω mass was therefore measured approximately 0.25% lower than expected; this is well within the expected 0.5% energy scale uncertainties.

The linearity of the energy scale was examined using the η sample as a function of p_T and energy (Figure 6.19). The energy scale was found to be linear and accurate to well within the 0.5% goal.

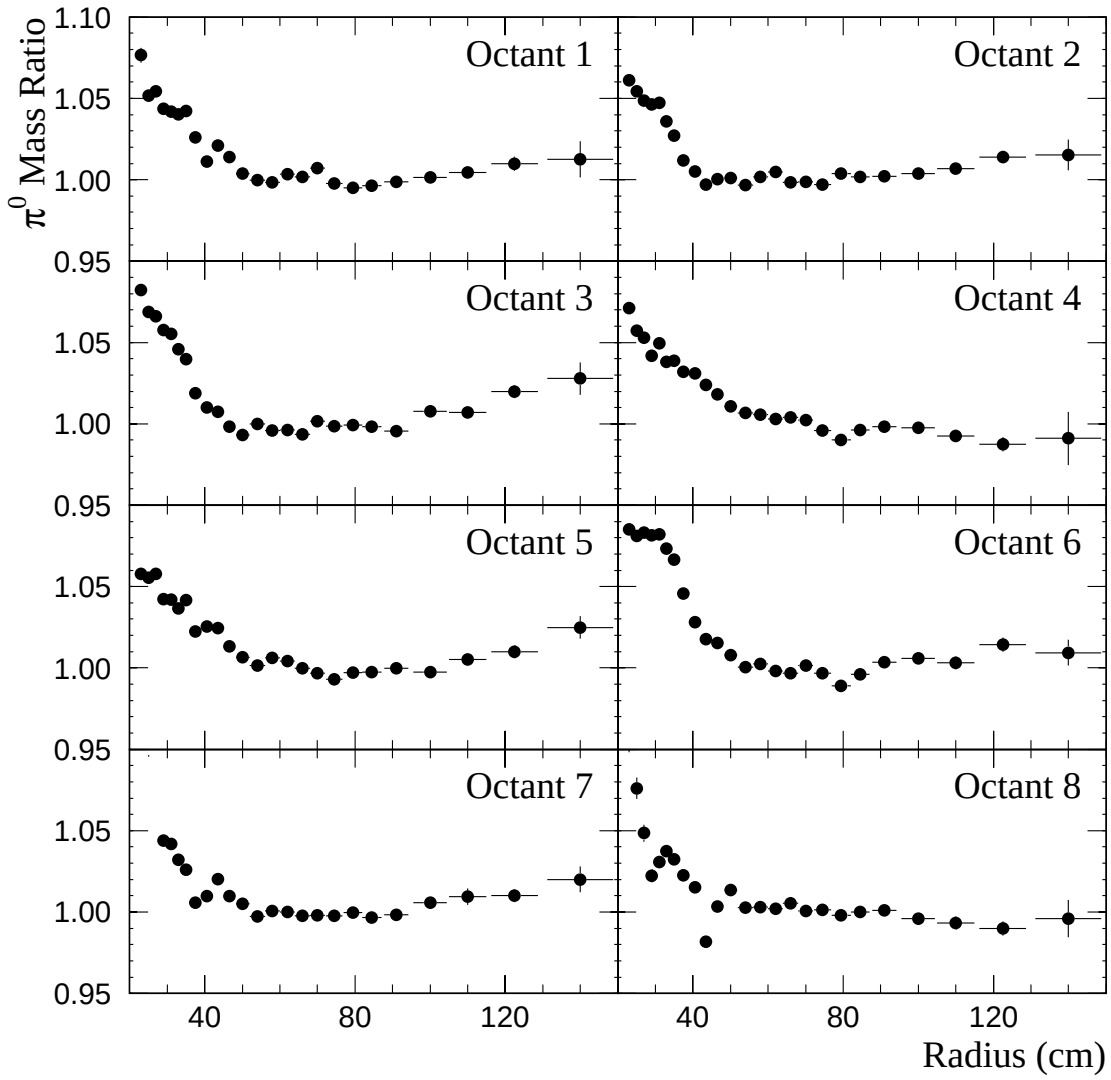

Figure 6.14 Radial dependence of the reconstructed π^0 mass with $p_T > 3.0$ GeV/c relative to its accepted value by octant from 1991.

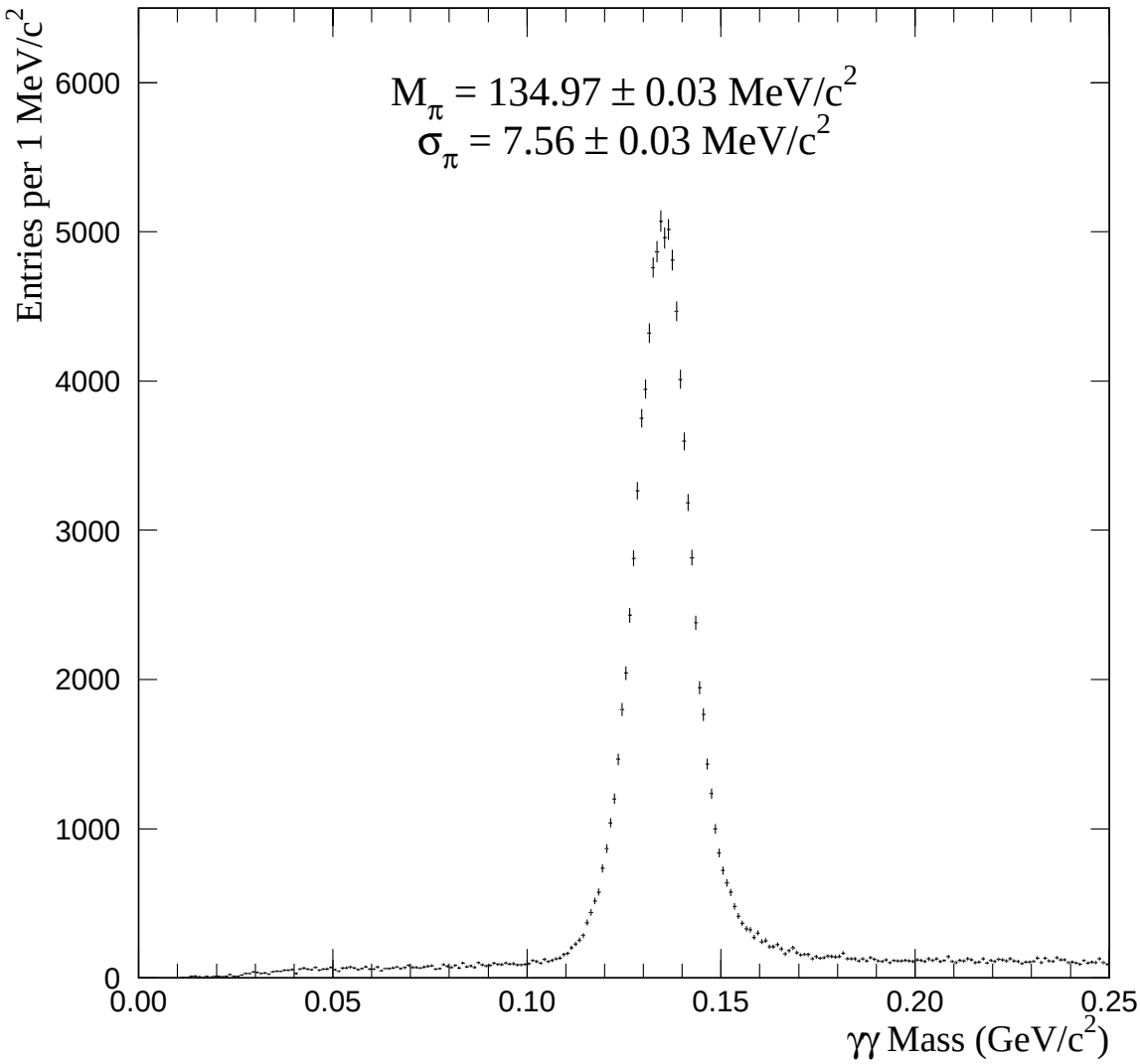

Figure 6.15 The calibrated two-photon mass distribution in the π^0 mass region for $\gamma\gamma$ pairs with $p_T > 3$ GeV/c and R > 50 cm from the 1991 data sample.

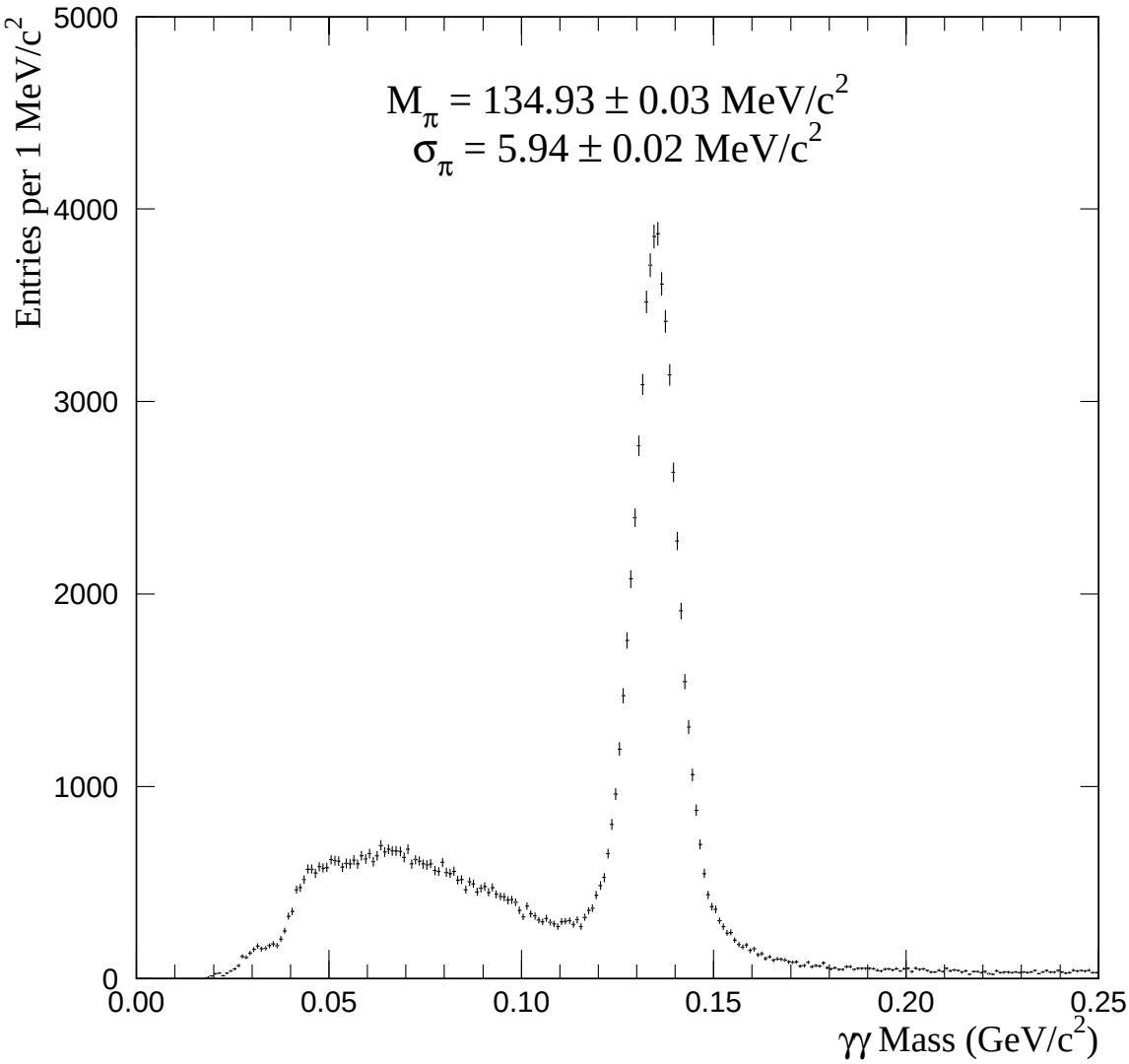

Figure 6.16 The calibrated two-photon mass distribution in the π^0 mass region for $\gamma\gamma$ pairs with $p_T > 5$ GeV/c and R > 50 cm from the 1991 data sample. The peak at low mass is due to muon bremsstrahlung. See Section 7.3 for more details.

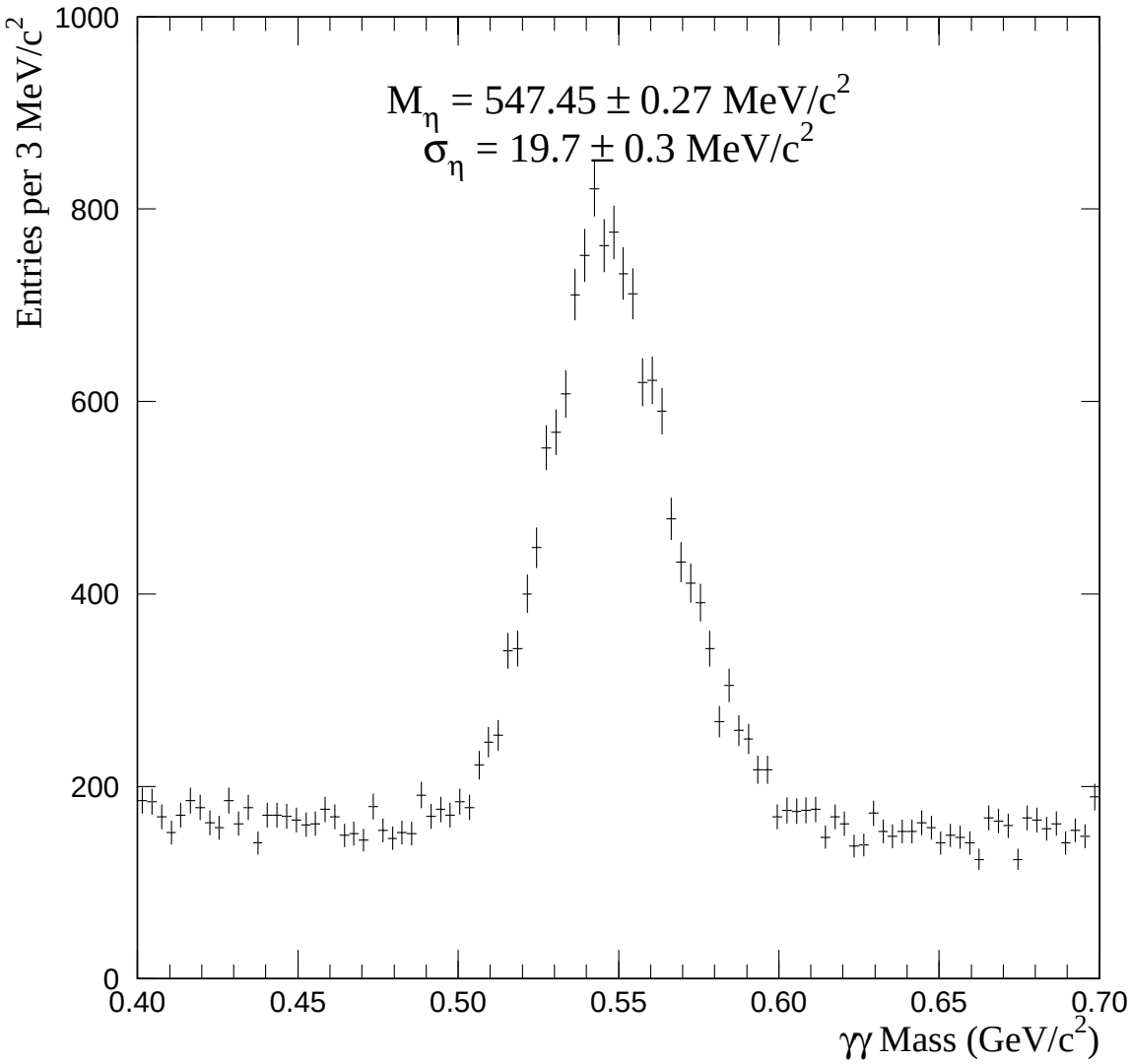

Figure 6.17 The calibrated two-photon mass distribution in the η mass region for $\gamma\gamma$ pairs with $p_T > 5$ GeV/c from the 1991 data sample.

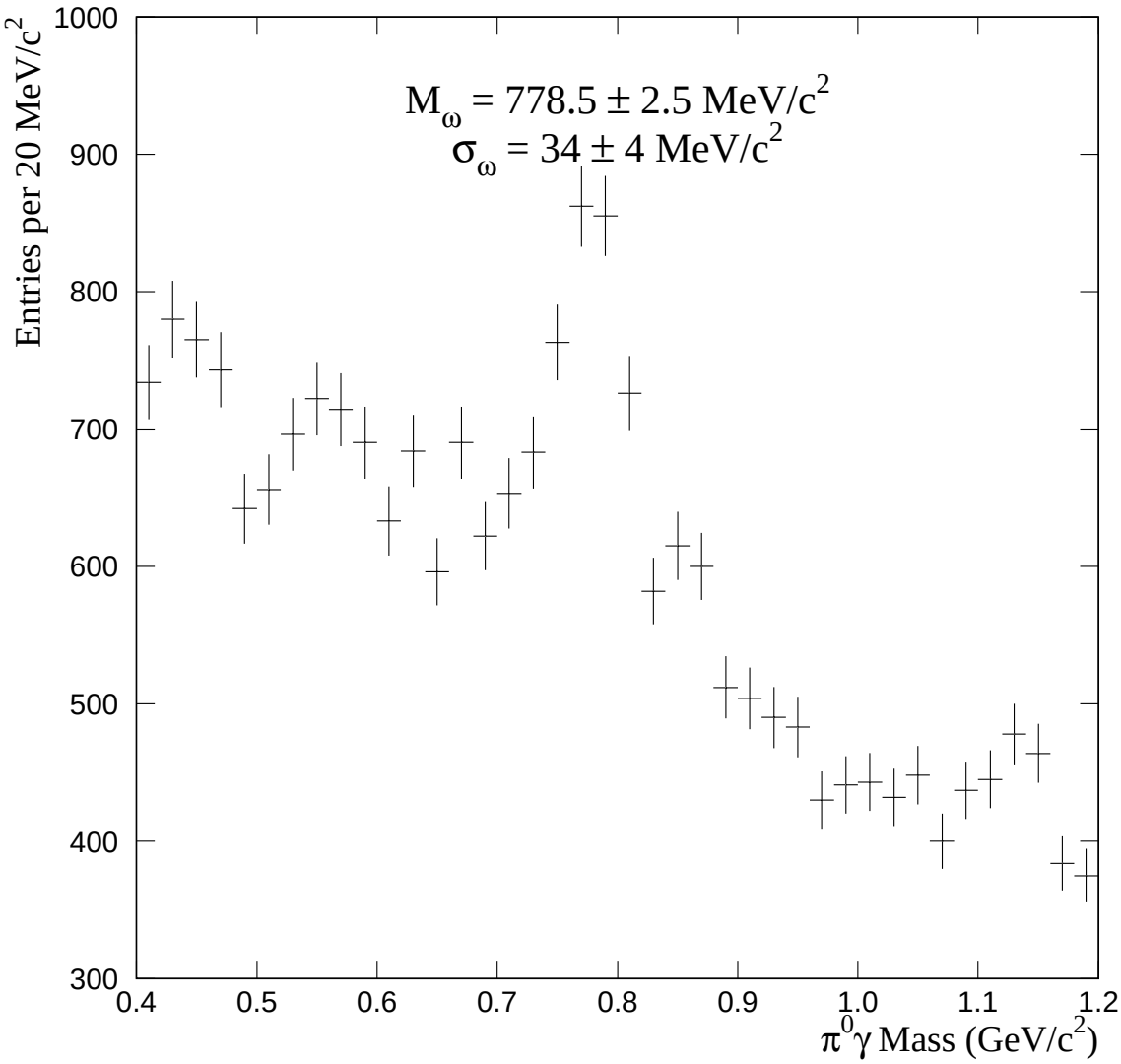

Figure 6.18 The calibrated $\gamma\pi^0$ mass distribution in the ω mass region for $\gamma\pi^0$ $p_T > 5$ GeV/c from the 1991 data sample.

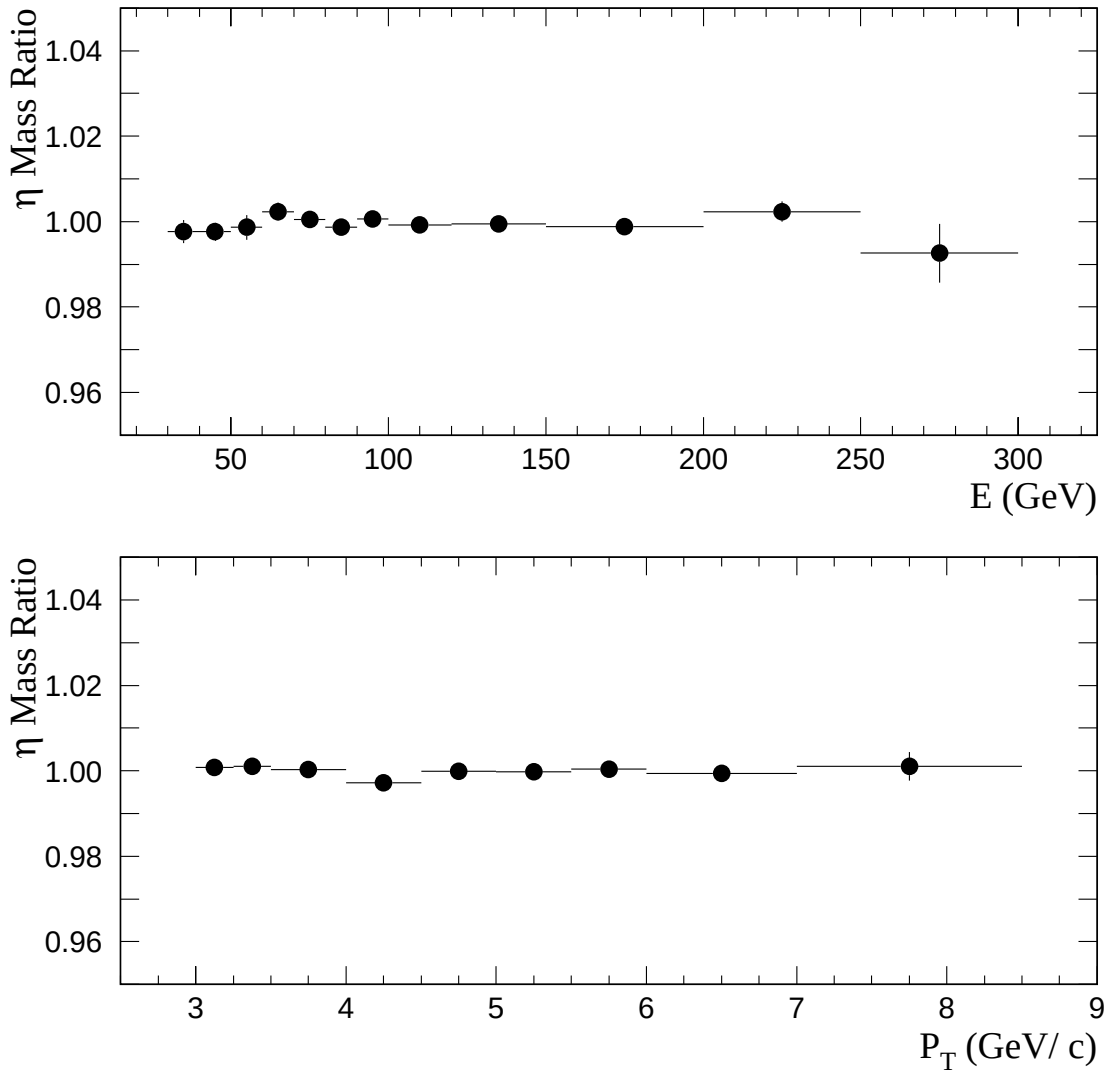

Figure 6.19 The mean η mass as a function of the η's energy (top) and p_T (bottom) from the 1991 data sample.

Meson	1990		1991	
	Mass (MeV/c^2)	Width (MeV/c^2)	Mass (MeV/c^2)	Width (MeV/c^2)
π^0	135.02 ± 0.06	5.58 ± 0.05	134.93 ± 0.03	5.94 ± 0.02
η	547.0 ± 0.4	17.3 ± 0.4	547.5 ± 0.3	19.7 ± 0.3
ω	779 ± 5	47 ± 7	778.5 ± 2.5	34 ± 4

Table 6.3 Reconstructed masses of the neutral mesons in the data. All of the standard cuts are applied. All mesons have $p_T > 5$ GeV/c. The π^0 is measured on the outside of the detector (R > 50 cm) only. The 1990 data sample includes both the early and late samples.

6.6 Electron Cross Checks

The high quality ZMP sample was used to explore residual energy dependences. Energy scale linearity was examined using π^0's and η's where one photon converted into a ZMP (Figure 6.20). This involved a comparison of the γe^+e^- mass as a function of the photon energy. A comparison of the ZMP electron's reconstructed energy to its measured momentum served as another useful cross check. There are caveats associated with this comparison (Section 6.4.1), but useful information was extracted.

6.6.1 Search for Residual Corrections Using the γe^+e^- Sample

The linearity of the energy scale was checked by examining η's, one of whose photons converted into an e^+e^- pair. The measured γe^+e^- mass of the η peak was compared against the photon's energy as shown in Figure 6.21. The electrons in this case used only tracking information for the mass calculation. The reconstructed γe^+e^- mass ratio versus photon energy is flat but it is also low by about 1%. A similar plot can be made for the π^0 signal, but in this case both a low-p_T cut and a cut to ensure these are away-side π^0's must be made to

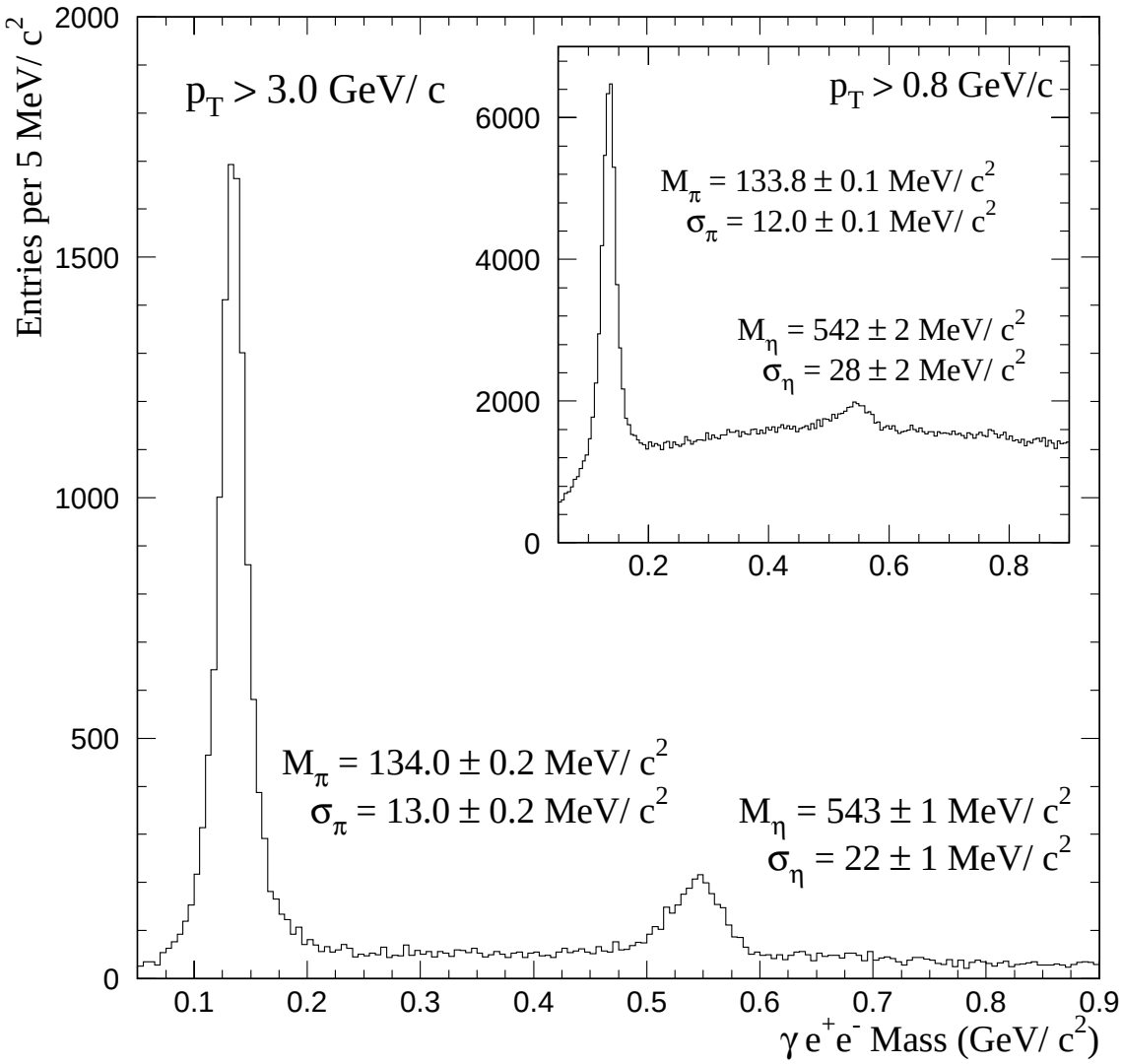

Figure 6.20 The γe^+e^- mass distribution from the combined 1990 and 1991 data samples.

avoid trigger biases and the resulting separation effects. This data fills in the low energy region.

Figure 6.22 shows a comparison between the ratio of the π^0 mass to its nominal value versus the number of radiation lengths traversed by the π^0's photons in the target region. The π^0 mass ratio for the case when one of the photons converted into an e^+e^- pair displays a linear decrease (with an intercept of one at zero radiation lengths) as a function of radiation length. This dependence is consistent with an energy loss in the target by the electrons via bremsstrahlung. This effect is also reproducible in the parameterized Monte Carlo using the `GEANT` parameterization of bremsstrahlung radiation (Section 5.2).

This effect can also be seen in the measured mass of the J/ψ (Figure 6.23). In this case, the J/ψ mass is 1% low when it is reconstructed in its electron decay mode as compared to the muon decay mode. Finally, when both π^0 photons convert in the material upstream of the magnet, the mass is lower than nominal by approximately 2% (Figure 6.24), again, consistent with energy losses due to bremsstrahlung radiation. On average this energy loss due to bremsstrahlung decreases the reconstructed γe^+e^- mass by 1% indicating there is no need for additional corrections.

6.6.2 Another Look at Electrons

We can compare the ZMP electron's reconstructed energy to its measured momentum to gain additional information about the energy scale. Although there are numerous caveats (Section 6.4.1), useful information about the absolute scale was extracted.

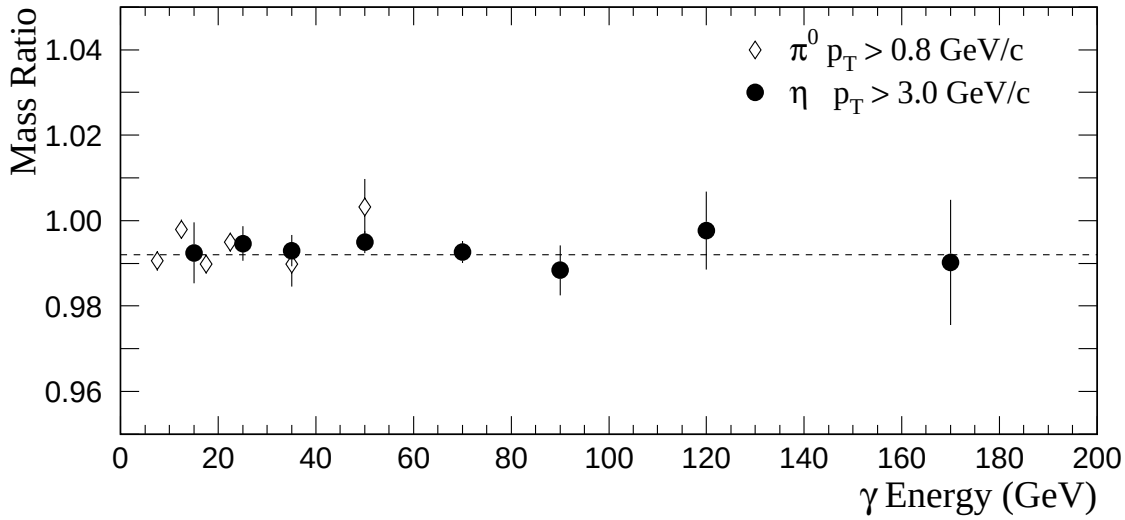

Figure 6.21 Ratio of the η mass to its nominal value when one of its photons converted into an e^+e^- pair versus the energy of the other photon. To fill in the low energy region, the same ratio is shown for the away-side π^0 mass.

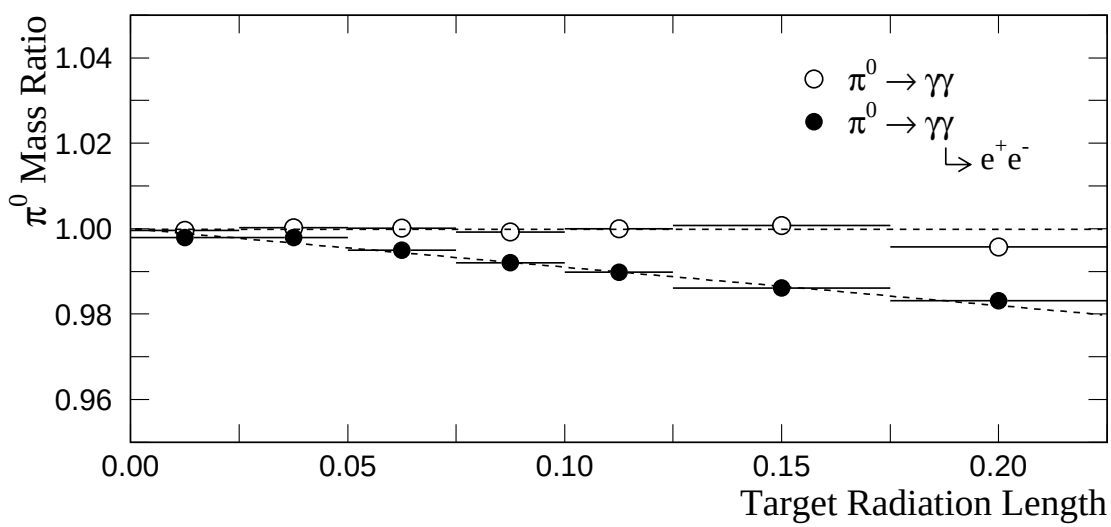

Figure 6.22 Ratio of the π^0 mass to its nominal value versus the number of radiation lengths of target material traversed by the photons. The closed circles (•) represent the π^0 mass ratio when one of the photons converted to an e^+e^- pair with the three particle γe^+e^- system $p_T > 0.8$ GeV/c. The open circles (○) represent π^0's with $p_T > 3.0$ GeV/c reconstructed from non-converted photons. The lines are fits to the data.

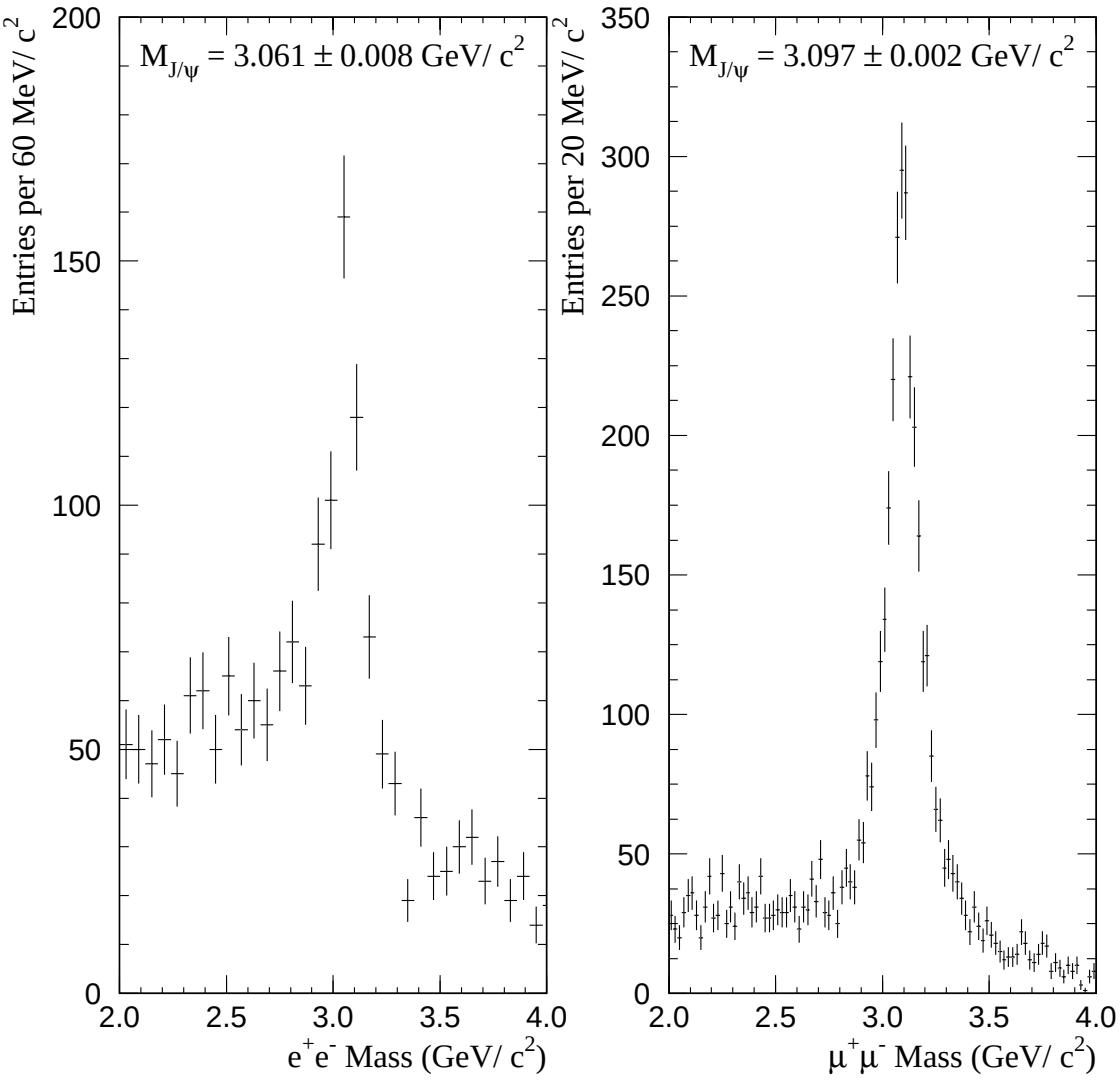

Figure 6.23 The J/ψ mass in its e^+e^- and $\mu^+\mu^-$ decay modes. These data are from the 1990 sample.

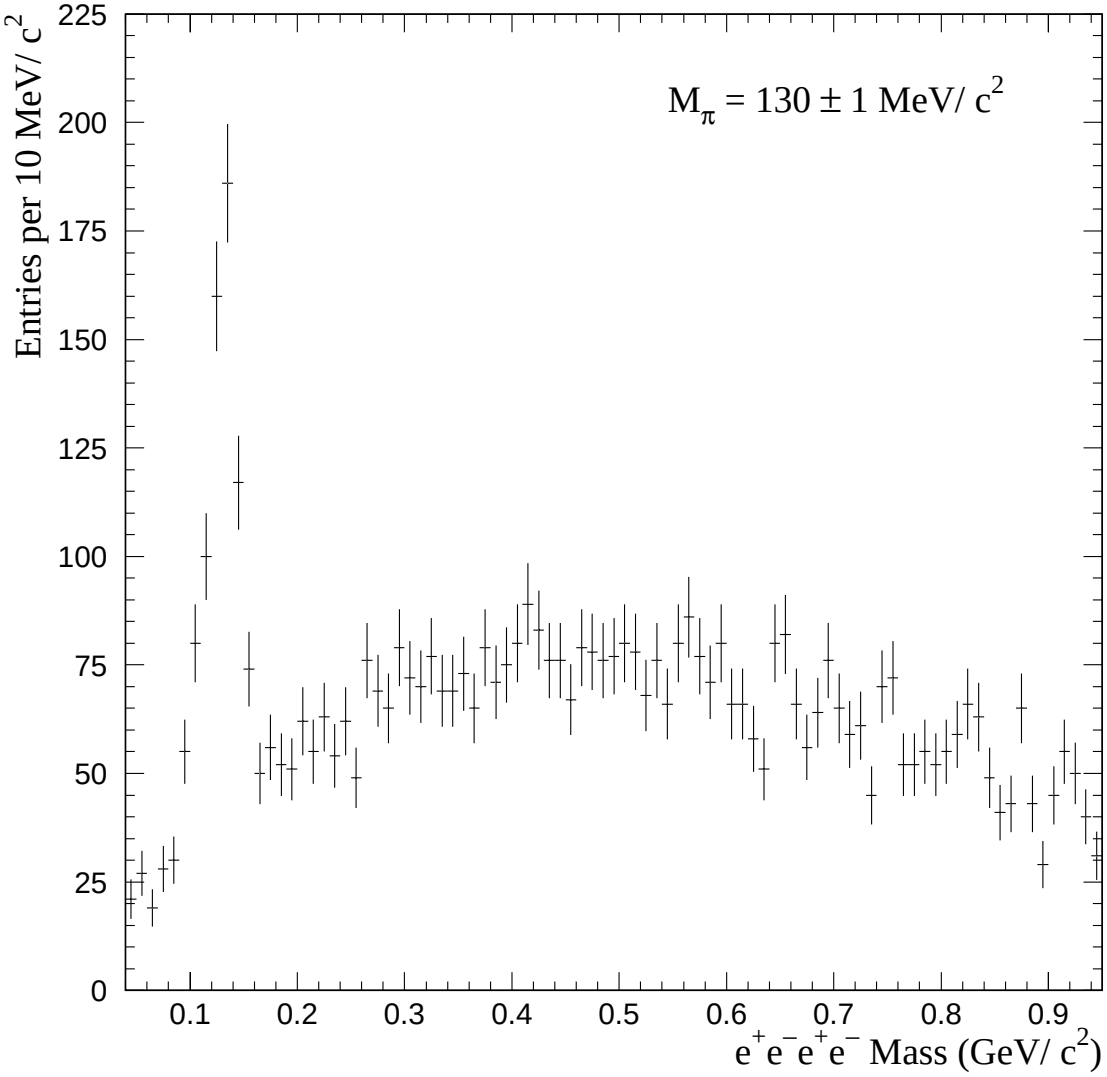

Figure 6.24 The $e^+e^-e^+e^-$ invariant mass distribution from the 1990 π^- sample with $p_T > 0.5$ GeV/c. The π^0 peak is clearly visible. Only information from the tracking system was used in this mass calculation. The electrons were not required to match with showers in the calorimeter.

This sample is more easily affected by contamination, so the cuts were tightened:

- $|\Delta S_Y| < 2$ mrad;
- Z–X intersection point within 5 cm of the center of the magnet;
- $0.10 < M_{\gamma e^+e^-} < 0.18$ GeV/c^2;
- $M_{e^+e^-} < 1.5$ MeV/c^2;
- π^0 $p_T > 0.8$ GeV/c;
- π^0 energy asymmetry < 0.5;
- Only 1 ZMP was reconstructed in the event.

The ZMP electron's reconstructed energy to its measured momentum as a function of its energy is shown in Figure 6.25. A line at 1.0 has been drawn to guide the eye. The E/P distribution rises with energy; it reaches a plateau value of 1.0 above ≈ 40 GeV.

This rise in the E/P ratio is due to differences in the shapes of electron- and photon-induced showers in the EMLAC. Because electron-induced showers are, on average, wider than photon-induced showers at corresponding energies, EMREC tends to underestimate the energies of electron-induced showers. This is due to our decision to use a shower shape in `EMREC` optimized for photon-induced showers (Section 4.3.5). It was not necessary to correct for this effect because we do not use electron shower energies in our analyses.

At high energies, where the differences between the electron-induced and photon-induced showers are minimized, the E/P ratio is approximately 1.0 (Figure 6.26).

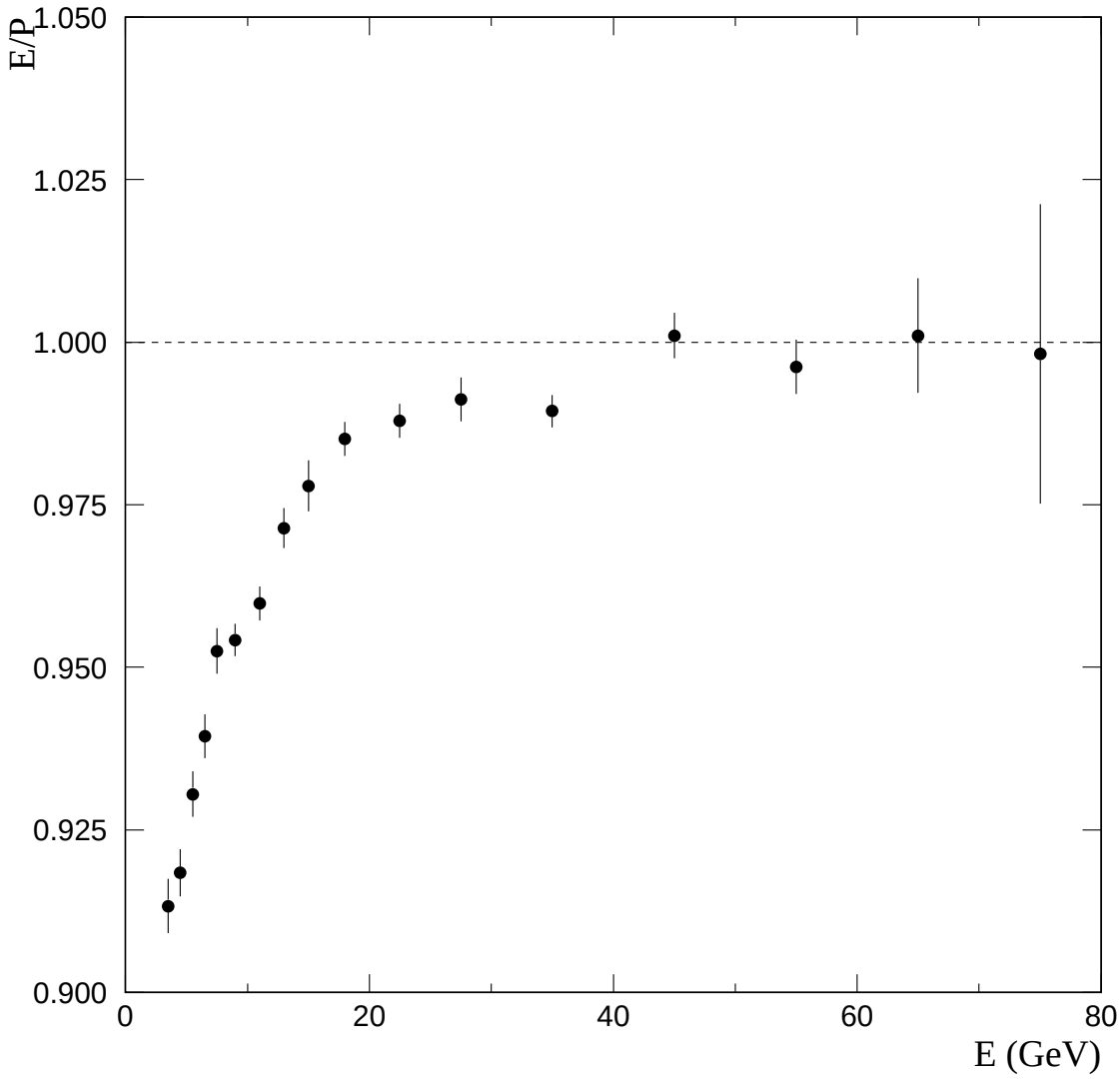

Figure 6.25 The dependence of ZMP electron's reconstructed energy to its measured momentum as a function of its energy. The line at 1.0 is intended to guide the eye. These data are from the 1991 sample.

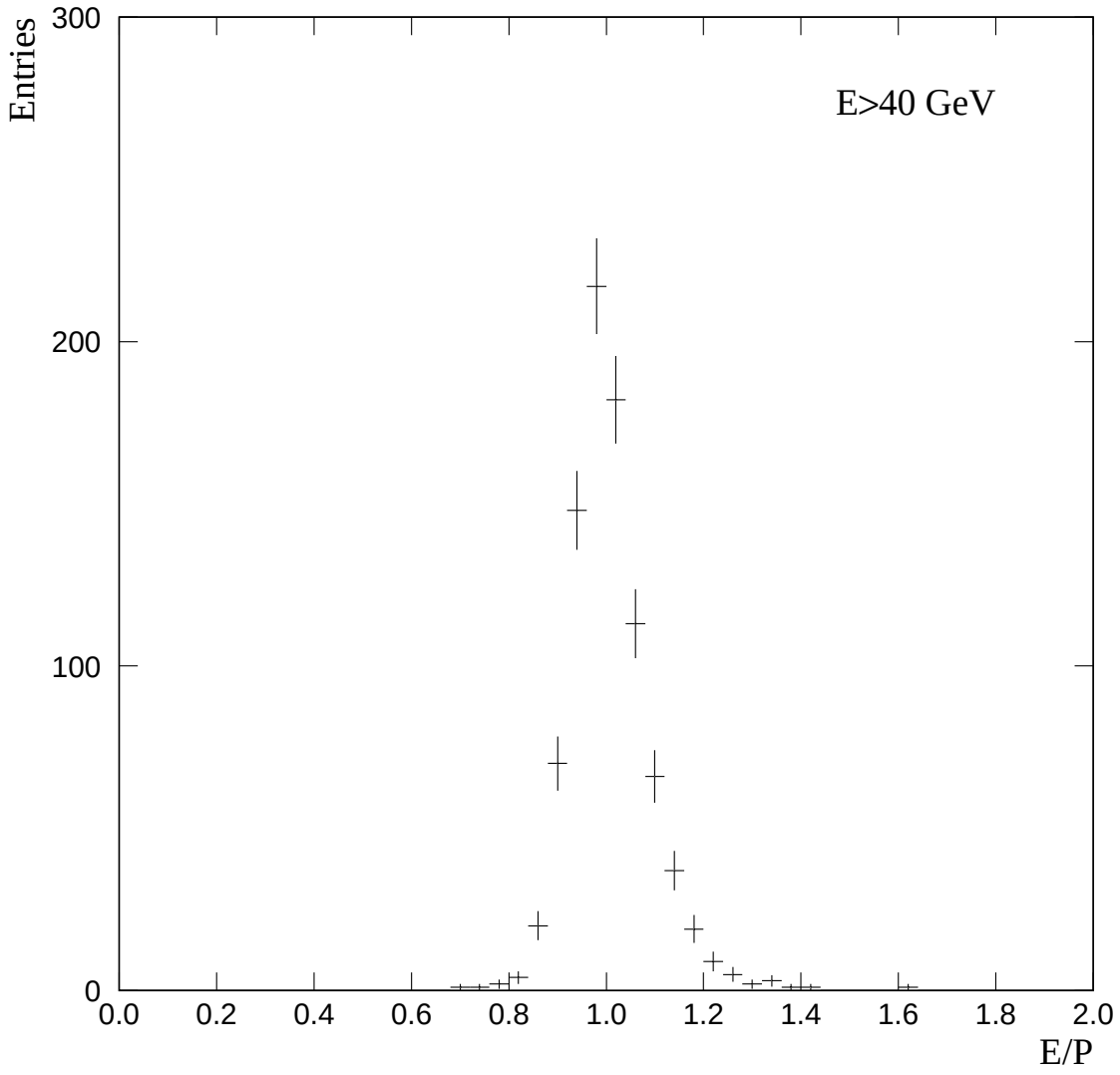

Figure 6.26 The ratio of a ZMP electron's reconstructed energy to its measured momentum for E > 40 GeV. Here the π^0 p_T cut has been raised to 3 GeV/c. The mean E/P is 1.000 ± 0.003 (Gaussian fit). These data are from the 1991 sample.

6.7 Full Monte Carlo Energy Scale

The energy response of the simulated EMLAC was calibrated in the same manner as the data. Corrections included setting the absolute scale, fixing the energies at the inner/outer ϕ boundary, and accounting for material energy loss. Because of the EMLAC's energy resolution (Figure 5.14) and the p_T requirement, there is a natural dependence of the photon energy on radius (Figure 6.27). This radial dependence was removed from the data while correcting for the effects of the BEFORE/AFTER timing (Section 6.5.5). It needed to be removed from the Monte Carlo to avoid an over-correction in the reconstruction efficiencies (Section 5.1.4).

Each Monte Carlo sample was corrected independently with regards to both the radial dependence and the absolute scale.

6.7.1 Initial Scale

A scale was initially created for the full Monte Carlo using information from the `GEANT` banks. This scale took into account factors dealing with the various parameterizations of the EMLAC [118]. It was determined by directing 100 GeV photons into the center of Octant 1 at a radius of 60 cm. These isolated showers were reconstructed and the resulting energy was rescaled to the generated value. This scale was applied at the preprocessor level (Section 5.1.3) and was in place during the reconstruction pass.

6.7.2 Radial Dependence and Absolute Scale

It was more difficult to measure the radial dependence in the full Monte Carlo than it was in the data. There were very few statistics as every sample, filter, and threshold had to be examined independently. Additionally, the full Monte Carlo

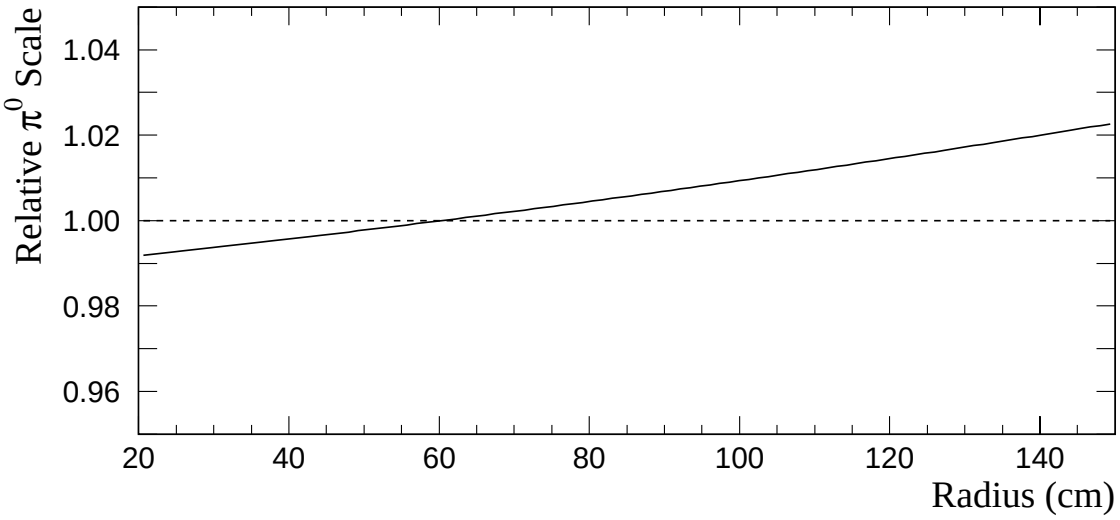

Figure 6.27 The relative change in the energy scale as a function of radius due to the energy resolution of the EMLAC (Figure 5.14). This was determined using the parameterized Monte Carlo (Section 5.2). The dashed line at 1.0 is intended to guide the eye.

suffers from the same separation issues as the data (Figure 6.6); this makes the high-p_T^{MIN} samples difficult to interpret. Also, the data events were triggered; this had effects on the sample and spectrum not accounted for by the `HERWIG`-to-Data surfaces or by the trigger simulation (Figures 6.28 and 6.30). This made the low-p_T^{MIN} samples difficult to interpret. To account for these statistical limitations, the parameterized Monte Carlo (Section 5.2) was used to guide the correction (Figure 6.27). This allowed more consistent results from sample-to-sample.

The absolute energy scale for the full Monte Carlo was established using the $p_T^{MIN} = 5.0$ GeV/c samples (the only common p_T threshold amongst the major samples). Both the π^0 and η were given equal weight (depending upon filter type).

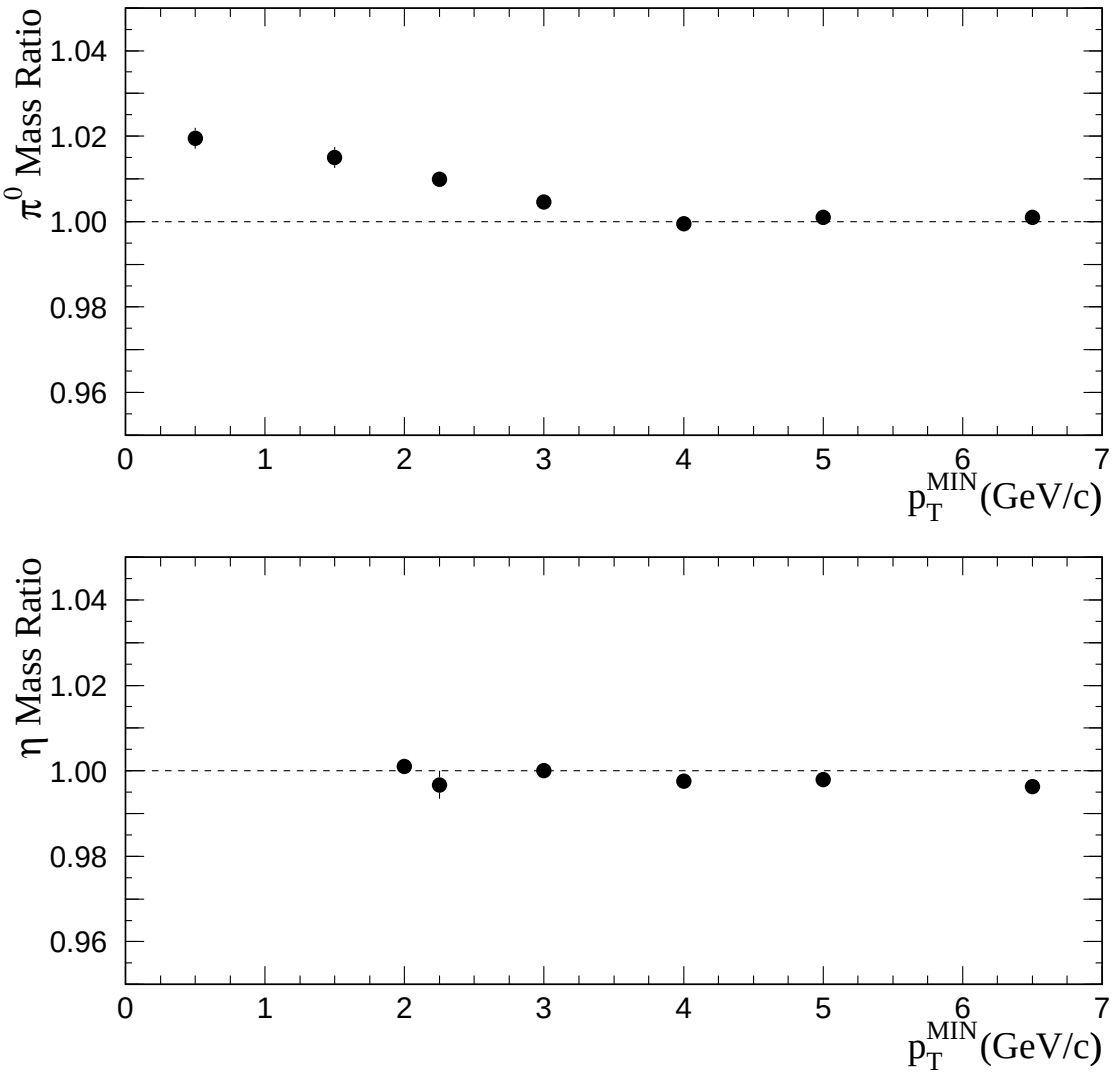

Figure 6.28 The π^0 (top) and η (bottom) masses versus p_T^{MIN} from the 1990 515 GeV/c π^- full Monte Carlo. This data is untriggered and is a composite of all the available filters. The π^0 mass is from the outside of the detector (R > 50 cm).

6.7.3 Results

Figure 6.28 displays the final Monte Carlo energy scale results as distributions of the π^0 and η meson masses with respect to p_T^{MIN}. In general the points are scattered about unity with the lower-p_T π^0 points higher than the higher-p_T points. This rise can be clearly seen in Figure 6.29 where these distributions are plotted to examine the effects of filter type on the final scale. This rise at low p_T is associated with the spectrum as the π^0 cross section is steeper at low p_T than at higher-p_T values (Figure 6.1). Placing trigger requirements on the Monte Carlo has the impact of flattening the spectrum at low p_T; this reduced the observed scale at these p_T values. This effect can be seen in Figure 6.30 where trigger probabilities have been applied as weights in an effort to simulate the effects of the trigger on the energy scale. The resulting distributions are clearly p_T dependent; furthermore, as we move to successively higher threshold triggers, the meson masses come closer to unity. Finally, the parameterized Monte Carlo (Section 5.2) was used to examine this effect. The rise at low p_T was reproduced; this can be seen in Figure 6.31. The rise at low p_T can therefore be discounted for the purposes of measuring the systematic uncertainty associated with the Monte Carlo energy scale.

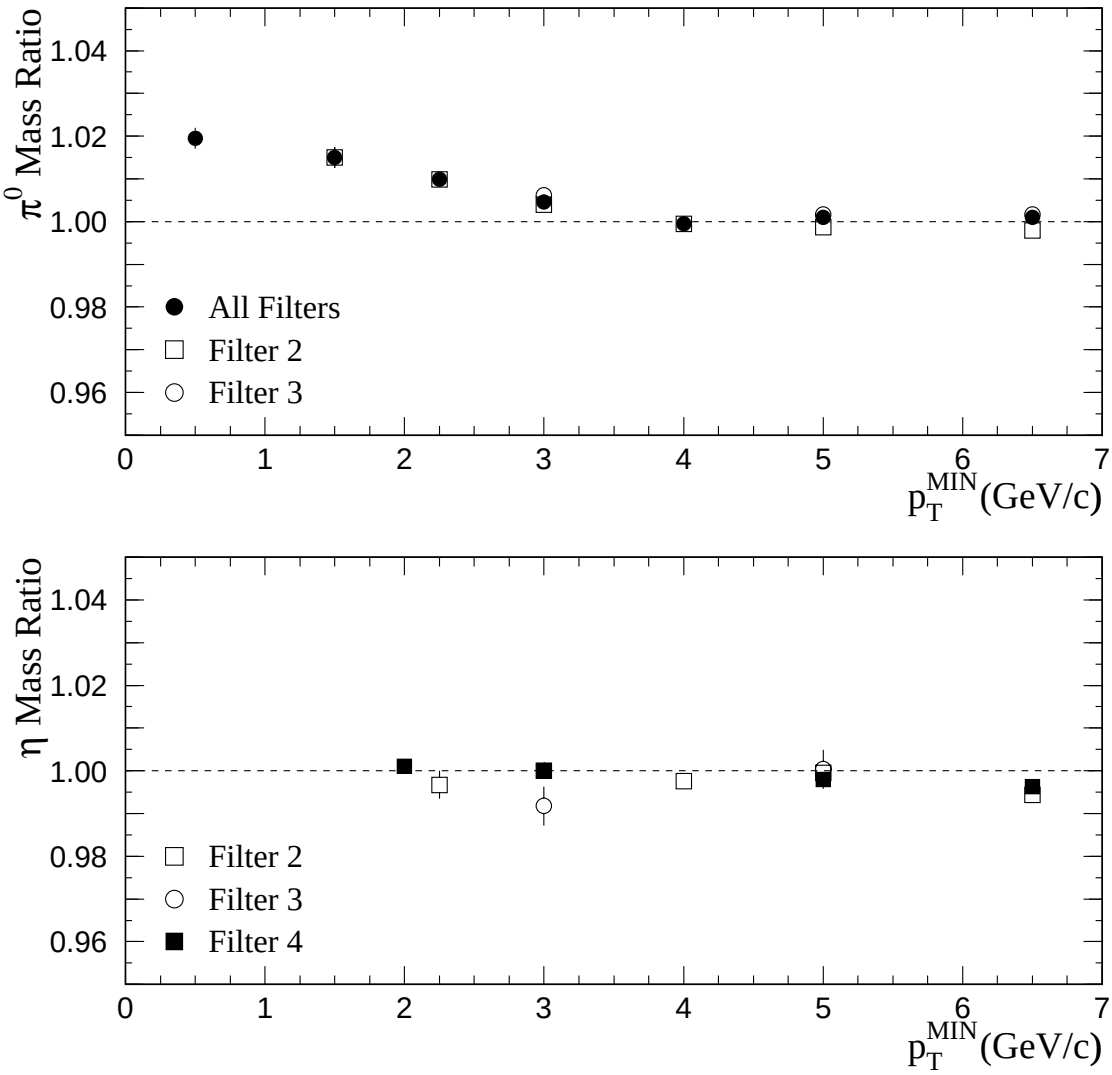

Figure 6.29 The π^0 (top) and η (bottom) masses versus p_T^{MIN} from the 1990 515 GeV/c π^- full Monte Carlo for different filter types. This data is untriggered. The π^0 mass is from the outside of the detector (R > 50 cm).

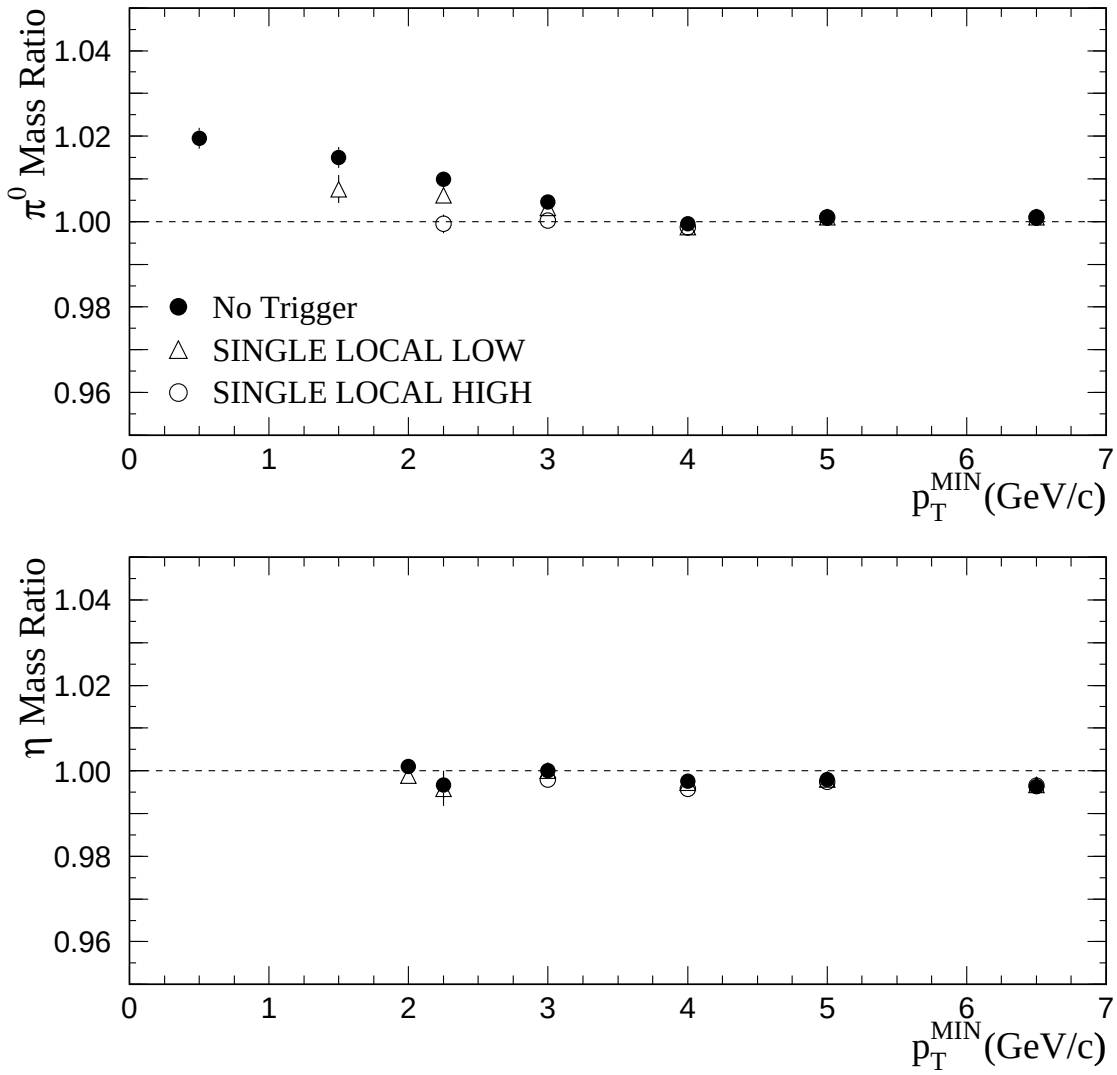

Figure 6.30 The π^0 (top) and η (bottom) masses versus p_T^{MIN} from the 1990 515 GeV/c π^- full Monte Carlo for the local triggers. This data is a composite of the available filters. The π^0 mass is from the outside of the detector (R > 50 cm).

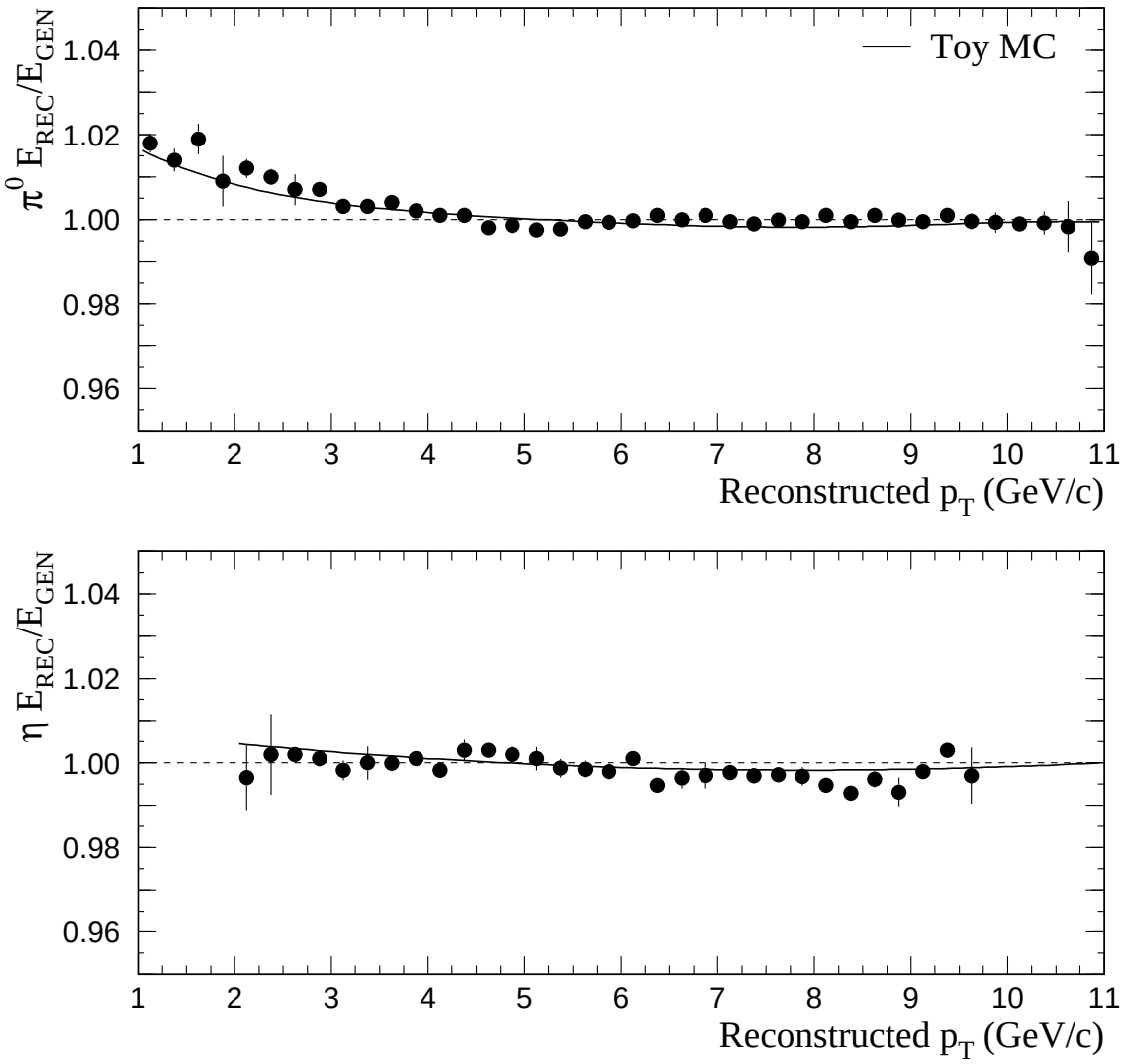

Figure 6.31 E_{REC}/E_{GEN} from the 1990 515 GeV/c π^- full Monte Carlo sample for π^0's and η's as functions of their reconstructed p_T values. Overlayed on each are the results from the parameterized Monte Carlo (Section 5.2).

6.8 Systematic Uncertainty

One, two! One, two! And through and through
The vorpal blade went snicker–snack!
He left it dead, and with its head
He went galumphing back.

Lewis Carroll
"Jabberwocky" in Through the Looking Glass

Evaluating the systematic uncertainty in the measured cross sections due to the uncertainty in the calibration of the energy response of the EMLAC is a tricky and complicated issue. The cross sections are very steeply falling functions of p_T so uncertainties in the calibration can be greatly magnified when applied to the cross sections. This uncertainty involves several pieces including the uncertainty associated with the calibration procedure (the mapping of reconstructed to actual photon energies), and the execution of the calibration in both the data and the Monte Carlo samples. There are also additional sample dependences since the samples used to calibrate the detector differed slightly from the samples used the cross section measurements.

6.8.1 Energy Scale Calibration

The procedure used to calibrate the energy response of the calorimeter was to set the average π^0 mass to its nominal value (Table 6.2). The uncertainty in following this procedure can be found by comparing the final, calibrated, measured π^0 mass against its nominal value for the interesting projections.

The systematic uncertainty associated with the energy scale calibration procedure came primarily from five sources: the fitting procedure, the non-Gaussian shape of the mass peaks, the radial correction, the correction for energy loss in the material upstream of the EMLAC, and the absolute scale. The

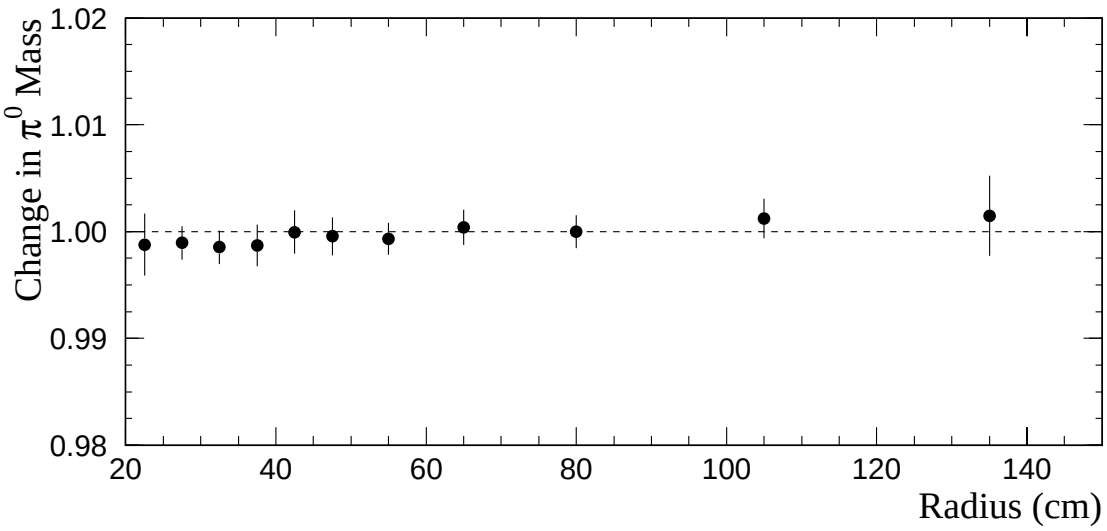

Figure 6.32 The relative change between Monte Carlo and data in the mean π^0 mass when the "high-mass bump" has been removed from consideration.

systematic uncertainty due to the fitting procedure is estimated to be 0.1%. Where appropriate this fundamental measurement uncertainty will be removed in quadrature from each individual systematic uncertainty and added back once in the final analysis.

The π^0 mass peak is non-Gaussian; there is a "high-mass bump" associated with this peak that has an independent radial dependence. Portions of this tail are reproduced in the Monte Carlo simulation of the detector and portions are due to interactions that occur upstream of the target (for example, in the beam hodoscope) [132]. The mass peak was fit using a Gaussian with a linear background. The effect of this bump was to "pull" the mean of the Gaussian high; consequently this affected the radial distributions. The size of this uncertainty can be estimated by refitting the radial dependence with this high-mass bump region

explicitly removed from the fit. The difference in the result between the Monte Carlo and the data was then taken to be the level of uncertainty (Figure 6.32). The effect is order 0.1%.

During the 1990–1 data taking, three different BEFORE/AFTER integration times were used. The resulting radial dependences were each individually corrected (Section 6.5.5). Each run region has a systematic uncertainty associated with its radial correction. As the sample used to correct the 1991 data had the highest statistics and was the most studied, this sample will be used as the baseline for the uncertainty estimation.

There were two uncertainties associated with the radial correction: one from the actual correction, and one from the addition of the radial dependence on separation taken from the η sample (Section 6.5.5). The size of the radial correction uncertainty in the 1991 data was determined by taking the distribution of the mean π^0 mass as a function of radius for each octant, projecting these values onto the mass axis and fitting the resulting Gaussian (Figure 6.33). These data were taken at the point in the correction just prior to the proper adjustment of the radial dependence due to separation biases inherent in the sample. The systematic uncertainty in this correction is 0.2%. To gauge the level of this uncertainty measurement, I added an arbitrary $\pm 0.2\%$ radial dependence to the energy scale and examined its effect on the standard distributions. Looking at the results, I think that a change of this size was on the edge of what I would have corrected. Bearing in mind that I *knew* that a change had been made, this indicates that 0.2% is not an unreasonable uncertainty to claim for the radial corrections. The uncertainty in the adjustment for separation was determined with the same procedure, using the mean η mass as a function of radius for $p_T > 3$ GeV/c and $p_T > 5$ GeV/c. This uncertainty is estimated to be 0.1%.

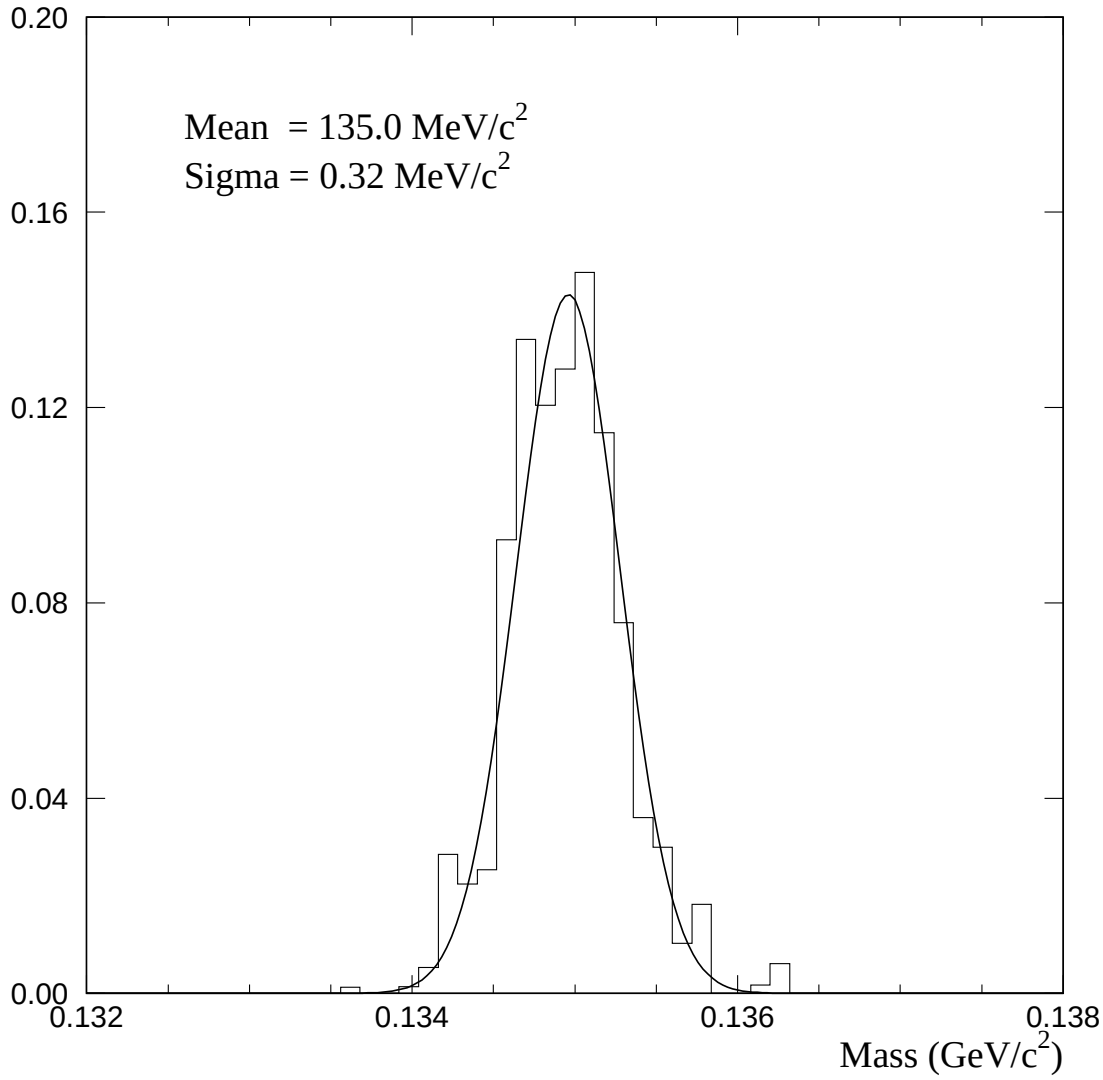

Figure 6.33 Residual systematic uncertainty in the radial correction for the 1991 data sample.

The π^0 mass as a function of radius following all energy scale corrections, can now be compared for each of the run regions to estimate the uncertainties of the two 1990 radial corrections (the π^0 sample used was at a low enough p_T that an additional separation correction was unnecessary). From these comparisons, the uncertainty of the radial correction was found to be 0.25% for the late 1990 sample. For the early 1990 data, this uncertainty is 0.4%. Because one section of the 1990 data (run numbers 7908 to 8628) was not included in the calculation of the late 1990 energy scale, this run region has an additional uncertainty of +0.2% for R < 35 cm, and +0.1% for 35 < R < 45 cm. Additionally, the samples used for these energy scales were determined in a slightly different fashion than that used for the 1991 sample. Since these extra requirements affect our final cross sections, they have additional systematic uncertainties. These uncertainties total less than 0.05% (when calculated in an internally consistent manner).

The uncertainty in the radial correction for the Monte Carlo is about 0.25%.

Finally, there is another systematic uncertainty associated with conversion of strip position into radius. A conversion factor is used that was determined from measurements of the strip layout on the G-10 prior to its installation in the cryostat. However, G-10 shrinks by 0.25% when immersed in liquid argon [134]. This means the conversion factor is improper for the cold geometry. The Monte Carlo uses the warm geometry and so we do not account for this effect. A study of the parameterized Monte Carlo indicates this effect is linear with the shrinkage rate and, for the most part, only affects masses in the inner radius region. On average, this adds a systematic uncertainty of -0.1% for R < 35 cm.

There is a systematic uncertainty associated with the correction for the energy loss in the material upstream of the first active layer of the EMLAC. Since the

correction was determined through a Monte Carlo analysis, it is possible that some material was not accounted for properly. Any difference in the material in front of the EMLAC between the real detector and the Monte Carlo simulation would lead to an offset in the energy loss correction which would show up as an additional radial dependence. This offset was estimated to be at most 150 MeV by studying ZMP electron energies versus their momenta. As the offset would cause a radial dependence that would be removed through the radial correction, there is the possibility we would have made a gains correction to a pedestal effect. The parameterized Monte Carlo was used to examine the effects of this on the energy scale. From the parameterized Monte Carlo, a total uncertainty of 0.1% can be assigned to this source.

In the region $35 < R < 45$ cm there is an additional uncertainty associated with the choice of $2E_R$ rather than E_R+E_ϕ for the photon's energy (Section 6.5.3). This systematic uncertainty is estimated to be less than 0.1%.

The systematic uncertainty associated with the absolute scale was determined in a similar fashion to that of the radial correction. In this case the η mass as a function of its p_T and energy was used (from Figure 6.19). The systematic uncertainty associated with the scale in the 1991 data sample is 0.1% (Figure 6.34). This uncertainty is slightly larger (0.15%) for the late 1990 data sample. The uncertainty is larger for the early 1990 data sample. In this sample the π^0 mass is approximately 1% above the η mass (compared to $< 0.1\%$ for the other samples). The η mass was used for the absolute scale since it appeared that the differential shower shape (due to the short integration time) was seriously impacting the reconstructed π^0 mass. To check the reality of this mass difference, the η/π^0 cross-section ratio was compared between the early and late 1990 data samples [135]. The η/π^0 ratio is effectively flat in both p_T and rapidity (Figure 5.12) and so any

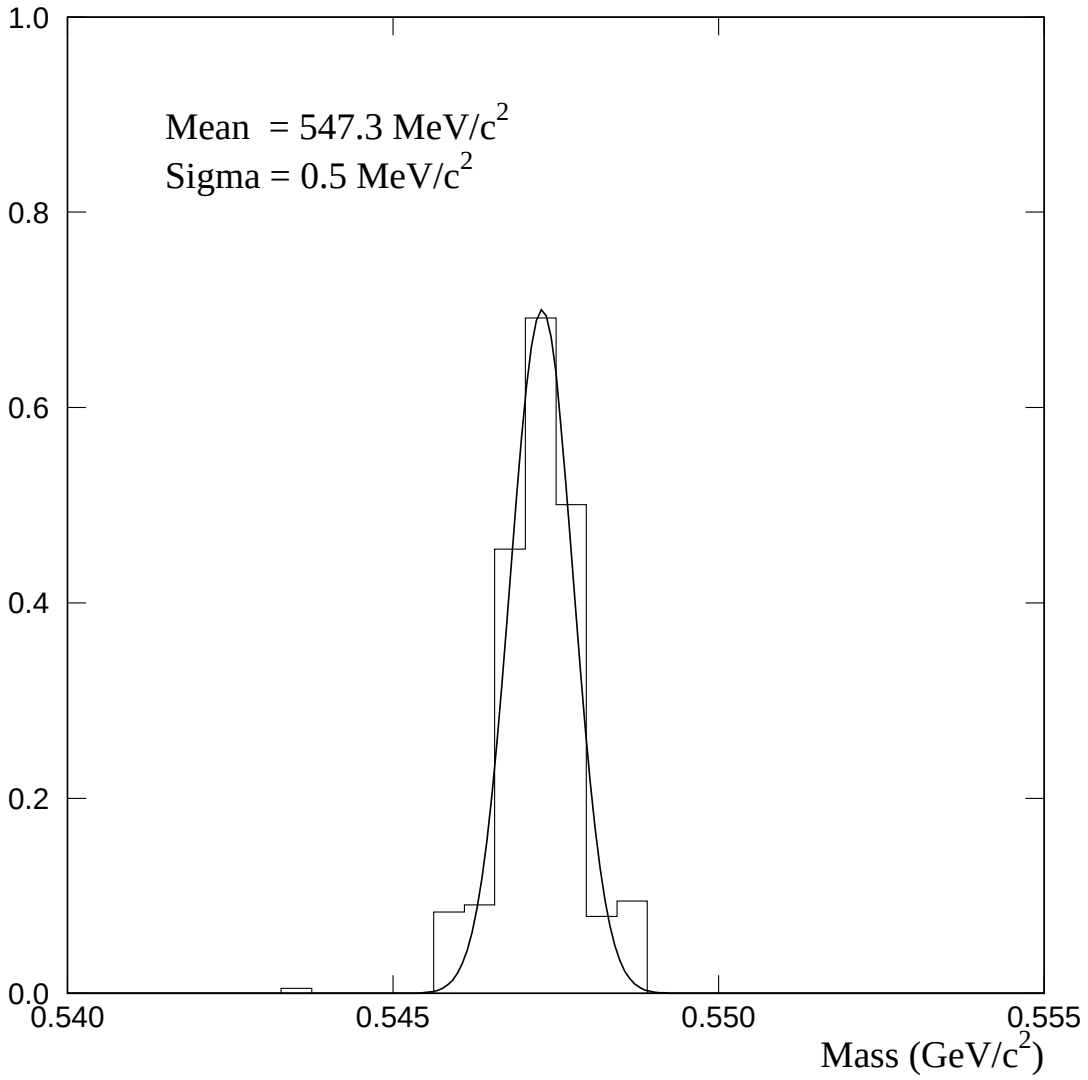

Figure 6.34 Residual systematic uncertainty in the absolute energy scale from the 1991 data sample.

Systematic Effect		Uncertainty (%)
Fitting procedure		± 0.1
Mass peak shape		± 0.1
Energy loss		± 0.1
Radial corrections	Data	± 0.22
	MC	± 0.25
Boundary ($35 < R < 45$ cm)		± 0.1
Cold vs. warm geometry		-0.1 to 0.0
Absolute scale	Data	± 0.1
	MC	± 0.1
Spectral Effects		± 0.1

Table 6.4 The systematics associated with the energy scale calibration of the EMLAC for the data composed with the Monte Carlo and their respective uncertainties.

real difference in the energy scale will show up. The η/π^0 ratios agreed remarkably well (better than 3%) and so the apparent difference is only a mass effect, not an energy effect. The systematic uncertainty for the absolute scale is taken to be less than 0.25% for the early 1990 run region.

The systematic uncertainty associated with the absolute scale in the Monte Carlo was determined in a similar fashion to that of the data. In this case the π^0 and η masses from all Monte Carlo samples with $p_T^{MIN} = 5$ GeV/c (as this p_T^{MIN} existed for all samples). The systematic uncertainty associated with the scale is $\approx 0.1\%$. As the energy scale depends, in part, on the input spectrum, a systematic uncertainty must be established for the use of `HERWIG`-to-data surfaces. This uncertainty was estimated by arbitrarily changing the surfaces and is less than 0.1%.

Summing up these uncertainties (Table 6.4), we find the average systematic uncertainty associated with the energy scale is 0.4% for the 1991 data and 0.5% for the 1990 data (using a rough luminosity weighting).

6.8.2 Mesons versus Photons

The goal of E706 is to make precision measurements of direct-photon production. The energy response of the calorimeter was calibrated using π^0's and cross checked using η's, ω's, and converted photons. It is therefore important to ensure this calibration is also appropriate for direct photons. This is particularly true as the energy response of the EMLAC is sensitive to event structure; direct photons are expected to be more isolated than corresponding photons from meson decays which are accompanied by other particles from the jet.

There are very few ways to check the energy scale of single photons in the data. The only two reasonable channels are η's whose decay results in photons in different quadrants, and very isolated electrons. Both of these samples had very limited statistics; both gave the result that single photons have a scale at least within 1% of that for π^0's.

It was much easier to check the single photon energy scale in the Monte Carlo as we had access to both reconstructed and generated energies. Of course, we needed to make the assumption that the Monte Carlo simulation responds in the same fashion as the real detector to single isolated photons. This is not a bad assumption, but it does influence the systematic uncertainties. We also needed to be careful when making this comparison that we accounted for any differences due to the spectrum. Direct photons have different slopes than π^0's as a function of p_T (Figure 6.1). To minimize this effect, we looked at E_{REC}/E_{GEN} binned in the generated p_T of the π^0 or direct photon. Of course, the average E_{REC}/E_{GEN} is

less than 1.0 as the energy scale was set using the reconstructed (hence smeared by detector resolution) energies.

A comparison of E_{REC}/E_{GEN} for π^0's and direct photons is shown in Figure 6.35. The top plot shows a scale shift of approximately 0.45% between direct photons and π^0's. The slight p_T dependence of the shift is a residual spectral effect and can be ignored. It was conjectured that this energy scale shift was due to differences in the response of `EMREC` to single and multiple photons. To test this hypothesis, cuts were introduced into the analysis to ensure that all photon energies were reconstructed in exactly the same manner. These results are shown in the bottom plot of Figure 6.35; it is clear the apparent energy scale shift is an `EMREC` artifact. This was confirmed by Monte Carlo studies where mono-energetic "beams" of photons and π^0's were employed to examine the calorimeter's response.

As the energy scale shift between direct photons and π^0's is reasonable, only a small addition was made to the systemic uncertainties. Because there is a systematic shift of the mean, an additional 0.1% uncertainty was added linearly to the systematic uncertainty. This uncertainty also includes the small differential energy scale between fake direct photons and π^0's (due to the separation effect discussed in Section 6.4).

6.8.3 P_T Scale

The relevant quantity for determining the systematic uncertainties associated with the energy scale is the uncertainty in the p_T scale since the cross sections are typically measured as functions of p_T.

$$p_T = E \sin\theta = \frac{ER}{Z} \tag{6.3}$$

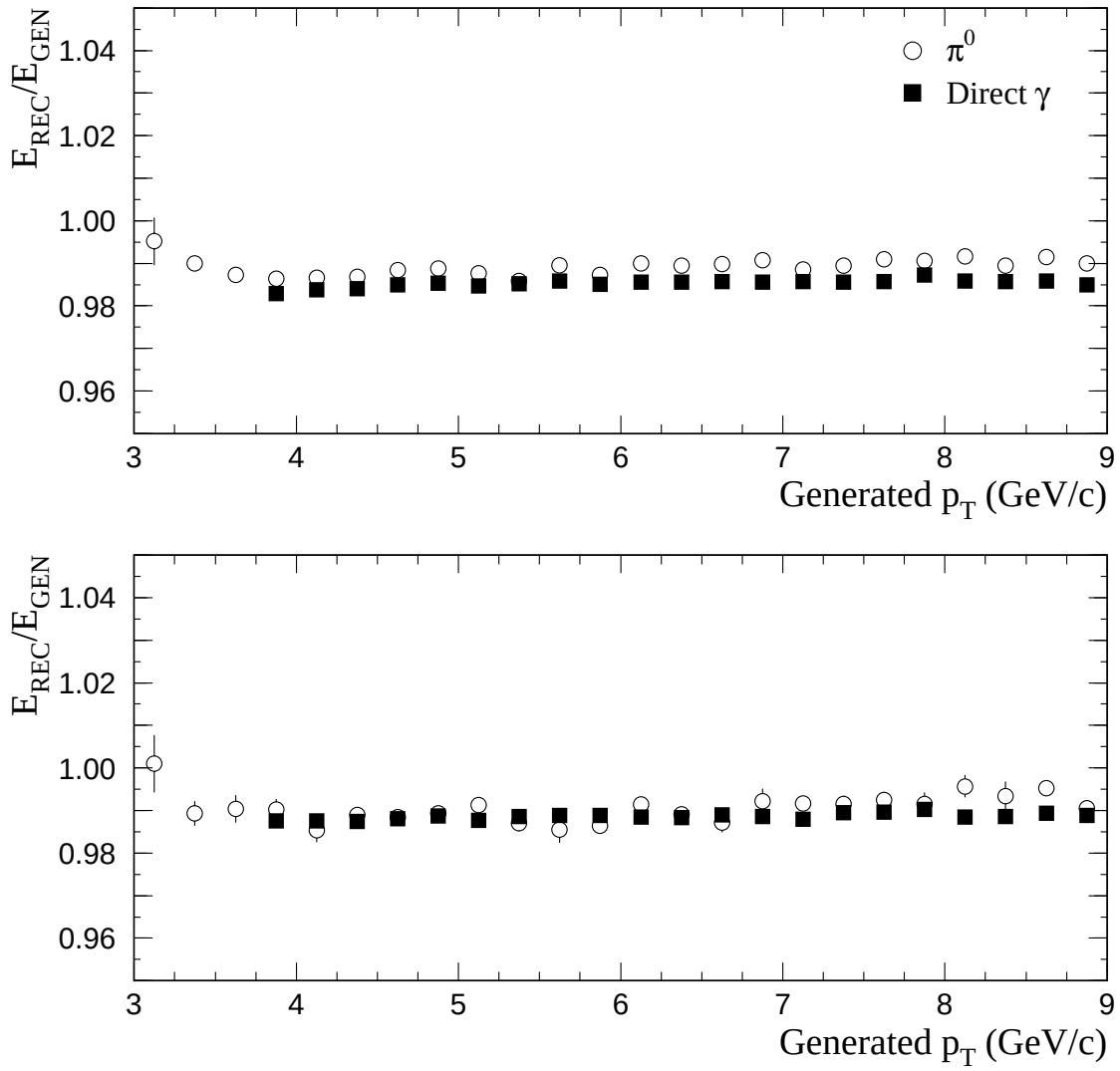

Figure 6.35 E_{REC}/E_{GEN} from the 1991 800 GeV/c proton full Monte Carlo sample for π^0's and direct photons as functions of their generated p_T values. The top plot is for the standard energy scale sample, the bottom plot has additional requirements assuring that all photons were reconstructed in the same manner by `EMREC`.

The fractional uncertainty in p_T is

$$\frac{\Delta p_T}{p_T} = \sqrt{\left(\frac{\Delta E}{E}\right)^2 + \left(\frac{\Delta R}{R}\right)^2 + \left(\frac{\Delta Z}{Z}\right)^2}. \tag{6.4}$$

The position uncertainty comes from the uncertainty in the alignment of the EMLAC to the tracking system (Section 6.3). The maximum uncertainty in X and Y were each 0.1 mm so that the fractional uncertainty in radius was at most 0.07%. The uncertainty in the Z-position of the EMLAC is order 0.5 cm, so the fractional uncertainty in Z is approximately 0.06%. Neither of these uncertainties are significant when added in quadrature with the uncertainties from the energy calibration. The uncertainty in the p_T scale can be taken to be the uncertainty due solely to the calibration of the EMLAC energy response.

6.8.4 Cross-Section Uncertainties

The differential cross sections measured by this experiment have uncertainties associated with both the data analysis and corrections. Several of these corrections (such as the reconstruction efficiency [Section 5.1.4]) involve the Monte Carlo analysis, therefore, the energy scale uncertainty folded together both the data and Monte Carlo uncertainties. Uncertainties in common were reduced by this technique (e.g., the uncertainty due to the fitting procedure). The energy scale uncertainties were then combined properly in quadrature and placed into the parameterized Monte Carlo to determine the systematic uncertainties associated with the energy scale on the cross sections. The systematic uncertainty in a few of the differential cross sections due to the calibration of the energy response of the electromagnetic calorimeter are displayed in Figures 6.36 through 6.40.

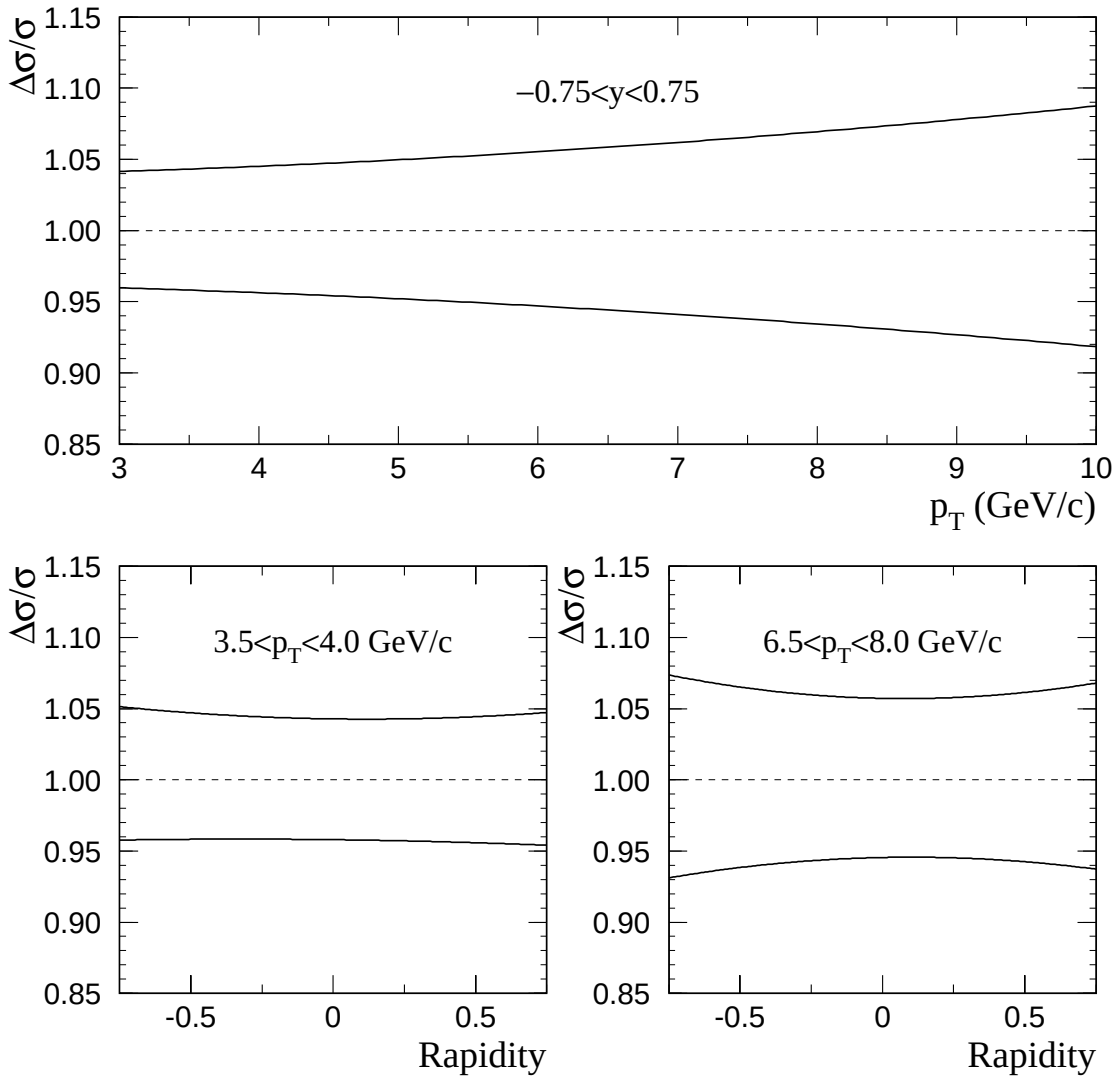

Figure 6.36 The systematic uncertainty in the π^0 cross section as functions of the π^0 p_T (top) and rapidity (bottom) for the data displayed in Figure 6.1. The energy scale systematic uncertainty was taken to be 0.5%.

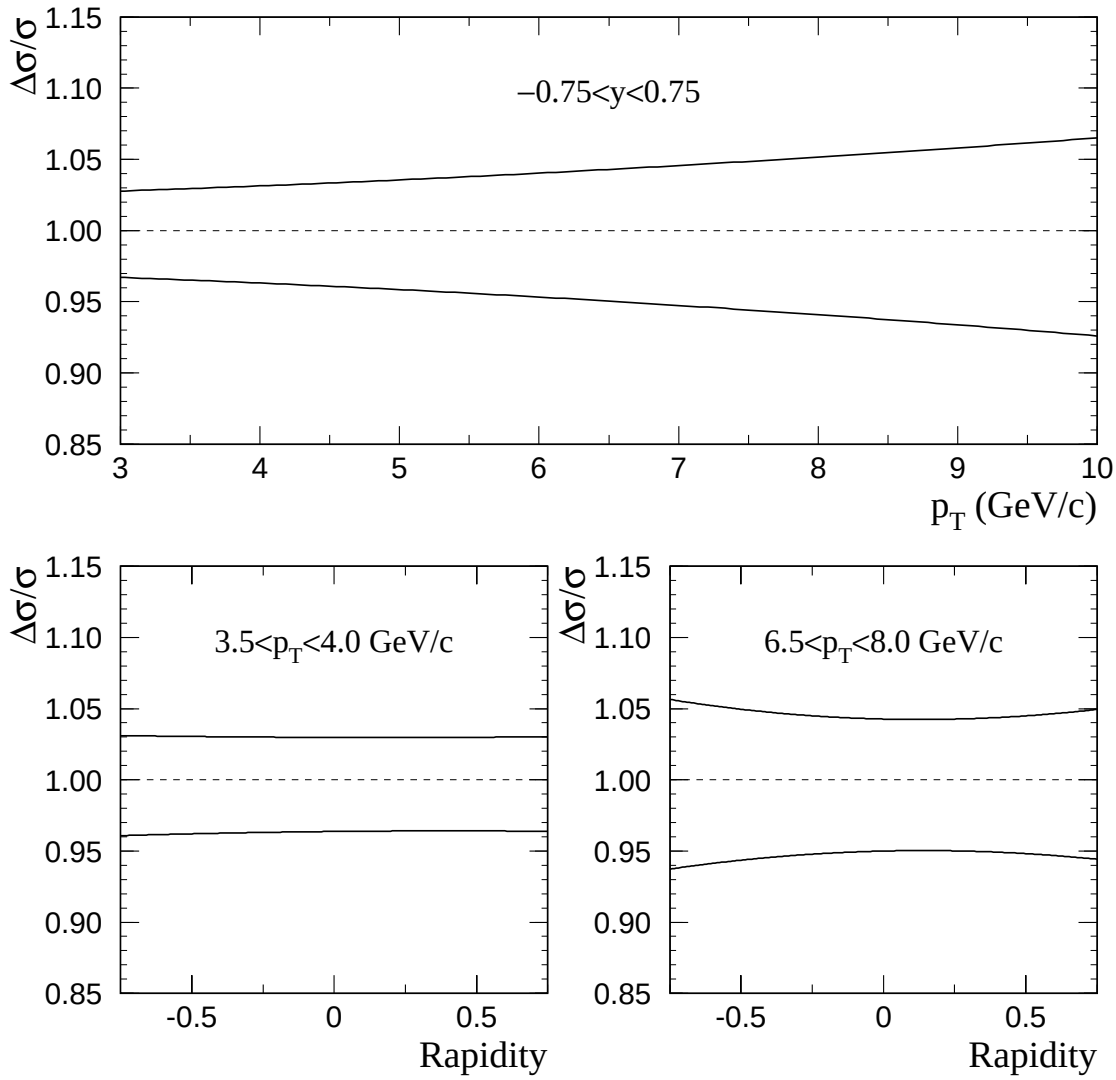

Figure 6.37 The systematic uncertainty in the direct-photon cross section as functions of p_T (top) and rapidity (bottom) for the data displayed in Figure 6.1. The energy scale systematic uncertainty was taken to be 0.6%.

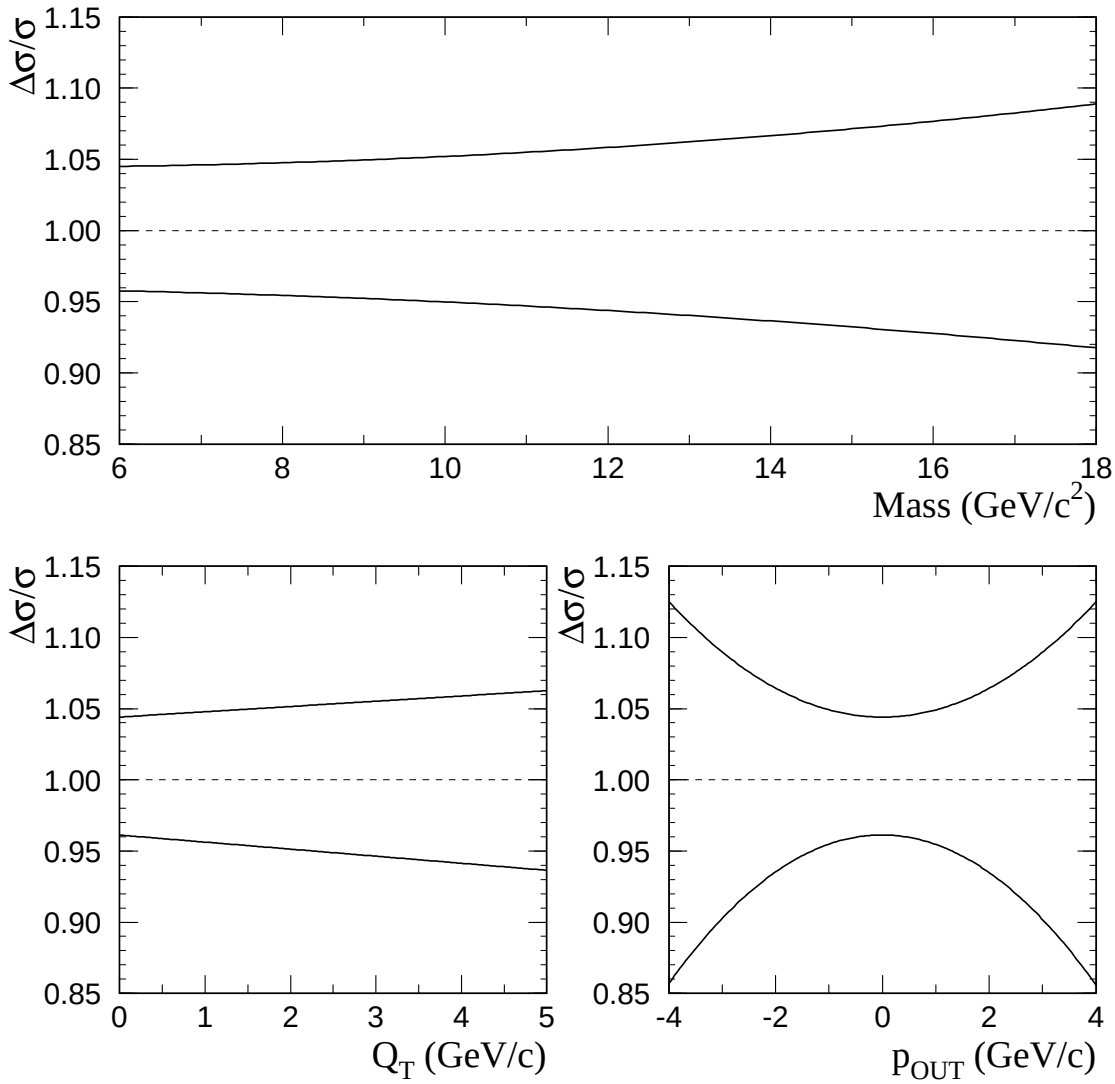

Figure 6.38 The systematic uncertainty in the $\pi^0\pi^0$ cross section as functions of mass (top), Q_T (bottom-right), and p_{OUT} (bottom-left) for the 515 GeV π^- data.

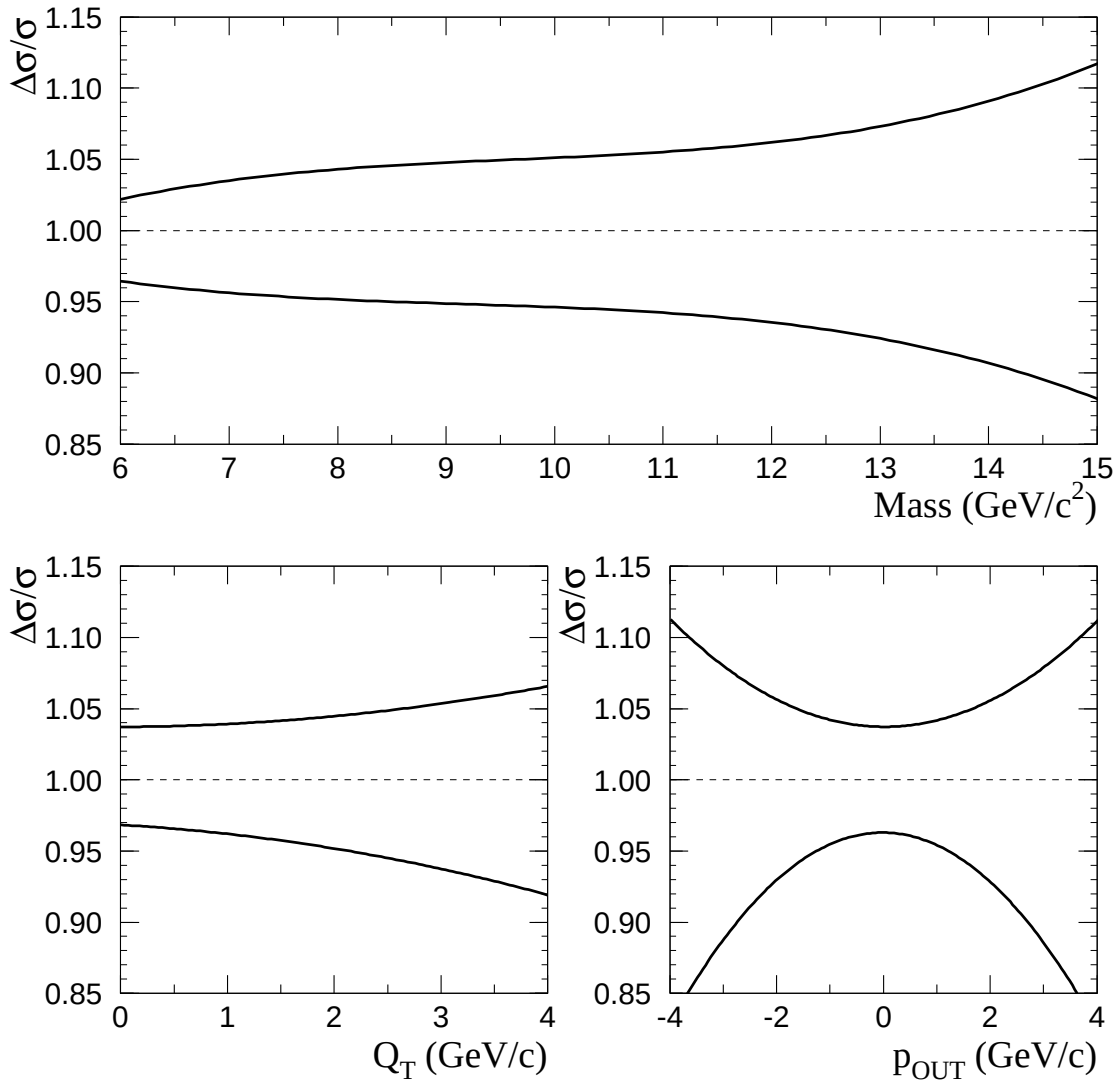

Figure 6.39 The systematic uncertainty in the direct photon–π^0 cross section as functions of mass (top), Q_T (bottom-right), and p_{OUT} (bottom-left) for the 515 GeV π^- data.

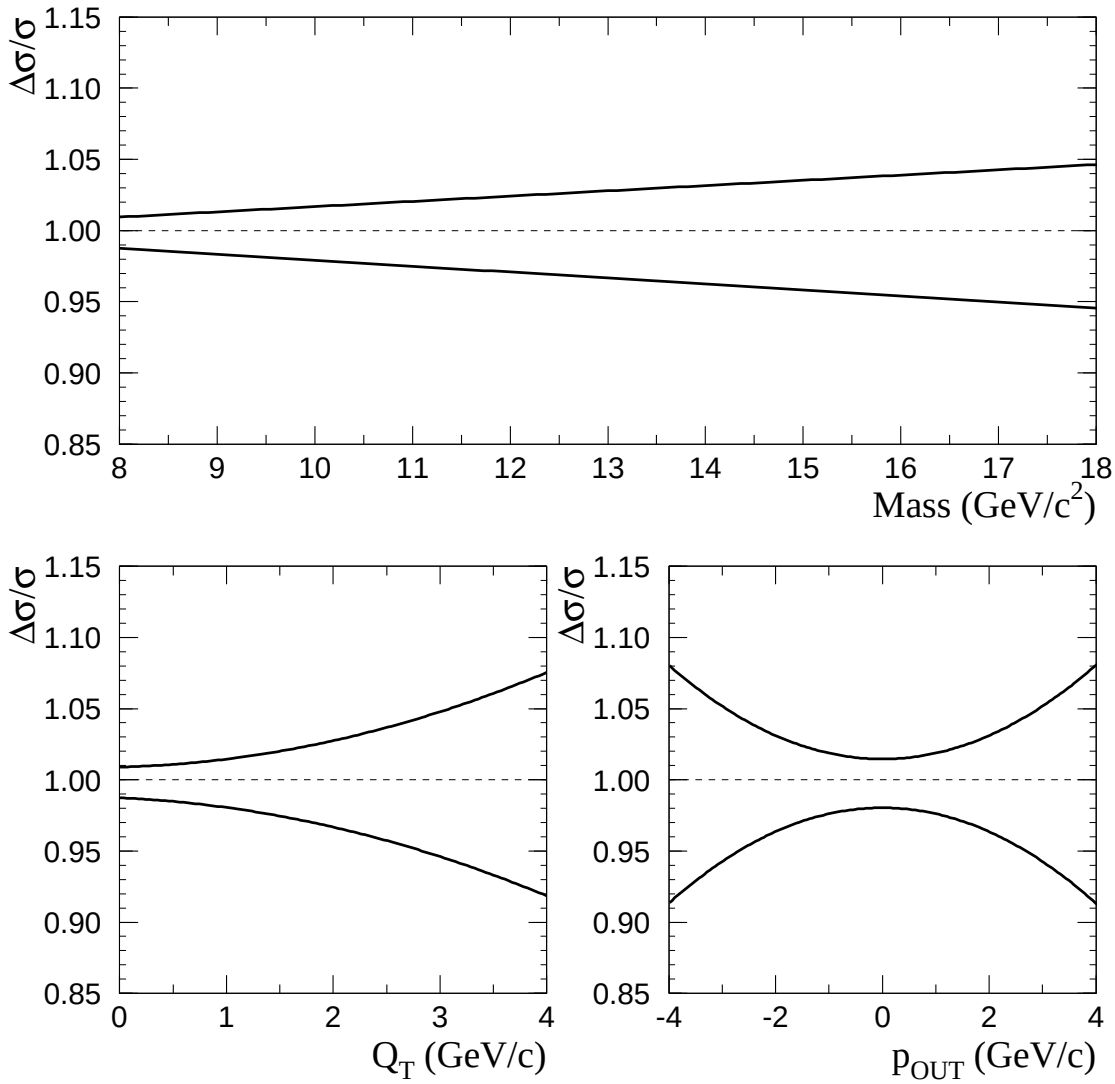

Figure 6.40 The systematic uncertainty in the double direct-photon cross section as functions of mass (top), Q_T (bottom-right), and p_{OUT} (bottom-left) for the 515 GeV π^- data.

Chapter 7 Event Selection and Analysis

This chapter describes the underlying selection criteria and analysis techniques used to explore high-mass pairs. This analysis is based upon data recorded during the 1990 and 1991 fixed target runs. These samples contain interactions between pion and proton beams incident upon targets of beryllium, copper, and hydrogen.

7.1 Cross Section Definition

The measured cross section, σ, for a process is evaluated via the expression

$$\sigma = \frac{1}{\mathcal{L}\,\mathrm{B}}\,\frac{\mathrm{N}}{\epsilon}, \tag{7.1}$$

where N is the number of events measured, B is the branching ratio for the specific measured subprocess (Table 5.5), ϵ is the efficiency for selecting, detecting, and reconstructing those events, and $\mathcal{L}$ represents the sensitivity to that process (*luminosity*), in units of events/pb. Differential cross sections, $\mathrm{d}\sigma/\mathrm{dX} = \Delta\sigma/\Delta\mathrm{X}$, will be presented in this document, where X represents a kinematic quantity such as $\mathrm{p_T}$ or mass.

7.2 Normalization

7.2.1 Beam

The Meson West beam line (Section 2.2.2) transported a 0.8 TeV proton beam and secondary beams consisting of admixtures of 0.5 TeV protons, pions, and kaons to the experimental hall. The beamline Čerenkov detector (Section 2.2.3) identified secondary beam particles [76]. Čerenkov light emitted by the particles passing through the helium medium was detected by rings of photomultiplier tubes. The optics were configured to allow simultaneous measurement of each

kind of beam particle during a single spill without requiring changes in the helium pressure. Logical combinations of the photomultiplier signals (Figure 7.1) were used to identify the particles based on a probabilistic analysis. A study of the incident positive 530 GeV/c secondary beam showed that it contained a mix of 96.7% protons, 2.75% pions, and 0.54% kaons [76]. The normalization was corrected for the tag efficiency. An overall systematic uncertainty was included for tag contamination.

The secondary beams also contained a small fraction of muons. The contamination level was determined using the FCAL (Section 2.4.4) and beam particles that did not interact in the target. The level of muon contamination was estimated to be 0.5% for the negative beam data, and 0.3% for the positive beam data [94, 136].

During data taking, online scalers were used to record aggregate statistics (counts) for various portions of the spectrometer. This information was analyzed offline on a spill-by-spill basis. In particular, scalers from the hodoscope, interaction counters, and beam hole counters (Section 2.2.5) were used to determine the number of beam particles available to the experiment. Other scalers were used to determine the *live fraction* (fraction of time available for data taking) of the DAQ and trigger components. Taken in combination, this information was used to calculate spill-by-spill counts of the beam particles that produced the data, LIVE TRIGGERABLE BEAM (LTB) [137].

7.2.2 Target

Every event required a reconstructed vertex in the target region (Figures 7.2 and 7.3). Longitudinal and transverse requirements were placed on the vertices to provide clean data samples. The longitudinal cuts selected the target in

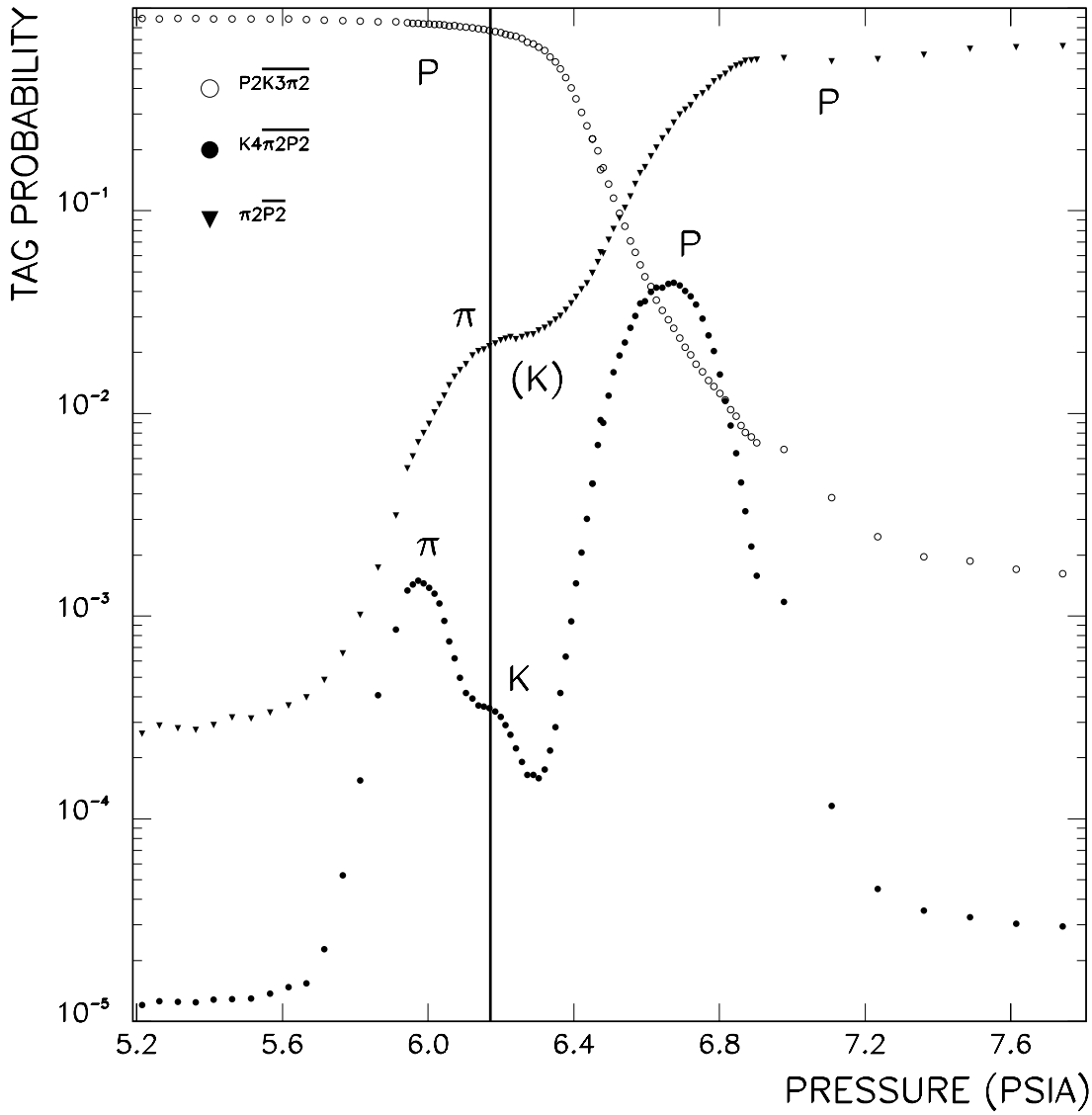

Figure 7.1 Pressure curves for the pion, kaon, and proton tags with incident +530 GeV/c beam. Each curve is labeled by tag logic. Peaks/plateaus are labeled by the associated particle type. The solid vertical line represents a typical Čerenkov operating pressure. The line clearly passes through the desired peaks for tagging each particle type with the appropriate coincidence logic [76].

Beam and Configuration	Target Material	Beam Absorption	Conversion (per photon)
1990 π^-	Be	1.06	1.09
	Cu	1.02	1.19
1991 π^-	H	1.04	1.11
	Be	1.08	1.08
	Cu	1.01	1.16
1991 p	H	1.03	1.11
	Be	1.08	1.08
	Cu	1.01	1.16

Table 7.1 Average weight for beam absorption and photon conversion for the various materials in the 1990 and 1991 target configurations.

which the incident beam interacted. The transverse cuts ensured the interaction occurred within the target material; this avoided biases in the normalization due to counting beam particles that missed the target. The correction was made by counting vertices in the upstream set of beam SSDs, both inside and outside the fiducial region, and adjusting the beam count accordingly. For the 1990 target configuration, this correction was ≈ 1.35; in 1991 it was close to unity [94].

Additional corrections were necessary to account for inefficiencies and biases in the vertex finding algorithms (Section 4.2.3). The vertex reconstruction efficiency, averaged over the entire target, was 99.6% [84]. A calculation was also performed to correct for the fraction of beam particles absorbed by the materials upstream of the primary vertex (Table 7.1).

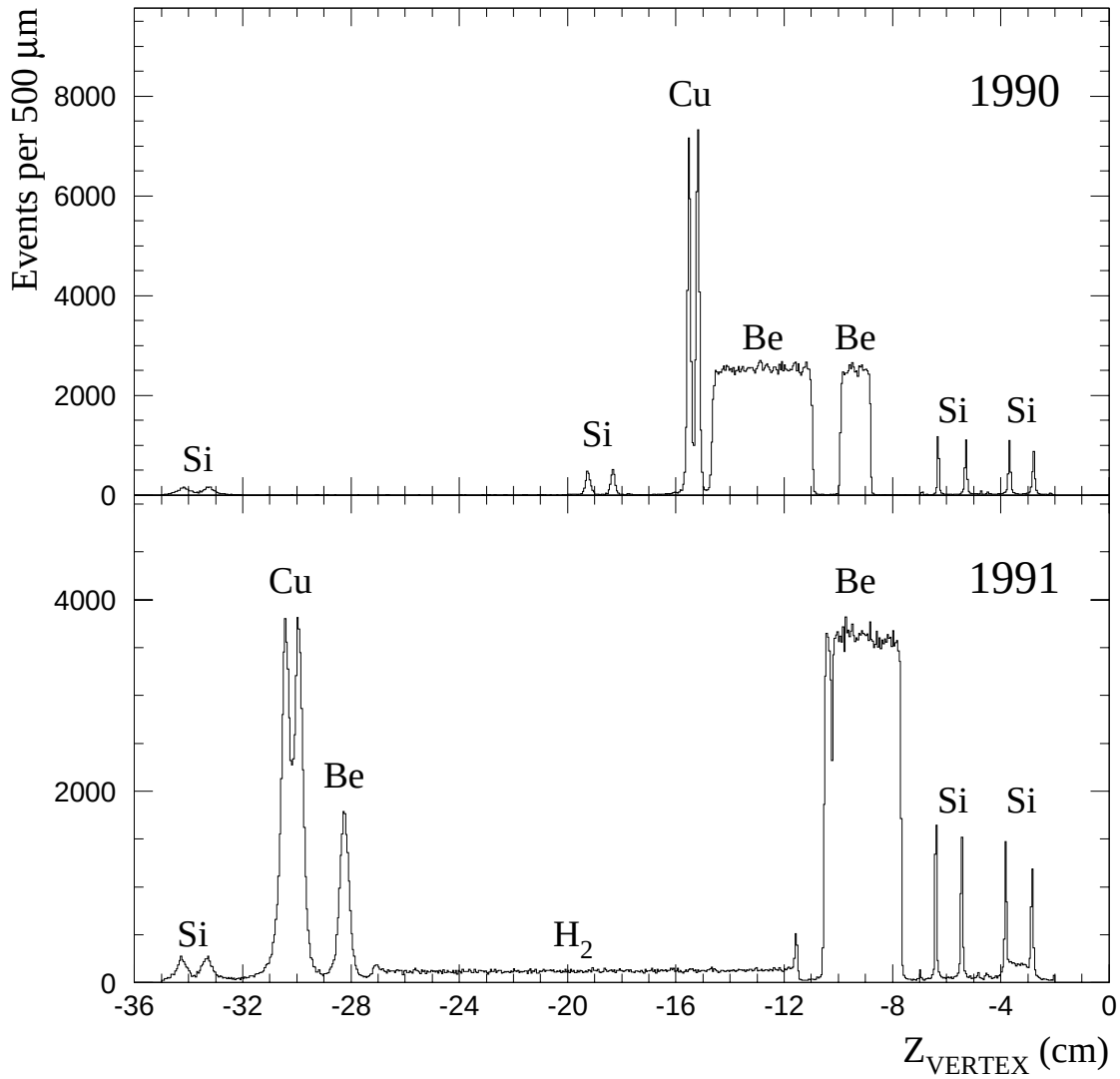

Figure 7.2 The longitudinal distribution of reconstructed vertices for 1990 (top) and 1991 (bottom) target configurations. The events contributing to these plots were selected by requiring a π^0 with $p_T > 4.0$ GeV/c.

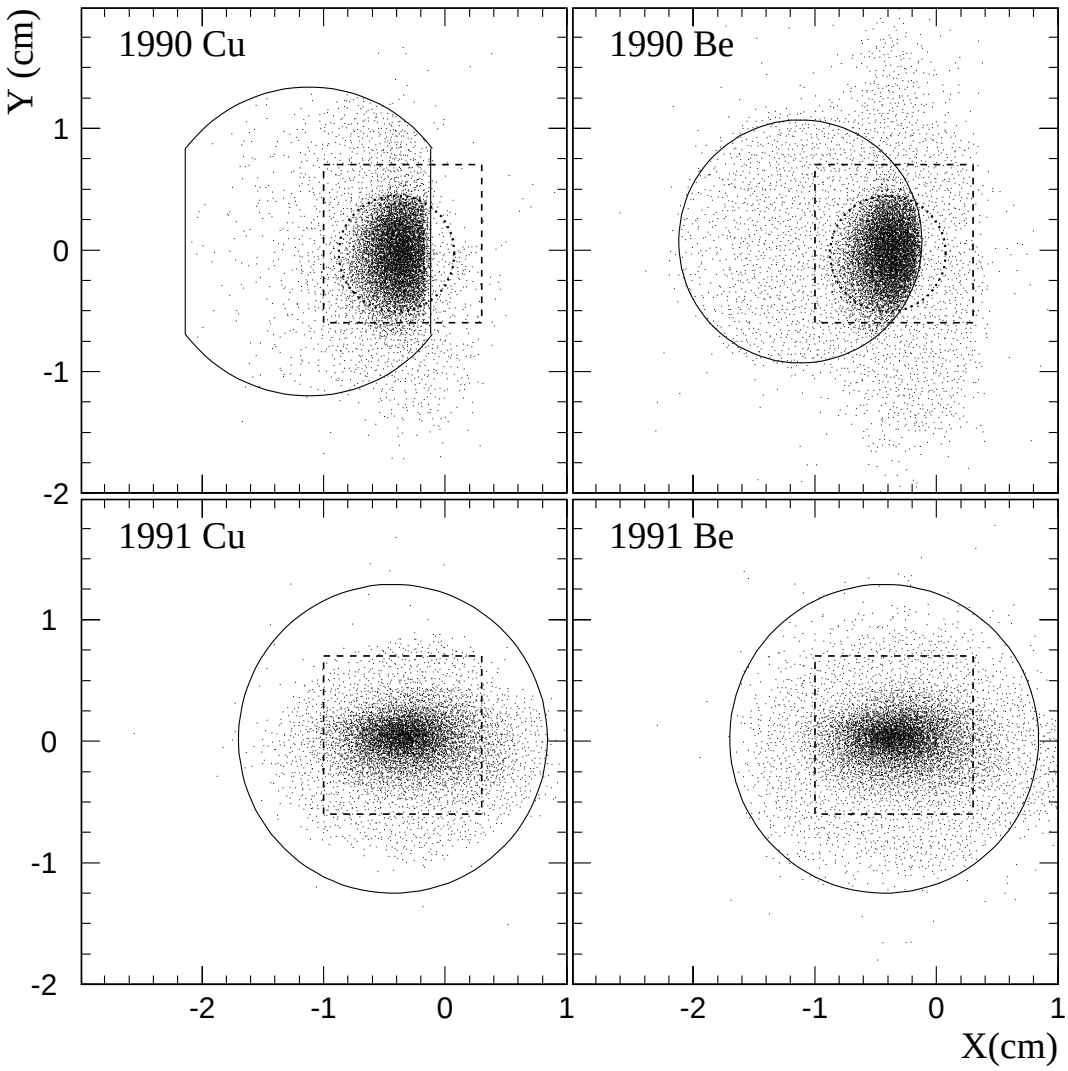

Figure 7.3 X–Y distribution of vertices in the copper and beryllium targets for the 1990 515 GeV/c π^- data and the 1991 530 GeV/c proton data. Each event required a π^0 with $p_T > 3.5$ GeV/c. The solid lines mark the edges of the target; the dashed lines represent the instrumented region of the beam SSDs; the dotted circle is the beam hole counter. Vertices outside the Cu and Be target area in the 1990 data are primarily due to interactions in the Rohacell target stand [119].

7.2.3 Integrated Luminosity

The integrated luminosity, $\mathcal{L}$, is the product of the number of available beam particles with the number of targets per unit area. It is expressed as

$$\mathcal{L} = \text{LTB}\ \rho\ \ell\ \text{N}_\text{A}, \tag{7.2}$$

where LTB is LIVE TRIGGERABLE BEAM, ρ is the target density, ℓ is the target fiducial length (Table 2.2), and N_A is Avogadro's number. The luminosity for each of the beam samples and targets considered in this analysis can be found in Table 7.2.

E706 accumulated statistics from 515 GeV/c π^- beams during both the 1990 and 1991 fixed target runs. As both samples have independent normalizations (although both are normalized using similar procedures) and since many of their corrections are measured independently, a comparison of the π^0 (Figure 7.4) and $\pi^0\pi^0$ (Figure 7.5) cross sections in both samples tests aspects of the normalization. Additional tests included comparisons of the π^0 cross section measured using the BEAM1 and INT1 triggers normalized by counting beam–target interactions to the cross sections using EMLAC triggers and LTB [138, 137]. For the analyses presented below, the 1990 and 1991 π^- samples have been combined together.

Beam Particle	Momentum (GeV/c)	Luminosity (pb^{-1})		
		Be	Cu	H
π^-	515	6.8	1.2	0.2
π^+	515	0.05	0.01	0.01
p	530	6.7	1.6	1.2
p	800	2.3	0.6	0.4

Table 7.2 Luminosity as a function of beam and target for data samples used in this analysis.

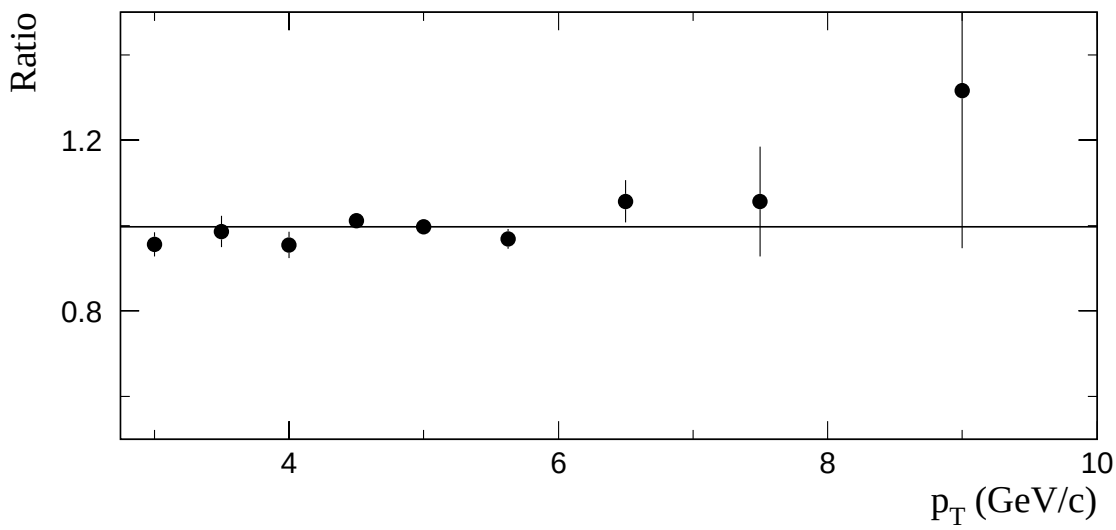

Figure 7.4 The ratio of inclusive differential π^0 cross sections as a function of p_T from the 515 GeV/c π^-Be data for the 1990 and 1991 fixed target runs. The luminosities (and most of the corrections) were calculated independently for these two samples. The line is a fit; the ratio is 0.998 ± 0.007.

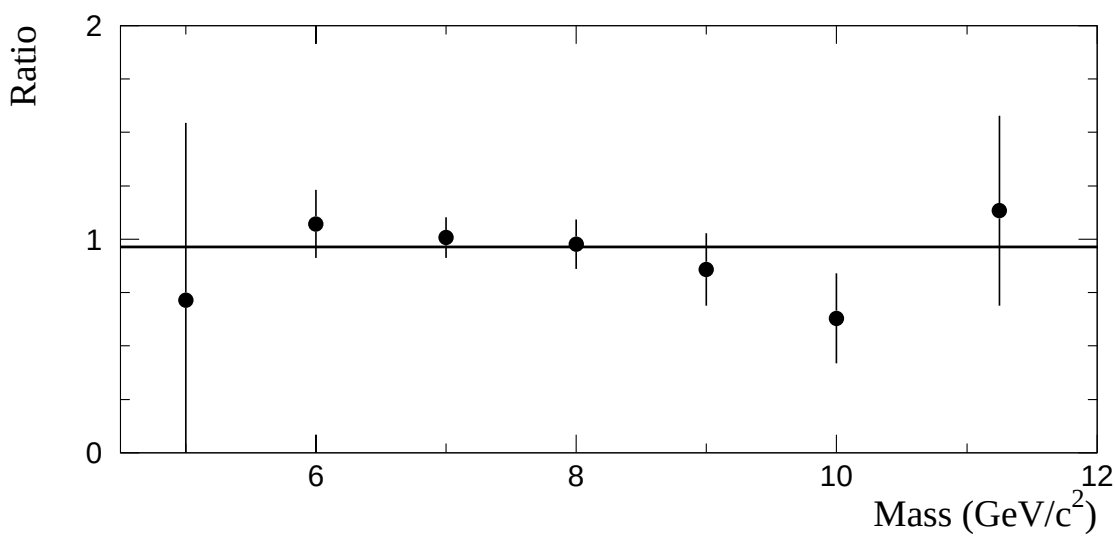

Figure 7.5 The ratio of $\pi^0\pi^0$ cross sections as a function of mass from the 515 GeV/c π^-Be data for the 1990 and 1991 fixed target runs. The luminosities (and most of the corrections) were calculated independently for these two samples. The line is a fit; the ratio is 0.96 ± 0.06.

7.3 Trigger

This analysis is based upon data acquired using the TWO GAMMA trigger (Section 3.1.5). The trigger was required to have fired (in each octant) with a probability of at least 10%. The full Monte Carlo was used to correct for events that had a lower trigger probability (Section 5.1.4). A Δoctant cut was applied so that the octants corresponded to the appropriate TWO GAMMA trigger configuration. The geometrical acceptance correction (Section 7.5) accounted for the Δoctant cut. As an additional test of the trigger corrections, a double-octant trigger was created by taking events where the SINGLE LOCAL HIGH trigger (Section 3.1.3) fired in two (or more) octants conforming to the TWO GAMMA acceptance. SINGLE LOCAL HIGH triggers were integrated into the analysis for the 800 GeV/c proton data to increase statistics (Figure 7.6)[1]. The prescaled TWO GAMMA PRETRIGGER (Section 3.1.2) was used to extend the mass spectrum to low p_T.

Spurious triggers were produced by beam halo muons that deposited energy in the electromagnetic calorimeter. Particularly in the outer regions of the EMLAC, this energy appeared as a high-p_T deposition that satisfied the local trigger requirement. This effect was much less pronounced in the TWO GAMMA trigger where high p_T was simultaneously required on both sides of the calorimeter (Figure 7.7). No offline muon cuts were required for this analysis.

[1] The TWO GAMMA trigger was not available during much of the 800 GeV/c proton running (Section 3.1.5).

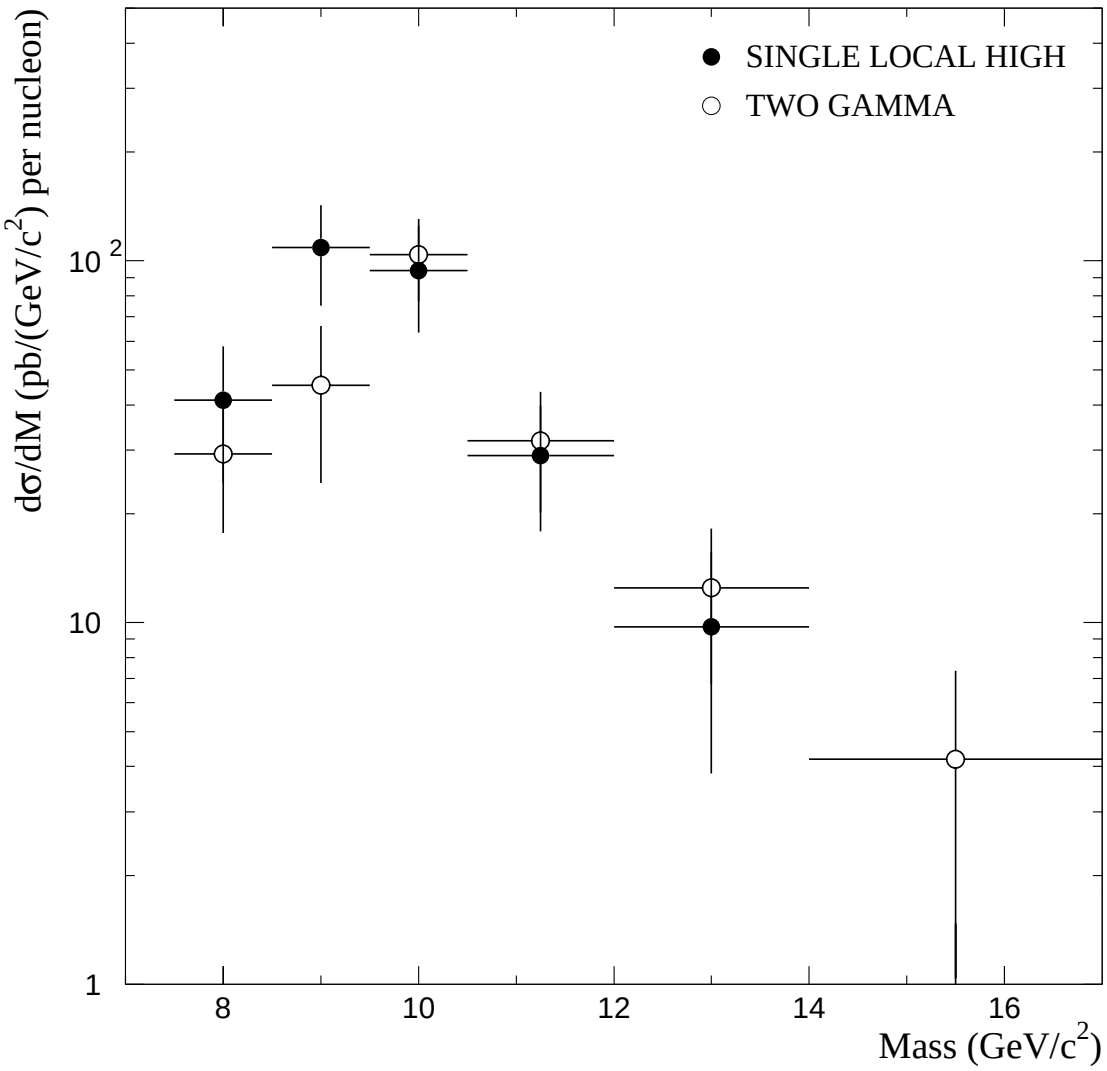

Figure 7.6 Comparison of $\pi^0\pi^0$ events for the TWO GAMMA trigger and for the SINGLE LOCAL HIGH trigger from the 800 GeV/c pBe data sample. These data are from independent run ranges. The π^0 was required to have $p_T^{\pi^0} > 4$ GeV/c to conform with the SINGLE LOCAL HIGH turn-on.

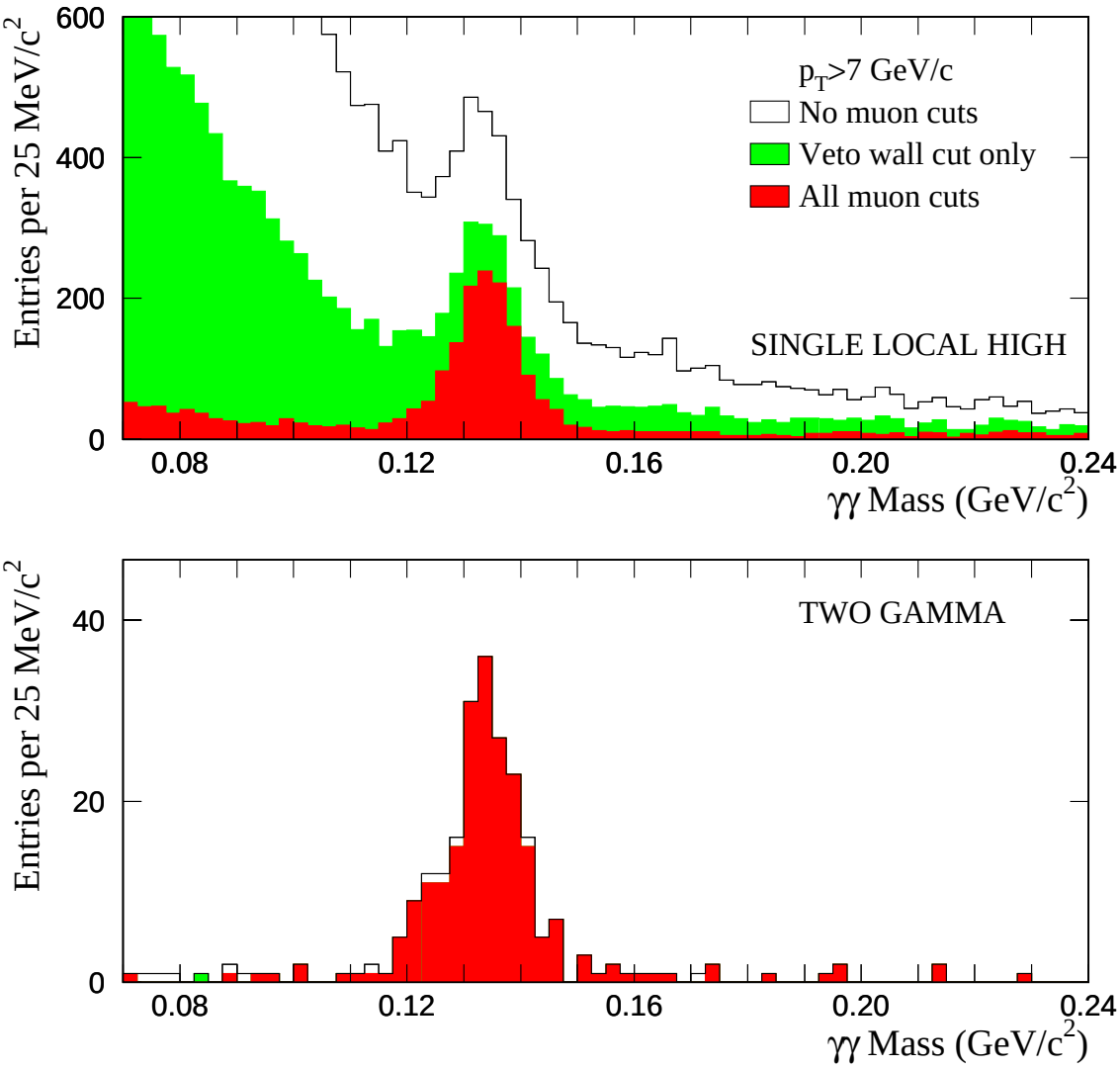

Figure 7.7 The π^0 mass plot with $p_T > 7.0$ GeV/c and R > 50 cm for top) the SINGLE LOCAL HIGH trigger and bottom) the TWO GAMMA trigger. The rise at low mass (M < 0.1 GeV/c^2) is due to muon bremsstrahlung. The *all muon cuts* includes all requirements listed in [79].

7.4 Photon Definition

In order to remove electrons (and many hadrons) from the direct-photon sample, a cut was placed upon the distance between reconstructed shower and the nearest reconstructed charged particle track (as projected onto the EMLAC) (Figure 7.8). Showers were excluded from the sample if this distance was less than 1 cm. The $\pi^0\pi^0$ cross section was used to account for accidentals (ratios with and with-out the cut) since this cross section is relatively independent of the cut. The correction was $\approx 1\%$ per photon.

Photons, passing through the materials upstream of the EMLAC can covert (Equation 4.5) into ZMP electrons (Section 4.5). By carefully accounting for this material (Figure 6.10) one can use Equation 4.5 to calculate the number of converted photons and correct for them (Table 7.1).

The active volume of the EMLAC consisted of 26 radiation lengths but less than 2 interaction lengths of material so, while electromagnetic showers were contained within the detector, only a fraction of the hadron's energy was deposited there. The front/back division of the EMLAC was therefore used to discriminate between hadronic and electromagnetic showers. Figure 7.9 displays the fraction of energy reconstructed in the front section compared to the total reconstructed energy in the EMLAC for hadronic showers ($\pi^{\pm}$ from K^0_S decays) and electromagnetic showers (ZMP electrons). Photons deposit most of their energy in the front section of the detector; the requirement that at least 20% of the shower energy be reconstructed within the EMLAC front section was sufficient to remove a large fraction of the hadronic background without compromising the photon signal. Photon losses due to this cut are corrected within the reconstruction efficiencies (Section 5.1.4). The correction totaled $\approx$ 2% per photon.

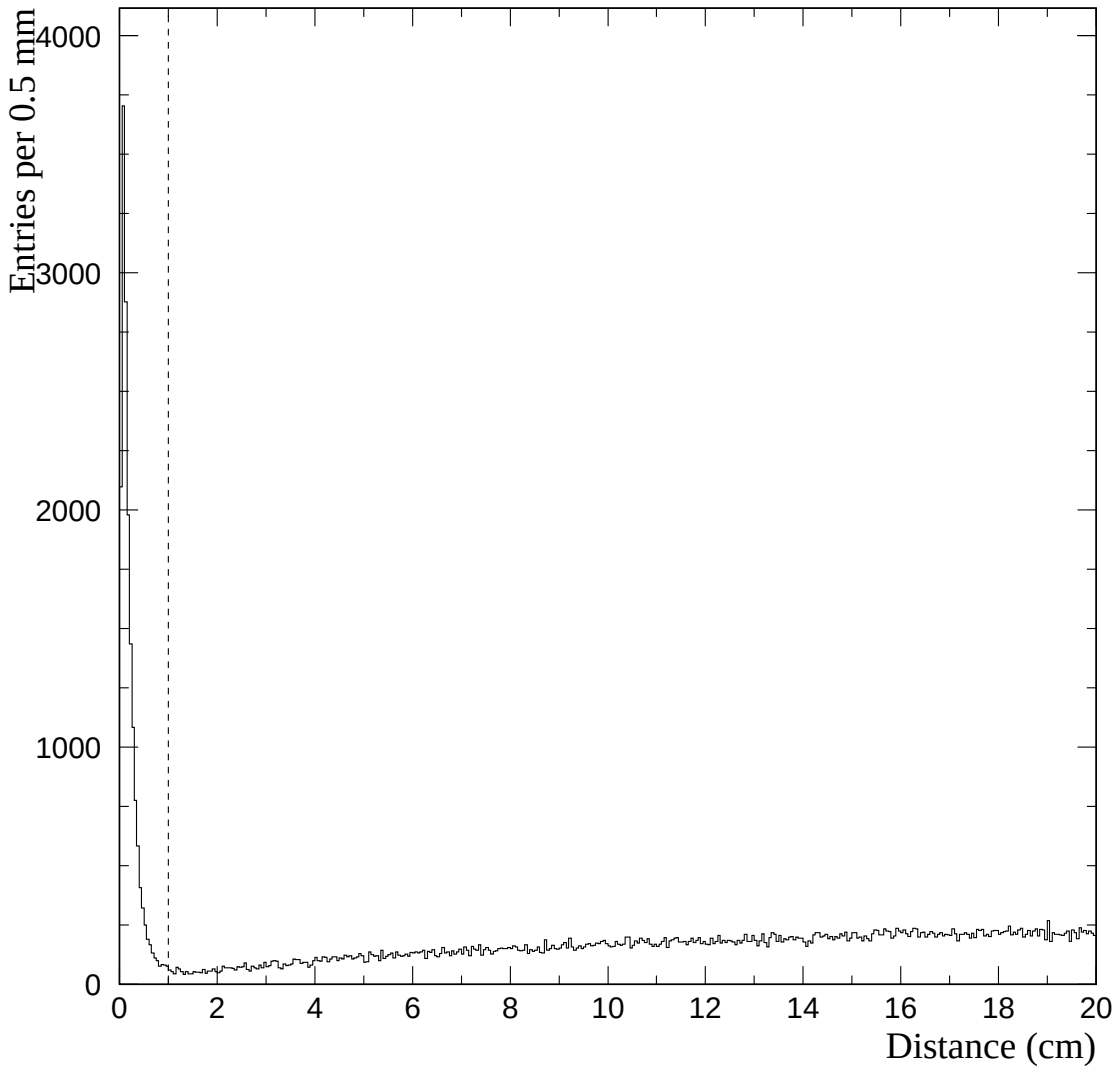

Figure 7.8 The distance to the nearest track for direct-photon candidates having $p_T > 4$ GeV/c. The dashed line is a representation of the cut value. Entries to the left of the line are primarily electrons.

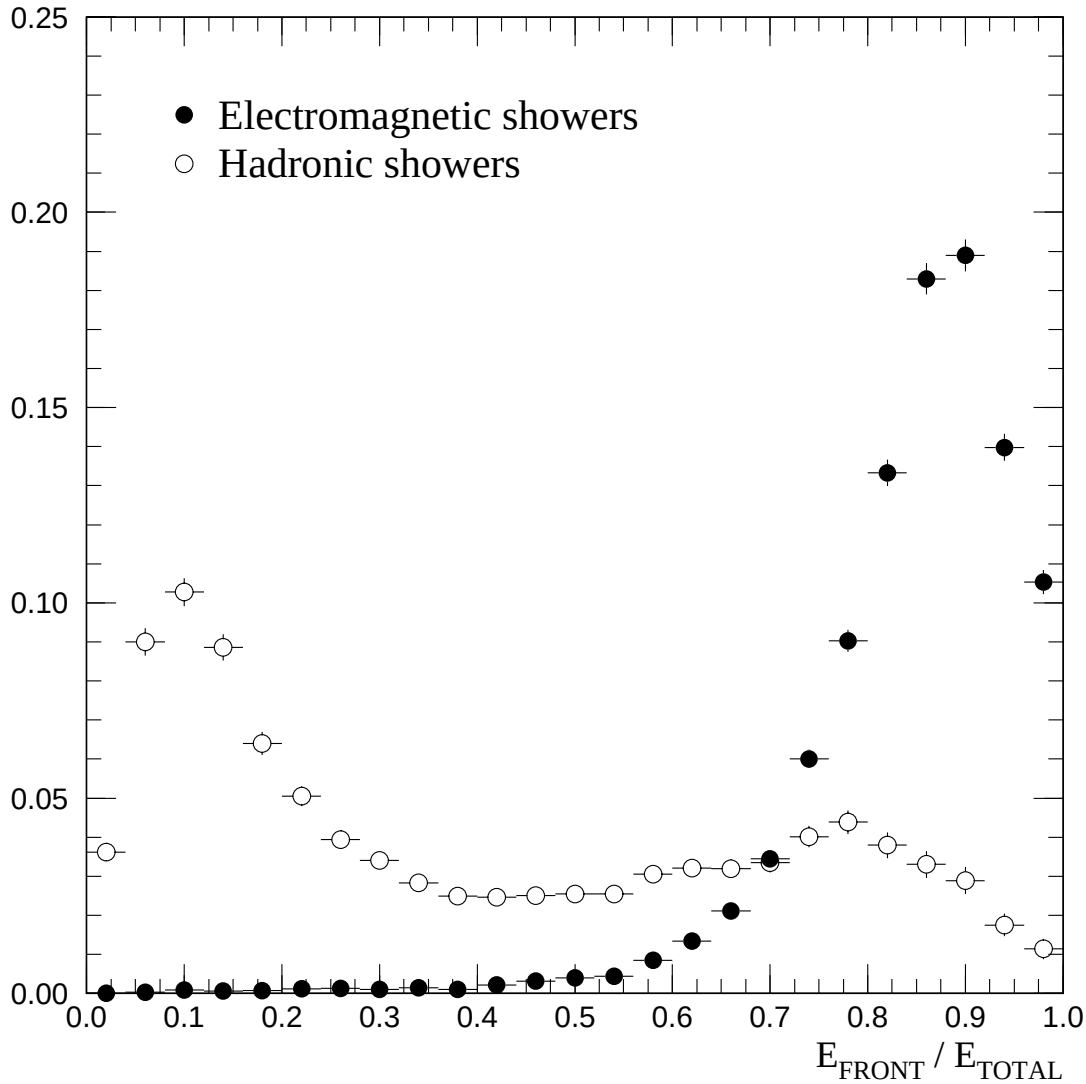

Figure 7.9 E_{FRONT}/E_{TOTAL} distribution for (•) electromagnetic showers (ZMP electrons) and (○) hadronic showers ($\pi^{\pm}$ from K^0_S decays).

7.5 EMLAC Geometrical Acceptance

Photons with reconstructed positions near the edges of the detector (quadrant and octant boundaries) were excluded from the sample (Figure 7.10). Additionally, photons reconstructed within two strips of the partial strip region in outer-R were rejected. These photons had biased energies since the electromagnetic reconstructor forced showers near the boundaries to correlate (Section 4.3.6).

A portion of quadrant 4 was excluded from the EMLAC fiducial volume[2] in the 1991 data analysis because it was found that the two LAC amplifier cards responsible for this detector region[3] (front section, radial view) were bad. Several pairs of the 16 amplifier channels on each card were capacitively coupled so that the individual channels each had the average energy deposited in the pair. This energy averaging compromised the pattern recognition and energy determination during photon reconstruction.

The acceptance of the EMLAC was accounted for by a simplistic ray trace Monte Carlo. Every reconstructed pair (e.g., $\pi^0\pi^0$ or $\gamma\pi^0$) was used as a seed. Keeping $\Delta\phi$ between the particles constant, the 4-vectors of the pair were rotated and redecayed 2000 times. These photons were then checked against the EMLAC fiducial volume. Additionally, photons from π^0 or η decays were required to be within the same octant with A < 0.75. Finally, a Δoctant cut was placed on the pair to simulate the TWO GAMMA trigger configuration. The effect of placing this cut in the geometrical acceptance calculation was to convert it into a $\Delta\phi$ cut. The correction was then the inverse of the survival fraction (Figure 7.11).

[2] This region corresponds to R < 29 cm in octant 7 and R < 31 cm in octant 8.

[3] This is an unfortunate happenstance as these cards are in different crates and have no other connection.

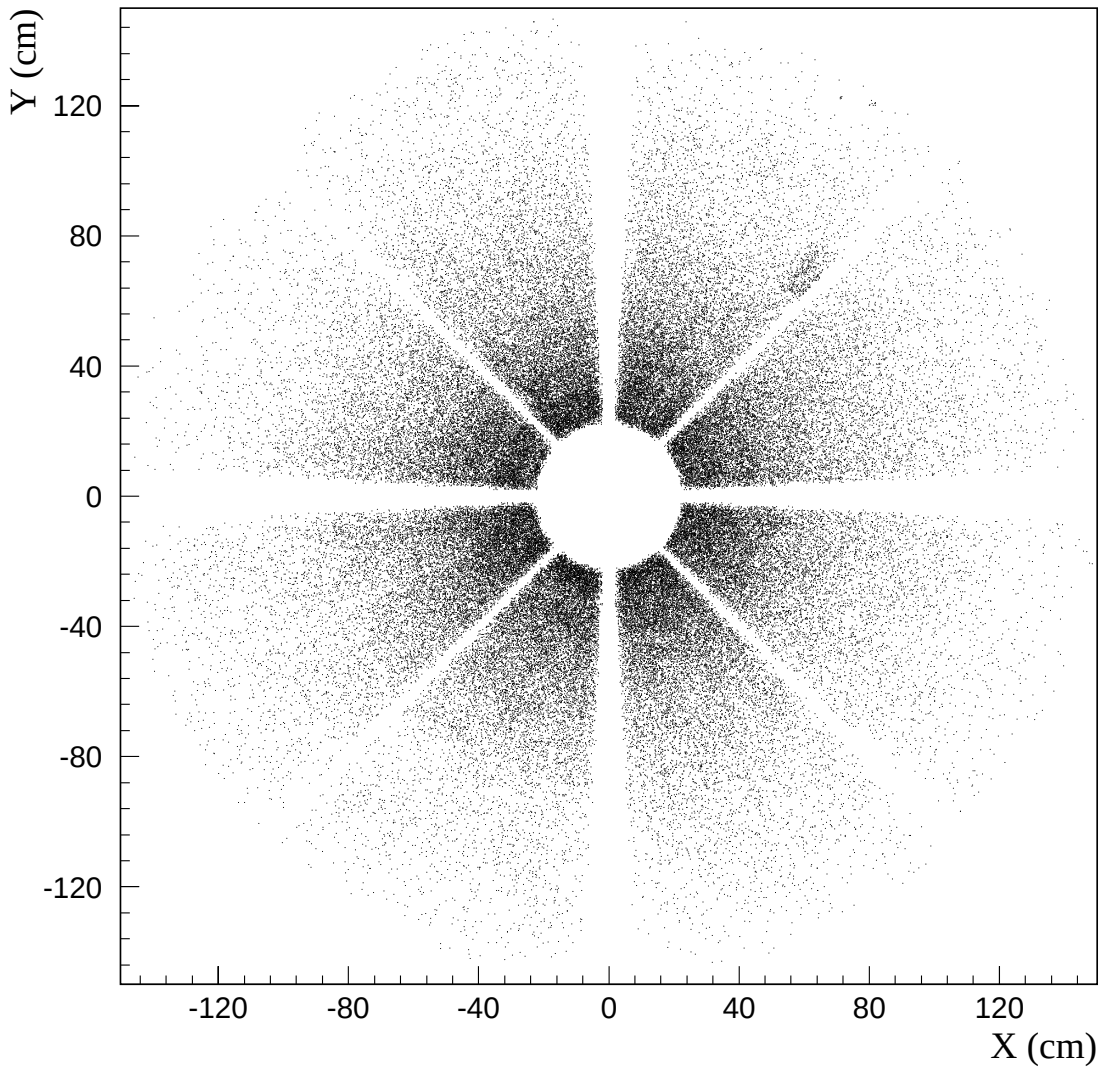

Figure 7.10 The positions of photons reconstructed in the EMLAC from the 1990 data. Each photon is required to fall within the EMLAC's fiducial volume. The octant structure is clearly visible.

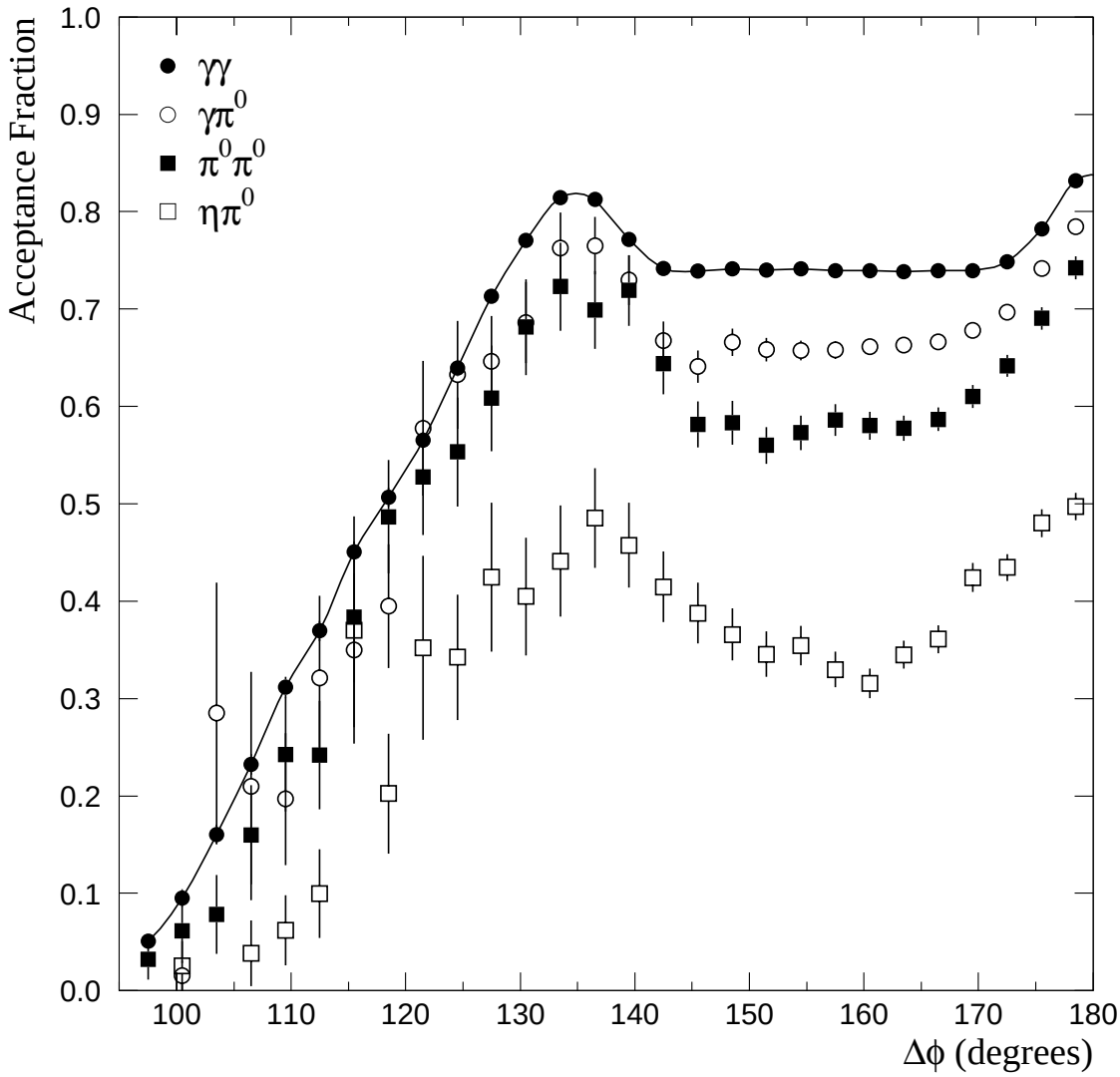

Figure 7.11 Geometrical acceptance for $\gamma\gamma$, $\gamma\pi^0$, $\pi^0\pi^0$, and $\eta\pi^0$ pairs as a function of $\Delta\phi$. The maxima and minima reflect the octant boundaries and the Δoctant cut. The line is a parameterization of the $\gamma\gamma$ geometrical acceptance.

Meson	Low Sideband (MeV/c^2)	Candidates (MeV/c^2)	High Sideband (MeV/c^2)
π^0	60—100	100—180	190—230
η	350—450	450—650	650—750

Table 7.3 Candidate and sideband ranges for π^0's and η's reconstructed from two-photon combinations.

The impact of this correction was limited by requiring central rapidities ($-0.8 < y < 0.8$ for the 0.5 TeV beams and $-1.05 < y < 0.55$ for the 0.8 TeV beam) and azimuthal separations of at least 105°.

7.6 Signal Definitions

All photons that survived the above cuts were taken in combination with each other (photons were required to be in the same EMLAC octant to avoid any reconstruction or trigger biases). The resulting mass distribution (Figure 7.12) was used to define the π^0 and η signals. The mass peaks contain an admixture of signal and background. The linear combinatorial background was removed by the side-band subtraction technique. In this method, regions of the mass spectrum are defined such that the total width of the background regions (one to either side of the peak) is equal to the width of the peaked candidate region (Table 7.3). The resulting side-band area is then equal to the amount of background contained under the peak. Statistics are accumulated for both candidate (c_{π^0} or c_η) and side-band regions (b_{π^0} or b_η); the signal (s_{π^0} or s_η) is measured by subtracting, $s = c - b$.

An energy asymmetry cut (Equation 4.4), $A < 0.75$, was used to ensure the background shape was suitable for sideband subtraction (Figure 7.13). Since the π^0 and η are spin-0 particles which therefore decay isotropically, the correction for this cut is 1/0.75.

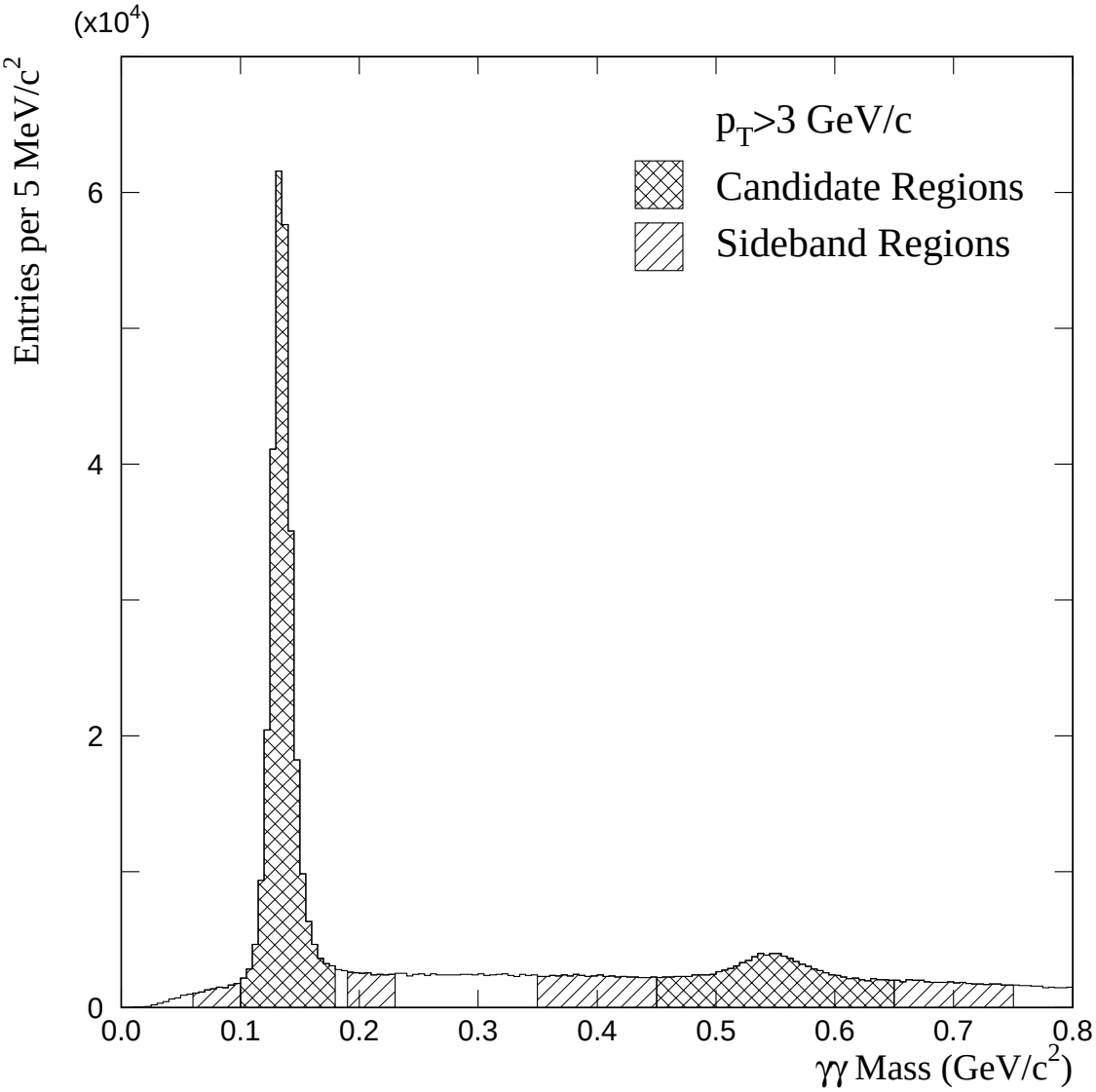

Figure 7.12 The π^0 and η masses showing the candidate and sideband regions used in this analysis.

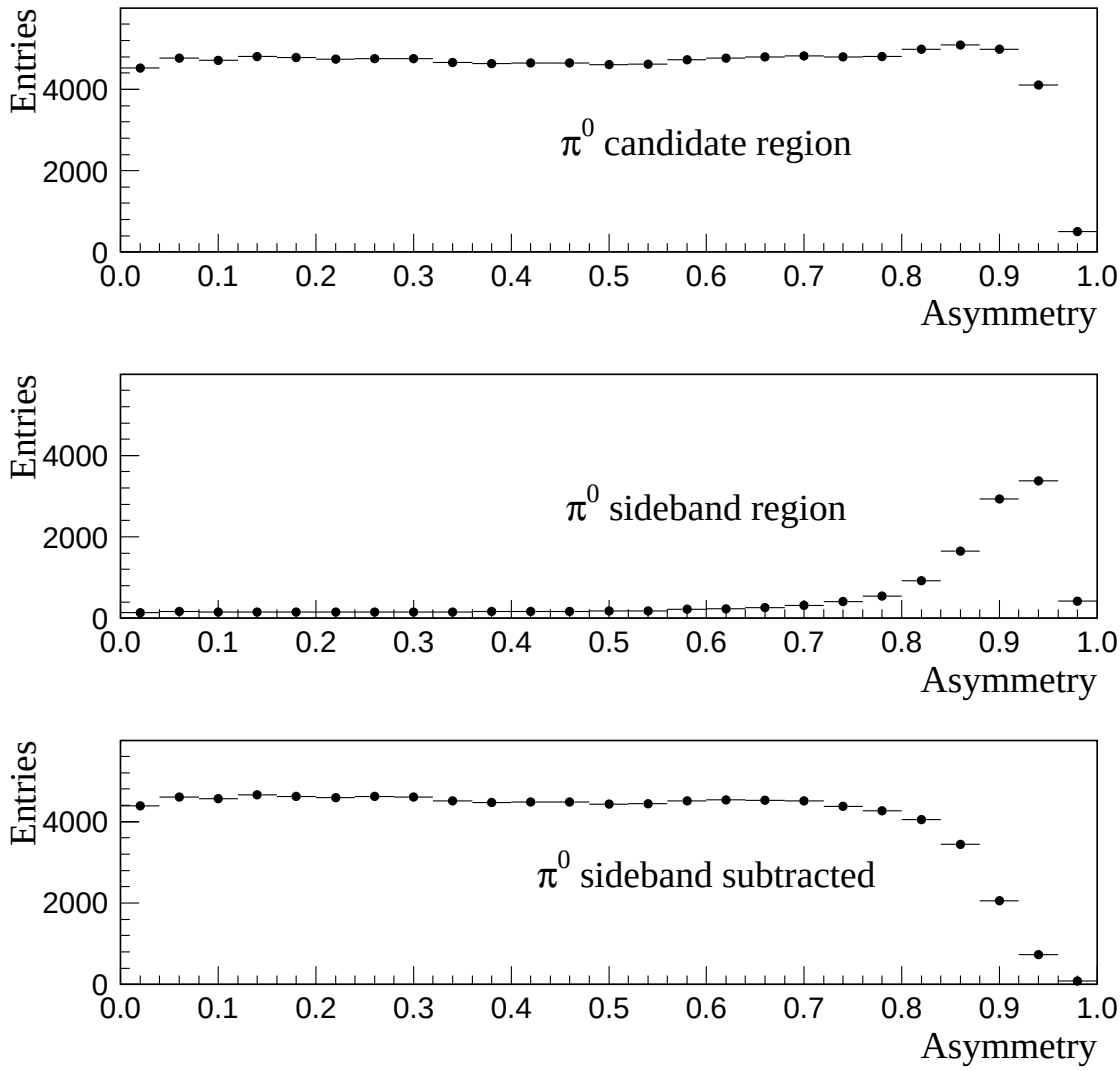

Figure 7.13 The energy asymmetry distribution for π^0 mesons ($4.0 < p_T < 5.5$ GeV) in the top) candidate region; middle) sideband region; bottom) sideband subtracted (signal region).

Photons which, in combination with other photons, did not have reconstructed masses within the candidate region of the π^0 with A < 0.75 or η with A < 0.8 were considered as direct-photon candidates[4] (c_γ).

7.6.1 Meson–Meson Background Subtraction

The background subtraction for pairs of mesons (Figure 7.14) is more complicated than for single mesons; the subtraction can be expressed as

$$s_{\pi_1^0} s_{\pi_2^0} = (c_{\pi_1^0} - b_{\pi_1^0})(c_{\pi_2^0} - b_{\pi_2^0}) \tag{7.3}$$

since each π^0 has combinatorial background under the peak. Expanding,

$$s_{\pi_1^0} s_{\pi_2^0} = c_{\pi_1^0} c_{\pi_2^0} - c_{\pi_1^0} b_{\pi_2^0} - b_{\pi_1^0} c_{\pi_2^0} + b_{\pi_1^0} b_{\pi_2^0}. \tag{7.4}$$

The same relation holds for $\pi^0\eta$ and $\eta\eta$ events.

7.6.2 Direct Photon–Meson Background Subtraction

In the case of $\gamma\pi^0$ events, signal extraction involves both the parameterized Monte Carlo (Section 5.2.3) and the side-band subtraction.

$$s_\gamma s_{\pi^0} = (c_\gamma - b_\gamma)(c_{\pi^0} - b_{\pi^0}) \tag{7.5}$$

$$s_\gamma s_{\pi^0} = c_\gamma c_{\pi^0} - c_\gamma b_{\pi^0} - b_\gamma s_{\pi^0} \tag{7.6}$$

Here b_γ is a background photon that fakes a real direct photon (s_γ), and the last term, $b_\gamma s_{\pi^0}$, is taken from the $s_{\pi^0} s_{\pi^0}$ parameterized Monte Carlo[5]. A similar relation applies to $\gamma\eta$ events. The size of the subtraction is illustrated in Figure 7.15 which shows a comparison of c_γ/s_{π^0} to b_γ/s_{π^0} as a function of ${p_T}^\gamma$ when there was a π^0 with ${p_T}^{\pi^0} > 2.5$ GeV/c reconstructed on the other side of the calorimeter.

[4] For comparison with other E706 analyses, this is the 75N photon definition.

[5] Background photons can arise from π^0's, $\pi^\pm$'s, η's, ω's, or η''s in the parameterized Monte Carlo (Section 5.2.1).

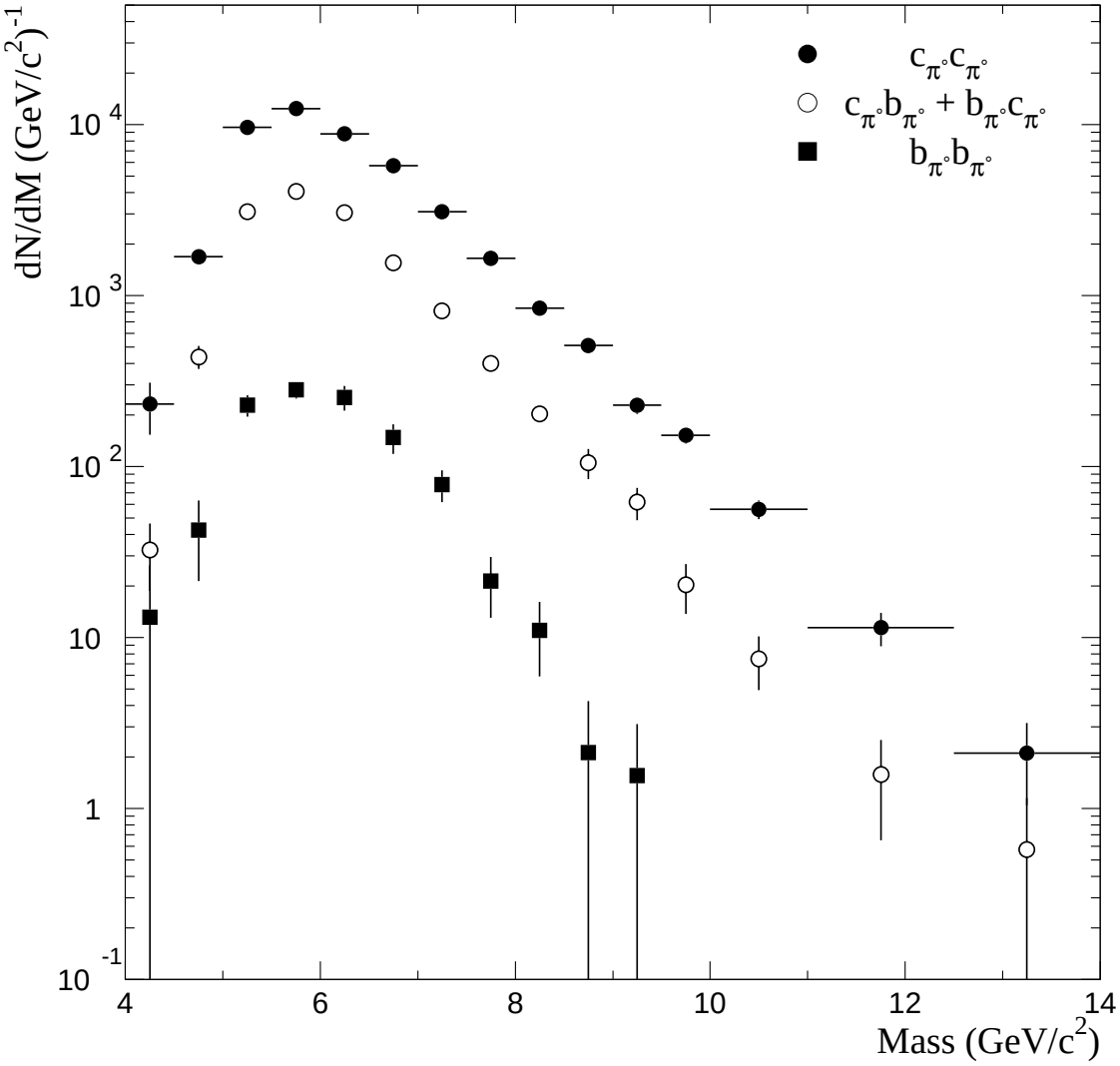

Figure 7.14 Candidate and side-band distributions for $\pi^0\pi^0$ events as a function of mass from the 530 GeV/c pBe sample.

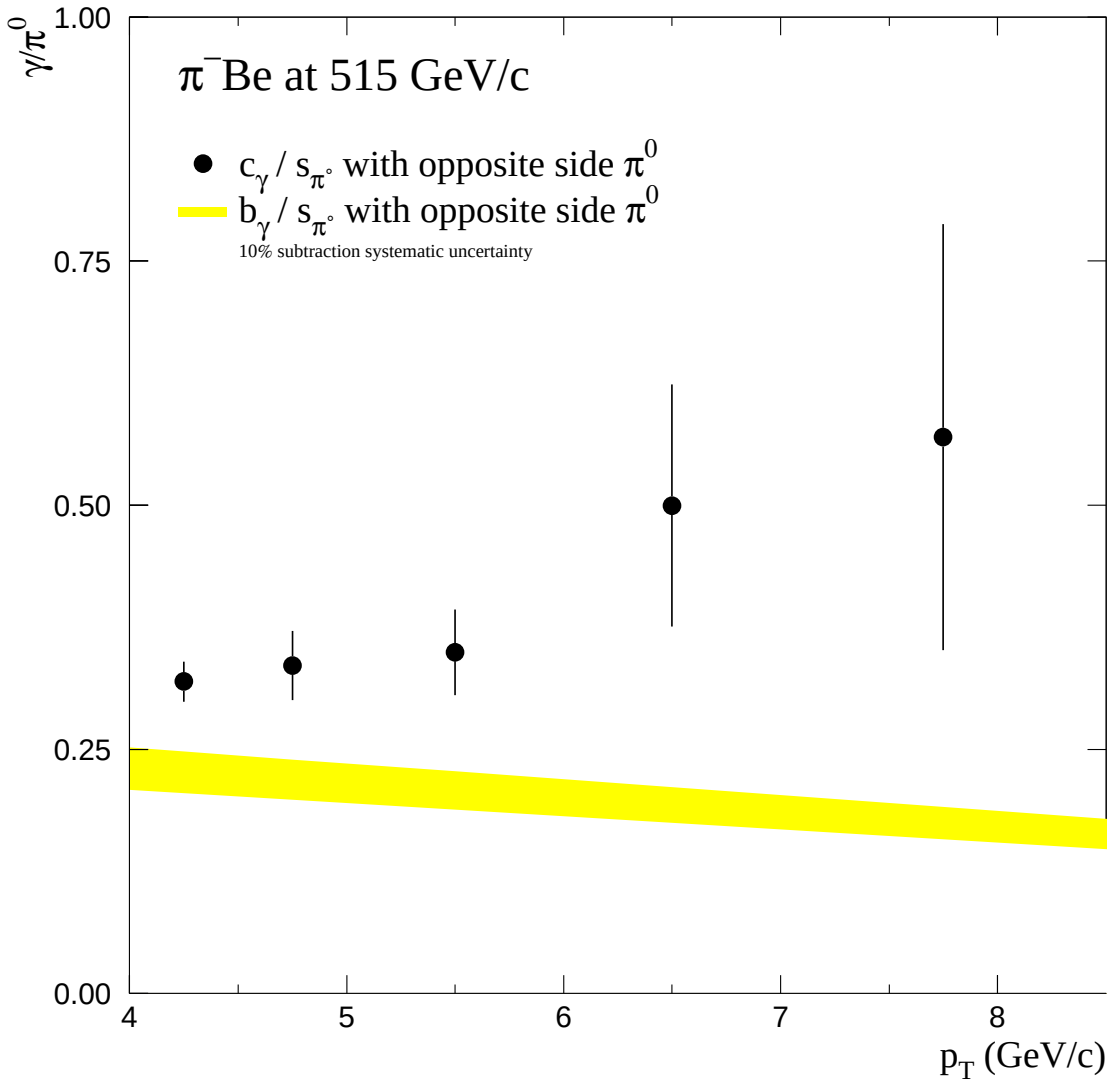

Figure 7.15 Comparison of signal and background for $\gamma\pi^0$ data from the 515 GeV/c π^-Be sample. The ratios c_γ/s_{π^0} and b_γ/s_{π^0} are plotted for the case when a π^0 with ${p_T}^{\pi^0} > 2.5$ GeV/c is reconstructed on the other side of the calorimeter.

7.6.3 Double Direct Photon Background Subtraction

Two major background sources are considered in double direct-photon production: direct photon–meson events and meson–meson events where the mesons decay into photons. Photons that survive the above cuts contribute to the direct-photon candidate sample (b_γ). These background contributions are estimated with the parameterized Monte Carlo (Section 5.2.3).

The background subtraction can be expressed as

$$s_{\gamma_1} s_{\gamma_2} = (c_{\gamma_1} - b_{\gamma_2})(c_{\gamma_1} - b_{\gamma_2}), \tag{7.7}$$

which expands to

$$s_{\gamma_1} s_{\gamma_2} = c_{\gamma_1} c_{\gamma_2} - (s_{\gamma_1} b_{\gamma_2} + b_{\gamma_1} s_{\gamma_2}) - b_{\gamma_1} b_{\gamma_2}. \tag{7.8}$$

The term $b_\gamma b_\gamma$ is derived from the $s_{\pi^0} s_{\pi^0}$ parameterized Monte Carlo. The middle term (delineated by the parenthesis) requires the use of a parameterized Monte Carlo that reproduces the $s_\gamma s_{\pi^0}$ distributions. It is difficult to tune the Monte Carlo generator (Section 5.2.1) for this sample since it requires the background subtraction described in Section 7.6.2 ($b_\gamma s_{\pi^0}$).

Alternatively, we can form an equivalent expression,

$$s_{\gamma_1} s_{\gamma_2} = c_{\gamma_1} c_{\gamma_2} - (c_{\gamma_1} b_{\gamma_2} + b_{\gamma_1} c_{\gamma_2}) + b_{\gamma_1} b_{\gamma_2}. \tag{7.9}$$

For this subtraction the parameterized Monte Carlo needs to reproduce the $c_\gamma s_{\pi^0}$ distributions. These are easily accessible from the data ($c_\gamma s_{\pi^0} = c_\gamma c_{\pi^0} - c_\gamma b_{\pi^0}$) and allow for simpler tunes of the parameterized Monte Carlo generator. Equation 7.9 will be used for the double direct-photon background subtraction (Chapter 11).

The statistical significance of the diphoton data is better than four sigma using this subtraction technique (Figure 7.16). This is comparable to other diphoton measurements (Table 1.9).

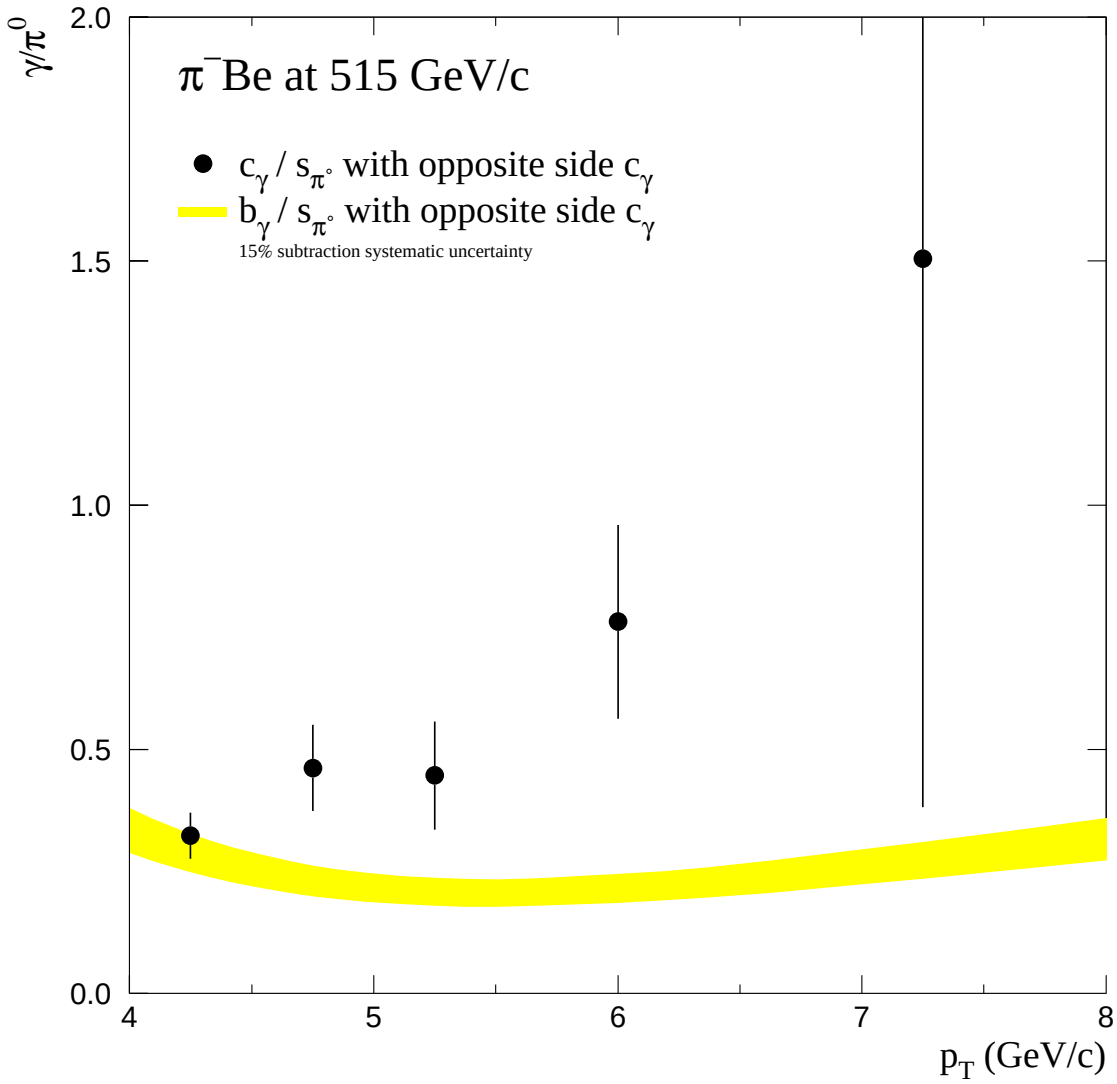

Figure 7.16 Comparison of signal and background for $\gamma\gamma$ data from the 515 GeV/c π^-Be sample. The ratios c_γ/s_{π^0} and b_γ/s_{π^0} are shown for the case when a photon (c_γ) with $p_T{}^\gamma > 4.0$ GeV/c is reconstructed on the other side of the calorimeter.

7.7 Systematic Uncertainties

It is important to assess the systematic uncertainties associated with measuring cross sections. Major sources of systematic uncertainty include the normalization, energy scale calibration, efficiency, and the background subtraction. Uncertainties from these sources are generally considered uncorrelated and will be added together in quadrature.

The systematic uncertainty in the normalization (Section 7.2) was assessed by comparing the results of various scalers and by cross checking samples in which the normalization is calculated independently (Figures 7.4 and 7.5). This uncertainty is estimated to be approximately 15% [137] and includes other small sources of uncertainty such as those associated with the interaction definition (Section 3.1.1) and contamination in the Čerenkov tag [76].

It is possible, though very unlikely, that the high-p_T particles in a high-mass pair can be produced by independent beam–target interactions. Figure 7.17 shows the difference in arrival time with respect to the trigger (Section 4.3.7) between particles in a reconstructed high-mass pair. The Δtime distribution for the $\pi^0\pi^0$ data is consistent with the single-bucket TVC resolution (Figure 4.8) indicating the π^0's were probably produced by the same interacting beam particle. Also shown in Figure 7.17 is the Δtime distribution for diphoton events; overlayed on these data is a fit to the shape of the $\pi^0\pi^0$ Δtime distribution. The shapes are very similar. There is one diphoton event with Δtime ≈ -50 ns ($\approx$ 2–3 bucket separation), but it is consistent with the tail of the $\pi^0\pi^0$ distribution.

The uncertainty in the energy scale has been discussed previously (Section 6.8.1) and has a 5–10% impact on the cross section (Figures 6.38, 6.39, and 6.40).

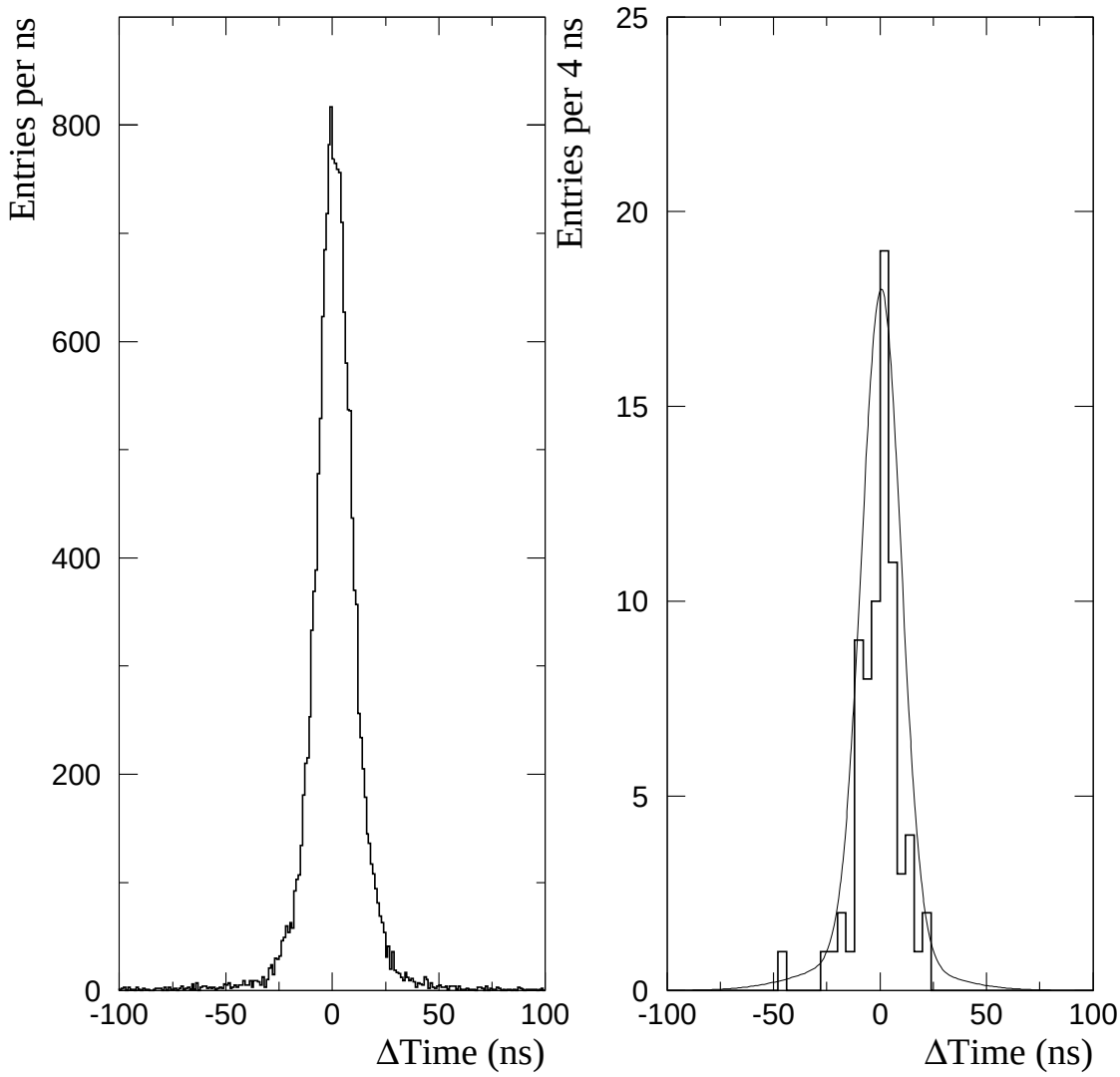

Figure 7.17 Difference in the time between left) two π^0's with $p_T^{\pi^0} > 2.5$ GeV/c from the 530 GeV/c proton sample and right) two direct-photon candidates with $p_T^{\gamma} > 4$ GeV/c from the 515 GeV/c π^- sample. A fit to shape of the $\pi^0\pi^0$ distribution has been overlayed on the diphoton data.

The uncertainty in the reconstruction efficiency (Section 5.1.4) is $\approx 3\%$ for π^0's and η's and 2% for direct photons [119]. When both particles in the pair are the same (e.g., π^0's from $\pi^0\pi^0$), then mistakes in the efficiency function affect both particles in the same manner since the efficiency functions are slowly varying functions of p_T and rapidity (e.g., Figure 5.8) and since both particles tend to have similar p_T's and rapidities. For this case, uncertainties are added linearly rather than quadratically. When the particles in the pair are different (e.g., $\gamma\pi^0$ and $\eta\pi^0$) then the uncertainties add in quadrature. The systematic uncertainty for the spectral unsmearing correction (Section 5.2.4) is approximately 3%. The correction for the geometrical acceptance (Section 7.5) has a systematic uncertainty of $\approx 2\%$. There are additional small ($< 0.5\%$) uncertainties for the corrections described in Section 7.4.

The systematic uncertainties associated with the background subtractions are slightly more complicated than the uncertainties discussed above. The impact of these uncertainties on the cross section depends upon the size of the subtraction. The method used in the parameterized Monte Carlo (Section 5.2) to produce background photons (Section 5.2.3) introduces $\approx 3\%$ systematic uncertainty [128]. The parameterized Monte Carlo was required to reproduce b_γ/s_{π^0} (Figure 5.22) from the full Monte Carlo, adding another $\approx 3\%$ uncertainty. Each of these uncertainties enters twice for the diphoton subtraction. The parameterization of the two arm production spectra (Section 5.2.1) added an additional 2–5% systematic uncertainty with another $\approx 1.5\%$ due to the relative normalization between the Monte Carlo and the data.

Chapter 8 Production of High-Mass Pion Pairs

In this chapter we present measurements of pairs of π^0 mesons produced by 515 GeV/c π^- and π^+ beams and 530 GeV/c and 800 GeV/c proton beams incident upon beryllium, copper, and hydrogen targets. Tables for these, and supporting, measurements can be found in Appendix A. Unless otherwise noted, there is a minimum p_T requirement on each π^0 of 2.5 GeV/c. Pions were also required to be central, with rapidities of $-0.8 < y < 0.8$ for the 0.5 TeV/c beams and $-1.05 < y < 0.55$ for the 0.8 TeV/c beam. The azimuthal angle between the π^0's was required to be at least 105°.

All theory curves [11] presented in this chapter use the BKK fragmentation function [20]. The fragmentation scale was fixed at $m_F = {p_T}^{\pi^0}/2$. The parton distribution function used was GRV92LO [18] for the data produced by pion beams and CTEQ4L [17] for the data produced by proton beams.

8.1 Cross Section Measurements

We can test pQCD theory by comparing the calculated and measured cross sections as functions of several variables. Mass is a useful variable for this purpose as it is invariant under transverse boosts and therefore insensitive to k_T effects (excepting for smearing across the p_T cut). Other variables insensitive to k_T effects include ${p_T}^{\pi^0}$ (for symmetric p_T cuts [30]), rapidity, and $\cos\theta^\star$.

8.1.1 Mass Distributions

The dipion mass spectrum for π^-Be interactions is presented in Figure 8.1. The cross section rises at low mass, peaks, and then falls exponentially with increasing mass; this shape is due to the minimum p_T requirement. The π^0's are

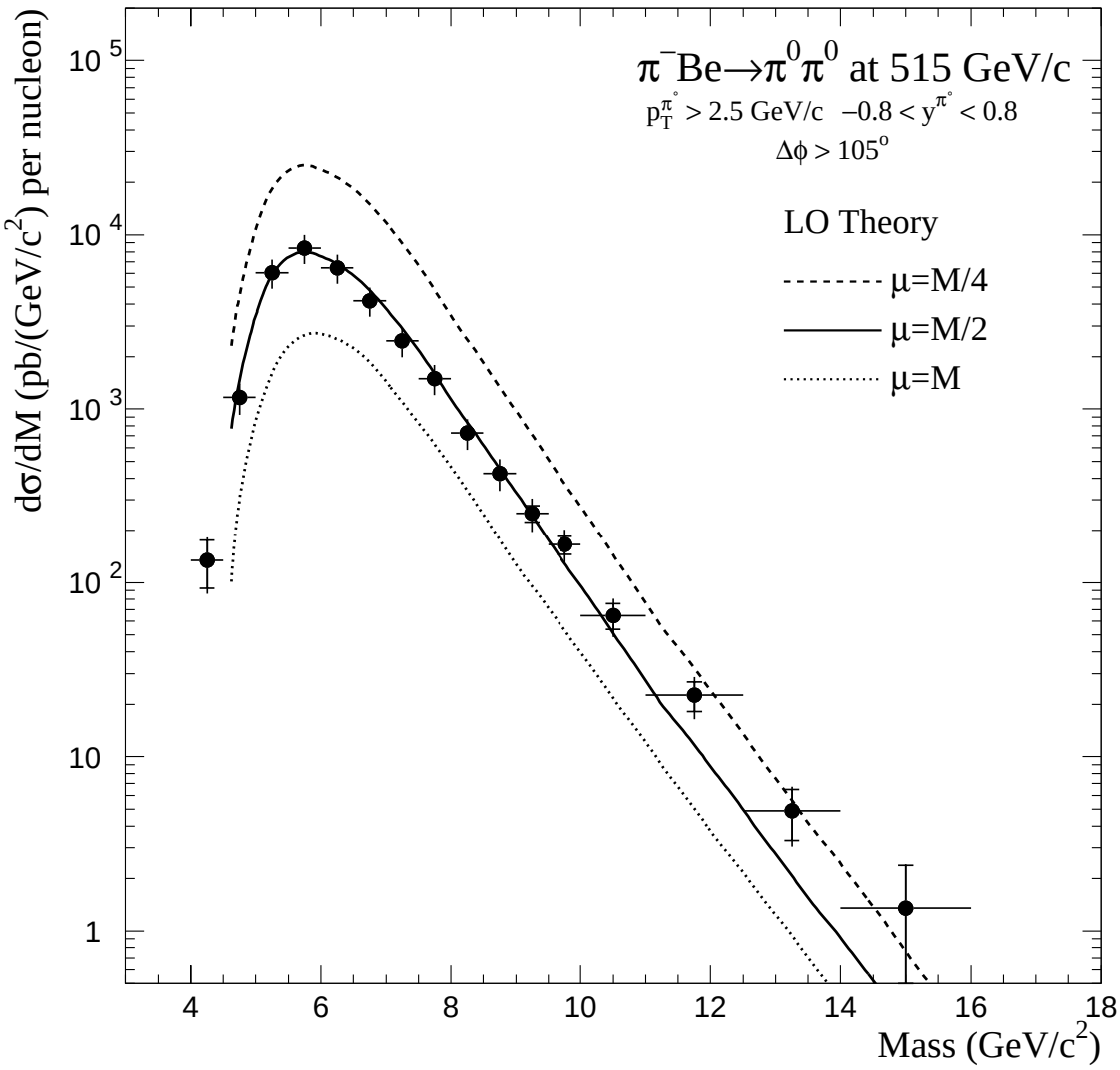

Figure 8.1 The dipion mass distribution produced by 515 GeV/c π^- incident on beryllium. The results of corresponding LO theory calculations [11] for several choices of scale are also shown.

jet fragments, therefore, a p_T requirement placed upon the π^0 causes an uneven sampling of the parent dijet mass spectrum. This bias is worst for dipion masses close to threshold, $M \approx 2p_T^{\pi^0}$, and decreases with increasing mass. Eventually, the mass is sufficiently large that this bias is negligible; the cross section then decreases with increasing mass[1]. This effect is illustrated in Figure 8.2 where the dipion mass spectrum is shown for several symmetric $p_T^{\pi^0}$ choices. The unbiased distribution ($p_T^{\pi^0} > 1.5$ GeV/c has no impact for the mass range shown) is exponentially falling. The mass distributions with larger $p_T^{\pi^0}$ requirements display peaked shapes; the spectra smoothly match for masses sufficiently large compared to the $p_T^{\pi^0}$ threshold.

The results from a LO pQCD theory calculation [11] for several choices of factorization scale are also shown in Figure 8.1. (The fragmentation scale was $p_T^{\pi^0}/2$ for each of these curves.) The scale $\mu = M/2$ provides a reasonable representation of the data over most of the mass range; this scale will be used as the default for all comparisons for all data samples (Figure 8.3). The theory characterizes the data normalization and shape, however, it appears to systematically underestimate the cross section at high mass. Similar distributions are presented for the hydrogen target in Figure 8.4. There is a similar level of agreement between the data and theory.

Two other experiments, CCOR [139] and NA24 [67], have published $\pi^0\pi^0$ measurements as a function of the mass of the pair. Both experiments used a more restrictive set of kinematic requirements than is used above; these cuts were intended to select a back-to-back sample of dipions. They required the

[1] k_T smearing across the $p_T^{\pi^0}$ threshold produces a similar, though smaller, effect. This effect is most visible for $M < 2p_T^{\pi^0}$ since the events cannot pass the kinematic requirements unless there is a non-zero k_T.

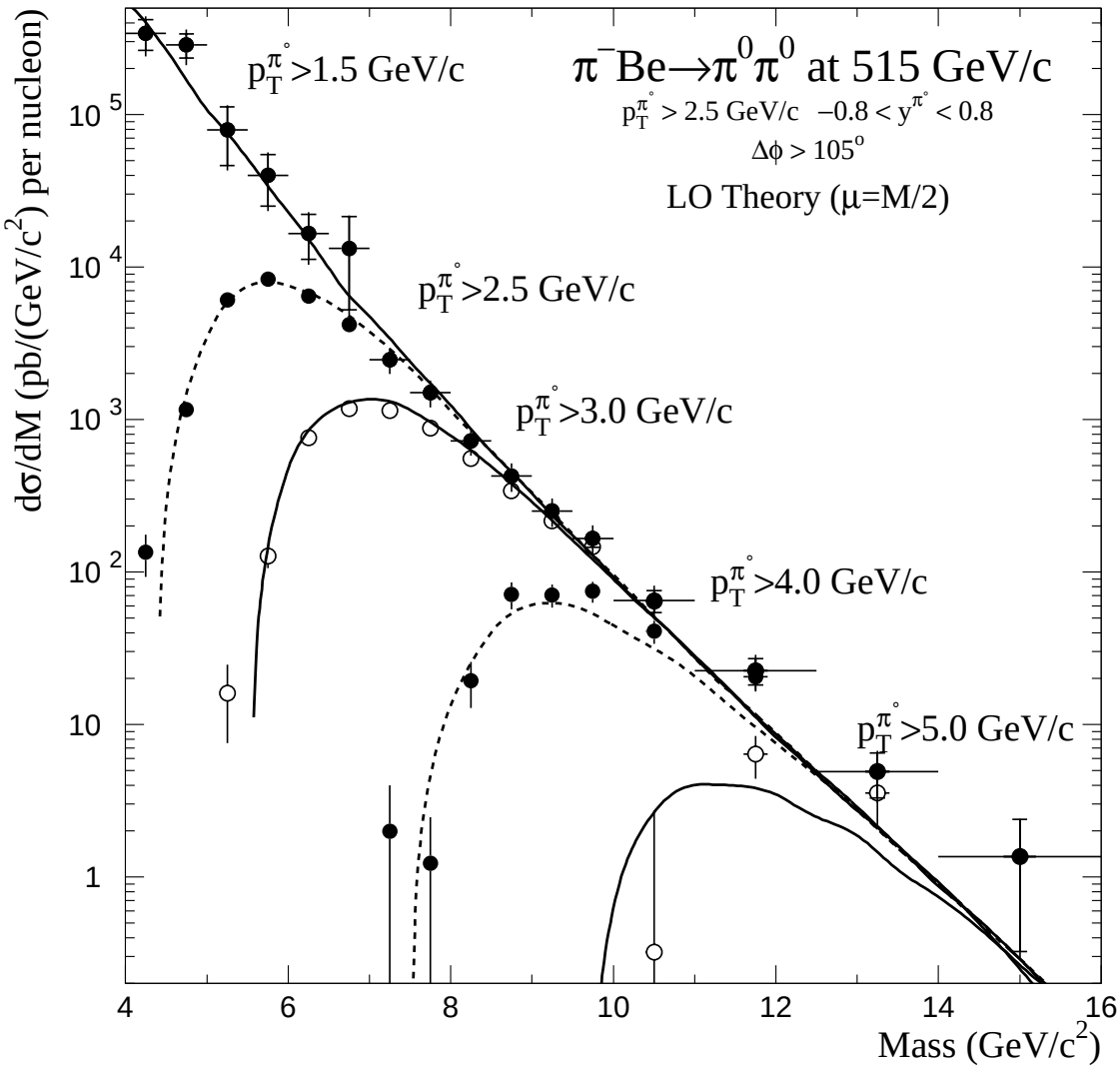

Figure 8.2 The dipion mass distribution for several different minimum $p_T^{\pi^0}$ requirements. Systematic uncertainties have only been displayed for the $p_T^{\pi^0} > 1.5$ GeV/c points. The results of corresponding LO theory calculations [11] are also shown.

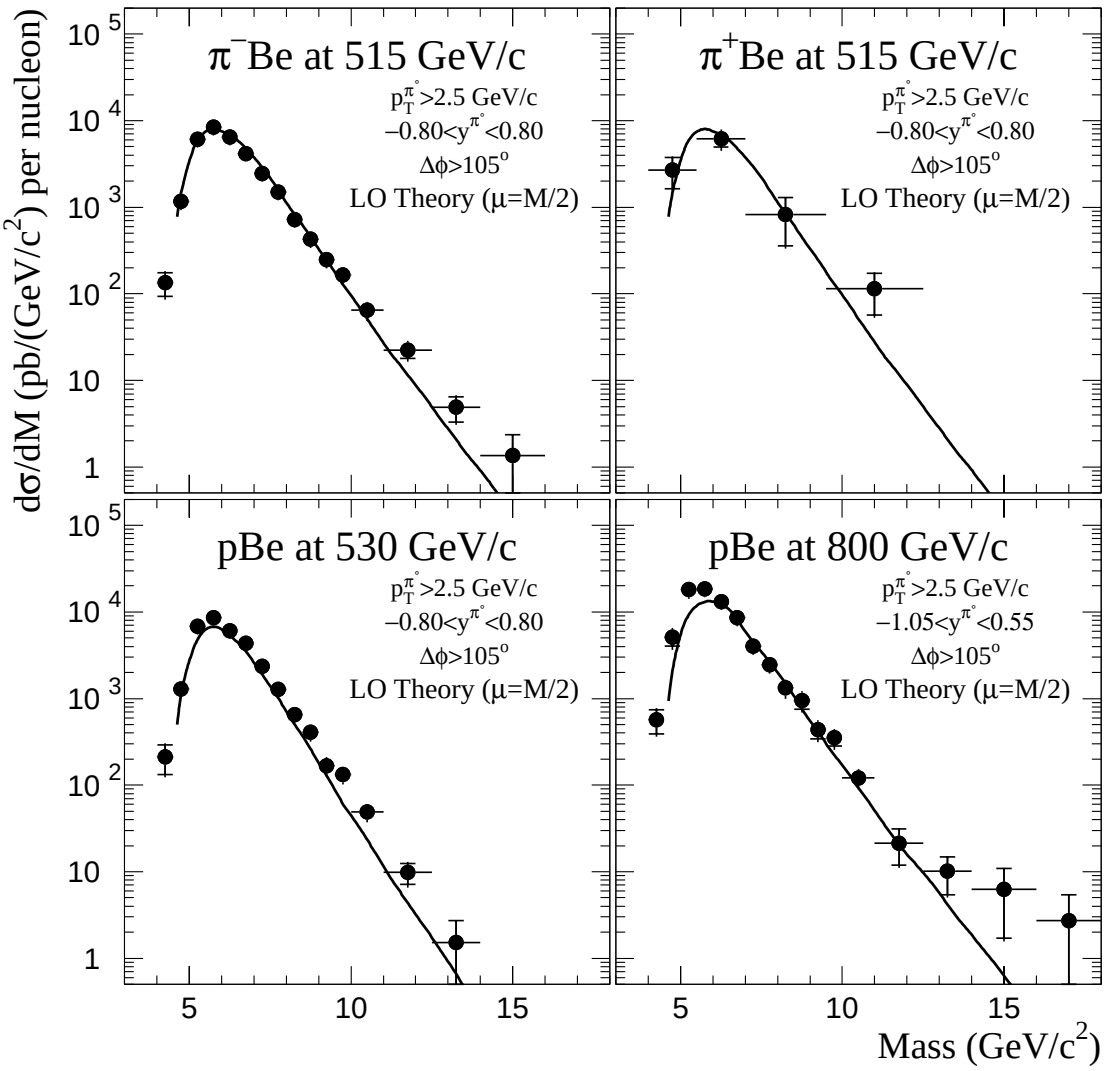

Figure 8.3 The dipion mass distribution produced by interactions of various beams on beryllium. The results of corresponding LO theory calculations [11] are also shown.

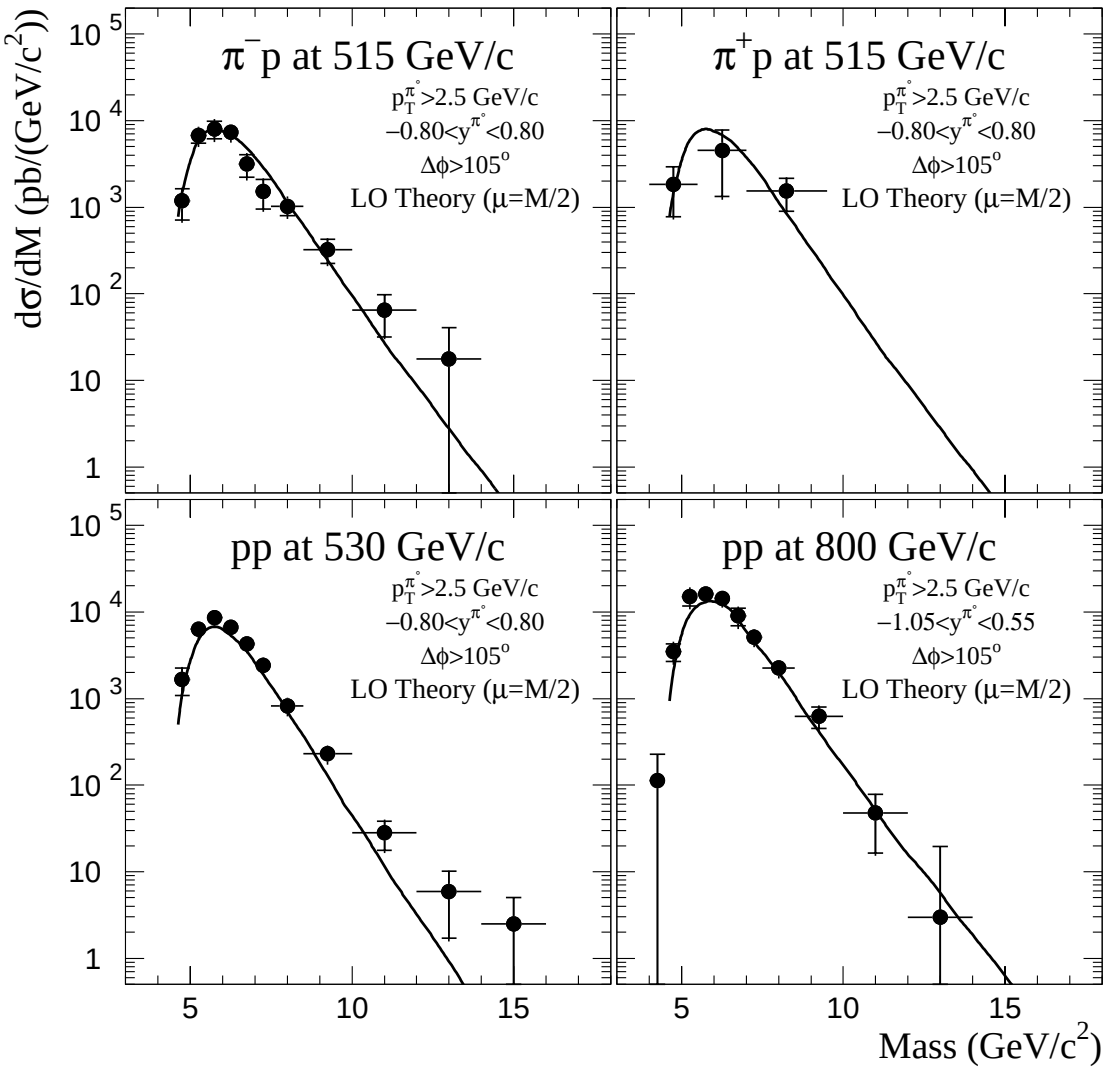

Figure 8.4 The dipion mass distribution produced by interactions of various beams on hydrogen. The results of corresponding LO theory calculations [11] are also shown.

azimuthal angle between the pions to be $\Delta\phi > 140°$, the rapidity of the pair to be $-0.35 < Y < 0.35$, and $|\cos\theta^\star| < 0.4$. They also required the total transverse momentum of the dipion system to be less than 1 GeV/c. Figure 8.5 is a comparison with the more restrictive requirements applied to the E706 data. Figure 8.6 is a comparison that uses the full range of our data. In both cases, the comparisons are made as Data/Theory ratios as a function of the scaling variable $\sqrt{\tau} \equiv M/\sqrt{s}$.

There are two different versions of the LO theory in Figures 8.5 and 8.6. The top plots in each figure use the LO theory without k_T ($\langle k_T \rangle = 0$ GeV/c). For the data to theory ratios in the bottom plots, we used $\langle k_T \rangle = 1.7$ GeV/c and 1.4 GeV/c for the CCOR experiment [28] at $\sqrt{s} = 62.4$ GeV and 44.7 GeV respectively. For E706 ($\sqrt{s} = 31.6$ GeV and 38.8 GeV) we used $\langle k_T \rangle = 1.4$ GeV/c, and for NA24 ($\sqrt{s} = 23.7$ GeV) we used $\langle k_T \rangle = 0.9$ GeV/c. Even though $\sqrt{\tau}$ should be unaffected by the addition of k_T to the system, there are noticeable differences between the top and bottom plots. In the case of Figure 8.5 these differences are principally due to the $Q_T < 1$ GeV/c requirement; this requirement has a strong impact on the theory as a function of input k_T. Since all three experiments have the same requirement, and since both the CCOR and NA24 experiments imposed minimum mass requirements to avoid ${p_T}^{\pi^0}$ threshold effects, the addition of k_T primarily changes the normalization. For the E706 data, there are additional differences at low $\sqrt{\tau}$ (corresponding to the peak region of the mass spectrum) as this region of mass is somewhat sensitive to k_T effects because of the ${p_T}^{\pi^0}$ requirements.

The restricted kinematic requirements were removed from the E706 data in Figure 8.6. Here the differences between the E706 data and the CCOR and NA24 samples are considerably larger when there is no k_T added to the LO theory.

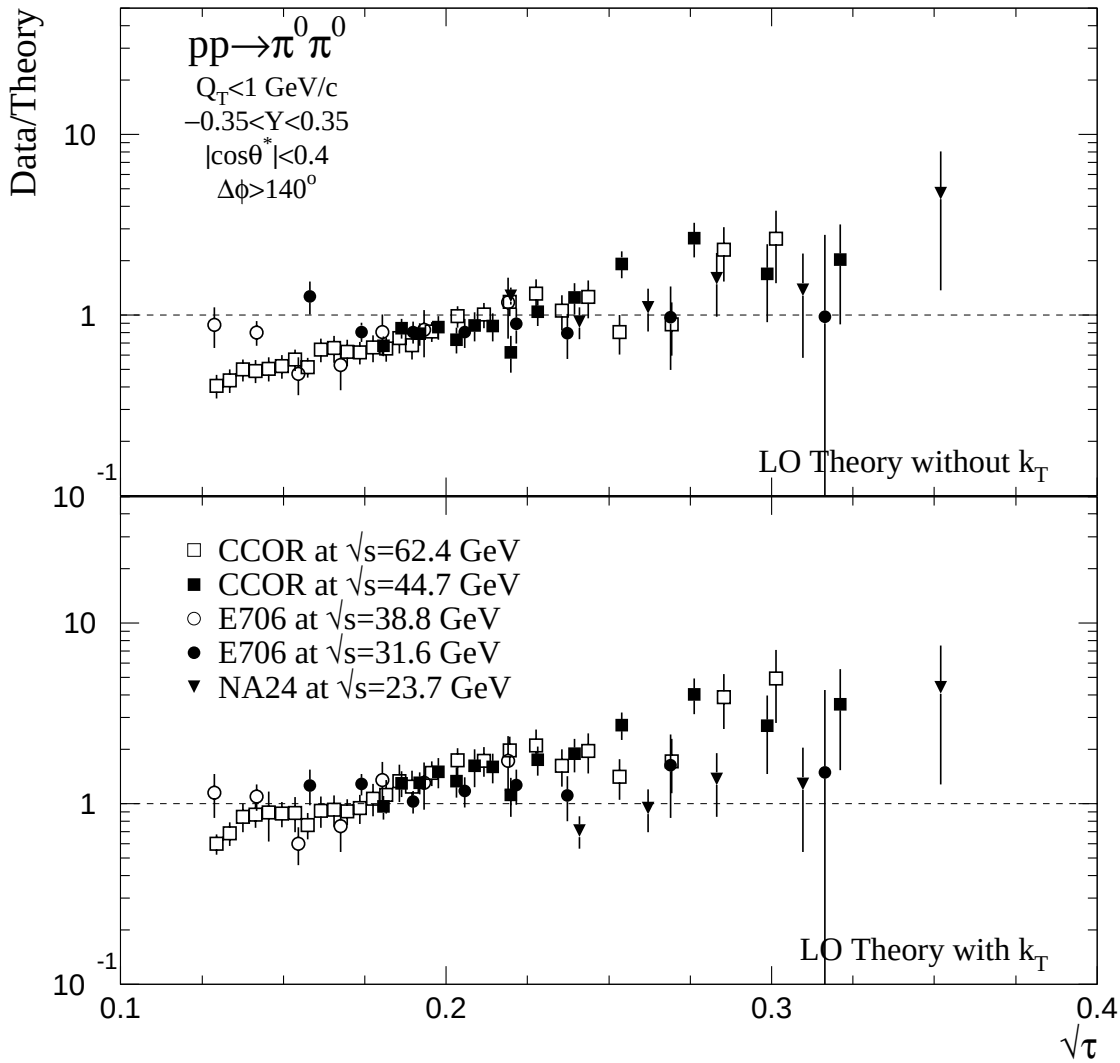

Figure 8.5 Data to theory comparison for $\pi^0\pi^0$ data produced in pp interactions from NA24, E706, and CCOR. Each sample has the same kinematic requirements. The LO theory [11] is described in the text; the theory in the top plot has $\langle k_T \rangle = 0$ GeV/c, the theory in the bottom plot has $\langle k_T \rangle$ as described in the text.

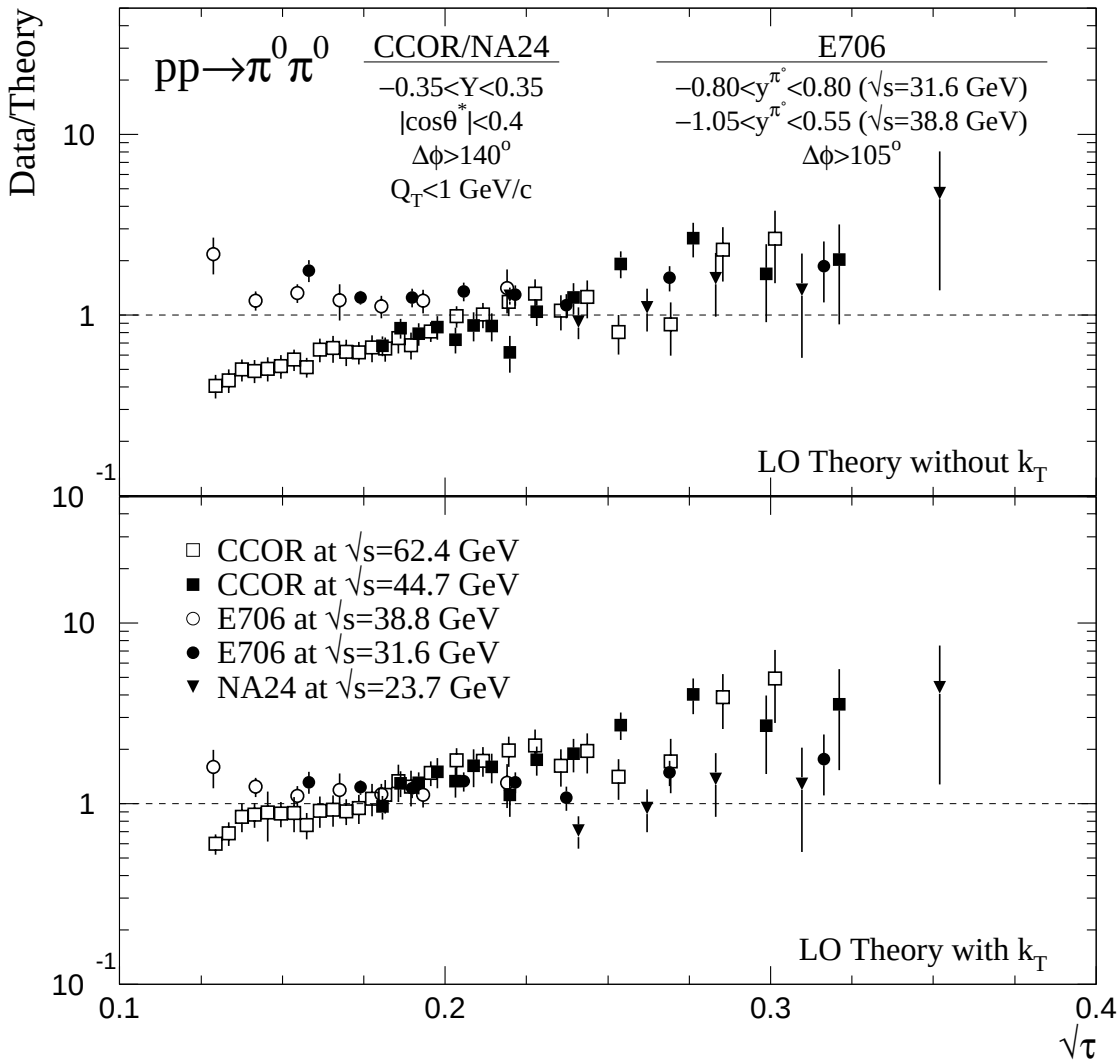

Figure 8.6 Data to theory comparison for $\pi^0\pi^0$ data produced in pp interactions from NA24, E706, and CCOR. The NA24 and CCOR data are the same as in Figure 8.5; the E706 data has the kinematic requirements used in Figure 8.4. The LO theory is described in the text; the theory in the top plot has $\langle k_T \rangle = 0$ GeV/c, the theory in the bottom plot has $\langle k_T \rangle$ as described in the text.

However, since the standard set of E706 kinematic requirements do not include cuts that strongly bias against k_T, there are only slight differences in the data to theory ratio for the without-k_T and with-k_T comparisons. (There are still some differences as explained above.) In both Figures 8.5 and 8.6, the E706 data compares well with the CCOR and NA24 data samples. There is general agreement for all of the $\pi^0\pi^0$ data.

E711 has published measurements of the production of high-mass pairs of charged pions in pBe interactions at 800 GeV [140]. Since we have a corresponding sample, we can directly compare the cross sections as a function of mass from the two experiments. Figure 8.7 displays the E711 data along with the E706 data (with the E711 kinematic requirements). For this comparison, since E711 measured $\pi^+\pi^-$, we have reduced their cross section by a factor of two to account for the difference in the number of final states. The two data samples agree rather well in both slope and normalization. There is some disagreement in the lowest mass bin, however, this is probably due to the different minimum ${p_T}^{\pi^0}$ requirements — the lowest E706 data point is affected by these requirements while the E711 data points are presented for masses that are insensitive to their ${p_T}^{\pi^0}$ requirements.

The LO pQCD theory has a large scale dependence and mismatches the data in several key areas (particularly at large mass) indicating that higher order terms can be significant. A NLO calculation of $\pi^0\pi^0$ production exists [141], however, results are not available for the range populated by our data. For self-consistency, this theory requires sufficiently high p_T cuts that few data statistics remain for comparison. In addition, this calculation integrates analytically over transverse elements making it difficult to compare against k_T-sensitive variables [142]. Another group has undertaken the effort to produce a NLO calculation that can also include resummed contributions [143], however, that result is not anticipated to be available for some time.

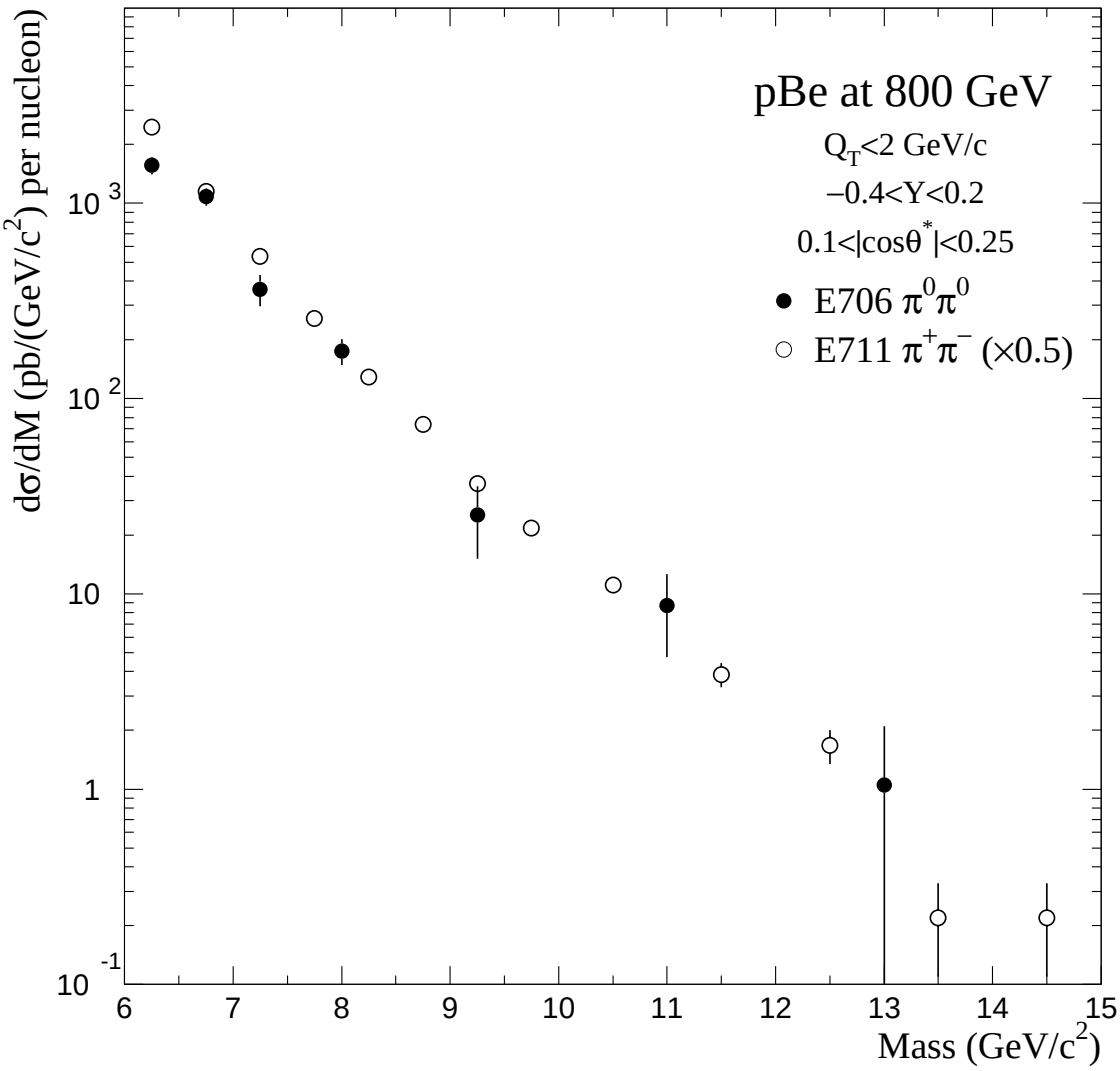

Figure 8.7 Comparison between the $\pi^0\pi^0$ cross section measured by E706 and the $\pi^+\pi^-$ cross section measured by E711 in pBe interactions at 800 GeV/c. For this comparison, the E711 kinematic requirements were placed on the E706 data. The E711 charged dipion cross section was reduced by a factor of two to account for the difference in the final states.

8.1.2 Pion Transverse Momentum

Another set of distributions that can be used to test the theory is the distribution of ${p_T}^{\pi^0}$. This projection is insensitive to k_T effects as long as both π^0's have symmetric p_T requirements [30]. The dipion ${p_T}^{\pi^0}$ spectrum for pBe interactions at 800 GeV/c is presented in Figure 8.8. There are two entries per pair. Results of calculations for several choices of factorization scales are presented. The calculation provides a reasonable description of the data using the scale $\mu = M/2$. Figures 8.9 and 8.10 display the ${p_T}^{\pi^0}$ spectrum for each of our four beam samples for data accumulated on the beryllium and hydrogen targets respectively. The theory provides a reasonable match to the data, although there are small slope differences (corresponding with the differences observed in the mass distributions).

8.1.3 Angular Distributions

Another way to test pQCD is to measure the parton–parton scattering angular distribution. For $\pi^0\pi^0$ production, the angular distribution is expected to be sharply peaked in the forward and backward directions (Section 1.2.3). The angular distribution is typically parameterized as in Equation 1.9. Experimentally, the $\cos\theta^\star$ distribution can be biased by detector acceptance and minimum p_T requirements. Since $\cos\theta^\star$ is related to rapidity, the amount of boost ($\eta_{\rm boost}$) between the hadron–hadron and parton–parton center-of-momentum systems can be used to ensure the $\cos\theta^\star$ distribution is populated evenly across the detector [87]. The size of this requirement depends upon the desired range in $\cos\theta^\star$. For measurements around $\cos\theta^\star = 0$, the full detector acceptance is available, $|\eta_{\rm boost}| < 0.8$. As the range of $\cos\theta^\star$ increases, the $\eta_{\rm boost}$ requirement must be tightened to ensure unbiased coverage. The measurement of $\cos\theta^\star$ over

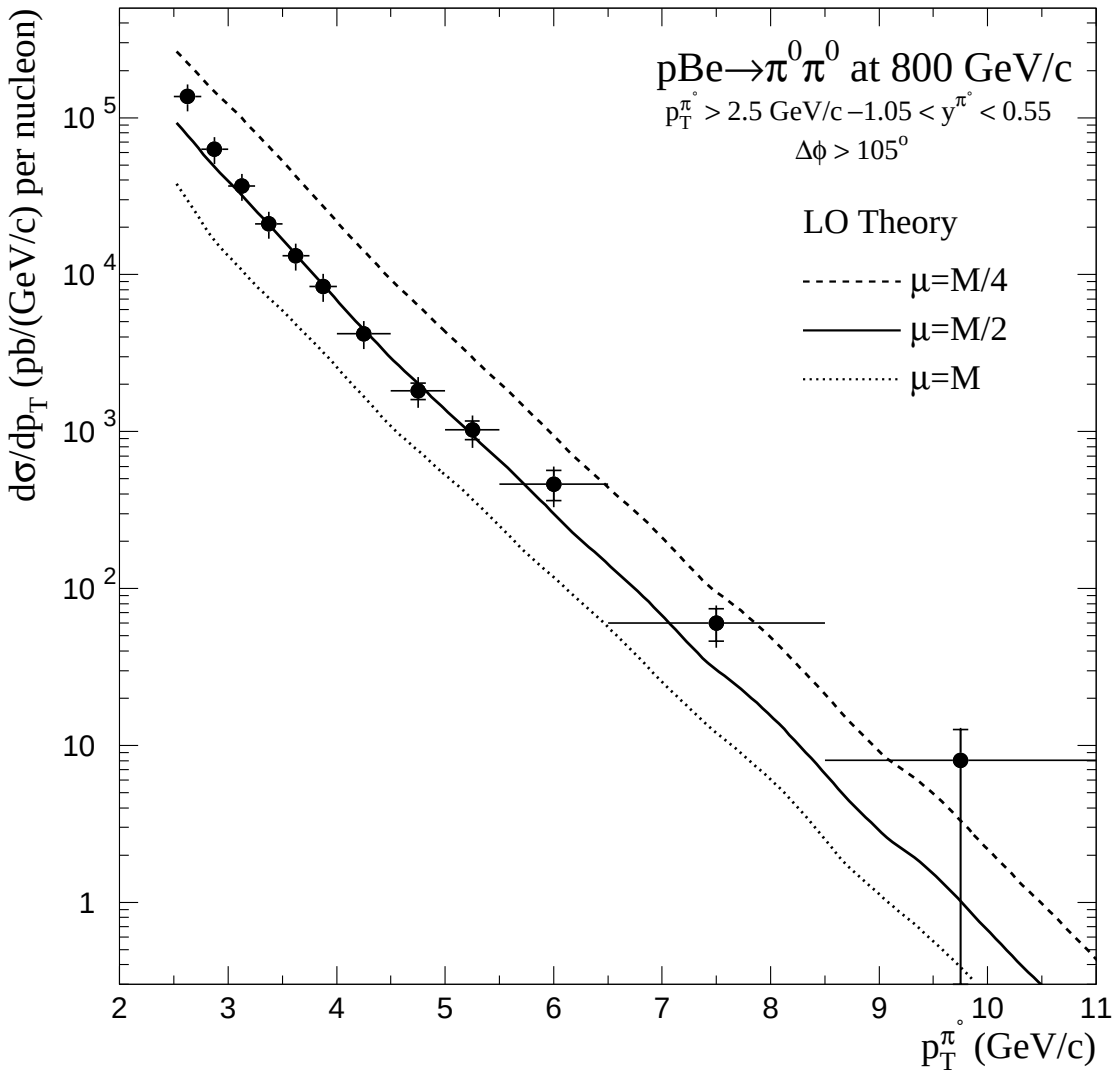

Figure 8.8 The dipion $p_T^{\pi^0}$ distribution produced by 800 GeV/c protons incident on beryllium. There are two entries per pair. The results of corresponding LO theory calculations [11] for several choices of scale are also shown.

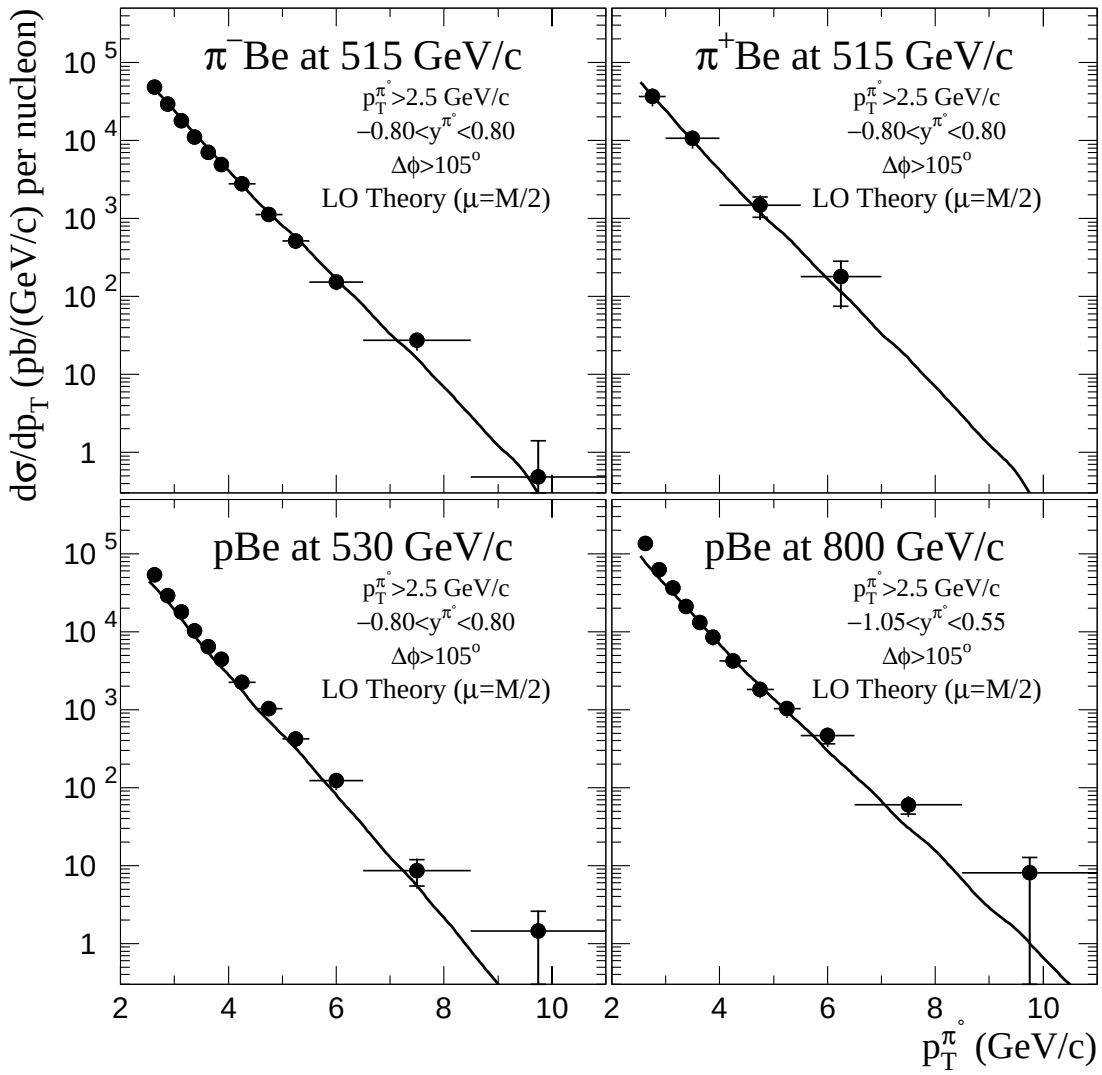

Figure 8.9 The dipion $p_T^{\pi^0}$ distribution produced by interactions of various beams on beryllium. There are two entries per pair. The results of corresponding LO theory calculations [11] are also shown.

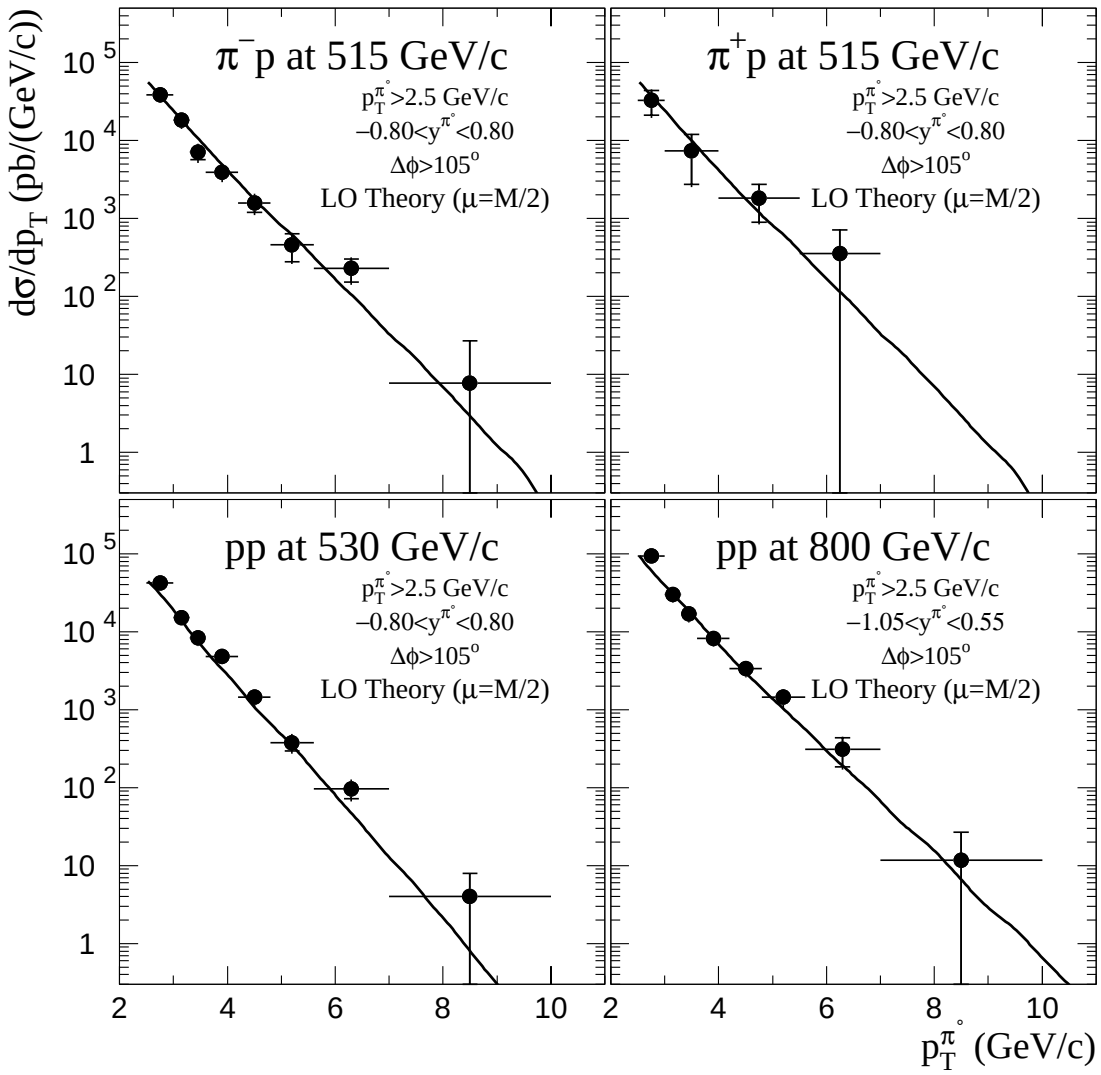

Figure 8.10 The dipion $p_T^{\pi^0}$ distribution produced by interactions of various beams on hydrogen. There are two entries per pair. The results of corresponding LO theory calculations [11] are also shown.

the range $|\cos\theta^\star| < 0.5$ requires $|\eta_{\rm boost}| < 0.25$. An additional mass requirement is placed on the data to avoid ${p_T}^{\pi^0}$ threshold effects [144]. This prevents low mass regions, which are heavily populated and which have a limited phase space (due to the ${p_T}^{\pi^0}$ requirement), from dominating the measurement.

The $\cos\theta^\star$ distributions for the 0.5 TeV/c π^- and proton samples are displayed in Figure 8.11. The measurement was normalized (using the parameterization) at $\cos\theta^\star = 0$. The parameter α was determined to be $\alpha = 2.7 \pm 0.2 \pm 0.3$ for the π^- data and $\alpha = 2.5 \pm 0.2 \pm 0.3$ for the proton data. The CCOR [139] and E711 [140] experiments measured this parameter with incident proton beams. CCOR measured[2] $\alpha = 2.97 \pm 0.05 \pm 0.2$ for $\pi^0\pi^0$ while E711 measured $\alpha = 3.01 \pm 0.04 \pm 0.5$ and $\alpha = 3.30 \pm 0.07 \pm 0.5$ for opposite sign and same sign dihadron data respectively. Our measurements of α are slightly smaller than the values reported by CCOR and E711.

The results from the theoretical calculation (with the same physics cuts) are also overlayed on the data in Figure 8.11. The LO theory is systematically less steep than the data. E711 finds this result as well.

A comparison is also made for rapidity of the pion pair in four mass bins (Figure 8.12). The peaked structure of the $\pi^0\pi^0$ rapidity distribution is due to the π^0 rapidity cuts.

[2] CCOR employed a global fit to their data incorporating the mass dependence of their $\cos\theta^\star$ distributions.

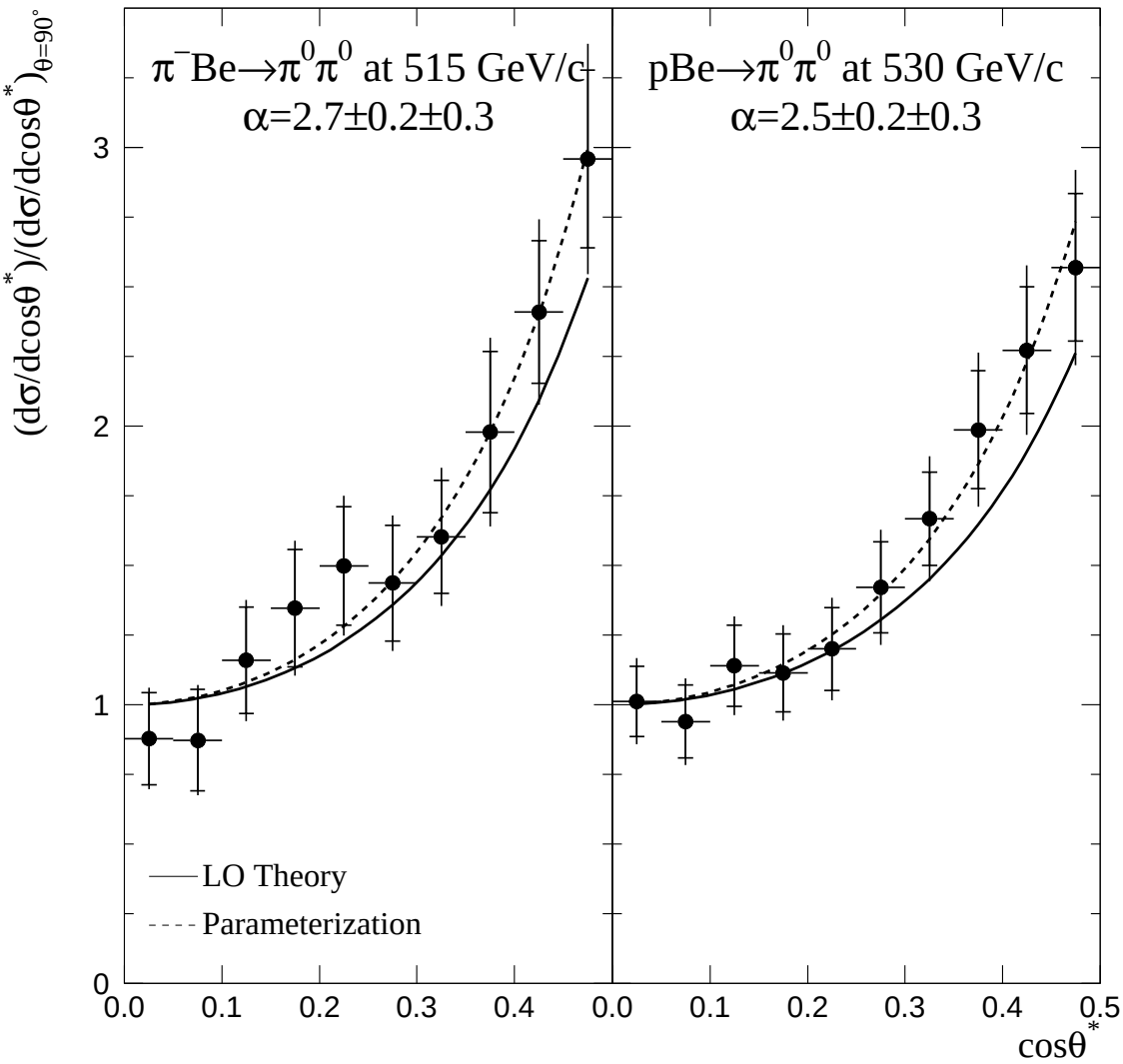

Figure 8.11 Dipion distributions in $\cos\theta^\star$ for the 515 GeV/c π^-Be data (M > 7.5 GeV/c) and the 530 GeV/c pBe data (M > 7.0 GeV/c). The parameterization refers to Equation 1.9 (dashed curve); the data was normalized at $\cos\theta^\star = 0$ using this function. Also overlayed are the results from the LO theory calculation [11] (solid curve).

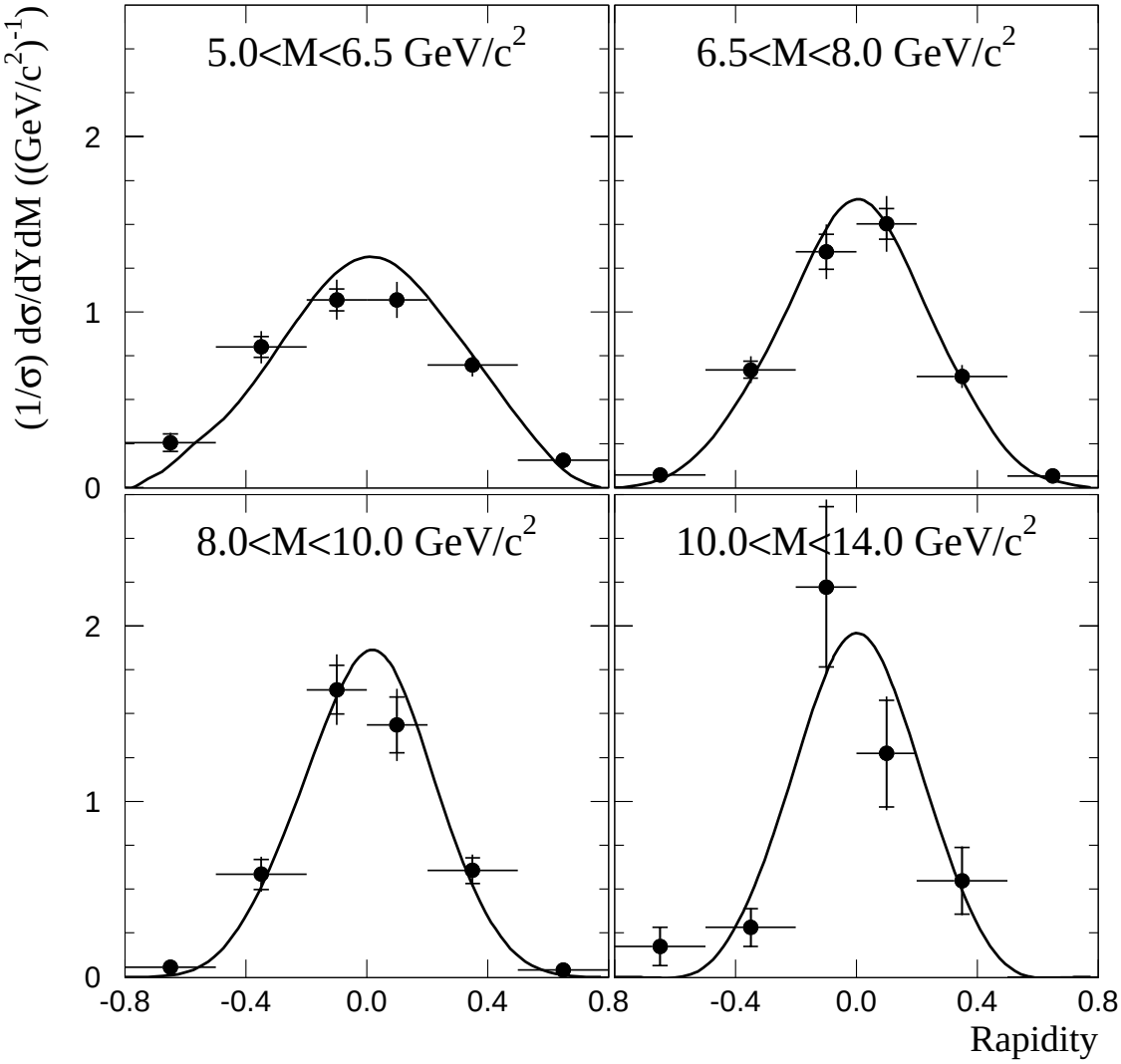

Figure 8.12 The dipion rapidity distribution in several mass bins produced by 530 GeV/c protons incident on beryllium. Additional requirements on the combinations contributing to this distribution are summarized at the beginning of Chapter 8. The results of corresponding LO theory calculations [11] are also shown.

8.2 Kinematic Correlations

Correlations between high-p_T π^0's can be used to investigate the transverse momentum of partons (k_T) prior to the hard scatter (Section 1.2.4). Dipion events are more complicated to interpret than dijet, diphoton, or dimuon events since the π^0's are jet fragments and consequently have additional transverse momentum (q_T) with respect to the jet axis and also are affected by longitudinal fragmentation effects. The LO pQCD theory [11] used in this study provides for both k_T and q_T effects through a Gaussian smearing model [145].

Several kinematic quantities were used to study k_T in the dipion system. These included the azimuthal angle between the π^0's ($\Delta\phi$), the momentum in and out of the plane (p_{IN} and p_{OUT}), the total p_T of the pair (Q_T), and the p_T-balance of the two π^0's (z). Interpreting these variables as representations of k_T outside the LO theory framework is difficult as each variable is affected to some degree by longitudinal fragmentation effects (Section 1.2.4). Some variables are more sensitive to these effects than others. Figure 8.13 shows the average azimuthal angle between the two π^0's as a function of the $\pi^0\pi^0$ mass. Overlayed on the data are two results from the LO theory. The dashed line represents the case when there is no additional transverse momentum added to the system ($\langle k_T \rangle = 0$ GeV/c and $\langle q_T \rangle = 0$ GeV/c) so that the results are purely due to longitudinal fragmentation effects. For this case, the π^0's are back-to-back as the fragmentation function doesn't affect the angular distribution. The $\langle \Delta\phi \rangle$ distribution is, however, affected by the incorporation of transverse momentum (k_T and q_T). These results are represented by the solid curve; on average, the π^0's are no longer back-to-back.

Fixing $\langle q_T \rangle = 600$ MeV/c [28, 29], we can vary k_T in the LO theory to estimate its effect upon the shape of the $\Delta\phi$ distributions as illustrated in Figure 8.14. Here

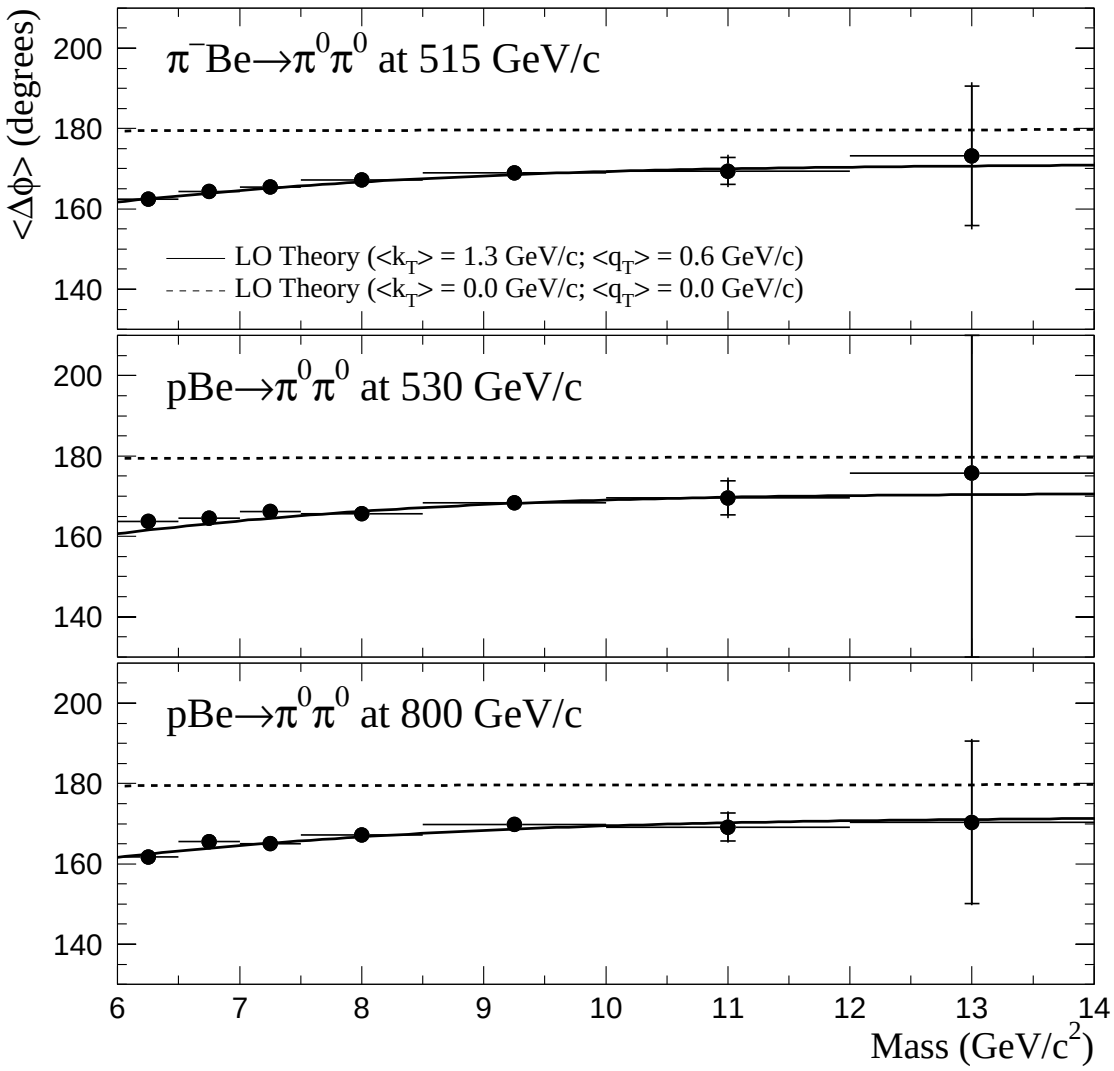

Figure 8.13 Average values of $\Delta\phi$ as a function of mass for $\pi^0\pi^0$ pairs. Curves from the LO theory [11] are overlayed on the data.

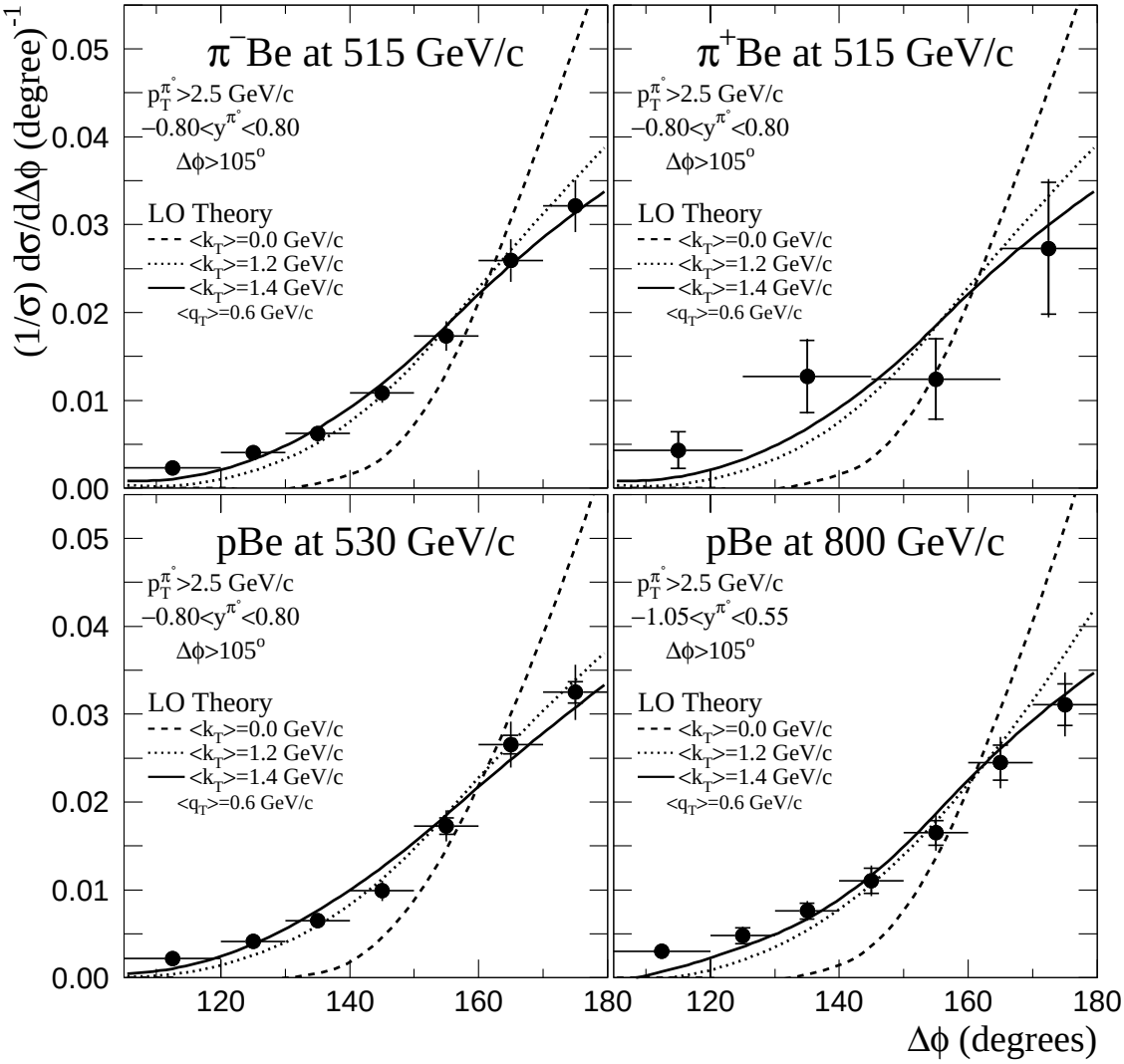

Figure 8.14 The dipion $\Delta\phi$ distribution produced by interactions of various beams on beryllium. The results of corresponding LO theory calculations [11] are also shown.

the dotted curve represents the theoretical shape with $\langle k_T \rangle = 0.0$ GeV/c. This distribution is too narrow to match well with the data. Two additional curves are overlayed on the data, one with $\langle k_T \rangle = 1.2$ GeV/c (dashed) and one with $\langle k_T \rangle = 1.4$ GeV/c (solid). (The spread in these values is provided to illustrate the impact of small changes in k_T.) The curves with non-zero k_T better represent the data. Similar distributions measured for the hydrogen target are given in Figure 8.15.

Average values for selected kinematic quantities (p_{OUT}, p_{IN}, and Q_T) as a function of mass are shown in Figure 8.16. The size of the longitudinal fragmentation contribution varies for these variables. Like $\Delta\phi$, p_{OUT} is not very sensitive to these longitudinal fragmentation effects. Variables such as Q_T and p_{IN} (and the π^0 p_T-balance, z) are sensitive to them and, consequently, are less sensitive to the impact of k_T. The LO theory includes both the transverse and longitudinal contributions and successfully characterizes these data distributions.

Shape comparisons between the data and the theory for these variables are presented in Figures 8.17, 8.18, 8.19, and 8.20 in the same fashion as the $\Delta\phi$ comparisons above. For p_{OUT}, the shapes of the $\langle k_T \rangle = 0$ GeV/c curves are narrower than the data and the non-zero k_T curves reasonably reproduce the shape of the data distributions. The other distributions (p_{IN}, Q_T, and z), are less sensitive to k_T effects; still, the theory with k_T represents the data better than the theory without k_T. These distributions were measured with data from interactions in the beryllium target. Corresponding comparisons for data from interactions in the hydrogen target for p_{OUT} (Figure 8.21) and p_{IN} (Figure 8.22) are also shown. As with the $\Delta\phi$ distributions, the theory also agrees with the hydrogen data.

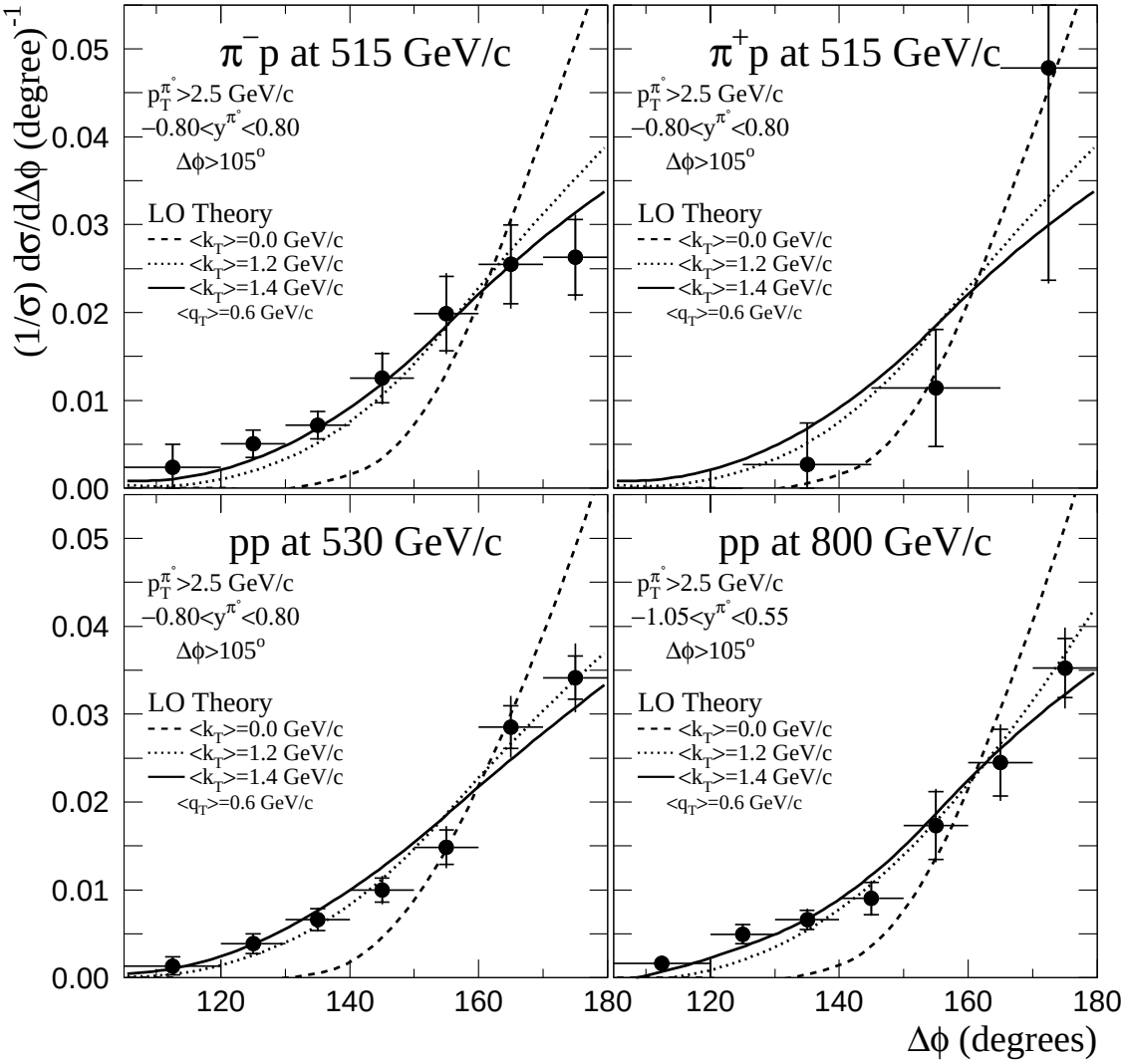

Figure 8.15 The dipion $\Delta\phi$ distribution produced by interactions of various beams on hydrogen. The results of corresponding LO theory calculations [11] are also shown.

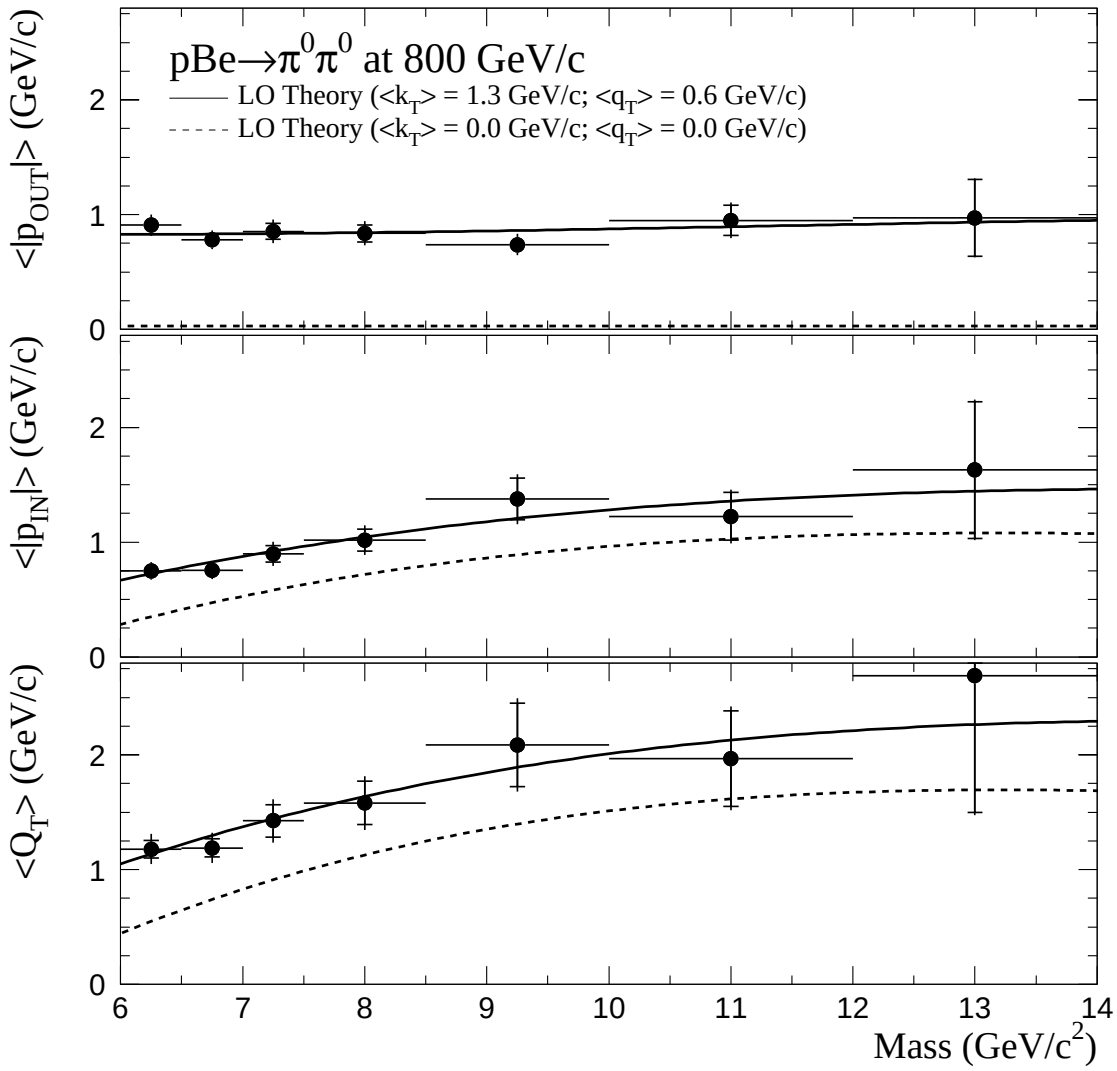

Figure 8.16 Average values of selected kinematic quantities as functions of mass for $\pi^0\pi^0$ pairs produced by pBe interactions at 800 GeV/c. Curves from the LO theory [11] are overlayed on the data.

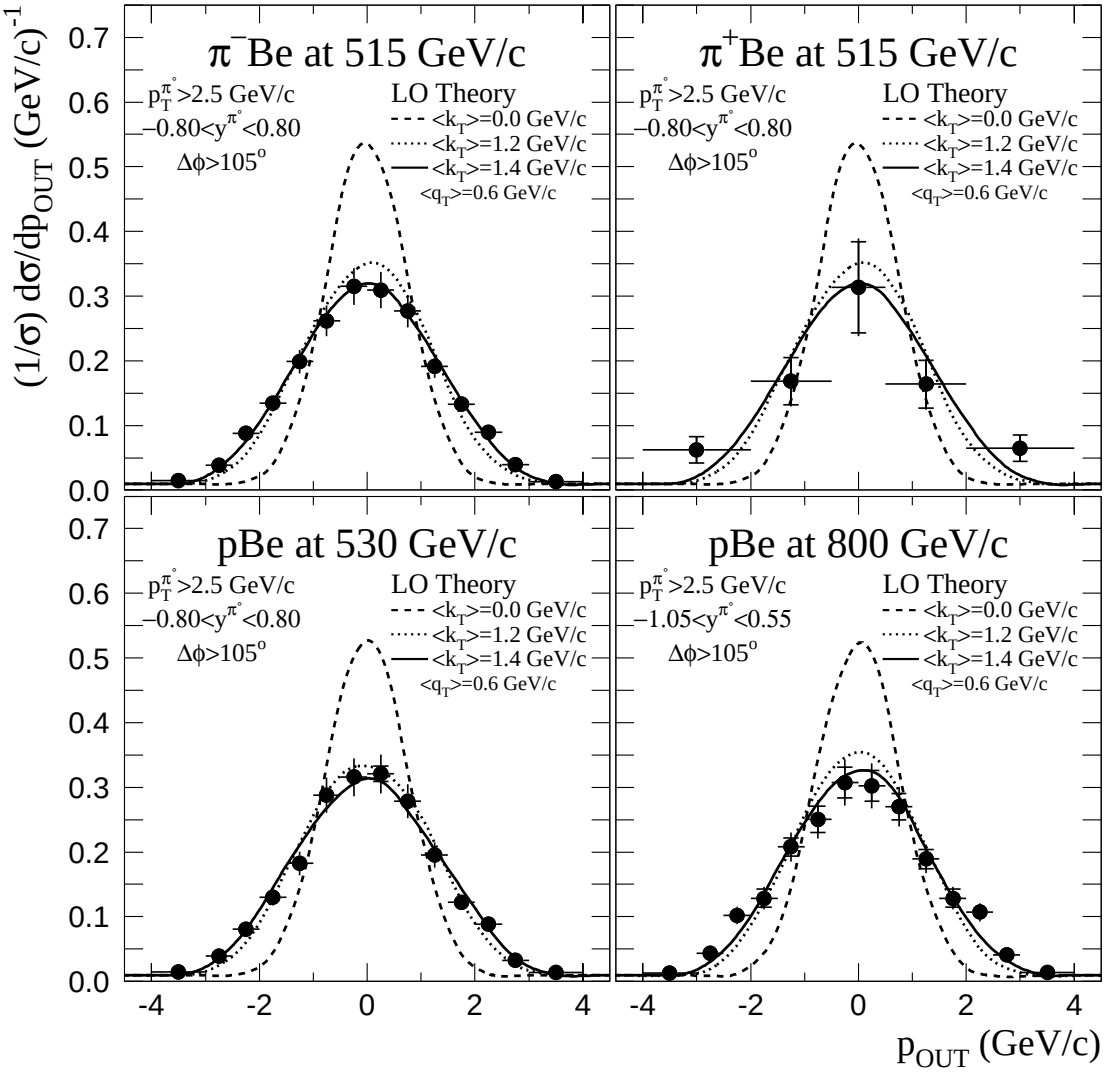

Figure 8.17 The dipion p_{OUT} distribution produced by interactions of various beams on beryllium. There are two entries per pair. The results of corresponding LO theory calculations [11] are also shown.

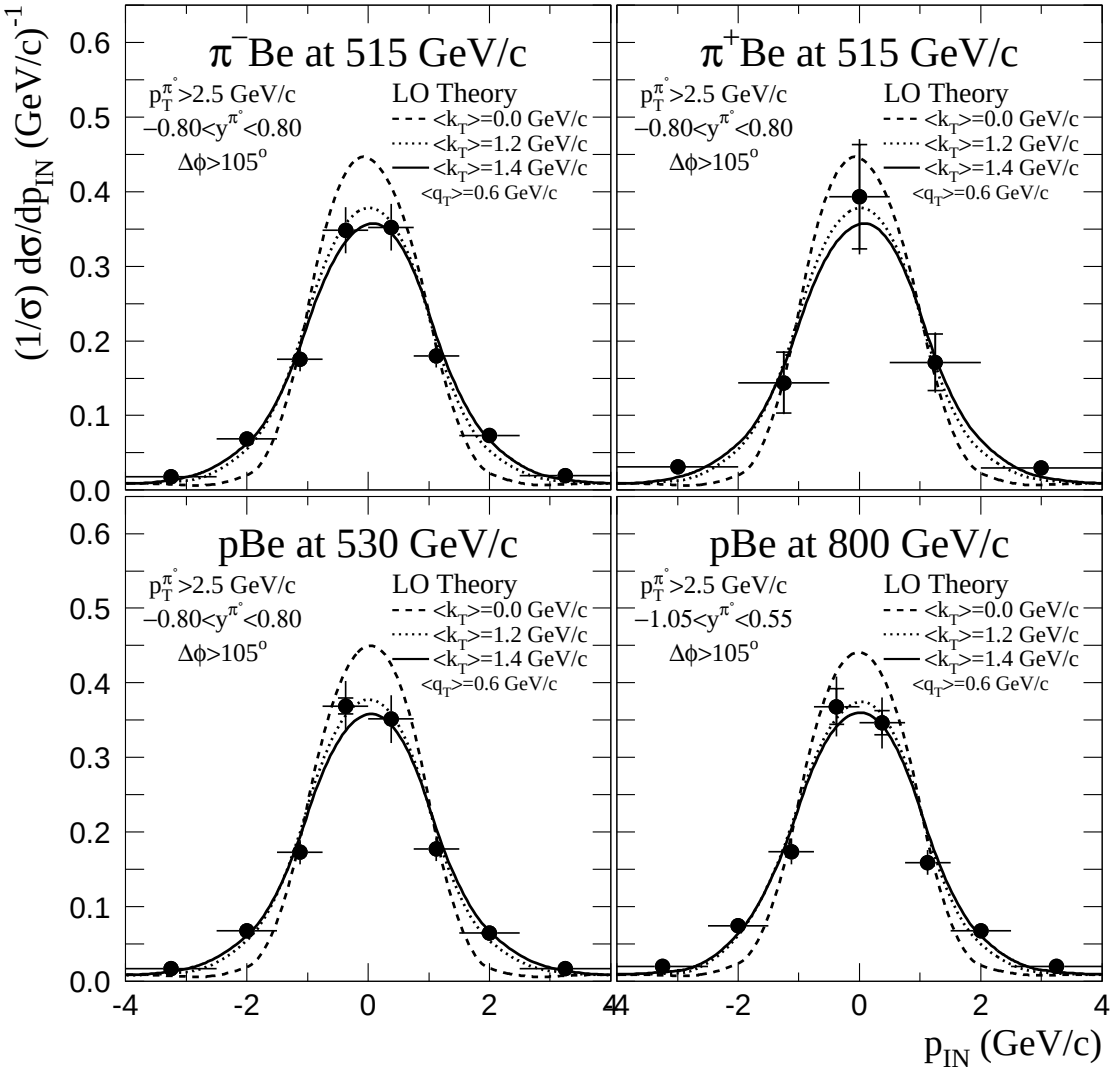

Figure 8.18 The dipion p_{IN} distribution produced by interactions of various beams on beryllium. There are two entries per pair. The results of corresponding LO theory calculations [11] are also shown.

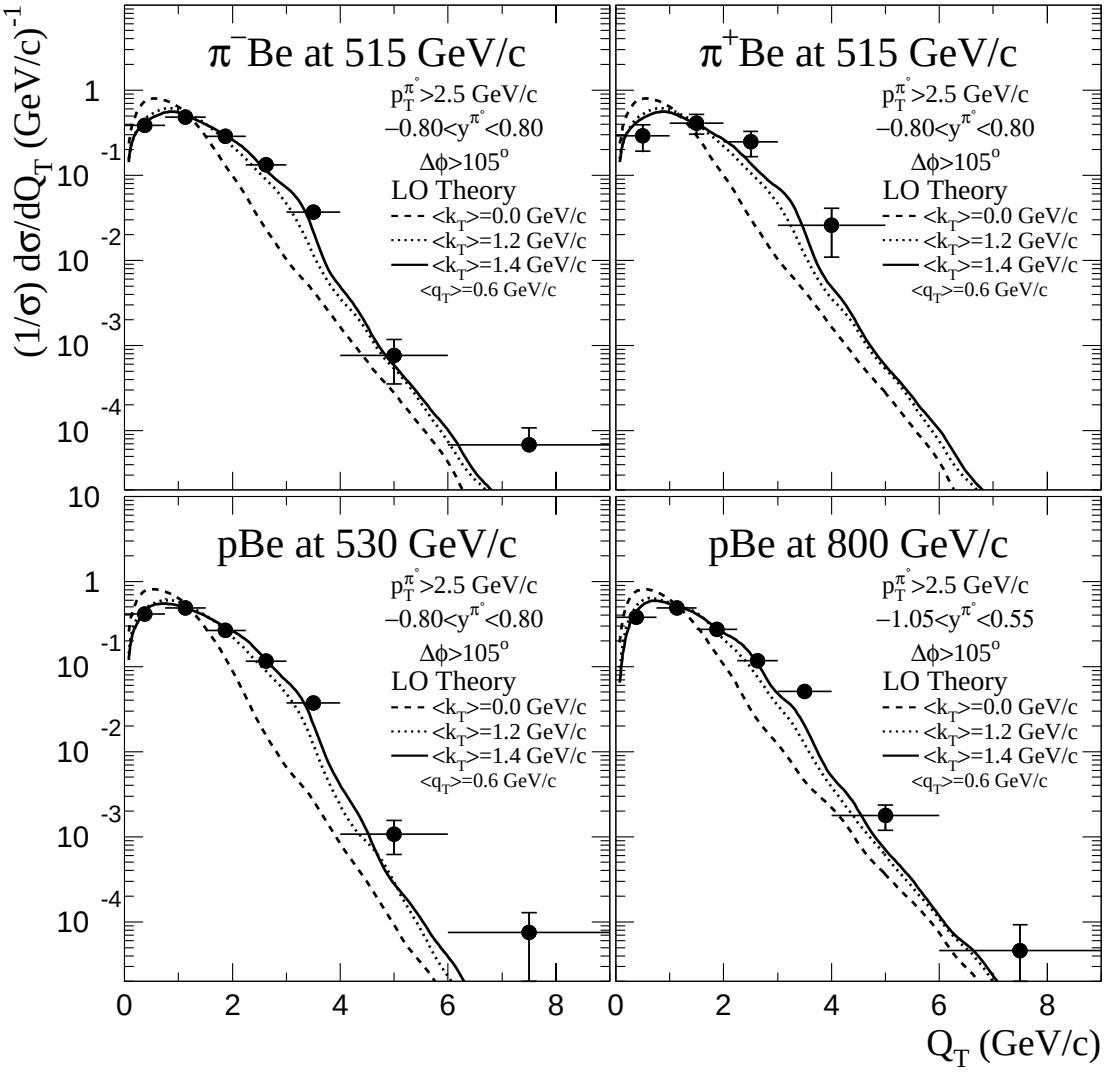

Figure 8.19 The dipion Q_T distribution produced by interactions of various beams on beryllium. The results of corresponding LO theory calculations [11] are also shown.

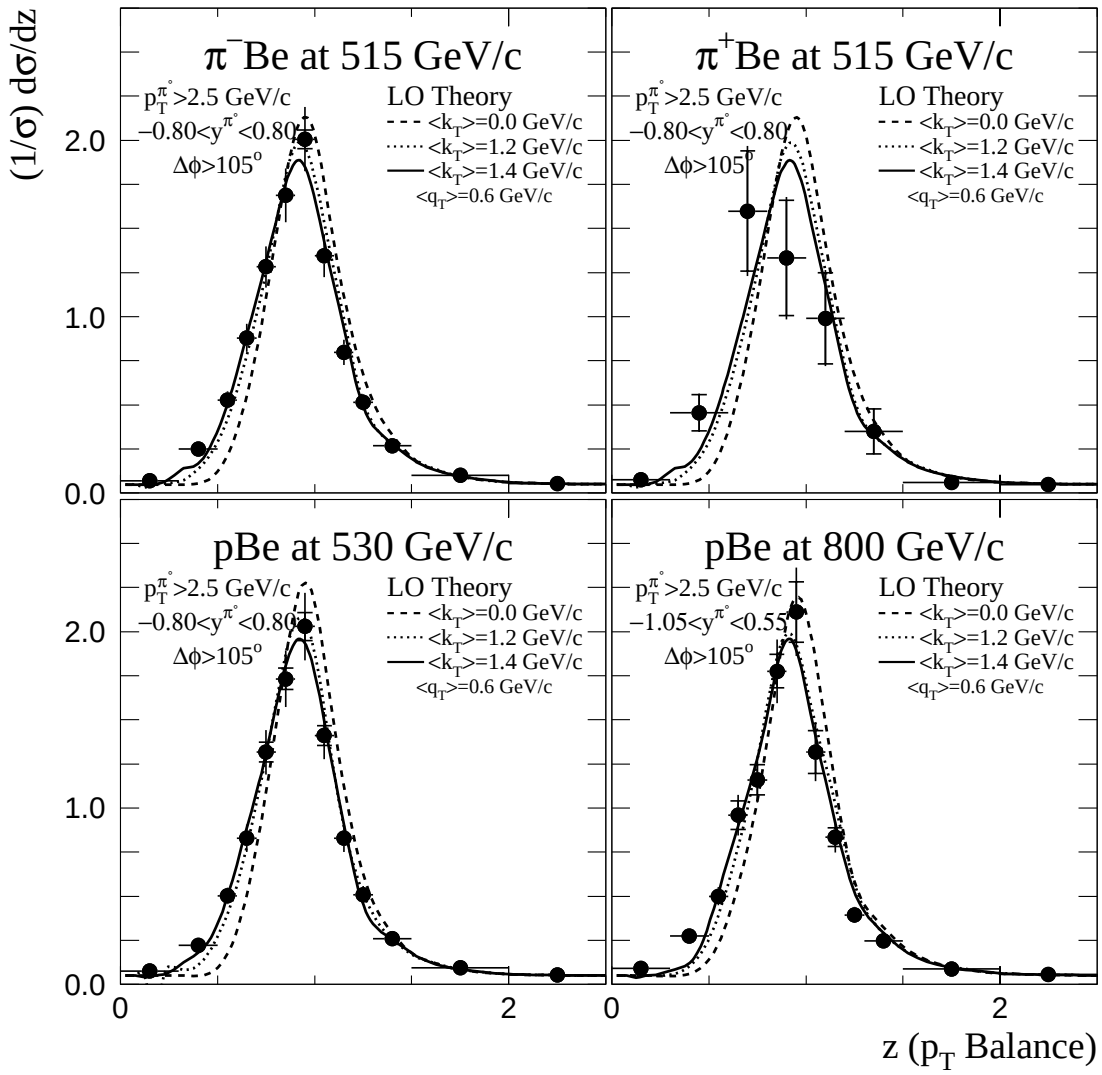

Figure 8.20 The dipion z distribution produced by interactions of various beams on beryllium. There are two entries per pair. The results of corresponding LO theory calculations [11] are also shown.

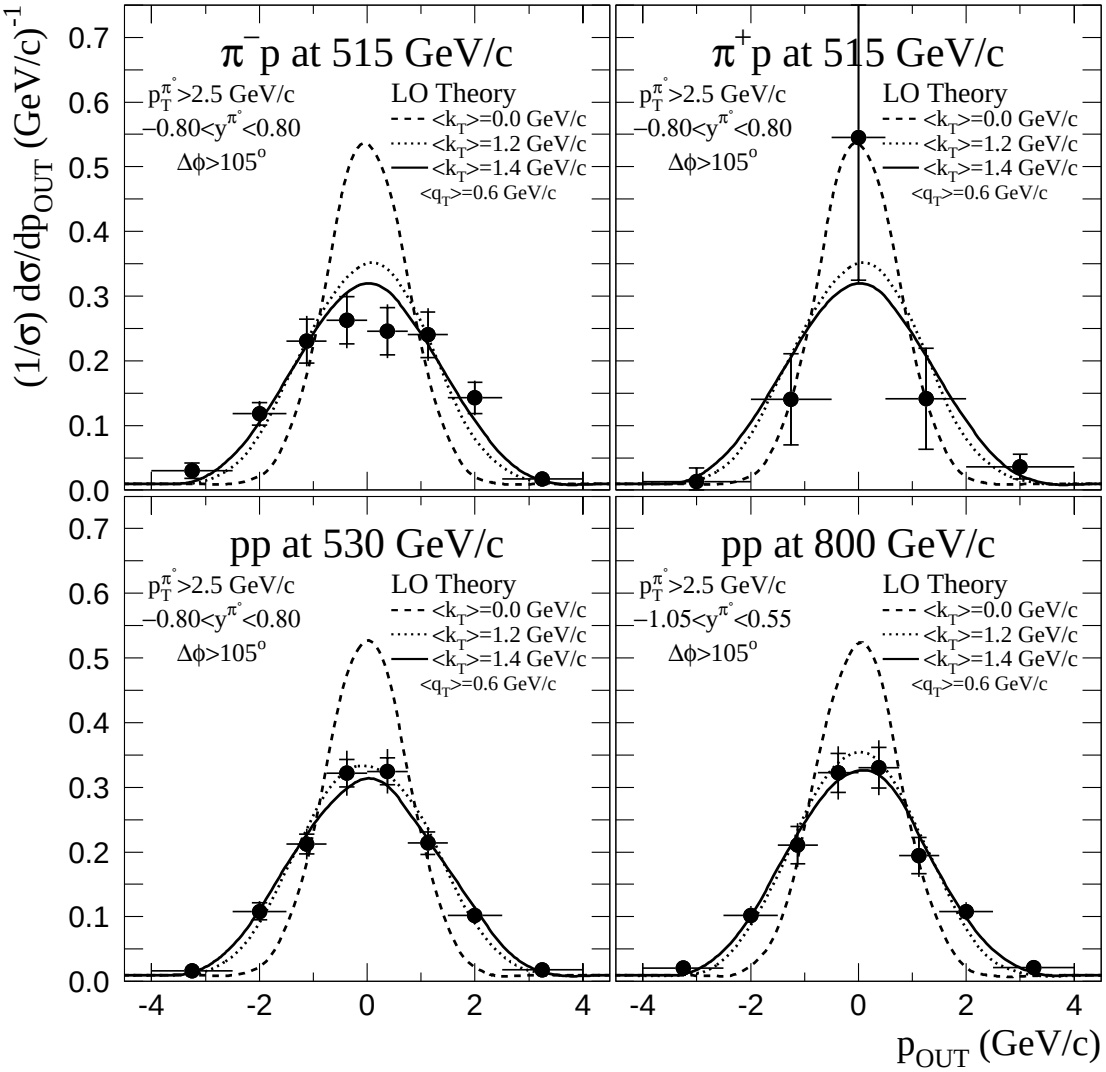

Figure 8.21 The dipion p_{OUT} distribution produced by interactions of various beams on hydrogen. There are two entries per pair. The results of corresponding LO theory calculations [11] are also shown.

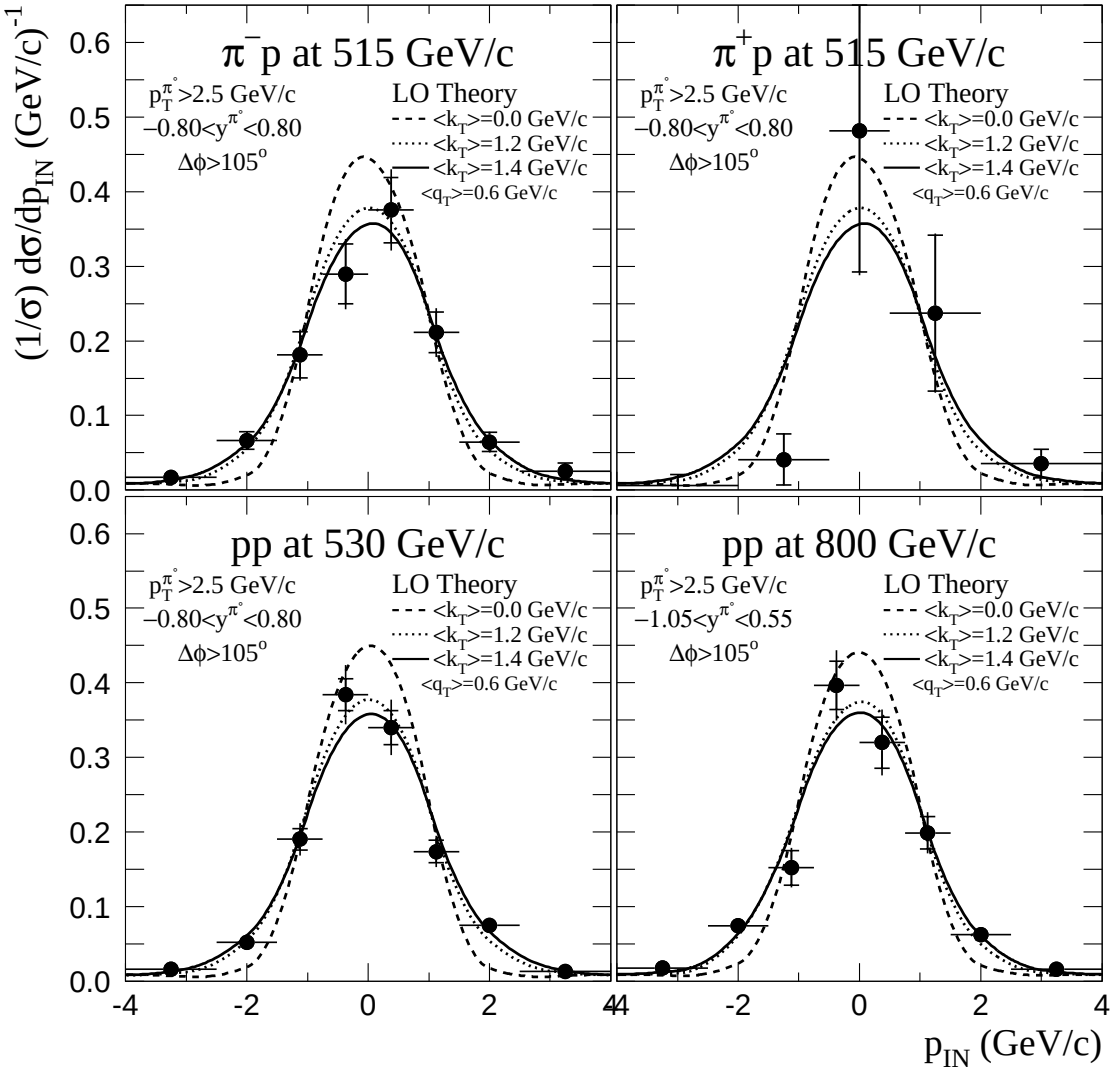

Figure 8.22 The dipion p_{IN} distribution produced by interactions of various beams on hydrogen. There are two entries per pair. The results of corresponding LO theory calculations [11] are also shown.

Chapter 9 Production of High-Mass Eta and Pion Pairs

9.1 Eta–Pion Production

In this chapter we present measurements of the production of high-mass $\eta\pi^0$ pairs produced by 515 GeV/c π^- and 530 GeV/c and 800 GeV/c proton beams incident upon the beryllium target. Tables for these measurements can be found in Appendix B. There is a minimum p_T requirement on each η and π^0 of 2.5 GeV/c. Mesons were also required to be central, with rapidities of $-0.8 < y < 0.8$ for the 0.5 TeV/c beams and $-1.05 < y < 0.55$ for the 0.8 TeV/c beam. The azimuthal angle between the η and π^0 was required to be at least 105°.

Assuming the two final state partons fragment into hadrons independently, the ratio $\sigma(\eta\pi^0)/\sigma(\pi^0\pi^0)$ is expected to be twice the inclusive ratio, $\sigma(\eta)/\sigma(\pi^0)$. This comparison is presented in Figure 9.1 as a function of mass. We use constant values for the $\sigma(\eta)$ to $\sigma(\pi^0)$ ratios as they are flat functions of p_T and rapidity [119]. Given the statistics, there is good agreement between these ratios, indicating the independent fragmentation hypothesis is reasonable.

High-mass $\eta\pi^0$ events display similar k_T signatures to those found in dipion events (Section 8.2). Shape comparisons between the $\eta\pi^0$ and the $\pi^0\pi^0$ in $\Delta\phi$, p_{OUT}, and Q_T are presented in Figures 9.2, 9.3, and 9.4. Theory overlays are not shown as there are no available fragmentation functions that describe η production appropriately for the available LO pQCD theory [11].

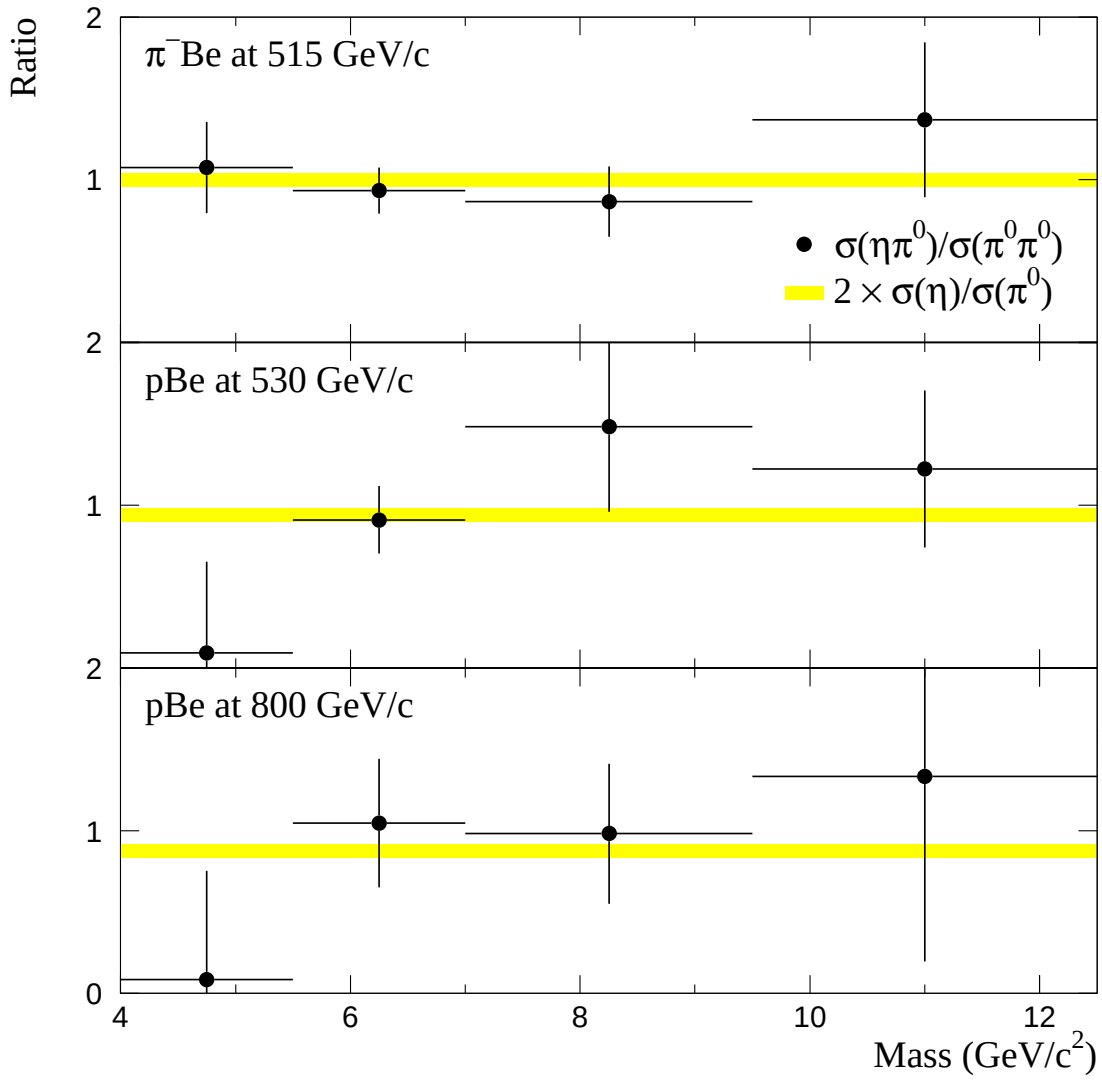

Figure 9.1 Ratio of $\sigma(\eta\pi^0)$ to $\sigma(\pi^0\pi^0)$ as a function of mass. Additional requirements on the combinations contributing to this distribution are summarized at the beginning of Chapter 9. Twice the measured inclusive ratio $\sigma(\eta)/\sigma(\pi^0)$ (Figure 5.12) is presented as an overlay.

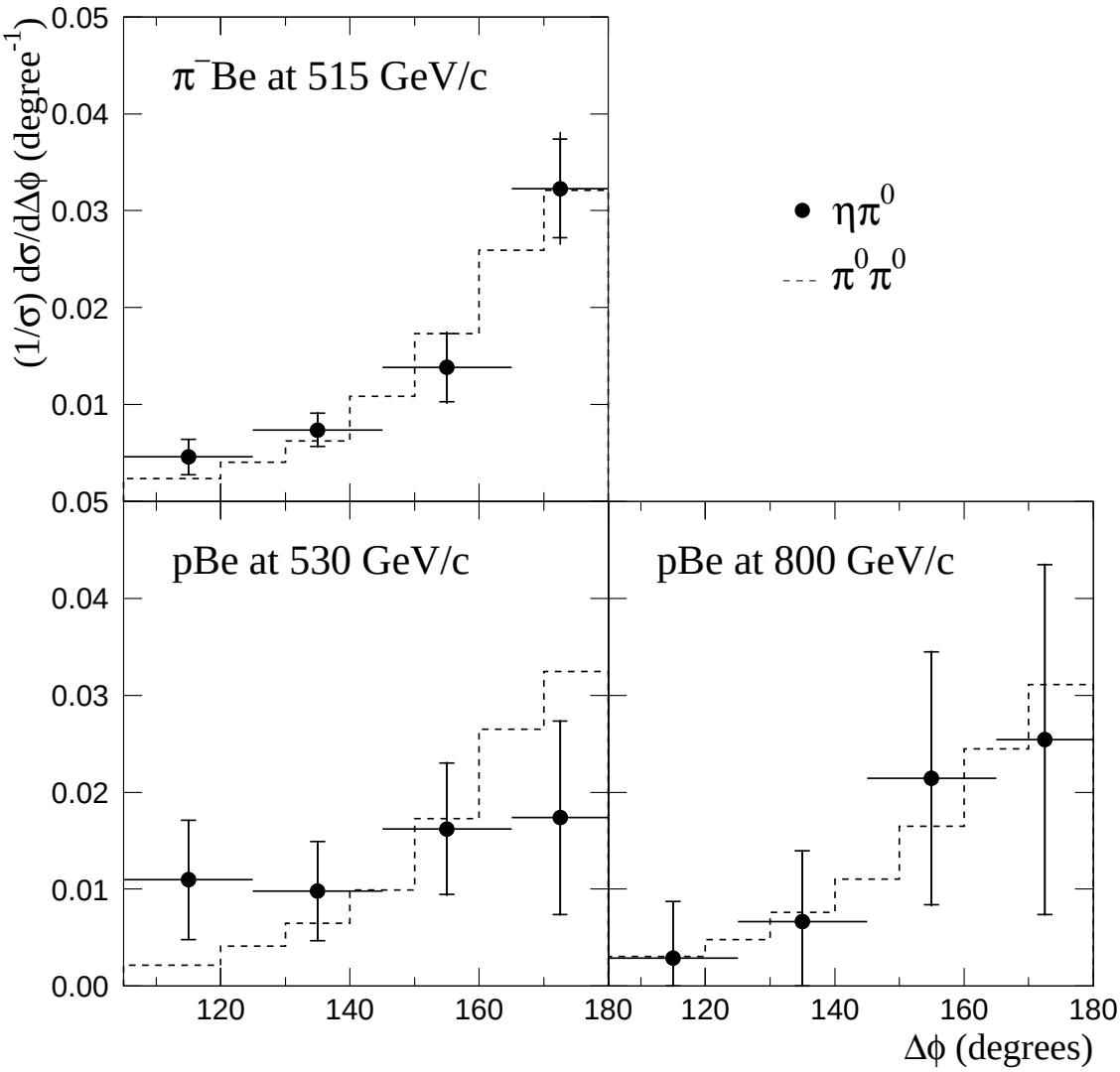

Figure 9.2 Shape comparison in $\Delta\phi$ between $\eta\pi^0$ (points) and $\pi^0\pi^0$ events (histogram). Additional requirements on the combinations contributing to this distribution are summarized at the beginning of Chapter 9.

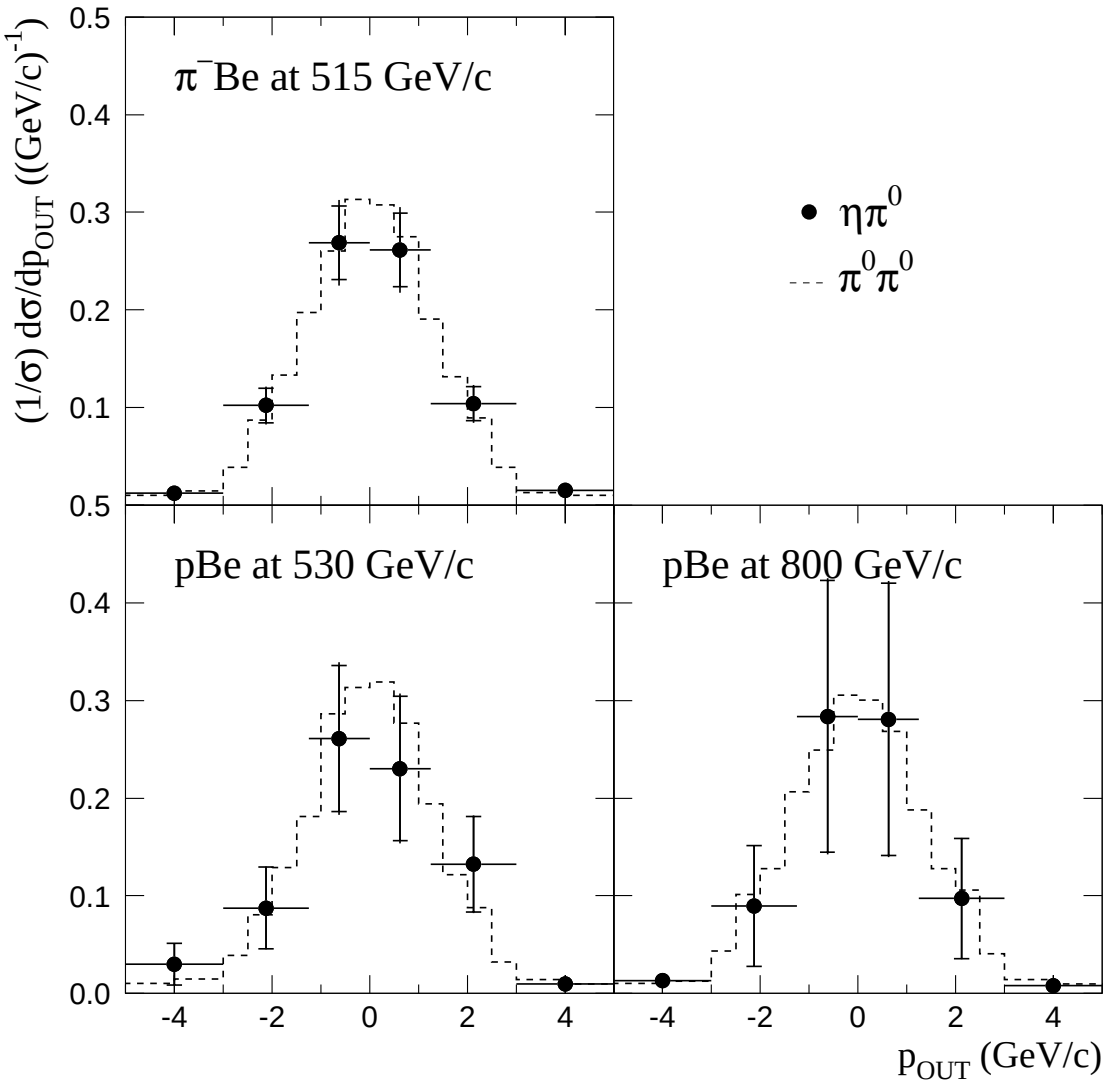

Figure 9.3 Shape comparison in p_{OUT} between $\eta\pi^0$ (points) and $\pi^0\pi^0$ events (histogram). There are two entries per pair. Additional requirements on the combinations contributing to this distribution are summarized at the beginning of Chapter 9.

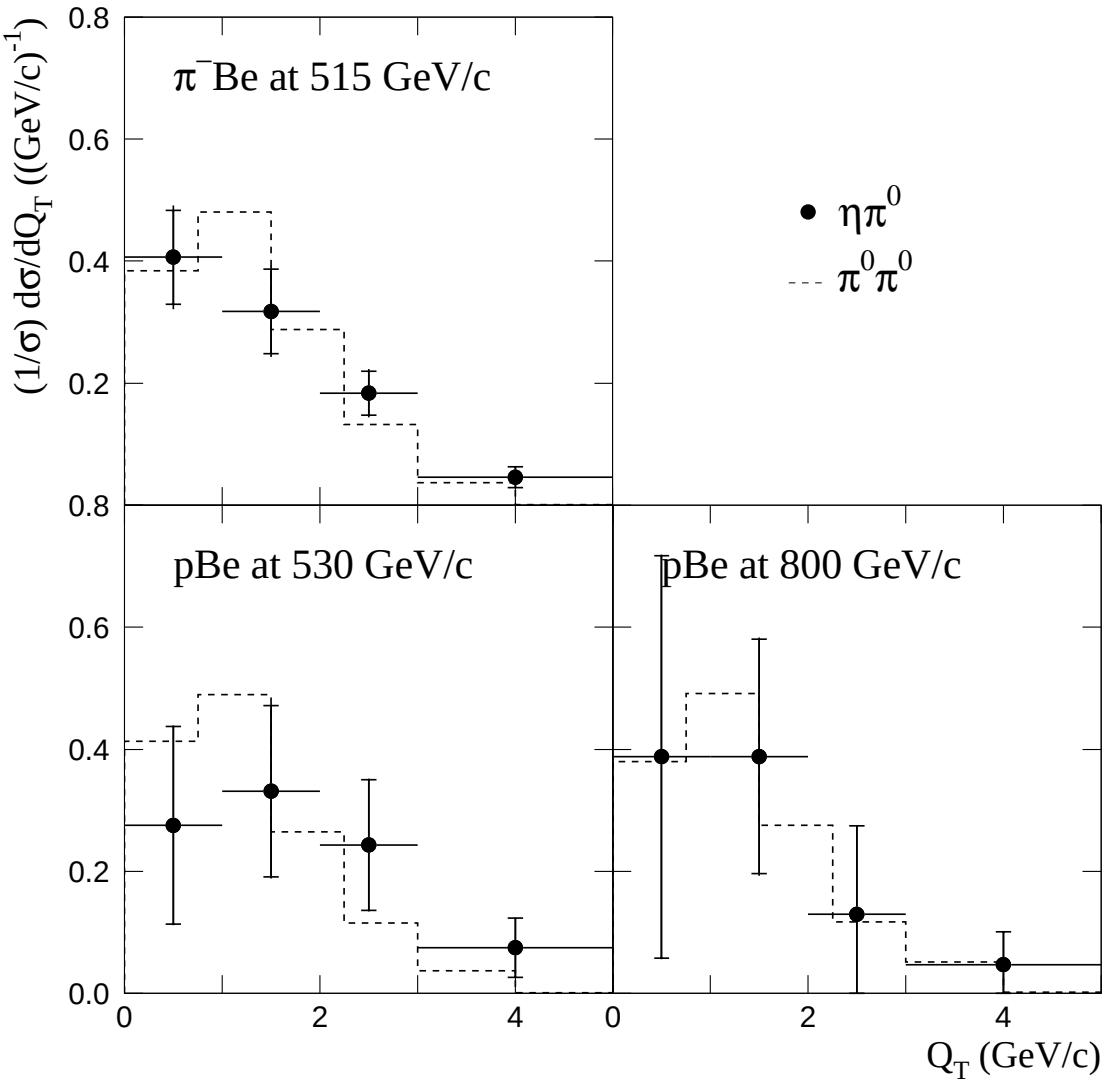

Figure 9.4 Shape comparison in Q_T between $\eta\pi^0$ (points) and $\pi^0\pi^0$ events (histogram). Additional requirements on the combinations contributing to this distribution are summarized at the beginning of Chapter 9.

9.2 Eta–Eta Production

There was very little reconstructed signal for $\eta\eta$ production. This was expected since the combination of production rate, branching ratio, and acceptance reduce the measurable rate of $\eta\eta$ production by a factor of ≈ 1000. The integrated cross section was measured for $p_T^{\eta} > 2.5$ GeV/c in π^-Be interactions at 515 GeV/c as 7400 ± 6300 pb. All other samples had null results. Assuming the two outgoing partons from the hard-scatter fragment independently, we expect $\sigma(\eta\eta)/\sigma(\pi^0\pi^0) = 0.25$. The measured value of this ratio is 0.5 ± 0.4 which is not inconsistent with the hypothesis.

Chapter 10 Production of Photon—Pion Pairs

In this chapter we present measurements of the high-mass production of $\gamma\pi^0$ pairs produced by 515 GeV/c π^- incident upon beryllium and copper targets. Tables for these, and supporting, measurements can be found in Appendix C. Unless otherwise noted, there is a minimum p_T requirement of 2.5 GeV/c on each π^0 and 4.0 GeV/c on each photon. Particles were required to be central, with rapidities in the range $-0.8 < y < 0.8$. The azimuthal angle between the photon and the π^0 was required to be at least 105°.

All theory curves [11] presented in this chapter use the BKK fragmentation function [20] for π^0 production. The fragmentation scale was fixed at $m_F = {p_T}^{\pi^0}/2$. GRV92LO [18] was used for the parton distribution function.

10.1 Cross Section Measurements

We can test the underlying pQCD theory by examining the cross section as a function of several variables. Mass is a useful variable for this purpose as it is invariant under transverse boosts and therefore insensitive to k_T effects (except for smearing across the p_T cut). Other variables insensitive to k_T effects include p_T, rapidity, and $\cos\theta^\star$.

10.1.1 Mass Distributions

The $\gamma\pi^0$ mass spectrum for π^-Be interactions is presented in Figure 10.1. The cross section rises at low mass, peaks, and then falls exponentially with increasing mass. This behavior is due to the minimum p_T requirements (Section 8.1.1). Changing the minimum ${p_T}^\gamma$ requirement illustrates this effect; Figure 10.2 displays the mass distribution for several choices of the minimum p_T requirement on the photon.

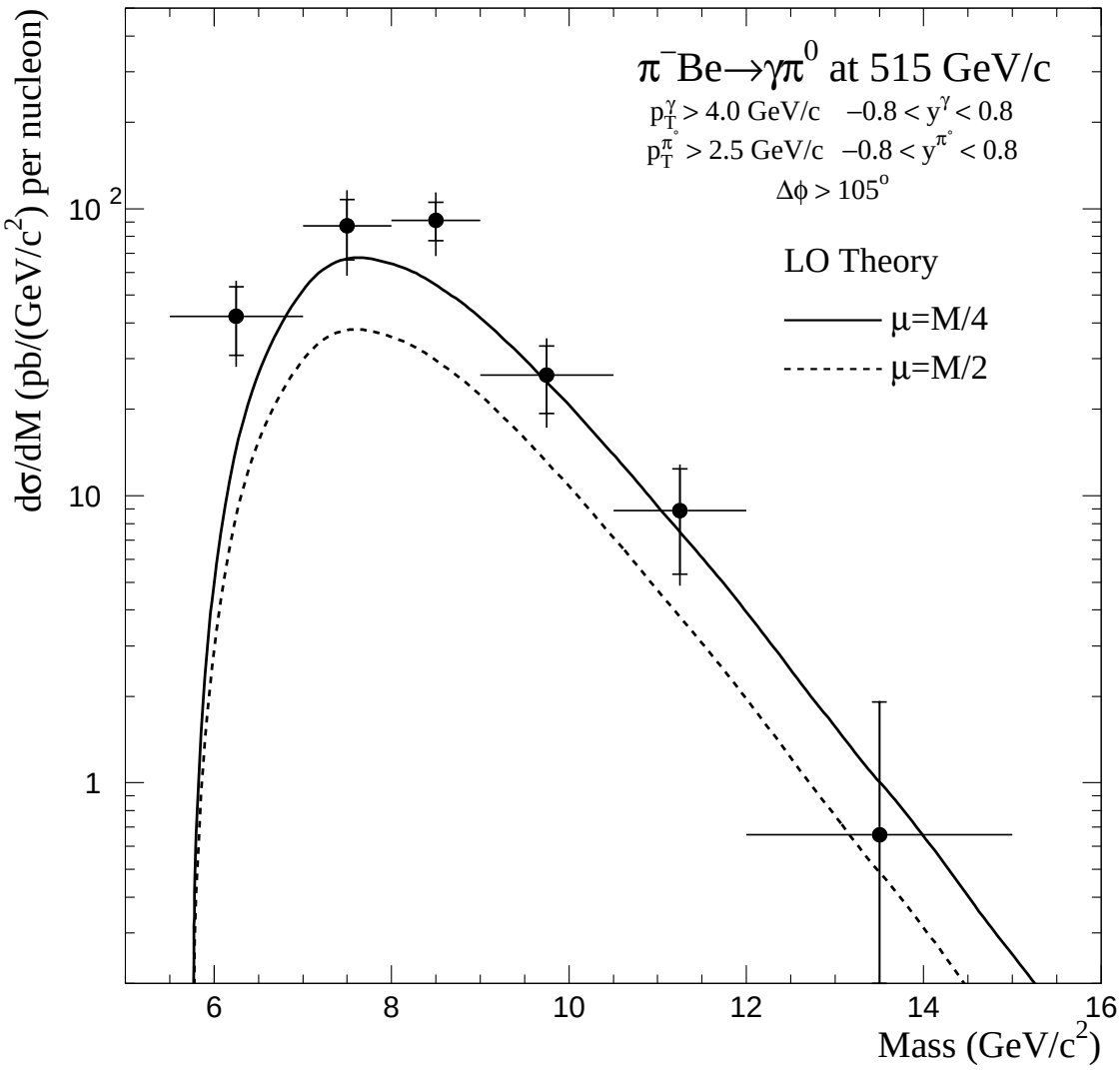

Figure 10.1 The $\gamma\pi^0$ mass distribution produced by 515 GeV/c π^- incident on beryllium. The results of corresponding LO theory calculations [11] for two choices of scale are also shown.

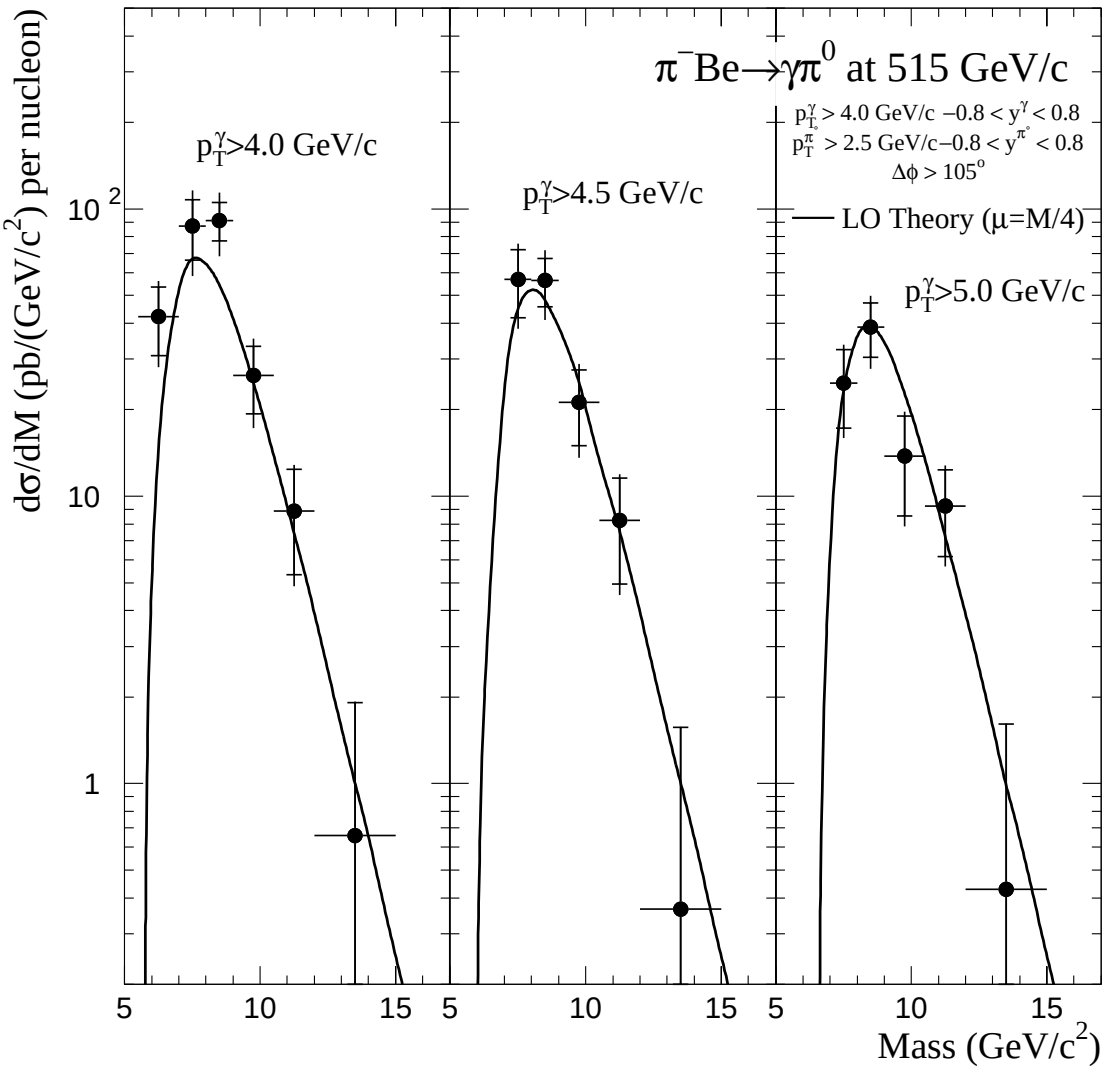

Figure 10.2 The $\gamma\pi^0$ mass distribution for several different minimum $p_T{}^\gamma$ requirements. The results of corresponding LO theory calculations [11] are also shown.

Overlayed on the data in Figure 10.1 are the results from the LO pQCD theory calculation [11] for two choices of factorization scale. (The fragmentation scale was ${p_T}^{\pi^0}/2$ for each of these curves.) The scale that best describes the data is $\mu = M/4$; this scale is used as the default. The theory characterizes the data normalization and shape, however, it systematically underestimates the cross section at low mass.

10.1.2 Transverse Momentum and the Fragmentation Function

A pseudo-fragmentation distribution can be created by comparing ${p_T}^{\pi^0}$ to ${p_T}^{\gamma}$ event-by-event (pseudo-z = ${p_T}^{\pi^0}/{p_T}^{\gamma}$). Defined in this manner, the pseudo-fragmentation distribution is insensitive to k_T effects. The distribution was then normalized to the integrated $\gamma\pi^0$ cross section. Given the relatively high p_T requirement placed on the π^0 (${p_T}^{\pi^0} > 2.5$ GeV/c), this sample is only sensitive to the high-z portion of the fragmentation function. Figure 10.3 shows the pseudo-fragmentation function for a high-${p_T}^{\gamma}$ bin. The turn-over at low z is due to the unequal coverage in pseudo-z across the ${p_T}^{\gamma}$ bin ($z_{min} \approx 0.45$ for ${p_T}^{\gamma} = 5.5$ GeV/c versus $z_{min} \approx 0.33$ for ${p_T}^{\gamma} = 7.5$ GeV/c). The distribution falls exponentially at higher values of pseudo-z.

Overlayed on the left side of Figure 10.3 are the results from the LO theory using the BKK fragmentation function [20]. The theory calculation represents the overall shape of the data distributions, but seems to have a slightly steeper slope at high z. Since the data have low statistics, a comparison is made on the right side of Figure 10.3 between the pseudo-fragmentation function measured from $\gamma\pi^0$ events produced in π^-Be interactions at 515 GeV/c and the z distribution of charged particles in a jet opposite an isolated direct photon produced in pBe interactions at 800 GeV/c [146]. This latter sample used a slightly different definition of z

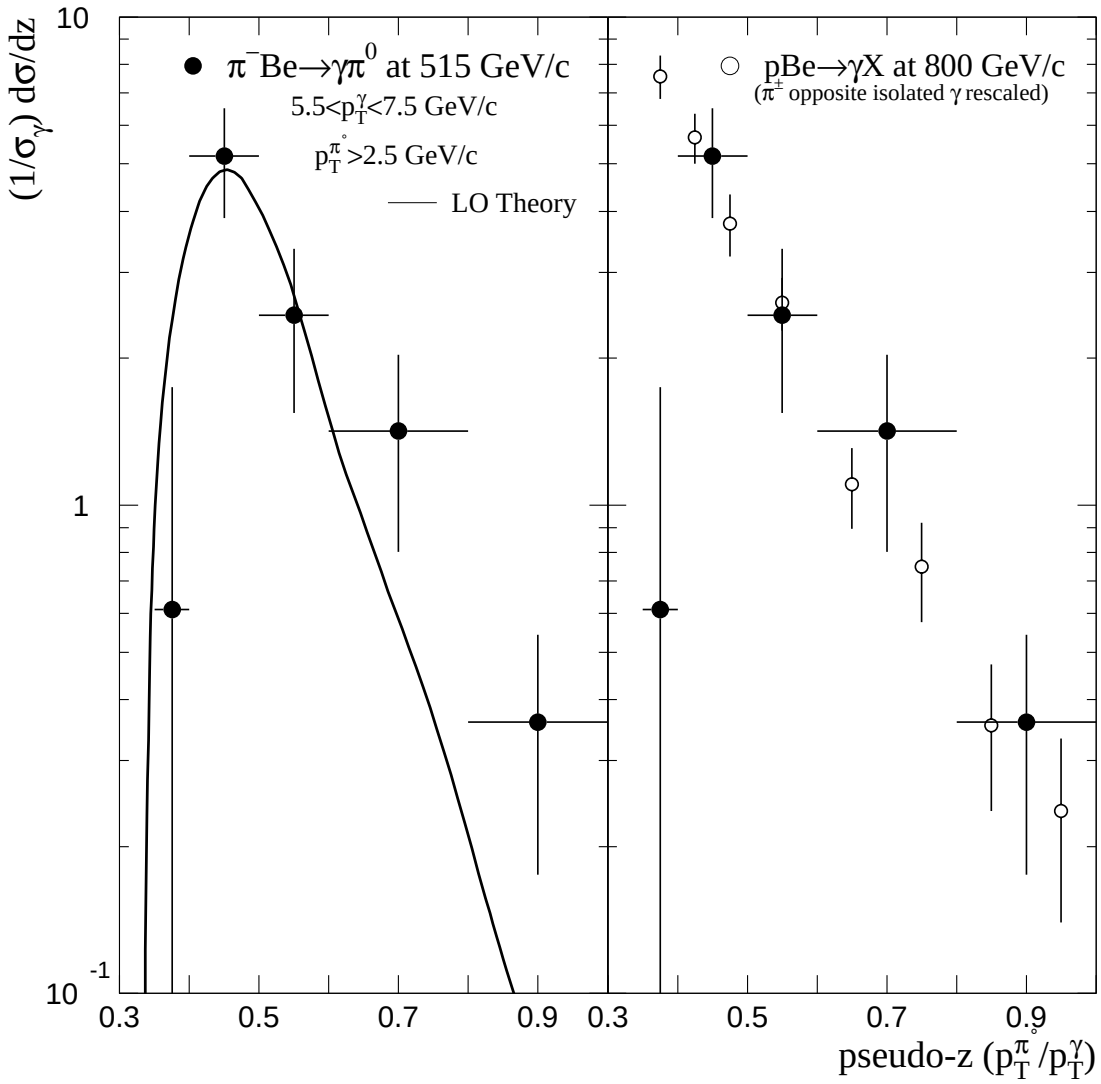

Figure 10.3 Pseudo-fragmentation function, $(1/\sigma_\gamma)d\sigma/dz$, where pseudo-z = ${p_T}^{\pi^0}/{p_T}^{\gamma}$. On the left is a comparison between the data and the results of the LO theory calculation. On the right is a comparison between the same data and the results from a study of charged hadrons in a jet opposite an isolated direct photon from the pBe at 800 GeV/c sample [146].

($z_{rescaled} = z \times (p_T^{jet}/p_T^{\gamma})$ [147]); the normalization has been floated to allow for the slope comparison. Although differences have been seen in distributions of charged particles opposite direct photons between the π^- and proton beams at high z, these differences are fairly small [147]. The slopes of the two data fragmentation distributions are in agreement.

10.1.3 Angular Distributions

Another way to test pQCD is to measure the parton–parton scattering angular distribution. For $\gamma\pi^0$ production, the angular distribution is expected to be relatively flat (Section 1.2.3). Parameterizing the angular distribution as given in Equation 1.9, it is expected that $\alpha \approx 1$ for direct-photon data [11]. The $\cos\theta^\star$ distribution is displayed in Figure 10.4; the measurement was normalized at $\cos\theta^\star = 0$. Additional requirements were placed on the sample to avoid biases due to the p_T and rapidity cuts [87, 144]. The result from the theoretical calculation (with the same physics cuts) is also overlayed on the data in Figure 10.4. The LO theory provides a reasonable description of the data; the best α value for this data is $\alpha = 1.1$ (the data statistics do not allow for a precise measurement of this value). The $\gamma\pi^0$ data is much flatter than the corresponding dipion sample (Figure 8.11) which has $\alpha = 2.7 \pm 0.2 \pm 0.3$.

A comparison is also made in Figure 10.5 for the $\gamma\pi^0$ rapidity in three mass bins. The theory nicely agrees with the shape of the data.

10.2 Kinematic Correlations

Correlations between high-p_T photons and π^0's can be used to investigate the transverse momentum of partons (k_T) prior to the hard scatter (Section 1.2.4). The photon–pion events are more complicated to interpret than dijet, diphoton,

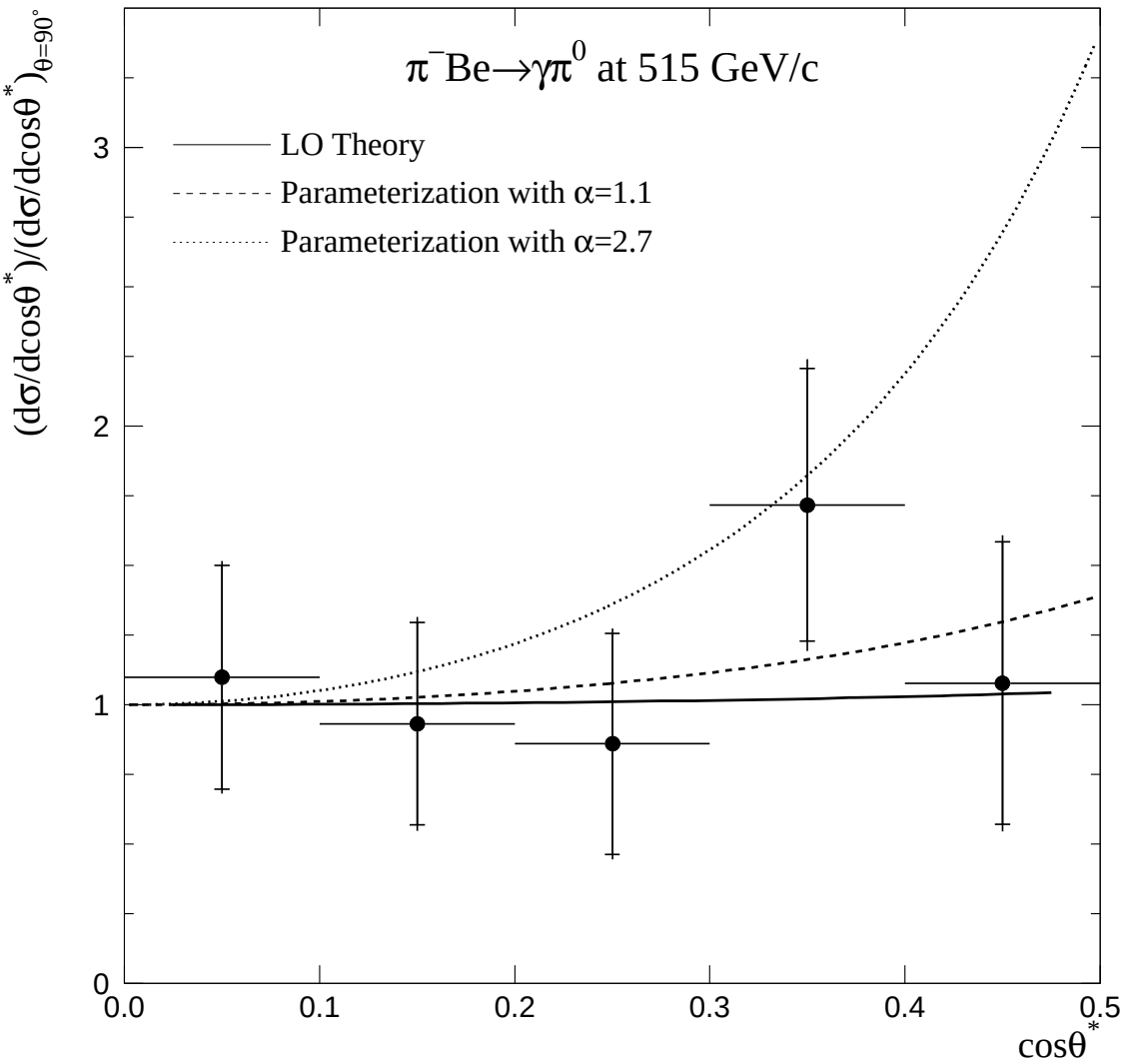

Figure 10.4 Distributions in $\cos\theta^\star$ for the 515 GeV/c π^-Be $\longrightarrow \gamma\pi^0$ data with M $>$ 7.5 GeV/c. Additional requirements on the combinations contributing to this distribution are summarized at the beginning of Chapter 10. The parameterization refers to Equation 1.9 (dashed curve); the data was normalized at $\cos\theta^\star = 0$ using this function. The dipion result from Figure 8.11 is shown as the dotted curve. Also overlayed are the results from the LO theory calculation [11] (solid curve).

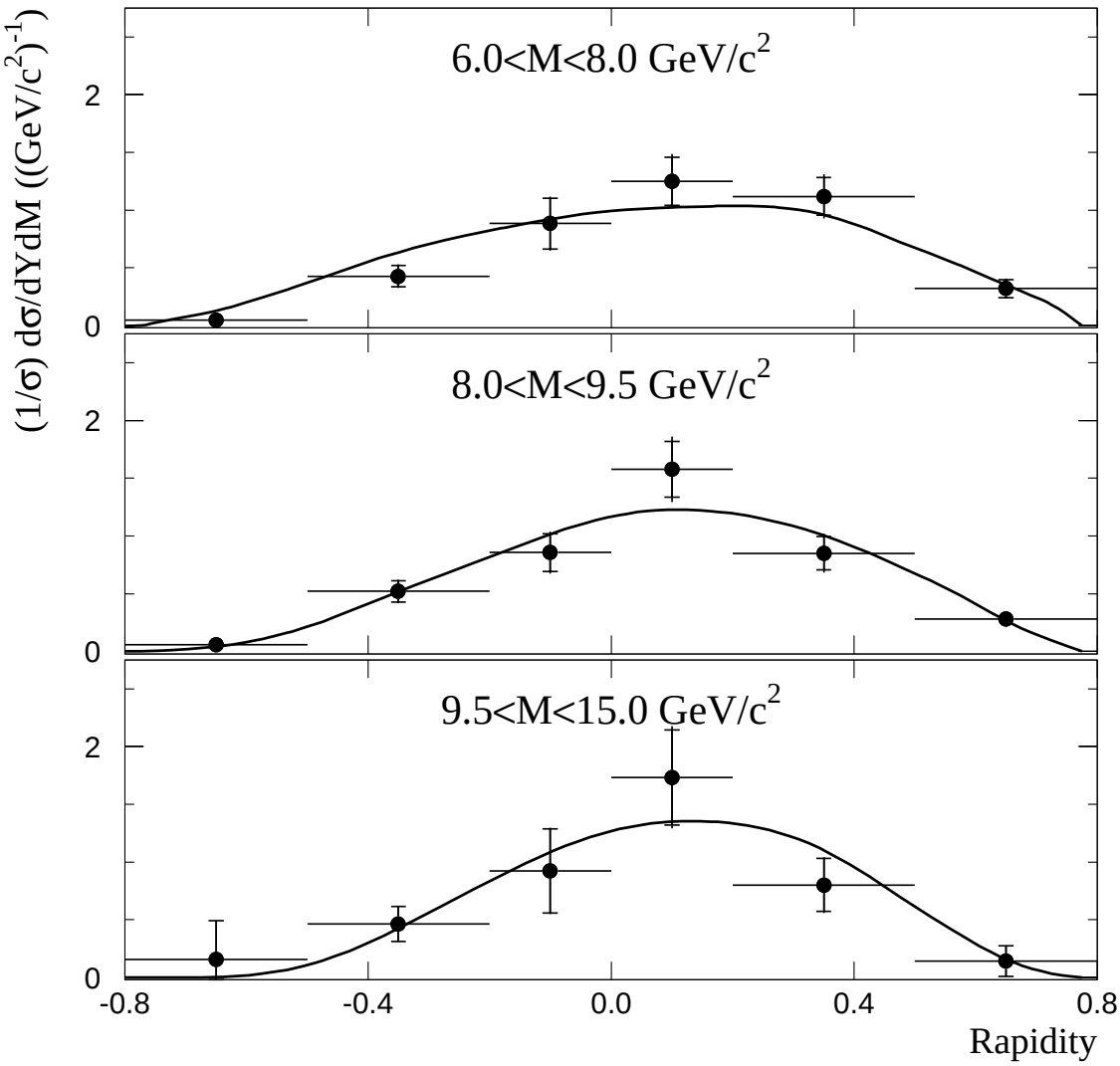

Figure 10.5 The $\gamma\pi^0$ rapidity distribution in three mass bins produced by 515 GeV/c π^- incident on beryllium. Additional requirements on the combinations contributing to this distribution are summarized at the beginning of Chapter 10. The results of corresponding LO theory calculations [11] are also shown.

or dimuon events since the π^0's are jet fragments and have additional transverse momentum (q_T) with respect to the jet axis and also are affected by longitudinal fragmentation effects. The LO pQCD theory [11] used in this study provides for both k_T and q_T effects through a Gaussian smearing model [145].

Several kinematic quantities were used to study k_T in the $\gamma\pi^0$ system. These included the azimuthal angle between the particles ($\Delta\phi$), the out-of-plane momentum (p_{OUT}), and the total p_T of the pair (Q_T). Interpretation of these variables as representations of k_T outside of the LO theory framework is difficult as each variable is affected to some degree by the asymmetric p_T requirements between direct photons and π^0's and by longitudinal fragmentation effects (Section 1.2.4). Some variables are more sensitive to these effects than others. Figure 10.6 shows the average azimuthal angle between the two particles as a function of the $\gamma\pi^0$ mass. Overlayed on the data are two results from the LO theory. The dashed line represents the case when there is no additional transverse momentum added to the system ($\langle k_T \rangle = 0$ GeV/c and $\langle q_T \rangle = 0$ GeV/c) so that the results are purely due to longitudinal fragmentation effects. For this case, the particles are still back-to-back as neither the asymmetric p_T requirements nor the fragmentation function affect the angular distribution. This distribution is, however, affected by the addition of transverse momentum (k_T and q_T) which is represented as the solid curve; on average, the particles are no longer back-to-back. Average values for p_{OUT} and Q_T as a function of mass are also shown in Figure 10.6. The size of the asymmetric p_T requirement and longitudinal fragmentation contributions varies for these two variables. Like $\Delta\phi$, p_{OUT} is not very sensitive to these longitudinal fragmentation effects nor is it sensitive to the asymmetric p_T requirements. Q_T is sensitive to them which reduces sensitivity to the impact of k_T. The LO theory includes both the transverse and longitudinal contributions and reasonably accommodates these distributions.

Fixing $\langle q_T \rangle = 600$ MeV/c [28, 29], we can vary k_T in the LO theory to estimate its effect upon the shape of the $\Delta\phi$, p_{OUT}, and Q_T distributions shown in Figures 10.7, 10.8, and 10.9. The dotted curves represent the theoretical shapes with $\langle k_T \rangle = 0.0$ GeV/c. These distributions are too narrow to describe the data. Two additional curves are overlayed on the data, one with $\langle k_T \rangle = 1.2$ GeV/c (dashed) and one with $\langle k_T \rangle = 1.4$ GeV/c (solid). (The spread in these values is given to illustrate the impact of small changes in $\langle k_T \rangle$.) The distributions with non-zero k_T give a much better representation of the $\Delta\phi$ and p_{OUT} data. The Q_T distribution is less sensitive to k_T effects and the data does not provide much discrimination between the theory curves.

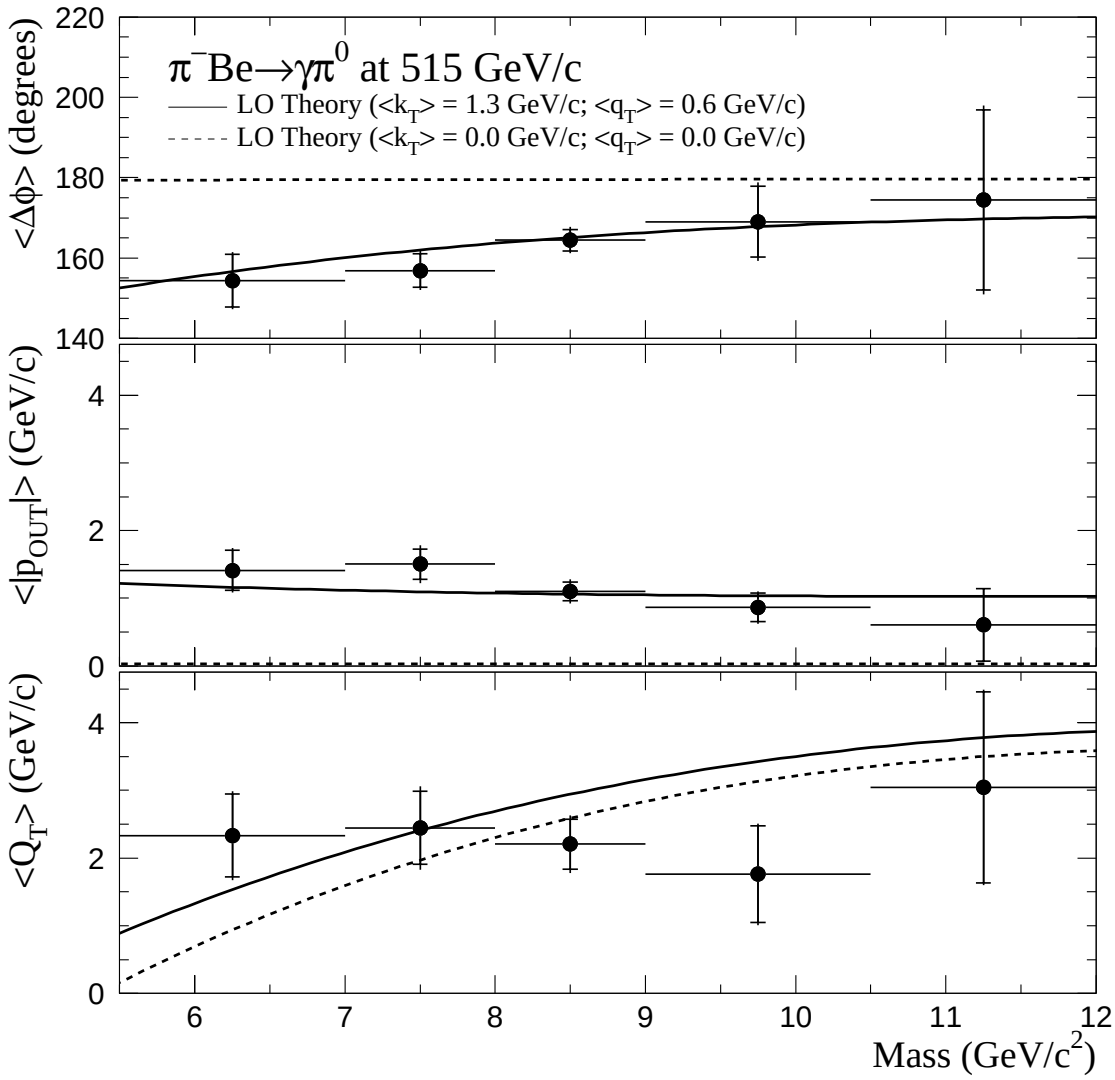

Figure 10.6 Average values of selected kinematic quantities as functions of mass for $\gamma\pi^0$ events. Additional requirements on the combinations contributing to this distribution are summarized at the beginning of Chapter 10. Curves from the LO theory are overlayed on the data.

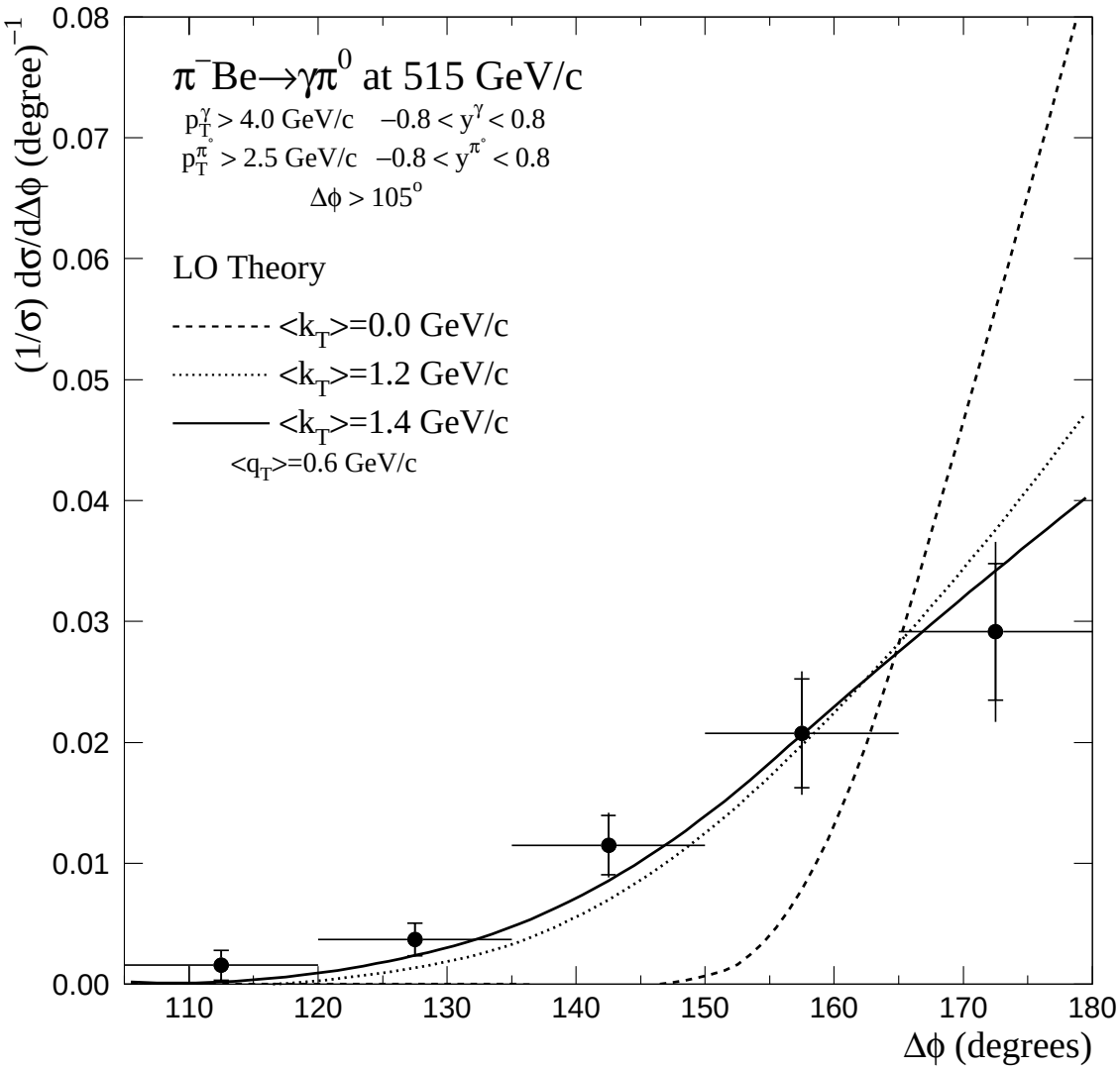

Figure 10.7 The $\gamma\pi^0$ $\Delta\phi$ distribution produced by 515 GeV/c π^- incident on beryllium. The results of corresponding LO theory calculations [11] are also shown.

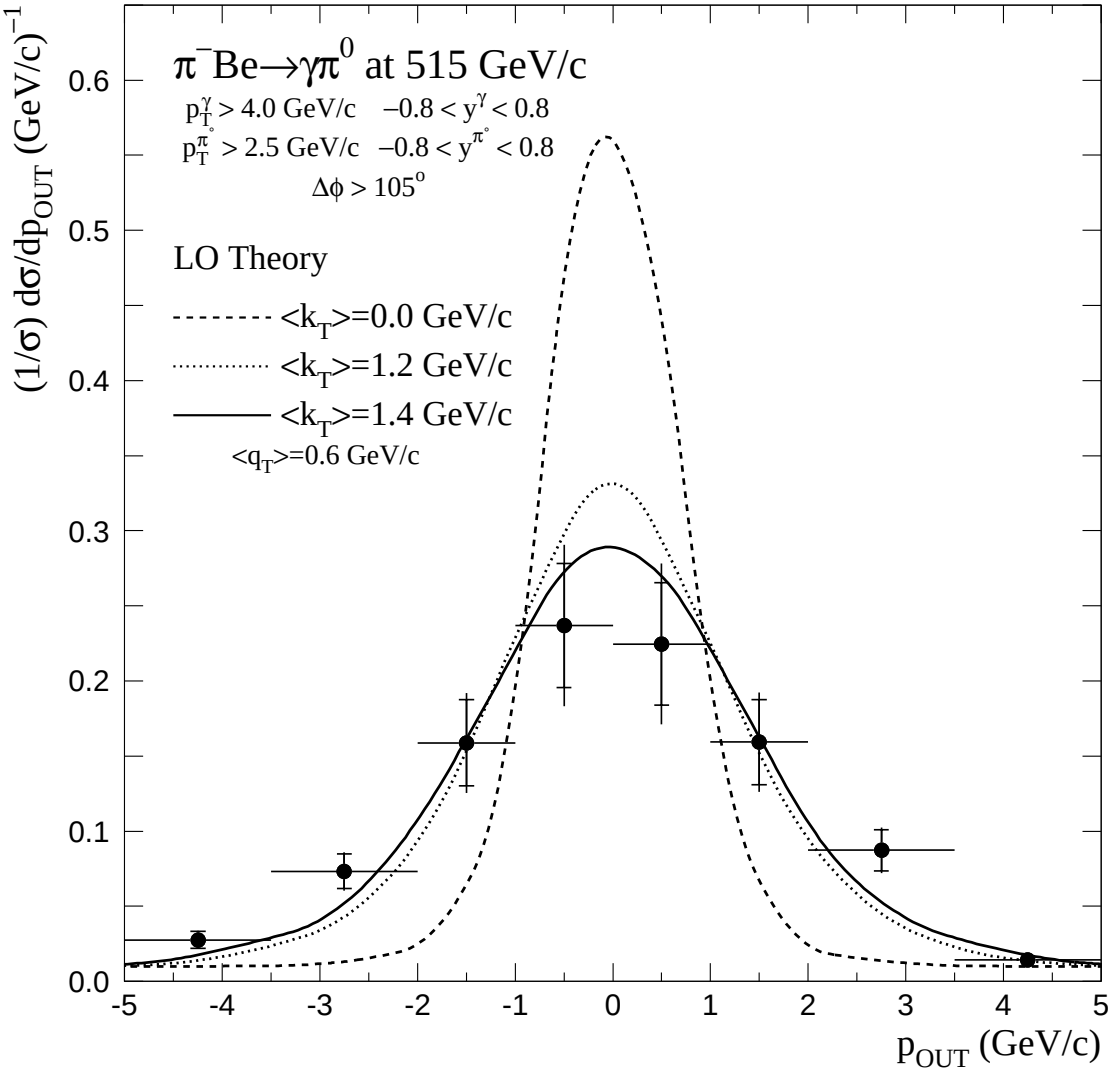

Figure 10.8 The $\gamma\pi^0$ p_{OUT} distribution produced by 515 GeV/c π^- incident on beryllium. There are two entries per pair. The results of corresponding LO theory calculations [11] are also shown.

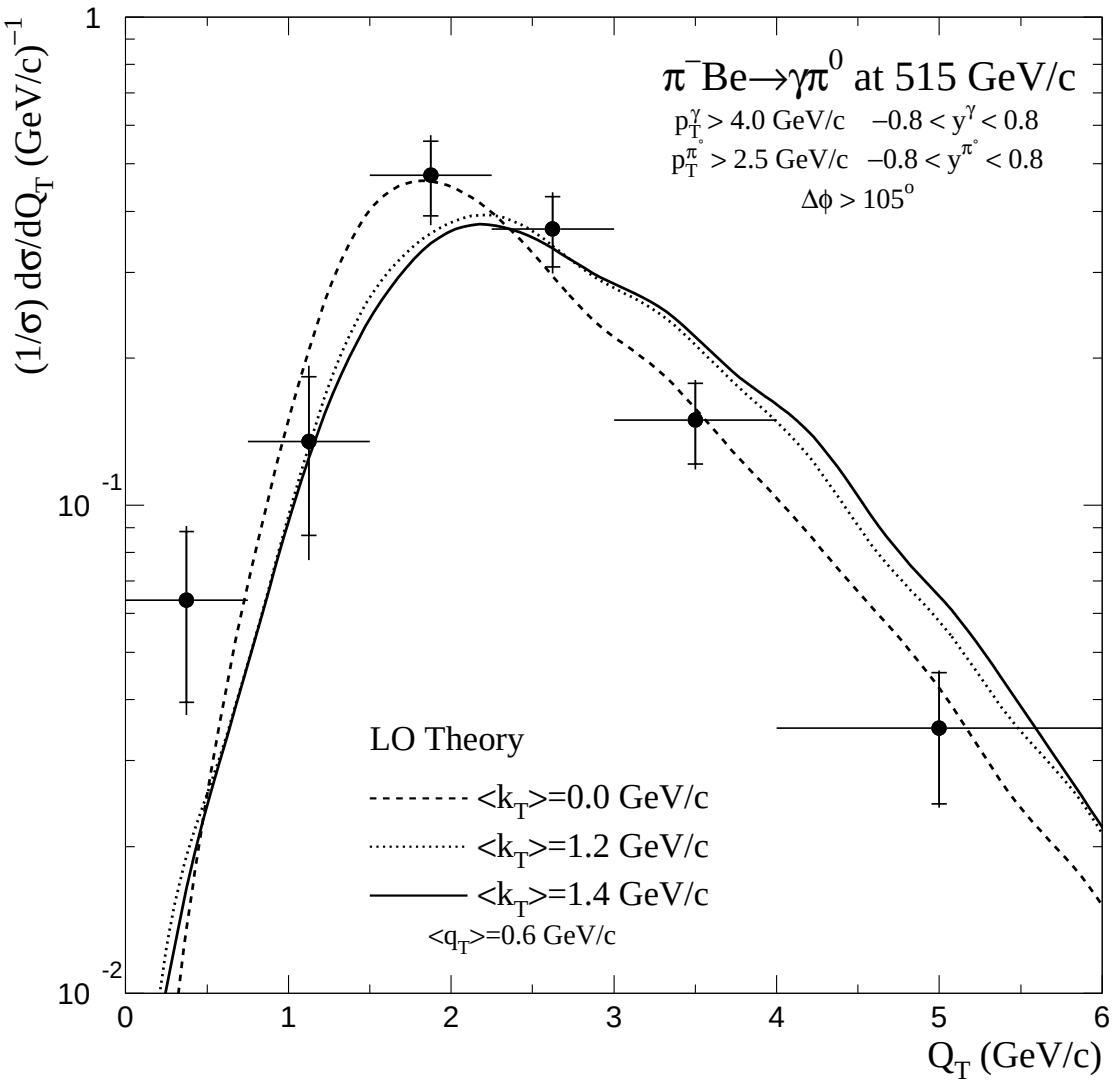

Figure 10.9 The $\gamma\pi^0$ Q_T distribution produced by 515 GeV/c π^- incident on beryllium. The results of corresponding LO theory calculations [11] are also shown.

Chapter 11 Production of High-Mass Direct Photon Pairs

In this chapter we present measurements of the high-mass production of photon pairs produced by 515 GeV/c π^- incident upon beryllium. Unless otherwise noted, there is a minimum p_T requirement of 4.0 GeV/c on each photon. Photons were required to be central, with rapidities in the range $-0.8 < y < 0.8$. The azimuthal angle between the photons was required to be at least 105°. All of the calculations in this chapter use the GRV92 [18, 148] parton distribution functions.

Correlations between high-p_T photons provide useful tests of pQCD. Comparisons between data and theory for k_T-insensitive and k_T-sensitive distributions shed light on fundamental differences between different theories. Two NLO pQCD calculations are considered in this analysis. The first is the NLO theory by Bailey, Owens, and Ohnemus [149]. This theory includes the subprocesses listed in Table 1.5. The second theory is `RESBOS` [150], an NLO calculation that has been resummed according to the Collins-Soper-Sterman (CSS) soft-gluon resummation formalism [151], originally developed for Drell-Yan production. As a function of $\gamma\gamma$ mass, or of $p_T{}^\gamma$, these two theories should yield similar results since these variables are insensitive to transverse boosts due to incident soft-gluon emission [152]. Figures 11.1 and 11.2 show comparisons between data and theory for these two distributions. Both theories agree with the shape of the data, although the resummed theory seems to provide slightly better agreement. This is particularly true near the $p_T{}^\gamma$ threshold, where k_T effects are expected to have greater impact. Still, the differences between the theory calculations are small and the data statistics are insufficient to distinguish between them.

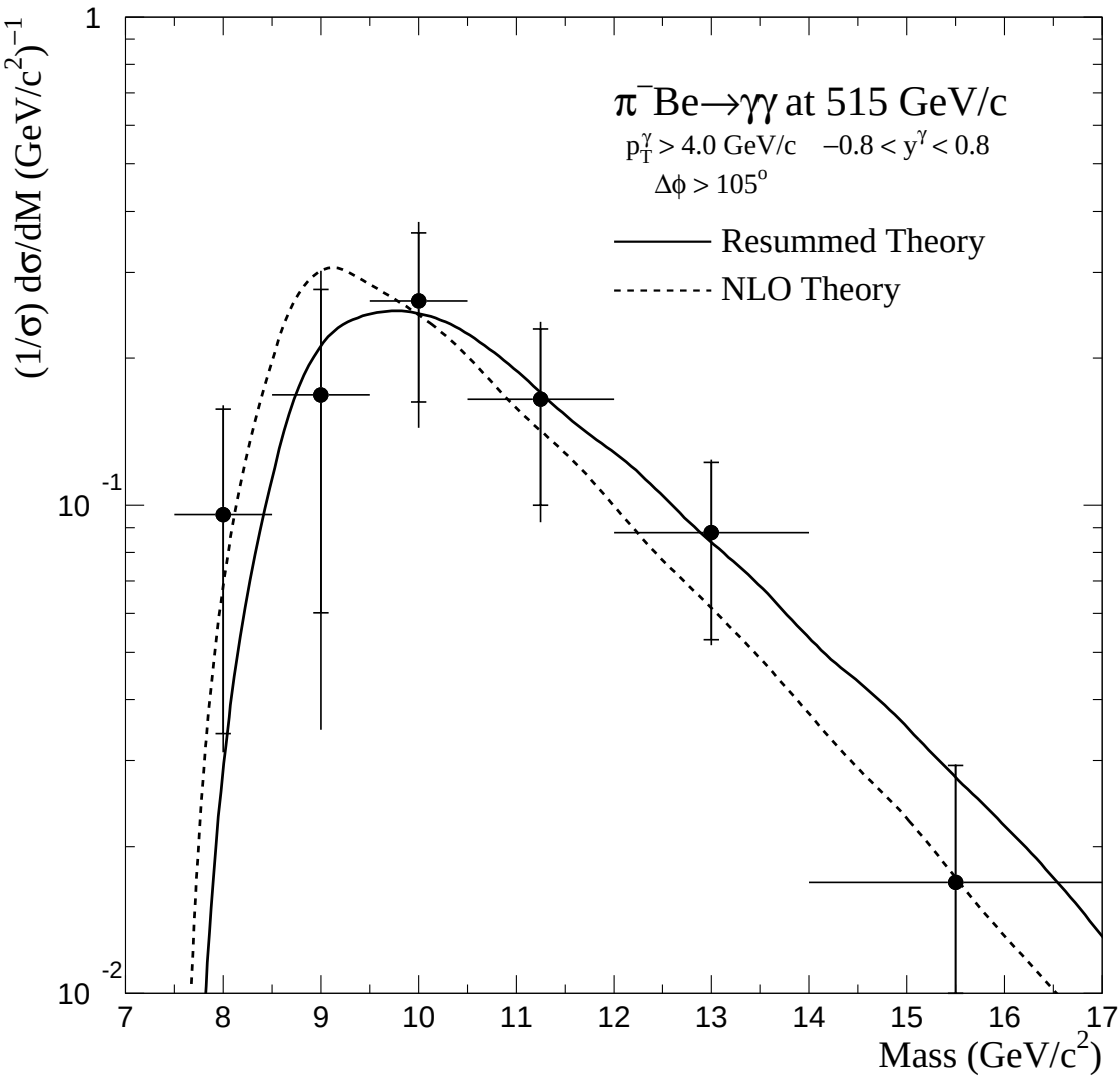

Figure 11.1 The diphoton mass distribution produced by 515 GeV/c π^- incident on beryllium. Overlayed on the data are the results from NLO [149] (dashed) and resummed [150] (solid) calculations.

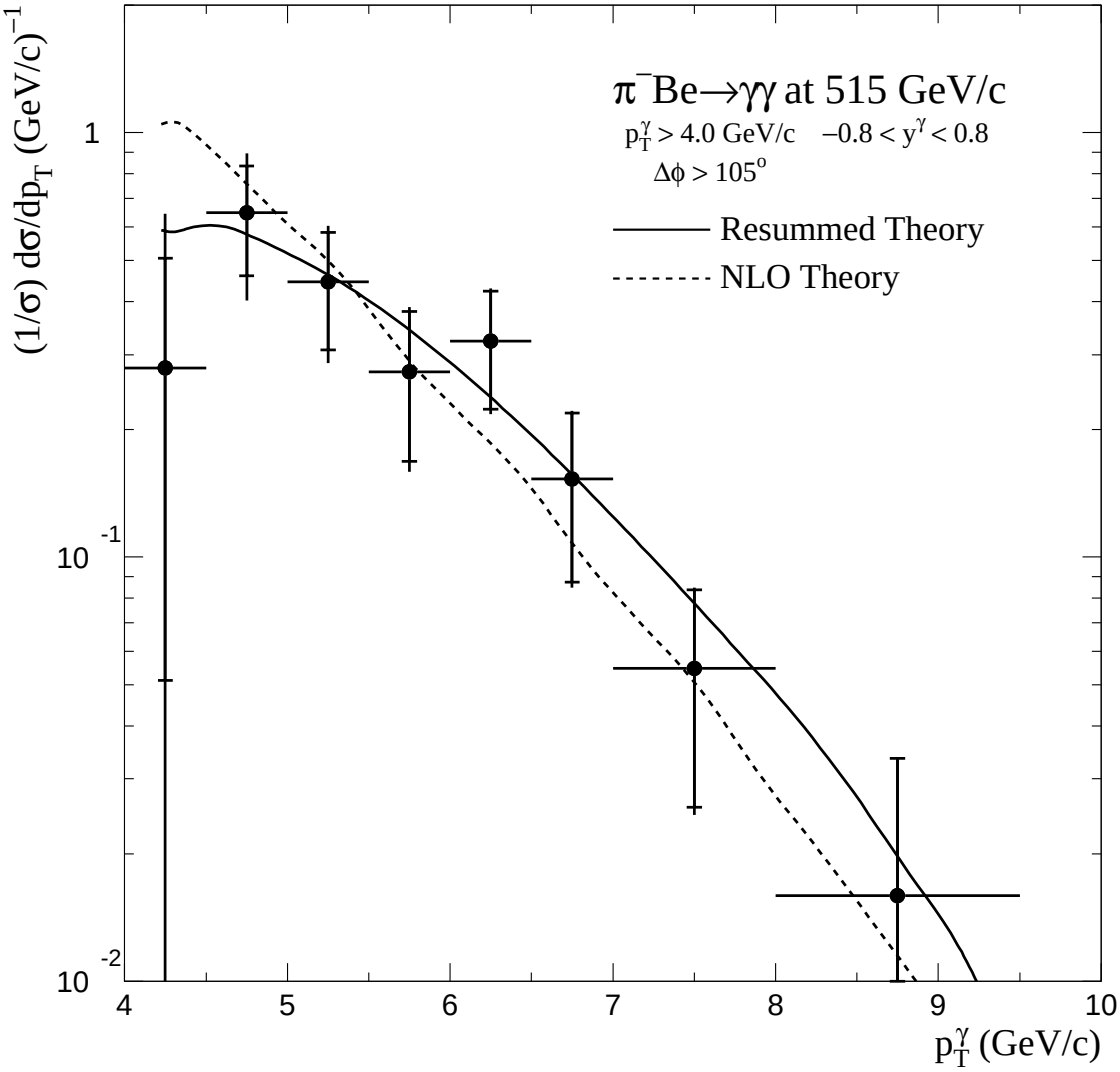

Figure 11.2 The diphoton $p_T{}^\gamma$ distribution produced by 515 GeV/c π^- incident on beryllium. There are two entries per pair. Overlayed on the data are the results from NLO [149] (dashed) and resummed [150] (solid) calculations.

Larger differences between the two theories are expected for distributions sensitive to the effects of multiple soft-gluon emission [153]. Such distributions include the azimuthal angle between the particles ($\Delta\phi$), the out-of-plane-momentum (p_{OUT}), the total p_T of the pair (Q_T), and the p_T balance of the photons (z). Figures 11.3, 11.4, 11.5, and 11.6 display comparisons between the shapes of data and theory for these variables. There was a minimum mass requirement of 10 GeV/c^2 for these distributions to avoid effects due to the large background subtraction at low mass (Figure 7.16).

There are large differences between the shapes of the theories. At leading order, each of these distributions would consist of a delta function. While the NLO theory has non-zero width due to the radiation of a single hard gluon, the resummed theory, which also includes the effects of multiple soft-gluon emission, characterizes the data shapes much better. This is particularly true for the Q_T distribution (Figure 11.5) where the NLO calculation tends towards infinity as $Q_T \rightarrow 0$ GeV/c, while the `RESBOS` calculation follows the shape of the data and goes to zero.

From these data distributions we can estimate a value for $\langle k_T \rangle$ assuming the diphoton distributions directly reflect the transverse momentum of the interacting partons. As discussed in Section 1.2.4, the total p_T of the pair of photons is related to k_T/parton by $\langle k_T \rangle \approx \langle Q_T \rangle / \sqrt{2}$. Assuming all of the out-of-plane momentum is due to k_T effects, then the mean of the p_{OUT} distribution, $\langle |p_{OUT}| \rangle \approx \langle k_T \rangle$, and the width (assuming a Gaussian distribution), $\sigma(p_{OUT}) \approx \sqrt{4/\pi}\ \langle k_T \rangle$, can also be used to extract values for $\langle k_T \rangle$. Values for these quantities are listed in Table 11.1. Using the parameterized Monte Carlo (Section 5.2), we can estimate the contribution to the widths of these distributions due to the resolution of the EMLAC. For the Q_T distribution the experimental resolution is approximately

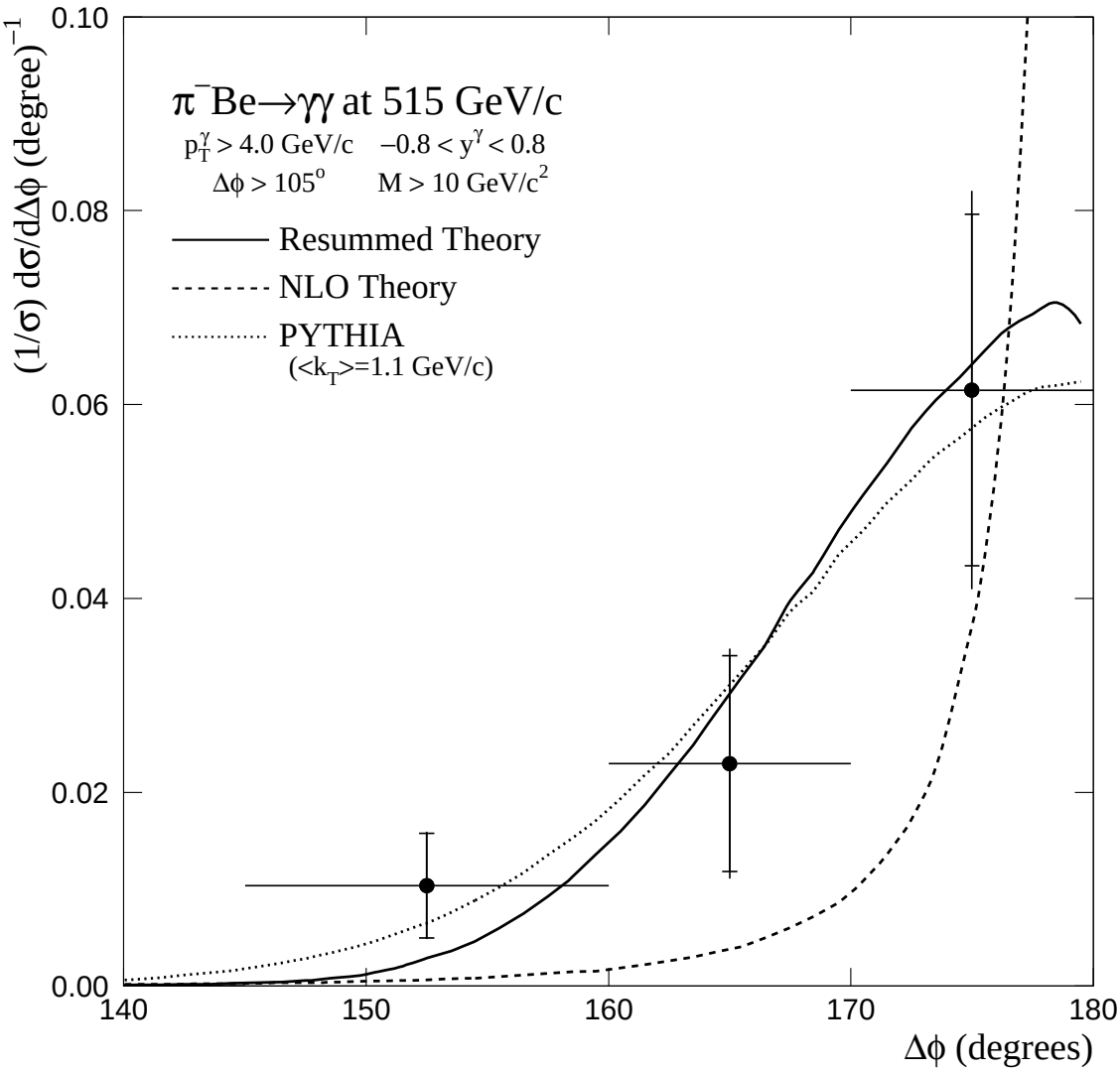

Figure 11.3 The diphoton $\Delta\phi$ distribution produced by 515 GeV/c π^- incident on beryllium. Overlayed on the data are the results from NLO [149] (dashed) and resummed [150] (solid) calculations. `PYTHIA` [121] results (dotted) with $\langle k_T \rangle = 1.1$ GeV/c are also shown.

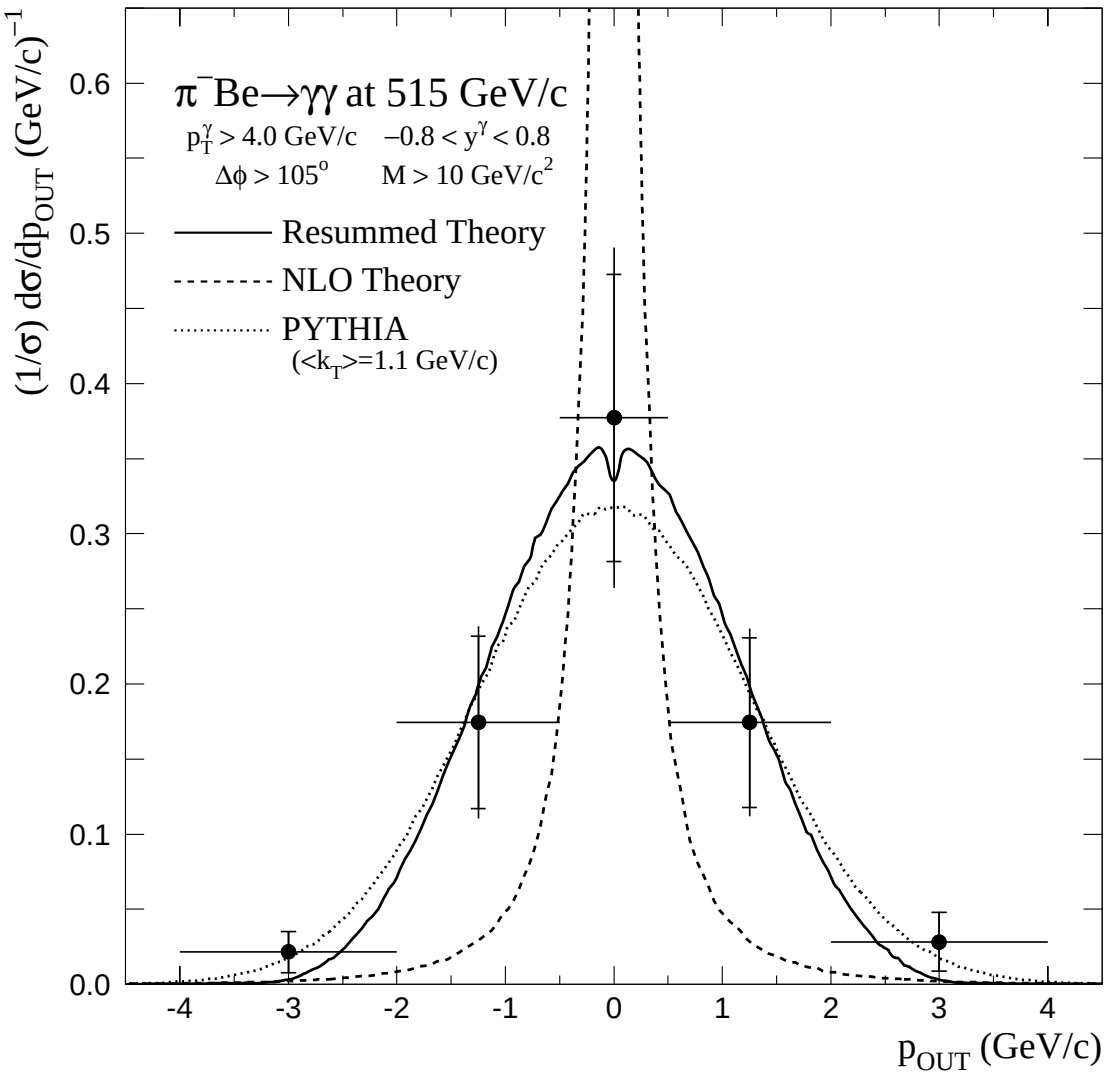

Figure 11.4 The diphoton p_{OUT} distribution produced by 515 GeV/c π^- incident on beryllium. There are two entries per pair. Overlayed on the data are the results from NLO [149] (dashed) and resummed [150] (solid) calculations. `PYTHIA` [121] results (dotted) with $\langle k_T \rangle = 1.1$ GeV/c are also shown. (The dip at $p_{OUT} = 0$ GeV/c is an artifact of `RESBOS` and is not intentional.)

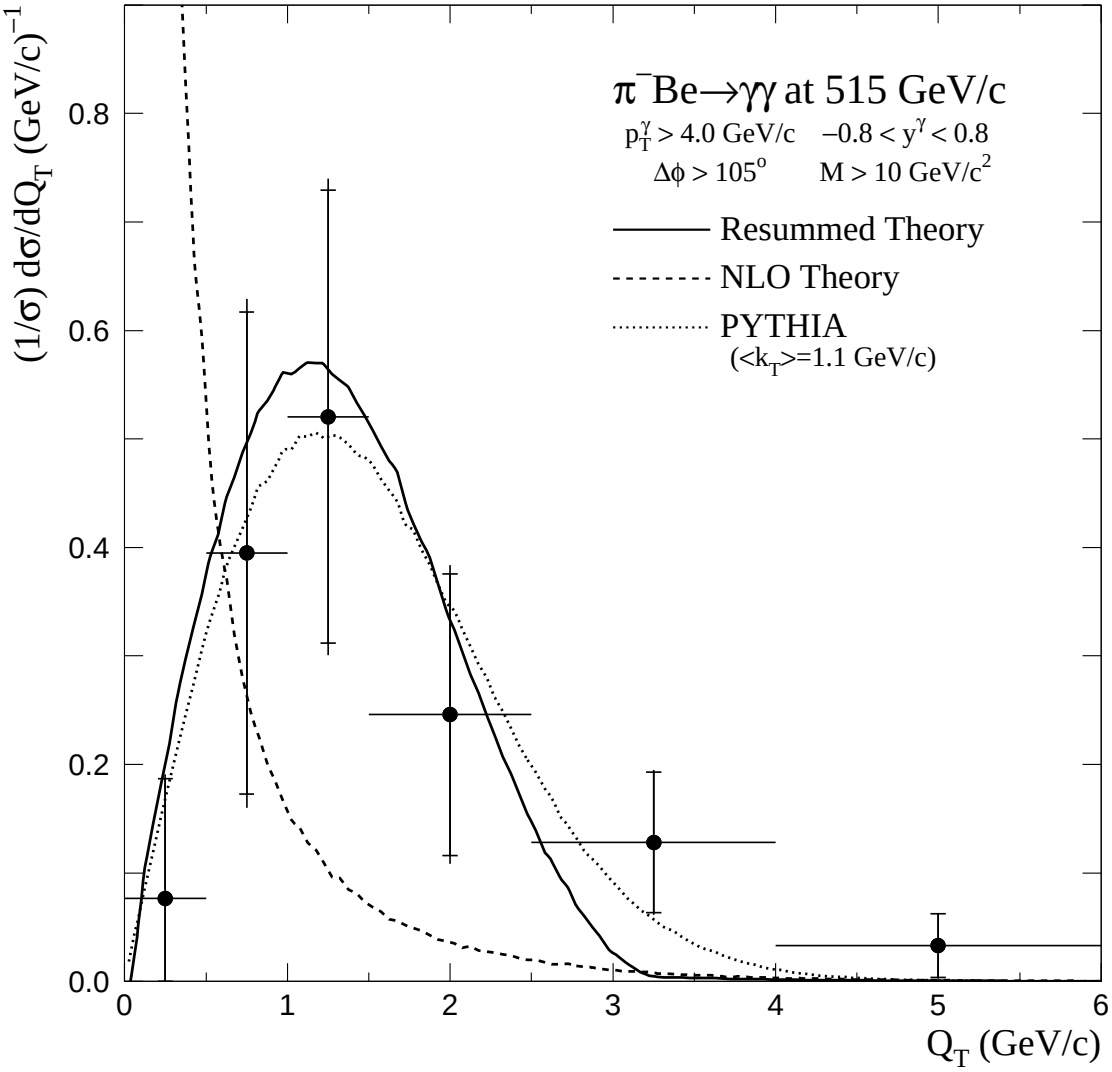

Figure 11.5 The diphoton Q_T distribution produced by 515 GeV/c π^- incident on beryllium. Overlayed on the data are the results from NLO [149] (dashed) and resummed [150] (solid) calculations. `PYTHIA` [121] results (dotted) with $\langle k_T \rangle = 1.1$ GeV/c are also shown.

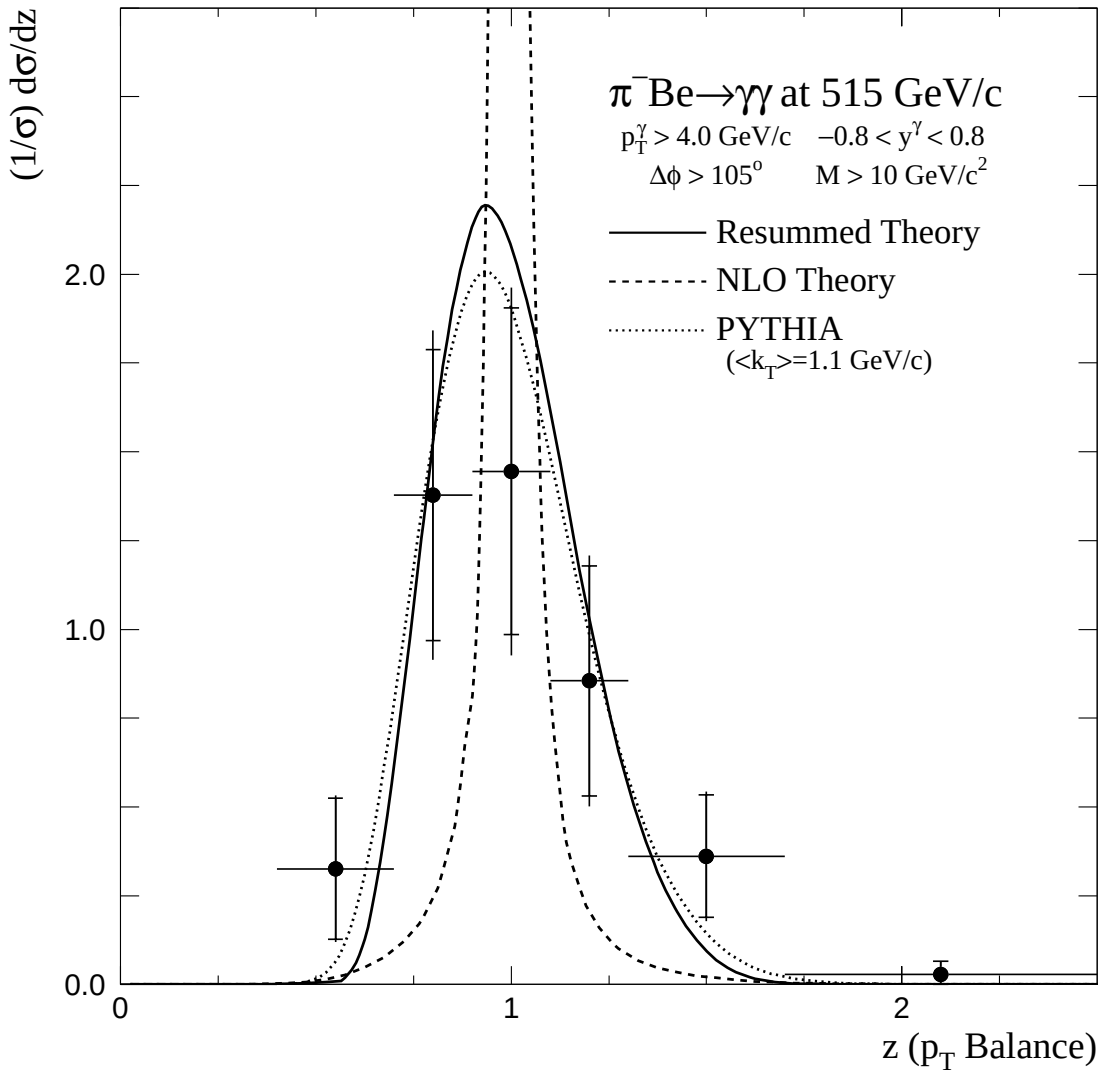

Figure 11.6 The diphoton z distribution produced by 515 GeV/c π^- incident on beryllium. There are two entries per pair. Overlayed on the data are the results from NLO [149] (dashed) and resummed [150] (solid) calculations. `PYTHIA` [121] results (dotted) with $\langle k_T \rangle = 1.1$ GeV/c are also shown.

Quantity	Experimental Resolution (MeV/c)	Measured Value (GeV/c)	$\langle k_T \rangle$ (GeV/c)
$\langle Q_T \rangle$	100	1.6 ± 0.5	1.1 ± 0.4
$\sigma(p_{OUT})$	10	1.3 ± 0.2	1.1 ± 0.2
$\langle \lvert p_{OUT} \rvert \rangle$	10	1.1 ± 0.3	1.1 ± 0.3

Table 11.1 Effective $\langle k_T \rangle$ values from several diphoton distributions.

100 MeV/c and for p_{OUT} it is approximately 10 MeV/c (for $\Delta\phi$ the resolution is approximately 0.4 degrees). These values are negligible on the scale of the measurements. All three quantities yield approximately the same value for $\langle k_T \rangle$ with the best estimate $\langle k_T \rangle = 1.1 \pm 0.2$ GeV/c. It is possible to approximate k_T effects in `PYTHIA`[1] using a Gaussian smearing technique. This program, using the value $\langle k_T \rangle = 1.1$ GeV/c, also provides a reasonable match to the distributions in Figures 11.3, 11.4, 11.5, and 11.6.

A measurement of the diphoton angular distribution provides another test of QCD. The $\cos\theta^\star$ distribution is displayed in Figure 11.7. Using the parameterization for this distribution given in Equation 1.9, the $\cos\theta^\star$ distribution was normalized at $\cos\theta^\star = 0$. Additional requirements were placed on the sample to avoid biases due to the p_T and rapidity cuts [87, 144]. The result from the resummed theoretical calculation [150] with the same physics cuts is overlayed on the data in Figure 11.7. The theory provides a good description of the data (though the data has poor statistics). For this data, the best α value is $\alpha = 0.9$ (the data statistics do not allow for a precise measurement of this value). The $\gamma\gamma$ $\cos\theta^\star$ distribution is flatter than that for the corresponding dipion sample (Figure 8.11).

[1] `PYTHIA` is an event generator that produces diphotons via the $q\bar{q}$ and gg processes (Table 1.5).

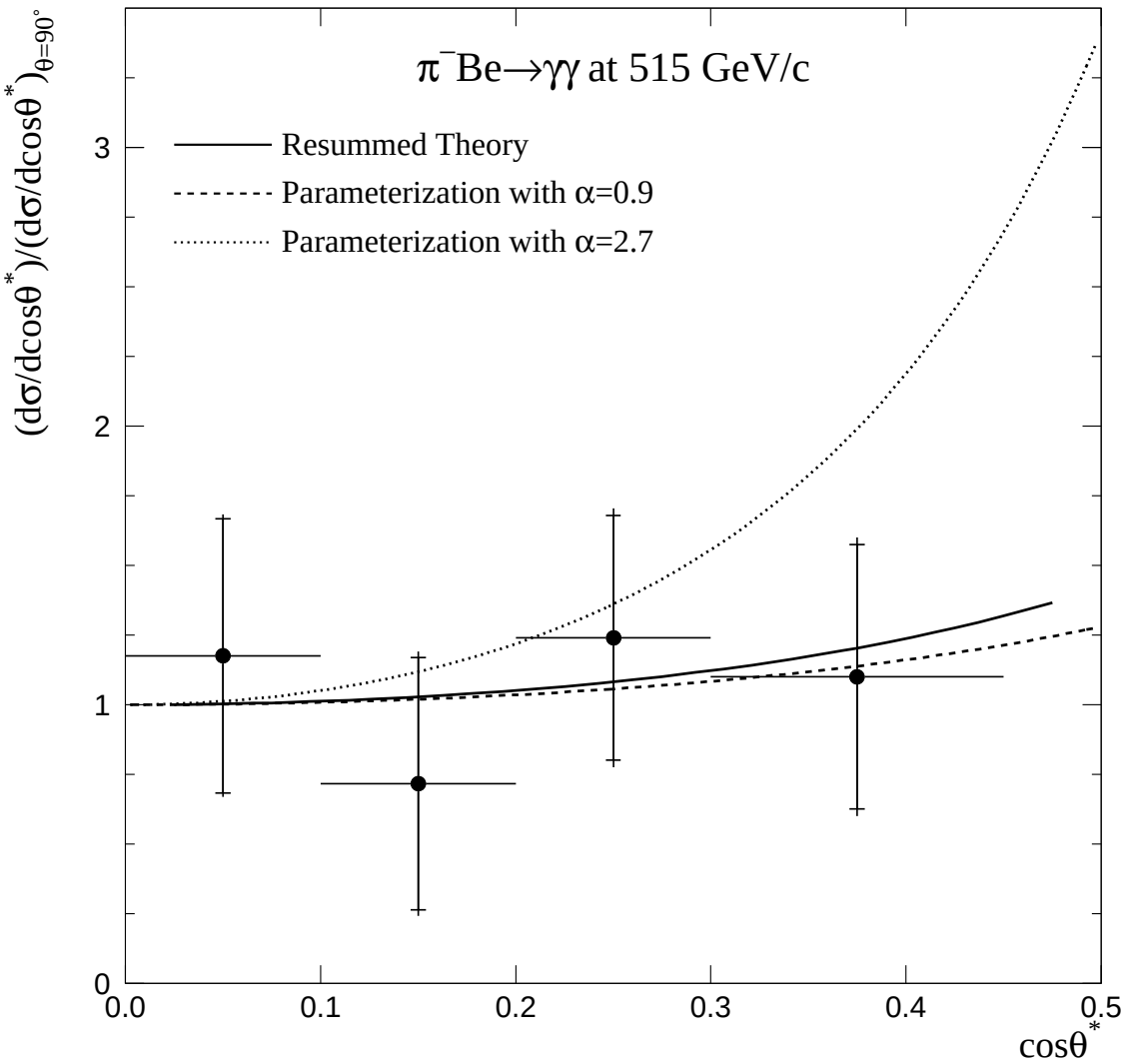

Figure 11.7 Distributions in $\cos\theta^\star$ for the 515 GeV/c π^-Be $\longrightarrow \gamma\gamma$ data with M $>$ 9.5 GeV/c. Additional requirements on the combinations contributing to this distribution are summarized at the beginning of Chapter 11. The parameterization refers to Equation 1.9 (dashed curve); the data was normalized at $\cos\theta^\star = 0$ using this function. The parameterization of the dipion result from Figure 8.11 is shown as the dotted curve. Also overlayed are the results from the resummed theory calculation [150] (solid curve).

Chapter 12 Conclusions

Direct-photon production has long been viewed as an ideal process for measuring the gluon distribution in the proton, and has been calculated to NLO in pQCD [154]. The quark–gluon Compton scattering subprocess ($gq \rightarrow \gamma q$ as shown in Figure 1.4) provides a large contribution to inclusive direct-photon production. The gluon distribution is relatively well constrained for $x < 0.1$ by deep-inelastic scattering and Drell-Yan data, but less so at larger x [155]. Direct-photon data can constrain the fits at large x, and consequently has been incorporated in several modern global parton distribution analyses [17, 18, 156]. In this chapter we summarize the results discussed in this thesis, placing them in the context of the other results obtained in E706 and other experiments that measured the production of direct photons.

A pattern of deviation has been observed between measured direct-photon cross sections and NLO calculations (Figures 12.1 and 12.2). The suspected origin of the disagreement is the effect of initial-state soft-gluon radiation [157, 145]. Correlations between high-p_T particles probe aspects of the hard scatter not easily accessible via studies of single inclusive particle production. In particular, studies of high-mass pairs of particles such as direct photons and π^0's can be used to extract information about the transverse momentum of partons prior to the hard scatter. Evidence of significant k_T has long been observed in measurements of dimuon, diphoton, and dijet production. A collection of measurements of the average transverse momentum of the pairs ($\langle Q_T \rangle$) is displayed in Figure 12.3 for a wide range of $\sqrt{s}$. The values of $\langle Q_T \rangle$ are large, and increase with increasing $\sqrt{s}$. The values of $\langle k_T \rangle$ per parton (estimated as $\approx \langle Q_T \rangle / \sqrt{2}$) indicated by these data are too large to be interpreted as only due to the size of the proton. From these

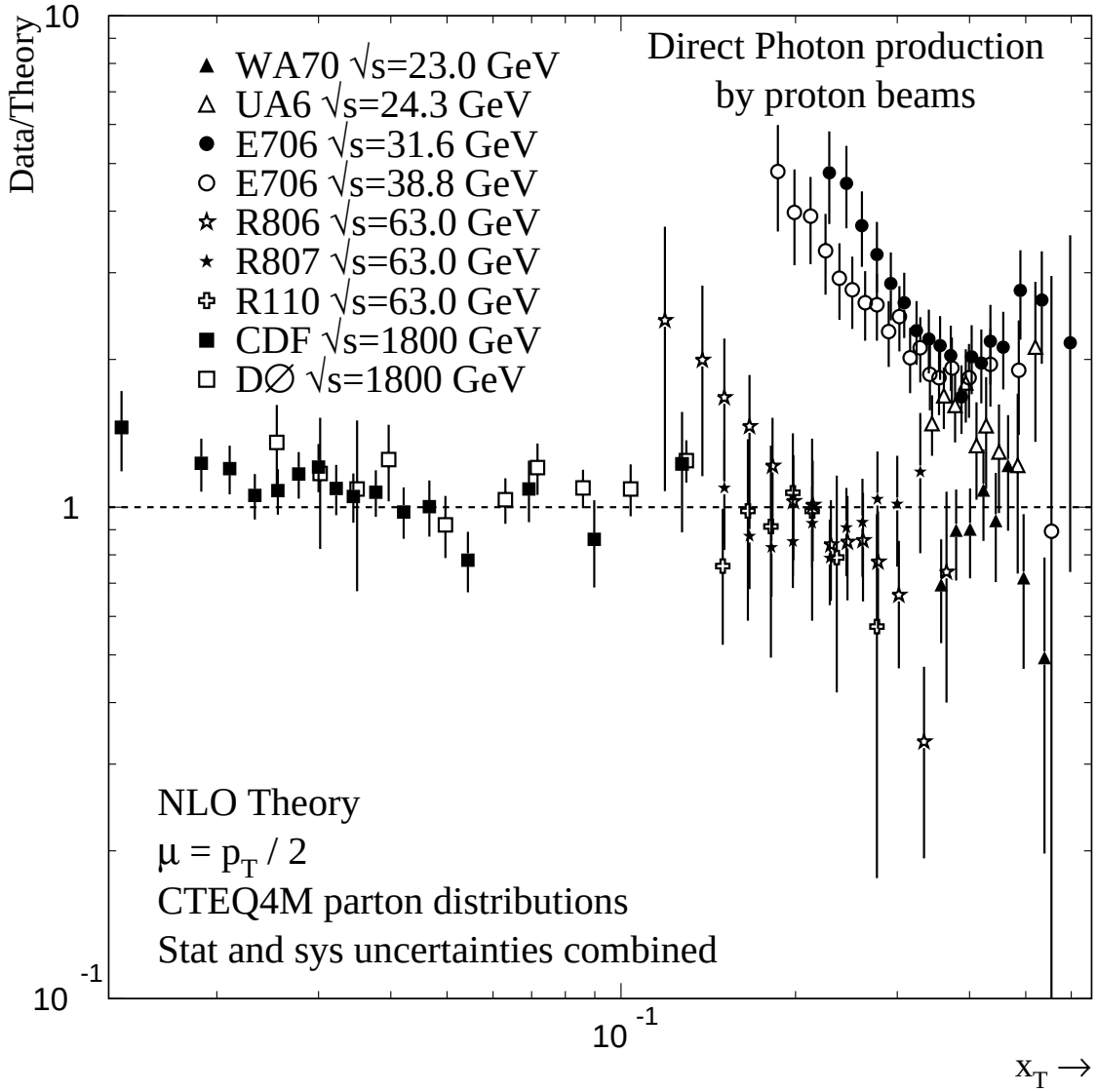

Figure 12.1 Comparison between proton-induced direct-photon data and NLO pQCD calculations for several experiments as a function of photon x_T.

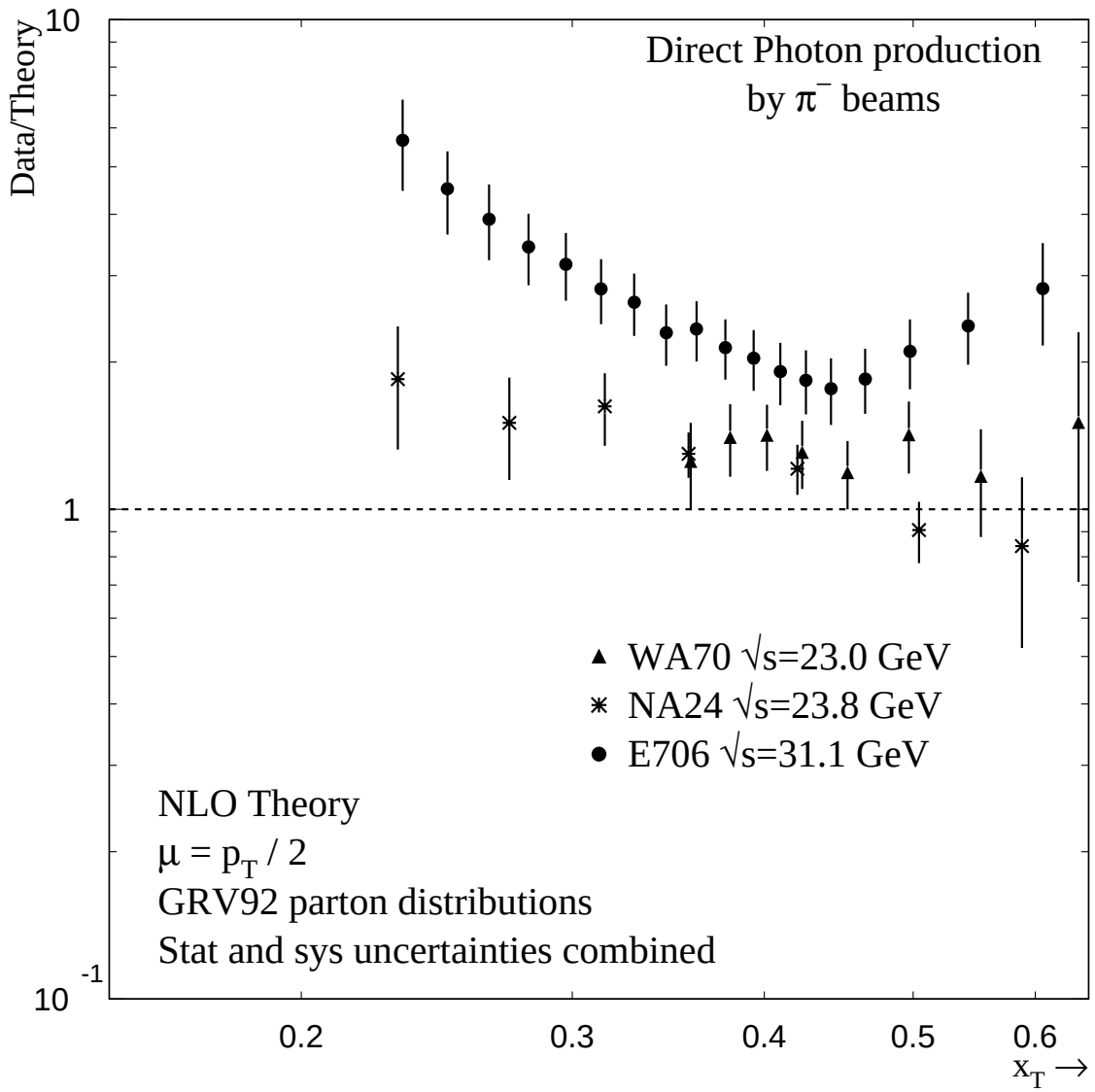

Figure 12.2 Comparison between π^- induced direct-photon data and NLO pQCD calculations for several experiments as a function of photon x_T.

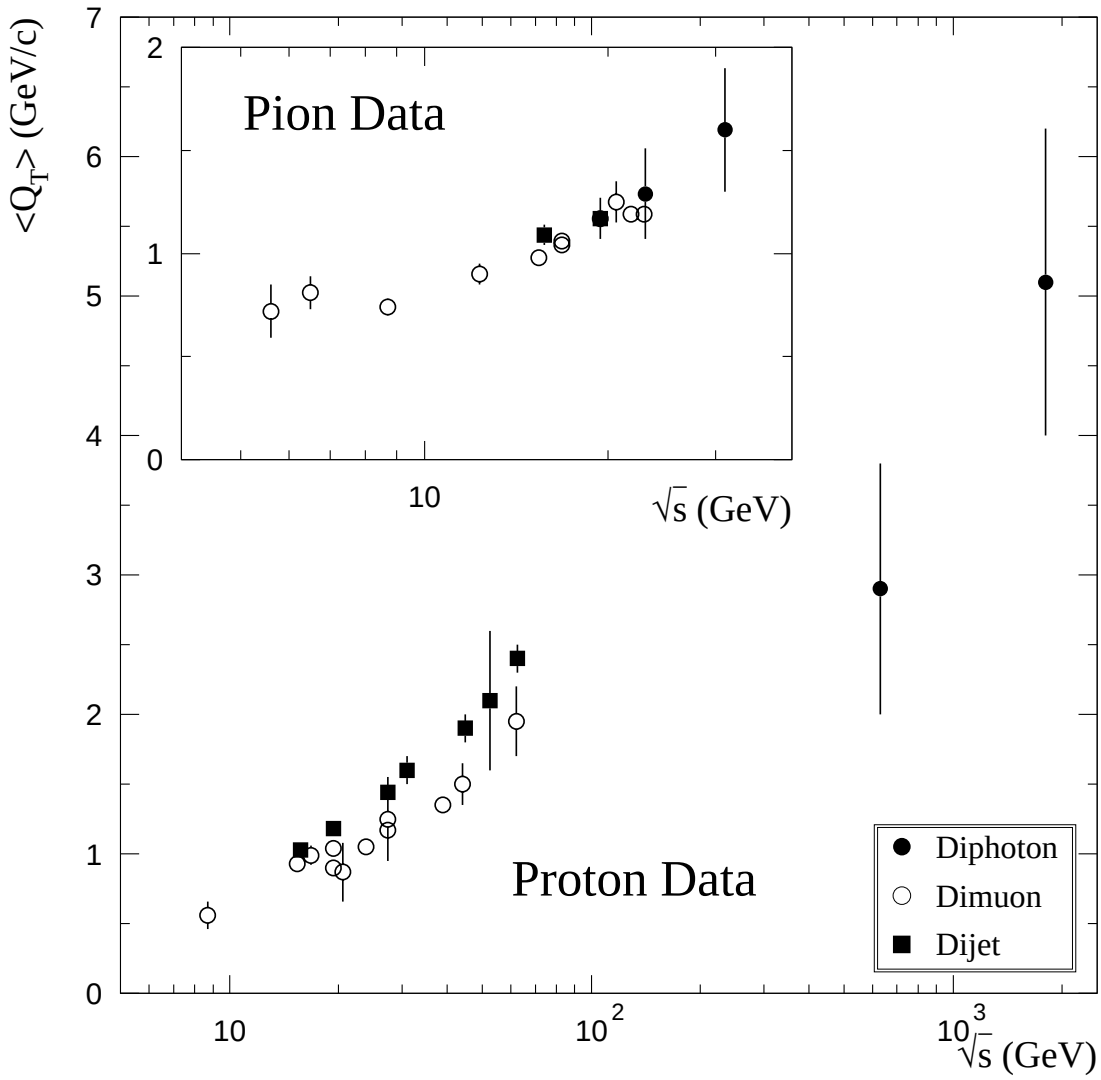

Figure 12.3 $\langle Q_T \rangle$ of pairs of muons, photons, and jets produced in hadronic collisions versus $\sqrt{s}$. The data point from Chapter 11 has been included on this plot.

observations, one can infer the $\langle k_T \rangle$ per parton is of order 1 GeV/c at fixed-target energies, increasing to 3 to 4 GeV/c at the Tevatron collider, whereas one would expect $\langle k_T \rangle$ values on the order of 0.3 to 0.5 GeV/c based solely on proton size.

The distributions of high-mass direct-photon pairs as a function of $\Delta\phi$, p_{OUT}, Q_T, and z are shown in Figure 12.4 for 515 GeV/c π^-Be interactions. Overlayed on the data are the results from both NLO [149] and resummed [150] pQCD calculations. The shape of the NLO calculation is inconsistent with the data distributions. The resummed calculation (`RESBOS`), which incorporates the effects of multiple soft-gluon emission, provides a reasonable match to the shape of the data. Also shown are the double direct-photon distributions from `PYTHIA` [121], where k_T effects have been approximated by a Gaussian smearing technique. `PYTHIA` provides a reasonable description of the diphoton data using a value for $\langle k_T \rangle$ consistent with the measurements displayed in Figure 12.4.

Similar signatures for k_T effects were seen in the analyses of high-mass $\pi^0\pi^0$ (Chapter 8), $\eta\pi^0$ (Chapter 9), and $\gamma\pi^0$ (Chapter 10). This is illustrated by Figure 12.5 which shows a comparison of the p_{OUT} distribution from each of the samples. The LO pQCD calculation [11], which incorporates k_T effects using a Gaussian smearing technique similar to that used in `PYTHIA` [121], provides a reasonable characterization of k_T-sensitive variables such as $\Delta\phi$ and p_{OUT} for $\langle k_T \rangle$ values similar to that measured for diphotons. The $\langle k_T \rangle$ values necessary to provide good matches to the data are slightly larger for $\pi^0\pi^0$ and $\gamma\pi^0$ than for $\gamma\gamma$, but that is expected since π^0's emanate from final-state quarks and gluons which can produce additional gluon radiation.

A comparison between our measured high-p_T $D^\pm$ cross section and NLO pQCD [158] (Figure 12.6) also shows evidence of substantial k_T. Similar soft-gluon effects are expected in other hard-scattering processes, such as the inclusive

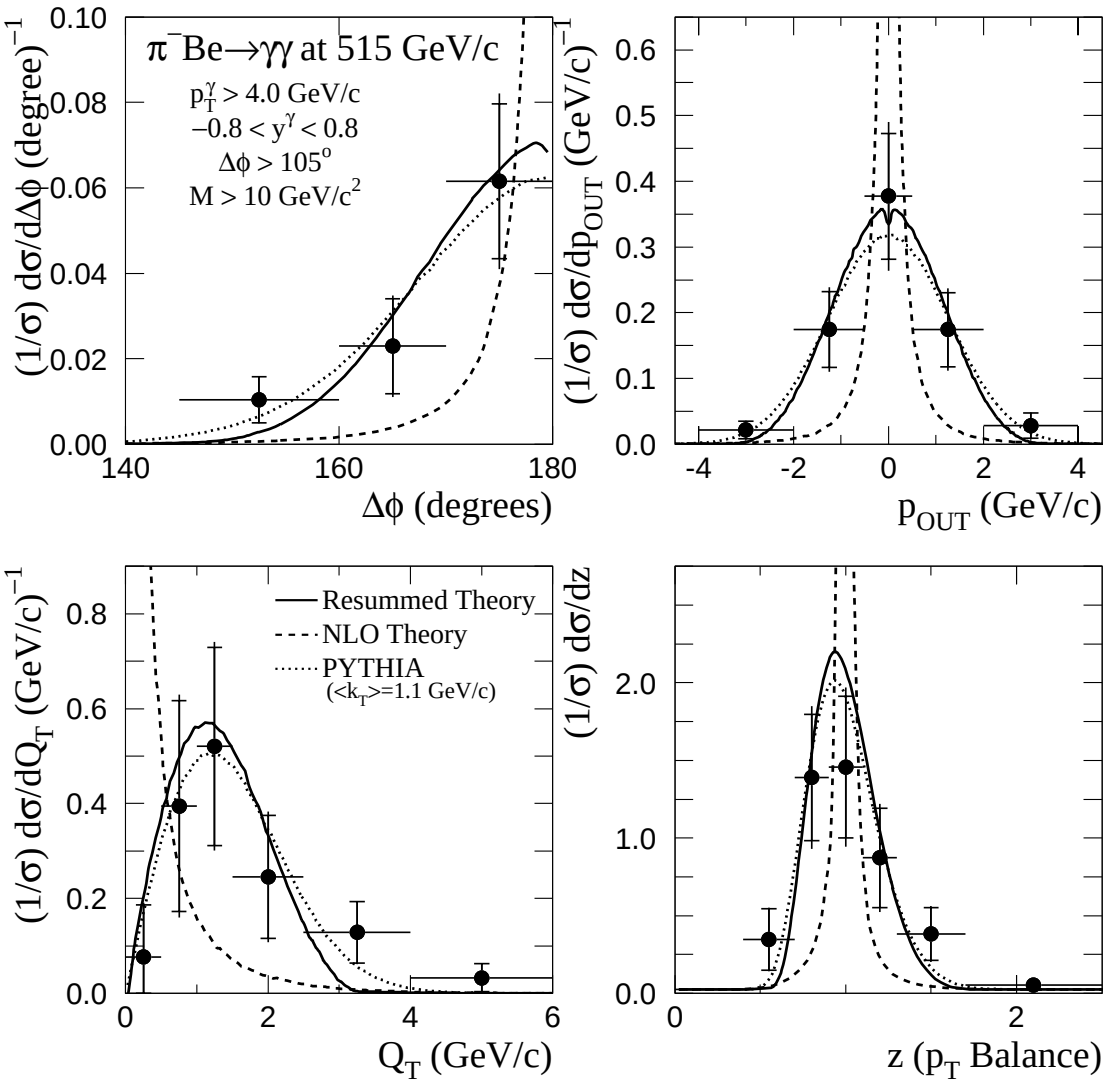

Figure 12.4 Diphoton $\Delta\phi$, p_{OUT}, Q_T, and z distributions produced by 515 GeV/c π^- incident on beryllium. The p_{OUT} and z distributions have two entries per pair. Overlayed on the data are the results from NLO [149] (dashed) and resummed [150] (solid) calculations. `PYTHIA` [121] results (dotted) with $\langle k_T \rangle = 1.1$ GeV/c are also shown.

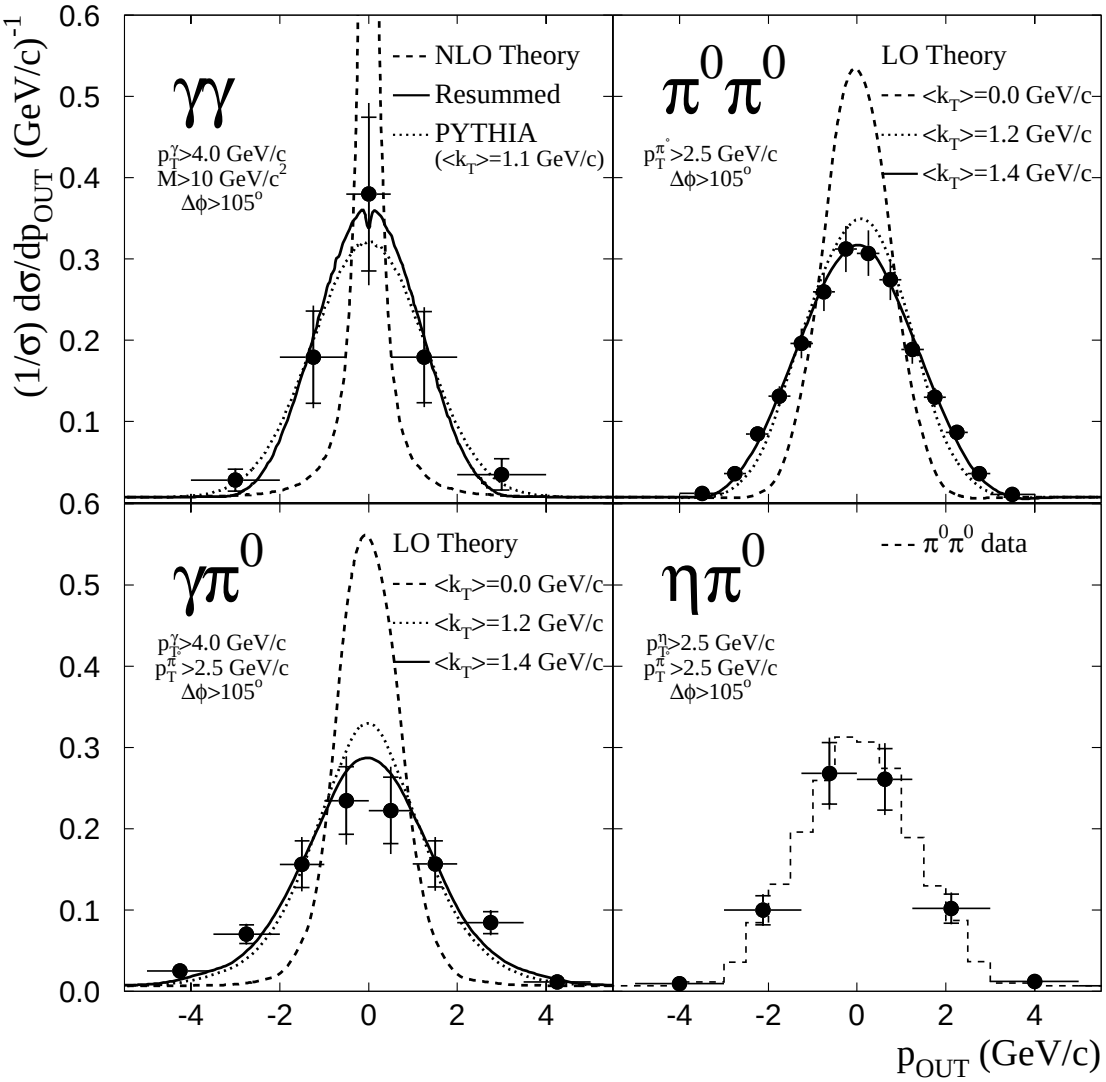

Figure 12.5 p_{OUT} distributions for $\gamma\gamma$, $\pi^0\pi^0$, $\gamma\pi^0$, and $\eta\pi^0$ produced by 515 GeV/c π^- incident on beryllium. There are two entries per pair. Overlayed on the diphoton data are the results from NLO [149] and resummed [150] pQCD calculations. `PYTHIA` [121] results with $\langle k_T \rangle = 1.1$ GeV/c are also shown. Overlayed on the $\pi^0\pi^0$ and $\gamma\pi^0$ are the results from LO pQCD calculations [11] for various values of $\langle k_T \rangle$ and fixed $\langle q_T \rangle = 0.6$ GeV/c. The $\pi^0\pi^0$ data has been overlayed on the $\eta\pi^0$ data for comparison.

production of jets or direct photons [159, 160, 161, 15]. Invariant cross sections for inclusive direct-photon and π^0 production are displayed for the 515 GeV/c π^-Be sample in Figure 12.7 with overlays from theory. Discrepancies between the NLO theory (dotted curves) and the data are particularly striking.

Fully resummed pQCD calculations for single direct-photon production are anticipated shortly [162, 163, 143]. Two independent threshold resummed pQCD calculations now exist [164, 165]; this resummed theory, which does not include k_T effects, exhibits less dependence on scale than the NLO theory (Figure 12.8). The threshold resummed calculation agrees with the NLO calculation for scale $\mu = p_T/2$. This scale was chosen for our inclusive comparisons with NLO pQCD. The equivalent scale, $\mu = p_T/2 \approx M/4$, successfully characterized the $\gamma\pi^0$ cross section as a function of the k_T-insensitive mass variable (Figure 10.2). Since current NLO calculations do not account for the effects of multiple soft-gluon emission, we employed a phenomenological model to incorporate k_T effects in pQCD calculations of direct-photon and π^0 production [166, 145].

We use the same LO pQCD [11], which successfully characterized the high-mass pairs, to create K-factors for inclusive cross sections (Figure 12.9), and then apply these K-factors to the NLO calculations. We recognize that this procedure involves a risk of double-counting since some of the k_T-enhancement may already be contained in the NLO calculation. However, we expect the effects of such double-counting to be small. The generated k_T-enhancements, using $\langle k_T \rangle$ values consistent with the high-mass pair data, describe both the shape and normalization of direct-photon and π^0 inclusive cross sections (Figures 12.7 and 12.10).

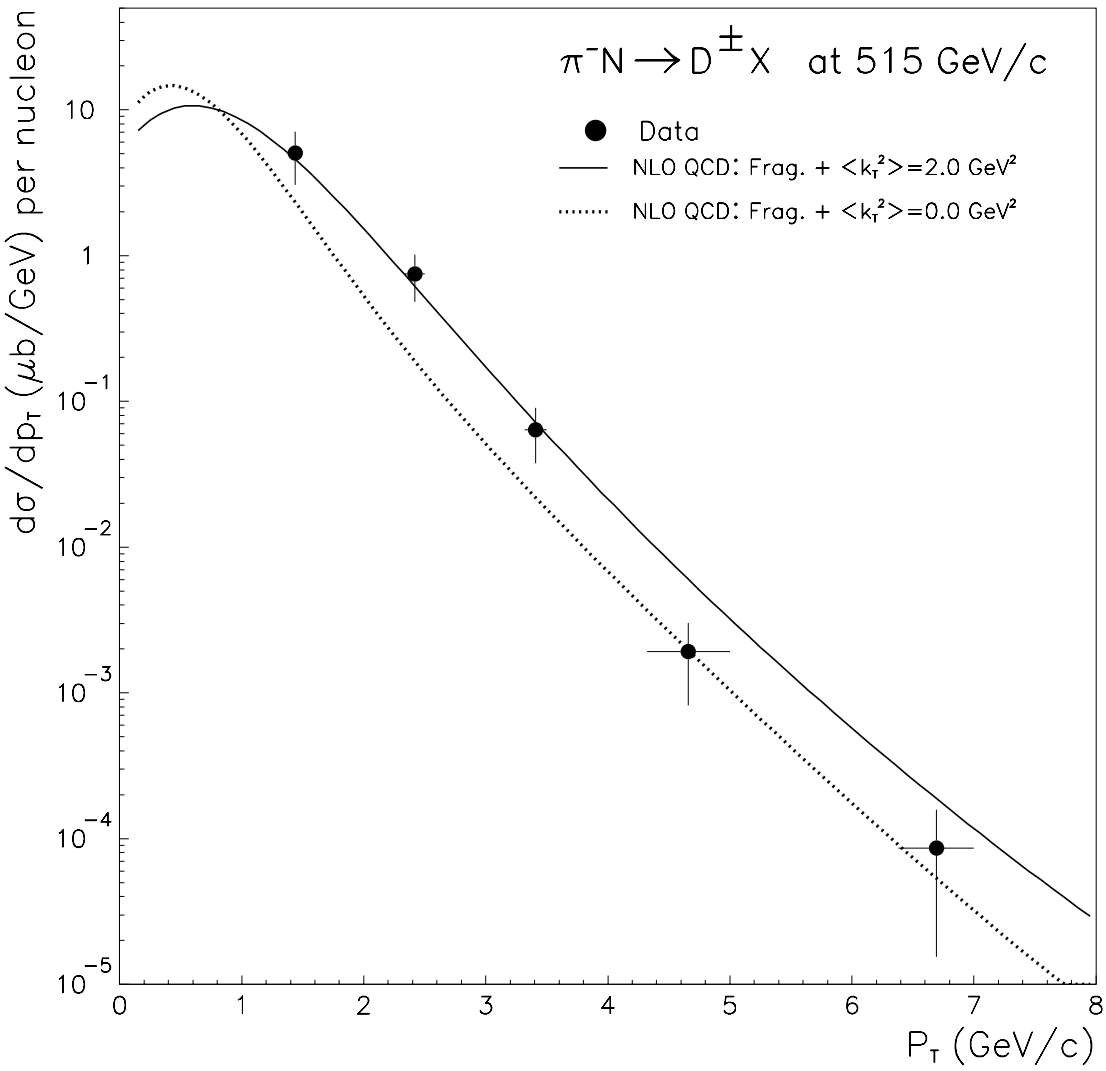

Figure 12.6 Charged D meson production for 515 GeV/c π^-N interactions as a function of the p_T of the charged D. Overlayed are the results of NLO calculations with and without k_T [158].

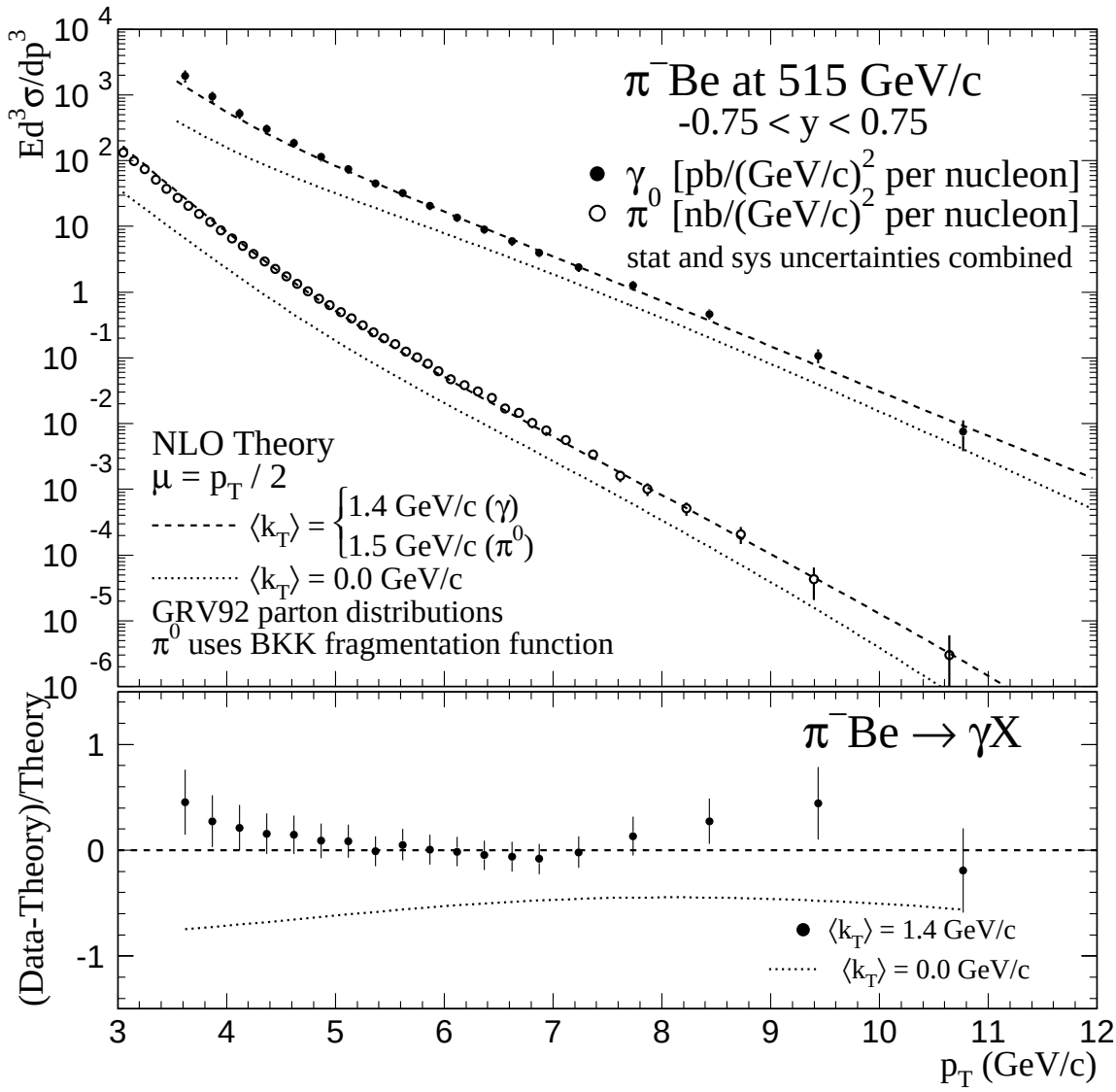

Figure 12.7 Top: The photon and π^0 cross sections at $\sqrt{s} = 31.1$ GeV compared to the k_T-enhanced NLO calculations. Bottom: The quantity (Data - Theory)/Theory for direct-photon production.

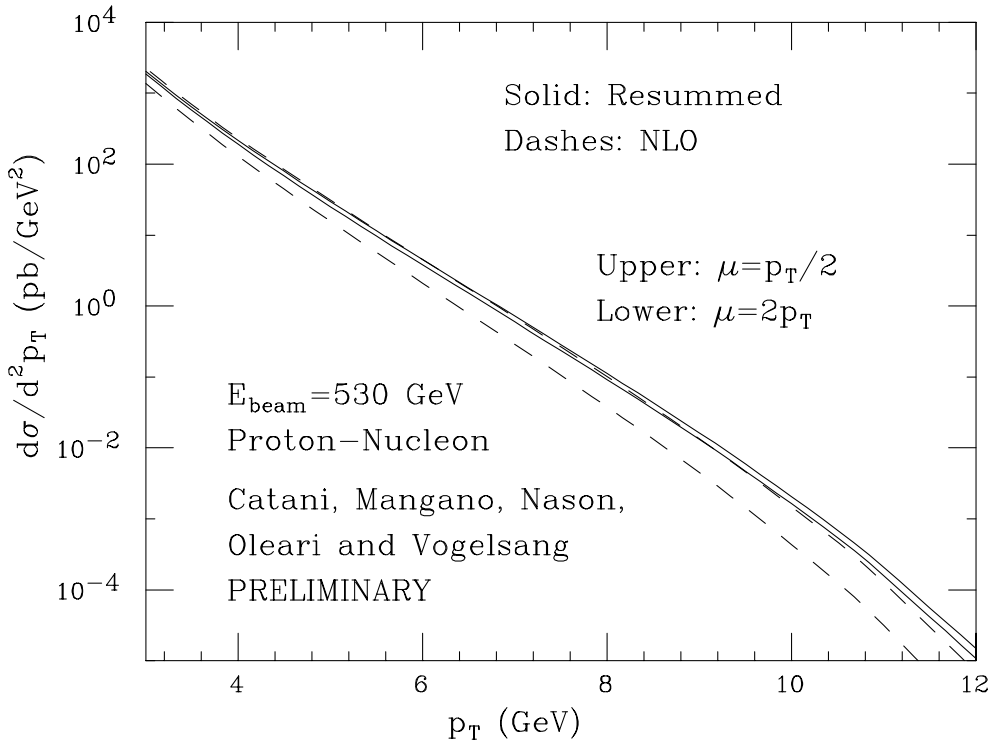

Figure 12.8 Comparison between a threshold resummed and a NLO theory calculation for direct-photon production for two scale choices: $p_T/2$ and $2p_T$ [164]. The threshold resummed theory exhibits a smaller dependence on scale than the NLO calculation and corresponds to the NLO theory with $\mu = p_T/2$.

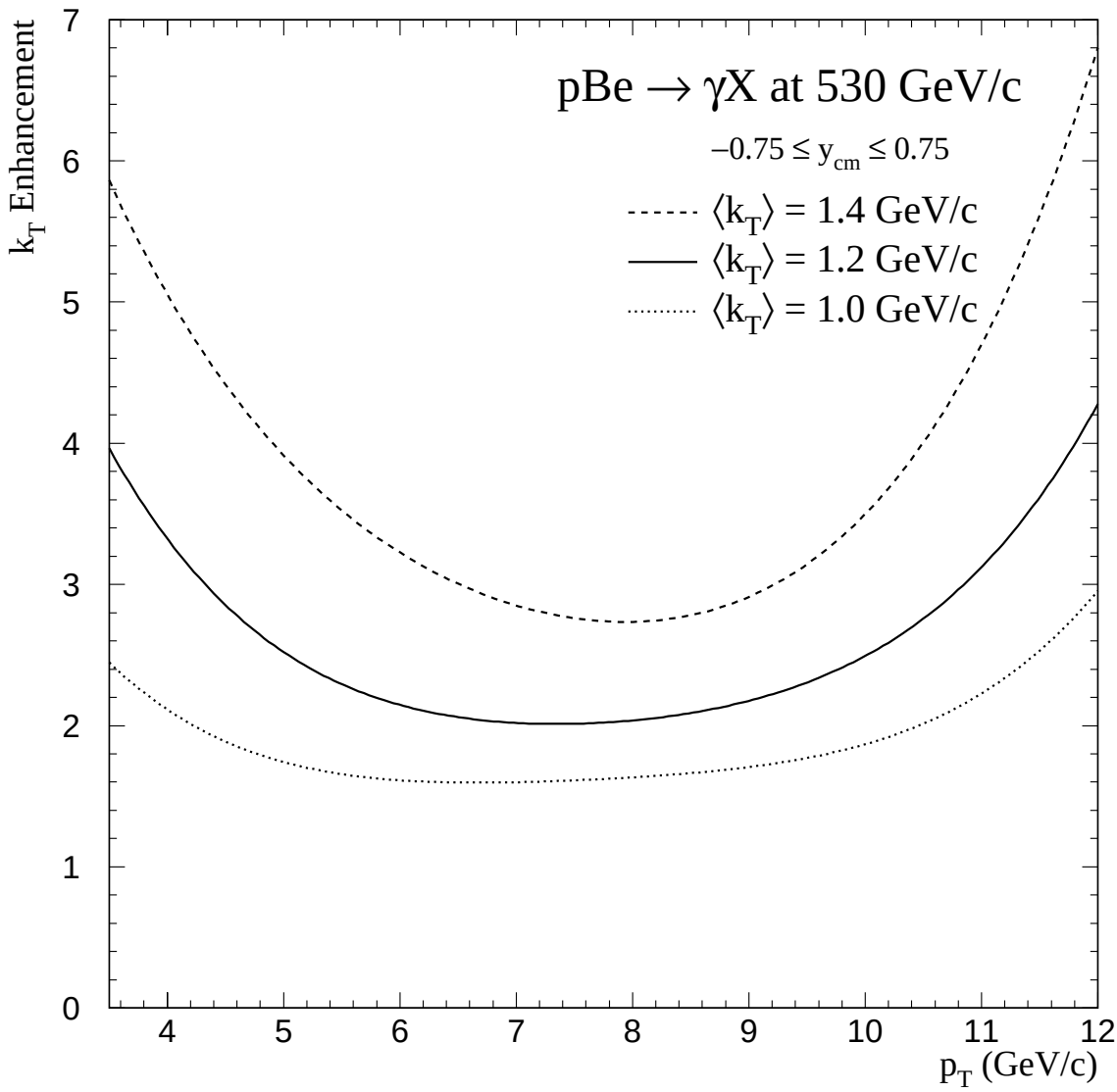

Figure 12.9 The variation of k_T enhancements, $K(p_T)$, for the 530 GeV/c pBe data.

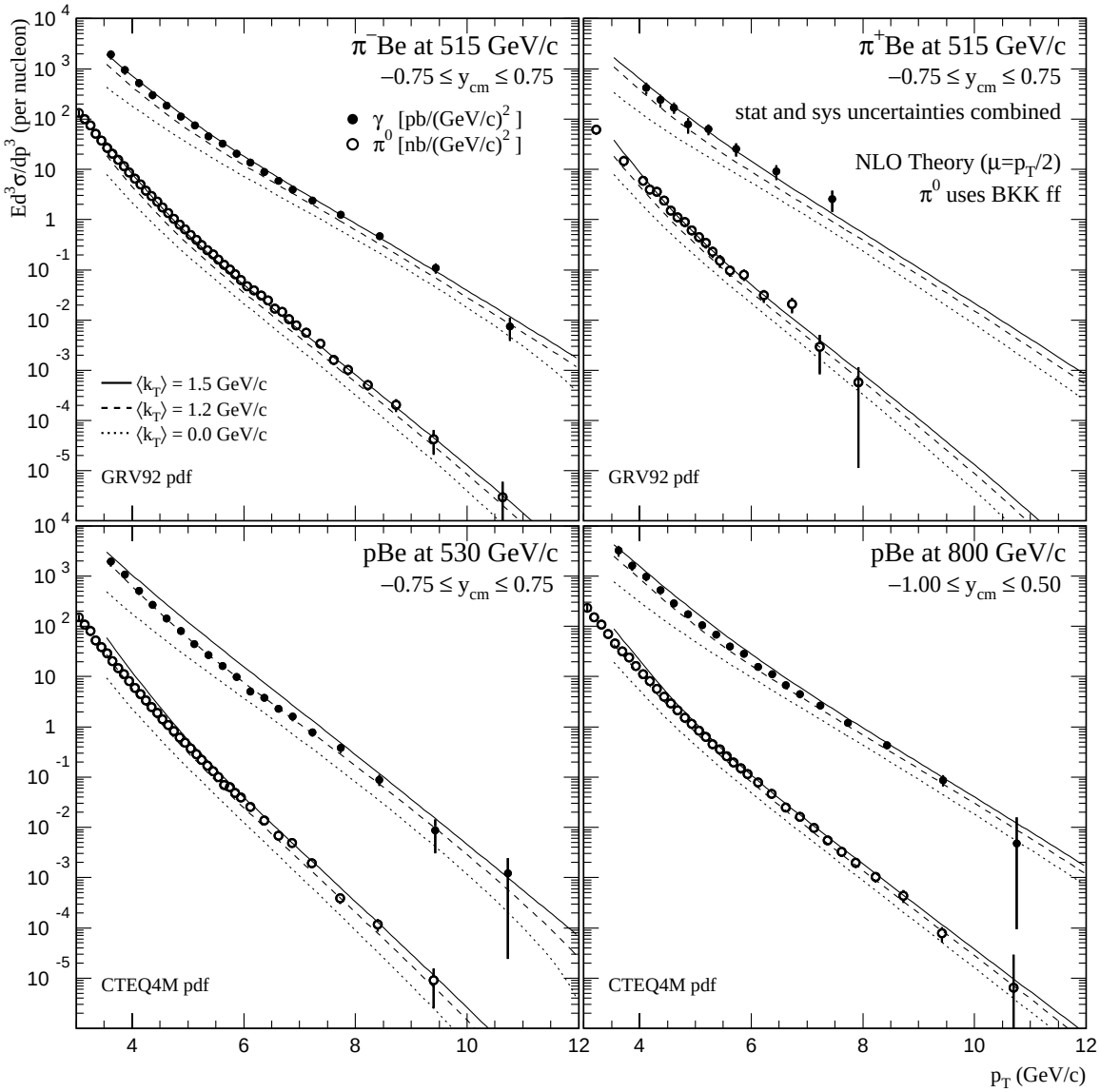

Figure 12.10 Invariant differential cross sections per nucleon for direct-photon and π^0 production in π^-Be and π^+Be interactions at 515 GeV/c and pBe interactions at 530 GeV/c and 800 GeV/c. Cross sections are shown as a function of p_T averaged over the full rapidity range. Overlayed on the data are the results of the NLO calculation with k_T enhancements for several values of $\langle k_T \rangle$.

We can use this phenomenological k_T model to compare with results of other experiments. The consequences of k_T smearing are expected to depend on $\sqrt{s}$ (Figure 12.3). At the Tevatron collider [167], where p_T is large compared to k_T, the above model of soft-gluon radiation leads to a relatively small modification of the NLO cross section. Only the lowest end of the p_T spectrum is modified significantly (Figure 12.11). Using diphotons, CDF has measured $\langle k_T \rangle = 3.6 \pm 0.8$ GeV/c at $\sqrt{s} = 1.8$ TeV [24]. Employing this value, the phenomenological model adequately describes the excess over NLO theory at low p_T for both CDF and DØ. The agreement between the phenomenological model and the collider direct-photon data can also be seen in preliminary CDF data at $\sqrt{s} = 630$ GeV (Figure 12.12).

Comparisons are also shown for WA70 [169, 54, 55] and UA6 [58] data (Figure 12.13). Both WA70 and UA6 have measured direct-photon and π^0 production with good statistics, and their direct-photon data have been included in recent global fits of parton distributions. The center-of-mass energies for these two experiments ($\sqrt{s} \approx 24$ GeV) are lower than those for E706. Correspondingly, $\langle k_T \rangle$ values for these experiments are expected to be slightly smaller than the values used for E706. WA70 measured $\langle k_T \rangle = 0.9 \pm 0.1 \pm 0.2$ GeV/c using their diphoton sample [66, 23]. We therefore use this $\langle k_T \rangle$ as the central value for the k_T-enhancement factors for both experiments, and vary the $\langle k_T \rangle$ by ± 0.2 GeV/c (Figure 12.13). Over the narrower p_T range of the WA70 and UA6 measurements, the effect of k_T is essentially to produce a shift in normalization. The k_T-enhanced theory compares well with the π^0 cross sections and with the UA6 and π^- beam WA70 direct-photon cross sections.

There are other, similar, phenomenological models that account for k_T effects in direct-photon and π^0 production [170, 171]. Such models are motivated by

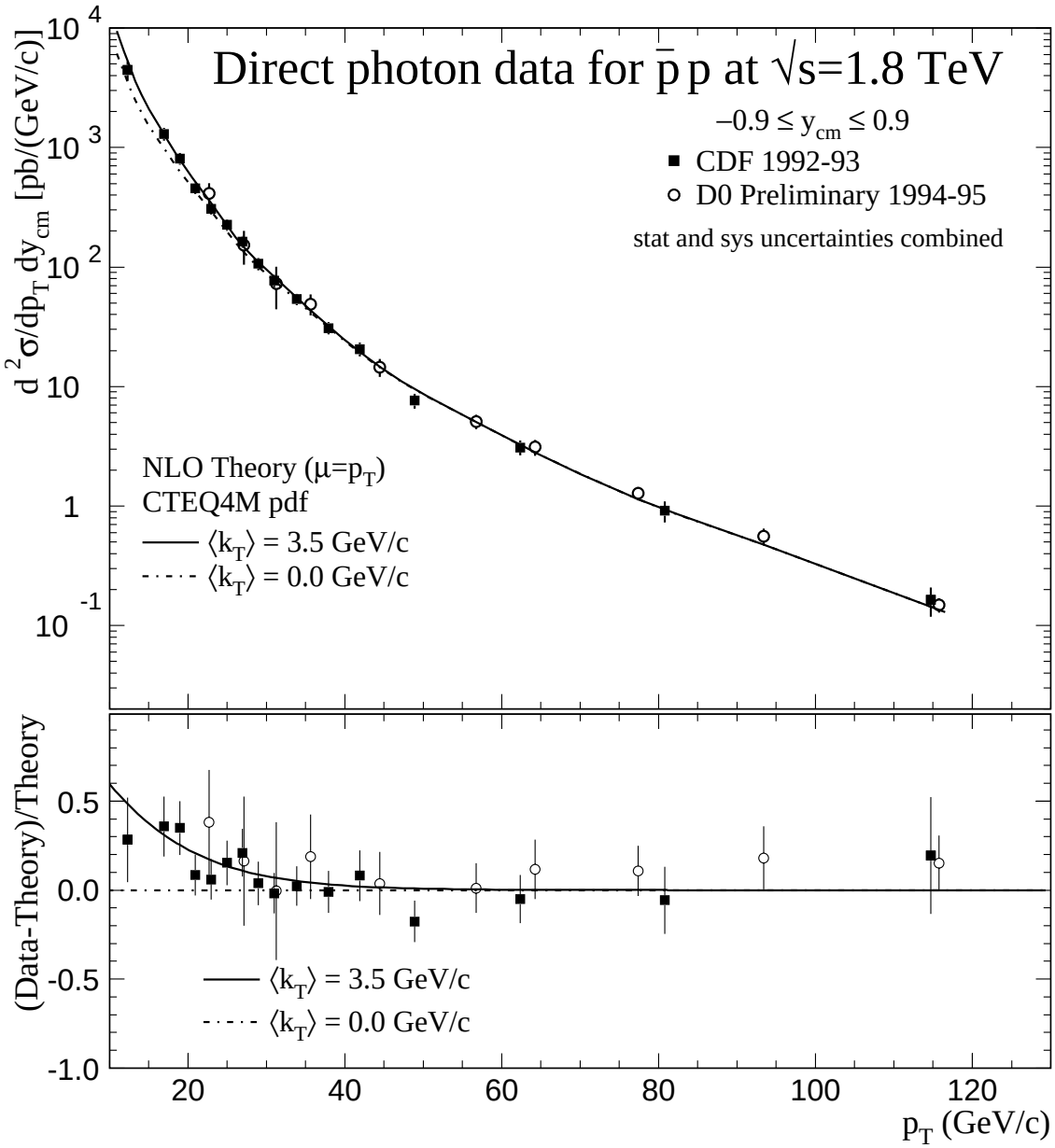

Figure 12.11 Isolated direct-photon cross sections from CDF and DØ at $\sqrt{s}$ = 1.8 TeV. Overlayed on the data are the results of the NLO calculations with (solid) and without (dashed) k_T enhancements for $\langle k_T \rangle$ = 3.5 GeV/c.

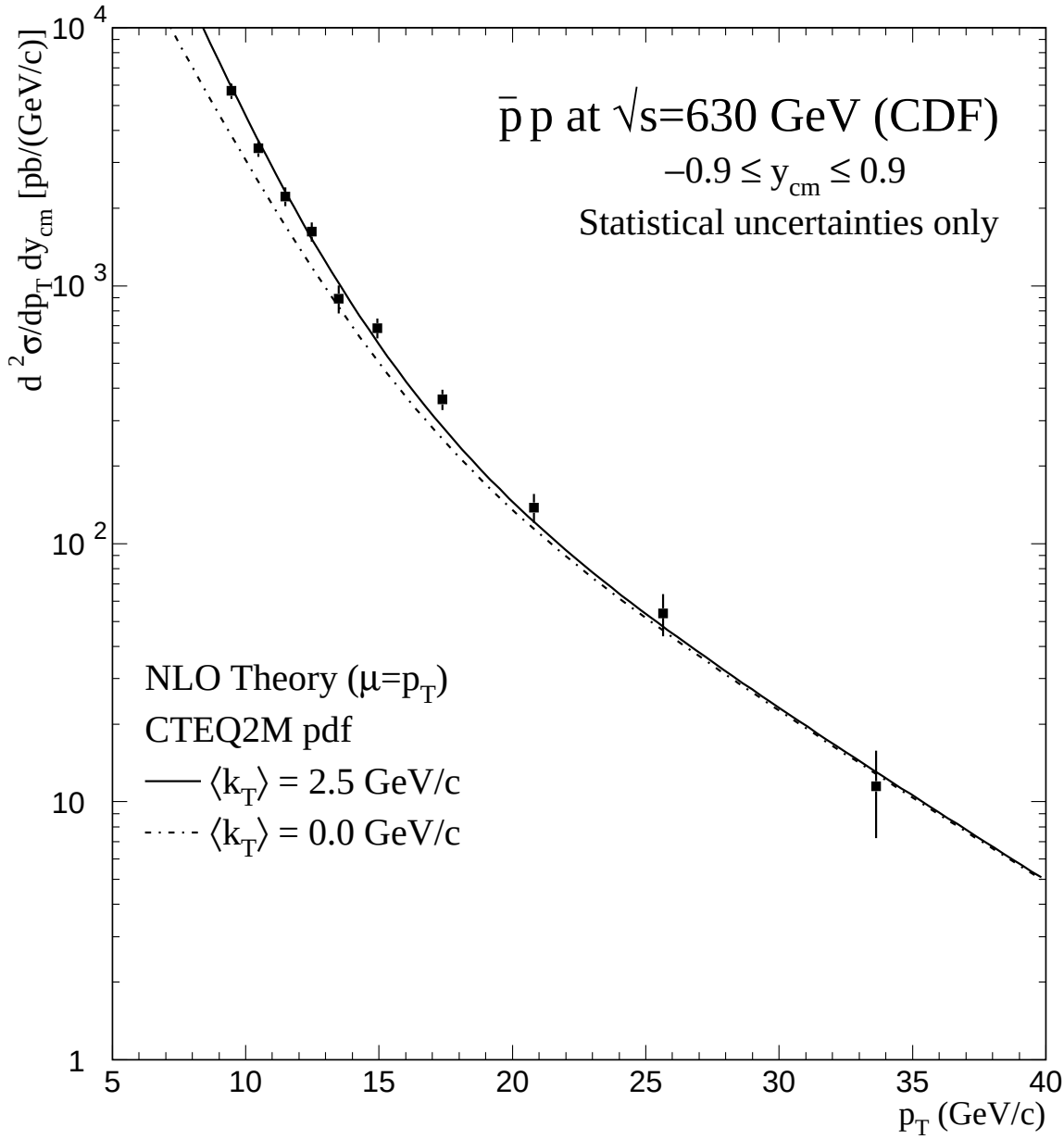

Figure 12.12 Preliminary, isolated direct-photon cross section for CDF at $\sqrt{s}$ = 630 GeV [168]. Overlayed on the data are the results of the NLO calculations with (solid) and without (dashed) k_T enhancements for $\langle k_T \rangle$ = 2.5 GeV/c.

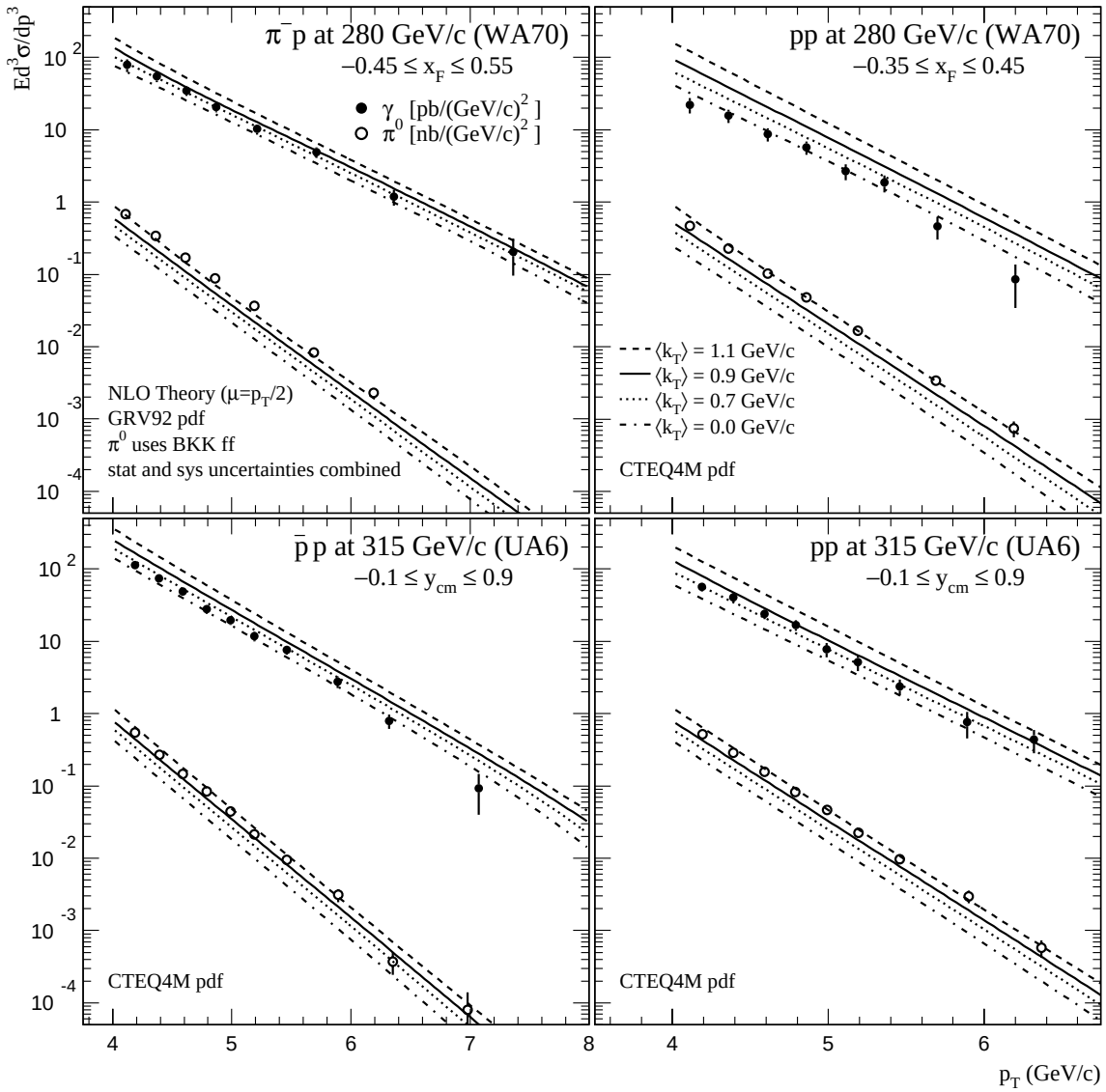

Figure 12.13 Invariant cross sections for direct-photon and π^0 production from WA70 (top) and UA6 (bottom). Overlayed on the data are the results of the NLO calculation with k_T enhancements for several values of $\langle k_T \rangle$.

studies for the Relativistic Heavy Ion Collider (RHIC) where it is hoped that direct-photon production can be used as one indication of quark–gluon plasma formation. Direct photons are expected to emerge without much rescattering in the final state, but the production rates of hadrons such as the π^0 should be suppressed [172]. Analyses of pairs of direct photons and π^0's are particularly interesting since they can be used to examine features of the quark–gluon plasma formation that are not easily studied by measurements of single-particle production [173].

Measurements of the production of high-mass pairs of high-p_T particles at E706 provide a consistent picture of k_T. NLO pQCD calculations [149], which include effects due to the radiation of a single hard gluon, compare poorly to k_T-sensitive distributions in diphoton data. `RESBOS` [150], a NLO pQCD calculation, which also includes the effects of multiple soft-gluon emission through the CSS resummation technique, compares well with the shape of the diphoton data. LO pQCD calculations [11, 121] that incorporate k_T effects through Gaussian smearing techniques, provide reasonable characterizations of distributions for pairs of direct photons, π^0's, and η's. LO theory can also be used to estimate the impact of k_T on the inclusive production of high-p_T direct photons and π^0's. This simple phenomenological model is able to account for differences between NLO pQCD calculations and inclusive data over a wide range in $\sqrt{s}$. This, and the success of the k_T-resummed pQCD calculation in describing the shapes of the double direct-photon distributions, point to the need for a k_T-resummed pQCD calculation for single direct-photon production. Such a calculation would be of benefit in the extraction of the gluon distribution function at medium to high-x values, where G(x) is not well constrained.

References

[1] M. Begel, *Photon Interference with Independent Laser Beams*, Senior Thesis, Reed College, 1991.

[2] M. de León, *Zohar: The Book of Enlightenment* (Paulist Press, Ramsey, NJ, 1983), Translated by D. Matt.

[3] Titus Lucretius Carus, *On the Nature of the Universe* (Penguin Books, London, 1951), Translated by R. E. Latham.

[4] Aristotle, *Physics* (Oxford University Press, 1996), Translated by R. Waterfield.

[5] H. Haber, *The Walt Disney story of Our Friend The Atom* (Dell Publishing Co., New York, 1956).

[6] R. Cahn and G. Goldhaber, *The Experimental Foundations of Particle Physics* (Cambridge University Press, 1989).

[7] F. Halzen and A. Martin, *Quarks and Leptons* (John Wiley and Sons, 1984).

[8] D. Perkins, *Introduction to High Energy Physics* (Addison-Wesley, 1987).

[9] C. Quigg, *Gauge Theories of the Strong, Weak, and Electromagnetic Interactions* (Addison-Wesley, 1983).

[10] R. M. Barnett *et al.*, *Review of particle properties*, Phys. Rev. **D54**, 1 (1996).

[11] J. F. Owens, *Large-momentum-transfer production of direct photons, jets, and particles*, Rev. Mod. Phys. **59**, 465 (1987).

[12] E. Rutherford, *The scattering of α and β particles by matter and the structure of the atom*, Philosophical Magazine **21**, 669 (1911).

[13] E. Bloom *et al.*, *High-energy inelastic e–p scattering at* $6°$ *and* $10°$, Phys. Rev. Lett. **23** (1969).

[14] M. Breidenbach *et al.*, *Observed behavior of highly inelastic electron–proton scattering*, Phys. Rev. Lett. **23** (1969).

[15] R. P. Feynman, R. D. Field, and G. C. Fox, *A quantum chromodynamic approach for the large transverse momentum production of particles and jets*, Phys. Rev. **D18**, 3320 (1978).

[16] CTEQ Collaboration, G. Sterman *et al.*, *Handbook of perturbative QCD*, Rev. Mod. Phys. **67**, 157 (1995).

[17] CTEQ Collaboration, H. L. Lai *et al.*, *Improved parton distributions from global analysis of recent deep inelastic scattering and inclusive jet data*, Phys. Rev. **D55**, 1280 (1997).

[18] M. Gluck, E. Reya, and A. Vogt, *Parton distributions for high-energy collisions*, Z. Phys. **C53**, 127 (1992).

[19] H. Plothow-Besch, *The parton distribution function library*, Int. J. Mod. Phys. **A10**, 2901 (1995).

[20] J. Binnewies, B. A. Kniehl, and G. Kramer, *Pion and kaon production in e^+e^- and ep collisions at next-to-leading order*, Phys. Rev. **D52**, 4947 (1995).

[21] E. L. Berger, E. Braaten, and R. D. Field, *Large-p_T production of single and double photons in proton-proton and pion-proton collisions*, Nucl. Phys. **B239**, 52 (1984).

[22] R. D. Field, *Applications of Perturbative QCD* (Addison-Wesley, 1989).

[23] WA70 Collaboration, E. Bonvin *et al.*, *Intrinsic transverse momentum in the $\pi^- p \longrightarrow \gamma\gamma X$ reaction at 280 GeV/c*, Phys. Lett. **B236**, 523 (1990).

[24] CDF Collaboration, F. Abe *et al.*, *Measurement of the cross section for the production of two isolated prompt photons in $p\bar{p}$ collisions at $\sqrt{s} = 1.8$ TeV*, Phys. Rev. Lett. **70**, 2232 (1993).

[25] WA11 Collaboration, R. Barate *et al.*, Phys. Rev. Lett. **21**, 1541 (1979); WA12 Collaboration, M. J. Corden *et al.*, Phys. Lett. **76B**, 226 (1978); R209 Collaboration, D. Antreasyan *et al.*, Phys. Rev. Lett. **47**, 12 (1981); NA3 Collaboration, J. Badier *et al.*, Phys. Lett. **117B**, 372 (1982); E288 Collaboration, A. S. Ito *et al.*, Phys Rev. **D23**, 604 (1981); E300 Collaboration, D. Antreaysan *et al.*, Phys. Rev. Lett. **39**, 906 (1977); E444 Collaboration, K. J. Anderson *et al.*, Phys. Rev. Lett. **42**, 944 (1979); E537 Collaboration, E. Anassontzis *et al.*, Phys Rev. **D38**, 1377 (1988); E605 Collaboration, G. Moreno *et al.*, Phys Rev. **D43**, 2815 (1991); E615 Collaboration, S. Palestini *et al.*, Phys. Rev. Lett. **55**, 2649 (1985); E615 Collaboration, J. S. Conway *et al.*, Phys Rev. **D39**, 92 (1989); E687 Collaboration, J. Alspector *et al.*, Phys. Lett. **81B**, 397 (1979).

[26] E395 Collaboration, M. D. Corcoran *et al.*, *A study of parton transverse momentum using jets from hadron interactions*, Phys. Rev. **D21**, 641 (1980).

[27] CCOR (R108) Collaboration, A. L. S. Angelis *et al.*, *Results on correlations and jets in high transverse momentum pp collisions at the CERN ISR*, Phys. Scripta **19**, 116 (1979).

[28] CCOR (R108) Collaboration, A. L. S. Angelis *et al.*, *A measurement of the transverse momenta of partons, and of jet fragmentation as a function of* $\sqrt{s}$ *in pp collisions*, Phys. Lett. **97B**, 163 (1980).

[29] R702 Collaboration, A. G. Clark *et al.*, *Large transverse momentum jets in high-energy proton-proton collisions*, Nucl. Phys. **B160**, 397 (1979).

[30] R. Baier, J. Engels, and B. Petersson, *Symmetric hadron pairs at large transverse momenta as a test of hard scattering models*, Z. Phys. **C2**, 265 (1979).

[31] CDF Collaboration, F. Abe *et al.*, *The CDF detector: An overview*, Nucl. Instrum. Methods **A271**, 387 (1988).

[32] DØ Collaboration, S. Abachi *et al.*, *The DØ detector*, Nucl. Instrum. Methods **A338**, 185 (1994).

[33] E629 Collaboration, C. Nelson *et al.*, *Operational performance of a large liquid argon photon calorimeter*, Nucl. Instrum. Methods **216**, 381 (1983).

[34] E704 Collaboration, D. Adams *et al.*, *Measurement of single spin asymmetry for direct photon production in pp collisions at 200 GeV/c*, Phys. Lett. **B345**, 569 (1995).

[35] E706 Collaboration, L. Apanasevich *et al.*, *Calibration and performance of the E706 lead and liquid-argon electromagnetic calorimeter*, Nucl. Instrum. Methods **A417**, 50 (1998).

[36] NA3 Collaboration, J. Badier *et al.*, *A large acceptance spectrometer to study high mass muon pairs*, Nucl. Instrum. Methods **175**, 319 (1980).

[37] NA3 Collaboration, F. Costantini *et al.*, *A new fine grained three coordinate readout shower chamber*, Nucl. Instrum. Methods **A225**, 463 (1984).

[38] NA24 Collaboration, C. D. Marzo *et al.*, *A segmented photon–hadron calorimeter using a two colored wavelength shifter optical readout system*, Nucl. Instrum. Methods **217**, 405 (1983).

[39] NA24 Collaboration, V. Artemev *et al.*, *Performance of a fine grained photon position detector using proportional tubes*, Nucl. Instrum. Meth. **A224**, 408 (1984).

[40] CCOR (R108) Collaboration, A. L. S. Angelis *et al.*, *Search for direct single photon production at large* p_T *in proton-proton collisions at* $\sqrt{s} = 62.4$ *GeV*, Phys. Lett. **94B**, 106 (1980).

[41] CMOR (R110) Collaboration, A. L. S. Angelis *et al.*, *Direct photon production at the CERN ISR*, Nucl. Phys. **B327**, 541 (1989).

[42] R806 Collaboration, J. H. Cobb *et al.*, *A large liquid argon shower detector for an ISR experiment*, Nucl. Instrum. Methods **158**, 93 (1979).

[43] AFS Collaboration, R. Carosi *et al.*, *A hexagonal uranium calorimeter for measuring electromagnetic showers at the CERN ISR*, Nucl. Instrum. Methods **A219**, 311 (1984).

[44] AFS Collaboration, T. Åkesson *et al.*, *Properties of a fine sampling uranium–copper scintillator hadron calorimeter*, Nucl. Instrum. Methods **A241**, 17 (1985).

[45] UA1 Collaboration, C. Albajar *et al.*, *Direct photon production at the CERN proton - anti-proton collider*, Phys. Lett. **209B**, 385 (1988).

[46] UA2 Collaboration, J. A. Appel *et al.*, *Direct photon production at the CERN* $\bar{p}p$ *collider*, Phys. Lett. **176B**, 239 (1986).

[47] UA6 Collaboration, L. Camilleri *et al.*, *A lead/proportional tube electromagnetic calorimeter for direct photon detection*, Nucl. Instrum. Methods **A286**, 49 (1990).

[48] WA70 Collaboration, M. Bonesini *et al.*, *Calibration of an electromagnetic calorimeter for direct photon physics*, Nucl. Instrum. Methods **A270**, 32 (1988).

[49] T. Ferbel and W. R. Molzon, *Direct-photon production in high-energy collisions*, Rev. Mod. Phys. **56**, 181 (1984).

[50] W. Vogelsang and M. R. Whalley, *A compilation of data on single and double prompt photon production in hadron-hadron interactions*, J. Phys. **G23**, Suppl. 7A (1997).

[51] P. Slattery *et al.*, P695: A Proposal to Measure Direct Photon Production at Tevatron Energies, October 26, 1981.

[52] E629 Collaboration, M. McLaughlin *et al.*, *Inclusive production of direct photons in 200 GeV/c collisions*, Phys. Rev. Lett. **51**, 971 (1983).

[53] NA3 Collaboration, J. Badier *et al.*, *Direct photon production from pions and protons at 200 GeV/c*, Z. Phys. **C31**, 341 (1986).

[54] WA70 Collaboration, M. Bonesini *et al.*, *High transverse momentum prompt photon production by π^- and π^+ on protons at 280 GeV/c*, Z. Phys. **C37**, 535 (1988).

[55] WA70 Collaboration, M. Bonesini *et al.*, *Production of high transverse momentum prompt photons and neutral pions in proton-proton interactions at 280 GeV/c*, Z. Phys. **C38**, 371 (1988).

[56] NA24 Collaboration, C. D. Marzo *et al.*, *A measurement of direct photon production at large transverse momentum in $\pi^- p$, $\pi^+ p$ and pp collisions at 300 GeV/c*, Phys. Rev. **D36**, 8 (1987).

[57] UA6 Collaboration, G. Sozzi *et al.*, *Direct photon production in $\bar{p}p$ and pp interactions at $\sqrt{s} = 24.3$ GeV*, Phys. Lett. **B317**, 243 (1993).

[58] UA6 Collaboration, G. Ballocchi *et al.*, *Direct photon cross-sections in proton–proton and anti-proton–proton interactions at $\sqrt{s} = 24.3$ GeV*, Phys. Lett. **B436**, 222 (1998).

[59] E706 Collaboration, G. Alverson *et al.*, *Production of direct photons and neutral mesons at large transverse momenta by π^- and p beams at 500 GeV/c*, Phys. Rev. **D48**, 5 (1993).

[60] R806 Collaboration, E. Anassontzis *et al.*, *High-p_T direct photon production in pp collisions*, Z. Phys. **C13**, 277 (1982).

[61] AFS Collaboration, T. Åkesson *et al.*, *A comparison of direct photon, π^0, and η production in $p\bar{p}$ and pp interactions at the CERN ISR*, Phys. Lett. **158B**, 282 (1985).

[62] UA2 Collaboration, J. Alitti *et al.*, *A measurement of the direct photon production cross-section at the CERN $\bar{p}p$ collider*, Phys. Lett. **B263**, 544 (1991).

[63] CDF Collaboration, F. Abe *et al.*, *A precision measurement of the prompt photon cross-section in $p\bar{p}$ collisions at $\sqrt{s} = 1.8$ TeV*, Phys. Rev. Lett. **73**, 2662 (1994).

[64] DØ Collaboration, S. Abachi *et al.*, *The isolated photon cross-section in the central and forward rapidity regions in $p\bar{p}$ collisions at $\sqrt{s} = 1.8$ TeV*, Phys. Rev. Lett. **77**, 5011 (1996).

[65] NA3 Collaboration, J. Badier *et al.*, *Direct photon pair production from pions and protons at 200 GeV/c*, Phys. Lett. **164B**, 184 (1985).

[66] WA70 Collaboration, E. Bonvin *et al.*, *Double prompt photon production at high transverse momentum by π^- on protons at 280 GeV/c*, Z. Phys. **C41**, 591 (1989).

[67] NA24 Collaboration, C. D. Marzo *et al.*, *Measurement of the production of high mass $\gamma\gamma$, $\pi^0\pi^0$, and $\gamma\pi^0$ pairs in π^-p, π^+p, and pp collisions at 300 GeV/c*, Phys. Rev. **D42**, 748 (1990).

[68] R806 Collaboration, C. Kourkoumelis *et al.*, *Search for massive photon pair production at the CERN Intersecting Storage Rings*, Z. Phys. **C16**, 101 (1982).

[69] AFS Collaboration, T. Åkesson *et al.*, *A study of the production of two direct photons in pp collisions at the CERN ISR*, Z. Phys. **C32**, 491 (1986).

[70] UA2 Collaboration, J. Alitti *et al.*, *A measurement of single and double prompt photon production at the CERN $\bar{p}p$ collider*, Phys. Lett. **B288**, 386 (1992).

[71] W. Chen, *Isolated Direct Double Photon Production in $\bar{p}p$ collisions at $\sqrt{s} = 1.8$ TeV with the DØ Detector*, Ph.D. thesis, State University of New York at Stony Brook, 1997.

[72] E706 Collaboration, L. Apanasevich *et al.*, *π^0 and η meson production at large transverse momenta in pp and pBe interactions at 530 and 800 GeV/c*, Phys. Rev. D (in preparation).

[73] W. Długosz, *The Production of High p_T π^0 Mesons in 515 GeV/c π^- - Nucleus Collisions*, Ph.D. thesis, Northeastern University, 1994.

[74] E706 Collaboration, W. Baker *et al.*, A-dependence of leading particle production by 800 GeV protons, in *Proceedings of the XXIV International*

Conference on High Energy Physics, München, Fed. Rep. of Germany, August 4-10, 1988, edited by R. Kotthaus and J. Kühn, p. 1400, Berlin, 1989, Springer-Verlag.

[75] W. DeSoi, *Construction and Performance of a Liquid Argon Calorimeter for Use in E706 at the Fermi National Accelerator Laboratory*, Ph.D. thesis, University of Rochester, 1990.

[76] D. Striley, *Large Transverse Momentum π^0 Meson Production by 0.5 TeV/c p, π^+, and K^+ Incident on Beryllium*, Ph.D. thesis, University of Missouri at Columbia, 1996.

[77] I. Kourbanis, *The A–dependence of Leading Particle Production by 800 GeV Protons*, Ph.D. thesis, Northeastern University, 1989.

[78] L. Sorrell, *Measurement of the Nuclear Dependence of Direct Photon and Neutral Meson Production at High Transverse Momentum by Negative 515 GeV/c Pions Incident on Beryllium and Copper Targets*, Ph.D. thesis, Michigan State University, 1995.

[79] V. Zutshi, *Direct Photon Production in Hadron Induced Collisions*, Ph.D. thesis, University of Delhi, 1997.

[80] L. Sorrell, *The E706 Trigger System*, E706 Note 201.

[81] E629 Collaboration, C. Bromberg *et al.*, *A scintillation counter hodoscope for 10 MHz beams*, Nucl. Instrum. Methods **200**, 245 (1982), [a third plane was added for E706].

[82] D. Allspach *et al.*, Design and performance of liquid hydrogen target systems for the Fermilab fixed target program, in *Advances in Cyrogenic Engineering*, edited by R. W. Fast, Vol.37, p. 1495, June, 1991.

[83] S. Mani, *A Silicon Microvertex Detector for Studying QCD Jets Associated with Direct Photons*, Ph.D. thesis, University of Pittsburgh, 1986.

[84] S. Blusk, *Measurement of the Production Cross Section of Charm Mesons at High Transverse Momentum in 515 GeV/c π^-Nucleon Collisions*, Ph.D. thesis, University of Pittsburgh, 1995.

[85] E706 Collaboration, E. Engels Jr. *et al.*, *A silicon microstrip vertex detector for direct photon physics*, Nucl. Instrum. Methods **A253**, 523 (1987).

[86] E706 Collaboration, E. Engels Jr. *et al.*, *Performance characteristics and radiation damage results from the Fermilab E706 silicon microstrip detector system*, Nucl. Instrum. Methods **A279**, 272 (1989).

[87] P. Chang, *Massive $\pi^0\pi^0$, $\pi^0\pi^-$, and $\pi^0\pi^+$ Production from 515 GeV/c π^- Collisions with Beryllium and Copper Targets*, Ph.D. thesis, Northeastern University, 1994.

[88] K. Hartman, *Hadronic Production of π^0 Pairs and Associated Event Structure at 530 GeV*, Ph.D. thesis, Pennsylvania State University, 1990.

[89] E706 Collaboration, C. Bromberg *et al.*, *Design and operation of large straw–tube drift chamber planes*, Nucl. Instrum. Methods **A307**, 292 (1991).

[90] J. Bacigalupi, *Strange Particle Production In Awayside Jets In High p_T π^0 And Direct Photon Triggered Events In π^- + Be/Cu Interactions at 515 GeV*, Ph.D. thesis, University of California at Davis, 1996.

[91] J. Urbin *et al.*, Cyrogenic design and operation of a liquid argon photon/hadron calorimeter at Fermilab, in *Advances in Cryogenic Engineering, Proceedings of the 1989 Cyrogenic Engineering Conference, July 24-28 1989, UCLA, California*, edited by R. W. Fast, Vol.35, Part B, p. 1803, New York, 1990, Plenum Press.

[92] E706 Collaboration, F. Lobkowicz *et al.*, *A large liquid argon photon/hadron calorimeter for FNAL*, Nucl. Instrum. Methods **A235**, 332 (1985).

[93] R. Benson, *Characteristics of Forward Energy Production in Proton-Nucleus and Pion-Nucleus Collisions at 530 GeV/c*, Ph.D. thesis, University of Minnesota, 1989.

[94] G. Osborne, *Direct Photon and Neutral Meson Production at High Transverse Momentum by Negative 515 GeV/c Pions and 530 GeV/c Protons Incident upon Hydrogen, Beryllium and Copper Targets*, Ph.D. thesis, University of Rochester, 1996.

[95] E672/E706 Collaboration, A. Gribushin *et al.*, *Production of J/ψ and $\psi(2S)$ mesons in π^-Be collisions at 515 GeV/c*, Phys. Rev. **D53**, 4732 (1996).

[96] E672/E706 Collaboration, A. Gribushin *et al.*, *Production of J/ψ mesons in pBe collisions at 530 and 800 GeV/c*, hep-ex/9910005, submitted to Phys. Rev. D.

[97] E672/E706 Collaboration, V. Koreshev *et al.*, *Production of charmonium states in π^-Be collisions at 515 GeV/c*, Phys. Rev. Lett. **77**, 4294 (1996).

[98] E672/E706 Collaboration, R. Jesik *et al.*, *Bottom production in π^--Be collisions at 515 GeV/c*, Phys. Rev. Lett. **74**, 495 (1995).

[99] C. Moore, The 1991 Fixed-Target Run, in *Fermilab Report, Fall 1992*, edited by C. Crego, p. 12, Fermilab Publications Office, Batavia, Illinois, 1992.

[100] E706 Collaboration, C. Lirakis, E706 Data Acquisition System, in *Proceedings of the First Annual Conference on Electronics for Future Colliders*, p. 37, New York, 1991, LeCroy Corporation.

[101] G. Drake *et al.*, *CDF front end electronics: The Rabbit system*, Nucl. Instrum. Methods **A269**, 68 (1988).

[102] D. D. Skow, *A Study of High Momentum Eta Meson Production*, Ph.D. thesis, University of Rochester, 1990.

[103] E. Prebys, *A Study of High Transverse Momentum Direct Photon Production from Beryllium and Copper Targets with 530 GeV/c Incident π^- and Proton Beams*, Ph.D. thesis, University of Rochester, 1990.

[104] ANSI/IEEE Std 960-1986, *IEEE Standard FASTBUS Modular High-Speed Data Aquisition and Control System* (The Institute of Electrical and Electronics Engineers, Inc., New York, 1985).

[105] N. Varelas, *π^0 Production at High Transverse Momenta from π^- Collisions at 520 GeV/c on Be and Cu Targets*, Ph.D. thesis, University of Rochester, 1994.

[106] CAMAC Instrumentation and Interface Standards, IEEE 1982, ISBN 0-471-89737.

[107] FNAL Computer Department, Fermilab, Batavia, Ill., *VAXONLINE Users Guide*, PN-252.

[108] G. O. Alverson and E. L. Pothier, *Preliminary E706 MAGIC Guide*, E706 Note 139.

[109] R. Brun *et al.*, *ZEBRA User's Guide*, Cern Computer Center Program Library, DD/EE/85-6 Q100, or FNAL Software Note PU-0046, 1992.

[110] C. Yosef, *Production of High Transverse Momentum π^0 Mesons in Interactions of 530 GeV/c proton and π^- Beams on Beryllium and Copper Targets*, Ph.D. thesis, Northeastern University, 1990.

[111] P. D. D. S. Weerasundara, *A Study of Large Transverse Momentum Direct Photon plus Away-Side Jet Production using 500 GeV/c proton and π^- Beams Incident on a Beryllium Target*, Ph.D. thesis, University of Pittsburgh, 1993.

[112] L. de Barbaro, *Omega Production at High Transverse Momentum by Negative 515 GeV/c Pions Incident on Beryllium and Copper Targets*, Ph.D. thesis, University of Rochester, 1995.

[113] E. Prebys, *Does Anybody Really Know What Time It Is?*, E706 Note .

[114] R. Roser, *Do TVC's Deserve Their Current Bad Reputation?*, E706 Note 193.

[115] J. Shiers *et al.*, *HBOOK Reference Manual*, 1993.

[116] J. W. Motz *et al.*, *Pair production by photons*, Rev. Mod. Phys. **41**, 581 (1969).

[117] R. Fernow, *Introduction to experimental particle physics* (Cambridge University Press, Cambridge, 1986).

[118] R. Roser, *Eta Production at High Transverse Momentum by Negative 520 GeV/c Pions Incident on Beryllium and Copper Targets*, Ph.D. thesis, University of Rochester, 1994.

[119] L. Apanasevich, Ph.D. thesis, Michigan State University, 1999.

[120] G. Marchesini, I.G. Knowles, M.H. Seymour, and B.R. Webber, *HERWIG Reference Manual*, , v5.6 ed.

[121] H.-U. Bengtsson and T. Sjostrand, *The LUND Monte Carlo for hadronic processes*, Comput. Phys. Commun. **46**, 43 (1987), (`Pythia` v5.7 and `Jetset` v7.4).

[122] F. Carminati *et al.*, *GEANT: Detector Description and Simulation Tool*, 1993.

[123] E706 Collaboration, L. Apanasevich *et al.*, *Omega meson production at large transverse momenta in π^-Be interactions at 515 GeV/c*, Phys. Rev. D (in preparation).

[124] R806 Collaboration, M. Diakonou *et al.*, *Inclusive high p_T ω and η' production at the ISR*, Phys. Lett. **89B**, 432 (1980).

[125] W. M. Geist *et al.*, *Hadronic production of particles at large transverse momentum: Its relevance to hadron structure, parton fragmentation and scattering*, Phys. Rept. **197**, 263 (1990).

[126] J. Bacigalupi, private communication.

[127] E706 Collaboration, N. Varelas *et al.*, *Calibration of the Fermilab E706 liquid argon electromagnetic calorimeter*, Nucl. Phys. B. (Proc. Suppl.) **44**, 153 (1995).

[128] L. Apanasevich, private communication.

[129] L. de Barbaro, private communication.

[130] K. W. Hartman, *Alignment of the EMLAC Relative to the PWCs using 1988 Data*, E706 Note 191.

[131] F. James *et al.*, *MINUIT: Function Minimization and Error Analysis*, 1992.

[132] W. Długosz, private communication.

[133] L. Carroll, *Alice's Adventures in Wonderland and Through the Looking Glass* (Oxford University Press, Oxford, 1982).

[134] M. B. Kasen *et al.*, Mechanical, electrical and thermal characterization of G-10CR and G-11CR glass-cloth/epoxy laminates between room temperature and 4 K, in *Advances in Cryogenic Engineering Materials*, edited by A. F. Clark and R. P. Reed, Vol.26, p. 235, New York, 1979, Plenum Press.

[135] M. Zielinski, private communication.

[136] G. Osborne, *A Measurement of the Muon Content of the 1991 MWest Beam*, E706 Note 197.

[137] G. Ginther, private communication.

[138] J. Kuehler, *An analysis of π^0 mesons produced in minimum bias 515 GeV/c π^- nuclear collisions*, Ph.D. thesis, University of Oklahoma, 1995.

[139] CCOR (R108) Collaboration, A. L. S. Angelis *et al.*, *Determination of the angular and energy dependence of hard constituent scattering from π^0 pair*

events at the CERN Intersecting Storage Rings, Nucl. Phys. **B209**, 284 (1982).

[140] E711 Collaboration, H. B. White *et al.*, *Massive hadron pair production by 800 GeV/c protons on nuclear targets*, Phys. Rev. **D48**, 3996 (1993).

[141] P. Chiappetta, R. Fergani, and J. P. Guillet, *Production of two large p_T hadrons from hadronic collisions*, Z. Phys. **C69**, 443 (1996).

[142] J. P. Guillet, private communication.

[143] J. F. Owens, private communication.

[144] D. Brown, *A Comparison of High Transverse Momentum Direct Photon and Neutral Pion Events in Negative Pion and Proton-Nucleus Collisions at 31.5 GeV Center of Mass Energy*, Ph.D. thesis, Michigan State University, 1992.

[145] L. Apanasevich *et al.*, *k_T effects in direct photon production*, Phys. Rev. **D59**, 074007 (1999).

[146] A. Maul, private communication.

[147] W. Chung, *A Study of the Event Structure in High p_T Direct Photon and π^0 Production by 515 GeV/c π^- and 800 GeV/c Proton Beams Incident on Nuclear Targets*, Ph.D. thesis, University of Pittsburgh, 1995.

[148] M. Gluck, E. Reya, and A. Vogt, *Pionic parton distributions*, Z. Phys. **C53**, 651 (1992).

[149] B. Bailey, J. F. Owens, and J. Ohnemus, *An order alpha-s Monte Carlo calculation of hadronic double photon production*, Phys. Rev. **D46**, 2018 (1992).

[150] C. Balazs *et al.*, *Photon pair production with soft gluon resummation in hadronic interactions*, Phys. Rev. **D57**, 6934 (1998).

[151] J. C. Collins, D. E. Soper, and G. Sterman, *Transverse momentum distribution in Drell-Yan pair and W and Z boson production*, Nucl. Phys. **B250**, 199 (1985).

[152] C. Balázs, private communication.

[153] C. Balázs, *Soft gluon effects on electroweak boson production in hadron colliders*, Ph.D. thesis, Michigan State University, 1999.

[154] P. Aurenche *et al.*, *Prompt photon production at large p_T in QCD beyond the leading order*, Phys. Lett. **140B**, 87 (1984).

[155] CTEQ Collaboration, J. Huston *et al.*, *Study of the uncertainty of the gluon distribution*, Phys. Rev. **D58**, 114034 (1998).

[156] A. D. Martin, R. G. Roberts, W. J. Stirling, and R. S. Thorne, *Parton distributions: A new global analysis*, Eur. Phys. J. **C4**, 463 (1998).

[157] CTEQ Collaboration, J. Huston *et al.*, *A global QCD study of direct photon production*, Phys. Rev. **D51**, 6139 (1995).

[158] E706 Collaboration, L. Apanasevich *et al.*, *Production of charm mesons at high transverse momentum in 515-GeV/c π^- nucleon collisions*, Phys. Rev. **D56**, 1391 (1997).

[159] A. P. Contogouris, S. Papadopoulos, and C. Papavassiliou, *Large p_T direct photon production and opposite side photon – hadron correlations in QCD*, Nucl. Phys. **B179**, 461 (1981).

[160] A. P. Contogouris *et al.*, *Direct photon production by positive and negative pion beams*, Phys. Rev. **D32**, 1134 (1985).

[161] M. Fontannaz and D. Schiff, *The effect of the parton transverse motion in large p_T reactions*, Nucl. Phys. **B132**, 457 (1978).

[162] H.-L. Lai and H. nan Li, *Origin of the k_T smearing in direct photon production*, Phys. Rev. **D58**, 114020 (1998).

[163] S. Catani, M. L. Mangano, and P. Nason, *Sudakov resummation for prompt photon production in hadron collisions*, JHEP **07**, 024 (1998).

[164] S. Catani *et al.*, *Sudakov resummation effects in prompt photon hadroproduction*, JHEP **03**, 025 (1999).

[165] N. Kidonakis, *NNLO results for heavy quark and direct photon production near threshold*, (1999), hep-ph/9905480.

[166] E706 Collaboration, L. Apanasevich *et al.*, *Evidence for parton k_T effects in high-p_T particle production*, Phys. Rev. Lett. **81**, 2642 (1998).

[167] See, e.g., S. Linn at the ICHEP conference in Vancouver, July 1998.

[168] J. Huston, private communication.

[169] WA70 Collaboration, M. Bonesini *et al.*, *High transverse momentum π^0 production by π^- and π^+ on protons at 280 GeV/c*, Z. Phys. **37**, 39 (1987).

[170] X.-N. Wang, *Systematic study of high p_T hadron spectra in p p, p A and A A collisions from SPS to RHIC energies*, (1998), nucl-th/9812021.

[171] G. Papp, G. Fai, and P. Levai, *Hard photons and neutral pions from RHIC*, (1999), hep-ph/9904503.

[172] X.-N. Wang, *Effect of jet quenching on high p_T hadron spectra in high-energy nuclear collisions*, Phys. Rev. **C58**, 2321 (1998).

[173] X.-N. Wang, Z. Huang, and I. Sarcevic, *Jet quenching in the opposite direction of a tagged photon in high-energy heavy ion collisions*, Phys. Rev. Lett. **77**, 231 (1996).

Appendix A Tabulated Cross Sections: $\pi^0\pi^0$

This appendix contains the tabulated cross sections for the data described in Chapter 8 along with additional, supporting, information. Unless otherwise noted, there is a minimum p_T requirement on each π^0 of 2.5 GeV/c. Mesons were also required to be central, with rapidities of $-0.8 < y < 0.8$ for the 0.5 TeV/c beams and $-1.05 < y < 0.55$ for the 0.8 TeV/c beam. The azimuthal angle between the π^0's was required to be at least 105°.

Cross sections are presented as $A \pm B \pm C$ where A represents the measured value, B is the statistical uncertainty on A, and C is the systematic uncertainty on the measurement calculated with the information presented in Section 7.7.

Mass	$d\sigma/dM$ $\left(pb/(GeV/c^2)\right)$				
(GeV/c^2)	${p_T}^{\pi^0} > 1.5$ GeV/c	${p_T}^{\pi^0} > 2.5$ GeV/c	${p_T}^{\pi^0} > 3.0$ GeV/c	${p_T}^{\pi^0} > 4.0$ GeV/c	${p_T}^{\pi^0} > 5.0$ GeV/c
$4.0 \longleftrightarrow 4.5$	$342000 \pm 78000 \pm 64000$	$134 \pm 41 \pm 25$	—	—	—
$4.5 \longleftrightarrow 5.0$	$287000 \pm 52000 \pm 54000$	$1160 \pm 100 \pm 220$	—	—	—
$5.0 \longleftrightarrow 5.5$	$79000 \pm 33000 \pm 15000$	$6060 \pm 250 \pm 1140$	$16.1 \pm 8.5 \pm 3.0$	—	—
$5.5 \longleftrightarrow 6.0$	$40000 \pm 15000 \pm 7000$	$8360 \pm 250 \pm 1570$	$127 \pm 21 \pm 24$	—	—
$6.0 \longleftrightarrow 6.5$	$16600 \pm 5400 \pm 3100$	$6450 \pm 220 \pm 1210$	$762 \pm 53 \pm 143$	—	—
$6.5 \longleftrightarrow 7.0$	$13300 \pm 8100 \pm 2500$	$4180 \pm 170 \pm 780$	$1180 \pm 63 \pm 221$	—	—
$7.0 \longleftrightarrow 7.5$	$2460 \pm 130 \pm 460$	$2460 \pm 130 \pm 460$	$1142 \pm 61 \pm 214$	$2.0 \pm 2.0 \pm 0.4$	—
$7.5 \longleftrightarrow 8.0$	$1498 \pm 92 \pm 281$	$1498 \pm 92 \pm 281$	$877 \pm 54 \pm 164$	$1.2 \pm 1.2 \pm 0.2$	—
$8.0 \longleftrightarrow 8.5$	$727 \pm 52 \pm 136$	$727 \pm 52 \pm 136$	$554 \pm 41 \pm 104$	$19.3 \pm 6.5 \pm 3.6$	—
$8.5 \longleftrightarrow 9.0$	$425 \pm 39 \pm 80$	$425 \pm 39 \pm 80$	$342 \pm 34 \pm 64$	$71 \pm 15 \pm 13$	—
$9.0 \longleftrightarrow 9.5$	$251 \pm 27 \pm 47$	$251 \pm 27 \pm 47$	$215 \pm 23 \pm 40$	$71 \pm 12 \pm 13$	—
$9.5 \longleftrightarrow 10.0$	$165 \pm 20 \pm 31$	$165 \pm 20 \pm 31$	$147 \pm 19 \pm 27$	$75 \pm 12 \pm 14$	—
$10.0 \longleftrightarrow 11.0$	$65 \pm 11 \pm 12$	$65 \pm 11 \pm 12$	$65 \pm 11 \pm 12$	$40.8 \pm 7.2 \pm 7.7$	—
$11.0 \longleftrightarrow 12.5$	$22.5 \pm 4.4 \pm 4.2$	$22.5 \pm 4.4 \pm 4.2$	$22.5 \pm 4.4 \pm 4.2$	$20.5 \pm 3.8 \pm 3.8$	$6.4 \pm 2.0 \pm 1.2$
$12.5 \longleftrightarrow 14.0$	$4.9 \pm 1.6 \pm 0.9$	$4.9 \pm 1.6 \pm 0.9$	$4.9 \pm 1.6 \pm 0.9$	$4.9 \pm 1.6 \pm 0.9$	$3.6 \pm 1.4 \pm 0.7$
$14.0 \longleftrightarrow 16.0$	$1.4 \pm 1.0 \pm 0.3$	$1.4 \pm 1.0 \pm 0.3$	$1.4 \pm 1.0 \pm 0.3$	$1.78 \pm 0.94 \pm 0.33$	$1.78 \pm 0.94 \pm 0.33$

Table A.1 Differential cross section per nucleon, $d\sigma/dM$, for several minimum ${p_T}^{\pi^0}$ requirements for $\pi^0\pi^0$ events produced in π^-Be interactions at 515 GeV/c. Additional requirements on the combinations contributing to this distribution are summarized at the beginning of Appendix A.

Mass (GeV/c^2)	$d\sigma/dM$ (pb/(GeV/c^2)) Be	Cu	H
$4.0 \longleftrightarrow 4.5$	$134 \pm 41 \pm 25$	$290 \pm 150 \pm 50$	—
$4.5 \longleftrightarrow 5.0$	$1160 \pm 100 \pm 220$	$1290 \pm 380 \pm 240$	$1180 \pm 470 \pm 220$
$5.0 \longleftrightarrow 5.5$	$6060 \pm 250 \pm 1140$	$6100 \pm 890 \pm 1140$	$6800 \pm 1300 \pm 1300$
$5.5 \longleftrightarrow 6.0$	$8360 \pm 250 \pm 1570$	$11100 \pm 1100 \pm 2100$	$8100 \pm 1900 \pm 1500$
$6.0 \longleftrightarrow 6.5$	$6450 \pm 220 \pm 1210$	$7610 \pm 670 \pm 1430$	$7300 \pm 1100 \pm 1400$
$6.5 \longleftrightarrow 7.0$	$4180 \pm 170 \pm 780$	$5130 \pm 600 \pm 960$	$3140 \pm 920 \pm 590$
$7.0 \longleftrightarrow 7.5$	$2460 \pm 130 \pm 460$	$2390 \pm 340 \pm 450$	$1520 \pm 570 \pm 290$
$7.5 \longleftrightarrow 8.5$	$1113 \pm 53 \pm 209$	$1260 \pm 130 \pm 240$	$1030 \pm 230 \pm 190$
$8.5 \longleftrightarrow 10.0$	$280 \pm 17 \pm 53$	$251 \pm 50 \pm 47$	$330 \pm 100 \pm 60$
$10.0 \longleftrightarrow 12.0$	$46.1 \pm 6.2 \pm 8.6$	$67 \pm 24 \pm 13$	$65 \pm 33 \pm 12$
$12.0 \longleftrightarrow 14.0$	$6.9 \pm 1.9 \pm 1.3$	$5.3 \pm 3.8 \pm 1.0$	$18 \pm 23 \pm 3$
$14.0 \longleftrightarrow 16.0$	$1.4 \pm 1.0 \pm 0.3$	—	—

Table A.2 Differential cross section per nucleon, $d\sigma/dM$, for various targets for $\pi^0\pi^0$ from the 515 GeV/c π^- sample. Additional requirements on the combinations contributing to this distribution are summarized at the beginning of Appendix A.

Mass (GeV/c^2)	$d\sigma/dM$ (pb/(GeV/c^2)) Be	Cu	H
$4.0 \longleftrightarrow 5.5$	$2700 \pm 1100 \pm 500$	$5300 \pm 2900 \pm 1000$	$1900 \pm 1100 \pm 300$
$5.5 \longleftrightarrow 7.0$	$6200 \pm 1200 \pm 1200$	$10100 \pm 3300 \pm 1900$	$4600 \pm 3200 \pm 900$
$7.0 \longleftrightarrow 9.5$	$830 \pm 470 \pm 160$	$510 \pm 870 \pm 90$	$1540 \pm 640 \pm 290$
$9.5 \longleftrightarrow 12.5$	$115 \pm 58 \pm 22$	—	—

Table A.3 Differential cross section per nucleon, $d\sigma/dM$, for various targets for $\pi^0\pi^0$ from the 515 GeV/c π^+ sample. Additional requirements on the combinations contributing to this distribution are summarized at the beginning of Appendix A.

Mass	$d\sigma/dM$ (pb/(GeV/c^2))			
(GeV/c^2)	$p_T^{\pi^0} > 2.5$ GeV/c	$p_T^{\pi^0} > 3.0$ GeV/c	$p_T^{\pi^0} > 4.0$ GeV/c	$p_T^{\pi^0} > 5.0$ GeV/c
$4.0 \longleftrightarrow 4.5$	$212 \pm 81 \pm 40$	—	—	—
$4.5 \longleftrightarrow 5.0$	$1300 \pm 160 \pm 240$	—	—	—
$5.0 \longleftrightarrow 5.5$	$6780 \pm 420 \pm 1270$	$27 \pm 13 \pm 5$	—	—
$5.5 \longleftrightarrow 6.0$	$8560 \pm 350 \pm 1600$	$101 \pm 28 \pm 19$	—	—
$6.0 \longleftrightarrow 6.5$	$6050 \pm 280 \pm 1130$	$649 \pm 48 \pm 122$	—	—
$6.5 \longleftrightarrow 7.0$	$4350 \pm 210 \pm 820$	$1074 \pm 58 \pm 201$	—	—
$7.0 \longleftrightarrow 7.5$	$2360 \pm 120 \pm 440$	$1008 \pm 55 \pm 189$	—	—
$7.5 \longleftrightarrow 8.0$	$1274 \pm 90 \pm 239$	$663 \pm 49 \pm 124$	—	—
$8.0 \longleftrightarrow 8.5$	$651 \pm 50 \pm 122$	$488 \pm 37 \pm 91$	$28.9 \pm 8.1 \pm 5.4$	—
$8.5 \longleftrightarrow 9.0$	$408 \pm 43 \pm 76$	$344 \pm 31 \pm 65$	$55 \pm 10 \pm 10$	—
$9.0 \longleftrightarrow 9.5$	$168 \pm 28 \pm 32$	$151 \pm 24 \pm 28$	$47.0 \pm 9.4 \pm 8.8$	—
$9.5 \longleftrightarrow 10.0$	$132 \pm 18 \pm 25$	$128 \pm 16 \pm 24$	$71 \pm 11 \pm 13$	—
$10.0 \longleftrightarrow 11.0$	$48.7 \pm 7.5 \pm 9.1$	$48.3 \pm 7.1 \pm 9.0$	$29.4 \pm 5.4 \pm 5.5$	$1.2 \pm 1.4 \pm 0.2$
$11.0 \longleftrightarrow 12.5$	$9.8 \pm 2.7 \pm 1.8$	$9.8 \pm 2.7 \pm 1.8$	$8.2 \pm 2.4 \pm 1.5$	$2.9 \pm 1.3 \pm 0.6$
$12.5 \longleftrightarrow 14.0$	$1.5 \pm 1.2 \pm 0.3$	$1.5 \pm 1.2 \pm 0.3$	$1.5 \pm 1.2 \pm 0.3$	$1.0 \pm 1.1 \pm 0.2$

Table A.4 Differential cross section per nucleon, $d\sigma/dM$, for several minimum $p_T^{\pi^0}$ requirements for $\pi^0\pi^0$ events produced in pBe interactions at 530 GeV/c. Additional requirements on the combinations contributing to this distribution are summarized at the beginning of Appendix A.

Mass	$d\sigma/dM$ $\left(pb/(GeV/c^2)\right)$		
(GeV/c^2)	Be	Cu	H
$4.0 \longleftrightarrow 4.5$	$212 \pm 81 \pm 40$	$70 \pm 140 \pm 10$	—
$4.5 \longleftrightarrow 5.0$	$1300 \pm 160 \pm 240$	$1260 \pm 860 \pm 240$	$1660 \pm 580 \pm 310$
$5.0 \longleftrightarrow 5.5$	$6780 \pm 420 \pm 1270$	$6900 \pm 1000 \pm 1300$	$6300 \pm 770 \pm 1180$
$5.5 \longleftrightarrow 6.0$	$8560 \pm 350 \pm 1600$	$9100 \pm 1200 \pm 1700$	$8630 \pm 700 \pm 1620$
$6.0 \longleftrightarrow 6.5$	$6050 \pm 280 \pm 1130$	$6460 \pm 580 \pm 1210$	$6580 \pm 740 \pm 1230$
$6.5 \longleftrightarrow 7.0$	$4350 \pm 210 \pm 820$	$3650 \pm 410 \pm 680$	$4300 \pm 500 \pm 810$
$7.0 \longleftrightarrow 7.5$	$2360 \pm 120 \pm 440$	$1630 \pm 280 \pm 310$	$2400 \pm 300 \pm 450$
$7.5 \longleftrightarrow 8.5$	$962 \pm 51 \pm 180$	$570 \pm 100 \pm 110$	$820 \pm 120 \pm 150$
$8.5 \longleftrightarrow 10.0$	$236 \pm 18 \pm 44$	$204 \pm 31 \pm 38$	$229 \pm 36 \pm 43$
$10.0 \longleftrightarrow 12.0$	$30.1 \pm 4.1 \pm 5.6$	$27.2 \pm 8.0 \pm 5.1$	$28 \pm 10 \pm 5$
$12.0 \longleftrightarrow 14.0$	$2.8 \pm 1.3 \pm 0.5$	$7.6 \pm 4.4 \pm 1.4$	$5.9 \pm 4.2 \pm 1.1$
$14.0 \longleftrightarrow 16.0$	—	—	$2.5 \pm 2.5 \pm 0.5$

Table A.5 Differential cross section per nucleon, $d\sigma/dM$, for various targets for $\pi^0\pi^0$ events from the 530 GeV/c proton sample. Additional requirements on the combinations contributing to this distribution are summarized at the beginning of Appendix A.

Mass	$d\sigma/dM$ $\left(pb/(GeV/c^2)\right)$			
(GeV/c^2)	$p_T^{\pi^0} > 2.5$ GeV/c	$p_T^{\pi^0} > 3.0$ GeV/c	$p_T^{\pi^0} > 4.0$ GeV/c	$p_T^{\pi^0} > 5.0$ GeV/c
$4.0 \longleftrightarrow 4.5$	$570 \pm 180 \pm 110$	—	—	—
$4.5 \longleftrightarrow 5.0$	$5100 \pm 1100 \pm 1000$	—	—	—
$5.0 \longleftrightarrow 5.5$	$18200 \pm 2200 \pm 3400$	$28 \pm 21 \pm 5$	—	—
$5.5 \longleftrightarrow 6.0$	$18300 \pm 1100 \pm 3400$	$334 \pm 65 \pm 63$	—	—
$6.0 \longleftrightarrow 6.5$	$13190 \pm 810 \pm 2470$	$1410 \pm 130 \pm 260$	—	—
$6.5 \longleftrightarrow 7.0$	$8570 \pm 570 \pm 1610$	$2000 \pm 160 \pm 380$	—	—
$7.0 \longleftrightarrow 7.5$	$4020 \pm 310 \pm 750$	$1570 \pm 140 \pm 290$	—	—
$7.5 \longleftrightarrow 8.0$	$2470 \pm 260 \pm 460$	$1390 \pm 120 \pm 260$	$4.1 \pm 2.9 \pm 0.8$	—
$8.0 \longleftrightarrow 8.5$	$1340 \pm 220 \pm 250$	$1040 \pm 140 \pm 200$	$66 \pm 18 \pm 12$	—
$8.5 \longleftrightarrow 9.0$	$980 \pm 190 \pm 180$	$622 \pm 98 \pm 117$	$75 \pm 20 \pm 14$	—
$9.0 \longleftrightarrow 9.5$	$474 \pm 95 \pm 89$	$433 \pm 69 \pm 81$	$79 \pm 26 \pm 15$	—
$9.5 \longleftrightarrow 10.0$	$351 \pm 64 \pm 66$	$263 \pm 44 \pm 49$	$117 \pm 20 \pm 22$	$4.5 \pm 3.2 \pm 0.9$
$10.0 \longleftrightarrow 11.0$	$109 \pm 20 \pm 20$	$105 \pm 20 \pm 20$	$70 \pm 14 \pm 13$	$10.2 \pm 3.8 \pm 1.9$
$11.0 \longleftrightarrow 12.5$	$25.1 \pm 7.2 \pm 4.7$	$25.1 \pm 7.2 \pm 4.7$	$17.4 \pm 5.8 \pm 3.3$	$4.9 \pm 2.8 \pm 0.9$
$12.5 \longleftrightarrow 14.0$	$8.5 \pm 4.1 \pm 1.6$	$8.5 \pm 4.1 \pm 1.6$	$8.5 \pm 4.1 \pm 1.6$	$5.8 \pm 3.5 \pm 1.1$
$14.0 \longleftrightarrow 16.0$	$3.7 \pm 2.4 \pm 0.7$	$3.7 \pm 2.4 \pm 0.7$	$3.7 \pm 2.4 \pm 0.7$	$3.7 \pm 2.4 \pm 0.7$
$16.0 \longleftrightarrow 18.0$	$1.4 \pm 1.4 \pm 0.3$	$1.4 \pm 1.4 \pm 0.3$	$1.4 \pm 1.4 \pm 0.3$	$1.4 \pm 1.4 \pm 0.3$

Table A.6 Differential cross section per nucleon, $d\sigma/dM$, for several minimum $p_T^{\pi^0}$ requirements for $\pi^0\pi^0$ events produced in pBe interactions at 800 GeV/c. Additional requirements on the combinations contributing to this distribution are summarized at the beginning of Appendix A.

Mass	$d\sigma/dM$ $\left(pb/(GeV/c^2)\right)$		
(GeV/c^2)	Be	Cu	H
$4.0 \longleftrightarrow 4.5$	$570 \pm 180 \pm 110$	$1050 \pm 640 \pm 200$	$110 \pm 110 \pm 20$
$4.5 \longleftrightarrow 5.0$	$5100 \pm 1100 \pm 1000$	$5000 \pm 1500 \pm 900$	$3490 \pm 800 \pm 650$
$5.0 \longleftrightarrow 5.5$	$18200 \pm 2200 \pm 3400$	$14900 \pm 4700 \pm 2800$	$15000 \pm 3200 \pm 2800$
$5.5 \longleftrightarrow 6.0$	$18300 \pm 1100 \pm 3400$	$18700 \pm 2200 \pm 3500$	$16100 \pm 1800 \pm 3000$
$6.0 \longleftrightarrow 6.5$	$13190 \pm 810 \pm 2470$	$12000 \pm 2200 \pm 2200$	$14400 \pm 1700 \pm 2700$
$6.5 \longleftrightarrow 7.0$	$8570 \pm 570 \pm 1610$	$9300 \pm 1300 \pm 1700$	$9000 \pm 2000 \pm 1700$
$7.0 \longleftrightarrow 7.5$	$4020 \pm 310 \pm 750$	$5030 \pm 1000 \pm 940$	$5110 \pm 720 \pm 960$
$7.5 \longleftrightarrow 8.5$	$1900 \pm 170 \pm 360$	$2160 \pm 420 \pm 410$	$2250 \pm 330 \pm 420$
$8.5 \longleftrightarrow 10.0$	$602 \pm 75 \pm 113$	$320 \pm 110 \pm 60$	$710 \pm 180 \pm 130$
$10.0 \longleftrightarrow 12.0$	$69 \pm 11 \pm 13$	$47 \pm 20 \pm 9$	$26 \pm 27 \pm 5$
$12.0 \longleftrightarrow 14.0$	$11.1 \pm 3.8 \pm 2.1$	$8.9 \pm 5.3 \pm 1.7$	—
$14.0 \longleftrightarrow 16.0$	$3.7 \pm 2.4 \pm 0.7$	—	—
$16.0 \longleftrightarrow 18.0$	$1.4 \pm 1.4 \pm 0.3$	—	—

Table A.7 Differential cross section per nucleon, $d\sigma/dM$, for various targets for $\pi^0\pi^0$ from the 800 GeV/c proton sample. Additional requirements on the combinations contributing to this distribution are summarized at the beginning of Appendix A.

p_T (GeV/c)	$d\sigma/dp_T$ (pb/(GeV/c)) Be	Cu	H
$2.50 \longleftrightarrow 2.75$	$48400 \pm 1000 \pm 9100$	$54300 \pm 3700 \pm 10200$	$43400 \pm 5500 \pm 8100$
$2.75 \longleftrightarrow 3.00$	$29400 \pm 660 \pm 5510$	$39100 \pm 2400 \pm 7300$	$34100 \pm 4500 \pm 6400$
$3.00 \longleftrightarrow 3.25$	$17940 \pm 450 \pm 3360$	$19800 \pm 1800 \pm 3700$	$19100 \pm 2500 \pm 3600$
$3.25 \longleftrightarrow 3.50$	$11040 \pm 340 \pm 2070$	$12700 \pm 1200 \pm 2400$	$8800 \pm 1800 \pm 1700$
$3.50 \longleftrightarrow 3.75$	$7030 \pm 310 \pm 1320$	$8010 \pm 840 \pm 1500$	$5500 \pm 1400 \pm 1000$
$3.75 \longleftrightarrow 4.00$	$4920 \pm 240 \pm 920$	$5920 \pm 710 \pm 1110$	$4300 \pm 990 \pm 810$
$4.00 \longleftrightarrow 4.50$	$2790 \pm 110 \pm 520$	$2900 \pm 360 \pm 540$	$1920 \pm 540 \pm 360$
$4.50 \longleftrightarrow 5.00$	$1114 \pm 64 \pm 209$	$1230 \pm 190 \pm 230$	$1120 \pm 350 \pm 210$
$5.00 \longleftrightarrow 5.50$	$516 \pm 50 \pm 97$	$620 \pm 150 \pm 120$	$500 \pm 180 \pm 90$
$5.50 \longleftrightarrow 6.50$	$153 \pm 18 \pm 29$	$98 \pm 46 \pm 18$	$196 \pm 83 \pm 37$
$6.50 \longleftrightarrow 8.50$	$27.3 \pm 5.0 \pm 5.1$	$20 \pm 14 \pm 4$	$85 \pm 49 \pm 16$
$8.50 \longleftrightarrow 11.00$	$0.49 \pm 0.93 \pm 0.09$	$2.2 \pm 2.2 \pm 0.4$	—

Table A.8 Differential cross section per nucleon, $d\sigma/dp_T$, for several targets for $\pi^0\pi^0$ from the 515 GeV/c π^- sample. There are two entries per pair. Additional requirements on the combinations contributing to this distribution are summarized at the beginning of Appendix A.

p_T (GeV/c)	$d\sigma/dp_T$ (pb/(GeV/c)) Be	Cu	H
$2.5 \longleftrightarrow 3.0$	$36900 \pm 6500 \pm 6900$	$71000 \pm 17000 \pm 13000$	$32000 \pm 12000 \pm 6000$
$3.0 \longleftrightarrow 4.0$	$10600 \pm 1900 \pm 2000$	$8600 \pm 3800 \pm 1600$	$7400 \pm 4700 \pm 1400$
$4.0 \longleftrightarrow 5.5$	$1470 \pm 430 \pm 280$	$2500 \pm 2300 \pm 500$	$1820 \pm 920 \pm 340$
$5.5 \longleftrightarrow 7.0$	$180 \pm 100 \pm 30$	$590 \pm 590 \pm 110$	$360 \pm 360 \pm 70$

Table A.9 Differential cross section per nucleon, $d\sigma/dp_T$, for several targets for $\pi^0\pi^0$ from the 515 GeV/c π^+ sample. There are two entries per pair. Additional requirements on the combinations contributing to this distribution are summarized at the beginning of Appendix A.

p_T (GeV/c)	$d\sigma/dp_T$ (pb/(GeV/c)) Be	Cu	H
$2.50 \longleftrightarrow 2.75$	$53400 \pm 1500 \pm 10000$	$52500 \pm 4300 \pm 9800$	$57200 \pm 3500 \pm 10700$
$2.75 \longleftrightarrow 3.00$	$29000 \pm 830 \pm 5440$	$29000 \pm 2600 \pm 5400$	$27100 \pm 1800 \pm 5100$
$3.00 \longleftrightarrow 3.25$	$17750 \pm 570 \pm 3330$	$15200 \pm 1800 \pm 2900$	$15600 \pm 1200 \pm 2900$
$3.25 \longleftrightarrow 3.50$	$10370 \pm 440 \pm 1940$	$10030 \pm 880 \pm 1880$	$10180 \pm 760 \pm 1910$
$3.50 \longleftrightarrow 3.75$	$6480 \pm 260 \pm 1210$	$6380 \pm 650 \pm 1200$	$6330 \pm 760 \pm 1190$
$3.75 \longleftrightarrow 4.00$	$4430 \pm 250 \pm 830$	$4310 \pm 560 \pm 810$	$5340 \pm 500 \pm 1000$
$4.00 \longleftrightarrow 4.50$	$2250 \pm 110 \pm 420$	$1870 \pm 220 \pm 350$	$1980 \pm 310 \pm 370$
$4.50 \longleftrightarrow 5.00$	$1038 \pm 81 \pm 195$	$740 \pm 130 \pm 140$	$1160 \pm 270 \pm 220$
$5.00 \longleftrightarrow 5.50$	$426 \pm 42 \pm 80$	$295 \pm 86 \pm 55$	$263 \pm 90 \pm 49$
$5.50 \longleftrightarrow 6.50$	$124 \pm 19 \pm 23$	$88 \pm 31 \pm 17$	$152 \pm 36 \pm 29$
$6.50 \longleftrightarrow 8.50$	$8.7 \pm 3.2 \pm 1.6$	$6.8 \pm 4.0 \pm 1.3$	$20.5 \pm 8.4 \pm 3.8$
$8.50 \longleftrightarrow 11.00$	$1.5 \pm 1.1 \pm 0.3$	$1.5 \pm 1.5 \pm 0.3$	—

Table A.10 Differential cross section per nucleon, $d\sigma/dp_T$, for several targets for $\pi^0\pi^0$ from the 530 GeV/c proton sample. There are two entries per pair. Additional requirements on the combinations contributing to this distribution are summarized at the beginning of Appendix A.

p_T (GeV/c)	$d\sigma/dp_T$ (pb/(GeV/c)) Be	Cu	H
$2.50 \longleftrightarrow 2.75$	$136600 \pm 7300 \pm 25600$	$119000 \pm 14000 \pm 22000$	$130000 \pm 11000 \pm 24000$
$2.75 \longleftrightarrow 3.00$	$62800 \pm 2900 \pm 11800$	$67200 \pm 8100 \pm 12600$	$57800 \pm 5400 \pm 10800$
$3.00 \longleftrightarrow 3.25$	$36700 \pm 1600 \pm 6900$	$35300 \pm 4300 \pm 6600$	$30000 \pm 3700 \pm 5600$
$3.25 \longleftrightarrow 3.50$	$21100 \pm 1100 \pm 3900$	$20900 \pm 3600 \pm 3900$	$21000 \pm 2400 \pm 3900$
$3.50 \longleftrightarrow 3.75$	$13210 \pm 730 \pm 2480$	$17400 \pm 2500 \pm 3300$	$11900 \pm 1700 \pm 2200$
$3.75 \longleftrightarrow 4.00$	$8430 \pm 700 \pm 1580$	$11100 \pm 2000 \pm 2100$	$8400 \pm 1200 \pm 1600$
$4.00 \longleftrightarrow 4.50$	$4200 \pm 330 \pm 790$	$4130 \pm 560 \pm 770$	$4710 \pm 660 \pm 880$
$4.50 \longleftrightarrow 5.00$	$1820 \pm 220 \pm 340$	$2280 \pm 380 \pm 430$	$2390 \pm 370 \pm 450$
$5.00 \longleftrightarrow 5.50$	$1030 \pm 140 \pm 190$	$880 \pm 370 \pm 160$	$1040 \pm 280 \pm 200$
$5.50 \longleftrightarrow 6.50$	$460 \pm 100 \pm 90$	$340 \pm 130 \pm 60$	$620 \pm 230 \pm 120$
$6.50 \longleftrightarrow 8.50$	$60 \pm 14 \pm 11$	$34 \pm 23 \pm 6$	$81 \pm 29 \pm 15$
$8.50 \longleftrightarrow 11.00$	$8.0 \pm 4.6 \pm 1.5$	—	—

Table A.11 Differential cross section per nucleon, $d\sigma/dp_T$, for several targets for $\pi^0\pi^0$ from the 800 GeV/c proton sample. There are two entries per pair. Additional requirements on the combinations contributing to this distribution are summarized at the beginning of Appendix A.

Rapidity	$d\sigma/dYdM$ (pb/(GeV/c^2))			
	$5.0 < M < 6.5$ GeV/c^2	$6.5 < M < 8.0$ GeV/c^2	$8.0 < M < 10.0$ GeV/c^2	$10.0 < M < 14.0$ GeV/c^2
Beryllium				
$-0.8 \longleftrightarrow -0.5$	$1220 \pm 170 \pm 230$	$137 \pm 27 \pm 26$	$8.0 \pm 4.7 \pm 1.5$	—
$-0.5 \longleftrightarrow -0.2$	$4200 \pm 230 \pm 790$	$1160 \pm 100 \pm 220$	$140 \pm 19 \pm 26$	$3.4 \pm 5.4 \pm 0.6$
$-0.2 \longleftrightarrow 0.0$	$6330 \pm 310 \pm 1190$	$3040 \pm 200 \pm 570$	$462 \pm 45 \pm 87$	$38.2 \pm 7.6 \pm 7.2$
$0.0 \longleftrightarrow 0.2$	$7990 \pm 310 \pm 1500$	$4110 \pm 210 \pm 770$	$634 \pm 54 \pm 119$	$58.2 \pm 8.8 \pm 10.9$
$0.2 \longleftrightarrow 0.5$	$6480 \pm 210 \pm 1210$	$2410 \pm 120 \pm 450$	$387 \pm 31 \pm 73$	$19.0 \pm 4.9 \pm 3.6$
$0.5 \longleftrightarrow 0.8$	$1750 \pm 100 \pm 330$	$567 \pm 58 \pm 106$	$41 \pm 12 \pm 8$	$1.6 \pm 1.2 \pm 0.3$
Copper				
$-0.8 \longleftrightarrow -0.5$	$930 \pm 920 \pm 170$	—	$10 \pm 15 \pm 2$	$4.3 \pm 4.3 \pm 0.8$
$-0.5 \longleftrightarrow -0.2$	$3920 \pm 910 \pm 740$	$1320 \pm 260 \pm 250$	$135 \pm 61 \pm 25$	$4.1 \pm 4.1 \pm 0.8$
$-0.2 \longleftrightarrow 0.0$	$9680 \pm 930 \pm 1810$	$4170 \pm 680 \pm 780$	$470 \pm 140 \pm 90$	$95 \pm 45 \pm 18$
$0.0 \longleftrightarrow 0.2$	$9090 \pm 930 \pm 1710$	$5300 \pm 730 \pm 990$	$620 \pm 150 \pm 120$	$75 \pm 33 \pm 14$
$0.2 \longleftrightarrow 0.5$	$8000 \pm 630 \pm 1500$	$2230 \pm 330 \pm 420$	$351 \pm 71 \pm 66$	—
$0.5 \longleftrightarrow 0.8$	$2240 \pm 530 \pm 420$	$530 \pm 120 \pm 100$	$50 \pm 42 \pm 9$	—
Hydrogen				
$-0.8 \longleftrightarrow -0.5$	$1120 \pm 570 \pm 210$	—	—	—
$-0.5 \longleftrightarrow -0.2$	$4000 \pm 1300 \pm 800$	$1720 \pm 540 \pm 320$	$410 \pm 170 \pm 80$	—
$-0.2 \longleftrightarrow 0.0$	$8600 \pm 1700 \pm 1600$	$1580 \pm 930 \pm 300$	$640 \pm 240 \pm 120$	$58 \pm 41 \pm 11$
$0.0 \longleftrightarrow 0.2$	$7400 \pm 2400 \pm 1400$	$3600 \pm 1200 \pm 700$	$340 \pm 240 \pm 60$	$114 \pm 85 \pm 21$
$0.2 \longleftrightarrow 0.5$	$6700 \pm 1200 \pm 1300$	$1310 \pm 470 \pm 250$	$290 \pm 150 \pm 50$	—
$0.5 \longleftrightarrow 0.8$	$2090 \pm 560 \pm 390$	$290 \pm 300 \pm 50$	—	$23 \pm 23 \pm 4$

Table A.12 Differential cross section per nucleon, $d\sigma/dYdM$, for several targets for $\pi^- N \longrightarrow \pi^0\pi^0$ at 515 GeV/c. Additional requirements on the combinations contributing to this distribution are summarized at the beginning of Appendix A.

Rapidity	$d\sigma/dY$ (pb)
$-0.8 \longleftrightarrow -0.5$	—
$-0.5 \longleftrightarrow -0.2$	$5400 \pm 2300 \pm 1000$
$-0.2 \longleftrightarrow 0.0$	$15400 \pm 4600 \pm 2900$
$0.0 \longleftrightarrow 0.2$	$12200 \pm 4000 \pm 2300$
$0.2 \longleftrightarrow 0.5$	$12800 \pm 3100 \pm 2400$
$0.5 \longleftrightarrow 0.8$	$330 \pm 980 \pm 60$

Table A.13 Differential cross section per nucleon, $d\sigma/dY$, for $\pi^+\text{Be} \longrightarrow \pi^0\pi^0$ at 515 GeV/c. Additional requirements on the combinations contributing to this distribution are summarized at the beginning of Appendix A.

Table A.14 Differential cross section per nucleon, $d\sigma/dYdM$, for various targets for pN $\longrightarrow$ $\pi^0\pi^0$ at 530 GeV/c. Additional requirements on the combinations contributing to this distribution are summarized at the beginning of Appendix A.

Rapidity	$d\sigma/dYdM$ (pb/(GeV/c^2))			
	$5.0 < M < 6.5$ GeV/c^2	$6.5 < M < 8.0$ GeV/c^2	$8.0 < M < 10.0$ GeV/c^2	$10.0 < M < 14.0$ GeV/c^2
Beryllium				
$-0.8 \longleftrightarrow -0.5$	$1830 \pm 350 \pm 340$	$187 \pm 36 \pm 35$	$18.9 \pm 5.9 \pm 3.5$	$2.9 \pm 1.8 \pm 0.5$
$-0.5 \longleftrightarrow -0.2$	$5700 \pm 420 \pm 1070$	$1780 \pm 130 \pm 330$	$198 \pm 29 \pm 37$	$4.6 \pm 1.7 \pm 0.9$
$-0.2 \longleftrightarrow 0.0$	$7630 \pm 450 \pm 1430$	$3570 \pm 270 \pm 670$	$556 \pm 47 \pm 104$	$36.5 \pm 7.5 \pm 6.9$
$0.0 \longleftrightarrow 0.2$	$7610 \pm 280 \pm 1430$	$4000 \pm 240 \pm 750$	$488 \pm 54 \pm 91$	$20.9 \pm 5.0 \pm 3.9$
$0.2 \longleftrightarrow 0.5$	$4980 \pm 170 \pm 930$	$1680 \pm 89 \pm 315$	$206 \pm 25 \pm 39$	$9.0 \pm 3.1 \pm 1.7$
$0.5 \longleftrightarrow 0.8$	$1100 \pm 77 \pm 206$	$173 \pm 26 \pm 32$	$13.6 \pm 6.4 \pm 2.6$	—
Copper				
$-0.8 \longleftrightarrow -0.5$	$2070 \pm 670 \pm 390$	$171 \pm 72 \pm 32$	$6 \pm 12 \pm 1$	—
$-0.5 \longleftrightarrow -0.2$	$4600 \pm 1000 \pm 900$	$1360 \pm 240 \pm 250$	$180 \pm 42 \pm 34$	$10.1 \pm 5.9 \pm 1.9$
$-0.2 \longleftrightarrow 0.0$	$9900 \pm 1100 \pm 1900$	$2610 \pm 510 \pm 490$	$463 \pm 94 \pm 87$	$51 \pm 17 \pm 10$
$0.0 \longleftrightarrow 0.2$	$9100 \pm 1700 \pm 1700$	$2630 \pm 530 \pm 490$	$269 \pm 92 \pm 50$	$16 \pm 11 \pm 3$
$0.2 \longleftrightarrow 0.5$	$4510 \pm 390 \pm 850$	$1420 \pm 200 \pm 270$	$170 \pm 57 \pm 32$	$3.6 \pm 3.6 \pm 0.7$
$0.5 \longleftrightarrow 0.8$	$1130 \pm 180 \pm 210$	$228 \pm 73 \pm 43$	$17 \pm 12 \pm 3$	—
Hydrogen				
$-0.8 \longleftrightarrow -0.5$	$1960 \pm 640 \pm 370$	$420 \pm 250 \pm 80$	$9.1 \pm 9.1 \pm 1.7$	—
$-0.5 \longleftrightarrow -0.2$	$4900 \pm 620 \pm 920$	$1560 \pm 270 \pm 290$	$175 \pm 50 \pm 33$	$11.8 \pm 6.8 \pm 2.2$
$-0.2 \longleftrightarrow 0.0$	$8500 \pm 1100 \pm 1600$	$3400 \pm 600 \pm 640$	$650 \pm 100 \pm 120$	$17 \pm 12 \pm 3$
$0.0 \longleftrightarrow 0.2$	$8100 \pm 1000 \pm 1500$	$4110 \pm 580 \pm 770$	$370 \pm 110 \pm 70$	$40 \pm 17 \pm 7$
$0.2 \longleftrightarrow 0.5$	$4590 \pm 420 \pm 860$	$1390 \pm 190 \pm 260$	$244 \pm 60 \pm 46$	$7 \pm 11 \pm 1$
$0.5 \longleftrightarrow 0.8$	$1370 \pm 200 \pm 260$	$175 \pm 72 \pm 33$	$8.2 \pm 8.2 \pm 1.5$	—

Table A.15 Differential cross section per nucleon, $d\sigma/dYdM$, for various targets for pN $\longrightarrow$ $\pi^0\pi^0$ at 800 GeV/c. Additional requirements on the combinations contributing to this distribution are summarized at the beginning of Appendix A.

Rapidity	$d\sigma/dYdM$ (pb/(GeV/c^2))			
	$5.0 < M < 6.5$ GeV/c^2	$6.5 < M < 8.0$ GeV/c^2	$8.0 < M < 10.0$ GeV/c^2	$10.0 < M < 14.0$ GeV/c^2
Beryllium				
$-1.05 \longleftrightarrow -0.65$	$7300 \pm 1700 \pm 1400$	$650 \pm 150 \pm 120$	$30 \pm 14 \pm 6$	$1.4 \pm 1.4 \pm 0.3$
$-0.65 \longleftrightarrow -0.35$	$13700 \pm 1400 \pm 2600$	$4060 \pm 440 \pm 760$	$550 \pm 110 \pm 100$	$17.4 \pm 7.1 \pm 3.3$
$-0.35 \longleftrightarrow -0.05$	$16460 \pm 870 \pm 3090$	$7080 \pm 520 \pm 1330$	$1170 \pm 200 \pm 220$	$77 \pm 14 \pm 14$
$-0.05 \longleftrightarrow 0.25$	$11930 \pm 510 \pm 2240$	$3870 \pm 310 \pm 730$	$690 \pm 130 \pm 130$	$46 \pm 14 \pm 9$
$0.25 \longleftrightarrow 0.55$	$3360 \pm 240 \pm 630$	$860 \pm 100 \pm 160$	$100 \pm 37 \pm 19$	—
Copper				
$-1.05 \longleftrightarrow -0.65$	$2800 \pm 3900 \pm 500$	$420 \pm 170 \pm 80$	$17 \pm 17 \pm 3$	—
$-0.65 \longleftrightarrow -0.35$	$17000 \pm 2700 \pm 3200$	$4500 \pm 1200 \pm 800$	$370 \pm 130 \pm 70$	—
$-0.35 \longleftrightarrow -0.05$	$14400 \pm 1800 \pm 2700$	$9200 \pm 1500 \pm 1700$	$980 \pm 280 \pm 180$	$99 \pm 37 \pm 19$
$-0.05 \longleftrightarrow 0.25$	$11500 \pm 1200 \pm 2200$	$4300 \pm 570 \pm 810$	$540 \pm 170 \pm 100$	$25 \pm 18 \pm 5$
$0.25 \longleftrightarrow 0.55$	$4040 \pm 540 \pm 760$	$620 \pm 230 \pm 120$	$113 \pm 75 \pm 21$	—
Hydrogen				
$-1.05 \longleftrightarrow -0.65$	$2100 \pm 1900 \pm 400$	$360 \pm 250 \pm 70$	$19 \pm 19 \pm 4$	—
$-0.65 \longleftrightarrow -0.35$	$16600 \pm 2900 \pm 3100$	$4680 \pm 770 \pm 880$	$660 \pm 290 \pm 120$	$10 \pm 10 \pm 2$
$-0.35 \longleftrightarrow -0.05$	$17400 \pm 2000 \pm 3300$	$7400 \pm 2200 \pm 1400$	$1790 \pm 440 \pm 340$	—
$-0.05 \longleftrightarrow 0.25$	$10500 \pm 1100 \pm 2000$	$4850 \pm 650 \pm 910$	$540 \pm 190 \pm 100$	$51 \pm 32 \pm 10$
$0.25 \longleftrightarrow 0.55$	$3320 \pm 550 \pm 620$	$1040 \pm 290 \pm 200$	$166 \pm 82 \pm 31$	$15 \pm 15 \pm 3$

$\lvert\cos\theta^\star\rvert$	$d\sigma/d\lvert\cos\theta^\star\rvert$ (pb)	
	π^-Be at 515 GeV/c	pBe at 530 GeV/c
$0.00 \longleftrightarrow 0.05$	$850 \pm 160 \pm 160$	$1620 \pm 200 \pm 300$
$0.05 \longleftrightarrow 0.10$	$850 \pm 180 \pm 160$	$1510 \pm 210 \pm 280$
$0.10 \longleftrightarrow 0.15$	$1130 \pm 190 \pm 210$	$1830 \pm 230 \pm 340$
$0.15 \longleftrightarrow 0.20$	$1310 \pm 200 \pm 250$	$1790 \pm 230 \pm 330$
$0.20 \longleftrightarrow 0.25$	$1460 \pm 210 \pm 270$	$1920 \pm 240 \pm 360$
$0.25 \longleftrightarrow 0.30$	$1400 \pm 200 \pm 260$	$2280 \pm 260 \pm 430$
$0.30 \longleftrightarrow 0.35$	$1560 \pm 200 \pm 290$	$2670 \pm 270 \pm 500$
$0.35 \longleftrightarrow 0.40$	$1920 \pm 280 \pm 360$	$3180 \pm 340 \pm 600$
$0.40 \longleftrightarrow 0.45$	$2340 \pm 250 \pm 440$	$3640 \pm 360 \pm 680$
$0.45 \longleftrightarrow 0.50$	$2880 \pm 310 \pm 540$	$4120 \pm 420 \pm 770$

Table A.16 Differential cross section per nucleon, $d\sigma/d\lvert\cos\theta^\star\rvert$. To avoid rapidity biases, we require $\lvert\eta_{\rm boost}\rvert < 0.25$. To avoid biases due to the p_T requirements, there is a minimum mass requirement of 7.5 GeV/c for the π^- beam and 7.0 GeV/c for the proton beam. Additional requirements on the combinations contributing to this distribution are summarized at the beginning of Appendix A.

$\Delta\phi$ (degrees)	$d\sigma/d\Delta\phi$ (pb/degree) Be	Cu	H
$105 \longleftrightarrow 120$	$37.5 \pm 3.9 \pm 7.0$	$64 \pm 17 \pm 12$	$37 \pm 40 \pm 7$
$120 \longleftrightarrow 130$	$64.9 \pm 4.9 \pm 12.2$	$70 \pm 13 \pm 13$	$78 \pm 24 \pm 15$
$130 \longleftrightarrow 140$	$99.9 \pm 5.3 \pm 18.7$	$154 \pm 18 \pm 29$	$111 \pm 24 \pm 21$
$140 \longleftrightarrow 150$	$174.0 \pm 8.5 \pm 32.6$	$253 \pm 28 \pm 48$	$194 \pm 43 \pm 36$
$150 \longleftrightarrow 160$	$278 \pm 11 \pm 52$	$266 \pm 43 \pm 50$	$308 \pm 66 \pm 58$
$160 \longleftrightarrow 170$	$416 \pm 12 \pm 78$	$492 \pm 48 \pm 92$	$394 \pm 69 \pm 74$
$170 \longleftrightarrow 180$	$515 \pm 14 \pm 97$	$542 \pm 45 \pm 102$	$407 \pm 66 \pm 76$

Table A.17 Differential cross section per nucleon, $d\sigma/d\Delta\phi$, for various targets for $\pi^0\pi^0$ from the 515 GeV/c π^- sample. Additional requirements on the combinations contributing to this distribution are summarized at the beginning of Appendix A.

$\Delta\phi$ (degrees)	$d\sigma/d\Delta\phi$ (pb/degree)
$105 \longleftrightarrow 125$	$68 \pm 33 \pm 13$
$125 \longleftrightarrow 145$	$201 \pm 65 \pm 38$
$145 \longleftrightarrow 165$	$196 \pm 72 \pm 37$
$165 \longleftrightarrow 180$	$430 \pm 120 \pm 80$

Table A.18 Differential cross section per nucleon, $d\sigma/d\Delta\phi$, for $\pi^+\mathrm{Be} \longrightarrow \pi^0\pi^0$ at 515 GeV/c. Additional requirements on the combinations contributing to this distribution are summarized at the beginning of Appendix A.

$\Delta\phi$ (degrees)	$d\sigma/d\Delta\phi$ (pb/degree) Be	Cu	H
$105 \longleftrightarrow 120$	$35.1 \pm 4.4 \pm 6.6$	$54 \pm 39 \pm 10$	$22 \pm 16 \pm 4$
$120 \longleftrightarrow 130$	$66.5 \pm 6.6 \pm 12.5$	$93 \pm 20 \pm 17$	$63 \pm 18 \pm 12$
$130 \longleftrightarrow 140$	$104.7 \pm 7.3 \pm 19.6$	$100 \pm 19 \pm 19$	$107 \pm 20 \pm 20$
$140 \longleftrightarrow 150$	$160 \pm 12 \pm 30$	$185 \pm 21 \pm 35$	$161 \pm 22 \pm 30$
$150 \longleftrightarrow 160$	$280 \pm 15 \pm 52$	$215 \pm 40 \pm 40$	$240 \pm 32 \pm 45$
$160 \longleftrightarrow 170$	$429 \pm 17 \pm 80$	$374 \pm 43 \pm 70$	$461 \pm 39 \pm 87$
$170 \longleftrightarrow 180$	$526 \pm 19 \pm 99$	$498 \pm 38 \pm 93$	$552 \pm 40 \pm 104$

Table A.19 Differential cross section per nucleon, $d\sigma/d\Delta\phi$, for various targets for $\pi^0\pi^0$ from the 530 GeV/c proton sample. Additional requirements on the combinations contributing to this distribution are summarized at the beginning of Appendix A.

$\Delta\phi$ (degrees)	$d\sigma/d\Delta\phi$ (pb/degree) Be	Cu	H
$105 \longleftrightarrow 120$	$112 \pm 17 \pm 21$	$225 \pm 51 \pm 42$	$56 \pm 17 \pm 10$
$120 \longleftrightarrow 130$	$177 \pm 33 \pm 33$	$159 \pm 41 \pm 30$	$173 \pm 37 \pm 32$
$130 \longleftrightarrow 140$	$280 \pm 33 \pm 53$	$256 \pm 66 \pm 48$	$230 \pm 38 \pm 43$
$140 \longleftrightarrow 150$	$407 \pm 52 \pm 76$	$511 \pm 92 \pm 96$	$314 \pm 64 \pm 59$
$150 \longleftrightarrow 160$	$609 \pm 51 \pm 114$	$650 \pm 150 \pm 120$	$600 \pm 130 \pm 110$
$160 \longleftrightarrow 170$	$903 \pm 73 \pm 169$	$500 \pm 160 \pm 90$	$850 \pm 130 \pm 160$
$170 \longleftrightarrow 180$	$1148 \pm 87 \pm 215$	$1170 \pm 160 \pm 220$	$1230 \pm 120 \pm 230$

Table A.20 Differential cross section per nucleon, $d\sigma/d\Delta\phi$, for various targets for $\pi^0\pi^0$ from the 800 GeV/c proton sample. Additional requirements on the combinations contributing to this distribution are summarized at the beginning of Appendix A.

Q_T (GeV/c)	$d\sigma/dQ_T$ (pb/(GeV/c)) Be	Cu	H
$0.00 \longleftrightarrow 0.75$	$6150 \pm 170 \pm 1150$	$6230 \pm 600 \pm 1170$	$5050 \pm 960 \pm 950$
$0.75 \longleftrightarrow 1.50$	$7690 \pm 220 \pm 1440$	$8610 \pm 840 \pm 1610$	$7500 \pm 1100 \pm 1400$
$1.50 \longleftrightarrow 2.25$	$4610 \pm 140 \pm 860$	$6230 \pm 430 \pm 1170$	$4890 \pm 720 \pm 920$
$2.25 \longleftrightarrow 3.00$	$2120 \pm 100 \pm 400$	$2720 \pm 320 \pm 510$	$1920 \pm 500 \pm 360$
$3.00 \longleftrightarrow 4.00$	$590 \pm 52 \pm 111$	$800 \pm 220 \pm 150$	$890 \pm 570 \pm 170$
$4.00 \longleftrightarrow 6.00$	$12.3 \pm 6.6 \pm 2.3$	$44 \pm 33 \pm 8$	$24 \pm 23 \pm 5$
$6.00 \longleftrightarrow 9.00$	$1.09 \pm 0.63 \pm 0.20$	$1.8 \pm 1.8 \pm 0.3$	—

Table A.21 Differential cross section per nucleon, $d\sigma/dQ_T$, for various targets for $\pi^0\pi^0$ from the 515 GeV/c π^- sample. Additional requirements on the combinations contributing to this distribution are summarized at the beginning of Appendix A.

Q_T (GeV/c)	$d\sigma/dQ_T$ (pb/(GeV/c))
$0 \longleftrightarrow 1$	$4600 \pm 1600 \pm 900$
$1 \longleftrightarrow 2$	$6500 \pm 1700 \pm 1200$
$2 \longleftrightarrow 3$	$3900 \pm 1300 \pm 700$
$3 \longleftrightarrow 5$	$410 \pm 240 \pm 80$

Table A.22 Differential cross section per nucleon, $d\sigma/dQ_T$, for $\pi^0\pi^0$ from the 515 GeV/c π^+Be sample. Additional requirements on the combinations contributing to this distribution are summarized at the beginning of Appendix A.

Q_T (GeV/c)	$d\sigma/dQ_T$ (pb/(GeV/c)) Be	Cu	H
$0.00 \longleftrightarrow 0.75$	$6670 \pm 270 \pm 1250$	$6030 \pm 600 \pm 1130$	$6690 \pm 600 \pm 1250$
$0.75 \longleftrightarrow 1.50$	$7910 \pm 290 \pm 1480$	$7360 \pm 700 \pm 1380$	$7970 \pm 550 \pm 1490$
$1.50 \longleftrightarrow 2.25$	$4280 \pm 170 \pm 800$	$3770 \pm 420 \pm 710$	$4860 \pm 490 \pm 910$
$2.25 \longleftrightarrow 3.00$	$1870 \pm 110 \pm 350$	$2350 \pm 270 \pm 440$	$1550 \pm 390 \pm 290$
$3.00 \longleftrightarrow 4.00$	$606 \pm 69 \pm 114$	$760 \pm 580 \pm 140$	$347 \pm 89 \pm 65$
$4.00 \longleftrightarrow 6.00$	$17.5 \pm 7.5 \pm 3.3$	$37 \pm 20 \pm 7$	$9 \pm 19 \pm 2$
$6.00 \longleftrightarrow 9.00$	$1.22 \pm 0.86 \pm 0.23$	—	—

Table A.23 Differential cross section per nucleon, $d\sigma/dQ_T$, for various targets for $\pi^0\pi^0$ from the 530 GeV/c proton sample. Additional requirements on the combinations contributing to this distribution are summarized at the beginning of Appendix A.

Q_T (GeV/c)	$d\sigma/dQ_T$ (pb/(GeV/c)) Be	Cu	H
$0.00 \longleftrightarrow 0.75$	$14000 \pm 1200 \pm 2600$	$12100 \pm 2600 \pm 2300$	$15100 \pm 2000 \pm 2800$
$0.75 \longleftrightarrow 1.50$	$18100 \pm 1200 \pm 3400$	$15300 \pm 2500 \pm 2900$	$15700 \pm 2100 \pm 2900$
$1.50 \longleftrightarrow 2.25$	$10140 \pm 850 \pm 1900$	$10100 \pm 1300 \pm 1900$	$9500 \pm 1100 \pm 1800$
$2.25 \longleftrightarrow 3.00$	$4310 \pm 340 \pm 810$	$6360 \pm 790 \pm 1190$	$4490 \pm 660 \pm 840$
$3.00 \longleftrightarrow 4.00$	$1890 \pm 250 \pm 360$	$2880 \pm 740 \pm 540$	$1210 \pm 280 \pm 230$
$4.00 \longleftrightarrow 6.00$	$66 \pm 22 \pm 12$	$34 \pm 19 \pm 6$	$43 \pm 27 \pm 8$
$6.00 \longleftrightarrow 9.00$	$1.7 \pm 1.7 \pm 0.3$	—	—

Table A.24 Differential cross section per nucleon, $d\sigma/dQ_T$, for various targets for $\pi^0\pi^0$ from the 800 GeV/c proton sample. Additional requirements on the combinations contributing to this distribution are summarized at the beginning of Appendix A.

p_{OUT} (GeV/c)	$d\sigma/dp_{OUT}$ $\left(pb/(GeV/c^2)\right)$	$d\sigma/dp_{OUT}dM$ $\left(pb/(GeV^2/c^3)\right)$ $5.0 < M < 6.5$ GeV/c^2	$6.5 < M < 8.0$ GeV/c^2	$8.0 < M < 10.0$ GeV/c^2	$10.0 < M < 14.0$ GeV/c^2
$-8.0 \longleftrightarrow -6.0$	$0.58 \pm 0.58 \pm 0.11$	—	—	$0.29 \pm 0.29 \pm 0.05$	—
$-6.0 \longleftrightarrow -4.0$	$1.4 \pm 3.6 \pm 0.3$	$0.44 \pm 0.44 \pm 0.08$	—	$0.47 \pm 0.27 \pm 0.09$	—
$-4.0 \longleftrightarrow -3.0$	$150 \pm 25 \pm 28$	$68 \pm 15 \pm 13$	$22.4 \pm 5.8 \pm 4.2$	$2.3 \pm 1.5 \pm 0.4$	$0.57 \pm 0.33 \pm 0.11$
$-3.0 \longleftrightarrow -2.5$	$946 \pm 97 \pm 177$	$339 \pm 46 \pm 64$	$63 \pm 13 \pm 12$	$19.4 \pm 4.2 \pm 3.6$	$2.4 \pm 1.2 \pm 0.4$
$-2.5 \longleftrightarrow -2.0$	$2530 \pm 140 \pm 470$	$1052 \pm 71 \pm 197$	$214 \pm 27 \pm 40$	$22.3 \pm 7.2 \pm 4.2$	$3.1 \pm 1.1 \pm 0.6$
$-2.0 \longleftrightarrow -1.5$	$4040 \pm 170 \pm 760$	$1867 \pm 96 \pm 350$	$536 \pm 52 \pm 100$	$65 \pm 11 \pm 12$	$2.3 \pm 1.5 \pm 0.4$
$-1.5 \longleftrightarrow -1.0$	$6140 \pm 240 \pm 1150$	$2770 \pm 140 \pm 520$	$1066 \pm 63 \pm 200$	$124 \pm 14 \pm 23$	$12.6 \pm 2.6 \pm 2.4$
$-1.0 \longleftrightarrow -0.5$	$8210 \pm 260 \pm 1540$	$3610 \pm 140 \pm 680$	$1513 \pm 95 \pm 284$	$223 \pm 19 \pm 42$	$11.0 \pm 2.9 \pm 2.1$
$-0.5 \longleftrightarrow 0.0$	$9920 \pm 260 \pm 1860$	$4140 \pm 150 \pm 780$	$1991 \pm 87 \pm 373$	$322 \pm 23 \pm 60$	$21.1 \pm 4.5 \pm 4.0$
$0.0 \longleftrightarrow 0.5$	$9740 \pm 270 \pm 1830$	$4040 \pm 150 \pm 760$	$1960 \pm 100 \pm 370$	$325 \pm 23 \pm 61$	$22.9 \pm 3.9 \pm 4.3$
$0.5 \longleftrightarrow 1.0$	$8680 \pm 250 \pm 1630$	$3780 \pm 140 \pm 710$	$1659 \pm 84 \pm 311$	$232 \pm 21 \pm 43$	$10.1 \pm 3.5 \pm 1.9$
$1.0 \longleftrightarrow 1.5$	$5910 \pm 240 \pm 1110$	$2760 \pm 150 \pm 520$	$950 \pm 59 \pm 178$	$122 \pm 14 \pm 23$	$8.2 \pm 2.7 \pm 1.5$
$1.5 \longleftrightarrow 2.0$	$3990 \pm 160 \pm 750$	$1824 \pm 85 \pm 342$	$530 \pm 53 \pm 99$	$58 \pm 10 \pm 11$	$5.3 \pm 1.6 \pm 1.0$
$2.0 \longleftrightarrow 2.5$	$2600 \pm 140 \pm 490$	$1045 \pm 74 \pm 196$	$216 \pm 24 \pm 41$	$23.2 \pm 5.7 \pm 4.3$	$2.8 \pm 1.4 \pm 0.5$
$2.5 \longleftrightarrow 3.0$	$957 \pm 87 \pm 179$	$368 \pm 41 \pm 69$	$91 \pm 15 \pm 17$	$14.8 \pm 4.4 \pm 2.8$	$1.99 \pm 0.90 \pm 0.37$
$3.0 \longleftrightarrow 4.0$	$110 \pm 16 \pm 21$	$53.1 \pm 9.3 \pm 10.0$	$12.0 \pm 4.6 \pm 2.2$	$4.3 \pm 1.5 \pm 0.8$	$0.63 \pm 0.38 \pm 0.12$
$4.0 \longleftrightarrow 6.0$	—	—	—	$0.28 \pm 0.41 \pm 0.05$	$0.08 \pm 0.15 \pm 0.01$

Table A.25 Differential cross sections per nucleon $d\sigma/dp_{OUT}$ and $d\sigma/dp_{OUT}dM$ for $\pi^-\mathrm{Be} \longrightarrow \pi^0\pi^0$ at 515 GeV/c. There are two entries per pair. Additional requirements on the combinations contributing to this distribution are summarized at the beginning of Appendix A.

p_{OUT} (GeV/c)	$d\sigma/dp_{OUT}$ (pb/(GeV/c)) Be	Cu	H
$-8.00 \longleftrightarrow -6.00$	$0.58 \pm 0.58 \pm 0.11$	—	—
$-6.00 \longleftrightarrow -4.00$	$1.4 \pm 3.6 \pm 0.3$	$22 \pm 21 \pm 4$	—
$-4.00 \longleftrightarrow -2.50$	$416 \pm 36 \pm 78$	$760 \pm 170 \pm 140$	$630 \pm 380 \pm 120$
$-2.50 \longleftrightarrow -1.50$	$3290 \pm 110 \pm 620$	$4530 \pm 330 \pm 850$	$3400 \pm 550 \pm 640$
$-1.50 \longleftrightarrow -0.75$	$6650 \pm 190 \pm 1250$	$7200 \pm 780 \pm 1350$	$6900 \pm 1100 \pm 1300$
$-0.75 \longleftrightarrow 0.00$	$9530 \pm 220 \pm 1790$	$10170 \pm 730 \pm 1910$	$7900 \pm 1100 \pm 1500$
$0.00 \longleftrightarrow 0.75$	$9550 \pm 220 \pm 1790$	$10120 \pm 720 \pm 1900$	$7400 \pm 1100 \pm 1400$
$0.75 \longleftrightarrow 1.50$	$6670 \pm 200 \pm 1250$	$7340 \pm 800 \pm 1380$	$7200 \pm 1100 \pm 1400$
$1.50 \longleftrightarrow 2.50$	$3290 \pm 110 \pm 620$	$4810 \pm 370 \pm 900$	$4160 \pm 760 \pm 780$
$2.50 \longleftrightarrow 4.00$	$392 \pm 31 \pm 74$	$580 \pm 110 \pm 110$	$230 \pm 110 \pm 40$
$4.00 \longleftrightarrow 6.00$	—	—	—

Table A.26 Differential cross section per nucleon, $d\sigma/dp_{OUT}$, for various targets for $\pi^0\pi^0$ from the 515 GeV/c π^- sample. There are two entries per pair. Additional requirements on the combinations contributing to this distribution are summarized at the beginning of Appendix A.

p_{OUT} (GeV/c)	$d\sigma/dp_{OUT}$ (pb/(GeV/c)) Be	Cu	H
$-4.0 \longleftrightarrow -2.0$	$1680 \pm 650 \pm 310$	$4400 \pm 2000 \pm 800$	—
$-2.0 \longleftrightarrow -0.5$	$5100 \pm 1200 \pm 900$	$5500 \pm 3200 \pm 1000$	$3500 \pm 1900 \pm 700$
$-0.5 \longleftrightarrow 0.5$	$9700 \pm 2300 \pm 1800$	$13000 \pm 4000 \pm 2400$	$14600 \pm 6000 \pm 2700$
$0.5 \longleftrightarrow 2.0$	$4900 \pm 1200 \pm 900$	$6700 \pm 3200 \pm 1300$	$3600 \pm 2100 \pm 700$
$2.0 \longleftrightarrow 4.0$	$1750 \pm 640 \pm 330$	$2800 \pm 1300 \pm 500$	$720 \pm 530 \pm 140$
$4.0 \longleftrightarrow 6.0$	—	$1500 \pm 1500 \pm 300$	—

Table A.27 Differential cross section per nucleon, $d\sigma/dp_{OUT}$, for various targets for $\pi^0\pi^0$ from the 515 GeV/c π^+ sample. There are two entries per pair. Additional requirements on the combinations contributing to this distribution are summarized at the beginning of Appendix A.

p_{OUT} (GeV/c)	$d\sigma/dp_{OUT}$ $\left(pb/(GeV/c^2)\right)$	$d\sigma/dp_{OUT}dM$ $\left(pb/(GeV^2/c^3)\right)$			
		$5.0 < M < 6.5$ GeV/c^2	$6.5 < M < 8.0$ GeV/c^2	$8.0 < M < 10.0$ GeV/c^2	$10.0 < M < 14.0$ GeV/c^2
$-6.0 \longleftrightarrow -4.0$	$8.1 \pm 5.8 \pm 1.5$	—	$0.41 \pm 0.41 \pm 0.08$	$3.3 \pm 2.8 \pm 0.6$	$0.23 \pm 0.23 \pm 0.04$
$-4.0 \longleftrightarrow -3.0$	$156 \pm 36 \pm 29$	$66 \pm 21 \pm 12$	$20.5 \pm 5.3 \pm 3.8$	$4.6 \pm 2.2 \pm 0.9$	$0.23 \pm 0.23 \pm 0.04$
$-3.0 \longleftrightarrow -2.5$	$960 \pm 120 \pm 180$	$378 \pm 45 \pm 71$	$50 \pm 20 \pm 9$	$18.1 \pm 4.3 \pm 3.4$	$0.50 \pm 0.50 \pm 0.09$
$-2.5 \longleftrightarrow -2.0$	$2340 \pm 150 \pm 440$	$884 \pm 67 \pm 166$	$169 \pm 30 \pm 32$	$24.1 \pm 5.1 \pm 4.5$	$1.55 \pm 0.78 \pm 0.29$
$-2.0 \longleftrightarrow -1.5$	$3930 \pm 230 \pm 740$	$1770 \pm 120 \pm 330$	$506 \pm 48 \pm 95$	$65 \pm 11 \pm 12$	$3.5 \pm 1.3 \pm 0.7$
$-1.5 \longleftrightarrow -1.0$	$5660 \pm 320 \pm 1060$	$2600 \pm 200 \pm 490$	$971 \pm 63 \pm 182$	$86 \pm 13 \pm 16$	$5.0 \pm 1.9 \pm 0.9$
$-1.0 \longleftrightarrow -0.5$	$9120 \pm 370 \pm 1710$	$4140 \pm 220 \pm 780$	$1610 \pm 110 \pm 300$	$222 \pm 21 \pm 42$	$9.8 \pm 2.4 \pm 1.8$
$-0.5 \longleftrightarrow 0.0$	$10020 \pm 380 \pm 1880$	$4360 \pm 230 \pm 820$	$1974 \pm 95 \pm 370$	$241 \pm 22 \pm 45$	$11.1 \pm 2.4 \pm 2.1$
$0.0 \longleftrightarrow 0.5$	$10190 \pm 390 \pm 1910$	$4420 \pm 240 \pm 830$	$2015 \pm 95 \pm 378$	$248 \pm 22 \pm 47$	$12.4 \pm 2.7 \pm 2.3$
$0.5 \longleftrightarrow 1.0$	$8820 \pm 350 \pm 1650$	$4000 \pm 210 \pm 750$	$1600 \pm 110 \pm 300$	$187 \pm 20 \pm 35$	$10.1 \pm 2.4 \pm 1.9$
$1.0 \longleftrightarrow 1.5$	$6080 \pm 330 \pm 1140$	$2910 \pm 210 \pm 540$	$923 \pm 65 \pm 173$	$108 \pm 14 \pm 20$	$7.2 \pm 2.0 \pm 1.3$
$1.5 \longleftrightarrow 2.0$	$3690 \pm 210 \pm 690$	$1580 \pm 110 \pm 300$	$496 \pm 46 \pm 93$	$85 \pm 15 \pm 16$	$2.11 \pm 0.95 \pm 0.40$
$2.0 \longleftrightarrow 2.5$	$2580 \pm 180 \pm 480$	$990 \pm 85 \pm 186$	$168 \pm 26 \pm 31$	$28.3 \pm 5.5 \pm 5.3$	$0.66 \pm 0.90 \pm 0.12$
$2.5 \longleftrightarrow 3.0$	$730 \pm 100 \pm 140$	$260 \pm 37 \pm 49$	$68 \pm 13 \pm 13$	$12.3 \pm 3.6 \pm 2.3$	—
$3.0 \longleftrightarrow 4.0$	$136 \pm 28 \pm 26$	$54 \pm 12 \pm 10$	$27 \pm 14 \pm 5$	$5.0 \pm 2.8 \pm 0.9$	$0.23 \pm 0.23 \pm 0.04$
$4.0 \longleftrightarrow 6.0$	$0.9 \pm 1.3 \pm 0.2$	—	$0.70 \pm 0.50 \pm 0.13$	—	—

Table A.28 Differential cross sections per nucleon $d\sigma/dp_{OUT}$ and $d\sigma/dp_{OUT}dM$ for pBe $\longrightarrow \pi^0\pi^0$ at 530 GeV/c. There are two entries per pair. Additional requirements on the combinations contributing to this distribution are summarized at the beginning of Appendix A.

p_{OUT} (GeV/c)	$d\sigma/dp_{OUT}$ (pb/(GeV/c)) Be	Cu	H
$-6.00 \longleftrightarrow -4.00$	$8.1 \pm 5.8 \pm 1.5$	$7.8 \pm 6.2 \pm 1.5$	—
$-4.00 \longleftrightarrow -2.50$	$422 \pm 46 \pm 79$	$200 \pm 250 \pm 40$	$209 \pm 58 \pm 39$
$-2.50 \longleftrightarrow -1.50$	$3140 \pm 140 \pm 590$	$3990 \pm 560 \pm 750$	$3230 \pm 420 \pm 600$
$-1.50 \longleftrightarrow -0.75$	$6560 \pm 250 \pm 1230$	$5650 \pm 660 \pm 1060$	$6630 \pm 510 \pm 1240$
$-0.75 \longleftrightarrow 0.00$	$9970 \pm 320 \pm 1870$	$9220 \pm 670 \pm 1730$	$10220 \pm 690 \pm 1920$
$0.00 \longleftrightarrow 0.75$	$9970 \pm 320 \pm 1870$	$9060 \pm 680 \pm 1700$	$10310 \pm 670 \pm 1930$
$0.75 \longleftrightarrow 1.50$	$6760 \pm 260 \pm 1270$	$6070 \pm 650 \pm 1140$	$6670 \pm 580 \pm 1250$
$1.50 \longleftrightarrow 2.50$	$3140 \pm 140 \pm 590$	$2800 \pm 480 \pm 520$	$3020 \pm 370 \pm 570$
$2.50 \longleftrightarrow 4.00$	$334 \pm 39 \pm 63$	$860 \pm 310 \pm 160$	$256 \pm 86 \pm 48$
$4.00 \longleftrightarrow 6.00$	$0.9 \pm 1.3 \pm 0.2$	$12 \pm 12 \pm 2$	$14 \pm 14 \pm 3$

Table A.29 Differential cross section per nucleon, $d\sigma/dp_{OUT}$, for various targets for $\pi^0\pi^0$ from the 530 GeV/c proton sample. There are two entries per pair. Additional requirements on the combinations contributing to this distribution are summarized at the beginning of Appendix A.

p_{OUT} (GeV/c)	$d\sigma/dp_{OUT}$ $\left(pb/(GeV/c^2)\right)$	$d\sigma/dp_{OUT}dM$ $\left(pb/(GeV^2/c^3)\right)$			
		$5.0 < M < 6.5$ GeV/c^2	$6.5 < M < 8.0$ GeV/c^2	$8.0 < M < 10.0$ GeV/c^2	$10.0 < M < 14.0$ GeV/c^2
$-6.0 \longleftrightarrow -4.0$	$13 \pm 15 \pm 2$	$2.0 \pm 2.0 \pm 0.4$	$6.1 \pm 9.6 \pm 1.1$	—	$0.24 \pm 0.24 \pm 0.04$
$-4.0 \longleftrightarrow -3.0$	$215 \pm 72 \pm 40$	$106 \pm 27 \pm 20$	$35 \pm 18 \pm 7$	$5.0 \pm 6.1 \pm 0.9$	—
$-3.0 \longleftrightarrow -2.5$	$2530 \pm 300 \pm 470$	$760 \pm 130 \pm 140$	$145 \pm 34 \pm 27$	$36 \pm 13 \pm 7$	$2.7 \pm 1.9 \pm 0.5$
$-2.5 \longleftrightarrow -2.0$	$6890 \pm 830 \pm 1290$	$2490 \pm 260 \pm 470$	$298 \pm 66 \pm 56$	$101 \pm 28 \pm 19$	$3.5 \pm 2.0 \pm 0.7$
$-2.0 \longleftrightarrow -1.5$	$8900 \pm 1000 \pm 1700$	$4100 \pm 580 \pm 770$	$880 \pm 140 \pm 170$	$111 \pm 33 \pm 21$	$9.1 \pm 3.9 \pm 1.7$
$-1.5 \longleftrightarrow -1.0$	$14800 \pm 1100 \pm 2800$	$7180 \pm 570 \pm 1350$	$1700 \pm 190 \pm 320$	$300 \pm 70 \pm 56$	$16.2 \pm 5.6 \pm 3.0$
$-1.0 \longleftrightarrow -0.5$	$18000 \pm 1500 \pm 3400$	$8470 \pm 990 \pm 1590$	$2980 \pm 250 \pm 560$	$312 \pm 87 \pm 59$	$25.9 \pm 7.9 \pm 4.9$
$-0.5 \longleftrightarrow 0.0$	$22200 \pm 1800 \pm 4200$	$9900 \pm 1100 \pm 1900$	$3950 \pm 310 \pm 740$	$660 \pm 100 \pm 120$	$26.0 \pm 8.0 \pm 4.9$
$0.0 \longleftrightarrow 0.5$	$21900 \pm 1700 \pm 4100$	$9800 \pm 1100 \pm 1800$	$3880 \pm 300 \pm 730$	$600 \pm 100 \pm 110$	$25.3 \pm 7.8 \pm 4.7$
$0.5 \longleftrightarrow 1.0$	$19500 \pm 1500 \pm 3600$	$9140 \pm 980 \pm 1710$	$3100 \pm 260 \pm 580$	$443 \pm 65 \pm 83$	$21.7 \pm 7.0 \pm 4.1$
$1.0 \longleftrightarrow 1.5$	$13400 \pm 1100 \pm 2500$	$6330 \pm 610 \pm 1190$	$1610 \pm 180 \pm 300$	$302 \pm 78 \pm 57$	$17.1 \pm 5.3 \pm 3.2$
$1.5 \longleftrightarrow 2.0$	$8900 \pm 1000 \pm 1700$	$4190 \pm 560 \pm 790$	$750 \pm 130 \pm 140$	$105 \pm 60 \pm 20$	$19.3 \pm 6.3 \pm 3.6$
$2.0 \longleftrightarrow 2.5$	$7240 \pm 830 \pm 1360$	$2460 \pm 230 \pm 460$	$485 \pm 99 \pm 91$	$45 \pm 19 \pm 8$	—
$2.5 \longleftrightarrow 3.0$	$2300 \pm 300 \pm 430$	$850 \pm 130 \pm 160$	$151 \pm 49 \pm 28$	$17 \pm 12 \pm 3$	—
$3.0 \longleftrightarrow 4.0$	$318 \pm 61 \pm 60$	$158 \pm 38 \pm 30$	$35 \pm 12 \pm 7$	$7.9 \pm 3.7 \pm 1.5$	$0.47 \pm 0.47 \pm 0.09$
$4.0 \longleftrightarrow 6.0$	$7.1 \pm 3.7 \pm 1.3$	$3.0 \pm 2.1 \pm 0.6$	$0.96 \pm 0.96 \pm 0.18$	$0.60 \pm 0.60 \pm 0.11$	—

Table A.30 Differential cross sections per nucleon $d\sigma/dp_{OUT}$ and $d\sigma/dp_{OUT}dM$ for pBe $\longrightarrow \pi^0\pi^0$ at 800 GeV/c. There are two entries per pair. Additional requirements on the combinations contributing to this distribution are summarized at the beginning of Appendix A.

p_{OUT} (GeV/c)	$d\sigma/dp_{OUT}$ (pb/(GeV/c)) Be	Cu	H
$-6.00 \longleftrightarrow -4.00$	$13 \pm 15 \pm 2$	—	$26 \pm 16 \pm 5$
$-4.00 \longleftrightarrow -2.50$	$990 \pm 110 \pm 180$	$1760 \pm 440 \pm 330$	$760 \pm 190 \pm 140$
$-2.50 \longleftrightarrow -1.50$	$7890 \pm 660 \pm 1480$	$9000 \pm 1100 \pm 1700$	$6500 \pm 820 \pm 1220$
$-1.50 \longleftrightarrow -0.75$	$15500 \pm 1000 \pm 2900$	$13400 \pm 2300 \pm 2500$	$14200 \pm 2100 \pm 2700$
$-0.75 \longleftrightarrow 0.00$	$21200 \pm 1400 \pm 4000$	$18900 \pm 2900 \pm 3500$	$22100 \pm 2100 \pm 4100$
$0.00 \longleftrightarrow 0.75$	$20900 \pm 1300 \pm 3900$	$18800 \pm 3000 \pm 3500$	$22600 \pm 2200 \pm 4200$
$0.75 \longleftrightarrow 1.50$	$15600 \pm 1200 \pm 2900$	$13600 \pm 2300 \pm 2600$	$13000 \pm 2000 \pm 2400$
$1.50 \longleftrightarrow 2.50$	$8060 \pm 660 \pm 1510$	$9000 \pm 1100 \pm 1700$	$6940 \pm 780 \pm 1300$
$2.50 \longleftrightarrow 4.00$	$980 \pm 110 \pm 180$	$1670 \pm 350 \pm 310$	$800 \pm 170 \pm 150$
$4.00 \longleftrightarrow 6.00$	$7.1 \pm 3.7 \pm 1.3$	$11 \pm 11 \pm 2$	—

Table A.31 Differential cross section per nucleon, $d\sigma/dp_{OUT}$, for various targets for $\pi^0\pi^0$ from the 800 GeV/c proton sample. There are two entries per pair. Additional requirements on the combinations contributing to this distribution are summarized at the beginning of Appendix A.

p_{IN} (GeV/c)	$d\sigma/dp_{IN}dM$ $\left(pb/(GeV^2/c^3)\right)$			
	$5.0 < M < 6.5$ GeV/c^2	$6.5 < M < 8.0$ GeV/c^2	$8.0 < M < 10.0$ GeV/c^2	$10.0 < M < 14.0$ GeV/c^2
$-6.00 \longleftrightarrow -4.00$	—	—	$2.19 \pm 0.89 \pm 0.41$	$0.12 \pm 0.18 \pm 0.02$
$-4.00 \longleftrightarrow -2.50$	$100 \pm 16 \pm 19$	$45.0 \pm 8.0 \pm 8.4$	$15.0 \pm 3.8 \pm 2.8$	$0.91 \pm 0.56 \pm 0.17$
$-2.50 \longleftrightarrow -1.50$	$730 \pm 46 \pm 137$	$396 \pm 26 \pm 74$	$80.4 \pm 8.2 \pm 15.1$	$6.5 \pm 1.9 \pm 1.2$
$-1.50 \longleftrightarrow -0.75$	$2430 \pm 110 \pm 460$	$1152 \pm 67 \pm 216$	$139 \pm 13 \pm 26$	$10.9 \pm 2.0 \pm 2.0$
$-0.75 \longleftrightarrow 0.00$	$5650 \pm 150 \pm 1060$	$1800 \pm 76 \pm 338$	$236 \pm 15 \pm 44$	$16.4 \pm 2.6 \pm 3.1$
$0.00 \longleftrightarrow 0.75$	$5550 \pm 140 \pm 1040$	$1920 \pm 71 \pm 360$	$230 \pm 16 \pm 43$	$12.4 \pm 2.2 \pm 2.3$
$0.75 \longleftrightarrow 1.50$	$2460 \pm 86 \pm 461$	$1178 \pm 59 \pm 221$	$156 \pm 13 \pm 29$	$7.6 \pm 2.6 \pm 1.4$
$1.50 \longleftrightarrow 2.50$	$780 \pm 44 \pm 146$	$386 \pm 26 \pm 72$	$71.8 \pm 8.2 \pm 13.5$	$7.4 \pm 1.5 \pm 1.4$
$2.50 \longleftrightarrow 4.00$	$125 \pm 12 \pm 23$	$27.3 \pm 5.9 \pm 5.1$	$20.2 \pm 3.5 \pm 3.8$	$1.20 \pm 0.70 \pm 0.23$
$4.00 \longleftrightarrow 6.00$	$0.93 \pm 0.93 \pm 0.17$	—	$1.5 \pm 1.0 \pm 0.3$	—
$6.00 \longleftrightarrow 8.00$	—	—	$0.29 \pm 0.29 \pm 0.05$	—

Table A.32 Differential cross section per nucleon $d\sigma/dp_{IN}dM$ for $\pi^-\mathrm{Be} \longrightarrow \pi^0\pi^0$ at 515 GeV/c. There are two entries per pair. Additional requirements on the combinations contributing to this distribution are summarized at the beginning of Appendix A.

p_{IN} (GeV/c)	$d\sigma/dp_{IN}$ (pb/(GeV/c)) Be	Cu	H
$-8.00 \longleftrightarrow -6.00$	—	$2.8 \pm 2.8 \pm 0.5$	—
$-6.00 \longleftrightarrow -4.00$	$5.5 \pm 4.5 \pm 1.0$	$4 \pm 11 \pm 1$	—
$-4.00 \longleftrightarrow -2.50$	$305 \pm 31 \pm 57$	$530 \pm 100 \pm 100$	$280 \pm 140 \pm 50$
$-2.50 \longleftrightarrow -1.50$	$2091 \pm 87 \pm 392$	$2140 \pm 260 \pm 400$	$1940 \pm 390 \pm 360$
$-1.50 \longleftrightarrow -0.75$	$5820 \pm 190 \pm 1090$	$7710 \pm 620 \pm 1450$	$5800 \pm 1000 \pm 1100$
$-0.75 \longleftrightarrow 0.00$	$11870 \pm 250 \pm 2230$	$12900 \pm 1100 \pm 2400$	$9500 \pm 1400 \pm 1800$
$0.00 \longleftrightarrow 0.75$	$12010 \pm 240 \pm 2250$	$13720 \pm 820 \pm 2570$	$12400 \pm 1500 \pm 2300$
$0.75 \longleftrightarrow 1.50$	$5980 \pm 160 \pm 1120$	$6830 \pm 590 \pm 1280$	$6830 \pm 930 \pm 1280$
$1.50 \longleftrightarrow 2.50$	$2229 \pm 89 \pm 418$	$2740 \pm 260 \pm 510$	$1880 \pm 430 \pm 350$
$2.50 \longleftrightarrow 4.00$	$357 \pm 28 \pm 67$	$620 \pm 140 \pm 120$	$560 \pm 370 \pm 100$
$4.00 \longleftrightarrow 6.00$	$4.4 \pm 3.5 \pm 0.8$	—	—
$6.00 \longleftrightarrow 8.00$	$0.58 \pm 0.58 \pm 0.11$	—	—

Table A.33 Differential cross section per nucleon, $d\sigma/dp_{IN}$, for various targets for $\pi^0\pi^0$ from the 515 GeV/c π^- sample. There are two entries per pair. Additional requirements on the combinations contributing to this distribution are summarized at the beginning of Appendix A.

p_{IN} (GeV/c)	$d\sigma/dp_{IN}$ (pb/(GeV/c)) Be	Cu	H
$-4.0 \longleftrightarrow -2.0$	$760 \pm 300 \pm 140$	$990 \pm 590 \pm 180$	—
$-2.0 \longleftrightarrow -0.5$	$4600 \pm 1400 \pm 900$	$5600 \pm 2400 \pm 1100$	$900 \pm 1000 \pm 200$
$-0.5 \longleftrightarrow 0.5$	$13200 \pm 2400 \pm 2500$	$16400 \pm 5600 \pm 3100$	$14000 \pm 5600 \pm 2600$
$0.5 \longleftrightarrow 2.0$	$5600 \pm 1300 \pm 1000$	$8000 \pm 3500 \pm 1500$	$6700 \pm 3100 \pm 1300$
$2.0 \longleftrightarrow 4.0$	$720 \pm 290 \pm 140$	$3500 \pm 1700 \pm 700$	$790 \pm 560 \pm 150$
$4.0 \longleftrightarrow 6.0$	—	$1500 \pm 1500 \pm 300$	—

Table A.34 Differential cross section per nucleon, $d\sigma/dp_{IN}$, as a for various targets for $\pi^0\pi^0$ from the 515 GeV/c π^+ sample. There are two entries per pair. Additional requirements on the combinations contributing to this distribution are summarized at the beginning of Appendix A.

p_{IN} (GeV/c)	$d\sigma/dp_{IN}dM$ $\left(pb/(GeV^2/c^3)\right)$			
	$5.0 < M < 6.5$ GeV/c^2	$6.5 < M < 8.0$ GeV/c^2	$8.0 < M < 10.0$ GeV/c^2	$10.0 < M < 14.0$ GeV/c^2
$-8.00 \longleftrightarrow -6.00$	—	—	—	$0.23 \pm 0.23 \pm 0.04$
$-6.00 \longleftrightarrow -4.00$	—	$1.14 \pm 0.66 \pm 0.21$	$2.38 \pm 0.89 \pm 0.45$	$0.43 \pm 0.27 \pm 0.08$
$-4.00 \longleftrightarrow -2.50$	$111 \pm 14 \pm 21$	$35.6 \pm 6.5 \pm 6.7$	$7.4 \pm 2.8 \pm 1.4$	$0.85 \pm 0.41 \pm 0.16$
$-2.50 \longleftrightarrow -1.50$	$704 \pm 47 \pm 132$	$358 \pm 32 \pm 67$	$67.9 \pm 8.0 \pm 12.7$	$2.79 \pm 0.89 \pm 0.52$
$-1.50 \longleftrightarrow -0.75$	$2380 \pm 140 \pm 450$	$1108 \pm 60 \pm 208$	$153 \pm 12 \pm 29$	$7.1 \pm 1.4 \pm 1.3$
$-0.75 \longleftrightarrow 0.00$	$6100 \pm 230 \pm 1140$	$1976 \pm 90 \pm 371$	$179 \pm 15 \pm 34$	$8.9 \pm 1.7 \pm 1.7$
$0.00 \longleftrightarrow 0.75$	$5780 \pm 210 \pm 1080$	$1829 \pm 76 \pm 343$	$206 \pm 15 \pm 39$	$7.7 \pm 1.8 \pm 1.4$
$0.75 \longleftrightarrow 1.50$	$2520 \pm 140 \pm 470$	$1140 \pm 73 \pm 214$	$130 \pm 13 \pm 24$	$6.7 \pm 1.7 \pm 1.2$
$1.50 \longleftrightarrow 2.50$	$664 \pm 47 \pm 124$	$311 \pm 27 \pm 58$	$62.1 \pm 9.1 \pm 11.6$	$3.12 \pm 0.91 \pm 0.58$
$2.50 \longleftrightarrow 4.00$	$92 \pm 17 \pm 17$	$39.1 \pm 9.4 \pm 7.3$	$20.9 \pm 6.2 \pm 3.9$	$1.08 \pm 0.50 \pm 0.20$
$4.00 \longleftrightarrow 6.00$	—	$0.39 \pm 0.58 \pm 0.07$	$0.48 \pm 0.35 \pm 0.09$	—

Table A.35 Differential cross section per nucleon $d\sigma/dp_{IN}dM$ for pBe $\longrightarrow \pi^0\pi^0$ at 530 GeV/c. There are two entries per pair. Additional requirements on the combinations contributing to this distribution are summarized at the beginning of Appendix A.

p_{IN} (GeV/c)	$d\sigma/dp_{IN}$ (pb/(GeV/c)) Be	Cu	H
$-8.00 \longleftrightarrow -6.00$	$0.93 \pm 0.93 \pm 0.17$	—	—
$-6.00 \longleftrightarrow -4.00$	$8.2 \pm 2.3 \pm 1.5$	$2.2 \pm 2.2 \pm 0.4$	$13 \pm 15 \pm 2$
$-4.00 \longleftrightarrow -2.50$	$289 \pm 29 \pm 54$	$620 \pm 310 \pm 120$	$247 \pm 62 \pm 46$
$-2.50 \longleftrightarrow -1.50$	$2080 \pm 100 \pm 390$	$2200 \pm 280 \pm 410$	$1520 \pm 240 \pm 290$
$-1.50 \longleftrightarrow -0.75$	$5790 \pm 240 \pm 1080$	$6090 \pm 600 \pm 1140$	$6400 \pm 500 \pm 1200$
$-0.75 \longleftrightarrow 0.00$	$12720 \pm 370 \pm 2380$	$12420 \pm 970 \pm 2330$	$13240 \pm 760 \pm 2480$
$0.00 \longleftrightarrow 0.75$	$12100 \pm 340 \pm 2270$	$10970 \pm 840 \pm 2060$	$11680 \pm 800 \pm 2190$
$0.75 \longleftrightarrow 1.50$	$5960 \pm 250 \pm 1120$	$5000 \pm 600 \pm 940$	$5820 \pm 540 \pm 1090$
$1.50 \longleftrightarrow 2.50$	$1970 \pm 110 \pm 370$	$1570 \pm 380 \pm 290$	$2330 \pm 290 \pm 440$
$2.50 \longleftrightarrow 4.00$	$293 \pm 36 \pm 55$	$210 \pm 250 \pm 40$	$160 \pm 150 \pm 30$
$4.00 \longleftrightarrow 6.00$	$1.6 \pm 1.1 \pm 0.3$	$23 \pm 14 \pm 4$	—

Table A.36 Differential cross section per nucleon, $d\sigma/dp_{IN}$, for various targets $\pi^0\pi^0$ from the 530 GeV/c proton sample. There are two entries per pair. Additional requirements on the combinations contributing to this distribution are summarized at the beginning of Appendix A.

p_{IN} (GeV/c)	$d\sigma/dp_{IN}dM$ $\left(pb/(GeV^2/c^3)\right)$ $5.0 < M < 6.5$ GeV/c^2	$6.5 < M < 8.0$ GeV/c^2	$8.0 < M < 10.0$ GeV/c^2	$10.0 < M < 14.0$ GeV/c^2
$-6.00 \longleftrightarrow -4.00$	—	$1.5 \pm 1.1 \pm 0.3$	$3.5 \pm 3.0 \pm 0.7$	$0.30 \pm 0.58 \pm 0.06$
$-4.00 \longleftrightarrow -2.50$	$273 \pm 43 \pm 51$	$61 \pm 17 \pm 11$	$54 \pm 14 \pm 10$	$2.5 \pm 1.4 \pm 0.5$
$-2.50 \longleftrightarrow -1.50$	$1740 \pm 260 \pm 330$	$731 \pm 81 \pm 137$	$214 \pm 50 \pm 40$	$15.8 \pm 3.7 \pm 3.0$
$-1.50 \longleftrightarrow -0.75$	$6230 \pm 430 \pm 1170$	$2010 \pm 170 \pm 380$	$295 \pm 53 \pm 55$	$11.2 \pm 4.1 \pm 2.1$
$-0.75 \longleftrightarrow 0.00$	$14100 \pm 1200 \pm 2600$	$3500 \pm 240 \pm 660$	$385 \pm 45 \pm 72$	$20.2 \pm 4.8 \pm 3.8$
$0.00 \longleftrightarrow 0.75$	$13270 \pm 810 \pm 2490$	$3650 \pm 230 \pm 680$	$335 \pm 51 \pm 63$	$25.9 \pm 6.1 \pm 4.9$
$0.75 \longleftrightarrow 1.50$	$4970 \pm 390 \pm 930$	$2110 \pm 160 \pm 400$	$278 \pm 62 \pm 52$	$11.2 \pm 4.6 \pm 2.1$
$1.50 \longleftrightarrow 2.50$	$1690 \pm 150 \pm 320$	$630 \pm 77 \pm 118$	$173 \pm 49 \pm 33$	$6.6 \pm 3.0 \pm 1.2$
$2.50 \longleftrightarrow 4.00$	$246 \pm 43 \pm 46$	$88 \pm 26 \pm 16$	$51 \pm 20 \pm 10$	$2.9 \pm 1.7 \pm 0.5$
$4.00 \longleftrightarrow 6.00$	$4.2 \pm 3.0 \pm 0.8$	$4.7 \pm 9.5 \pm 0.9$	$3.8 \pm 2.9 \pm 0.7$	$0.93 \pm 0.67 \pm 0.18$

Table A.37 Differential cross sections per nucleon $d\sigma/dp_{IN}dM$ for pBe $\longrightarrow$ $\pi^0\pi^0$ at 800 GeV/c. There are two entries per pair. Additional requirements on the combinations contributing to this distribution are summarized at the beginning of Appendix A.

p_{IN} (GeV/c)	$d\sigma/dp_{IN}$ (pb/(GeV/c)) Be	Cu	H
$-6.00 \longleftrightarrow -4.00$	$10.4 \pm 6.6 \pm 1.9$	—	$17 \pm 18 \pm 3$
$-4.00 \longleftrightarrow -2.50$	$890 \pm 110 \pm 170$	$1110 \pm 360 \pm 210$	$630 \pm 150 \pm 120$
$-2.50 \longleftrightarrow -1.50$	$5270 \pm 550 \pm 990$	$6740 \pm 770 \pm 1260$	$4950 \pm 630 \pm 930$
$-1.50 \longleftrightarrow -0.75$	$13280 \pm 710 \pm 2490$	$12000 \pm 1500 \pm 2300$	$10900 \pm 1800 \pm 2000$
$-0.75 \longleftrightarrow 0.00$	$28900 \pm 1900 \pm 5400$	$21700 \pm 3600 \pm 4100$	$29500 \pm 2500 \pm 5500$
$0.00 \longleftrightarrow 0.75$	$27200 \pm 1300 \pm 5100$	$28100 \pm 3000 \pm 5300$	$23600 \pm 2600 \pm 4400$
$0.75 \longleftrightarrow 1.50$	$12100 \pm 750 \pm 2270$	$11000 \pm 2200 \pm 2100$	$14400 \pm 1700 \pm 2700$
$1.50 \longleftrightarrow 2.50$	$4710 \pm 420 \pm 880$	$6210 \pm 990 \pm 1160$	$4080 \pm 560 \pm 760$
$2.50 \longleftrightarrow 4.00$	$890 \pm 110 \pm 170$	$1630 \pm 380 \pm 310$	$550 \pm 140 \pm 100$
$4.00 \longleftrightarrow 6.00$	$25 \pm 16 \pm 5$	$18 \pm 13 \pm 3$	$13 \pm 15 \pm 2$

Table A.38 Differential cross section per nucleon, $d\sigma/dp_{IN}$, for various targets for $\pi^0\pi^0$ from the 800 GeV/c proton sample. There are two entries per pair. Additional requirements on the combinations contributing to this distribution are summarized at the beginning of Appendix A.

z	$d\sigma/dz$ (pb)	$d\sigma/dzdM$ $\left(pb/(GeV/c^2)\right)$			
		$5.0 < M < 6.5$ GeV/c^2	$6.5 < M < 8.0$ GeV/c^2	$8.0 < M < 10.0$ GeV/c^2	$10.0 < M < 14.0$ GeV/c^2
$0.0 \longleftrightarrow 0.3$	$680 \pm 140 \pm 130$	$224 \pm 62 \pm 42$	—	$7.6 \pm 3.8 \pm 1.4$	—
$0.3 \longleftrightarrow 0.6$	$9620 \pm 360 \pm 1800$	$2910 \pm 170 \pm 550$	$1497 \pm 90 \pm 281$	$319 \pm 34 \pm 60$	$15.3 \pm 4.8 \pm 2.9$
$0.6 \longleftrightarrow 0.8$	$33650 \pm 780 \pm 6310$	$13840 \pm 400 \pm 2590$	$6160 \pm 300 \pm 1160$	$808 \pm 59 \pm 151$	$56 \pm 11 \pm 11$
$0.8 \longleftrightarrow 1.0$	$58600 \pm 1100 \pm 11000$	$30470 \pm 690 \pm 5710$	$6880 \pm 250 \pm 1290$	$821 \pm 52 \pm 154$	$58 \pm 10 \pm 11$
$1.0 \longleftrightarrow 1.2$	$33330 \pm 780 \pm 6250$	$15960 \pm 470 \pm 2990$	$5300 \pm 220 \pm 990$	$624 \pm 47 \pm 117$	$46.8 \pm 8.0 \pm 8.8$
$1.2 \longleftrightarrow 1.5$	$9850 \pm 340 \pm 1850$	$2940 \pm 150 \pm 550$	$2980 \pm 170 \pm 560$	$417 \pm 35 \pm 78$	$35.5 \pm 5.4 \pm 6.7$
$1.5 \longleftrightarrow 2.0$	$1719 \pm 98 \pm 322$	$84 \pm 18 \pm 16$	$809 \pm 58 \pm 152$	$169 \pm 18 \pm 32$	$10.0 \pm 3.9 \pm 1.9$
$2.0 \longleftrightarrow 2.5$	$136 \pm 29 \pm 26$	—	$30 \pm 13 \pm 6$	$45 \pm 10 \pm 8$	$0.8 \pm 1.4 \pm 0.2$
$2.5 \longleftrightarrow 4.0$	$4.5 \pm 4.0 \pm 0.8$	—	—	$2.1 \pm 2.0 \pm 0.4$	—

Table A.39 Differential cross section per nucleon $d\sigma/dzdM$ for $\pi^-Be \longrightarrow \pi^0\pi^0$ at 515 GeV/c. There are two entries per pair. Additional requirements on the combinations contributing to this distribution are summarized at the beginning of Appendix A.

z	$d\sigma/dz$ (pb)		
	Be	Cu	H
$0.0 \longleftrightarrow 0.3$	$680 \pm 140 \pm 130$	$1580 \pm 670 \pm 300$	—
$0.3 \longleftrightarrow 0.5$	$6610 \pm 400 \pm 1240$	$10000 \pm 1600 \pm 1900$	$9100 \pm 4300 \pm 1700$
$0.5 \longleftrightarrow 0.6$	$15630 \pm 720 \pm 2930$	$16700 \pm 1800 \pm 3100$	$14000 \pm 3100 \pm 2600$
$0.6 \longleftrightarrow 0.7$	$27100 \pm 970 \pm 5080$	$33600 \pm 3000 \pm 6300$	$29900 \pm 4600 \pm 5600$
$0.7 \longleftrightarrow 0.8$	$40200 \pm 1200 \pm 7500$	$50100 \pm 4300 \pm 9400$	$36000 \pm 6100 \pm 6800$
$0.8 \longleftrightarrow 0.9$	$53400 \pm 1400 \pm 10000$	$69800 \pm 5400 \pm 13100$	$53800 \pm 8200 \pm 10100$
$0.9 \longleftrightarrow 1.0$	$63800 \pm 1700 \pm 12000$	$59300 \pm 5900 \pm 11100$	$64300 \pm 9900 \pm 12100$
$1.0 \longleftrightarrow 1.1$	$42200 \pm 1200 \pm 7900$	$52300 \pm 5400 \pm 9800$	$41200 \pm 6800 \pm 7700$
$1.1 \longleftrightarrow 1.2$	$24410 \pm 930 \pm 4580$	$25100 \pm 3800 \pm 4700$	$22500 \pm 4800 \pm 4200$
$1.2 \longleftrightarrow 1.3$	$15230 \pm 680 \pm 2860$	$19400 \pm 2200 \pm 3600$	$9800 \pm 3300 \pm 1800$
$1.3 \longleftrightarrow 1.5$	$7170 \pm 390 \pm 1340$	$8100 \pm 950 \pm 1520$	$6500 \pm 1500 \pm 1200$
$1.5 \longleftrightarrow 2.0$	$1719 \pm 98 \pm 322$	$1340 \pm 300 \pm 250$	$1210 \pm 460 \pm 230$
$2.0 \longleftrightarrow 2.5$	$136 \pm 29 \pm 26$	$146 \pm 78 \pm 27$	$270 \pm 170 \pm 50$
$2.5 \longleftrightarrow 4.0$	$4.5 \pm 4.0 \pm 0.8$	$15 \pm 13 \pm 3$	—

Table A.40 Differential cross section per nucleon, $d\sigma/dz$, for various targets for $\pi^0\pi^0$ from the 515 GeV/c π^- sample. There are two entries per pair. Additional requirements on the combinations contributing to this distribution are summarized at the beginning of Appendix A.

z	$d\sigma/dz$ (pb)		
	Be	Cu	H
$0.0 \longleftrightarrow 0.3$	$860 \pm 860 \pm 160$	$10000 \pm 10000 \pm 2000$	—
$0.3 \longleftrightarrow 0.6$	$13100 \pm 3300 \pm 2400$	$42000 \pm 15000 \pm 8000$	$3500 \pm 4200 \pm 700$
$0.6 \longleftrightarrow 0.8$	$50000 \pm 11000 \pm 9000$	$57000 \pm 28000 \pm 11000$	$23200 \pm 9600 \pm 4300$
$0.8 \longleftrightarrow 1.0$	$41000 \pm 10000 \pm 8000$	$60000 \pm 21000 \pm 11000$	$58000 \pm 27000 \pm 11000$
$1.0 \longleftrightarrow 1.2$	$30300 \pm 8300 \pm 5700$	$31000 \pm 16000 \pm 6000$	$28000 \pm 23000 \pm 5000$
$1.2 \longleftrightarrow 1.5$	$9700 \pm 4100 \pm 1800$	$6700 \pm 7200 \pm 1200$	$9500 \pm 4800 \pm 1800$
$1.5 \longleftrightarrow 2.0$	$410 \pm 690 \pm 80$	$1200 \pm 2300 \pm 200$	$1400 \pm 1400 \pm 300$
$2.0 \longleftrightarrow 2.5$	—	$1800 \pm 1800 \pm 300$	$1100 \pm 1100 \pm 200$

Table A.41 Differential cross section per nucleon, $d\sigma/dz$, for various targets for $\pi^0\pi^0$ from the 515 GeV/c π^+ sample. There are two entries per pair. Additional requirements on the combinations contributing to this distribution are summarized at the beginning of Appendix A.

z	dσ/dz (pb)	dσ/dzdM (pb/(GeV/c^2))			
		$5.0 < M < 6.5$ GeV/c^2	$6.5 < M < 8.0$ GeV/c^2	$8.0 < M < 10.0$ GeV/c^2	$10.0 < M < 14.0$ GeV/c^2
$0.0 \longleftrightarrow 0.3$	$870 \pm 200 \pm 160$	$162 \pm 44 \pm 30$	$6.4 \pm 6.0 \pm 1.2$	$3.0 \pm 3.0 \pm 0.6$	$1.5 \pm 1.5 \pm 0.3$
$0.3 \longleftrightarrow 0.6$	$8730 \pm 400 \pm 1640$	$2720 \pm 170 \pm 510$	$1330 \pm 110 \pm 250$	$249 \pm 40 \pm 47$	$12.1 \pm 3.8 \pm 2.3$
$0.6 \longleftrightarrow 0.8$	$33700 \pm 1100 \pm 6300$	$13390 \pm 580 \pm 2510$	$6180 \pm 310 \pm 1160$	$658 \pm 53 \pm 123$	$30.8 \pm 5.7 \pm 5.8$
$0.8 \longleftrightarrow 1.0$	$60200 \pm 1600 \pm 11300$	$31900 \pm 1000 \pm 6000$	$6690 \pm 290 \pm 1250$	$833 \pm 51 \pm 156$	$35.6 \pm 7.3 \pm 6.7$
$1.0 \longleftrightarrow 1.2$	$35200 \pm 1100 \pm 6600$	$17210 \pm 690 \pm 3230$	$5370 \pm 250 \pm 1010$	$610 \pm 45 \pm 114$	$29.0 \pm 6.6 \pm 5.4$
$1.2 \longleftrightarrow 1.5$	$9610 \pm 440 \pm 1800$	$2890 \pm 220 \pm 540$	$3040 \pm 190 \pm 570$	$330 \pm 31 \pm 62$	$16.9 \pm 3.6 \pm 3.2$
$1.5 \longleftrightarrow 2.0$	$1450 \pm 110 \pm 270$	$73 \pm 24 \pm 14$	$690 \pm 62 \pm 129$	$137 \pm 23 \pm 26$	$8.1 \pm 2.1 \pm 1.5$
$2.0 \longleftrightarrow 2.5$	$119 \pm 23 \pm 22$	—	$36 \pm 10 \pm 7$	$31.1 \pm 8.4 \pm 5.8$	$0.88 \pm 0.62 \pm 0.16$
$2.5 \longleftrightarrow 4.0$	$1.3 \pm 3.1 \pm 0.2$	—	—	$0.5 \pm 1.3 \pm 0.1$	—

Table A.42 Differential cross section per nucleon dσ/dzdM for pBe $\longrightarrow \pi^0\pi^0$ at 530 GeV/c. There are two entries per pair. Additional requirements on the combinations contributing to this distribution are summarized at the beginning of Appendix A.

z	$d\sigma/dz$ (pb)		
	Be	Cu	H
$0.0 \longleftrightarrow 0.3$	$870 \pm 200 \pm 160$	$2300 \pm 2400 \pm 400$	$570 \pm 250 \pm 110$
$0.3 \longleftrightarrow 0.5$	$5630 \pm 450 \pm 1060$	$5900 \pm 2100 \pm 1100$	$3400 \pm 1700 \pm 600$
$0.5 \longleftrightarrow 0.6$	$14920 \pm 820 \pm 2800$	$17100 \pm 2000 \pm 3200$	$16000 \pm 2900 \pm 3000$
$0.6 \longleftrightarrow 0.7$	$25600 \pm 1100 \pm 4800$	$25400 \pm 3200 \pm 4800$	$25800 \pm 2900 \pm 4800$
$0.7 \longleftrightarrow 0.8$	$41700 \pm 1800 \pm 7800$	$39200 \pm 3500 \pm 7400$	$40600 \pm 3100 \pm 7600$
$0.8 \longleftrightarrow 0.9$	$55400 \pm 2000 \pm 10400$	$52500 \pm 5100 \pm 9800$	$59300 \pm 4500 \pm 11100$
$0.9 \longleftrightarrow 1.0$	$65100 \pm 2600 \pm 12200$	$59500 \pm 6000 \pm 11200$	$67300 \pm 5400 \pm 12600$
$1.0 \longleftrightarrow 1.1$	$44800 \pm 1800 \pm 8400$	$41000 \pm 4300 \pm 7700$	$42800 \pm 4000 \pm 8000$
$1.1 \longleftrightarrow 1.2$	$25700 \pm 1200 \pm 4800$	$26100 \pm 2500 \pm 4900$	$24500 \pm 2500 \pm 4600$
$1.2 \longleftrightarrow 1.3$	$15100 \pm 1100 \pm 2800$	$12200 \pm 1900 \pm 2300$	$15300 \pm 1900 \pm 2900$
$1.3 \longleftrightarrow 1.5$	$6900 \pm 390 \pm 1290$	$6380 \pm 810 \pm 1200$	$7210 \pm 840 \pm 1350$
$1.5 \longleftrightarrow 2.0$	$1450 \pm 110 \pm 270$	$850 \pm 170 \pm 160$	$1670 \pm 310 \pm 310$
$2.0 \longleftrightarrow 2.5$	$119 \pm 23 \pm 22$	$92 \pm 48 \pm 17$	$118 \pm 63 \pm 22$
$2.5 \longleftrightarrow 4.0$	$1.3 \pm 3.1 \pm 0.2$	$6.5 \pm 4.7 \pm 1.2$	—

Table A.43 Differential cross section per nucleon, $d\sigma/dz$, for various targets for $\pi^0\pi^0$ from the 530 GeV/c proton sample. There are two entries per pair. Additional requirements on the combinations contributing to this distribution are summarized at the beginning of Appendix A.

z	$d\sigma/dz$ (pb)	$d\sigma/dzdM$ $\left(pb/(GeV/c^2)\right)$			
		$5.0 < M < 6.5$ GeV/c^2	$6.5 < M < 8.0$ GeV/c^2	$8.0 < M < 10.0$ GeV/c^2	$10.0 < M < 14.0$ GeV/c^2
$0.0 \longleftrightarrow 0.3$	$3170 \pm 830 \pm 590$	$470 \pm 130 \pm 90$	$31 \pm 64 \pm 6$	$12.5 \pm 9.4 \pm 2.3$	—
$0.3 \longleftrightarrow 0.6$	$22500 \pm 1300 \pm 4200$	$6900 \pm 530 \pm 1290$	$2490 \pm 300 \pm 470$	$810 \pm 210 \pm 150$	$44 \pm 13 \pm 8$
$0.6 \longleftrightarrow 0.8$	$75600 \pm 4400 \pm 14200$	$30500 \pm 2100 \pm 5700$	$11160 \pm 750 \pm 2090$	$1410 \pm 170 \pm 260$	$51 \pm 20 \pm 10$
$0.8 \longleftrightarrow 1.0$	$141800 \pm 7300 \pm 26600$	$75700 \pm 4600 \pm 14200$	$13380 \pm 900 \pm 2510$	$1530 \pm 230 \pm 290$	$104 \pm 20 \pm 19$
$1.0 \longleftrightarrow 1.2$	$76800 \pm 5000 \pm 14400$	$40200 \pm 3200 \pm 7500$	$9420 \pm 750 \pm 1770$	$1040 \pm 140 \pm 190$	$95 \pm 18 \pm 18$
$1.2 \longleftrightarrow 1.5$	$18500 \pm 1100 \pm 3500$	$5150 \pm 550 \pm 970$	$5990 \pm 440 \pm 1120$	$810 \pm 87 \pm 152$	$25 \pm 12 \pm 5$
$1.5 \longleftrightarrow 2.0$	$2820 \pm 300 \pm 530$	$183 \pm 37 \pm 34$	$1300 \pm 150 \pm 240$	$252 \pm 94 \pm 47$	$20.8 \pm 7.5 \pm 3.9$
$2.0 \longleftrightarrow 2.5$	$630 \pm 190 \pm 120$	—	$101 \pm 54 \pm 19$	$223 \pm 87 \pm 42$	$7.8 \pm 3.7 \pm 1.5$
$2.5 \longleftrightarrow 4.0$	$11 \pm 11 \pm 2$	—	—	$5.9 \pm 5.4 \pm 1.1$	—

Table A.44 Differential cross section per nucleon $d\sigma/dzdM$ for pBe $\longrightarrow \pi^0\pi^0$ at 800 GeV/c. There are two entries per pair. Additional requirements on the combinations contributing to this distribution are summarized at the beginning of Appendix A.

z	$d\sigma/dz$ (pb)		
	Be	Cu	H
$0.0 \longleftrightarrow 0.3$	$3170 \pm 830 \pm 590$	$4600 \pm 1600 \pm 900$	$500 \pm 470 \pm 90$
$0.3 \longleftrightarrow 0.5$	$16900 \pm 1600 \pm 3200$	$28200 \pm 4200 \pm 5300$	$13300 \pm 2100 \pm 2500$
$0.5 \longleftrightarrow 0.6$	$33700 \pm 2400 \pm 6300$	$36300 \pm 6700 \pm 6800$	$33200 \pm 5100 \pm 6200$
$0.6 \longleftrightarrow 0.7$	$68100 \pm 6000 \pm 12800$	$65200 \pm 8900 \pm 12200$	$64900 \pm 7400 \pm 12200$
$0.7 \longleftrightarrow 0.8$	$83100 \pm 6300 \pm 15600$	$103000 \pm 13000 \pm 19000$	$69300 \pm 7800 \pm 13000$
$0.8 \longleftrightarrow 0.9$	$129200 \pm 7100 \pm 24200$	$120000 \pm 19000 \pm 23000$	$112000 \pm 14000 \pm 21000$
$0.9 \longleftrightarrow 1.0$	$154000 \pm 13000 \pm 29000$	$109000 \pm 26000 \pm 21000$	$163000 \pm 22000 \pm 31000$
$1.0 \longleftrightarrow 1.1$	$94900 \pm 9000 \pm 17800$	$83000 \pm 16000 \pm 16000$	$108000 \pm 14000 \pm 20000$
$1.1 \longleftrightarrow 1.2$	$58800 \pm 4100 \pm 11000$	$50200 \pm 7800 \pm 9400$	$41900 \pm 6400 \pm 7800$
$1.2 \longleftrightarrow 1.3$	$25800 \pm 2600 \pm 4800$	$27100 \pm 5900 \pm 5100$	$27900 \pm 5300 \pm 5200$
$1.3 \longleftrightarrow 1.5$	$14800 \pm 950 \pm 2770$	$17100 \pm 4000 \pm 3200$	$13500 \pm 1900 \pm 2500$
$1.5 \longleftrightarrow 2.0$	$2820 \pm 300 \pm 530$	$3210 \pm 570 \pm 600$	$3780 \pm 710 \pm 710$
$2.0 \longleftrightarrow 2.5$	$630 \pm 190 \pm 120$	$320 \pm 250 \pm 60$	$520 \pm 200 \pm 100$
$2.5 \longleftrightarrow 4.0$	$11 \pm 11 \pm 2$	—	$16 \pm 19 \pm 3$

Table A.45 Differential cross section per nucleon, $d\sigma/dz$, for various targets for $\pi^0\pi^0$ from the 800 GeV/c proton sample. There are two entries per pair. Additional requirements on the combinations contributing to this distribution are summarized at the beginning of Appendix A.

Mass (GeV/c^2)	$\langle Q_T \rangle$ (GeV/c)	$\langle Q_T{}^2 \rangle$ (GeV/c)^2	$\langle \lvert p_{OUT} \rvert \rangle$ (GeV/c)	$\langle \lvert p_{IN} \rvert \rangle$ (GeV/c)	$\langle \Delta\phi \rangle$ (degrees)
$4.0 \longleftrightarrow 4.5$	$3.0 \pm 1.3 \pm 0.8$	$9.0 \pm 4.1 \pm 2.4$	$1.80 \pm 0.73 \pm 0.48$	$2.45 \pm 0.93 \pm 0.65$	$111 \pm 48 \pm 29$
$4.5 \longleftrightarrow 5.0$	$2.42 \pm 0.31 \pm 0.64$	$6.24 \pm 0.86 \pm 1.65$	$1.51 \pm 0.17 \pm 0.40$	$2.11 \pm 0.23 \pm 0.56$	$126 \pm 15 \pm 33$
$5.0 \longleftrightarrow 5.5$	$1.332 \pm 0.084 \pm 0.353$	$2.49 \pm 0.18 \pm 0.66$	$0.846 \pm 0.047 \pm 0.224$	$1.214 \pm 0.065 \pm 0.322$	$152.2 \pm 9.1 \pm 40.4$
$5.5 \longleftrightarrow 6.0$	$1.109 \pm 0.052 \pm 0.294$	$1.77 \pm 0.11 \pm 0.47$	$0.708 \pm 0.029 \pm 0.188$	$0.953 \pm 0.038 \pm 0.253$	$159.8 \pm 6.9 \pm 42.4$
$6.0 \longleftrightarrow 6.5$	$1.165 \pm 0.061 \pm 0.309$	$1.87 \pm 0.12 \pm 0.49$	$0.740 \pm 0.034 \pm 0.196$	$0.890 \pm 0.041 \pm 0.236$	$162.4 \pm 7.7 \pm 43.1$
$6.5 \longleftrightarrow 7.0$	$1.261 \pm 0.080 \pm 0.334$	$2.03 \pm 0.16 \pm 0.54$	$0.802 \pm 0.045 \pm 0.213$	$0.856 \pm 0.048 \pm 0.227$	$164.3 \pm 9.7 \pm 43.6$
$7.0 \longleftrightarrow 7.5$	$1.39 \pm 0.10 \pm 0.37$	$2.42 \pm 0.20 \pm 0.64$	$0.882 \pm 0.059 \pm 0.234$	$0.845 \pm 0.055 \pm 0.224$	$165 \pm 12 \pm 44$
$7.5 \longleftrightarrow 8.5$	$1.51 \pm 0.11 \pm 0.40$	$2.94 \pm 0.26 \pm 0.78$	$0.963 \pm 0.061 \pm 0.255$	$0.810 \pm 0.050 \pm 0.215$	$167 \pm 11 \pm 44$
$8.5 \longleftrightarrow 10.0$	$1.86 \pm 0.18 \pm 0.49$	$4.71 \pm 0.56 \pm 1.25$	$1.19 \pm 0.10 \pm 0.32$	$0.810 \pm 0.067 \pm 0.215$	$169 \pm 15 \pm 45$
$10.0 \longleftrightarrow 12.0$	$1.82 \pm 0.40 \pm 0.48$	$4.5 \pm 1.2 \pm 1.2$	$1.14 \pm 0.22 \pm 0.30$	$0.91 \pm 0.16 \pm 0.24$	$169 \pm 32 \pm 45$
$12.0 \longleftrightarrow 14.0$	$1.81 \pm 0.82 \pm 0.48$	$3.6 \pm 2.5 \pm 0.9$	$1.21 \pm 0.46 \pm 0.32$	$0.71 \pm 0.36 \pm 0.19$	$173 \pm 65 \pm 46$
$14.0 \longleftrightarrow 16.0$	—	—	—	$0.95 \pm 0.88 \pm 0.25$	$170 \pm 190 \pm 50$

Table A.46 Averages of several kinematic quantities as functions of mass for $\pi^-\mathrm{Be} \longrightarrow \pi^0\pi^0$ at 515 GeV/c. Additional requirements on the combinations contributing to this distribution are summarized at the beginning of Appendix A.

Mass (GeV/c^2)	$\langle Q_T \rangle$ (GeV/c)	$\langle Q_T^2 \rangle$ (GeV/c)^2	$\langle \lvert p_{OUT} \rvert \rangle$ (GeV/c)	$\langle \lvert p_{IN} \rvert \rangle$ (GeV/c)	$\langle \Delta\phi \rangle$ (degrees)
4.0 $\longleftrightarrow$ 4.5	3.1 ± 2.3 ± 0.8	9.4 ± 7.3 ± 2.5	1.8 ± 1.3 ± 0.5	2.5 ± 1.6 ± 0.7	109 ± 82 ± 29
4.5 $\longleftrightarrow$ 5.0	2.8 ± 1.2 ± 0.8	8.0 ± 3.4 ± 2.1	1.71 ± 0.66 ± 0.45	2.40 ± 0.87 ± 0.64	117 ± 50 ± 31
5.0 $\longleftrightarrow$ 5.5	1.48 ± 0.28 ± 0.39	2.98 ± 0.60 ± 0.79	0.94 ± 0.17 ± 0.25	1.34 ± 0.23 ± 0.36	150 ± 32 ± 40
5.5 $\longleftrightarrow$ 6.0	1.05 ± 0.16 ± 0.28	1.55 ± 0.27 ± 0.41	0.674 ± 0.090 ± 0.179	0.92 ± 0.12 ± 0.24	161 ± 23 ± 43
6.0 $\longleftrightarrow$ 6.5	1.29 ± 0.16 ± 0.34	2.11 ± 0.30 ± 0.56	0.824 ± 0.093 ± 0.218	1.06 ± 0.11 ± 0.28	159 ± 20 ± 42
6.5 $\longleftrightarrow$ 7.0	1.38 ± 0.30 ± 0.37	2.68 ± 0.79 ± 0.71	0.86 ± 0.16 ± 0.23	0.98 ± 0.18 ± 0.26	161 ± 26 ± 43
7.0 $\longleftrightarrow$ 7.5	1.74 ± 0.35 ± 0.46	3.81 ± 0.94 ± 1.01	1.10 ± 0.20 ± 0.29	1.04 ± 0.19 ± 0.28	162 ± 33 ± 43
7.5 $\longleftrightarrow$ 8.5	1.64 ± 0.28 ± 0.44	3.34 ± 0.70 ± 0.88	1.06 ± 0.15 ± 0.28	0.92 ± 0.14 ± 0.24	165 ± 24 ± 44
8.5 $\longleftrightarrow$ 10.0	1.67 ± 0.54 ± 0.44	3.9 ± 1.6 ± 1.0	1.07 ± 0.30 ± 0.28	0.82 ± 0.23 ± 0.22	169 ± 48 ± 45
10.0 $\longleftrightarrow$ 12.0	2.0 ± 1.1 ± 0.5	5.4 ± 3.5 ± 1.4	1.31 ± 0.62 ± 0.35	0.84 ± 0.37 ± 0.22	170 ± 86 ± 45
12.0 $\longleftrightarrow$ 14.0	1.6 ± 1.7 ± 0.4	3.2 ± 3.8 ± 0.9	0.99 ± 0.97 ± 0.26	0.97 ± 0.90 ± 0.26	170 ± 170 ± 50

Table A.47 Averages of several kinematic quantities as functions of mass for π^-Cu $\longrightarrow$ $\pi^0\pi^0$ at 515 GeV/c. Additional requirements on the combinations contributing to this distribution are summarized at the beginning of Appendix A.

Mass (GeV/c^2)	$\langle Q_T \rangle$ (GeV/c)	$\langle Q_T^2 \rangle$ $(GeV/c)^2$	$\langle \lvert p_{OUT} \rvert \rangle$ (GeV/c)	$\langle \lvert p_{IN} \rvert \rangle$ (GeV/c)	$\langle \Delta\phi \rangle$ (degrees)
$4.0 \longleftrightarrow 4.5$	$2.9 \pm 3.3 \pm 0.8$	$8.4 \pm 9.7 \pm 2.2$	$1.9 \pm 2.0 \pm 0.5$	$2.4 \pm 2.4 \pm 0.6$	$110 \pm 130 \pm 30$
$4.5 \longleftrightarrow 5.0$	$2.6 \pm 1.5 \pm 0.7$	$6.8 \pm 4.0 \pm 1.8$	$1.56 \pm 0.81 \pm 0.41$	$2.3 \pm 1.1 \pm 0.6$	$122 \pm 69 \pm 32$
$5.0 \longleftrightarrow 5.5$	$1.22 \pm 0.35 \pm 0.32$	$1.79 \pm 0.67 \pm 0.48$	$0.78 \pm 0.20 \pm 0.21$	$1.14 \pm 0.27 \pm 0.30$	$154 \pm 40 \pm 41$
$5.5 \longleftrightarrow 6.0$	$1.43 \pm 0.56 \pm 0.38$	$3.0 \pm 1.5 \pm 0.8$	$0.87 \pm 0.30 \pm 0.23$	$1.21 \pm 0.39 \pm 0.32$	$152 \pm 49 \pm 40$
$6.0 \longleftrightarrow 6.5$	$1.19 \pm 0.26 \pm 0.32$	$1.82 \pm 0.43 \pm 0.48$	$0.76 \pm 0.15 \pm 0.20$	$1.00 \pm 0.19 \pm 0.26$	$160 \pm 34 \pm 42$
$6.5 \longleftrightarrow 7.0$	$1.27 \pm 0.50 \pm 0.34$	$1.99 \pm 0.80 \pm 0.53$	$0.83 \pm 0.30 \pm 0.22$	$0.88 \pm 0.32 \pm 0.23$	$164 \pm 69 \pm 43$
$7.0 \longleftrightarrow 7.5$	$1.20 \pm 0.70 \pm 0.32$	$2.0 \pm 1.3 \pm 0.5$	$0.76 \pm 0.39 \pm 0.20$	$0.94 \pm 0.43 \pm 0.25$	$164 \pm 88 \pm 44$
$7.5 \longleftrightarrow 8.5$	$1.84 \pm 0.57 \pm 0.49$	$4.0 \pm 1.4 \pm 1.1$	$1.18 \pm 0.33 \pm 0.31$	$0.92 \pm 0.26 \pm 0.24$	$165 \pm 52 \pm 44$
$8.5 \longleftrightarrow 10.0$	$2.04 \pm 0.97 \pm 0.54$	$5.4 \pm 3.0 \pm 1.4$	$1.29 \pm 0.54 \pm 0.34$	$1.10 \pm 0.43 \pm 0.29$	$165 \pm 72 \pm 44$
$10.0 \longleftrightarrow 12.0$	$2.7 \pm 2.0 \pm 0.7$	$8.4 \pm 6.5 \pm 2.2$	$1.8 \pm 1.2 \pm 0.5$	$0.90 \pm 0.60 \pm 0.24$	$170 \pm 120 \pm 40$
$12.0 \longleftrightarrow 14.0$	$1.5 \pm 3.4 \pm 0.4$	—	$0.6 \pm 1.6 \pm 0.2$	$1.3 \pm 1.8 \pm 0.3$	$170 \pm 310 \pm 40$

Table A.48 Averages of several kinematic quantities as functions of mass for $\pi^- p \longrightarrow \pi^0\pi^0$ at 515 GeV/c. Additional requirements on the combinations contributing to this distribution are summarized at the beginning of Appendix A.

Mass (GeV/c^2)	$\langle Q_T \rangle$ (GeV/c)	$\langle Q_T^2 \rangle$ (GeV/c)^2	$\langle \lvert p_{OUT} \rvert \rangle$ (GeV/c)	$\langle \lvert p_{IN} \rvert \rangle$ (GeV/c)	$\langle \Delta\phi \rangle$ (degrees)
		Beryllium			
$4.0 \longleftrightarrow 5.5$	$2.0 \pm 1.1 \pm 0.5$	$4.9 \pm 2.7 \pm 1.3$	$1.27 \pm 0.63 \pm 0.34$	$1.72 \pm 0.84 \pm 0.46$	$138 \pm 78 \pm 37$
$5.5 \longleftrightarrow 7.0$	$1.31 \pm 0.38 \pm 0.35$	$2.35 \pm 0.80 \pm 0.62$	$0.79 \pm 0.21 \pm 0.21$	$1.09 \pm 0.27 \pm 0.29$	$157 \pm 44 \pm 42$
$7.0 \longleftrightarrow 9.5$	$1.7 \pm 1.2 \pm 0.5$	$3.3 \pm 2.2 \pm 0.9$	$1.03 \pm 0.70 \pm 0.27$	$0.93 \pm 0.59 \pm 0.25$	$170 \pm 130 \pm 40$
$9.5 \longleftrightarrow 12.5$	$1.6 \pm 1.2 \pm 0.4$	$3.1 \pm 2.4 \pm 0.8$	$1.06 \pm 0.69 \pm 0.28$	$0.76 \pm 0.52 \pm 0.20$	$170 \pm 120 \pm 50$
		Copper			
$4.0 \longleftrightarrow 5.5$	$1.8 \pm 1.4 \pm 0.5$	$4.0 \pm 3.2 \pm 1.1$	$1.10 \pm 0.80 \pm 0.29$	$1.6 \pm 1.1 \pm 0.4$	$140 \pm 110 \pm 40$
$5.5 \longleftrightarrow 7.0$	$2.0 \pm 1.2 \pm 0.5$	$6.9 \pm 5.2 \pm 1.8$	$1.29 \pm 0.67 \pm 0.34$	$1.55 \pm 0.77 \pm 0.41$	$146 \pm 66 \pm 39$
$7.0 \longleftrightarrow 9.5$	$4.1 \pm 7.8 \pm 1.1$	$11 \pm 21 \pm 3$	$2.9 \pm 5.2 \pm 0.8$	$1.8 \pm 3.4 \pm 0.5$	$150 \pm 390 \pm 40$
		Hydrogen			
$4.0 \longleftrightarrow 5.5$	$5.3 \pm 4.3 \pm 0.4$	$11.6 \pm 9.4 \pm 0.6$	$3.2 \pm 2.4 \pm 0.2$	$4.7 \pm 3.3 \pm 0.4$	$400 \pm 320 \pm 40$
$5.5 \longleftrightarrow 7.0$	$4.5 \pm 4.0 \pm 0.2$	$15 \pm 15 \pm 0$	$2.9 \pm 2.3 \pm 0.1$	$3.5 \pm 2.8 \pm 0.1$	$330 \pm 250 \pm 50$
$7.0 \longleftrightarrow 9.5$	$1.4 \pm 1.2 \pm 0.4$	$3.6 \pm 3.1 \pm 0.8$	$0.94 \pm 0.67 \pm 0.24$	$0.59 \pm 0.50 \pm 0.12$	$51 \pm 97 \pm 46$

Table A.49 Averages of several kinematic quantities as functions of mass and target for $\pi^0\pi^0$ events from the 515 GeV/c π^+ sample. Additional requirements on the combinations contributing to this distribution are summarized at the beginning of Appendix A.

Mass (GeV/c^2)	$\langle Q_T \rangle$ (GeV/c)	$\langle Q_T{}^2 \rangle$ (GeV/c)^2	$\langle \lvert p_{OUT} \rvert \rangle$ (GeV/c)	$\langle \lvert p_{IN} \rvert \rangle$ (GeV/c)	$\langle \Delta\phi \rangle$ (degrees)
$4.0 \longleftrightarrow 4.5$	$3.1 \pm 1.7 \pm 0.8$	$9.7 \pm 5.4 \pm 2.6$	$1.98 \pm 0.97 \pm 0.53$	$2.5 \pm 1.2 \pm 0.7$	$108 \pm 58 \pm 29$
$4.5 \longleftrightarrow 5.0$	$2.33 \pm 0.41 \pm 0.62$	$5.8 \pm 1.0 \pm 1.5$	$1.49 \pm 0.23 \pm 0.39$	$2.06 \pm 0.31 \pm 0.55$	$128 \pm 23 \pm 34$
$5.0 \longleftrightarrow 5.5$	$1.27 \pm 0.11 \pm 0.34$	$2.28 \pm 0.21 \pm 0.60$	$0.807 \pm 0.062 \pm 0.214$	$1.156 \pm 0.086 \pm 0.306$	$154 \pm 14 \pm 41$
$5.5 \longleftrightarrow 6.0$	$1.061 \pm 0.065 \pm 0.281$	$1.65 \pm 0.12 \pm 0.44$	$0.679 \pm 0.037 \pm 0.180$	$0.905 \pm 0.048 \pm 0.240$	$160.8 \pm 9.4 \pm 42.6$
$6.0 \longleftrightarrow 6.5$	$1.098 \pm 0.072 \pm 0.291$	$1.63 \pm 0.12 \pm 0.43$	$0.694 \pm 0.041 \pm 0.184$	$0.828 \pm 0.048 \pm 0.219$	$164 \pm 11 \pm 43$
$6.5 \longleftrightarrow 7.0$	$1.197 \pm 0.085 \pm 0.317$	$1.86 \pm 0.15 \pm 0.49$	$0.756 \pm 0.048 \pm 0.200$	$0.833 \pm 0.051 \pm 0.221$	$164 \pm 11 \pm 44$
$7.0 \longleftrightarrow 7.5$	$1.35 \pm 0.10 \pm 0.36$	$2.33 \pm 0.21 \pm 0.62$	$0.861 \pm 0.058 \pm 0.228$	$0.797 \pm 0.054 \pm 0.211$	$166 \pm 12 \pm 44$
$7.5 \longleftrightarrow 8.5$	$1.65 \pm 0.15 \pm 0.44$	$3.51 \pm 0.43 \pm 0.93$	$1.051 \pm 0.082 \pm 0.279$	$0.910 \pm 0.075 \pm 0.241$	$166 \pm 12 \pm 44$
$8.5 \longleftrightarrow 10.0$	$1.58 \pm 0.21 \pm 0.42$	$3.56 \pm 0.62 \pm 0.94$	$1.02 \pm 0.11 \pm 0.27$	$0.831 \pm 0.087 \pm 0.220$	$168 \pm 18 \pm 45$
$10.0 \longleftrightarrow 12.0$	$2.04 \pm 0.48 \pm 0.54$	$6.3 \pm 2.5 \pm 1.7$	$1.32 \pm 0.26 \pm 0.35$	$0.91 \pm 0.18 \pm 0.24$	$170 \pm 33 \pm 45$
$12.0 \longleftrightarrow 14.0$	$1.4 \pm 1.3 \pm 0.4$	$2.9 \pm 4.9 \pm 0.8$	$0.89 \pm 0.70 \pm 0.23$	$0.40 \pm 0.38 \pm 0.11$	$180 \pm 120 \pm 50$

Table A.50 Averages of several kinematic quantities as functions of mass for pBe $\longrightarrow \pi^0\pi^0$ at 530 GeV/c. Additional requirements on the combinations contributing to this distribution are summarized at the beginning of Appendix A.

Mass (GeV/c^2)	$\langle Q_T \rangle$ (GeV/c)	$\langle Q_T{}^2 \rangle$ (GeV/c)^2	$\langle \lvert p_{OUT} \rvert \rangle$ (GeV/c)	$\langle \lvert p_{IN} \rvert \rangle$ (GeV/c)	$\langle \Delta\phi \rangle$ (degrees)
$4.0 \longleftrightarrow 4.5$	$3.4 \pm 8.5 \pm 0.9$	$11 \pm 27 \pm 3$	$1.3 \pm 3.7 \pm 0.4$	$2.7 \pm 6.1 \pm 0.7$	$110 \pm 290 \pm 30$
$4.5 \longleftrightarrow 5.0$	$2.1 \pm 2.6 \pm 0.6$	$4.1 \pm 7.6 \pm 1.1$	$1.1 \pm 1.3 \pm 0.3$	$1.9 \pm 1.8 \pm 0.5$	$130 \pm 120 \pm 30$
$5.0 \longleftrightarrow 5.5$	$1.24 \pm 0.25 \pm 0.33$	$2.23 \pm 0.45 \pm 0.59$	$0.78 \pm 0.14 \pm 0.21$	$1.14 \pm 0.20 \pm 0.30$	$154 \pm 32 \pm 41$
$5.5 \longleftrightarrow 6.0$	$1.38 \pm 0.38 \pm 0.37$	$2.8 \pm 1.1 \pm 0.8$	$0.86 \pm 0.20 \pm 0.23$	$1.15 \pm 0.24 \pm 0.31$	$154 \pm 26 \pm 41$
$6.0 \longleftrightarrow 6.5$	$1.12 \pm 0.14 \pm 0.30$	$1.81 \pm 0.28 \pm 0.48$	$0.712 \pm 0.081 \pm 0.189$	$0.855 \pm 0.096 \pm 0.227$	$163 \pm 21 \pm 43$
$6.5 \longleftrightarrow 7.0$	$1.37 \pm 0.22 \pm 0.36$	$2.35 \pm 0.43 \pm 0.62$	$0.86 \pm 0.13 \pm 0.23$	$0.96 \pm 0.14 \pm 0.25$	$163 \pm 26 \pm 43$
$7.0 \longleftrightarrow 7.5$	$1.09 \pm 0.32 \pm 0.29$	$1.51 \pm 0.61 \pm 0.40$	$0.68 \pm 0.17 \pm 0.18$	$0.63 \pm 0.17 \pm 0.17$	$170 \pm 41 \pm 45$
$7.5 \longleftrightarrow 8.5$	$1.46 \pm 0.44 \pm 0.39$	$3.0 \pm 1.0 \pm 0.8$	$0.94 \pm 0.25 \pm 0.25$	$0.90 \pm 0.24 \pm 0.24$	$165 \pm 43 \pm 44$
$8.5 \longleftrightarrow 10.0$	$1.74 \pm 0.42 \pm 0.46$	$4.4 \pm 1.3 \pm 1.2$	$1.12 \pm 0.24 \pm 0.30$	$0.67 \pm 0.14 \pm 0.18$	$171 \pm 37 \pm 45$
$10.0 \longleftrightarrow 12.0$	$2.14 \pm 0.93 \pm 0.57$	$5.7 \pm 2.6 \pm 1.5$	$1.38 \pm 0.53 \pm 0.37$	$1.03 \pm 0.41 \pm 0.27$	$168 \pm 70 \pm 44$
$12.0 \longleftrightarrow 14.0$	$1.3 \pm 1.2 \pm 0.3$	$2.2 \pm 2.0 \pm 0.6$	$0.73 \pm 0.61 \pm 0.19$	$0.67 \pm 0.54 \pm 0.18$	$170 \pm 140 \pm 50$

Table A.51 Averages of several kinematic quantities as functions of mass for pCu $\longrightarrow$ $\pi^0\pi^0$ at 530 GeV/c. Additional requirements on the combinations contributing to this distribution are summarized at the beginning of Appendix A.

Mass (GeV/c^2)	$\langle Q_T \rangle$ (GeV/c)	$\langle Q_T{}^2 \rangle$ (GeV/c)^2	$\langle \lvert p_{OUT} \rvert \rangle$ (GeV/c)	$\langle \lvert p_{IN} \rvert \rangle$ (GeV/c)	$\langle \Delta\phi \rangle$ (degrees)
$4.0 \longleftrightarrow 4.5$	—	—	—	—	—
$4.5 \longleftrightarrow 5.0$	$2.4 \pm 1.2 \pm 0.6$	$6.0 \pm 3.2 \pm 1.6$	$1.50 \pm 0.70 \pm 0.40$	$2.08 \pm 0.91 \pm 0.55$	$127 \pm 61 \pm 34$
$5.0 \longleftrightarrow 5.5$	$1.14 \pm 0.21 \pm 0.30$	$1.87 \pm 0.40 \pm 0.50$	$0.75 \pm 0.12 \pm 0.20$	$1.05 \pm 0.16 \pm 0.28$	$156 \pm 27 \pm 41$
$5.5 \longleftrightarrow 6.0$	$0.98 \pm 0.12 \pm 0.26$	$1.45 \pm 0.21 \pm 0.38$	$0.621 \pm 0.067 \pm 0.165$	$0.825 \pm 0.088 \pm 0.219$	$162 \pm 19 \pm 43$
$6.0 \longleftrightarrow 6.5$	$1.11 \pm 0.19 \pm 0.30$	$1.72 \pm 0.38 \pm 0.46$	$0.71 \pm 0.11 \pm 0.19$	$0.84 \pm 0.13 \pm 0.22$	$163 \pm 26 \pm 43$
$6.5 \longleftrightarrow 7.0$	$1.28 \pm 0.24 \pm 0.34$	$2.00 \pm 0.44 \pm 0.53$	$0.81 \pm 0.13 \pm 0.21$	$0.83 \pm 0.13 \pm 0.22$	$165 \pm 27 \pm 44$
$7.0 \longleftrightarrow 7.5$	$1.30 \pm 0.24 \pm 0.34$	$2.10 \pm 0.42 \pm 0.56$	$0.82 \pm 0.14 \pm 0.22$	$0.82 \pm 0.13 \pm 0.22$	$166 \pm 30 \pm 44$
$7.5 \longleftrightarrow 8.5$	$1.44 \pm 0.33 \pm 0.38$	$2.58 \pm 0.65 \pm 0.68$	$0.90 \pm 0.18 \pm 0.24$	$0.78 \pm 0.15 \pm 0.21$	$168 \pm 36 \pm 44$
$8.5 \longleftrightarrow 10.0$	$1.68 \pm 0.44 \pm 0.44$	$3.4 \pm 1.2 \pm 0.9$	$1.08 \pm 0.24 \pm 0.29$	$0.76 \pm 0.16 \pm 0.20$	$170 \pm 38 \pm 45$
$10.0 \longleftrightarrow 12.0$	$2.7 \pm 1.4 \pm 0.7$	$9.5 \pm 5.2 \pm 2.5$	$1.84 \pm 0.84 \pm 0.49$	$1.06 \pm 0.48 \pm 0.28$	$168 \pm 88 \pm 45$
$12.0 \longleftrightarrow 14.0$	$2.1 \pm 2.2 \pm 0.6$	$5.0 \pm 5.3 \pm 1.3$	$1.4 \pm 1.3 \pm 0.4$	$0.90 \pm 0.80 \pm 0.24$	$170 \pm 170 \pm 50$
$14.0 \longleftrightarrow 16.0$	$0.9 \pm 1.2 \pm 0.2$	$0.8 \pm 1.1 \pm 0.2$	$0.48 \pm 0.65 \pm 0.13$	$0.79 \pm 0.97 \pm 0.21$	$170 \pm 240 \pm 50$

Table A.52 Averages of several kinematic quantities as functions of mass for $pp \longrightarrow \pi^0\pi^0$ at 530 GeV/c. Additional requirements on the combinations contributing to this distribution are summarized at the beginning of Appendix A.

Mass (GeV/c^2)	$\langle Q_T \rangle$ (GeV/c)	$\langle {Q_T}^2 \rangle$ (GeV/c)^2	$\langle \lvert p_{OUT} \rvert \rangle$ (GeV/c)	$\langle \lvert p_{IN} \rvert \rangle$ (GeV/c)	$\langle \Delta\phi \rangle$ (degrees)
$4.0 \longleftrightarrow 4.5$	$3.1 \pm 1.4 \pm 0.8$	$9.6 \pm 4.2 \pm 2.5$	$1.77 \pm 0.73 \pm 0.47$	$2.49 \pm 0.94 \pm 0.66$	$108 \pm 47 \pm 29$
$4.5 \longleftrightarrow 5.0$	$2.27 \pm 0.65 \pm 0.60$	$5.6 \pm 1.6 \pm 1.5$	$1.36 \pm 0.36 \pm 0.36$	$1.99 \pm 0.50 \pm 0.53$	$129 \pm 39 \pm 34$
$5.0 \longleftrightarrow 5.5$	$1.13 \pm 0.18 \pm 0.30$	$2.00 \pm 0.31 \pm 0.53$	$0.71 \pm 0.10 \pm 0.19$	$1.03 \pm 0.15 \pm 0.27$	$156 \pm 28 \pm 41$
$5.5 \longleftrightarrow 6.0$	$1.176 \pm 0.099 \pm 0.312$	$1.92 \pm 0.18 \pm 0.51$	$0.748 \pm 0.057 \pm 0.198$	$1.020 \pm 0.075 \pm 0.270$	$158 \pm 13 \pm 42$
$6.0 \longleftrightarrow 6.5$	$1.18 \pm 0.11 \pm 0.31$	$1.91 \pm 0.19 \pm 0.51$	$0.749 \pm 0.060 \pm 0.199$	$0.908 \pm 0.072 \pm 0.241$	$162 \pm 14 \pm 43$
$6.5 \longleftrightarrow 7.0$	$1.19 \pm 0.11 \pm 0.32$	$1.85 \pm 0.19 \pm 0.49$	$0.755 \pm 0.064 \pm 0.200$	$0.782 \pm 0.068 \pm 0.207$	$166 \pm 16 \pm 44$
$7.0 \longleftrightarrow 7.5$	$1.42 \pm 0.18 \pm 0.38$	$2.61 \pm 0.50 \pm 0.69$	$0.898 \pm 0.099 \pm 0.238$	$0.855 \pm 0.096 \pm 0.227$	$165 \pm 18 \pm 44$
$7.5 \longleftrightarrow 8.5$	$1.58 \pm 0.24 \pm 0.42$	$3.35 \pm 0.60 \pm 0.89$	$1.02 \pm 0.13 \pm 0.27$	$0.84 \pm 0.11 \pm 0.22$	$167 \pm 21 \pm 44$
$8.5 \longleftrightarrow 10.0$	$2.09 \pm 0.45 \pm 0.55$	$5.7 \pm 1.4 \pm 1.5$	$1.37 \pm 0.26 \pm 0.36$	$0.74 \pm 0.12 \pm 0.20$	$170 \pm 32 \pm 45$
$10.0 \longleftrightarrow 12.0$	$1.97 \pm 0.54 \pm 0.52$	$5.3 \pm 1.7 \pm 1.4$	$1.22 \pm 0.30 \pm 0.32$	$0.95 \pm 0.21 \pm 0.25$	$169 \pm 42 \pm 45$
$12.0 \longleftrightarrow 14.0$	$2.7 \pm 1.6 \pm 0.7$	$8.1 \pm 5.3 \pm 2.2$	$1.63 \pm 0.91 \pm 0.43$	$0.97 \pm 0.53 \pm 0.26$	$170 \pm 100 \pm 50$
$14.0 \longleftrightarrow 16.0$	$3.0 \pm 3.1 \pm 0.8$	$9.0 \pm 9.6 \pm 2.4$	$2.0 \pm 1.8 \pm 0.5$	$0.67 \pm 0.60 \pm 0.18$	$170 \pm 180 \pm 50$
$16.0 \longleftrightarrow 18.0$	$1.5 \pm 2.2 \pm 0.4$	$2.3 \pm 3.3 \pm 0.6$	$1.1 \pm 1.3 \pm 0.3$	$0.14 \pm 0.17 \pm 0.04$	$180 \pm 250 \pm 50$

Table A.53 Averages of several kinematic quantities as functions of mass for pBe $\longrightarrow \pi^0\pi^0$ at 800 GeV/c. Additional requirements on the combinations contributing to this distribution are summarized at the beginning of Appendix A.

Mass (GeV/c^2)	$\langle Q_T \rangle$ (GeV/c)	$\langle Q_T^2 \rangle$ $(GeV/c)^2$	$\langle \lvert p_{OUT} \rvert \rangle$ (GeV/c)	$\langle \lvert p_{IN} \rvert \rangle$ (GeV/c)	$\langle \Delta\phi \rangle$ (degrees)
$4.0 \longleftrightarrow 4.5$	$3.1 \pm 2.7 \pm 0.8$	$9.7 \pm 8.3 \pm 2.6$	$1.7 \pm 1.4 \pm 0.4$	$2.5 \pm 1.9 \pm 0.7$	$108 \pm 92 \pm 29$
$4.5 \longleftrightarrow 5.0$	$2.33 \pm 0.89 \pm 0.62$	$6.0 \pm 2.2 \pm 1.6$	$1.45 \pm 0.51 \pm 0.38$	$2.04 \pm 0.70 \pm 0.54$	$128 \pm 55 \pm 34$
$5.0 \longleftrightarrow 5.5$	$1.50 \pm 0.59 \pm 0.40$	$3.3 \pm 1.2 \pm 0.9$	$0.91 \pm 0.34 \pm 0.24$	$1.33 \pm 0.48 \pm 0.35$	$149 \pm 68 \pm 39$
$5.5 \longleftrightarrow 6.0$	$1.12 \pm 0.22 \pm 0.30$	$1.80 \pm 0.53 \pm 0.48$	$0.72 \pm 0.12 \pm 0.19$	$0.97 \pm 0.16 \pm 0.26$	$160 \pm 27 \pm 42$
$6.0 \longleftrightarrow 6.5$	$1.27 \pm 0.32 \pm 0.34$	$2.14 \pm 0.55 \pm 0.57$	$0.79 \pm 0.18 \pm 0.21$	$0.94 \pm 0.21 \pm 0.25$	$162 \pm 42 \pm 43$
$6.5 \longleftrightarrow 7.0$	$1.36 \pm 0.27 \pm 0.36$	$2.40 \pm 0.48 \pm 0.64$	$0.86 \pm 0.15 \pm 0.23$	$0.98 \pm 0.17 \pm 0.26$	$161 \pm 33 \pm 43$
$7.0 \longleftrightarrow 7.5$	$1.87 \pm 0.63 \pm 0.49$	$4.6 \pm 2.0 \pm 1.2$	$1.22 \pm 0.35 \pm 0.32$	$1.23 \pm 0.38 \pm 0.33$	$157 \pm 43 \pm 42$
$7.5 \longleftrightarrow 8.5$	$1.95 \pm 0.68 \pm 0.52$	$4.9 \pm 2.2 \pm 1.3$	$1.26 \pm 0.37 \pm 0.33$	$1.18 \pm 0.38 \pm 0.31$	$160 \pm 42 \pm 42$
$8.5 \longleftrightarrow 10.0$	$1.8 \pm 1.0 \pm 0.5$	$4.7 \pm 3.0 \pm 1.2$	$1.06 \pm 0.55 \pm 0.28$	$0.89 \pm 0.36 \pm 0.24$	$168 \pm 79 \pm 45$
$10.0 \longleftrightarrow 12.0$	$1.6 \pm 1.2 \pm 0.4$	$3.7 \pm 3.4 \pm 1.0$	$0.99 \pm 0.63 \pm 0.26$	$0.85 \pm 0.49 \pm 0.22$	$170 \pm 100 \pm 40$
$12.0 \longleftrightarrow 14.0$	$1.5 \pm 1.5 \pm 0.4$	$3.4 \pm 3.7 \pm 0.9$	$1.05 \pm 0.86 \pm 0.28$	$0.43 \pm 0.32 \pm 0.12$	$180 \pm 150 \pm 50$

Table A.54 Averages of several kinematic quantities as functions of mass for pCu $\longrightarrow$ $\pi^0\pi^0$ at 800 GeV/c. Additional requirements on the combinations contributing to this distribution are summarized at the beginning of Appendix A.

Mass (GeV/c^2)	$\langle Q_T \rangle$ (GeV/c)	$\langle Q_T^2 \rangle$ (GeV/c)^2	$\langle \lvert p_{OUT} \rvert \rangle$ (GeV/c)	$\langle \lvert p_{IN} \rvert \rangle$ (GeV/c)	$\langle \Delta\phi \rangle$ (degrees)
$4.0 \longleftrightarrow 4.5$	$3.0 \pm 4.3 \pm 0.8$	$9 \pm 13 \pm 2$	$2.1 \pm 2.6 \pm 0.6$	$2.5 \pm 3.0 \pm 0.7$	$110 \pm 150 \pm 30$
$4.5 \longleftrightarrow 5.0$	$2.47 \pm 0.82 \pm 0.66$	$6.3 \pm 2.1 \pm 1.7$	$1.57 \pm 0.46 \pm 0.42$	$2.16 \pm 0.61 \pm 0.57$	$125 \pm 40 \pm 33$
$5.0 \longleftrightarrow 5.5$	$1.00 \pm 0.33 \pm 0.27$	$1.54 \pm 0.50 \pm 0.41$	$0.66 \pm 0.19 \pm 0.18$	$0.93 \pm 0.26 \pm 0.25$	$159 \pm 49 \pm 42$
$5.5 \longleftrightarrow 6.0$	$1.14 \pm 0.19 \pm 0.30$	$1.92 \pm 0.35 \pm 0.51$	$0.72 \pm 0.11 \pm 0.19$	$0.98 \pm 0.14 \pm 0.26$	$159 \pm 26 \pm 42$
$6.0 \longleftrightarrow 6.5$	$1.14 \pm 0.19 \pm 0.30$	$1.74 \pm 0.32 \pm 0.46$	$0.72 \pm 0.11 \pm 0.19$	$0.90 \pm 0.13 \pm 0.24$	$162 \pm 27 \pm 43$
$6.5 \longleftrightarrow 7.0$	$1.13 \pm 0.32 \pm 0.30$	$1.78 \pm 0.51 \pm 0.47$	$0.72 \pm 0.19 \pm 0.19$	$0.82 \pm 0.22 \pm 0.22$	$164 \pm 53 \pm 44$
$7.0 \longleftrightarrow 7.5$	$1.34 \pm 0.28 \pm 0.36$	$2.23 \pm 0.54 \pm 0.59$	$0.83 \pm 0.16 \pm 0.22$	$0.82 \pm 0.15 \pm 0.22$	$166 \pm 33 \pm 44$
$7.5 \longleftrightarrow 8.5$	$1.74 \pm 0.37 \pm 0.46$	$3.99 \pm 0.91 \pm 1.06$	$1.12 \pm 0.21 \pm 0.30$	$0.79 \pm 0.16 \pm 0.21$	$168 \pm 35 \pm 45$
$8.5 \longleftrightarrow 10.0$	$2.21 \pm 0.97 \pm 0.59$	$6.2 \pm 3.0 \pm 1.6$	$1.35 \pm 0.53 \pm 0.36$	$0.94 \pm 0.39 \pm 0.25$	$167 \pm 64 \pm 44$
$10.0 \longleftrightarrow 12.0$	$2.9 \pm 2.6 \pm 0.8$	$11 \pm 10 \pm 3$	$1.8 \pm 1.5 \pm 0.5$	$1.6 \pm 1.2 \pm 0.4$	$160 \pm 150 \pm 40$
$12.0 \longleftrightarrow 14.0$	—	—	—	—	—

Table A.55 Averages of several kinematic quantities as functions of mass for pp $\longrightarrow$ $\pi^0\pi^0$ at 800 GeV/c. Additional requirements on the combinations contributing to this distribution are summarized at the beginning of Appendix A.

Appendix B Tabulated Cross Sections: $\eta\pi^0$

This appendix contains the tabulated cross sections for the data described in Chapter 9 along with additional, supporting, information. For these data, there is a minimum p_T requirement on each meson of 2.5 GeV/c. Mesons were also required to be central, with rapidities of $-0.8 < y < 0.8$ for the 0.5 TeV/c beams and $-1.05 < y < 0.55$ for the 0.8 TeV/c beam. The azimuthal angle between the η and π^0 was required to be at least 105°.

Cross sections are presented as $A \pm B \pm C$ where A represents the measured value, B is the statistical uncertainty on A, and C is the systematic uncertainty on the measurement calculated with the information presented in Section 7.7.

Mass (GeV/c^2)	$d\sigma/dM$ (pb/(GeV/c^2)) $\pi^0\pi^0$	$\eta\pi^0$
π^-Be at 515 GeV/c		
$4.0 \longleftrightarrow 5.5$	$2453 \pm 92 \pm 460$	$2630 \pm 680 \pm 490$
$5.5 \longleftrightarrow 7.0$	$6330 \pm 130 \pm 1190$	$5900 \pm 880 \pm 1110$
$7.0 \longleftrightarrow 9.5$	$1072 \pm 34 \pm 201$	$930 \pm 230 \pm 170$
$9.5 \longleftrightarrow 12.5$	$60.4 \pm 5.4 \pm 11.3$	$83 \pm 28 \pm 15$
$12.5 \longleftrightarrow 16.0$	$2.87 \pm 0.90 \pm 0.54$	—
pBe at 530 GeV/c		
$4.0 \longleftrightarrow 5.5$	$2760 \pm 150 \pm 520$	—
$5.5 \longleftrightarrow 7.0$	$6320 \pm 160 \pm 1180$	$5700 \pm 1300 \pm 1100$
$7.0 \longleftrightarrow 9.5$	$972 \pm 33 \pm 182$	$1440 \pm 510 \pm 270$
$9.5 \longleftrightarrow 12.5$	$43.2 \pm 4.1 \pm 8.1$	$53 \pm 20 \pm 10$
$12.5 \longleftrightarrow 16.0$	$0.65 \pm 0.52 \pm 0.12$	$3.1 \pm 2.0 \pm 0.6$
pBe at 800 GeV/c		
$4.0 \longleftrightarrow 5.5$	$7940 \pm 820 \pm 1490$	—
$5.5 \longleftrightarrow 7.0$	$13360 \pm 490 \pm 2500$	$14000 \pm 5300 \pm 2600$
$7.0 \longleftrightarrow 9.5$	$1840 \pm 100 \pm 350$	$1810 \pm 790 \pm 340$
$9.5 \longleftrightarrow 12.5$	$110 \pm 14 \pm 21$	$150 \pm 120 \pm 30$
$12.5 \longleftrightarrow 16.0$	$7.9 \pm 3.3 \pm 1.5$	$12.6 \pm 5.9 \pm 2.4$

Table B.1 Differential cross section per nucleon, $d\sigma/dM$, for $\pi^0\pi^0$ and $\eta\pi^0$ events. Additional requirements on the combinations contributing to this distribution are summarized at the beginning of Appendix B.

Rapidity	$d\sigma/dY$ (pb)
π^-Be at 515 GeV/c	
$-0.8 \longleftrightarrow -0.5$	$3100 \pm 2600 \pm 600$
$-0.5 \longleftrightarrow -0.2$	$9800 \pm 3500 \pm 1800$
$-0.2 \longleftrightarrow 0.0$	$25900 \pm 5100 \pm 4800$
$0.0 \longleftrightarrow 0.2$	$26000 \pm 5700 \pm 4900$
$0.2 \longleftrightarrow 0.5$	$20400 \pm 4200 \pm 3800$
$0.5 \longleftrightarrow 0.8$	$4500 \pm 2400 \pm 800$
pBe at 530 GeV/c	
$-0.5 \longleftrightarrow -0.2$	$9000 \pm 7800 \pm 1700$
$-0.2 \longleftrightarrow 0.0$	$21000 \pm 10000 \pm 4000$
$0.0 \longleftrightarrow 0.2$	$28000 \pm 11000 \pm 5000$
$0.2 \longleftrightarrow 0.5$	$19200 \pm 3500 \pm 3600$
$0.5 \longleftrightarrow 0.8$	$2600 \pm 2500 \pm 500$
pBe at 800 GeV/c	
$-0.65 \longleftrightarrow -0.35$	$15000 \pm 31000 \pm 3000$
$-0.35 \longleftrightarrow -0.05$	$78000 \pm 21000 \pm 15000$
$-0.05 \longleftrightarrow 0.25$	$60000 \pm 11000 \pm 11000$
$0.25 \longleftrightarrow 0.55$	$8400 \pm 9100 \pm 1600$

Table B.2 Differential cross section per nucleon, $d\sigma/dY$, for $\eta\pi^0$ events. Additional requirements on the combinations contributing to this distribution are summarized at the beginning of Appendix B.

Q_T (GeV/c)	$d\sigma/dQ_T$ (pb/(GeV/c))		
	π^-Be at 515 GeV/c	pBe at 530 GeV/c	pBe at 800 GeV/c
$0 \longleftrightarrow 1$	$6200 \pm 1200 \pm 1200$	$3500 \pm 2100 \pm 700$	$10400 \pm 8900 \pm 2000$
$1 \longleftrightarrow 2$	$4900 \pm 1100 \pm 900$	$4200 \pm 1800 \pm 800$	$10400 \pm 5200 \pm 2000$
$2 \longleftrightarrow 3$	$2830 \pm 550 \pm 530$	$3100 \pm 1400 \pm 600$	$3500 \pm 3900 \pm 700$
$3 \longleftrightarrow 5$	$710 \pm 270 \pm 130$	$950 \pm 620 \pm 180$	$1300 \pm 1400 \pm 200$
$5 \longleftrightarrow 9$	—	$12.5 \pm 5.0 \pm 2.3$	$37 \pm 24 \pm 7$

Table B.3 Differential cross section per nucleon, $d\sigma/dQ_T$, for $\eta\pi^0$ events. Additional requirements on the combinations contributing to this distribution are summarized at the beginning of Appendix B.

$\Delta\phi$ (degrees)	$d\sigma/d\Delta\phi$ (pb/degree)		
	π^-Be at 515 GeV/c	pBe at 530 GeV/c	pBe at 800 GeV/c
$105 \longleftrightarrow 125$	$71 \pm 28 \pm 13$	$140 \pm 78 \pm 26$	$80 \pm 160 \pm 10$
$125 \longleftrightarrow 145$	$113 \pm 26 \pm 21$	$125 \pm 65 \pm 23$	$180 \pm 200 \pm 30$
$145 \longleftrightarrow 165$	$212 \pm 54 \pm 40$	$207 \pm 86 \pm 39$	$580 \pm 350 \pm 110$
$165 \longleftrightarrow 180$	$496 \pm 78 \pm 93$	$220 \pm 130 \pm 40$	$690 \pm 490 \pm 130$

Table B.4 Differential cross section per nucleon, $d\sigma/d\Delta\phi$, for $\eta\pi^0$ events. Additional requirements on the combinations contributing to this distribution are summarized at the beginning of Appendix B.

p_{OUT} (GeV/c)	$d\sigma/dp_{OUT}$ (pb/(GeV/c))		
	π^-Be at 515 GeV/c	pBe at 530 GeV/c	pBe at 800 GeV/c
$-5.00 \longleftrightarrow -3.00$	$86 \pm 74 \pm 16$	$520 \pm 560 \pm 100$	$180 \pm 280 \pm 30$
$-3.00 \longleftrightarrow -1.25$	$2890 \pm 560 \pm 540$	$2000 \pm 1100 \pm 400$	$4400 \pm 3400 \pm 800$
$-1.25 \longleftrightarrow 0.00$	$8100 \pm 1200 \pm 1500$	$6500 \pm 1900 \pm 1200$	$15200 \pm 7700 \pm 2800$
$0.00 \longleftrightarrow 1.25$	$7900 \pm 1200 \pm 1500$	$5700 \pm 1900 \pm 1100$	$15000 \pm 7700 \pm 2800$
$1.25 \longleftrightarrow 3.00$	$2950 \pm 550 \pm 550$	$3200 \pm 1300 \pm 600$	$4800 \pm 3400 \pm 900$
$3.00 \longleftrightarrow 5.00$	$160 \pm 100 \pm 30$	—	—

Table B.5 Differential cross section per nucleon, $d\sigma/dp_{OUT}$, for $\eta\pi^0$ events. There are two entries per pair. Additional requirements on the combinations contributing to this distribution are summarized at the beginning of Appendix B.

Appendix C Tabulated Cross Sections: $\gamma\pi^0$

This appendix contains the tabulated cross sections for the data described in Chapter 10 along with additional, supporting, information. Unless otherwise noted, there is a minimum p_T requirement on each π^0 of 2.5 GeV/c and on each photon of 4.0 GeV/c. Particles were required to be central, with rapidities of $-0.8 < y < 0.8$. The azimuthal angle between the photon and the π^0 was required to be at least 105°.

Cross sections are presented as $A \pm B \pm C$ where A represents the measured value, B is the statistical uncertainty on A, and C is the systematic uncertainty on the measurement calculated with the information presented in Section 7.7.

Mass	$d\sigma/dM$ $\left(pb/(GeV/c^2)\right)$		
(GeV/c^2)	$p_T{}^\gamma > 4.0$ GeV/c	$p_T{}^\gamma > 4.5$ GeV/c	$p_T{}^\gamma > 5.0$ GeV/c
$5.50 \longleftrightarrow 7.00$	$42 \pm 11 \pm 8$	—	—
$7.00 \longleftrightarrow 8.00$	$87 \pm 21 \pm 20$	$57 \pm 15 \pm 11$	$24.8 \pm 7.5 \pm 4.6$
$8.00 \longleftrightarrow 9.00$	$91 \pm 14 \pm 18$	$56 \pm 11 \pm 11$	$38.8 \pm 8.3 \pm 7.2$
$9.00 \longleftrightarrow 10.50$	$26.3 \pm 7.0 \pm 5.7$	$21.2 \pm 6.3 \pm 4.4$	$13.8 \pm 5.2 \pm 2.7$
$10.50 \longleftrightarrow 12.00$	$8.9 \pm 3.5 \pm 1.9$	$8.2 \pm 3.3 \pm 1.7$	$9.2 \pm 3.1 \pm 1.8$
$12.00 \longleftrightarrow 15.00$	$0.7 \pm 1.3 \pm 0.2$	$0.4 \pm 1.2 \pm 0.2$	$0.4 \pm 1.2 \pm 0.1$

Table C.1 Differential cross section per nucleon, $d\sigma/dM$, for several minimum $p_T{}^\gamma$ requirements for $\gamma\pi^0$ events produced in π^-Be interactions at 515 GeV/c. Additional requirements on the combinations contributing to this distribution are summarized at the beginning of Appendix C.

Mass	$d\sigma/dM$ $\left(pb/(GeV/c^2)\right)$	
(GeV/c^2)	Be	Cu
$6.0 \longleftrightarrow 7.5$	$73 \pm 15 \pm 15$	$75 \pm 35 \pm 16$
$7.5 \longleftrightarrow 9.0$	$88 \pm 13 \pm 18$	$103 \pm 41 \pm 21$
$9.0 \longleftrightarrow 10.5$	$26.3 \pm 7.0 \pm 5.7$	$33 \pm 18 \pm 7$
$10.5 \longleftrightarrow 12.0$	$8.9 \pm 3.5 \pm 1.9$	—
$12.0 \longleftrightarrow 15.0$	$0.7 \pm 1.3 \pm 0.2$	—

Table C.2 Differential cross section per nucleon, $d\sigma/dM$, for several targets for $\gamma\pi^0$ from the 515 GeV/c π^- sample. Additional requirements on the combinations contributing to this distribution are summarized at the beginning of Appendix C.

p_T^{γ} (GeV/c)	$d\sigma/dp_T^{\gamma}$ (pb/(GeV/c)) $p_T^{\gamma} > 4.0$ GeV/c	$p_T^{\gamma} > 4.5$ GeV/c
$4.0 \longleftrightarrow 4.5$	$275 \pm 47 \pm 61$	—
$4.5 \longleftrightarrow 5.0$	$126 \pm 34 \pm 27$	$133 \pm 33 \pm 28$
$5.0 \longleftrightarrow 6.0$	$50 \pm 12 \pm 10$	$53 \pm 12 \pm 11$
$6.0 \longleftrightarrow 7.0$	$25.8 \pm 7.0 \pm 4.8$	$25.0 \pm 7.0 \pm 4.7$
$7.0 \longleftrightarrow 8.0$	$7.1 \pm 4.1 \pm 1.3$	$6.4 \pm 4.1 \pm 1.2$
$8.0 \longleftrightarrow 10.0$	$2.6 \pm 3.5 \pm 0.5$	$2.6 \pm 3.6 \pm 0.5$
$10.0 \longleftrightarrow 14.0$	$0.39 \pm 0.42 \pm 0.07$	$0.29 \pm 0.32 \pm 0.05$

Table C.3 Differential cross section per nucleon, $d\sigma/dp_T^{\gamma}$, for π^-Be $\longrightarrow \gamma\pi^0$ at 515 GeV/c. These direct photons are opposite π^0's with $p_T^{\pi^0} > 2.5$ GeV/c. Additional requirements on the combinations contributing to this distribution are summarized at the beginning of Appendix C.

$p_T^{\pi^0}$ (GeV/c)	$d\sigma/dp_T^{\pi^0}$ (pb/(GeV/c)) $p_T^{\gamma} > 4.0$ GeV/c	$p_T^{\gamma} > 4.5$ GeV/c
$2.5 \longleftrightarrow 3.0$	$308 \pm 53 \pm 61$	$147 \pm 36 \pm 28$
$3.0 \longleftrightarrow 3.5$	$202 \pm 26 \pm 39$	$120 \pm 18 \pm 23$
$3.5 \longleftrightarrow 4.5$	$62 \pm 11 \pm 13$	$31.0 \pm 8.5 \pm 6.4$
$4.5 \longleftrightarrow 6.0$	$8.7 \pm 4.2 \pm 2.5$	$5.7 \pm 3.1 \pm 1.4$

Table C.4 Differential cross section per nucleon, $d\sigma/dp_T^{\pi^0}$, for π^-Be $\longrightarrow \gamma\pi^0$ at 515 GeV/c. These π^0's are opposite direct photons with $p_T^{\gamma} > 4.0$ GeV/c and $p_T^{\gamma} > 4.5$ GeV/c. Additional requirements on the combinations contributing to this distribution are summarized at the beginning of Appendix C.

Rapidity	$d\sigma/dYdM$ (pb/(GeV/c^2))		
	$6.0 < M < 8.0$ GeV/c^2	$8.0 < M < 9.5$ GeV/c^2	$9.5 < M < 15.0$ GeV/c^2
$-0.8 \longleftrightarrow -0.5$	$6.9 \pm 9.5 \pm 1.3$	$7.5 \pm 5.3 \pm 1.4$	$1.8 \pm 4.0 \pm 0.3$
$-0.5 \longleftrightarrow -0.2$	$63 \pm 14 \pm 12$	$68 \pm 12 \pm 13$	$5.5 \pm 1.8 \pm 1.0$
$-0.2 \longleftrightarrow 0.0$	$130 \pm 32 \pm 24$	$112 \pm 21 \pm 21$	$10.9 \pm 4.3 \pm 2.1$
$0.0 \longleftrightarrow 0.2$	$185 \pm 31 \pm 34$	$207 \pm 32 \pm 38$	$20.5 \pm 4.9 \pm 3.8$
$0.2 \longleftrightarrow 0.5$	$165 \pm 24 \pm 31$	$112 \pm 19 \pm 21$	$9.5 \pm 2.7 \pm 1.8$
$0.5 \longleftrightarrow 0.8$	$47 \pm 12 \pm 9$	$36.7 \pm 8.3 \pm 6.8$	$1.7 \pm 1.6 \pm 0.3$

Table C.5 Differential cross section per nucleon, $d\sigma/dYdM$, for π^-Be $\longrightarrow \gamma\pi^0$ at 515 GeV/c. Additional requirements on the combinations contributing to this distribution are summarized at the beginning of Appendix C.

$\lvert\cos\theta^\star\rvert$	$d\sigma/d\lvert\cos\theta^\star\rvert$ (pb)
$0.0 \longleftrightarrow 0.1$	$188 \pm 69 \pm 37$
$0.1 \longleftrightarrow 0.2$	$160 \pm 62 \pm 35$
$0.2 \longleftrightarrow 0.3$	$147 \pm 68 \pm 33$
$0.3 \longleftrightarrow 0.4$	$294 \pm 84 \pm 58$
$0.4 \longleftrightarrow 0.5$	$185 \pm 87 \pm 43$

Table C.6 Differential cross section per nucleon, $d\sigma/d\lvert\cos\theta^\star\rvert$ for π^-Be $\longrightarrow \gamma\pi^0$ at 515 GeV/c. To avoid rapidity biases, we require $\lvert\eta_{\rm boost}\rvert < 0.25$. To avoid biases due to the p_T requirements, there is a minimum mass requirement of 7.5 GeV/c. Additional requirements on the combinations contributing to this distribution are summarized at the beginning of Appendix C.

$\Delta\phi$ (degrees)	$d\sigma/d\Delta\phi$ (pb/degree)
$105 \longleftrightarrow 120$	$0.44 \pm 0.34 \pm 0.08$
$120 \longleftrightarrow 135$	$1.03 \pm 0.37 \pm 0.19$
$135 \longleftrightarrow 150$	$3.20 \pm 0.68 \pm 0.60$
$150 \longleftrightarrow 165$	$5.8 \pm 1.3 \pm 1.2$
$165 \longleftrightarrow 180$	$8.1 \pm 1.6 \pm 2.0$

Table C.7 Differential cross section per nucleon, $d\sigma/d\Delta\phi$, for $\pi^-\mathrm{Be} \longrightarrow \gamma\pi^0$ at 515 GeV/c. Additional requirements on the combinations contributing to this distribution are summarized at the beginning of Appendix C.

p_{OUT} (GeV/c)	$d\sigma/dp_{OUT}$ (pb/(GeV/c))
$-8.0 \longleftrightarrow -5.0$	$0.97 \pm 0.85 \pm 0.18$
$-5.0 \longleftrightarrow -3.5$	$10.7 \pm 3.5 \pm 2.0$
$-3.5 \longleftrightarrow -2.0$	$38.2 \pm 7.0 \pm 7.1$
$-2.0 \longleftrightarrow -1.0$	$90 \pm 17 \pm 18$
$-1.0 \longleftrightarrow 0.0$	$137 \pm 25 \pm 32$
$0.0 \longleftrightarrow 1.0$	$129 \pm 25 \pm 32$
$1.0 \longleftrightarrow 2.0$	$90 \pm 17 \pm 18$
$2.0 \longleftrightarrow 3.5$	$46.7 \pm 8.2 \pm 8.6$
$3.5 \longleftrightarrow 5.0$	$2.7 \pm 2.9 \pm 0.5$
$5.0 \longleftrightarrow 8.0$	$0.90 \pm 0.46 \pm 0.16$

Table C.8 Differential cross section per nucleon, $d\sigma/dp_{OUT}$, for $\pi^-\mathrm{Be} \longrightarrow \gamma\pi^0$ at 515 GeV/c. There are two entries per pair. Additional requirements on the combinations contributing to this distribution are summarized at the beginning of Appendix C.

Q_T (GeV/c)	$d\sigma/dQ_T$ (pb/(GeV/c))
$0.00 \longleftrightarrow 0.75$	$22.0 \pm 8.4 \pm 5.5$
$0.75 \longleftrightarrow 1.50$	$47 \pm 17 \pm 15$
$1.50 \longleftrightarrow 2.25$	$163 \pm 28 \pm 33$
$2.25 \longleftrightarrow 3.00$	$127 \pm 21 \pm 24$
$3.00 \longleftrightarrow 4.00$	$51.6 \pm 9.7 \pm 9.5$
$4.00 \longleftrightarrow 6.00$	$12.1 \pm 3.6 \pm 2.2$

Table C.9 Differential cross section per nucleon, $d\sigma/dQ_T$, for $\pi^-\mathrm{Be} \longrightarrow \gamma\pi^0$ at 515 GeV/c. Additional requirements on the combinations contributing to this distribution are summarized at the beginning of Appendix C.